ISSN 2312-4334

MINISTRY OF EDUCATION AND SCIENCE OF UKRAINE

East European Journal of Physics

No 4. 2021

2021

East European Journal of Physics

EEJP is an international peer-reviewed journal devoted to experimental and theoretical research on the nuclear physics, cosmic rays and particles, high-energy physics, solid state physics, plasma physics, physics of charged particle beams, plasma electronics, radiation materials science, physics of thin films, condensed matter physics, functional materials and coatings, medical physics and physical technologies in an interdisciplinary context.
Published quarterly in hard copy and online by V.N. Karazin Kharkiv National University Publishing.
ISSN 2312-4334 (Print), ISSN 2312-4539 (Online)

The editorial policy is to maintain the quality of published papers at the highest level by strict peer review.
Approved for publication by the Academic Council of the V.N. Karazin Kharkiv National University (November 29, 2021; Protocol No.12).
EEJP registered by the order of Ministry of Education and Science of Ukraine No. 1643 of 28.12.2019, and included in the list of scientific professional editions of Ukraine (category "A", specialty: 104, 105), in which can be published results of dissertations for obtaining Ph.D. and Dr. Sci. degrees in physical and mathematical sciences.
The Journal is a part of the Web of Science Core Collection (ESCI) scientometric platform and indexed by SCOPUS.

Editorial office
Department of Physics and Technologies, V.N. Karazin Kharkiv National University
Kurchatov av., 31, office 402, Kharkiv, 61108, Ukraine
Tel: +38-057-335-18-33,
E-mail: eejp@karazin.ua,
Web-pages: http://periodicals.karazin.ua/eejp (Open Journal System)
Certificate of State registration No.20644-10464P, 21.02.2014

East European Journal of Physics

No 4. 2021

REVIEWS

Recent Advances in Modeling of Perovskite Solar Cells Using SCAPs-1D: Effect of Absorber and ETM Thickness **5**
Eli Danladi, Douglas Saviour Dogo, Samuel Michael Udeh, Felix Omachoko Uloko, Abdul Azeez Omeiza Salavu

Останні досягнення в моделюванні перовскітних сонячних елементів з використанням SCAP-1D: вплив поглинача та товщини ETM
Е. Данладі, Д.С. Дого, С.М. Уде, Ф.О. Улоко, А.А.О. Салаву

Comparison of Anatase and Rutile for Photocatalytic Application: the Short Review **19**
Volodymyr Morgunov, Serhii Lytovchenko, Volodymyr Chyshkala, Dmytro Riabchykov, Dementii Matviienko

Порівняння властивостей анатаза і рутила для фотокаталитичного використання: короткий огляд
В.В. Моргунов, С.В. Літовченко, В.О. Чішкала, Д.Л. Рябчиков, Д.С. Матвієнко

ORIGINAL ARTICLES

The Effect of Hydrostatic Pressure and Cationic Vacancy on the Electronic and Magnetic Properties of the ZnSe:T Crystals (T = Ti, V, Cr, Mn, Fe, Co, Ni) **31**
Stepan V. Syrotyuk

Вплив гідростатичного тиску і катіонної вакансії на електронні та магнітні властивості кристалів ZnSe:T (T = Ti, V, Cr, Mn, Fe, Co, Ni)
Степан В. Сиротюк

Electrical and Photoelectric Properties of Organic-Inorganic Heterojunctions PEDOT:PSS/*n*-CdTe **43**
Hryhorii P. Parkhomenko, Mykhailo M. Solovan, Andrii I. Mostovyi, Ivan G. Orletskyi, Viktor V. Brus

Електричні та фотоелектричні властивості органічно-неорганічних гетеропереходів PEDOT:PSS/n-CdTe
Г.П. Пархоменко, М.М. Солован, А.І. Мостовий, І.Г. Орлецький, В.В. Брус

Family of the Atomic Radial Basis Functions of Three Independent Variables Generated by Helmholtz-Type Operator **49**
Denys O. Protektor

Родина атомно-радіальних функцій трьох незалежних змінних, згенерованих оператором типу Гельмгольца
Д.О. Протектор

Application of Particular Solutions of the Burgers Equation to Describe the Evolution of Shock Waves of Density of Elementary Steps **59**
Oksana L. Andrieieva, Victor I. Tkachenko, Oleksandr P. Kulyk, Oksana V. Podshyvalova, Volodymyr A. Gnatyuk, Toru Aoki

Застосування частинних розв'язків рівняння Бюргерса для опису еволюції ударних хвиль густини елементарних сходин
О.Л. Андрєєва, В.І. Ткаченко, О.П. Кулик, О.В. Подшивалова, В.А. Гнатюк, Т. Аокі

On the Impact Parameter Dependence of the Ionization Energy Loss of Fast Negatively Charged Particles in an Oriented Crystal **68**
Sergii V. Trofymenko, Igor V. Kyryllin, Oleksandr P. Shchus

Про залежність іонізаційних втрат енергії швидких негативно заряджених частинок в орієнтованому кристалі від прицільного параметра
С.В. Трофименко, І.В. Кирилін, О.Р. Щусь

Structural, Electrical and Optical Properties of CuO Thin Films Obtained by Reactive Magnetron Sputtering **76**
Serhii I. Kuryshchuk, Taras T. Kovalyuk, Hryhorii P. Parkhomenko, Mykhailo M. Solovan

Структурні, електричні та оптичні властивості тонких плівок CuO отриманих методом реактивного магнетронного розпилення
С.І. Курищук, Т.Т. Ковалюк, Г.П. Пархоменко, М.М. Солован

Thermal-Vacuum Method for Obtaining Nanodispersed Zirconium Dioxide **86**
Volodymyr O. Kutovyi, Dmitry G. Malykhin, Volodymyr D. Virych, Ruslan L. Vasilenko

Термовакуумний спосіб одержання нанодисперсного діоксиду цирконію
В.О. Кутовий, Д.Г. Малихін, В.Д. Вірич, Р.Л. Василенко

GEANT4 Modeling of the Bremsstrahlung Converter Optimal Thickness for Studying the Radiation Damage Processes in Organic Dyes Solutions **91**
Tetiana V. Malykhina, Vladimir E. Kovtun, Valentin I. Kasilov, Sergey P. Gokov

GEANT4-моделювання оптимальної товщини конвертеру гальмівного випромінювання для дослідження процесів радіаціних пошкоджень при взаємодії випромінювання з розчинами органічних барвників
Т.В. Малихіна, В.Є. Ковтун, В.Й. Касілов, С.П. Гоков

Thermodynamic and Kinetic Parameters of the Processes of Deuterium Interaction with Tungsten Protective Coatings **99**
Sergiy Karpov, Valeryi Ruzhytskyi, Galyna Tolstolutskaya, Ruslan Vasilenko, Oleksandr Kuprin, Sergiy Leonov

Термодинамічні та кінетичні параметри процесів взаємодії дейтерію із захисними покриттями вольфраму
С. Карпов, В. Ружицький, Г. Толстолуцька, Р. Василенко, О. Купрін, С. Леонов

Interactions of Novel Phosphonium Dye with Lipid Bilayers: A Fluorescence Study **107**
Olga Zhytniakivska

Взамодія нового фосфонієвого зоду з ліпідними мембранами: флуоресцентне дослідження
О. Житняківська

Clinical Commissioning and Dosimetric Verification of the Raystation Treatment Planning System **114**
Taylan Tuğrul

Клінічний пуск та дозиметрична верифікація системи планування лікування променевою станцією
Т. Тугрул

Investigation of the Structural Composition of Fe-Mn-Si-Ti-Al-N-C Alloys and the Solubility of Elements in α-Iron **120**
Nataliia Yu. Filonenko, Aleksander I. Babachenko, Hanna A. Kononenko, Alexander S. Baskevich

Дослідження структурного складу сплавів системи Fe-Mn-Si-Ti-Al-N-C та розчинності елементів в α- залізі
Н.Ю. Філоненко, О.І. Бабаченко, Г. А. Кононенко, А.С. Баскевич

East European Journal of Physics

No 4. 2021

Simulation of a High-Energy Electron Beam Transmission Through Titanium and Kapton® Thin Films **124**
Tetiana V. Malykhina, Stepan G. Karpus, Oleg O. Shopen, Valerii I. Prystupa

Моделювання проходження пучка високоенергетичних електронів через тонкі плівки титану та каптону
Т.В. Малихіна, С.Г. Карпусь, О.О. Шопен, В.І. Приступа

Research of Interaction Processes of Fast and Thermal Neutrons with Solution of Organic Dye Methyl Orange **130**
Sergey P. Gokov, Yuri G. Kazarinov, Sergiy A. Kalenik, Valentin Y. Kasilov, Tetiana V. Malykhina, Yegor V. Rudychev, Vitaliy V. Tsiats'ko

Дослідження процесів взаимодії потоків швидких і теплових нейтронів з розчином органічного барвника метиловий оранжевий
С.П. Гоков, Ю.Г. Казарінов, С.О. Каленик, В.І. Касілов, Т.В. Малихіна, Е.В. Рудичев, В.В. Цяцько

Positive Deviation of the Hall-Petch Relationship for Aluminum Condensates Alloyed with Iron **135**
Evgeniy Lutsenko, Anatoly Zubkov, Maria Zhadko, Eduard Zozulya

Позитивне відхилення співношення Hall-Petch для алюмінієвого конденсату, легованого з залізом
Є.А. Луценко, А.Б Зубков., М.Б. Жадько, Є.Б. Зозуля

X-Ray Induced Light Emission of Yttrium Oxide **140**
Sergiy Kononenko, Oganes Kalantaryan, Vitaliy Zhurenko, Volodymyr Chishkala, Sergii Lytovchenko, Ruslan Skyba

Люмінесценція оксиду ітрію, спричинена рентгенівським опроміненням
С. Кононенко, О. Калантар'ян, В. Журенко, В. Чішкала, С. Литовченко

Photoluminescence, Impedance, Thermal Characteristics and Hirshfeld Surface Analysis of Potassium Bisulphate Single Crystals for Third Order NLO Applications **145**
K. Thilaga, P. Selvarajan, S.M. Abdul Kader

Фотолюмінесценція, імпеданс, термічні характеристики та аналіз поверхні хіршфельда монокристалів бісульфату калію для застосувань NLO третього порядку
K. Thilaga, P. Selvarajan, S.M. Abdul Kader

Plasma Conversion of CO_2 in DC Glow Discharge with Distributed Gas Injection and Pumping **152**
Valeriy A. Lisovskiy, Stanislav V. Dudin, Pavlo P. Platonov, Vladimir D. Yegorenkov

Плазмова конверсія CO_2 у тліючому розряді постійного струму з розподіленим напуском та відкачуванням газу
В.А. Лісовський, С.В. Дудін, П.П. Платонов, В.Д. Єгоренков

Concept of Neutron Source Creation for Nuclear Medicine on the Basis of Linear Electron Accelerator **160**
Valentin I. Kasilov, Sergey P. Gokov, Sergiy A. Kalenik, Sergey S. Kochetov, Leonid D. Saliy, Vitaliy V. Tsyats'ko, Evgen V. Tsyats'ko, Oleg A. Shopen

Концепція створення джерела нейтронів для ядерної медицини на основі лінійного прискорювача електронів
В.Й. Касілов, С.П. Гоков, С.О. Каленик, С.С. Кочетов, Л.Д. Салій, В.В. Цяц'ко, Е.В. Цяц'ко, О.О. Шопен

Enhancing Si Solar Cells Efficiency by Adding SiO_2/TiO_2 Thin Films Using Transfer Matrix Method **164**
Wedad Ahmed Abdullah Garhoom, Zina A. Al Shadidi

Підвищення ефективності сонячних елементов Si за використання додавання тонкіх плівок SiO2/TiO2 за використанням методу передачної матриці
В.А.А. Гархум, З.А. аль Шадіді

Pressure of Electromagnetic Radiation on a Linear Vibrator **172**
Mykola G. Kokodii, Sergey L. Berdnik, Victor O. Katrich, Mikhail V. Nesterenko, Marina V. Kaydash

Тиск електромагнітного випромінювання на лінійний вібратор
М.Г. Кокодій, С.Л. Бердник, В.О. Катрич, М.В. Нестеренко, М.В. Кайдаш

The Nonlinear Magnetosonic Waves in Magnetized Dense Plasma for Quantum Effects of Degenerate Electrons **180**
Neelam Rani, Manikant Yadav

Нелінійні магнітозвукові хвилі в намагніченій щільній плазмі з квантовими ефектами вироджених електронів
Н. Рані, М. Ядав

Thermoelectric Coefficients of Heavily Doped N-Type Silicon **189**
Mulugeta Habte Gebru

Термоелектричні коефіцієнти сильно легованого кремнію n-типу
Мулугета Хабте Гебру

EAST EUROPEAN JOURNAL OF PHYSICS. 4. 5-17 (2021)
DOI: 10.26565/2312-4334-2021-4-01 ISSN 2312-4334

RECENT ADVANCES IN MODELING OF PEROVSKITE SOLAR CELLS USING SCAPS-1D: EFFECT OF ABSORBER AND ETM THICKNESS†

Eli Danladi[a,*], Douglas Saviour Dogo[b], Samuel Udeh Michael[c], Felix Omachoko Uloko[d], Abdul Azeez Omeiza Salawu[e]

[a]*Department of Physics, Federal University of Health Sciences, Otukpo, Benue State, Nigeria*
[b]*Department of Physics, Federal College of Education (Technical) Omoku, Rivers State, Nigeria*
[c]*Department of Physics, Nigerian Defence Academy, Kaduna, Nigeria*
[d]*Department of Physics, Federal University, Lokoja, Kogi State, Nigeria*
[e]*Department of Computer Science, Nile University of Nigeria*
**Corresponding Author: danladielibako@gmail.com, tel. +2348063307256*
Received August 28, 2021; revised November 15, 2021; accepted November 16, 2021

With the massive breakthrough recorded in the power conversion efficiency (PCE) of perovskite solar cells (PSCs) from 3.8 % to > 25 %, PSCs have attracted considerable attention in both the academia and industries. However, some challenges remain as barrier in realizing its deployment. To develop a highly efficient PSCs as well as environmentally benign device, simulation and optimization of such devices is desirable. Its impractical as well as wastage of time and money to design a solar cell without simulation works. It minimizes not only the risk, time and money rather analyzes layers' properties and role to optimize the solar cell to best performance. Numerical modeling to describe PV thin layer devices is a convenient tool to better understand the basic factors limiting the electrical parameters of the solar cells and to increase their performance. In this review article, we focused on the recent advances in modelling and optimization of PSCs using SCAPS-1D with emphasis on absorber and electron transport medium (ETM) thickness.
Keywords: perovskite solar cells, absorber, electron transport medium, SCAPS
PACS: 41.20.Cv; 61.43.Bn; 68.55.ag; 89.30.Cc; 68.55.jd; 73.25.+i; 72.80.Tm; 74.62.Dh; 78.20.Bh;

INTRODUCTION

Perovskite solar cells, as a promising class of device belonging to the third-generation solar cell, have gained global interest due to their simple processing procedure and low cost [1]. Hybrid perovskite are defined on the basis of AMX_3 crystal structure, where A is an organic cation, for example, methylammonium or formamidinium, M is a metal and X is a halogen atom. The combination of amazing advantages, such as excellent tolerance for perovskite crystal defects, availability for superior light absorption efficiency, efficient carrier mobility and enough carrier diffusion lifetimes promote this as a candidate for outstanding solar cell photovoltaic performance [1-7]. In general, the competitiveness of solar cells is evaluated by efficiency, cost and lifetime, where scalability is closely related to cost and lifetime has much to do with stability [8]. Achieving a balance of efficiency, cost and lifetime is the key to promote the commercialization of PSCs to grab a share of the energy market. Therefore, several research efforts are addressing these issues that are important for commercialization. A few unprecedented achievements have been made that are highly beneficial for the large-scale commercial application of PSCs in the future [9-11].

In PSCs, the absorber layer, which is used for harvesting photon energy is crucial. It is the central part of PSCs mostly determines the overall device performance. Many studies have demonstrated that the PCE of PSCs is generally dependent on thickness of the perovskite absorber [12-15]. Thickness of electron transport layers are also crucial for better efficiencies [13-17].

In this article, the progress of PSC development is reviewed, concentrating on the perovskite and electron transport functional layer, and valuable insights are provided. Other sections discussed the effect of thickness of absorber and ETM on the photovoltaic properties of perovskite solar devices.

OPERATION PRINCIPLE OF A PEROVSKITE SOLAR CELL

The working principle of the PSC is described in Figure 1. Photons from the light source reach the perovskite layer via glass (TCO) and transparent electrodes. In the active perovskite layer, photons are absorbed and excitons are excited when the incident energy of the photon is greater than that of the perovskite material. The exiton is split into electrons and holes by an internal potential created by the difference in the work function between the transparent electrode and metallic electrode. Electrons are transferred to Electron Transporting Layer (ETL) and holes are transferred to Hole Transporting Layer (HTL). From there, the electrons move to the transparent electrode and the holes move to the metal electrode. Next, the electrons travel through a network that connects the two electrodes, and the traveling electrons produce an electric current. For the PSC to function properly, the energy levels in each layer must be carefully configured to prevent the recombination of excited charge carriers. However, since they are also energy conservers, they always follow the path of least resistance [18]. The correct structure of the layers prevents recombination within the cell as the charge carriers pass through different paths. This is achieved by creating an ETL Lowest Unoccupied Molecular Orbital

† ***Cite as:*** E. Danladi, D.S. Dogo, S.U. Machael, F.O. Uloko, and A.O. Salawu, East. Eur. J. Phys. **4**, 5 (2021), https://doi.org/10.26565/2312-4334-2021-4-01

(LUMO) lower than the perovskite LUMO layer. This creates a more attractive way for electrons to move. The same applies to HTL Highest Occupied Molecular Orbital (HOMO). HTL HOMO must be higher than the perovskite HOMO layer. This creates a more attractive path for holes to go. This is the same for each layer in the cell. Each layer has a higher HOMO or lower LUMO for the normal operation of the charge carrier transport chain, as shown in Figure 1.

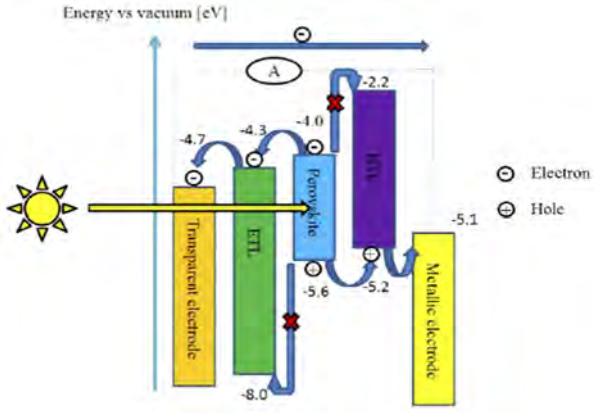

Figure 1. Schematic of the operational principle of perovskite solar cell [18]

Device Structure

The architecture of the device is a fundamental tool in evaluating the PCE of PSCs. Perovskite solar cells are generally classified into regular (n-i-p) and inverted (p-i-n) structures depending on which transport (electron/hole) material is present on the exterior portion of the cell/encountered by incident light first [19]. These two design are sub-divided into two classes: mesoscopic and planar structures. The mesoscopic structure is made of a mesoporous layer whereas the planar structure consists of all planar layers. Some design does not involve electron and hole-transporting layers. Summarily, about six types of perovskite solar cell architectures have been designed and tested by several researchers thus far: the mesoscopic n-i-p configuration, the planar n-i-p configuration, the planar p-i-n configuration, the mesoscopic p-i-n configuration, the ETL-free configuration, and the HTL-free configuration [19].

Regular n-i-p structure

The conventional n-i-p mesoscopic structure was the first structure developed and tested, it involves the replacement light-harvesting dye with lead halide perovskite absorber in a traditional dye sensitized solar cell (DSSC)-type architecture [20]. The interest was sold to many researchers when the initial structure (Fig. 2a) were built by replacing the liquid electrolyte with a solid-state hole-conductor [21]. This breakthrough in the architecture has created a pathway for photovoltaic scholars and consequently led to the development of other PSC device structures (Fig. 2b–d). The planar architecture is an evolution of the mesoscopic structure, where the perovskite light-harvesting layer is sandwiched between the ETM and HTM. The absence of a mesoporous metal oxide layer leads to an overall simpler structure.

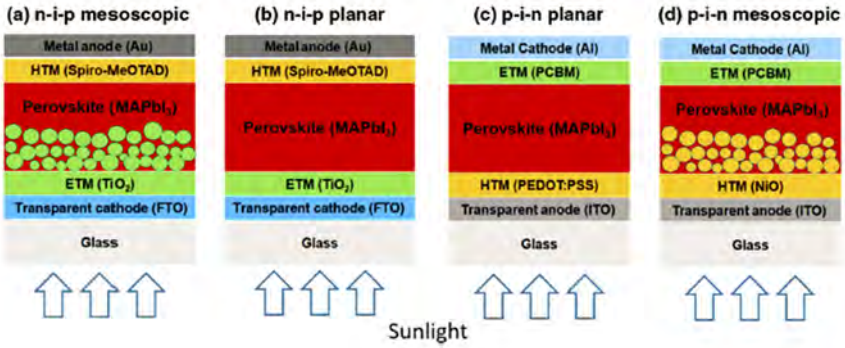

Figure 2. Schematic showing the layered structure four typical of perovskite solar cells (a) n-i-p mesoscopic, (b) n-i-p planar, (c) p-i-n planar, and (d) p-i-n mesoscopic [19,22]

Inverted p-i-n structure

The p-i-n perovskite solar cells design was first derived from the organic solar cell reported [23]. In the case of the p-i-n planar perovskite structure, the hole transport layer (HTL) is first deposited followed by the electron transport layer (ETL). It was discovered that perovskites absorbers can simultaneously absorbs photon energy and transport the holes themselves [19,24], and this led to the development of planar hetero-junction PSC with an inverted structural design [25]. With this record breakthrough, the inverted p-i-n structure has expanded the horizon of photovoltaics and permits mesoscopic p-i-n device architecture [19]. The device structure of the inverted p-i-n planar and mesoscopic PSC is shown in Fig. 2c, d.

Effect of thickness of absorber

The absorber layer of the perovskite solar cell plays an essential role in device performance and outcome. Therefore, the proper choice of thickness of the absorber can considerably affect the performance and results of a solar cells. Thickness of absorber is an essential factor to be considered in a solar cell device as such a comprehensive understanding of its role in solar cell is necessary. Eli et al. [26] investigated the effect of thickness of absorber with TiO_2 and inorganic cuprous oxide (Cu_2O) as ETM and HTM ranging from 0.2 to 0.9 μm. The influence of thickness of absorber on the solar cell parameters (V_{OC}, J_{SC}, *FF* and *PCE*) were evaluated. PCE is lower when thickness of the absorber is 0.2 μm which can be attributed to the poor light absorption by the layer. However an increased in PCE was observed as a result of increase of the absorber layer thickness from 0.20 to 0.40 μm, thereafter, it starts decreasing. For thickness beyond 0.4 μm, the collection of photo generated carriers decreased because of charge recombination [26]. The best performing device was observed with thickness of 0.40 μm which gave optimized parameters (PCE of 12.83%. Jsc of 21.43 mA/cm^2, Voc of 0.86V, and FF of 69.51%). The JV curve and variation of the thickness with parameters is as shown in Fig. 3 [26]. Their studies demonstrate that careful selection of absorber thickness results to good performing PSCs. Similar studies with variation in absorber thickness from 0.1 to 1.0 μm was carried out [27]. Short circuit current (Jsc) increases from 12.33 to 22.36 mAcm^{-2} with thickness increase from 0.1 to 0.6 μm which is attributed to the increase in carrier generation and dissociation, then starts decreasing from 0.7 to 1.0 μm. It was also observed that the Fill Factor (FF) decreases with thickness increase in the perovskite layer. The PCE increase with increase in layer thickness from 0.1 to 0.4 μm was due to the production of new charge carriers. However, PCE decreases from thickness of 0.5 μm to 1.0 μm (Table 1) due to lesser electron and hole pairs extraction rate that leads to recombination process [28].

Table 1. J-V characteristic parameters with the variation of thickness of absorber

Parameters T (μm)	J_{sc} (mAcm^{-2})	V_{oc} (V)	*FF*	PCE (%)
0.1	12.34	0.77	79.12	7.48
0.2	17.85	0.82	77.16	11.30
0.3	20.42	0.84	74.32	12.78
0.4	21.63	0.86	71.39	13.21
0.5	22.17	0.86	68.54	13.13
0.6	22.36	0.87	65.36	12.85
0.7	22.36	0.88	63.59	12.46
0.8	22.24	0.88	61.39	12.02
0.9	22.06	0.88	59.50	11.60
1.0	21.85	0.89	57.73	11.18

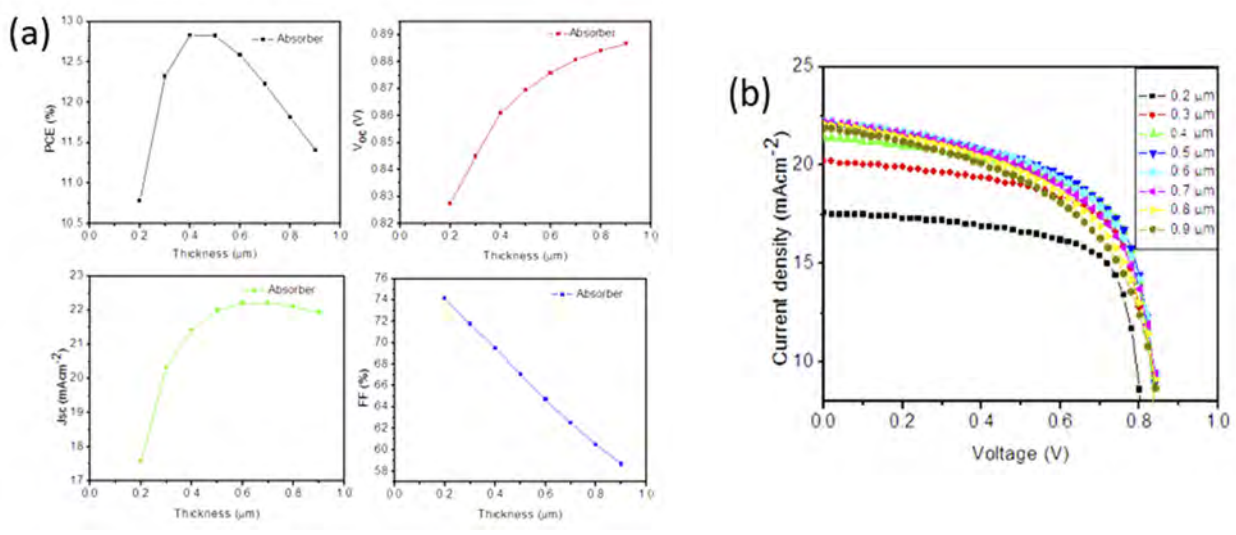

Figure 3. (a) Variation in performance parameters of PSC with thickness of Absorber, (b) J–V curves of PSC with different values of Absorber thickness [26].

Another study that show the beneficial role of absorber thickness on solar cell performance (V_{OC}, J_{SC}, FF and PCE) is described in Figure 4 (a). The J-V and QE of the varied absorber thickness is shown in Figure 4 (b) and (c).

Figure 4 (c) exhibits the spectral response of the PSCs as a function of wavelength with varied $CH_3NH_3PbI_3$ layer thickness within range of 300 nm to 900 nm. The QE first increases rapidly with the $CH_3NH_3PbI_3$ thickness increasing from 0.1 μm to 0.4 μm, and the QE increase slightly after the thickness is greater than 0.4 μm, which shows that 0.4 μm thickness of $CH_3NH_3PbI_3$ layer can absorb most of the incident photons and the part beyond 0.4 μm can only contribute little to the PSC performance. Therefore, the optimized perovskite absorber layer thickness is around 0.4 μm which gives V_{OC} of 0.86 V, J_{SC} of 21.63 mAcm^{-2}, FF of 71.31 % and PCE of 13.21 %.

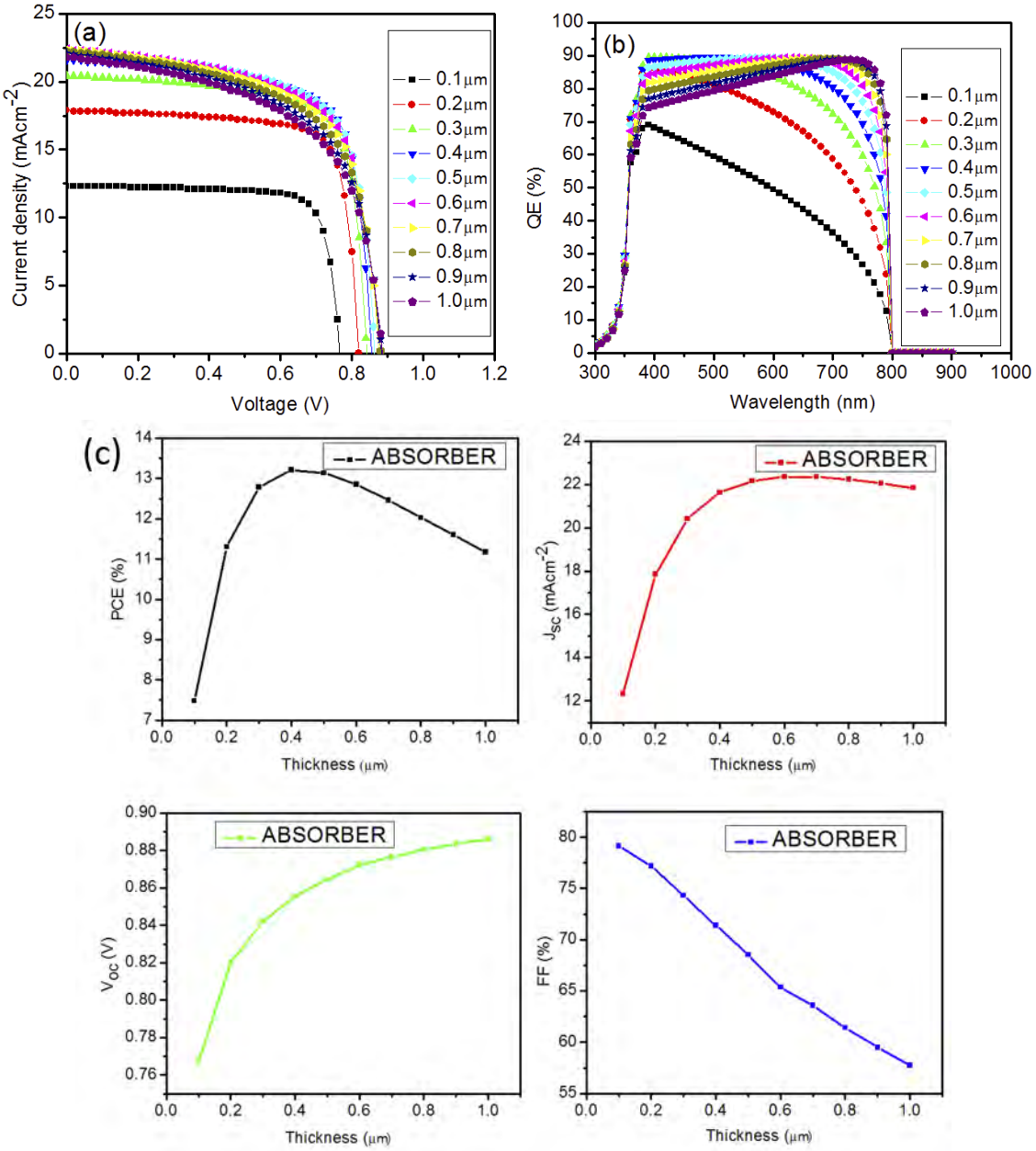

Figure 4 (a) J–V curves of PSC with different values of thickness of absorber layer, (b) QE with different values of thickness of absorber layer, (c) Variation in performance parameters of PSC with thickness of absorber layer [27].

The effect of thickness on PV and Quantum efficiencies of PSCs with ZnSe as ETL and Cu_2O as ETL was also studied [29]. The simulation was carried out in the range of 0.03 to 1.5 µm while other parameters are kept constant. Table 2 [29] shows the effect with respect to varied absorber thickness.

Similarly, Muhammad et al. [30] systematically investigated the effect of absorber thickness in lead free PSC with copper iodide as HTM and found out that the thickness of absorber affects the performance of perovskite solar cells as shown in Fig. 5 [30].

Hussain and co researchers [31] also studied the effect of absorber layer thickness on PCE of lead free hybrid double PSCs with spiro-meOtad as HTM. In their study, absorber layer thickness was varied from 100 nm to 1000 nm, and the effect was observed on the output parameters while all other parameters are set constant. The deviation in device outcomes with the thickness of the active layer is depicted in Fig 6 and Table 3 [31]. The simulation results show that with the

increase in thickness of the active layer, short-circuit current Jsc increases and approaches to the optimum value of ~39 $mAcm^{-2}$.

The influence of thickness of absorber on the performance parameters was also studied by Haider et al. [32]. They made used of lead based perovskite absorber with inorganic HTM and ETM as transport medium for holes and electrons. The variation of the absorber thickness was from 100 to 1000 nm. PCE is lower when thickness of the layer is too small due to the poor light absorption, which means that small thicknesses are not favorable for good light harvesting in PSC. PCE of PSCs increases with the increase of the thickness of the absorber before reaching a constant value at 600 nm. For absorber thicker than 600 nm, the collection of photo generated carriers decreased because of charge recombination, which also shows that thicker absorber layer act as center for recombination of charge carriers. Fig. 7(b) indicates that QE increases with the increase of absorber thickness up to 300 nm thickness. After 300 nm thickness, no significant increase in QE is observed. Carrier diffusion length is the crucial factor in designing perovskite solar cell structure [32-34] which depends on the absorber thickness (Fig. 7c).

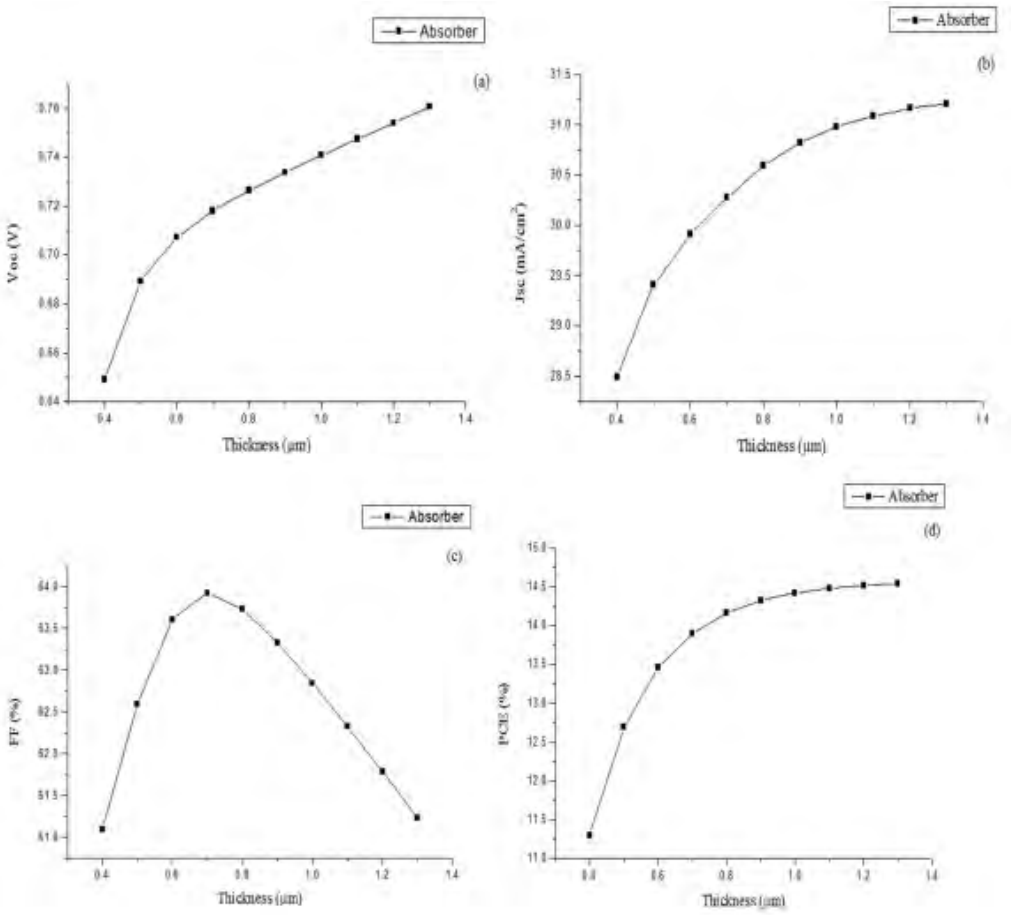

Figure 5. Variation of Absorber thickness with photovoltaic performance [30]

Table 2. Dependence of solar cell performance on absorber layer [29].

Absorber thickness (μm)	J_{SC} (mA/cm²)	V_{OC} (V)	FF (%)	PCE (%)
0.03	8.87	0.76	74.99	5.08
0.09	16.76	0.80	74.53	10.11
0.2	24.73	0.84	72.11	15.15
0.5	31.32	0.89	68.29	19.08
0.7	32.44	0.89	67.77	19.65
1.9	32.91	0.89	67.44	19.82
1.2	33.16	0.89	67.08	19.81
1.5	33.23	0.88	66.77	19.71

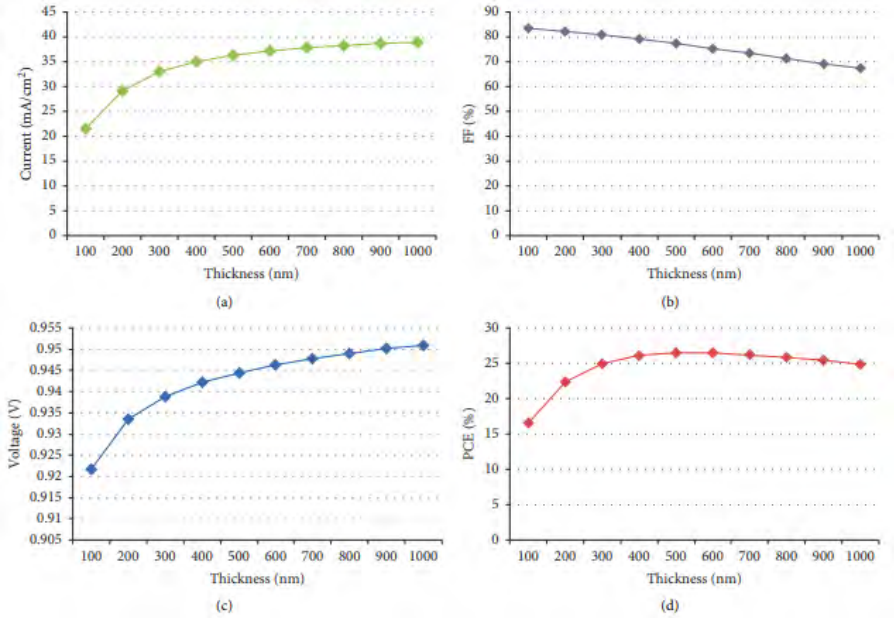

Figure 6. (a) Short-circuit current density as a function of absorber thickness. (b) Fill factor as a function of absorber thickness. (c) Open circuit voltage as a function of absorber thickness. (d) PCE as a function of absorber thickness [31].

Table 3. Device Performance at a different absorber layer thickness [31]

Thickness (nm)	V_{oc} (volt)	FF (%)	Jsc (mA/cm^2)	PCE (%)
100	0.9216	83.60	21.56	16.61
200	0.9335	82.24	29.18	22.40
300	0.9388	80.73	32.95	24.98
400	0.9421	79.08	35.03	26.10
500	0.9445	77.28	36.31	26.50
600	0.9463	75.36	37.16	26.50
700	0.9478	73.39	37.77	26.28
800	0.9491	71.38	38.23	25.90
900	0.9501	69.34	38.59	25.42
1000	0.9510	67.28	38.88	24.88

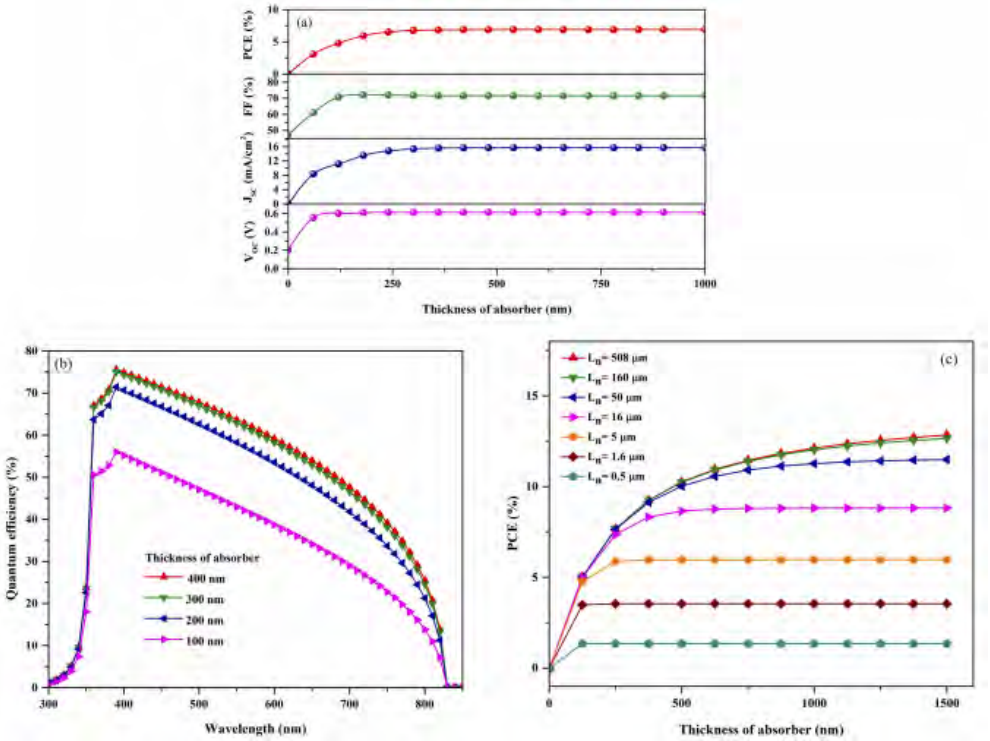

Figure 7. Variation in (a) performance parameters and (b) quantum efficiency of PSC with different thickness of absorber layer (c) variation in PCE with various diffusion lengths and thickness of absorber layer [32].

Also, a simulation was done by changing the absorber thickness from 0.1 μm to 2 μm and maintaining all the other device parameters constant [35]. As shown, Jsc increases with the increasing thickness (Fig. 8a), which is attributed to the generation of more electron-hole pairs in the perovskite leading to an efficiency enhancement. The highest efficiency of 21.42% is obtained at an optimum thickness of 0.5 μm. However, a decrease in efficiency in the thicker absorber layer is due to a reduced electric field, which affects the charge carriers' recombination behaviour within the absorber [36]. This statement has been confirmed in the recombination profile with an increasing recombination at the perovskite/Spiro-meOtad junction with a thickness (Fig. 8c). FF is inversely proportional to the perovskite thickness due to an increased series resistance and an internal power dissipation in a thicker absorber layer (Fig. 8b). The decrease in Voc with the thickness (Fig. 8b) is attributed to the increment in the dark saturation current, which increases the recombination of the charge carriers. That can be explained by the dependency of open-circuit voltage on the photo-generated current and dark saturation current, which is written as [37]:

$$v_{OC} = \frac{kT}{q} \ln\left[\frac{J_{SC}}{J_0} + 1\right], \tag{1}$$

where kT/q is the thermal voltage, J_{sc} is the photo-generated current density, and J_0 is the saturation current density.

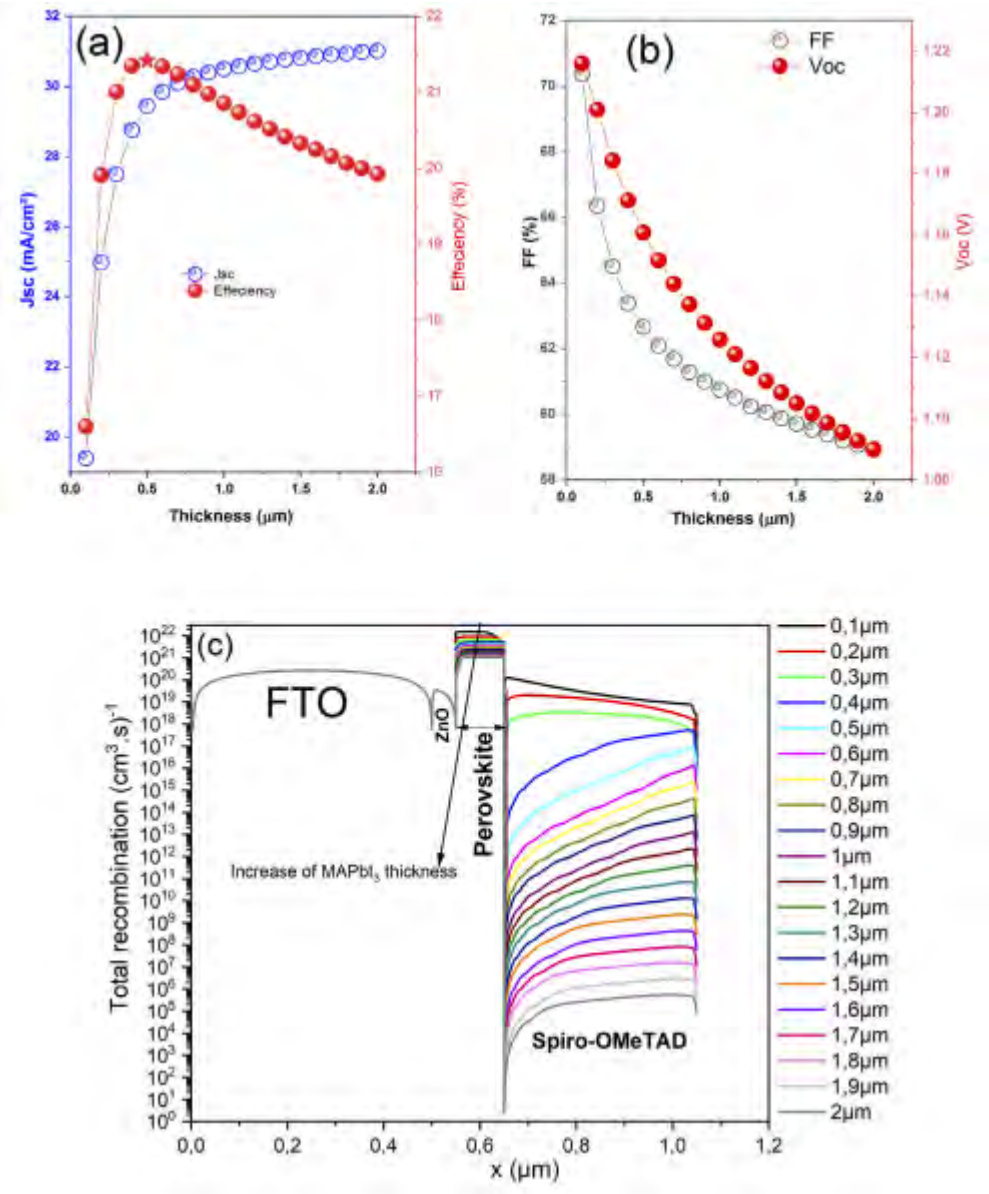

Figure 8. The variation of (a) Jsc, PCE, (b) FF, Voc as well as (c) total recombination profile versus the thickness of $MAPbI_3$ [35].

Soucase et al. [38], also studied the effect of thickness of absorber from 50 nm to 700 nm under 1 Sun (AM1.5G) illumination without considering interface trap density of states but consideration of inputs value of band tail density of states, and Gaussian acceptor/donor states of $MAPbI_3$ to be 10×10^{14} $eV^{-1}cm^{-3}$ and 10×10^{14} cm^{-3} respectively. The short

circuit current and PCE both are found to be increased sharply with increase in thickness up to 500 nm (Fig. 9a) [38]. After this, increment is very slow and reaches to almost optimal efficiency 25.22%, V_{OC} 1.2 V, J_{SC} 25.49 mA/cm^2 and FF 82.56% at 700 nm [38]. The quantum efficiency curves as a function of wavelength of incident light for different thickness of the absorber (Fig. 9b) also verifies the above mentioned upshot.

Several other authors have also studied the effect of perovskite thickness [39-47] using SCAPS and their studies show that, poor film quality can affect the coverage of perovskite on ETL. If the quality of film is poor, then defect density increases and recombination rate of carriers becomes dominant in absorber layer which determine the Voc of the solar cell [32]. Therefore, substantive studies should be carried out to determine the best thickness for optimum PSC performance.

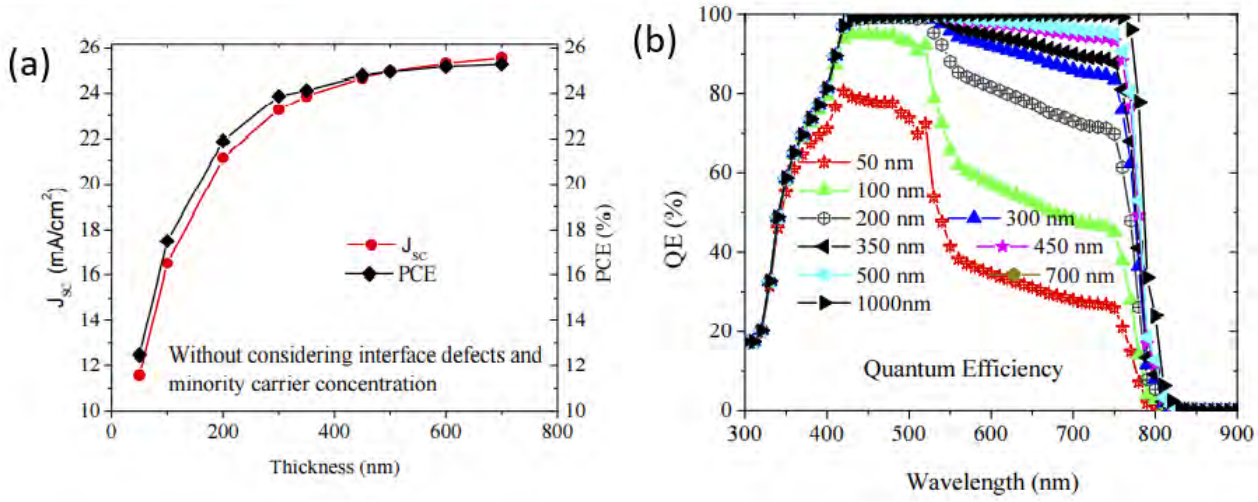

Figure 9. (a) J_{SC} and PCE vs Thickness, (b) Variation of quantum efficiency with thickness of absorber [38].

Effect of ETL thickness

The thickness properties of the ETM affect the conduction of charge carrier between the front and back contacts [48]. Efficient collection of the charge carriers depends on work function of the front contact material and rear metallization [60]. And most importantly, the selection of the appropriate ETM plays a significant role on the design and implementation of high efficiency perovskite solar cell as the energy band alignment between absorber and ETM layer is a crucial factor for the efficiency improvement of PSCs [48,49].

Soucase et al. [38] studied the effect of thickness of two ETMs (TiO_2 and ZnO) with spiro-meOtad as HTM. In both cases V_{OC}, J_{SC} and *PCE* gradually decreases due to fractional absorption of incident light by the ETMs layer, the bulk recombination and surface recombination at the interface and change in series resistance [38, 49]. The thickness of ETMs was varied from 50 nm to 450 nm to make the practical devices. Results from the studies showed that TiO_2 is more sensitive than that of ZnO due to its high absorption coefficient and reflectance and less transmittance than ZnO [38]. This shows that, increase in thickness of ETM lessen the performance of solar cells due to increase in partial absorption of photons and resistance of the device. Also, study was carried out by simulation by the same group of researchers with practically viable thickness of TiO_2 – ETM (Fig. 10).

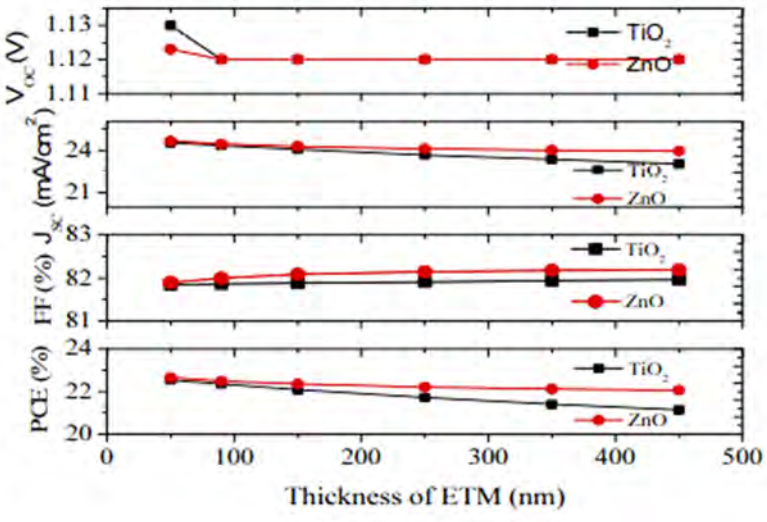

Figure 10. Variation of PV cells parameters with thickness of ETMs [38].

In a HTM free PSCs, where the absorber is simultaneously absorbing light and transporting holes, the thickness of ETM was varied from 0.02 to 0.10 μ m. The results show that both the PCE, Jsc, Voc and FF decrease with the thickness of ETM (Fig 11, Table 4) [27]. Fig. 11b, shows the QE of the PSCs as a function of wavelength in the range of 300-900 nm with varied ETM layer thickness. The studies show that QE maximum value was obtained in the wavelength range of 380−570 nm and gradually decreases at longer wavelengths until 800 nm, which corresponds to its absorption spectrum.

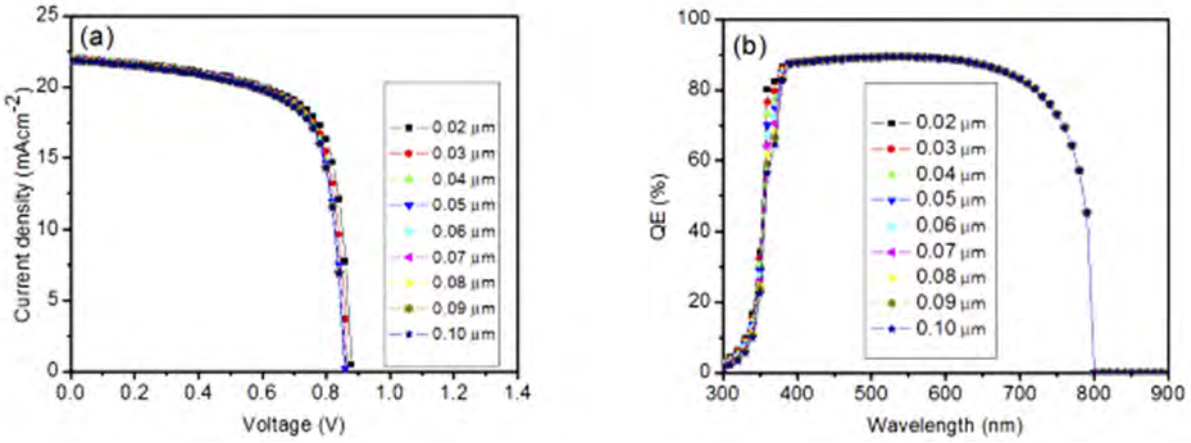

Figure 11. (a) J–V curves of PSC with different values of thickness of ETM, (b) QE with different values of thickness of ETM [27].

Table 4. J-V characteristic parameters with the variation of thickness of ETM [27]

Parameters T (μ m)	J_{sc} (mAcm^{-2})	V_{oc} (V)	*FF*	PCE (%)
0.02	22.05	0.88	70.17	13.63
0.03	22.01	0.87	70.11	13.40
0.04	21.98	0.86	69.96	13.28
0.05	21.96	0.86	69.94	13.22
0.06	21.94	0.86	69.91	13.18
0.07	21.93	0.86	69.91	13.17
0.08	21.92	0.86	69.91	13.15
0.09	21.90	0.86	69.91	13.15
0.10	21.89	0.86	69.92	13.14

Effect of ETL layer thickness in PSC with ZnSe and Cu_2O as ETM and HTM was explored in the range of 0.005 to 0.080 μm. The results after the simulation show that when there is an increase in the thickness of electron transporting material it results in decrease in J_{SC}, *FF* and *PCE* of the device while V_{OC} decreases but remain invariable from 0.89 V at the thickness of 0.010μm (Table 3).

Table 2. Dependence of solar cell performance of the thickness of ZnSe (ETL) [29].

ZnSe thickness (μm)	J_{SC} (mA/cm^2)	V_{OC} (V)	FF (%)	PCE (%)
0.0050	33.13	0.90	68.16	20.44
0.0100	32.91	0.89	67.76	20.03
0.0150	32.81	0.89	67.75	19.90
0.0300	32.63	0.89	67.75	19.77
0.0350	32.58	0.89	67.75	19.74
0.0450	32.49	0.89	67.76	19.68
0.0500	32.44	0.89	67.77	19.65
0.0800	32.18	0.89	67.79	19.50

Their study signifies that when the material is thicker, it provides a longer diffusion path for the electron to reach the electrode which limit (solar cell parameters) the charge collection efficiency and transmitting of incident photon

decreases with increasing thickness. The optimized device performance was obtained, when the thickness of ETL was 0.005µm with J_{SC} of 33.13mA/cm^2 V_{OC} of 0.90 V, FF of 68.16% and high PCE of 20.44% [29]. Also, different ETMs (TiO_2, ZnO and SnO_2) were simulated in PSCs with thickness variation from 90 nm to 200 nm. It was observed that with the increase of thickness >90 nm, a decrease in Voc, Jsc and thus PCE in case of TiO_2 and ZnO, was observed (Fig. 12) [50], while in the case of SnO_2, there was no noticeable change in its value. It was found that TiO_2 was more affected than ZnO and SnO_2 due to its lower transmittance in 300-400 nm range and possesses low electron mobility, thus reduction in Jsc value occurs as a function of increased ETM thickness, which can be ascribed to the partial absorption of incident light by thicker TiO_2 and ZnO layer.

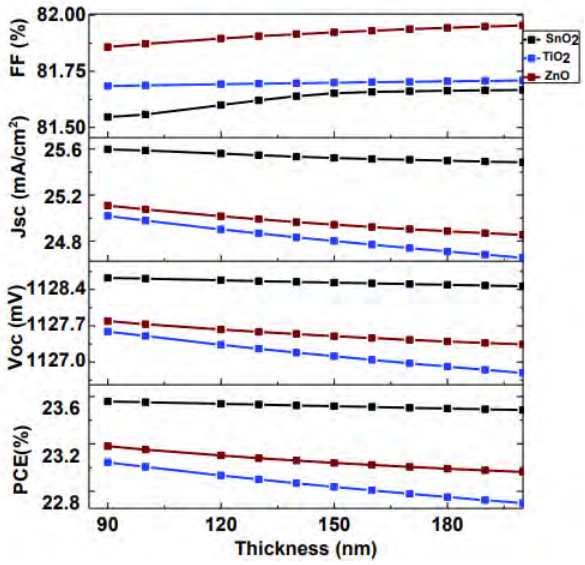

Figure 12. Effect of different ETM thickness on photovoltaic parameters of $MAPbI_3$ based planar perovskite solar cells using Spiro-OMeTAD as HTM [50].

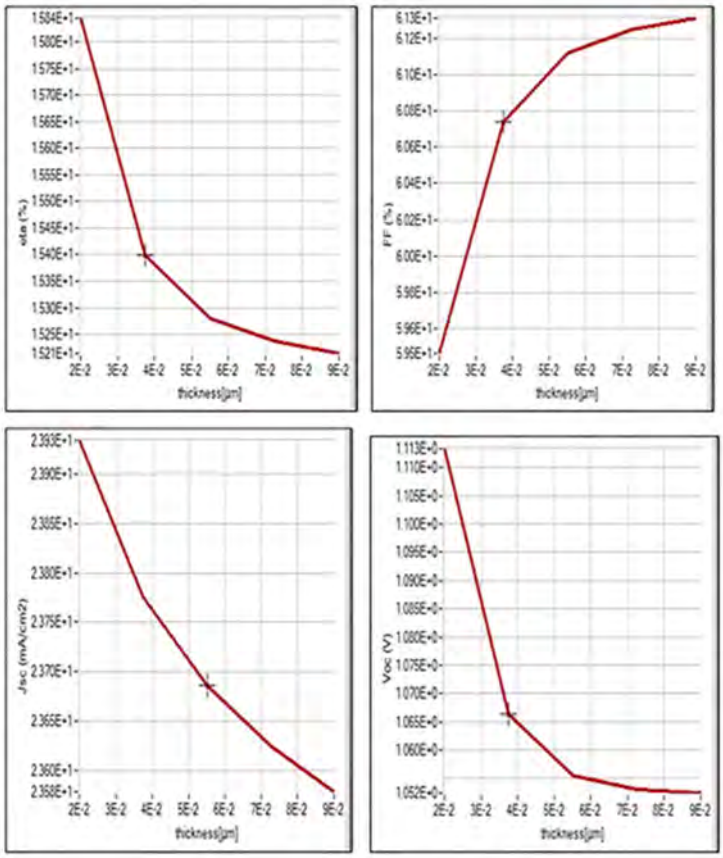

Figure 13. Variation of efficiency, fillfactor, Jsc, and Voc with respect to thickness of ETM layer [58].

Hence it decreases the rate of charge generation and collection and consequently short circuit current (Jsc) decreases [50-53]. However, in case of SnO_2, due to its high transparency, active layer absorption is less affected and Jsc did not decrease significantly up to a certain thickness of 150 nm thus rate of charge generation rate increases as compared to the recombination. Moreover, due to high carrier mobility and high carrier concentration of SnO_2, the series resistance decreases with the thickness due to increase in conductivity and thus fill factor also increases up to certain thickness of 150 nm and beyond this insignificant changes occurs. Some notable achievements in PSCs using SCAPS has been reported too [30,54-57]. Also, a studies with variation of thickness of ZnO as ETM was conducted by Aseena et al. [58]. The study explains the effect of ETM layer thickness on the PSC parameters. The results showed that the efficiency decreases slightly from 15.84% to 15.24% as thickness is increased from 20 nm to 90 nm (Fig. 13). This confirms that the electron transport layer does not have much effect on the electrical parameters of the perovskite solar cell [58]. An ETM free perovskite planar structure solar cells was designed and implemented [59]. This is explained on the basis of the fact that perovskite material itself could help the generation of charge carriers by photon

excitation and ETM layer is just a charge transport layer. Even in the absence of the ETM, the transparent conducting oxide (Fluorine doped tin oxide) layer will act as charge transport layer without affecting the efficiency [58,59]. But however, fill factor could be improved by the application of an optimal layer of ETM [60]. But the gradual increase in ETM layer thickness can also reduce the performance of PSC by increasing photon absorption and resistance of the cell [38].

Sultana et al. [49] also shows how the thickness of ETM affects photovoltaic parameters (Fig. 14). It was shown that, the variation of thickness towards getting optimum performance influence the performance of PSCs. From the three different ETMs (TiO_2, ZnO and SnO_2) used, 400 nm thicknesses are taken for both $MAPbI_3$(absorber) and spiro-OMeTAD (HTM) layer.

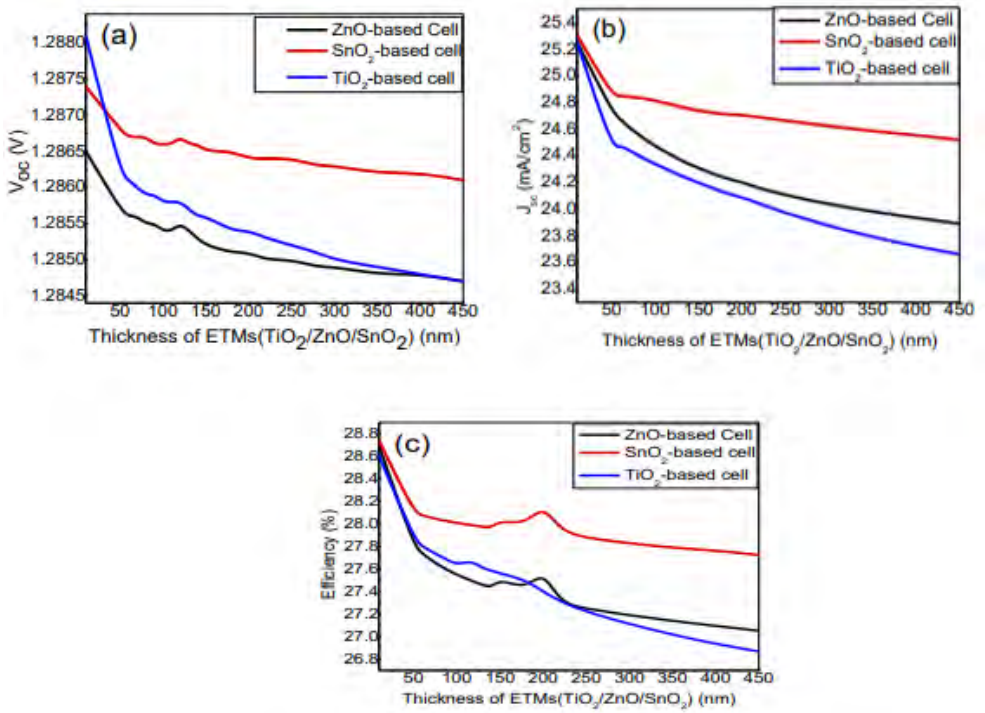

Figure 14. Photovoltaic performances of three models by varying thickness of ETM (a) Open circuit voltage; (b) Short circuit current density; (c) Photovoltaic conversion efficiency [49].

Their ETM layer thickness was varied from 10 nm to 450 nm and a gradual decrease of Voc, Jsc and PCE was observed. The overall performance of solar cell with SnO_2 as ETM is higher than other two models for the entire thickness range. At lower thickness (10 nm to 180 nm), TiO_2-based model gives better performance than ZnO based cell, but for thickness higher than 250 nm ZnO-base model shows better efficiency than TiO_2 [49]. The observation showed that TiO_2 is more responsive to sunlight than that of the other two electron collecting materials as it has higher absorption coefficient and reflectance and less transmittance [48, 49]. It was shown from their work that the increase in thickness of ETM result to poor performance of the solar cells. This can be ascribed to fractional absorption of incident light by ETMs and variation in series resistance of the device with increasing thickness of ETM layer [26,49]. Efficiencies of 27.6 %, 27.5% and 28.02% are found for TiO_2, ZnO and SnO_2-base cell respectively at 90 nm thickness of electron collecting material [48].

CONCLUSION

We have summarized and discussed recent developments in simulation of perovskite solar cells using solar capacitance simulator software with emphasis on thickness of absorber and ETM and its influence with variation on the photovoltaic performance of perovskite solar cells. The review shows that the proper choice of thickness of the absorber can considerably affect the performance and results of solar cells. Also, selection of the appropriate ETM and its thicknesses plays a significant role on the design and implementation of high efficiency perovskite solar cells as the energy band alignment between absorber and ETM layer is a crucial factor for the efficiency improvement of PSCs.

ORCID IDs

Eli Danladi, https://orcid.org/0000-0001-5109-4690

REFERENCES

[1] D. Eli, M.Y. Onimisi, S. Garba, and J. Tasiu, SN Applied Science, **2**, 1769 (2020), https://doi.org/10.1007/s42452-020-03597-y
[2] D. Eli, M.Y. Onimisi, S. Garba, P.M. Gyuk, T. Jamila, and H.P. Boduku, IOP Conference Series, Material Science and Engineering, **805**, 012005 (2020), https://doi.org/10.1088/1757-899X/805/1/012005
[3] M.U. Samuel, M.Y. Onimisi, J.A. Owolabi, D. Eli, and E.O. Mary, The Proceedings of the Nigerian Academy of Science, **13(1)**, 148 (2020), https://nasjournal.org.ng/index.php/pnas/article/view/320/162

[4] J. Jin, J. Li, Q. Tai, Y. Chen, D.D. Mishra, W. Deng, J. Xin, S. Guo, B. Xiao, and X. Wang, Journal of Power Sources, **482**, 228953 (2021), https://doi.org/10.1016/j.jpowsour.2020.228953
[5] M. Minbashi, A. Ghobadi, M.H. Ehsani, H. Rezagholipour Dizaji, and N. Memarian, Solar Energy, **176**, 520 (2018), http://dx.doi.org/10.1016/j.solener.2018.10.058
[6] K. Kumari, A. Jana, A. Dey, T. Chakrabarti, and S.K. Sarkar, Optical Materials, **111**, 110574 (2021), https://doi.org/10.1016/j.optmat.2020.110574
[7] P.K. Patel, Scientific Reports, **11**, 3082 (2021), https://doi.org/10.1038/s41598-021-82817-w
[8] X. Dai, K. Xu, and F. Wei Beilstein, Journal of Nanotechnology, **11**, 51 (2020), https://doi.org/10.3762/bjnano.11.5
[9] X. Zhu, Z. Xu, S. Zuo, J. Feng, Z. Wang, X. Zhang, K. Zhao, J. Zhang, H. Liu, S Priya, S. F. Liu, and D. Yang, Energy & Environmental Science, **11**, 3349 (2018), https://doi.org/10.1039/C8EE02284D
[10] F. Di Giacomo, S. Shanmugam, H. Fledderus, B.J. Bruijnaers, W.J.H. Verhees, M.S. Dorenkamper, S.C. Veenstra, W. Qiu, R. Gehlhaar, T. Merckx, T. Aernouts, R. Andriessen, and Y. Galagan, Solar Energy Materials and Solar Cells, **181**, 53 (2018**),** https://doi.org/10.1016/j.solmat.2017.11.010
[11] Y. Zong, Z. Zhou, M. Chen, N.P. Padture, and Y. Zhou, Advanced Energy Materials, **8**, 1800997 (2018), https://doi.org/10.1002/aenm.201800997
[12] I.J. Ogundana, and S.Y. Foo, Journal of Solar Energy, **2017**, Article ID 8549847, https://doi.org/10.1155/2017/8549847
[13] F. Izadi, A. Ghobadi, A. Gharaati, M. Minbashi, and A. Hajjiah, Optik, **227**, 166061 (2021), https://doi.org/10.1016/j.ijleo.2020.166061
[14] C.W. Chang, Z.W. Kwang, T.Y. Hsieh, T.C. Wei, and S.Y. Lu, Electrochimica Acta, **292**, 399 (2018), https://doi.org/10.1016/j.electacta.2018.09.161
[15] M. Rai, L.H. Wong, and L. Etgar, Journal of Physical Chemistry Letters, **11**(19), 8189 (2020), https://doi.org/10.1021/acs.jpclett.0c02363
[16] A. Sławek, Z. Starowicz, and M. Lipin´ski, Materials, **14,** 3295 (2021), https://doi.org/10.3390/ma14123295
[17] A. Kumar, S.K. Ojha, N. Vyas, and A.K. Ojha, ACS Omega, **6**(10), 7086 (2021), https://doi.org/10.1021/acsomega.1c00062
[18] J. Stenberg, Master's Thesis, Umea University, (2017).
[19] I. Hussain, H.P. Tran, J. Jaksik, J. Moore, N. Islam, and M.J. Uddin, Emergent materials, **1**, 133 (2018), https://doi.org/10.1007/s42247-018-0013-1
[20] A. Kojima, K. Teshima, Y. Shirai, and T. Miyasaka, Journal of American Chemical Society, **131**, 6050 (2009), https://doi.org/10.1021/ja809598r
[21] H.S. Kim, C.R. Lee, J.H. Im, K.B. Lee, T. Moehl, A. Marchioro, S.J. Moon, R. Humphry-Baker, J.H. Yum, J.E. Moser, M. Grätzel, and N.G. Park, Scientific Reports, **2**, 591 (2012), https://doi.org/10.1038/srep00591
[22] Z. Song, S.C. Watthage, A.B. Phillips, M.J. Heben, Journal of Photonics for Energy, **6**, 022001 (2016), https://doi.org/10.1117/1.JPE.6.022001
[23] L. Meng, J. You, T.-F. Guo, and Y. Yang, Accounts of Chemical Research, **49**(1), 155 (2016), https://doi.org/10.1021/acs.accounts.5b00404
[24] J.Y. Jeng, Y.F. Chiang, M.H. Lee, S.R. Peng, T.F. Guo, P. Chen, and T.C. Wen, Advanced Materials, **25**, 3727 (2013), https://doi.org/10.1002/adma.201301327
[25] L. Hu, K. Sun, M. Wang, W. Chen, B. Yang, J. Fu, Z. Xiong, X. Li, X. Tang, Z. Zang, S. Zhang, L. Sun, and M. Li, ACS Applied Materials & Interfaces, **9**(50), 43902 (2017), https://doi.org/10.1021/acsami.7b14592
[26] D. Eli, M.Y. Onimisi, S. Garba, R.U. Ugbe, J.A. Owolabi, O.O. Ige, G.J. Ibeh, and A.O. Muhammed, Journal of the Nigerian Society of Physical Sciences, **1**, 72 (2019), https://doi.org/10.46481/jnsps.2019.13
[27] E. Danladi, A. Shuaibu, M. S. Ahmad, and J. Tasiu, East European Journal of Physics, **2021**(2), 135 (2021), https://doi.org/10.26565/2312-4334-2021-2-11
[28] U. Mandadapu, S.V. Vedanayakam, and K. Thyagarajan, International Journal of Engineering Science and Invention, **2**, 40 (2017).
[29] J.A. Owolabi, M.Y. Onimisi, J.A. Ukwenya, A.B. Bature, U.R. Ushiekpan, American Journal of Physics and Applications, **8**(1), 8, (2020), http://dx.doi.org/10.11648/j.ajpa.20200801.12
[30] A.O. Muhammed, E. Danladi**,** H.P. Boduku, J. Tasiu, M.S. Ahmad, and N. Usman, East European Journal of Physics, **2021**(2), 146 (2021), https://doi.org/10.26565/2312-4334-2021-2-12
[31] S.S. Hussain, S. Riaz, G.A. Nowsherwan, K. Jahangir, A. Raza, M.J. Iqbal, I. Sadiq, S.M. Hussain, and S. Naseem, Journal of Renewable Energy, **2021**, Article ID 6668687 (2021), https://doi.org/10.1155/2021/6668687
[32] S.Z. Haider, H. Anwar, and M. Wang, Semiconductor Science and Technology, **33**, 035001 (2018), https://orcid.org/0000-0002-0473-850X
[33] M.M. Tavakoli, L. Gu, Y. Gao, C. Reckmeier, J. He, A.L. Rogach, Y. Yao, and Z. Fan, Scientific Reports, **5**, 14083 (2015), https://doi.org/10.1038/srep14083
[34] A.A. Paraecattil, J. De Jonghe-Risse, V. Pranculis, J. Teuscher, and J.E. Moser, Journal of Physical Chemistry C, **120**, 19595 (2016), https://doi.org/10.1021/acs.jpcc.6b08022
[35] T. Ouslimane, L. Et-taya, L. Elmaimouni, and A. Benami, Heliyon, **7**, e06379 (2021), https://doi.org/10.1016/j.heliyon.2021.e06379
[36] J.P. Correa-Baena, M. Anaya, G. Lozano, W. Tress, K. Domanski, M. Saliba, T. Matsui, T.J. Jacobsson, M.E. Calvo, A. Abate, M. Gratzel, H. Míguez, and A. Hagfeldt, Advanced Materials, **28**, 5031 (2016), https://doi.org/10.1002/adma.201600624
[37] P. Singh, and N.M. Ravindra, Solar Energy Materials and Solar Cells, **101**, 36 (2012), https://doi.org/10.1016/j.solmat.2012.02.019
[38] B.M. Soucase, I.G. Pradas, and K.R. Adhikari, in: *Perovskite Materials - Synthesis, Characterisation, Properties, and Applications*, (**49659**), 445 (2016), https://doi.org/10.5772/61751
[39] M. Kaifi, and S.K. Gupta, International Journal of Engineering Research and Technology, **12**(10), 1778 (2019).
[40] G.A. Nowsherwan, K. Jahangir, Y. Usman, M.W. Saleem, M. Khalid, Scholars Bulletin, **7**(7), 171 (2021), https://doi.org/10.36348/sb.2021.v07i07.004

[41] U.C. Obi, M.Sc. thesis, department of material science and engineering, African university of science and technology, Abuja, Nigeria (2019).
[42] M.T. Islam, M.R. Jani, S. Rahman, K.M. Shorowordi, S.S. Nishat, D. Hodges, S. Banerjee, H. Efstathiadis, J. Carbonara, and S. Ahmed, SN Applied Sciences, **3**, 504 (2021), https://doi.org/10.1007/s42452-021-04487-7
[43] M.I. Samiul, K. Sobayel, A. Al-Kahtani, M.A. Islam, G. Muhammad, N. Amin, M. Shahiduzzaman, and M. Akhtaruzzaman, Nanomaterials, **11**, 1218 (2021), https://doi.org/10.3390/nano11051218
[44] U. Mandadapu, S.V. Vedanayakam, and K. Thyagarajan, Indian Journal of Science and Technology, **10**(11), 1 (2017).
[45] U. Mandadapu, S.V. Vedanayakam, K.K. Thyagarajan, and B.J. Babu, International Journal of Simulation and Process Modelling, **13**(3), 221 (2018), https://dx.doi.org/10.1504/IJSPM.2018.093097
[46] M.R. Ahmadian-Yazdi, F. Zabihi, M. Habibi, and M. Eslamian, Nanoscale Research Letters, **11**, 408 (2016), https://doi.org/10.1186/s11671-016-1601-8
[47] J. Barbé, M.L. Tietze, M. Neophytou, B. Murali, E. Alarousu, A. El Labban, M. Abulikemu et al, ACS Appl. Mater. Interfaces, **9**, 11828 (2017), https://doi.org/10.1021/acsami.6b13675
[48] K.R. Adhikari, S. Gurung, B.K. Bhattarai, and B.M. Soucase, Physica Status Solidi C, **13**(1), 13 (2016), https://doi.org/10.1002/pssc.201510078
[49] N.A. Sultana, M.O. Islam, M. Hossain, and Z.H. Mahmood, Dhaka University Journal of Science, **66**(2), 109 (2018), http://dx.doi.org/10.3329/dujs.v66i2.54553
[50] Y. Raoui, H. Ez-Zahraouy, N. Tahiri, O. El Bounagui, S. Ahmad, and S. Kazim, Solar Energy, **193**, 948 (2019), https://doi.org/10.1016/j.solener.2019.10.009
[51] A. Singla, R. Pandey, R. Sharma, J. Madan, K. Singh, V.K. Yadav, and R. Chaujar, in: *2018 IEEE Electron Devices Kolkata Conference (EDKCON)*, pp. 278-282 (2018).
[52] T. Kirchartz, T. Agostinelli, M. Campoy-Quiles, W. Gong, and J. Nelson, The Journal of Physical Chemistry Letters, **3**, 3470 (2012), https://doi.org/10.1021/jz301639y
[53] I. Alam, and M.A. Ashraf, *Energy Sources, Part A: Recovery, Utilization, and Environmental Effects*, (2020).
[54] S. Yasin, T. Al Zoubi, and M. Moustafa, Optik, **229**, 166258 (2021), https://doi.org/10.1016/j.ijleo.2021.166258
[55] F.A. Afak, M. Nouredine, S.A. Meftah, Solar Energy, **181**, 372 (2019), https://doi.org/10.1016/j.solener.2019.02.017
[56] M. Kumar A. Raj, A. Kumar, and A. Anshul, Materials Today Communications, **26,** 101851 (2021), https://doi.org/10.1016/j.mtcomm.2020.101851
[57] N. Singh, A. Agarwal, and M. Agarwal, AIP Conference Proceedings, **2265**, 030672 (2020), https://doi.org/10.1063/5.0016929
[58] S. Aseena, N. Abraham, and V.S. Babu, Materials Today: Proceedings, **43**(6), 3432 (2021), https://doi.org/10.1016/j.matpr.2020.09.077
[59] L. Huang, X. Sun, C. Li, R. Xu, J. Xu, Y. Du, Y. Wu, J. Ni, H. Cai, et al, Solar Energy Materials and Solar Cells, **157**, 1038 (2016), https://doi.org/10.1016/j.solmat.2016.08.025
[60] A. Hima, N. Lakhdar, B. Benhaoua, A. Saadoune, I. Kemerchou, and F. Rogti, Superlattices and Microstructures, **129**, 240 (2019), https://doi.org/10.1016/j.spmi.2019.04.007

ОСНОВНІ УСПІХИ В МОДЕЛЮВАННІ ПЕРОВСКІТНИХ СОНЯЧНИХ ЕЛЕМЕНТІВ З ВИКОРИСТАННЯМ SCAPS-1D: ВПЛИВ ПОГЛИНАЧА ТА ТОВЩИНИ ЕТМ

Елі Данладі[a], Дуглас Сейвіор Дого[b], Семюел Уде Міхаел[c], Фелікс Омачоко Улоко[d], Абдул Азіз Омейза Салаву[e]

[a]Кафедра фізики, Федеральний університет медико-санітарних наук, Отукпо, штат Бенуе, Нігерія
[b]Кафедра фізики, Федеральний освітній (технічний) коледж Омоку, штат Ріверс, Нігерія
[c]Кафедра фізики, Нігерійська академія оборони, Кадуна, Нігерія
[d]Кафедра фізики, Федеральний університет, Локоджа, штат Когі, Нігерія
[e]Кафедра комп'ютерних наук Нігерійського університету Нілу

З великим проривом, зафіксованим у ефективності перетворення енергії (PCE) перовскітних сонячних елементів (PSC) з 3,8 % до > 25 %, PSC привернули значну увагу як у наукових колах, так і в промисловості. Однак деякі проблеми залишаються перешкодою для реалізації їх розгортання. Для розробки високоефективних PSC, а також екологічно безпечних пристроїв, бажано моделювати та оптимізувати такі пристрої. Проектувати сонячну батарею без імітаційних робіт непрактично, а також є витрачанням час та коштів. Проектування мінімізує не тільки ризик, час і гроші, а аналізує властивості та роль шарів для оптимізації сонячного елемента для досягнення найкращої продуктивності. Чисельне моделювання для опису фотоелементних тонкошарових пристроїв є зручним інструментом для кращого розуміння основних факторів, що обмежують електричні параметри сонячних елементів, і для підвищення їх продуктивності. У цій оглядовій статті ми зосередилися на останніх досягненнях у моделюванні та оптимізації PSC за допомогою SCAPS-1D з акцентом на товщину поглинача та електронно-транспортного середовища (ЕТМ).

Ключові слова: перовскітові сонячні батареї, поглинач, електронне транспортне середовище, SCAPS

East European Journal of Physics. 4. 18-30 (2021)
DOI: 10.26565/2312-4334-2021-4-02 ISSN 2312-4334

COMPARISON OF ANATASE AND RUTILE FOR PHOTOCATALYTIC APPLICATION: THE SHORT REVIEW †

Volodymyr Morgunov[*,a,b], **Serhii Lytovchenko**[a], **Volodymyr Chyshkala**[a], **Dmytro Riabchykov**[a], **Dementii Matviienko**[a]

[a] *V. N. Karazin Kharkiv National University, 4 Svobody Sq., Kharkiv, 61022, Ukraine;*

[b] *Ukrainian Engineering Pedagogic Academy, vul. Universitets'ka, 16, Kharkiv, 61003, Ukraine*

**Corresponding Author: v.morgunov@karazin.ua*

Received June 30, 2021; revised August 8, 2021; accepted September 16, 2021

The dioxide titanium (TiO_2) is attracting a great attention as semiconductor photocatalyst because of its high photoreactivity, non-toxicity, corrosion resistance, photostability, cheapness. It can be used in wide range of applications: air and water purification, hydrogen (H_2) generation, CO_2 reduction, in photovoltaic application and others. The efforts of scientists were applied to use solar light for dioxide titanium photocatalysis and to enhance the photocatalytic efficiency. In this article we review the properties difference of anatase and rutile modifications of TiO_2. The anatase has a higher photoefficiency. The higher photoefficiency of anatase is due to longer lifetime of charge carriers (lifetime of e^-/h^+ in anatase on 3 order higher than in rutile). But anatase has higher band gap energy (3.2 eV or 388 nm) in comparison with rutile (3.0 eV or 414 nm). Thus, anatase becomes photosensitive in ultraviolet (UV) diapason of light, meanwhile rutile - in violet spectrum of visible light. It is desirable to obtain TiO_2 semiconductor with properties combining best ones from anatase and rutile: higher photoreactivity and smaller band gap. It can be made by using external factors such as electric or magnetic fields, doping and etc.

Keywords: photocatalysis, dioxide titanium, anatase, rutile, band gap, photoefficiency, electron-hole generation.
PACS: 31.10.+z; 71.20.Nr ; 73.20.-r

INTRODUCTION

The photocatalytic properties of TiO_2 was firstly reported in 1972 [1]. After that an interest of researchers from whole the world to photocatalysis was attracted. On the fig. 1 it can be seen that the number of the publications from the 70s until 2020 has significantly increased. This can be explained by the following reasons:

- a wide range of TiO_2 photocatalyst applications:
  - environmental: purification of water and air, CO_2 reduction [2–7];
  - antibacterial and antimicrobial properties [8–11]
  - energy: electricity and hydrogen production [12–16];
  - self-cleaning material and antifogging [17–20];
- high photoreactivity (usually up to ζ (photonic efficiency) = 10 %)
- chemically and biologically inert and non-toxic;
- inexpensive;
- corrosion resistant and photostable [21, 22].

On the other hand, the disadvantages are the following [3, 15]:

- low photon utilization efficiency and slow removal rate;
- rapid recombination of photo-generated electron/hole pairs;
- the poor activation of TiO_2 by visible light.

†**Cite as:** V. Morgunov, S. Lytovchenko, V. Chyshkala, D. Riabchykov, and D. Matviienko, East. Eur. J. Phys. 4, 18 (2021), https://doi.org/10.26565/2312-4334-2021-4-02.

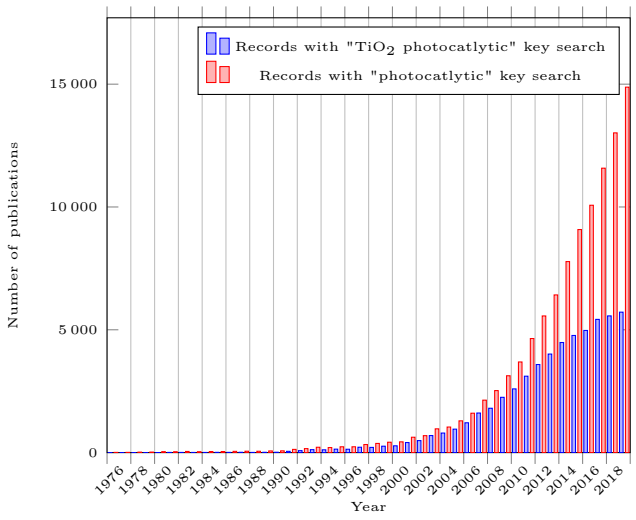

Figure 1: Number of publications of photocatalysis-related and TiO_2 photocatalysis-related papers for the period 1976 - 2020 years. (Source: Web of Science; date: June 9, 2021; keywords: "photocatalytic" and "TiO_2 photocatalytic".)

To solve first issue the nanosized particles of photocatalyst are used.

To reduce recombination electron/hole pairs (second items) some investigators added sacrificial reagents and carbonate salts [15, 23], doped with metals/non-metals [23, 24], loaded noble metal nanoparticles [25, 26] or applied external electrical field [27, 28].

To use visible light for the enhancement photocatalysis (third issue) some investigations focused on modification of TiO_2 by means of metal loading, metal ion doping, dye sensitization, anion doping and metal ion-implantation [29–36].

The aim of this short review is to summarize what was made in this field and elaborate an direction for further investigations.

THEORETICAL ASPECTS OF TIO_2 PHOTOCATALYSIS

We briefly consider the TiO_2 lattice structure and the theory of the photocatalysis. Photocatalysis is complicated phenomena and even definition this phenomena has several version [37]. IUPAC Commissions defined photocatalysis as “a catalytic reaction involving light absorption by a catalyst or a substrate” [38]. In a later revised glossary a complementary definition of a photo-assisted catalysis was also proposed: “catalytic reaction involving production of a catalyst by absorption of light” [39]. And in version of 2011 definition of photocatalysis sounds as following "Change in the rate of a chemical reaction or its initiation under the action of ultraviolet, visible, or infrared radiation in the presence of a substance—the photocatalyst—that absorbs light and is involved in the chemical transformation of the reaction partner" [40]. But more practical definition is "Photocatalysis is phenomena that accelerated chemical reaction in the presence of catalyst which absorbed photons".

A detailed knowledge of the surface structure is the crucial first step in obtaining a detailed knowledge of reaction mechanisms on the molecular scale.

The crystal structure of pure titanium lattice is hexagonal close-packed. The lattice constants of Ti have been determined as [41]

$$a_0 = 2.95111 \pm 0.000\,06\ \text{Å}$$
$$c_0 = 4.68433 \pm 0.000\,10\ \text{Å}$$
$$c/a = 1.5873$$

for a temperature of 25 °C.

Ti hexagonal alpha form changes into a body-centered cubic (lattice) beta form at 882 °C [42].

Titanium dioxide crystallizes in three major different structures:

- rutile (tetragonal, $D_{4h}{}^{14}$-$P4_2/mnm$, a=b=4.584 Å, c=2.953 Å [43]);
- anatase (tetragonal, $D_{4h}{}^{19}$-$I4_1/amd$, a=b=3.782 Å, c=9.502 Å [44]);
- brookite (rhombohedrical, $D_{2h}{}^{15}$-Pbca, a=5.436 Å, b=9.166 Å, c=5.135 Å [44])

Other structures exist as well, for example, cotunnite TiO_2 has been synthesized at high pressures and is one of the hardest polycrystalline materials known [45].

However, only rutile and anatase play any role in the applications of TiO_2 and are of any interest here as they have been studied with surface science techniques. Their unit cells are shown in Fig. 2. In both structures, the basic building block consists of a titanium atom surrounded by six oxygen atoms in a more or less distorted octahedral configuration. In each structure, the two bonds between the titanium and the oxygen atoms at the aspices of the octahedron are slightly longer. A sizable deviation from a 90° bond angle is observed in anatase. In rutile, neighboring octahedra share one corner along ⟨110⟩ – type directions, and are stacked with their long axis alternating by 90°. In anatase the corner-sharing octahedra form (0 0 1) planes. They are connected with their edges with the plane of octahedra below. In all three TiO_2 structures, the stacking of the octahedra results in threefold coordinated oxygen atoms [46].

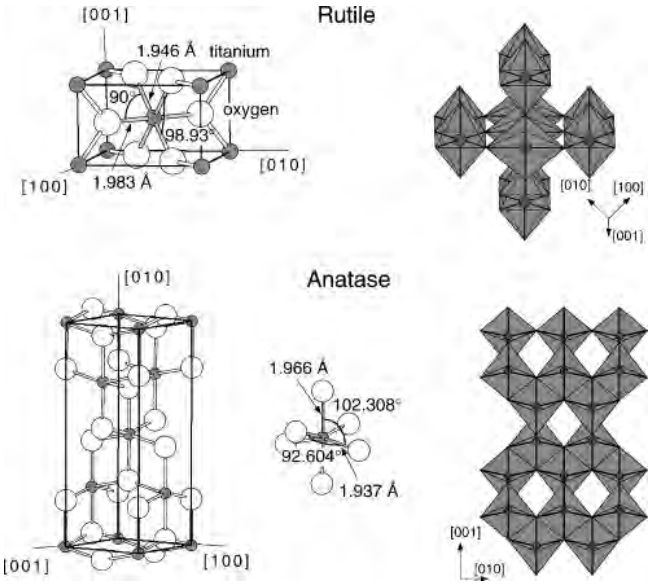

Figure 2: Unit cells of rutile and anatase [46]

.

TiO_2 is a n-type semiconductor [47]. The parameters of TiO_2 lattice at different temperatures are given in Table 1 [48]. Comparison of properties of anatase and rutile is given in Table 2 [49].

TiO_2 itself is not a magnetic material, but when it doped by a few percent of Co dioxide titanium becomes a ferromagnetic [60, 61].

Dark Processes in TiO_2

For semiconductor surface in contact with vacuum surface states are formed. These surfaces alter the electronic structure drastically [47]. As dioxide titanium is covalently bound semiconductor so it has covalent surface states (Shotkey states). Surface states on clean surfaces originate from dangling bonds [62]. These surface states introduce additional energy levels in the middle of the bandgap. To achieve electronic equilibrium between the surface and bulk, a positively charged space charged layer is formed just beneath the surface of an n-type semiconductor [21]. Also, usually, the defects on the TiO_2 surfaces exist in the form of O_vs (s – means surface) by removing surface lattice oxygen atoms in the preparation procedure, leaving behind unpaired electrons (in the Ti 3d orbitals) on the surfaces [63]. These two effects gives the band binding as illustrated on Fig. 3 [46].

Point defects, including O_vs, interstitial titanium ions (Ti^{3+}) and substituted ions, exist in all the crystalline materials of TiO_2. Vacancies and interstitial ions are intrinsic defects of crystalline materials, which may significantly affect the catalytic property, mass transport, and electrical conduction of the materials. The point defects introduce new electronic states in the bandgap of TiO_2, which are called as defect states. The positions of defect states in the bandgap are affected by the phases and surface structures of TiO_2. For example, the defect states of R-TiO_2(110) are located at $\approx 0.8 - 1.0\ eV$ below the CB edge [64]. However, the defect states of A-TiO_2(101) are located at $\approx 0.4 - 1.1\ eV$ below the CB edge [65–69]. Different types of deffects in TiO_2 are shown on Fig. 4 [70].

For realistic cases, when electron-rich TiO_2 surfaces adsorb different types of adsorbates, charge transfer between surfaces and adsorbates will occur, which may even revert the direction of band bending [69].

Table 1: The parameters of TiO_2 lattice at different temperatures

Lattice parameters		Temperature, °C
Dimensions	Lattice constant, Å	
a	3.7845	28
c	9.5143	
a	3.7855	84
c	9.5185	
a	3.7866	161
c	9.5248	
a	3.7875	210
c	9.5294	
a	3.7884	258
c	9.5342	
a	3.7894	306
c	9.5374	
a	3.7907	354
c	9.5432	
a	3.7923	449
c	9.5548	
a	3.7939	497
c	9.5595	
a	3.7948	534
c	9.5669	
a	3.7962	571
c	9.5754	
a	3.7970	608
c	9.5794	
a	3.7989	645
c	9.5872	
a	3.7998	679
c	9.5933	
a	3.8009	712
c	9.5975	

Table 2: Properties of anatase and rutile

Property	Anatase	Rutile	Reference
Crystal structure	Tetragonal	Tetragonal	[50]
Atoms per unit cell (Z)	4	2	[51]
Space group	$I\frac{4}{\alpha}md$	$P\frac{4_2}{m}nm$	[52]
Type of band gap	indirect	direct	[53]
Lattice parameters (nm)	a = 0.3785	a = 0.4594	
	c = 0.9514	c = 0.29589	[51]
Unit cell volume (nm^3)	0.1363	0.0624	[51]
Density (kg/m^3)	3894	4250	[51]
Calculated band gap			
(eV)	3.23–3.59	3.02–3.24	[54–57]
(nm)	345.4–383.9	382.7–410.1	
Experimental band gap			
(eV)	$\sim$ 3.2	$\sim$ 3.0	[56, 58]
(nm)	$\sim$ 387	$\sim$ 413	
Refractive index	2.54, 2.49	2.79, 2.903	[50]
Solubility in HF	Soluble	Insoluble	[59]
Solubility in H_2O	Insoluble	Insoluble	[50]
Hardness (Mohs)	5.5–6	6–6.5	[49]
Bulk modulus (GPa)	183	206	[57]

The accumulation of electrons at the surface determines the surface chemistry of TiO_2. All processes occurring at the surface of semiconductors are driven to achieve an equilibrium between the Fermi level potential and the chemical potential of the adsorbates, with the position of the Fermi level being equal to the work function of the semiconductor [21].

Deskins et al. [70] suggested that the relative electronegativity of TiO_2 surfaces and adsorbates may perhaps be the key parameter to understand the charge transfer between TiO_2 surfaces and adsorbates. Based on their theoretical works, electron transfer from the TiO_2 surface to adsorbates only occurs when the electronegativity of adsorbates ($\chi_{adsorbate}$) is larger than that of TiO_2 (χ_{TiO_2}) (Figure 5a). Otherwise, no charge transfer occurs (Figure 5b).

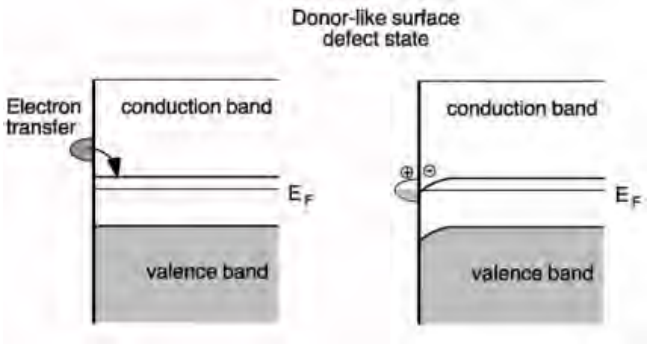

Figure 3: Schematic diagram of the band-bending effect due to donor-like surface defect states. Surface oxygen vacancies create a defect state and electrons are donated to the system. A charge accumulation layer is created in the near-surface region and the bands in the n-type semiconducting TiO_2 sample bend downwards.

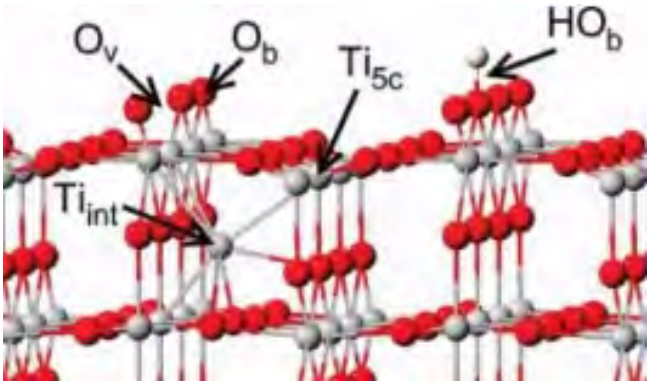

Figure 4: Structure of the rutile (110) surface. Red spheres represent O atoms, gray spheres represent Ti atoms, and white spheres represent H atoms. The notable surface sites are the bridging row O atoms (O_b) and the five-coordinated Ti sites (Ti_{5c}). Also shown are defects that lead to surface reduction: O vacancies (O_v), surface hydroxyls (HO_b), and interstitial Ti atoms (Ti_{int}).

Illumination of TiO_2

When exposed to light (sun- or ultraviolet- light), the semiconductor absorbs photons with sufficient energy (more or equal to band gap energy) to inject electrons from the valence band to its conduction band, creating electron/hole pairs [47] as shown on Fig. 6. As magnitude of the band gap for TiO_2 semiconductor is $\sim 3.2\ eV$ for anatase modification and $\sim 3.0\ eV$ for rutile modification, so there is wavelength threshold of $\lambda < 388\ nm$ for anatase and $\lambda < 414\ nm$ for rutile to become electronically conductive. It should be noted that in sunlight the percentage of ultraviolet is about 3 % [71].

Photocatalytic reactions can only occur at the TiO_2 surface. After migration to surface of TiO_2 electrons e^- and holes h^+ can oxidize and reduce absorbed molecules, respectively. Some of electrons and holes are recombined. In fact, time-resolved spectroscopy studies reveal that the most of photogenerated e^-/h^+ pairs (~ 90 %) recombine rapidly after excitation. This is assumed to be one reason for the relatively low values of photonic efficiency ζ (the rate of the formation of the reaction products divided by the incident flow) [21].

Schematically these steps are shown on Fig 7 [72] and in the following table [73]:

Table 3: Schematic model illustrating the main steps associated with TiO_2 photocatalysis

No of step	Reaction	Time
1	Charge carrier generation: $TiO_2 \xrightarrow{h\nu} TiO_2(e^-_{CB} + h^+_{VB})$ and thermalization: $e^{-*} \rightarrow e^- + heat(phonons)$ $h^{+*} \rightarrow h^+ + heat(phonons)$	<100 fs 10 fs
2	Trapping CB electrons (e^-_{cb}) at defect Ti^{4+} sites: $Ti^{4+}_{ds} + e^-_{cb} \rightarrow Ti^{3+}_{ds}$ [74]	200 fs
3	Trapping valence band holes (h^+_{vb}) at terminal Ti–OH or surface Ti–O–Ti sites: $Ti - O_sH\ or\ Ti - Os - Ti + h^+_{vb} \rightarrow Ti - O_sH^{\cdot +}\ or\ Ti - O^{\cdot +}_s - Ti$ [74]	200 fs
4	Reduction of adsorbed electron acceptor (A_{ad}) with e^-_{cb} at reduction sites: $e^-_{cb} + A_{ad} \rightarrow A^{\cdot -}_{ad}$	>10 ns
5	Reduction of A_{ad} with electrons trapped at defect sites (Ti^{3+}_{ds}): $Ti^{3+}_{ds} + A_{ad} \rightarrow Ti^{4+}_{ds} + A^{\cdot -}_{ad}$	slow process

6	Oxidation of adsorbed electron donor (D_{ad}) by trapped holes at oxidation sites: $Ti-O_sH^{\cdot+}$ *or* $Ti-O_s^{\cdot+}-Ti+D_{ad}\rightarrow Ti-O_sH$ *or* $Ti-O_s-Ti+D_{ad}^{\cdot+}$		100 ps-10 ns
7	Recombination of e_{cb}^- with trapped holes [75]:		
	$e_{cb}^-+Ti-O_sH^{\cdot+}$ *or* $Ti-O_s^{\cdot+}-Ti\rightarrow Ti-O_sH$ *or* $Ti-O_s-Ti$	*rutile* *anatase*	24 *ns* $\sim$ *few ms*
8	Recombination of Ti_{ds}^{3+} with trapped holes [75]:		
	$Ti_{ds}^{3+}+Ti-O_sH^{\cdot+}$ *or* $Ti-O_s^{\cdot+}-Ti\rightarrow Ti_{ds}^{4+}+Ti-O_sH$ *or* $Ti-O_s-Ti$	*rutile* *anatase*	[48 *ns*] [$\sim$ *few ns*]

Charge carrier generation and thermalization

Charge carrier generation in anatase and rutile is running in different ways because anatase belongs to indirect band gap semiconductor, rutile - to direct one [76]. The schemes of direct and indirect band gaps are shown on Fig. 8a. Indirect transitions involve either the absorption of both a photon and a phonon or the absorption of a photon and the emission of a phonon. The conditions for indirect transitions, as shown in Fig. 8a, can be summarized in the following way [76]. For the conservation of momentum,

$$k_{ph}=k_f-k_i$$

where k_{ph} is the wave vector for the phonon, and k_f and k_i are the wave vectors for the final and initial states of the transition, respectively.

For direct transitions $k_{ph}=0$ and for indirect transitions $k_{ph}\neq 0$.

After illumination of TiO_2 by UV photons with energy more or equal to band gap width free electrons and holes are generated (fig. 6). It should be noted that the penetration depth δ_p of ultraviolet light in TiO_2 is approximately equal to 160 nm [77]. Therefore electron-hole pairs are generated in the outer surface region of the TiO_2. Due to the near surface electric field the recombination of e^-/h^+ is retarded [21].

Continuous illumination will result in the annihilation of this electric field, that is, a band flattening [78]. Yates et al. [21, 79] explained the appearance of this band flattening by a band shifting at the surface, because the free electrons move to the bulk, while free holes accumulate at the surface where the negative charge is neutralized. However, band flattening can also be explained by a band shifting in the bulk region, as the number of electrons increases in the bulk upon illumination.

According to electron paramagnetic resonance (EPR) spectroscopy process of pair generation occurs in femtoseconds [80] (1 fs = $10^{-15}s$) up to 100 fs. But it is obviously that e^-/h^+ pair generation time for indirect and direct TiO_2 modifications(anatase and rutile, respectively) is differ. There is no data in literature concerning this difference in time of the charge carrier generation.

In an ideal photocatalyst, all photon energy invested in charge carrier generation would be available for redox reactions, namely, hot electrons (or deep holes) produced by shorter wavelength light have more reductive (or oxidative) capacity than those at the band edges of a photocatalyst [69]. However, charge carrier thermalization occurs rapidly.

After e^-/h^+ generation the energetic electrons continue to travel in the solid, losing its energy and producing shallower core holes. This cascade process, often called "thermalization", is repeated until the hole is created at the top of valence band and fully thermalized electrons settling in the bottom of the conduction band [81].

In [82] authors found that time of thermalization in TiO_2 (110) is equal to 10 fs.

These studies clearly demonstrate that charge carrier thermalization occurs prior to recombination or transfer.

Electron and hole trapping

Once produced, the charge carriers become trapped, either in shallow traps (ST) or in deep traps (DT) [80]. The photogenerated charge carriers can be trapped in either in bulk or on the surface. In generally, surface trapping at either the subsurface or the surface region is preferred in semiconductor nanoparticles [83, 84].

Because of the upward band bending in n-type TiO_2, the photogenerated electrons are forced to move from its surface into the bulk, where they can be delocalized over different Ti sites. Both theoretical and experimental studies are predicting bulk (subsurface) trapping rather than surface trapping of these electrons [85–87]. However, alternative studies also exist demonstrating that $Ti^{4+}OH$ groups located at the TiO_2 surface can act as trapping centers for the electrons, resulting in the formation of $Ti^{3+}OH$ species. Such species can attract holes, thus behaving as recombination centers [88–90].

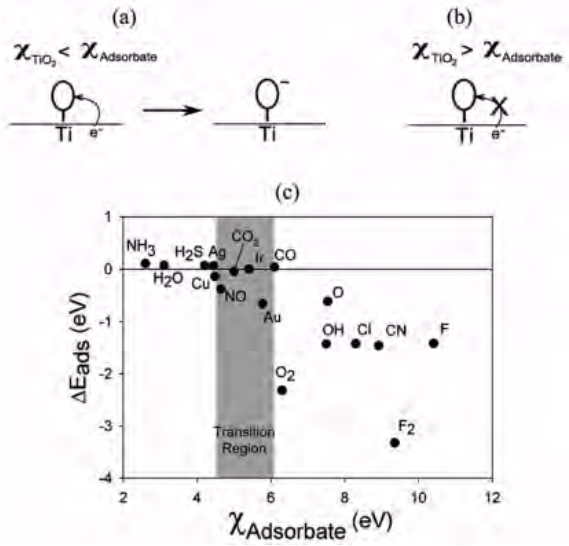

Figure 5: The effect of electronegativity on the adsorption energy of adsorbates on TiO_2.

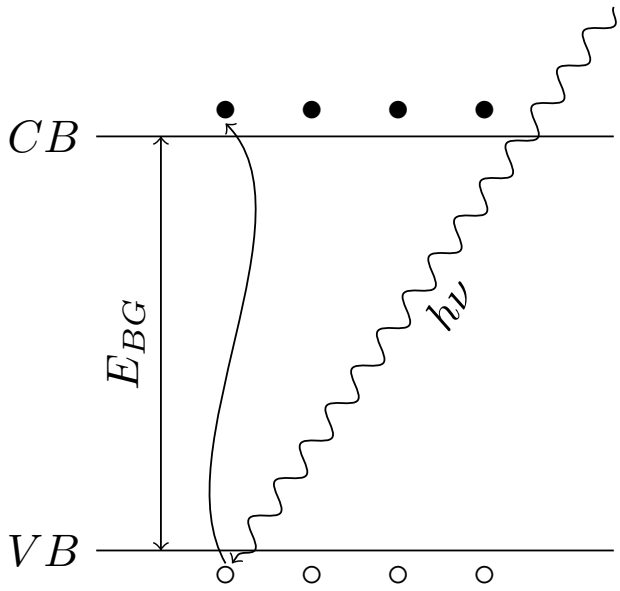

Figure 6: Scheme of electron/hole formation in the semiconductors. CB - conduction band, VB – valence band, E_{BG} – energy band gap, ○ - holes, ● - electrons, $h\nu$ - photon.

Upon 355 nm excitation, photogenerated electrons and holes are trapped very rapidly within 100 fs. However, the excess energy of free electrons in the TiO_2 CB slows the trapping time to ≈200 fs upon 266 nm irradiation [91].

Reduction of electron acceptors A_{ad} with electrons and oxidation of adsorbed electron donor D_{ad} by holes

Following their formation by light excitation, electrons and holes can easily be transferred to electron and hole acceptors, respectively. The quantum efficiency of these reactions depends on the charge-transfer rate at the interface, on the recombination rate within the particle, and on the transit time of the photogenerated charge carriers to the surface [21].

Photocatalytic reactions occur on the surface of semiconductor. Photocatalytic reactions can be reduction and oxidation ones. These reactions are form reactive oxygen species (ROS), such as superoxide anion radicals ($O_2^{\cdot -}$), hydroperoxy radicals ($\cdot OOH$), hydrogen peroxide (H_2O_2), and hydroxyl radicals ($\cdot OH$), under both aqueous and aerated conditions [21, 92]. These ROS play a crucial role in the photocatalysis on TiO_2 for water purification, air cleaning, self-cleaning, self-sterilization, etc. The reduction reactions on photo-irradiated TiO_2 under acidic conditions can be depicted as follows [21, 73, 92, 93]:

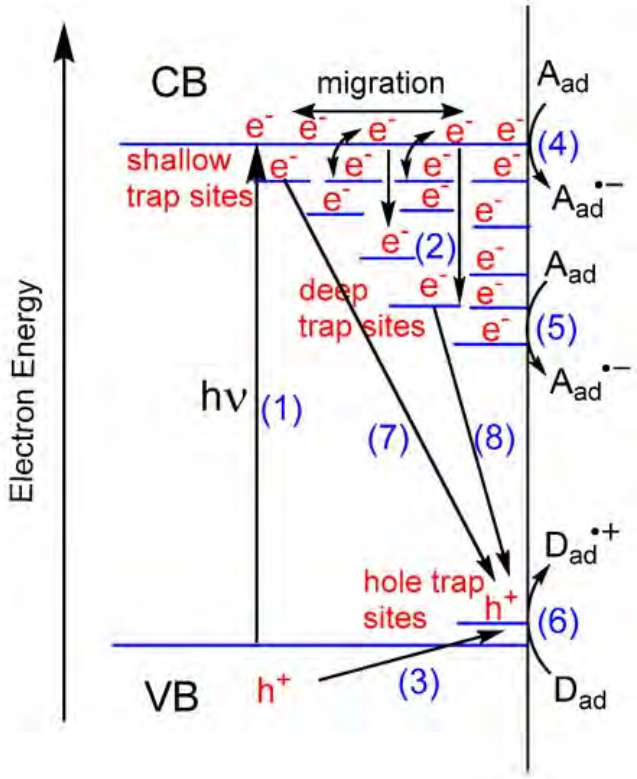

Figure 7: Schematic model illustrating the main steps associated with TiO_2 photocatalysis

Photoreduction: $O_2 + (Ti^{3+}_{ds} \ and \ e^-_{cb}) \rightarrow O_2^{\cdot -}$

Protonation: $O_2^{\cdot -} + H^+ \rightarrow \cdot OOH$

Disproportionation: $2 \cdot OOH \rightarrow H_2O_2 + O_2$

Photoreduction: $H_2O_2 + (Ti^{3+}_{ds} \ and \ e^-_{cb}) \rightarrow \cdot OH + OH^-$

In oxidation reactions hydroxyl radicals OH are formed via direct hole oxidation of adsorbed H_2O [94]:

$$h^+ + H_2O \rightarrow \cdot OH$$

There are two types of $\cdot OH$ radicals: free mobile (OH_f) and surface bound (OH_s) hydroxyl radicals, which exhibit different reactivities depending on the properties of target pollutants. The OH_f generation and the subsequent diffusion from the surface are critical in achieving the mineralization of non-adsorbing substrates by extending the reaction zone from the surface to the solution bulk [95].

For environmental application main role plays free hydroxyl radical OH_f. As mentioned in [95] these radicals are producing mainly by anatase modification of titanium dioxide.

The electron-hole recombination

The electron-hole recombination process is undesirable one because it reduce efficiency of photochemical reactions occurring on the surface of TiO_2. As it was above mentioned about 90 % of charge carriers recombine decreasing efficiency of the photocatalytic reactions.

The electron-hole recombination is found to be quite rapid cases, with a majority of recombination complete within 50 ps[96]. In [97] revealed significantly higher yields and longer lifetimes of charge carriers in the anatase powder. Yamada et al [75] stated that electrons lifetime in rutile is equal to 24 ns, in anatase - microseconds; lifetime of holes in rutile is equal to 48 ns, in anatase - nanoseconds. The longer charge carriers lifetime in anatase is one of the main reason why anatase has more photoactivity property.

There are three basic recombination mechanisms that are responsible for carrier annihilation in a semiconductor [98]:

1. band-to-band recombination, which occurs when an electron moves from the conduction band (CB) to the empty valence band (VB) containing a hole (the rate of band-to-band recombination depends on

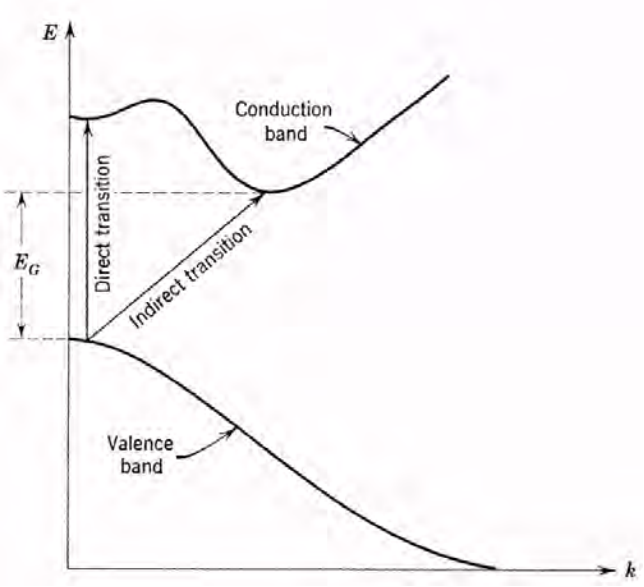

(a) Direct and indirect transitions between valence and conduction bands with extrema at different values of k.

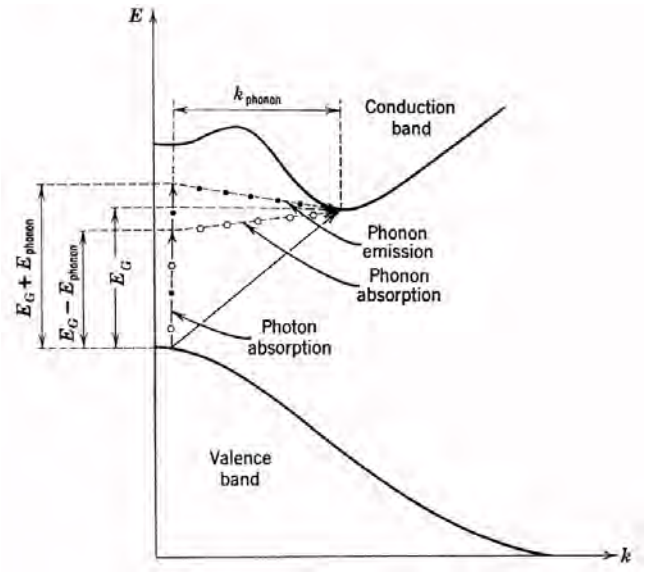

(b) Indirect transitions between conduction and valence bands with extrema at different values of k. Two processes are possible, one involving the absorption of a photon and a phonon, and the other involving the absorption of a photon and the emission of a phonon.

Figure 8: Direct and indirect transitions between valence and conduction bands [76].

the product of the concentrations of available electrons and holes and is second order in charge carrier concentration];

2. trap-assisted recombination (Shockley-Read-Hall Model, SRH model),which occurs when an electron in the CB recombines indirectly with a hole in the VB at a "trap" state;
3. Auger recombination, which occurs when an electron-hole pair recombine in a band-to-band transition giving off the generated energy to another electron or hole.

The electron-hole recombination process reaction successfully compete with the hole-transfer [99].

As it was mentioned earlier time of electron-pair recombination in rutile shorter than in anatase. This is one of the main reason why anatase is more photoactive. Thi is because of that anatase has indirect band gap and to recombine the

OH generation

CONCLUSION

In the article the difference between anatase and rutile was considered as from photocatalytic point of view as well as from structure point of view. The main differences are

- Cell volume of rutile smaller then anatase one by factor ≈ 2.
- Rutile is more stable modification of dioxide titanium in comparison with anatase.
- Width of band gap in anatase is equal to 3.2 eV (388 nm - ultraviolet light), meanwhile, rutile has width of band gap equal to 3.0 eV that corresponds to 414 nm that is in visible diapason of light.
- Anatase has indirect transitions between conduction and valence bands, rutile - direct.
- Recombination of electron/hole pairs is quicker in rutile then in anatase because recombination in anatase slower because it has indirect transition in band gap.
- Free radical OH_f can be generated by anatase only.

Thus, anatase has more photocatalytic activity in comparison with rutile because of more longer lifetime of charge carriers. But the width of rutile band gap is narrower so rutile has photocatalytic properties in visible diapason of light - the aim of last decade of investigations. It is desire to increase time life of electrons and holes in rutile. It can be done by external forces, for example electric or magnetic fields.

ORCID IDs

Volodymyr Morgunov, https://orcid.org/0000-0002-8681-1941,
Serhii Lytovchenko, https://orcid.org/0000-0002-3292-5468,
Volodymyr Chyshkala, https://orcid.org/0000-0002-8634-4212,
Dmytro Riabchykov, https://orcid.org/0000-0002-9529-0412,
Dementii Matviienko, https://orcid.org/0000-0001-9862-5815.

REFERENCES

[1] A. Fujishima and K. Honda, Nature **238**, 37–38 (1972), https://doi.org/10.1038/238037a0.

[2] T. Ochiai and A. Fujishima, Journal of Photochemistry and photobiology C: Photochemistry reviews **13**, 247–262 (2012), https://doi.org/10.1016/j.jphotochemrev.2012.07.001.

[3] F. He, W. Jeon, and W. Choi, Nature Communications **12**, 1–4 (2021), https://doi.org/10.1038/s41467-021-22839-0.

[4] A Fernandez, G Lassaletta, V. Jimenez, A Justo, A. Gonzalez-Elipe, J.-M. Herrmann, H Tahiri, and Y Ait-Ichou, Applied Catalysis B: Environmental **7**, 49–63 (1995), https://doi.org/10.1016/0926-3373(95)00026-7.

[5] K. Nakata, T. Ochiai, T. Murakami, and A. Fujishima, Electrochimica Acta **84**, ELECTROCHEMICAL SCIENCE AND TECHNOLOGYState of the Art and Future PerspectivesOn the occasion of the International Year of Chemistry (2011), 103–111 (2012), https://doi.org/10.1016/j.electacta.2012.03.035.

[6] J. Ângelo, L. Andrade, L. M. Madeira, and A. Mendes, en, Journal of Environmental Management **129**, 522–539 (2013), https://doi.org/10.1016/j.jenvman.2013.08.006.

[7] O. Ola and M. M. Maroto-Valer, en, Journal of Photochemistry and Photobiology C: Photochemistry Reviews **24**, 16–42 (2015), https://doi.org/10.1016/j.jphotochemrev.2015.06.001.

[8] G. Fu, P. S. Vary, and C.-T. Lin, The Journal of Physical Chemistry B **109**, 8889–8898 (2005), https://doi.org/10.1021/jp0502196.

[9] Y. Liu, X. Wang, F. Yang, and X. Yang, en, Microporous and Mesoporous Materials **114**, 431–439 (2008), https://doi.org/10.1016/j.micromeso.2008.01.032.

[10] U. Joost, K. Juganson, M. Visnapuu, M. Mortimer, A. Kahru, E. Nõmmiste, U. Joost, V. Kisand, and A. Ivask, en, Journal of Photochemistry and Photobiology B: Biology **142**, 178–185 (2015), https://doi.org/10.1016/j.jphotobiol.2014.12.010.

[11] A. Kubacka, M. Ferrer, M. L. Cerrada, C. Serrano, M. Sánchez-Chaves, M. Fernández-García, A. de Andrés, R. J. J. Riobóo, F. Fernández-Martín, and M. Fernández-García, en, Applied Catalysis B: Environmental **89**, 441–447 (2009), https://doi.org/10.1016/j.apcatb.2009.01.002.

[12] S. Sfaelou and P. Lianos, AIMS Mater. Sci. **3**, 270–288 (2016).

[13] M. Kaneko, N. Gokan, N. Katakura, Y. Takei, and M. Hoshino, Chem. Commun., 1625–1627 (2005), https://doi.org/10.1039/B418580C.

[14] K. Iyatani, Y. Horiuchi, M. Moriyasu, S. Fukumoto, S.-H. Cho, M. Takeuchi, M. Matsuoka, and M. Anpo, J. Mater. Chem. **22**, 10460–10463 (2012), https://doi.org/10.1039/C2JM32064A.

[15] M. Ni, M. K. Leung, D. Y. Leung, and K. Sumathy, Renewable Sustainable Energy Rev. **11**, 401–425 (2007), https://doi.org/10.1016/j.rser.2005.01.009.

[16] V. Kumaravel, S. Mathew, J. Bartlett, and S. C. Pillai, Applied Catalysis B: Environmental **244**, 1021–1064 (2019), https://doi.org/10.1016/j.apcatb.2018.11.080.

[17] S. Banerjee, D. D. Dionysiou, and S. C. Pillai, Applied Catalysis B: Environmental **176-177**, 396–428 (2015), https://doi.org/10.1016/j.apcatb.2015.03.058.

[18] C. Euvananont, C. Junin, K. Inpor, P. Limthongkul, and C. Thanachayanont, Ceramics International **34**, The Fifth Asian Meeting on Electroceramics (AMEC-5), 1067–1071 (2008), https://doi.org/10.1016/j.ceramint.2007.09.043.

[19] A. Folli, C. Pade, T. B. Hansen, T. De Marco, and D. E. Macphee, Cement and Concrete Research **42**, 539–548 (2012), https://doi.org/10.1016/j.cemconres.2011.12.001.

[20] C. Garlisi and G. Palmisano, en, Applied Surface Science **420**, 83–93 (2017), https://doi.org/10.1016/j.apsusc.2017.05.077.

[21] J. Schneider, M. Matsuoka, M. Takeuchi, J. Zhang, Y. Horiuchi, M. Anpo, and D. W. Bahnemann, Chemical reviews **114**, 9919–9986 (2014), https://doi.org/10.1021/cr5001892.

[22] O. Carp, C. L. Huisman, and A. Reller, en, Progress in Solid State Chemistry **32**, 33–177 (2004), https://doi.org/10.1016/j.progsolidstchem.2004.08.001.

[23] M. Yadav, A. Yadav, R. Fernandes, Y. Popat, M. Orlandi, A. Dashora, D. C. Kothari, A. Miotello, B. L. Ahuja, and N. Patel, en, Journal of Environmental Management **203**, 364–374 (2017), https://doi.org/10.1016/j.jenvman.2017.08.010.

[24] K. Subalakshmi and J. Senthilselvan, en, Solar Energy **171**, 914–928 (2018), 10.1016/j.solener.2018.06.077.

[25] M. Diak, E. Grabowska, and A. Zaleska, en, Applied Surface Science **347**, 275–285 (2015), https://10.1016/j.apsusc.2015.04.103.

[26] X. Pan and Y.-J. Xu, The Journal of Physical Chemistry C **117**, 17996–18005 (2013), 10.1021/jp4064802.

[27] Z. Jiang, H. Wang, H. Huang, and C. Cao, en, Chemosphere **56**, 503–508 (2004), https://doi.org/10.1016/j.chemosphere.2004.02.006.

[28] V. Morgunov and D. Rudenko, *Method of photocatalytic disinfection and purification of air from harmful gas compounds, dust*, UA Patent 108560, Jul. 2016.

[29] K.-H. Chung, S. Jeong, B.-J. Kim, K.-H. An, Y.-K. Park, and S.-C. Jung, en, International Journal of Hydrogen Energy **43**, 11422–11429 (2018), https://doi.org/10.1016/j.ijhydene.2018.03.190.

[30] J. F. Gomes, A. Lopes, K. Bednarczyk, M. Gmurek, M. Stelmachowski, A. Zaleska-Medynska, M. E. Quinta-Ferreira, R. Costa, R. M. Quinta-Ferreira, and R. C. Martins, en, ChemEngineering **2**, 4 (2018), https://doi.org/10.3390/chemengineering2010004.

[31] N. Singhal and U. Kumar, en, Molecular Catalysis **439**, 91–99 (2017), https://doi.org/10.1016/j.mcat.2017.06.031.

[32] J. Choi, H. Park, and M. R. Hoffmann, The Journal of Physical Chemistry C **114**, 783–792 (2010), https://doi.org/10.1021/jp908088x.

[33] J. M. Macák, H. Tsuchiya, A. Ghicov, and P. Schmuki, en, Electrochemistry Communications **7**, 1133–1137 (2005), https://doi.org/10.1016/j.elecom.2005.08.013.

[34] G. Yang, Z. Yan, and T. Xiao, en, Applied Surface Science **258**, 8704–8712 (2012), https://doi.org/10.1016/j.apsusc.2012.05.078.

[35] A. Zaleska, Recent Patents on Engineering **2**, 157–164 (2008), https://doi.org/10.2174/187221208786306289.

[36] S. G. Kumar and K. S. R. K. Rao, en, Applied Surface Science, 2nd International Symposium on Energy and Environmental Photocatalytic Materials **391**, 124–148 (2017), https://doi.org/10.1016/j.apsusc.2016.07.081.

[37] N. Serpone and A. V. Emeline, en, International Journal of Photoenergy **4**, 91–131 (2002), https://dpoi.org/10.1155/S1110662X02000144.

[38] S. E. Braslavsky and K. N. Houk, de, Pure and Applied Chemistry **60**, 1055–1106 (1988), https://doi.org/10.1351/pac198860071055.

[39] J. W. Verhoeven, de, Pure and Applied Chemistry **68**, 2223–2286 (1996), https://doi.org/10.1351/pac199668122223.

[40] S. E. Braslavsky, A. M. Braun, A. E. Cassano, A. V. Emeline, M. I. Litter, L. Palmisano, V. N. Parmon, and N. Serpone, de, Pure and Applied Chemistry **83**, 931–1014 (2011), https://doi.org/10.1351/PAC-REC-09-09-36.

[41] R. M. Wood, Proceedings of the Physical Society (1958-1967) **80**, 783 (1962), https://doi.org/10.1088/0370-1328/80/3/323.

[42] C. A. Hampel, *The encyclopedia of the chemical elements,* English, OCLC: 449569 (Reinhold Book Corp., New York, 1968).

[43] F. Grant, Reviews of Modern Physics **31**, 646–674 (1959), https://doi.org/10.1103/RevModPhys.31.646.

[44] G. V. Samsonov, *The Oxide Handbook*, en, IFI Data Base Library (Springer US, 1973),https://doi.org/10.1007/978-1-4615-9597-7.

[45] L. Dubrovinsky, N. Dubrovinskaia, V. Swamy, J. Muscat, N. Harrison, R. Ahuja, B. Holm, and B. Johansson, Nature **410**, 653–654 (2001), https://doi.org/10.1038/35070650.

[46] U. Diebold, en, Surface Science Reports **48**, 53–229 (2003), https://doi.org/10.1016/S0167-5729(02)00100-0.

[47] S. M. Bard A J and S Licht, *Encyclopedia of electrochemistry. Vol. 6. Semiconductor electrodes and photoelectrochemistry*, 2002.

[48] K. V. K. Rao, S. V. N. Naidu, and L. Iyengar, en, Journal of the American Ceramic Society **53**, 124–126 (1970), https://doi.org/10.1111/j.1151-2916.1970.tb12051.x.

[49] D. A. H. Hanaor and C. C. Sorrell, en, Journal of Materials Science **46**, 855–874 (2011), https://doi.org/10.1007/s10853-010-5113-0.

[50] T. Jones, J. Edwards, and J. Kallioinen, en, in *Kirk-Othmer Encyclopedia of Chemical Technology* (American Cancer Society, 2019), pp. 1–76,https://doi.org/10.1002/0471238961.0914151805070518.a01.pub4.

[51] J. K. Burdett, T. Hughbanks, G. J. Miller, J. W. Richardson, and J. V. Smith, Journal of the American Chemical Society **109**, 3639–3646 (1987), https://doi.org/10.1021/ja00246a021.

[52] T. Hahn and P. Paufler, en, Crystal Research and Technology **19**, 1306–1306 (1984), https://doi.org/10.1002/crat.2170191008.

[53] J. Zhang, P. Zhou, J. Liu, and J. Yu, en, Physical Chemistry Chemical Physics **16**, 20382–20386 (2014), https://doi.org/10.1039/C4CP02201G.

[54] K Madhusudan Reddy, S. V. Manorama, and A Ramachandra Reddy, en, Materials Chemistry and Physics **78**, 239–245 (2003), https://doi.org/10.1016/S0254-0584(02)00343-7.

[55] N. Serpone, The Journal of Physical Chemistry B **110**, 24287–24293 (2006), https://doi.org/10.1021/jp065659r.

[56] N. Daude, C. Gout, and C. Jouanin, Physical Review B **15**, 3229–3235 (1977), https://doi.org/10.1103/PhysRevB.15.3229.

[57] H. Wang and J. P. Lewis, en, Journal of Physics: Condensed Matter **18**, 421–434 (2005), https://doi.org/10.1088/0953-8984/18/2/006.

[58] D. Mardare, M. Tasca, M. Delibas, and G. I. Rusu, en, Applied Surface Science **156**, 200–206 (2000), https://doi.org/10.1016/S0169-4332(99)00508-5.

[59] T. Ohno, K. Sarukawa, and M. Matsumura, The Journal of Physical Chemistry B **105**, 2417–2420 (2001), https://doi.org/10.1021/jp003211z.

[60] S. Chambers, S. Thevuthasan, R. Farrow, R. Marks, J. Thiele, L. Folks, M. Samant, A. Kellock, N. Ruzycki, D. Ederer, and U. Diebold, Applied Physics Letters **79**, 3467–3469 (2001), https://doi.org/10.1063/1.1420434.

[61] Y. Matsumoto, M. Murakami, T. Shono, T. Hasegawa, T. Fukumura, M. Kawasaki, P. Ahmet, T. Chikyow, S.-Y. Koshihara, and H. Koinuma, Science **291**, 854–856 (2001), https://doi.org/10.1126/science.1056186.

[62] W. Mönch, *Semiconductor Surfaces and Interfaces*, en, 3rd ed., Springer Series in Surface Sciences (Springer-Verlag, Berlin Heidelberg, 2001),https://doi.org/10.1007/978-3-662-04459-9.

[63] P. J. D. Lindan, N. M. Harrison, M. J. Gillan, and J. A. White, Physical Review B **55**, 15919–15927 (1997), https://doi.org/10.1103/PhysRevB.55.15919.

[64] Z. Wang, B. Wen, Q. Hao, L.-M. Liu, C. Zhou, X. Mao, X. Lang, W.-J. Yin, D. Dai, A. Selloni, and X. Yang, Journal of the American Chemical Society **137**, 9146–9152 (2015), https://doi.org/10.1021/jacs.5b04483.

[65] B. Wen, Q. Hao, W.-J. Yin, L. Zhang, Z. Wang, T. Wang, C. Zhou, A. Selloni, X. Yang, and L.-M. Liu, en, Physical Chemistry Chemical Physics **20**, 17658–17665 (2018), https://doi.org/10.1039/C8CP02648C.

[66] W.-J. Yin, B. Wen, C. Zhou, A. Selloni, and L.-M. Liu, en, Surface Science Reports **73**, 58–82 (2018), https://doi.org/10.1016/j.surfrep.2018.02.003.

[67] A. G. Thomas, W. R. Flavell, A. K. Mallick, A. R. Kumarasinghe, D. Tsoutsou, N. Khan, C. Chatwin, S. Rayner, G. C. Smith, R. L. Stockbauer, S. Warren, T. K. Johal, S. Patel, D. Holland, A. Taleb, and F. Wiame, Physical Review B **75**, 035105 (2007), https://doi.org/10.1103/PhysRevB.75.035105.

[68] M. Setvin, C. Franchini, X. Hao, M. Schmid, A. Janotti, M. Kaltak, C. G. Van de Walle, G. Kresse, and U. Diebold, Physical Review Letters **113**, 086402 (2014), https://doi.org/10.1103/PhysRevLett.113.086402.

[69] Q. Guo, C. Zhou, Z. Ma, and X. Yang, en, Advanced Materials **31**, 1901997 (2019), https://doi.org/10.1002/adma.201901997.

[70] N. A. Deskins, R. Rousseau, and M. Dupuis, The Journal of Physical Chemistry C **114**, 5891–5897 (2010), https://doi.org/10.1021/jp101155t.

[71] R. R. D. Center, ASTM G173-03 Tables (2012).

[72] M. A. Henderson, en, Surface Science Reports **66**, 185–297 (2011), 10.1016/j.surfrep.2011.01.001.

[73] S. Kohtani, A. Kawashima, and H. Miyabe, en, Catalysts **7**, 303 (2017), https://doi.org/10.3390/catal7100303.

[74] Y. Tamaki, A. Furube, M. Murai, K. Hara, R. Katoh, and M. Tachiya, en, Physical Chemistry Chemical Physics **9**, 1453–1460 (2007), https://doi.org/10.1039/B617552J.

[75] Y. Yamada and Y. Kanemitsu, Applied Physics Letters **101**, 133907 (2012), https://doi.org/10.1063/1.4754831.

[76] R. H. Bube, *Photoconductivity of solids* (Wiley, New York, 1978).

[77] D. M. Eagles, Journal of Physics and Chemistry of Solids **25**, 1243–1251 (1964), https://doi.org/10.1016/0022-3697(64)90022-8.

[78] J. M. Lantz and R. M. Corn, The Journal of Physical Chemistry **98**, 9387–9390 (1994), https://doi.org/10.1021/j100069a022.

[79] A. Stevanovic and J. T. Yates, The Journal of Physical Chemistry C **117**, 24189–24195 (2013), https://doi.org/10.1021/jp407765r.

[80] T. Berger, M. Sterrer, O. Diwald, E. Knözinger, D. Panayotov, T. L. Thompson, and J. T. Yates, The Journal of Physical Chemistry B **109**, 6061–6068 (2005), https://doi.org/10.1021/jp0404293.

[81] L. Liu and T.-K. Sham, en, in *Titanium dioxide - material for a sustainable environment*, edited by D. Yang (InTech, June 2018),https://doi.org/10.5772/intechopen.72856.

[82] L. Gundlach, R. Ernstorfer, and F. Willig, Physical Review B **74**, 035324 (2006), 10.1103/PhysRevB.74.035324.

[83] R. Qian, H. Zong, J. Schneider, G. Zhou, T. Zhao, Y. Li, J. Yang, D. W. Bahnemann, and J. H. Pan, en, Catalysis Today, Advances in photo(electro)catalysis for environmental applications and chemical synthesis **335**, 78–90 (2019), https://doi.org/10.1016/j.cattod.2018.10.053.

[84] A. Stevanovic and J. T. Yates, Langmuir **28**, 5652–5659 (2012), 10.1021/la205032j.

[85] T. Bredow and K. Jug, The Journal of Physical Chemistry **99**, 285–291 (1995), https://doi.org/10.1021/j100001a044.

[86] V. Shapovalov, E. V. Stefanovich, and T. N. Truong, en, Surface Science **498**, L103–L108 (2002), https://doi.org/10.1016/S0039-6028(01)01595-3.

[87] Y. Ji, B. Wang, and Y. Luo, The Journal of Physical Chemistry C **116**, 7863–7866 (2012), https://doi.org/10.1021/jp300753f.

[88] M. Anpo, T. Shima, and Y. Kubokawa, Chemistry Letters **14**, 1799–1802 (1985), https://doi.org/10.1246/cl.1985.1799.

[89] O. I. Micic, Y. Zhang, K. R. Cromack, A. D. Trifunac, and M. C. Thurnauer, The Journal of Physical Chemistry **97**, 7277–7283 (1993), https://doi.org/10.1021/j100130a026.

[90] C. Di Valentin, G. Pacchioni, and A. Selloni, Physical Review Letters **97**, 166803 (2006), https://doi.org/10.1103/PhysRevLett.97.166803.

[91] Y. Tamaki, K. Hara, R. Katoh, M. Tachiya, and A. Furube, The Journal of Physical Chemistry C **113**, 11741–11746 (2009), 10.1021/jp901833j.

[92] M. R. Hoffmann, S. T. Martin, W. Choi, and D. W. Bahnemann, Chemical Reviews **95**, 69–96 (1995), https://doi.org/10.1021/cr00033a004.

[93] H. H. Mohamed, R. Dillert, and D. W. Bahnemann, en, Journal of Photochemistry and Photobiology A: Chemistry **217**, 271–274 (2011), https://doi.org/10.1016/j.jphotochem.2010.09.024.

[94] P. F. Schwarz, N. J. Turro, S. H. Bossmann, A. M. Braun, A.-M. A. A. Wahab, and H. Duerr, The Journal of Physical Chemistry B **101**, 7127–7134 (1997), https://doi.org/10.1021/jp971315c.

[95] S. Kim and W. Choi, Environmental Science & Technology **36**, 2019–2025 (2002), https://doi.org/10.1021/es015560s.

[96] D. P. Colombo Jr and R. M. Bowman, The Journal of Physical Chemistry **99**, 11752–11756 (1995), https://doi.org/10.1021/j100030a020.

[97] K. M. Schindler and M. Kunst, Journal of Physical Chemistry **94**, 8222–8226 (1990), https://doi.org/10.1021/j100384a045.

[98] Z. Zhang and J. T. Yates, The Journal of Physical Chemistry C **114**, 3098–3101 (2010), 10.1021/jp910404e.

[99] D. P. Colombo and R. M. Bowman, The Journal of Physical Chemistry **100**, 18445–18449 (1996), https://doi.org/10.1021/jp9610628.

ПОРІВНЯННЯ ВЛАСТИВОСТЕЙ АНАТАЗА І РУТИЛА ДЛЯ ФОТОКАТАЛІТИЧНОГО ВИКОРИСТАННЯ: КОРОТКИЙ ОГЛЯД

В. В. Моргунов[a,b], **С. В. Літовченко**[a], **В. О. Чішкала**[a], **Д. Л. Рябчиков**[a], **Д. С. Матвієнко**[a]
[a] *Харківський національний університет імені В. Н. Каразіна, Пл. Свободи, 4, Харків, 61022, Україна;*
[b] *Українська інженерно-педагогічна академія, вул. Університетська, 16, Харків, 61003, Україна*

Діоксид титану (TiO_2) привертає велику увагу як напівпровідниковий фотокаталізатор через свою високу фотореактивність, нетоксичність, корозійну стійкість, фотостійкість, дешевизну. Він може бути використаний у широкому спектрі застосувань: очищення повітря та води, генерування водню (H_2), зменшення вмісту CO_2, у фотоелектричних пристроях тощо. Зусилля вчених були направлені на пошук способів, що використовують сонячне світло для фотокаталізу за допомогою діоксиду титану та підвищення фотокаталітичної ефективності. У цій статті ми розглядаємо різницю властивостей модифікацій анатазу та рутилу TiO_2. Анатаз має більш високу фотоефективність. Більш висока фотоефективність анатазу обумовлена більш тривалим терміном життя носіїв заряду (час життя e^-/h^+ в анатазі на 3 порядки вище, ніж у рутилу). Але анатаз має більшу ширину забороненої зони (3,2 еВ або 388 нм) у порівнянні з рутилом (3,0 еВ або 414 нм). Таким чином, анатаз стає світлочутливим в ультрафіолетовому (УФ) діапазоні світла, тим часом рутил - у фіолетовому спектрі видимого світла. Бажано отримати напівпровідник TiO_2 з властивостями, що поєднують найкращі як для анатазу так і для рутилу: більша фотореактивність та менша забороненої зони. Це можна зробити за допомогою зовнішніх факторів, таких як електричне або магнітне поле, легування тощо.

Ключові слова: фотокаталіз, діоксид титану, анатаз, рутил, ширина забороненої зони, фотоефективність, генерація електронних дірок.

EAST EUROPEAN JOURNAL OF PHYSICS. 4. 31-42 (2021)
DOI: 10.26565/2312-4334-2021-4-03 ISSN 2312-4334

THE EFFECT OF HYDROSTATIC PRESSURE AND CATIONIC VACANCY ON THE ELECTRONIC AND MAGNETIC PROPERTIES OF THE ZnSe:T CRYSTALS (T = Ti, V, Cr, Mn, Fe, Co, Ni)†

Stepan V. Syrotyuk
Semiconductor Electronics Department, Lviv Polytechnic National University, 12 S. Bandera Str., 79013 Lviv Ukraine
**Corresponding Author: svsnpe@gmail.com*
Received August 7, 2021; revised November 17, 2021; accepted November 18, 2021

The parameters of the spin-polarized electronic energy spectrum of ZnSe:T crystals (T = Ti, V, Cr, Mn, Fe, Co, Ni) are studied on the basis of a 2 × 2 × 2 supercell built on the basis of a ZnSe unit cell with a sphalerite structure. The supercell contains 64 atoms, with one Zn atom replaced by one transition 3d element T. The first stage of this study is to calculate in the ideal material ZnTSe parameters of electronic energy bands, dependent on the external hydrostatic pressure. At the second stage, the effect of pressure on the parameters of the electronic energy spectrum in the ZnTSe materials is investigated, taking into account the Zn vacancy. The calculations were performed using the Abinit program. For a better description of strongly correlated 3d electrons of the element T, a hybrid exchange-correlation functional PBE0 with an admixture of the Hartree-Fock exchange potential was used, in which the self-interaction error of these electrons is removed. Based on the obtained spin-polarized electron densities of states, the magnetic moments of the supercells were also determined. A significant effect of pressure on the parameters of electronic energy zones was revealed. So, the ideal ZnTiSe material at zero pressure is a metal for both spin values, but under pressure it becomes a semiconductor. The same material with a point defect, i.e. a vacancy at the site of the Zn atom, exhibits semiconductor properties for both spin orientations at zero pressure. It was found that vacancies radically change the parameters of electronic energy bands. The magnetic moments of the supercell, as integral values of the spin-polarized densities of electronic states, also reflect these changes. Thus, in ZnTiSe material without defects, the magnetic moments of the supercell are 1.92, 2.0 and 2.0 μ_B, at pressures 0, 21 and 50 GPa, respectively, while in the same material with a vacancy, the corresponding values are 0.39, 0.02 and 0.36 μ_B. The ideal ZnVSe material at zero pressure is also a metal for both values of the spin moment, but in the presence of a cationic vacancy it is characterized by a pseudogap because the Fermi level is localized in the upper part of the valence band. Ideal ZnFeSe and ZnNiSe crystals are characterized by similar dependences of the electronic energy parameters on the pressure, for both spins. However, the same materials with a cationic vacancy are characterized by the Fermi level immersed in the valence band for a spin up.
Keywords: ZnSe, 3d impurity, cationic vacancy, electronic properties, spin, magnetic moment, strong correlations, hybrid functional.
PACS: 68.35.Dv, 71.15.Mb, 71.20.Nr, 71.27.+a, 81.05.Bx

The ultrashort pulse lasers of infrared (IR) light have gained great attentions for ophthalmic, surgical, dental, therapeutic, and aesthetic medical applications. The pulses from the picosecond (ps) to femtosecond (fs) require less energy to ablate biological tissues and the accuracy is in the micrometer range. The passively mode-locked femtosecond ZnSe:Cr laser was first reported in 2006, generating ~100 fs pulses at up to 75 mW power around 2.5 μm wavelength [1].

ZnSe is a wide band gap semiconductor, widely used in light-emitting devices, solar cells, and photodetectors because of its high excitation energy and excellent photoelectric performance [2]. The optical and electrical properties of semiconductor materials are the main factors that determine the performance of devices. At present, it is the most widely used way to regulate the photoelectric characteristics of semiconductors through morphology regulation or doping treatment. The doping technique by introducing donor impurities or acceptor impurities into the host lattice is one of the most effective ways to achieve regulatory effects, and it can accurately control the transport properties of the semiconductor by adjusting the type of doping element and the doping concentration. In addition, the mechanism of the change of optical and conductive properties of ZnSe caused by doping has not been studied deeply in theory.

The ZnS:Cr lasers have been extensively studied both experimentally and theoretically. The zinc-blende ZnS has the larger band gap of 3.8 eV, higher thermal conductivity of 27 W/mK, higher thermal shock parameter of 7.1 W/m$^{1/2}$, and lower dn/dT of $46 \cdot 10^{-6}$ K^{-1}, compared respectively to 2.8 eV, 18 W/mK, 5.3 W/m$^{1/2}$, and $70 \cdot 10^{-6}$ K^{-1} in ZnSe [3].

The physical, spectroscopic, and laser characteristics of the single crystal and polycrystalline II-VI chalcogenides are practically identical [4]. This is important since II-VI single-crystals of high optical quality are difficult to grow while chemically vapor grown II-VI polycrystals benefited from low-cost mass production technology of fabrication and were widely used as passive materials for middle-infrared technology [5]. The combination of low-cost and readily available polycrystalline II-VI materials with a quantitative and affordable post-growth TM doping procedure, preserving high optical quality of the starting materials, enabled an effective technology for fabrication of gain elements, which is quite rare for solid-state laser materials.

Since ZnS, ZnSe, ZnTe crystals with impurities of transition 3d elements are used in devices, particular in lasers, it is important to study their electronic structure from the unified theoretical methodology under the action of hydrostatic

† ***Cite as:*** S.V. Syrotyuk, East. Eur. J. Phys. **4**, 31 (2021), https://doi.org/10.26565/2312-4334-2021-4-03

pressure and vacancies at the site of the zinc atom. The aim of this study is also to take into account the strong correlations of 3d electrons using a hybrid exchange-correlation functional. Let us go to performing these tasks.

CALCULATION

We solve the Schrödinger equation in the basis of projectior augmented waves (PAW) [6], which combines the features of the pseudopotential approaches [7] and the all-electronic method of augmented plane waves (APW) [8]. In the PAW and APW methods, the crystal is divided into two regions. The first region is inside the atomic spheres, and the second one is interspherical. In the APW approach, the wave functions of both regions are joining at the surface of the sphere to ensure continuity throughout space. In the PAW method, an augmentation is performed using a projection procedure.

The all-electronic wave $|\psi_n>$ and pseudo-wave $|\tilde{\psi}_n>$ functions are connected as follows [6]:

$$|\psi_n(\mathbf{r})> = |\tilde{\psi}_n(\mathbf{r})> + \sum_a \sum_i (|\phi_i^a(\mathbf{r})> - |\tilde{\phi}_i^a(\mathbf{r})>) < \tilde{p}_i^a | \tilde{\psi}_n>, \tag{1}$$

where $|\phi_i^a(\mathbf{r})>$ is atomic wave, $|\tilde{\phi}_i^a(\mathbf{r})>$ pseudo-wave, and $<\tilde{p}_i^a|$ projector function, respectively. The summation in (1) is performed by the augmentation spheres, which are numbered by the index a, and the index $i = \{n, l, m\}$ incorporates the principal, orbital and magnetic quantum numbers, respectively.

From equation (1) we see that

$$|\psi_n(\mathbf{r})> = \tau |\tilde{\psi}_n(\mathbf{r})>, \tag{2}$$

where the τ operator converts a pseudo-wave $|\tilde{\psi}_n(\mathbf{r})>$ into an all-electron wave function $|\psi_n(\mathbf{r})>$.

The explicit form of the operator τ follows from equation (1):

$$\tau = 1 + \sum_a \sum_i (|\phi_i^a> - |\tilde{\phi}_i^a>) < \tilde{p}_i^a|. \tag{3}$$

Stationary Schrödinger equation

$$H|\psi_n> = \varepsilon_n |\psi_n>, \tag{4}$$

taking into account (2) takes the following form [4]:

$$\tau^+ H \tau |\tilde{\psi}_n> = \tau^+ \tau |\tilde{\psi}_n> \varepsilon_n, \tag{5}$$

in which the required electron spectrum ε_n is the same as in equation (4).

The idea of the PAW method is to convert the Schrödinger equation to an equation in which the unknown state function is $|\tilde{\psi}_n>$. If it is found, then with the help of (1) the all-electronic wave function is obtained. Through the latter we find the electron density and the corresponding Hartree potential.

The exchange-correlation potential was chosen in the form of PBE0 [9–12], according to which the exchange-correlation energy

$$E_{xc}^{PBE0}[\rho] = E_{xc}^{PBE}[\rho] + \alpha(E_x^{HF}[\psi_{3d}] - E_x^{PBE}[\rho_{3d}]), \tag{6}$$

where PBE corresponds to the generalized gradient approximation (GGA-PBE) of exchange-correlation functional [12], and $E_x^{HF}[\psi_{3d}]$ is the exchange energy in the Hartree-Fock theory. The recommended value of a mixing factor α is equal to $1/4$. In formula (6), the exchange energy $E_x^{PBE}[\rho_{3d}]$, in which the self-interaction error (SIE) of 3d electrons is the largest, is partially subtracted. In fact, these electrons move in narrow energy bands with a high density of states. In the included exact term of exchange energy $E_x^{HF}[\psi_{3d}]$ the SIE is absent in general. Neglecting the second term in formula (6) leads to a conventional GGA-PBE exchange-correlation functional suitable for describing materials with s (p) electrons.

The functional $E_{xc}^{PBE0}[\rho]$ is important for describing materials containing d (f) electrons. In particular, it has been successfully used to study nanostructures containing transition 3d elements [13, 14]. Energy band structure peculiarities and luminescent parameters of CeX_3 (X = Cl, Br, I) crystals were revealed and shown good comparison with experiment [15]. Electronic properties of orthorhombic InI and TlI crystals taking into account the quasiparticle corrections and spin-orbit interaction, have been evaluated based on the results, defined at the level of the hybrid functional as the starting point [16]. The combined approach of the hybrid functional and quasiparticle GW was successfully used in the calculations of the electronic structure in chalcogenides ZnX (X=O, S, Se, Te) [17]. The results obtained in works [16, 17] are in good agreement with experimental data. The electronic structure of the CdMnTe solid solution [18] is satisfactory agreed with the experimental results [19]. Electronic structure, magnetic and mechanical properties of MnCoSi half-Heusler alloy also have been found with the hybrid PBE0 exchange-correlation functional [20], where the different values of the mixing coefficient α were used.

All calculations were performed using the ABINIT program [21], in 2 × 2 × 2 supercells containing 64 atoms. At the first stage, the defect of substitution in the supercell $Zn_{32}Se_{32}$ of one Zn atom by transition element T, i.e. $Zn_{31}T_1Se_{32}$ is considered. At the second stage the supercell with a vacancy, $Zn_{30}v_1T_1Se_{32}$, is treated. The electronic structure of these materials was calculated under the action of hydrostatic pressure.

The calculations are performed on the basis of PAW. The following valence configurations of atoms were selected: Zn: $3d^{10}4s^2$, Se: $4s^24p^4$, Ti: $3s^23p^63d^24s^2$, V: $3s^23p^63d^34s^2$, Cr: $3s^23p^63d^54s^1$, Mn: $3s^23p^63d^54s^2$, Fe: $3s^23p^63d^64s^2$, Co: $3s^23p^63d^74s^2$, and Ni: $3s^23p^63d^84s^2$. Basic functions and pseudopotentials (PAW) were generated using AtomPAW code [22, 23]. The calculation of the wave function was performed on the basis of plane waves determined by the maximum kinetic energy ε_{cut} = 40 Ry, on a spatial grid of 90×90×90. Electron density and potentials were calculated on a denser grid of 125 × 125 × 125, determined by an energy ε_{cut} = 80 Ry.

RESULTS AND DISCUSSION

The spin-polarized electron energies in the ZnTiSe material are shown in Fig. 1. The parameters of the electronic energy band spectrum are denoted as follows: E_v - the energy of the top of the valence band, E_f - the Fermi energy, E_c - the lowest electron energy in the conduction band. Figures 1a and 1b show the electron energies in an ideal ZnSe crystal in which one Zn atom is replaced by a Ti atom. The parameters of supercell 2×2×2, which contains 64 atoms, correspond to the applied external pressures from 0 to 50 GPa. In other words, the value of the constant lattice for the supercell $a = 19.14$ Å corresponds to the pressure P = 50 GPa, and the value of $a =$ 21.64 Å corresponds to the pressure 0 GPa, i.e. to ambient conditions.

Note that under normal conditions (P = 0) the ZnTiSe material exhibits metallic properties for both spin orientations, i.e. $\varepsilon_g = 0$. The magnetic moment of the supercell $M = 1.92\,\mu_B$. However, under the action of hydrostatic pressure, this material reveals the properties of a semiconductor for both spins. Increasing the hydrostatic pressure leads to an increase in the width of the band gap ε_g, as it is shown in Figures 1a and 1b. At a pressure value of $P = 21$ GPa for spin up, the direct optical gap at the point Γ $\varepsilon_{gd} = 0.72$ eV, and the fundamental indirect one $\varepsilon_{gi} = 0.61$ eV.

For the spin down, the optical direct gap is identical with the fundamental one, and the numerical value is $\varepsilon_g = 2.19$ eV. Magnetic moment of the supercell $M = 2.0\,\mu_B$. At a pressure $P = 50$ GPa, for spin up, the direct optical gap at the Γ point $\varepsilon_{gd} =$ 0.69 eV, and the fundamental indirect one $\varepsilon_{gi} = 0.54$ eV. For the spin down, the optical and fundamental band gaps are equal, and the numerical value of $\varepsilon_g =$ 2.03 eV. Magnetic moment of the supercell $M = 2.0\,\mu_B$. As can be seen from Figs. 1a, 1b, and the Fermi level is located inside the forbidden gap.

However, the presence of a point defect, i.e. a vacancy at the Zn atom site, leads to a significant change in the dependence of the electronic energy spectrum in the ZnTiSe material on the external hydrostatic pressure. From Figures 1c and 1d, we see that for both spin orientations, the ZnTiSe material with a point defect exhibits semiconductor properties for all hydrostatic pressure values. At a pressure value $P = 0$, for the spin up, the optical gap at the point Γ $\varepsilon_{gd} = 0.20$ eV, and the fundamental indirect one $\varepsilon_{gi} = 0.18$ eV. For spin down, the optical gap $\varepsilon_{gd} =$ 0.71 eV, and the fundamental indirect one $\varepsilon_{gi} =$ 0.70 eV. The magnetic moment of the supercell $M = 0.39\,\mu_B$. At a pressure value of $P =$ 20 GPa, for the spin up, the optical gap at the point Γ $\varepsilon_{gd} = 0.38$ eV, and the fundamental indirect one $\varepsilon_{gi} =$ 0.35 eV. For spin down, the optical pap $\varepsilon_{gd} = 0.40$ eV, and the fundamental indirect one $\varepsilon_{gi} = 0.37$ eV. The magnetic moment of the supercell $M = 0.02\,\mu_B$. At a pressure value of 48 GPa, for the spin up, the optical gap at a point Γ $\varepsilon_{gd} = 0.43$ eV, and the fundamental indirect one $\varepsilon_{gi} = 0.38$ eV. For the spin down, the optical gap $\varepsilon_{gd} = 0.43$ eV, and the fundamental indirect one $\varepsilon_{gi} = 0.38$ eV. The magnetic moment of the supercell $M = 0.36\,\mu_B$. The largest band gap ε_g is expected under normal conditions for electrons with spins down. For this state, the band gap ε_g decreases with increasing pressure (decrease in the constant lattice of the crystal) from 0 to about 20 GPa, after which its values remain almost constant for both spin orientations, including the pressure value of 48 GPa.

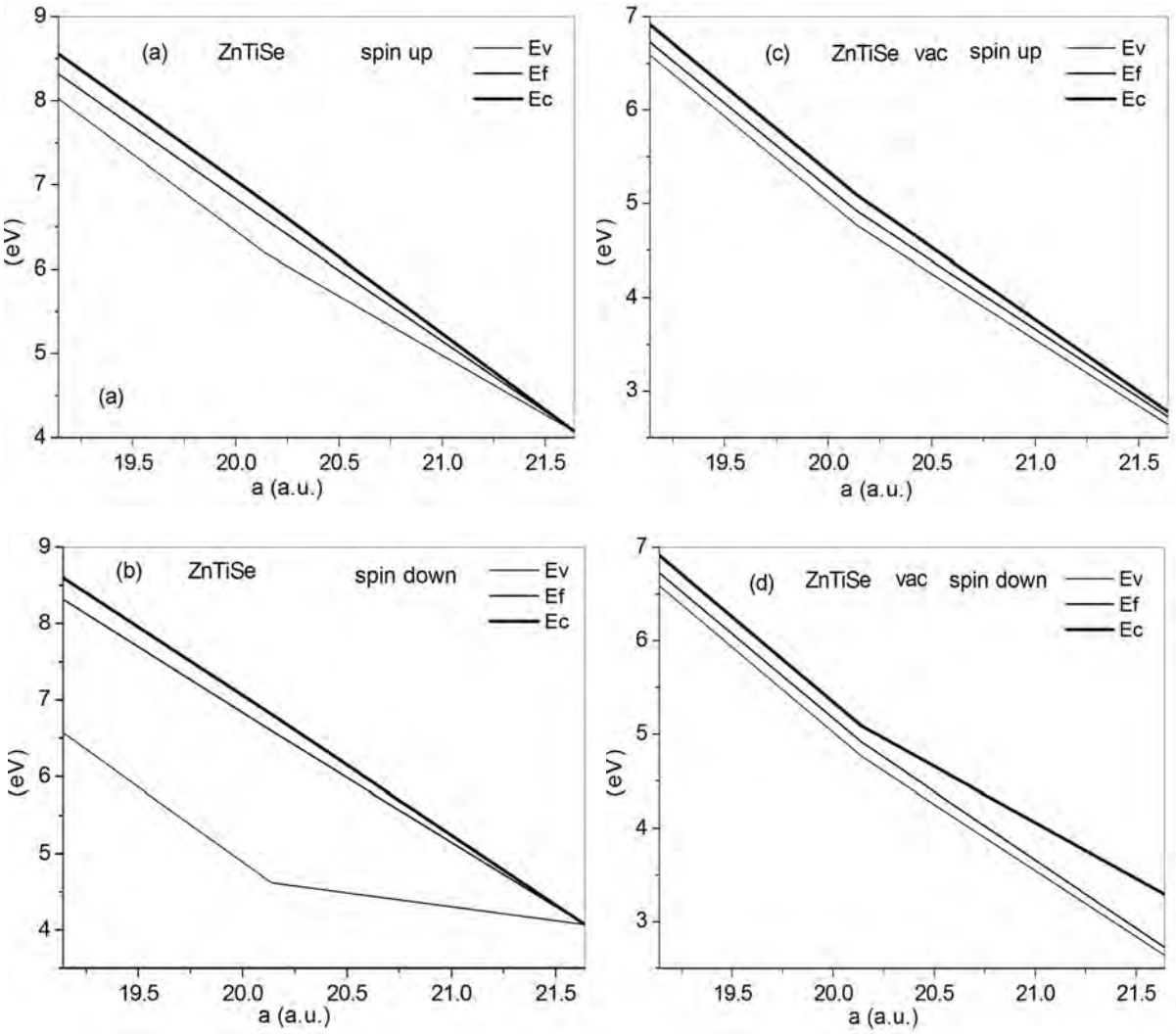

Figure 1. The spin-polarized electronic energy band parameters in the ZnTiSe material versus the 2×2×2 supercell lattice constant: top of valence band E_v, Fermi energy E_f and bottom of conduction band E_c.

The calculation results for the ZnVSe material are shown in Fig. 2. First, consider the parameters of an ideal crystal shown in Figures 2a and 2b. For a pressure $P = 0$, the material reveals a metallic state with a band gap $\varepsilon_g = 0$ for both spin values. The magnetic moment of the supercell $M = 2.7\,\mu_B$. However, at higher pressures, $0 < P \le 21$ GPa, and for states with spin up $E_v = E_c$, i.e. we again have a metallic state. For pressures $21 < P \le 50$ GPa, in states with spin up $E_f < E_v < E_c$, i.e. the Fermi level is localized in the valence band. On the contrary, for spin-down electronic states, the ZnVSe crystal is a semiconductor whose fundamental interband gap $\varepsilon_g = 0$ at a pressure $P = 0$, and for higher pressures $0 < P \le 21$ GPa it increases. At a pressure $P = 21$ GPa, the optical and fundamental gaps are the same, i.e. $\varepsilon_g = 2.20$ eV for both spin orientations. The value of the magnetic moment of the supercell $M = 3\,\mu_B$. At higher pressures, i.e. in the interval $21 < P \le 50$ GPa, the interband gap is almost constant, and the Fermi level is shifted toward the conduction band. At a pressure of 50 GPa, the optical and fundamental slits are the same, i.e. $\varepsilon_g = 1.99$ eV for both spin orientations. The magnetic moment of a supercell $M = 3\,\mu_B$.

If there is a vacancy, we have another picture, shown in Figures 2c and 2d. In fig. 2c we see that for states with spin up, at pressure $P = 0$, the Fermi level is localized inside the band gap, and in the upper part of the valence band at higher pressures. At a pressure of $P = 0$ we have a direct band gap $\varepsilon_g = 1.10$ eV at a point Γ. At pressures of 20 and 48 GPa, the values of the pseudogaps are 1.25 and 1.14 eV, respectively. At pressures of 0, 20 and 48 GPa, the magnetic moments of the supercell are 2.7, 3.0 and 3.0 μ_B, respectively.

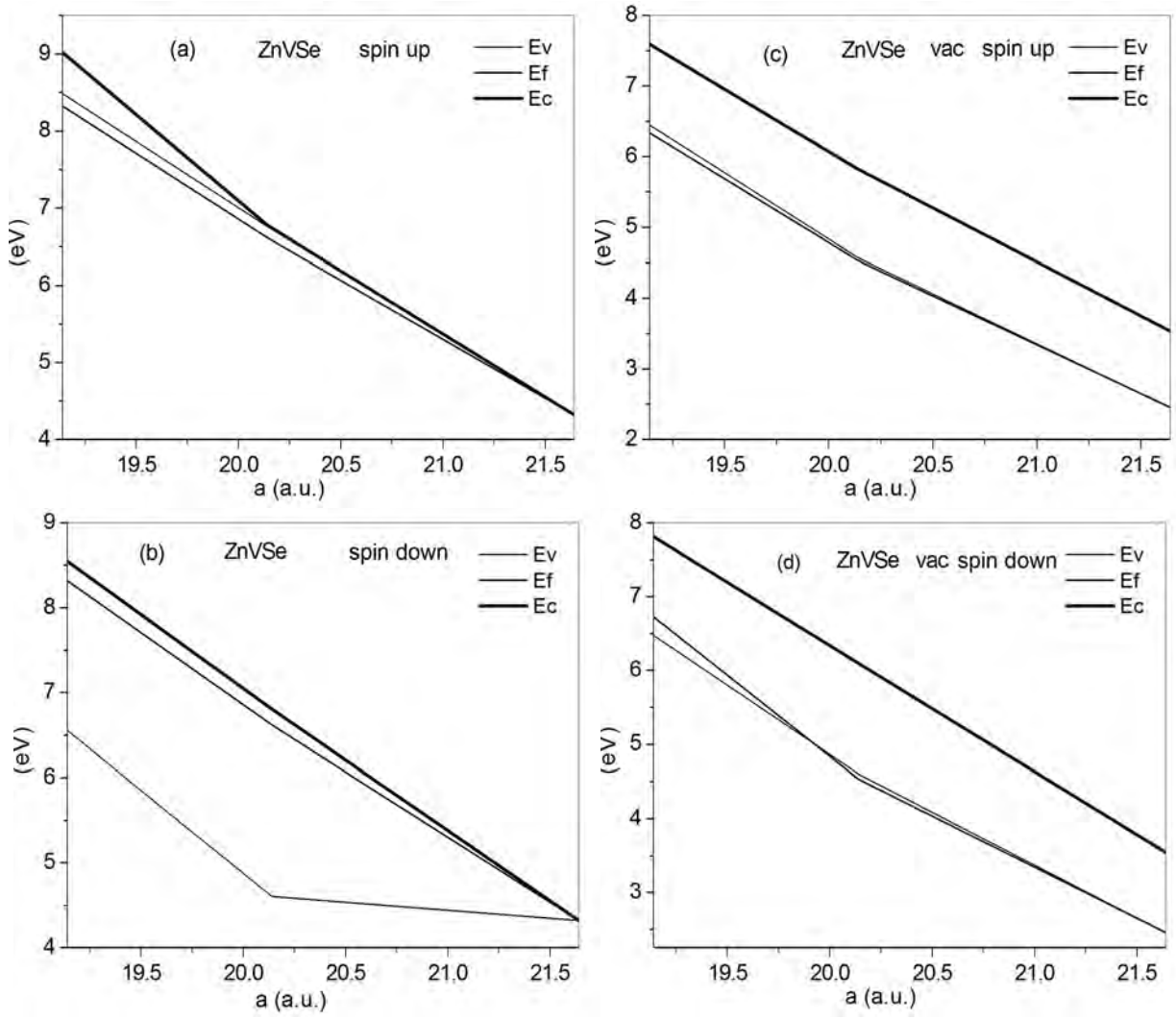

Figure 2. The spin-polarized electronic energy band parameters in the ZnVSe material versus the 2×2×2 supercell lattice constant: top of valence band E_v, Fermi energy E_f and bottom of conduction band E_c.

If there is a vacancy, we have another picture, shown in Figures 2c and 2d. In Fig. 2c we see that for states with spin up at pressure $P = 0$ the Fermi level is localized inside the band gap, and in the upper part of the valence band at higher pressures. At a pressure of $P = 0$ we have a direct band gap ε_g =1.10 eV at a point Γ. At pressures of 20 and 48 GPa, the values of the pseudogaps are 1.25 and 1.14 eV, respectively. At pressures 0, 21 and 50 GPa, the magnetic moments of the supercell are 2.7, 3.0 and 3.0 μ_B, respectively.

For electrons with spin down (Fig. 2 d), under pressure $P = 0$, we have a direct band gap ε_g =1.12 eV at a point Γ. At $0 < P \le 20$ GPa pressures, the Fermi level is localized at the top of the valence band, and the pseudogap value is 1.50 eV if $P = 20$ GPa. At $20 < P \le 48$ GPa pressures, the ZnVSe material with the vacancy is a semiconductor with a band gap of $\varepsilon_g = 1.33$ eV ($P = 48$ GPa). At pressures 0, 20 and 48 GPa, the magnetic moments of the supercell are 2.00, 2.05 and 2.05 μ_B, respectively.

The parameters of the ZnCrSe material E_v, E_f and E_c, depending on the pressure, differ from those shown in Figures 1 and 2 above. Let us first consider the results obtained for an ideal ZnCrSe crystal. They are shown in Figures 3a and 3b. For the spin up (Fig. 3a) we notice the immersion of the Fermi level in the valence band. The interband pseudogap increases with increasing pressure. For the spin down we have a semiconductor, the width of the band gap of which increases with increasing pressure. At pressure values of 0, 22 and 51 GPa, the magnetic moment of the supercell is the same and equal to 4 μ_B, and the values of the optical and fundamental gaps coincide and are 1.20, 2.22 and 1.99 eV, respectively.

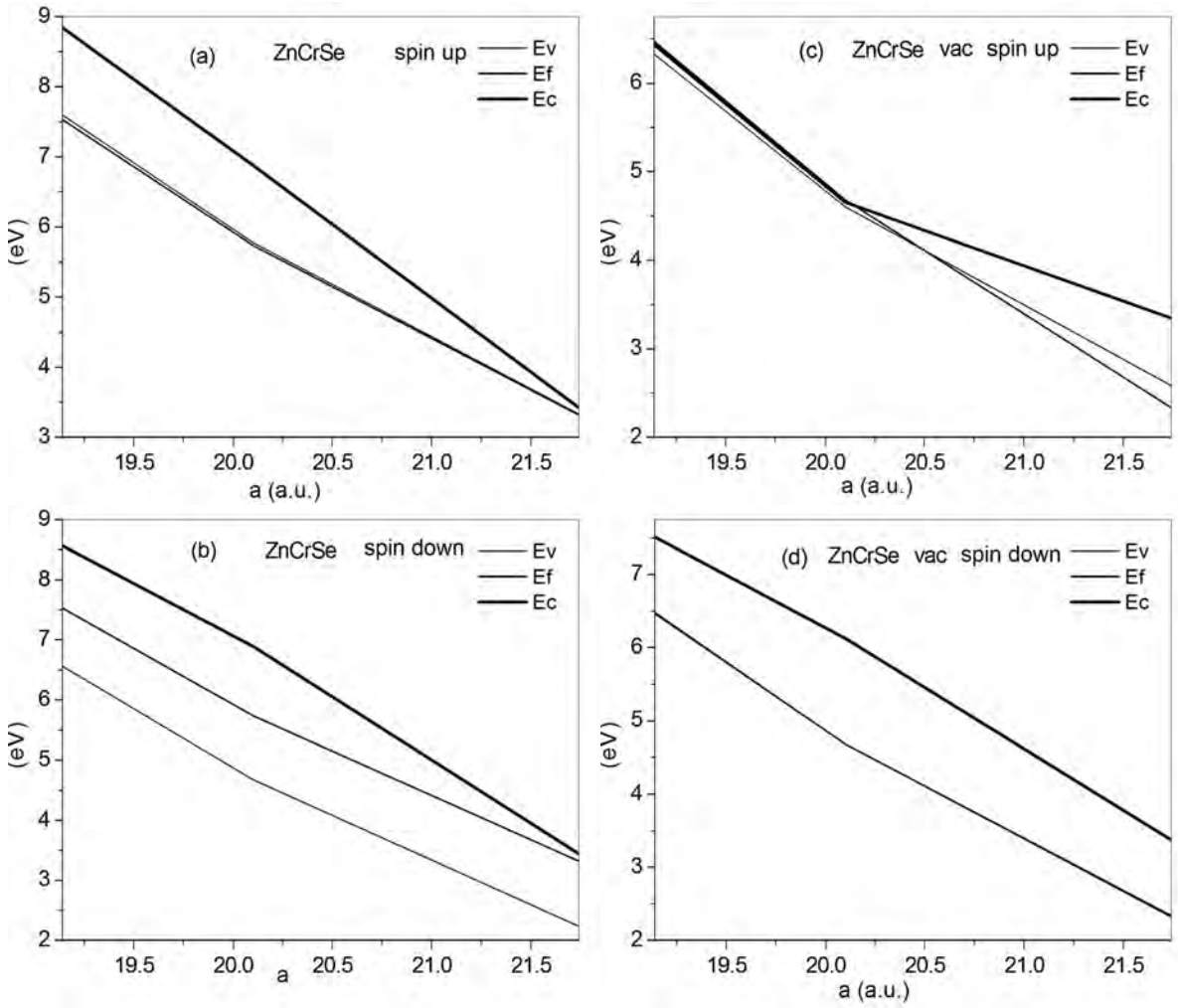

Figure 3. The spin-polarized electronic energy band parameters in the ZnCrSe material versus the 2×2×2 supercell lattice constant: top of valence band E_v, Fermi energy E_f and bottom of conduction band E_c.

Now consider the results obtained for a ZnCrSe crystal with a vacancy at the Zn atom site. At $0 < P \le 22$ GPa pressures, the Fermi level of electrons with spin up (Fig. 3c) is localized in the valence band, and the width of the pseudogap increases. A further increase in pressure leads the material to a metallic state. For electrons with spin down (Fig. 3d), the Fermi level is in the upper part of the valence band, and the pseudogap shows a slow change as a function of pressure. The values of pseudogaps at pressures 0, 20 and 49 GPa are 1.06 eV (optical and fundamental), 1.50 eV (optical) and 1.46 eV (indirect fundamental), and 0 eV, respectively. The magnetic moments of the supercell corresponding to these pressures are equal to 2.75, 2.57 and 2.37 μ_B, respectively.

The pressure-dependent parameters of the electronic energy spectrum of an ideal ZnMnSe material are shown in Figures 4a and 4b. Their change, if there is a vacancy, is shown in Figures 4c and 4d. In an ideal material at pressures of 0, 22 and 51 GPa, the optical band gaps coincide with the fundamental ones, and their values are 1.04, 1.96 and 1.85 eV for spin up, and 1.20, 2.21 and 1.95 eV for spin down, respectively. The magnetic moments of the supercell are the same for these pressure values and are equal to $5\,\mu_B$. Figures 4a and 4b indicate that for both spin up and down, the material is a semiconductor whose band gap slowly increases with increasing in pressure to 22 GPa, and a further increase in pressure causes a slow decrease in bandwidth.

In the presence of a vacancy at the Zn atom site, the picture changes radically. The Fermi level for both spin orientations is at the top of the valence band. At pressures of 0, 20 and 49 GPa, the values of pseudogaps 1.03, 1.96 and 1.85 eV for spin up, and 1.20, 2.07 and 1.55 eV for spin down, respectively. The values of the magnetic moments of the supercell at these values of pressure are equal to 4.16, 4.2 and 4 μ_B, respectively.

The parameters of the electronic energy bands in the ZnFeSe material, depending on the pressure, found without taking into account the vacancy, are shown in Figures 5a, 5b. For spin-up states, we have a direct-band material with interband gaps of 1.14, 1.83, and 1.94 eV, at corresponding pressure values of $P = 0$, 15, and 49 GPa. The increase in pressure leads to a gradual lowering of the Fermi level in the band gap, i.e. it shifts towards the top of the valence band (Fig. 5a).

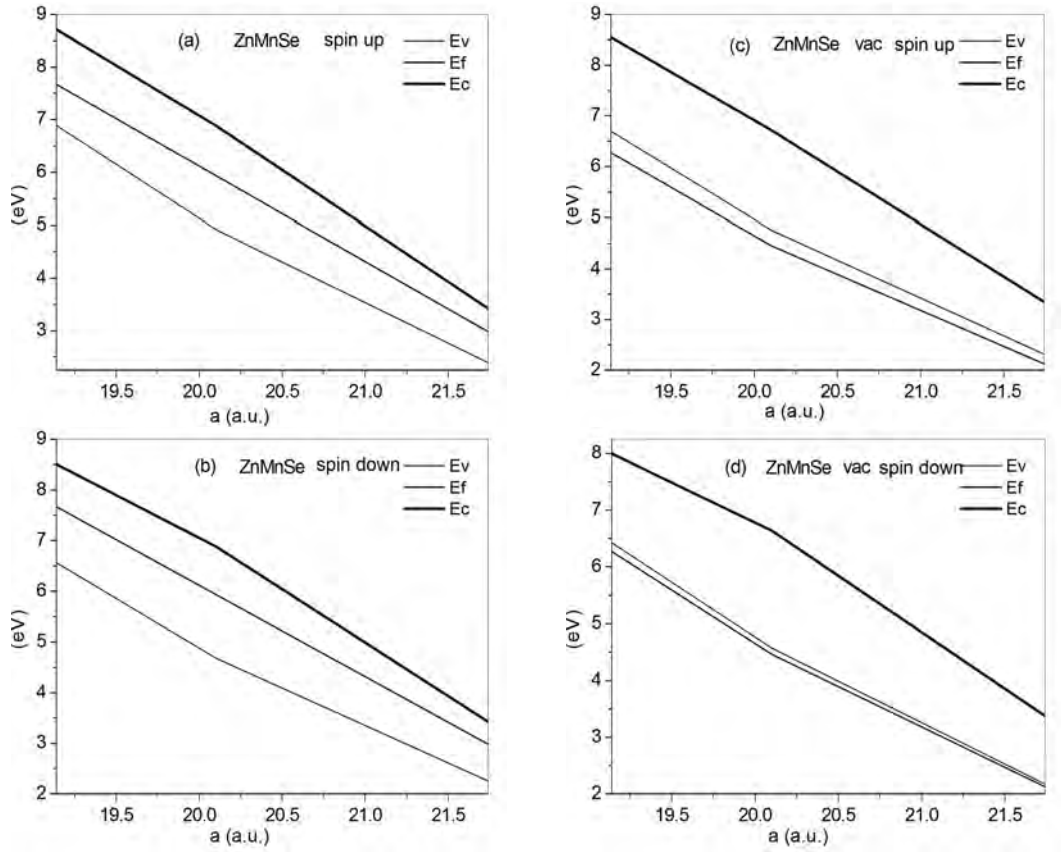

Figure 4. The spin-polarized electronic energy band parameters in the ZnMnSe material versus the 2×2×2 supercell lattice constant: top of valence band E_v, Fermi energy E_f and bottom of conduction band E_c.

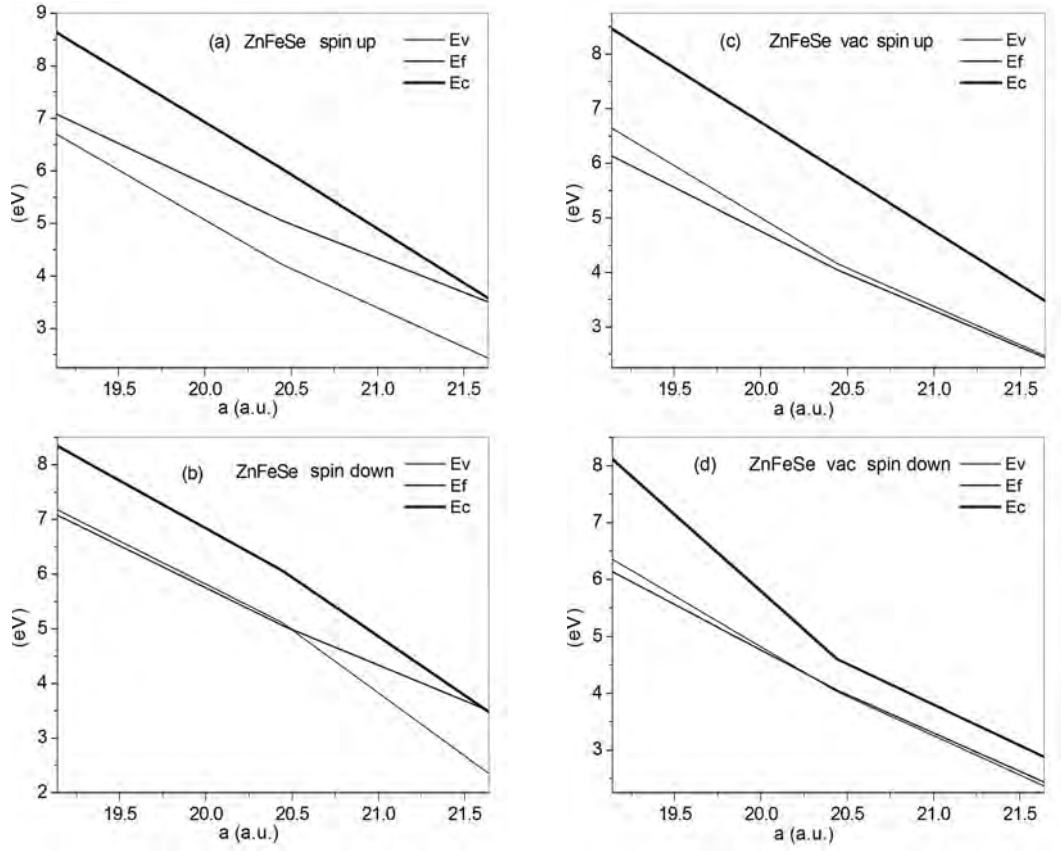

Figure 5. The spin-polarized electronic energy band parameters in the ZnFeSe material versus the 2×2×2 supercell lattice constant: top of valence band E_v, Fermi energy E_f and bottom of conduction band E_c.

A completely different picture is observed for the states of the electron with the spin down. At a pressure value of 0, the Fermi level is in the conduction band, and the pseudogap equals to 1.13 eV. An increase in pressure leads to a decrease in the Fermi level and its immersion in the valence band. The latter occurs at a pressure of $P = 15$ GPa, at which the pseudogap is 0.96 eV. A further increase in pressure leads to a slow increase in the pseudogap to 1.17 eV. The magnetic moment of the supercell at all pressure values $P = 0$, 14 та 47 GPa equals to $M = 4\ \mu_B$.

The presence of a vacancy radically changes the parameters of electronic energy zones. For the spin up, the Fermi level is in the valence band, and at pressure values of $P = 0$, 14, and 47 GPa, the values of the pseudogaps are 1.01, 1.71, and 1.82 eV, respectively.

For spin down at $0 < P \le 14$ GPa pressures, the material is a semiconductor with an optical gap of 0.59 eV and a fundamental indirect one of 0.53 eV. The increase in pressure leads to a slow growth of these gaps, i.e. if $P = 14$ GPa, the values of these gaps are 0.63 and 0.60 eV. At $14 < P \le 47$ GPa pressures, the Fermi level is immersed in the valence band. The corresponding value of the pseudogap at a pressure of $P = 47$ GPa is 1.80 eV. The magnetic moments of the supercell at pressures 0, 14 and 47 GPa are 4.56, 4.49 and 1.48 μ_B, respectively.

The results of calculations for an ideal ZnCoSe crystal are shown in Figures 6a, 6b. The ZnCoSe material exhibits semiconductor properties at all investigated pressure values for both spin orientations. For the spin up at pressures of 0, 20 and 49 GPa, the predicted optical gaps coincide with the fundamental ones and are equal to 1.15, 2.04 and 1.96 eV, respectively.

For spin down, at these pressure values, the optical gaps are 1.24, 2.11 and 1.71 eV, and the fundamental gaps equal 1.24 (direct at the Γ point), and two indirect gaps of 2.04 and 1.63 eV, respectively. The magnetic moments of the supercell are the same for all investigated pressure values and equal to 3 μ_B.

For a point-defect crystal, the data obtained are shown in Figures 6c, 6d. In the material with the vacancy for both values of the spin moment, the Fermi level is in the valence band. So, we can only talk about pseudo-gap. For spin up at pressures 0, 19 and 47 GPa, the values of pseudogaps equal to 1.12, 2.01 and 1.90 eV, and for spin down they are equal to 1.22, 1.74 and 1.31 eV, respectively. The magnetic moments of the supercell corresponding to pressures 0, 20 and 49 GPa are 2.26, 2.44 and 2.25 μ_B, respectively.

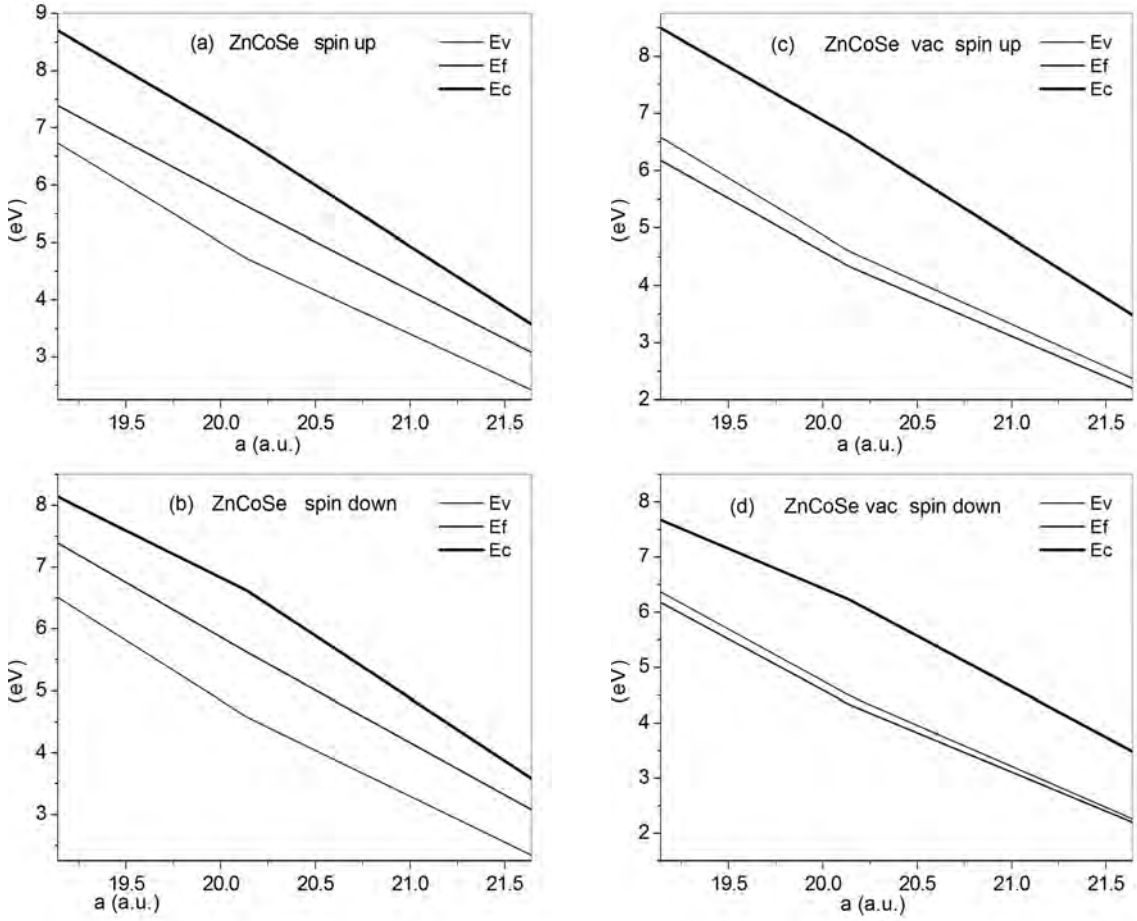

Figure 6. The spin-polarized electronic energy band parameters in the ZnCoSe material versus the 2×2×2 supercell lattice constant: top of valence band E_v, Fermi energy E_f and bottom of conduction band E_c.

The parameters of the electronic energy bands in an ideal ZnNiSe crystal are shown in Figures 7a and 7b. For the spin up, the Fermi level is inside the band gap, i.e. the material is a semiconductor. At pressure values of 0, 20 and 49 GPa, the optical and fundamental gaps are identical and equal to 1.19, 2.05 and 1.97 eV, respectively.

For spin down at $0 \le P \le 20$ GPa pressure values, the Fermi level is inside the band gap, i.e. the crystal is a semiconductor. At a pressure of $P = 0$, the band gap is 0.99 eV, at its value $P = 20$ GPa equals 1.24 eV. At higher $20 \le P \le 49$ GPa pressures, the Fermi level is in the valence band, and the pseudo gap corresponding to its largest value equals to 1.43 eV. The magnetic moments of the supercell are the same for the investigated pressure values and equal to 2 μ_B.

The introduction of the vacancy causes a radical change in the parameters of the electronic energy zones shown in Figures 7c, 7d. the magnetic moments of the supercell are 2.21, 2.15 and 1.94, respectively. For spin down at these pressures, the optical slits are 0.25, 0.29 and 0.21 eV, and the indirect fundamental slits are 0.19, 0.21 and 0.18 eV, respectively. The corresponding dependences of the parameters of the electronic energy zones are shown in Fig. 7d, allow to characterize the material as a narrow-band semiconductor.

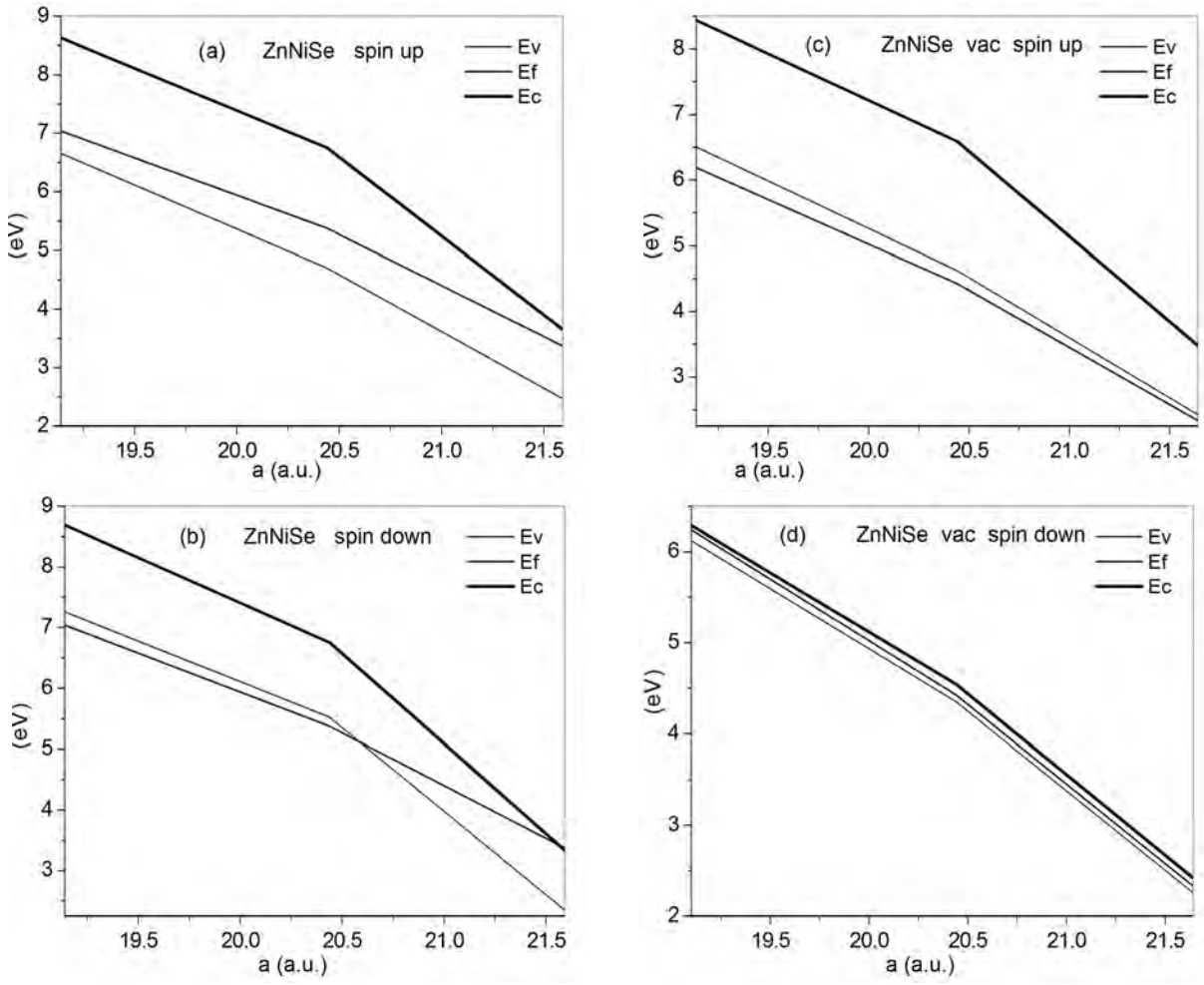

Figure 7. The spin-polarized electronic energy band parameters in the ZnNiSe material versus the 2×2×2 supercell lattice constant: top of valence band E_v, Fermi energy E_f and bottom of conduction band E_c.

In Figures 1–7, we observe a change in the dependence of the parameters of the electronic energy bands as a function of pressure (lattice parameter), which occurs at $20 \le P \le 21$ GPa pressure values. To reveal the nature of this behavior, let us consider the partial 3d DOS of transition elements. In Figures 8 a, b we notice a significant redistribution of the 3d DOS of the Ti atom caused by the increase in pressure. At pressure $P = 0$ we see the presence of 3d electrons of the Ti atom at the Fermi level for both values of the spin moment. This corresponds to the metallic state, as mentioned above. However, at a pressure of 21 GPa 3d states are absent at the Fermi level, and as noted above, the ideal ZnTiSe material exhibits semiconductor properties for both spin moments.

The magnetic moments on the Ti atom in an ideal ZnTiSe material at pressures of 0, 20, and 50 GPa are equal to 1.06, 1.00, and 0.92 μ_B, respectively. In the presence of a vacancy, their values vary greatly and at pressures of 0, 20 and 48 GPa are equal to 0.26, 0.01 and 0.00 μ_B, respectively.

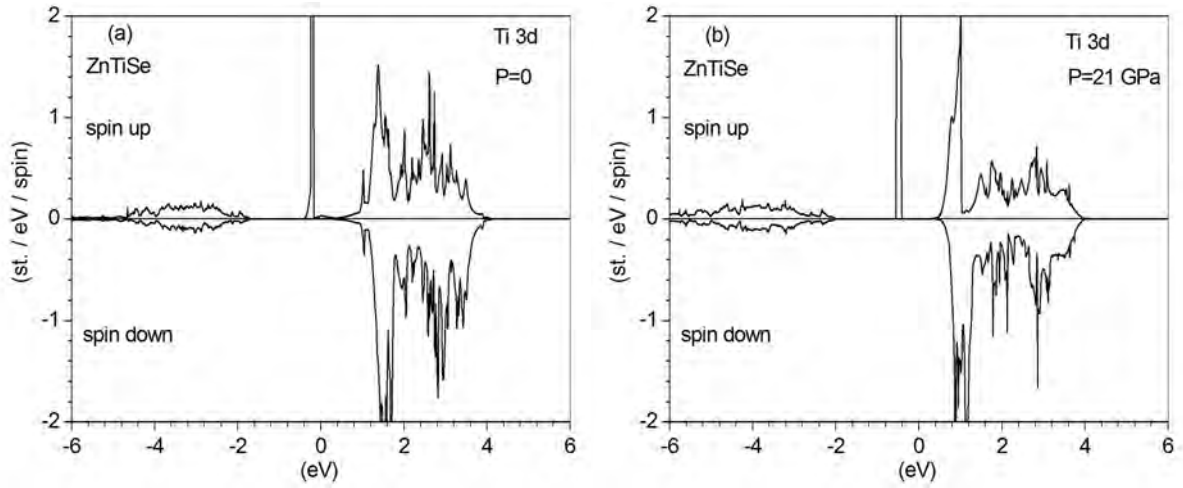

Figure 8. The spin-polarized DOS of the Ti 3d electrons in the ideal ZnTiSe material.

In Fig. 9 we also observe a significant redistribution of 3d electrons of the V atom caused by the increase in pressure. At a pressure $P = 0$ (Fig. 9 a) we see the presence of the V 3d electrons at the Fermi level for both spin orientations. However, at a pressure of 20 GPa (Fig. 9 b) we observe the presence of the V 3d electrons at the Fermi level only for the spin up.

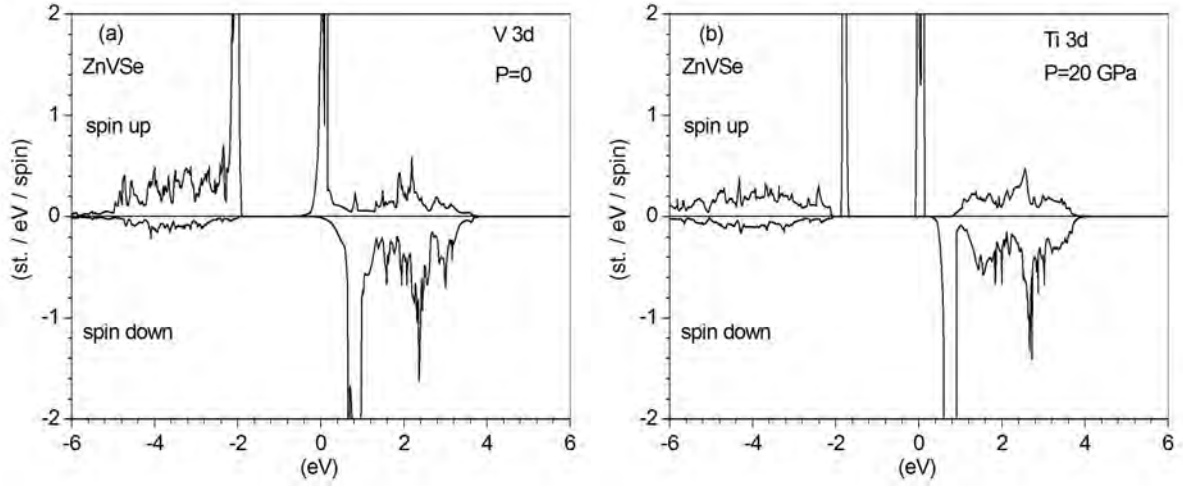

Figure 9. The spin-polarized DOS of the V 3d electrons in the ideal ZnVSe material.

The magnetic moments on the V atom in an ideal ZnVSe material at pressures of 0, 21, and 50 GPa are 1.72, 1.67, and 1.54 μ_B, respectively. If there is a vacancy, their values are much lower and at pressures 0, 20 and 48 GPa are equal to 1.44, 1.34 and 1.26 μ_B, respectively.

All the results of the electronic energy structure calculation were obtained here with the hybrid exchange-correlation functional PBE0. In this approach, it is possible to achieve a better positioning of 3d energy levels compared to that obtained using the usual GGA-PBE approximation [24].

We compare our results found in the PBE0 formalism for ZnCrSe and ZnFeSe materials with those obtained in the GGA-PBE approach [24]. From Figures 10 a, b we note that the Cr 3d states with higher energies and the spin up are located at the Fermi level, and those with lower energies are immersed in the valence band. This contradicts the results of [19], according to which the Fermi level and energy of 3d electrons are very close to the conduction band. For spin down approaches PBE0 and GGA-PBE [24] qualitatively give similar results, according to which 3d electrons form a conduction band. However, in the PBE0 approximation, the Fermi level is approximately 1.6 eV away from the lowest level of 3d electrons, whereas in the GGA-PBE formalism [24] this distance is approximately equal to 0.2 eV.

The results obtained for the ZnFeSe material are shown in Figures 10 c, d. In the PBE0 approach, we obtained the following results. For spin up, the smallest distance between the Fe 3d levels equals to 1.2 eV, whereas the GGA-PBE approximation [24] leads to its value of 0.6 eV. For spin down, part of the 3d states with lower energies is localized at the Fermi level, and the distance to the high-energy peak density of the 3d states is 1.6 eV. The same distance obtained in the GGA-PBE approach [24], approximately equal to 0.7 eV.

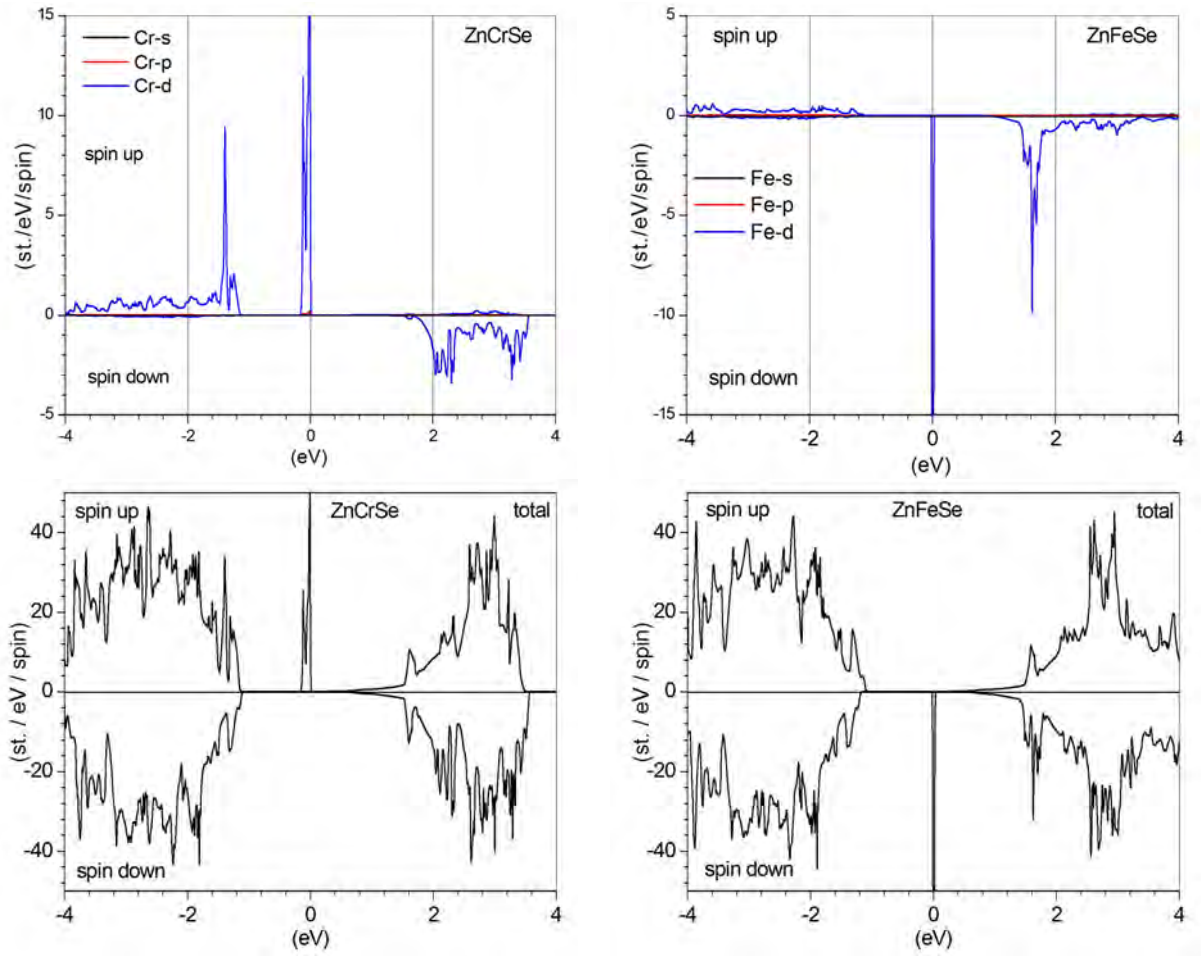

Figure 10. The spin-polarized partial DOS of the Cr (a) and Fe (c) atoms, and total DOS in the ideal materials ZnCrSe (c) and ZnFeSe (d).

Such differences between the parameters of the electronic energy bands obtained here in the PBE0 approach and in the GGA-PBE approximation [24], are explained by the fact that in the GGA-PBE formalism the electron density of s, p and d electrons is described by the same terms of the exchange-correlation functional. In the hybrid functional PBE0 s and p, electrons moving in wide energy zones are described in the GGA-PBE approximation. At the same time, the motion of 3d electrons in narrow energy zones with a high density of states is taken into account. The self-interaction error of 3d electrons is eliminated by adding the Hartree-Fock exchange potential, i.e. the PBE0 approach, which we apply here to all studied materials, has a significant advantage over the GGA-PBE approximation in describing the properties of materials containing d (f) electrons.

CONCLUSIONS

The electronic and magnetic properties in the ZnSe:T crystals have been evaluated for supercells $Zn_{31}T_1Se_{32}$ and $Zn_{30}v_1T_1Se_{32}$ under hydrostatic pressure. Here 3d transition atom T={Ti, V, Cr, Mn, Fe, Co, and Ni} substitutes the Zn one. The second supercells contain additionally a vacancy at Zn atom site. The strongly correlated 3d electrons are treated by means of the hybrid exchange-correlation functional PBE0, in which their self-interaction error is partly removed. It was found that under ambient conditions the materials $Zn_{31}Ti_1Se_{32}$ and $Zn_{31}V_1Se_{32}$ reveal metallic properties for both spin values. However, under the action of pressure, they become semiconductors. The introduction of a vacancy leads to a semiconductor state for all considered values of pressures and both spins in the $Zn_{30}v_1Ti_1Se_{32}$ material. But in the $Zn_{30}v_1V_1Se_{32}$ material the Fermi level is located in a valence band under low pressure, and it is a semiconductor under pressures $P > 21$ GPa. We have found that the combination of factors such as hydrostatic pressure and vacancy at the Zn atom site leads to a number of unexpected variety of the electronic and magnetic properties for the materials studied here. The results obtained in this work will be the basis for experiments to find effective materials for electronics application.

ORCID ID

Stepan V. Syrotyuk, https://orcid.org/0000-0003-4157-7351

REFERENCES

[1] Jen-Chuan Tung, Bang-Wun Lin, and Po-Liang Liu, ACS Omega, **10**(24), 8937 (2020), https://doi.org/10.3390/app10248937
[2] Fen Qiao, Rong Kang, Qichao Liang, Yongqing Cai, Jiming Bian, and Xiaoya Hou, ACS Omega **4**(7), 12271 (2019), https://doi.org/10.1021/acsomega.9b01539
[3] F. Trager, Lasers and Coherent Light Sources. In: *Springer Handbook of Lasers and Optics, 2nd ed.; T. Frank, Ed.* (Springer, Dordrecht, The Netherlands, 2012), **11**, pp. 749–750.
[4] S.B. Mirov, I.S. Moskalev, S. Vasilyev, V. Smolski, V.V. Fedorov, D. Martyshkin, J. Peppers , M. Mirov, A. Dergachev, and V. Gapontsev, IEEE Journal of Selected Topics in Quantum Electronics, **24**(5), 1601829 (2018), https://doi.org/10.1109/JSTQE.2018.2808284
[5] U. Demirbas, A. Sennaroglu, N. Vermeulen, H. Ottevaere, and H. Thienpont, *Proc. SPIE 6190, Solid State Lasers and Amplifiers II*, **61900A**(10), (2006), https://doi.org/10.1117/12.661725
[6] P.E. Blöchl, Phys. Rev. B. **50**, 17953 (1994), https://doi.org/10.1103/PhysRevB.50.17953
[7] M. Fuchs, M. Scheffler, Comput. Phys. Commun. **119**, 67 (1999).
[8] G.K.H. Madsen, P. Blaha, K. Schwarz, E. Sjöstedt, and Lars Nordström, Phys. Rev. B. **64**, 195134 (2001), https://doi.org/10.1103/PhysRevB.64.195134
[9] M. Ernzerhof, and G.E. Scuseria, J. Chem. Phys. **110**, 5029 (1999), https://doi.org/10.1063/1.478401
[10] P. Novák, J. Kunes, L. Chaput, and W.E. Pickett, Phys. Status Solidi B, **243**(3), 563 (2006), https://doi.org/10.1002/pssb.200541371
[11] E. Tran, P. Blaha, K. Schwarz, and P. Novák, Phys. Rev. B, **74**, 155108 (2006), https://doi.org/10.1103/PhysRevB. 74.155108
[12] J.P. Perdew, K. Burke, and M. Ernzerhof, Phys. Rev. Letters, **77**(18), 3865 (1996), https://doi.org/10.1103/PhysRevLett. 77.3865
[13] Y. Klysko, and S. Syrotyuk, Ukr. J. Phys. **66**(1), 55 (2021), https://ujp.bitp.kiev.ua/index.php/ujp/article/view/2019493
[14] S.V. Syrotyuk, and Yu.V. Klysko, Condens. Matter Phys. **23**(3), 33703 (2020), https://doi.org/10.5488/CMP.23.33703)
[15] Ya.M. Chornodolskyy, V.O. Karnaushenko, V.V. Vistovskyy, S.V. Syrotyuk, A.V. Gektin, and A.S. Voloshinovskii, Journal of Luminescence **237**, 118147 (2021), https://doi.org/10.1016/j.jlumin.2021.118147
[16] S.V. Syrotyuk, Physics and Chemistry of Solid State, **21**(4), 695 (2020), https://doi.org/10.15330/pcss.21.4.695-699)
[17] S.V. Syrotyuk, and O.P. Malyk, J. Nano- Electron. Phys. **11**(6), 06018 (2019), https://doi.org/10.21272/jnep.11(6).06018
[18] S.V. Syrotyuk, and O.P. Malyk, J. Nano- Electron. Phys. **11**(1), 01009 (2019), https://doi.org/10.21272/jnep.11(1).01009
[19] R.Yu. Petrus, H.A. Ilchuk, V.M. Sklyarchuk, A.I. Kashuba, I.V. Semkiv, and E.O. Zmiiovska, J. Nano- Electron. Phys. **10**, 06042 (2018), https://doi.org/10.21272/jnep.10(6).06042
[20] S.V. Syrotyuk, Metallofiz. Noveishie Tekhnol. **43**(4), 541 (2021), https://doi.org/10.15407/mfint.43.04.0541
[21] X. Gonze, F. Jollet, F. Abreu Araujo, D. Adams, B. Amadon, T. Applencourt, C. Audouze, et al, Comput. Phys. Commun. **205**, 106 (2016), https://doi.org/10.1016/j.cpc.2016.04.003
[22] N.A.W. Holzwarth, A.R. Tackett, and G.E. Matthews, Comput. Phys. Commun. **135**, 329 (2001), https://doi.org/10.1016/S0010-4655(00)00244-7)
[23] A.R. Tackett, N.A.W. Holzwarth, and G.E. Matthews, Comput. Phys. Commun. **135**, 348 (2001), https://doi.org/10.1016/S0010-4655(00)00241-1
[24] Y. Zhang, G. Feng, and S. Zhou, Proc. SPIE 9920, Active Photonic Materials VIII, 99200L (16 September 2016); SPIE Nanoscience + Engineering, 2016, San Diego, California, United States, https://doi.org/10.1117/12.2236152

ВПЛИВ ГІДРОСТАТИЧНОГО ТИСКУ І КАТІОННОЇ ВАКАНСІЇ НА ЕЛЕКТРОННІ ТА МАГНІТНІ ВЛАСТИВОСТІ КРИСТАЛІВ ZnSe:T (T = Ti, V, Cr, Mn, Fe, Co, Ni)

Степан В. Сиротюк
Національний університет "Львівська політехніка", 79013 Львів Україна

Параметри поляризованого за спіном електронного енергетичного спектру кристалів ZnSe: T (T = Ti, V, Cr, Mn, Fe, Co, Ni) вивчаються на основі надкомірки 2×2×2, побудованої на базі кристала ZnSe зі структурою сфалериту. Надкомірка містить 64 атоми, з яких один атом Zn заміщується перехідним 3d елементом T. Перший етап даного дослідження полягає в розрахунку в ідеальному матеріалі ZnTSe залежних від зовнішнього гідростатичного тиску параметрів електронних енергетичних зон. На другому етапі досліджується вплив тиску на значення параметрів електронного енергетичного спектру матеріалів ZnTSe з урахуванням вакансії на вузлі атома Zn. Розрахунки виконані за допомогою програми Abinit. Для кращого опису сильно скорельованих 3d електронів елемента T був застосований гібридний обмінно-кореляційний функціонал PBE0 з домішкою обмінного потенціала Хартрі-Фока, у якому відсутня самодія цих електронів. На основі отриманих електронних густин, поляризованих за спіном, були визначені також і магнітні моменти надкомірок. Виявлено значний вплив тиску на параметри електронних енергетичних зон. Так, ідеальний матеріал ZnTiSe за нульового тиску є металом для обидох значень спіна, але під дією тиску він стає напівпровідником. Цей же матеріал з точковим дефектом, тобто вакансією на вузлі атома Zn, виявляє властивості напівпровідника для обидвох орієнтацій спіна за нульового тиску. Виявлено, що вакансії докорінно змінюють параметри електронних енергетичних зон. Магнітні моменти надкомірки, як інтегральні величини поляризованих за спіном густин електронних станів, також відображають ці зміни. Так, у матеріалі ZnTiSe без дефектів магнітні моменти надкомірки становлять 1.92, 2.0 та 2.0 μ_B , за тисків 0, 21 та 50 GPa, тоді як тому ж матеріалі з вакансією відповідні значення становлять 0.39, 0.02 та 0.36 μ_B . Ідеальний матеріал ZnVSe за нульового тиску також є металом для обидвох значень спінового моменту, але за наявності катіонної вакансії він є характеризується псевдощілиною, оскільки рівень Фермі локалізований у верхній частині валентної зони. Ідеальні кристали ZnFeSe та ZnNiSe характеризуються подібними залежностями від тиску параметрів електронних енергетичних зон для обидвох спінів. Однак ці ж матеріали з катіонною вакансією характеризуються для спінів вгору рівнем Фермі, зануреним у валентну зону.

Ключові слова: ZnSe, домішка 3d, катіонна вакансія, електронні властивості, спін, магнітний момент, сильні кореляції, гібридний функціонал.

EAST EUROPEAN JOURNAL OF PHYSICS. 4. 43-48 (2021)
DOI: 10.26565/2312-4334-2021-4-04 ISSN 2312-4334

ELECTRICAL AND PHOTOELECTRIC PROPERTIES OF ORGANIC-INORGANIC HETEROJUNCTIONS PEDOT:PSS/*n*-CdTe†

Hryhorii P. Parkhomenko[a], Mykhailo M. Solovan[a], Andrii I. Mostovyi[a], Ivan G. Orletskyi[a], Viktor V. Brus[b,*]

[a]*Department of Electronics and Energy Engineering, Chernivtsi National University, 58012, Chernivtsi, Ukraine*
[b]*Department of Physics, Nazarbayev University, 010000, Nur-Sultan, Kazakhstan*
**Corresponding Author: viktor.brus@nu.edu.kz*
Received September 28, 2021; accepted November 14, 2021

PEDOT: PSS thin films are widely used as transparent coatings in flexible semiconductor devices including solar cells. However, they are not widely used as transparent coatings in combination with crystal substrates. This work shows the possibility of using PEDOT:PSS thin films as a frontal transparent conducting layer in hybrid organic-inorganic Schottky type heterojunctions of the PEDOT:PSS/*n*-CdTe, which were prepared by deposition of PEDOT:PSS thin films (using the spin-coating method) on crystalline cadmium telluride substrates. The current-voltage (in a wide temperature range) and capacitance-voltage (at room temperature) characteristics of heterojunctions were measurement and analyzed. It has been established that PEDOT:PSS/*n*-CdTe heterojunctions have good diode properties with a high rectification ratio RR≈10^5, a potential barrier height φ_0 = 0.95 eV, and series R_s = 91 Ohm and shunt R_{sh} = 5.7 × 10^7 Ohm resistances. Analysis of the forward branches of the *I–V* characteristics of heterojunctions showed that the dominant charge transfer mechanisms are determined by the processes of radiative recombination at low biases (3kT/e <*V* <0.3 V) and tunneling through a thin depleted layer at high biases (0.3 V <*V* <0.6 V). Capacity-voltage characteristics are plotted in the Mott-Schottky coordinate, taking into account the influence of series resistance, measured at a frequency of 1 MHz. Used the C-V characteristic was determined the value of the built-in potential V_c = 1.32 V (it correlates well with the cutoff voltage determined from the current-voltage characteristics) and the concentration of uncompensated donors in the *n*-CdTe substrate N_D-N_A = 8.79 × 10^{14} cm^{-3}. Although the photoelectric parameters of unoptimized PEDOT:PSS/*n*-CdTe heterojunctions are low, their photodiode characteristics (Detectivity D^*> 10^{13} Jones) are very promising for further detailed analysis and improvement. The proposed concept of a hybrid organic-inorganic heterojunction also has potential for use in inexpensive γ- and X-ray detectors.
Keywords: PEDOT:PSS, CdTe, heterojunction, photodetector, current transport.
PACS: 68.65.Pq, 68.55.Jk, 68.37.Hk, 68.37.−d, 71.20.−b, 71.20.Nr

For a long time, many scientific laboratories have been developing the technology to obtain high-quality crystals of cadmium telluride CdTe and study their physical properties. This material attracts materials scientists and device engineers involved in the development of new types of semiconductor devices for various applications.

Cadmium telluride (CdTe) is a direct-gap semiconductor of the $A^{II}B^{VI}$ group with a wide bandgap of 1.49 eV at 300 K [1,2]. Currently, CdTe semiconductor crystals find their application in different optoelectronic devices: solar cells, lasers, photoresistors, and ionizing radiation detectors [3-5].

Among the conductive polymers, PEDOT:PSS (polyenidoxythiophene) is widely used in organic and hybrid perovskite optoelectronics [6,7]. It can also replace transparent conductors such as ITO or FTO and is widely used on flexible substrates [8-10]. This degenerated p-type organic semiconductor is particularly interesting due to the synergy of its optical and electrical properties with the advantages of simple, low-cost solution processing.

So far, PEDOT:PSS films were used to fabricate ohmic back contacts to CdTe thin-film solar cells [11]. This is possible because of the large work function of PEDOT:PSS films close to that of p-type CdTe.

This contribution is the first to report on employing PEDOT:PSS thin films as the front transparent functional layer in a Schottky-type hybrid organic-inorganic heterojunction PEDOT:PSS/n-CdTe.

EXPERIMENTAL DETAILS

The heterojunctions were fabricated by spin-coating PEDOT:PSS water suspension at room temperature on freshly cleaved *n*-CdTe substrates (3.5×3.5×0.7 mm^3) at 2000 rpm. Afterward, the samples were annealed in air at the temperature of 370 K.Properties of the CdTe crystals are described in our previous paper [12].

The front electric contact to the PEDOT:PSS thin films was formed by using a graphite conductive paste. During the formation of the back electrical contact to the single-crystal n-CdTe substrate, a copper layer was deposited via the reduction from an aqueous solution of copper sulfate, followed by the thermal evaporation of indium [13].

A schematic representation of the fabricated photosensitive hybrid organic-inorganic heterostructures PEDOT:PSS/*n*-CdTe is shown in Figure 1a. The energy diagram of the PEDOT:PSS/n-CdTe heterojunction, built according to the Anderson model [14] is shown in Figure 1b. The energy parameters of the semiconductor components of the heterojunction were taken from the literature [5,14-17].

† ***Cite as:*** H.P. Parkhomenko, M.M. Solovan, A.I. Mostovyi, I.G. Orletskyi, and V.V. Brus, East. Eur. J. Phys. **4**, 43 (2021), https://doi.org/10.26565/2312-4334-2021-4-04

The current-voltage characteristics of the heterojunctions were measured according to the standard method using a Keysight B2985A precision Femto/pico-amperemeter in combination with a voltmeter Agilent 34410A. The measurements of the capacitance-voltage (*C–V*) characteristics of the heterojunctions were completed by an LCR Meter BR2876.

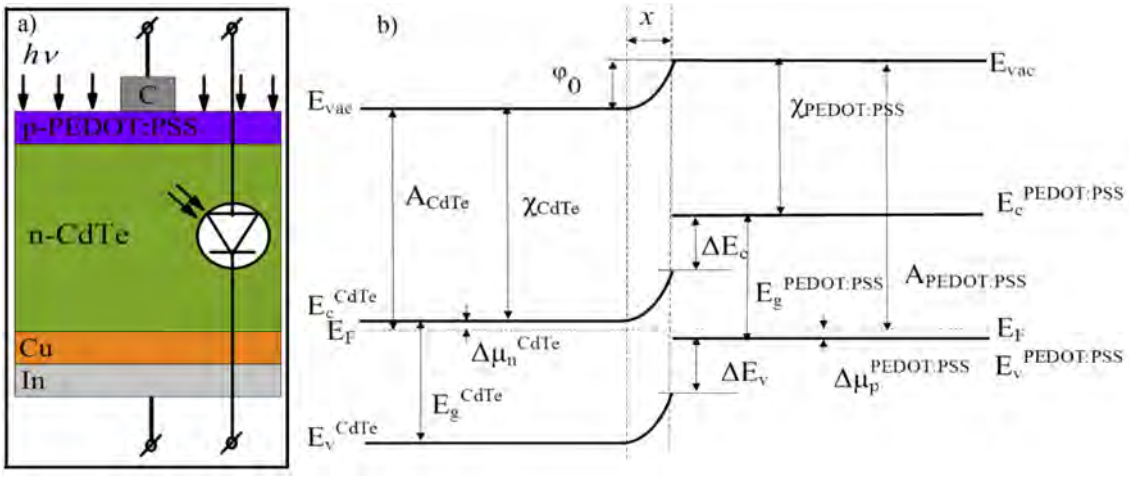

Figure 1. a) a schematic representation of the PEDOT:PSS/n-CdTe heterojunction photodiode; b) energy diagram of the PEDOT:PSS/n-CdTe heterojunction at zero bias: $E_g^{PEDOT:PSS}$ = 1.6 eV, $\chi_{PEDOT:PSS}$ = 3.6 eV, $A_{PEDOT:PSS}$ = 5.1 eV, E_g^{CdTe} = 1.5 eV, χ_{CdTe} = 4.28 eV, A_{CdTe} = 4.38 eV $\Delta\mu_p^{PEDOT:PSS} \approx 0.1$ eV, $\Delta\mu_n^{CdTe} = 0.1$ eV, $\Delta E_c = 0.68$ eV, $\Delta E_v = 0.58$ eV, $\varphi_0 = 0.72$ eV.

RESULTS AND DISCUSSIONS

Electrical properties of the PEDOT:PSS/n-CdTe heterostructures

Figure 2a reveals dark current-voltage characteristics of the hybrid heterojunctions PEDOT:PSS/n-CdTe. The work function difference between the PEDOT:PSS (5.1 eV) [17] and n-CdTe (4.38 eV) [5] resulted in a potential barrier for charge transport at the heterojunction interface with a high rectification ratio $RR_{2V} = 10^5$.

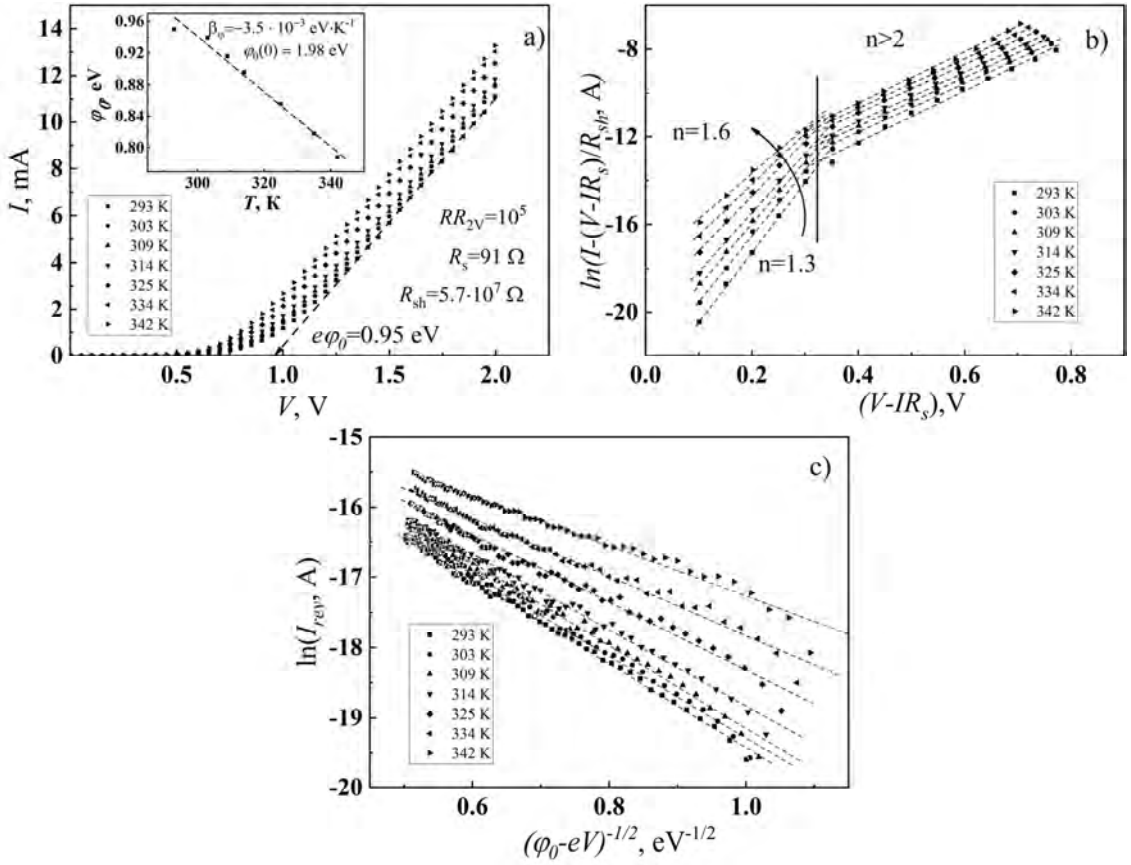

Figure 2. a) *I-V* characteristics of the PEDOT:PSS/*n*-CdTe heterojunctions (the inset: temperature dependence of the potential-barrier height); b) Forward branch of the *I–V* characteristics in a semi-logarithmic scale, taking into account the effect of series and shunt resistance; c) The tunneling current transport through the heterojunction under investigation at reverse bias.

Extrapolating the linear parts of the *I–V* characteristics towards their interception with the voltage axis allows to determine the height of the potential barrier at the PEDTO:PSS/n-CdTe heterojunction interface at different temperatures $\varphi_0 = eV_{bi}$, where V_{bi} is the built-in voltage, (see the inset in Fig. 2a). We have found that the temperature dependence of the potential-barrier height at the PEDOT:PSS/n-CdTe heterojunction is well described by the linear equation [12]:

$$\phi_0(T) = \phi_0(0) - \beta_\phi \cdot T \ , \tag{1}$$

where β_φ = -3.5 · 10^{-3} eV/K is the temperature coefficient of the potential-barrier height and $\varphi_0(0)$ = 1.98 eV is the potential-barrier height of the investigated heterojunction at the absolute zero temperature.

The series resistance R_s = 91 Ohm and shunt resistance R_{sh}=5.7·10^7 Ohm of the organic-inorganic heterojunction photodiode PEDOT:PSS/*n*-CdTe were established from the voltage dependence of its differential resistance R_{dif} at room temperature [18,19].

Charge transport mechanisms

Figure 2b shows the forward branches of the *I–V* characteristics of the hybrid PEDOT:PSS/*n*-CdTe heterojunction in the semi-logarithmic scale $\ln[I\text{-}(V\text{-}IR_s)/R_{sh}] = f(V\text{-}IR_s)$. The plot consists of two linear sections, that indicates an exponential dependence of current on voltage and the presence of two dominant charge transport mechanisms within the considered voltage range. The values of the ideality factor *n* ($\Delta\ln[I\text{-}(V\text{-}IR_s)/R_{sh}]/\Delta(V\text{-}IR_s) = e/nkT$) [20,21] for two voltage regions are shown in Figure 2b.

First, consider the voltage range ($3kT/e<V<0.3$ V). In this range, the measured *I–V* characteristics can be governed by the standard equation, which takes into account the effect of the series R_s and shunt R_{sh} resistance [22]:

$$I = I_0\left[\exp\left(\frac{e(V - IR_s(T))}{nkT}\right) - 1\right] + \frac{V - IR_s(T)}{R_{sh}(T)}, \tag{2}$$

where I_0 is the saturation current, *n* is the ideality factor, *k* is the Boltzmann constant and *T* is the absolute temperature.

The value of the nonideality factor changes from 1 to 2 with increasing temperature, which suggests that the current in this voltage range is well described by the emission-recombination model of current transport [15,20].

Now let us consider linear sections in the voltage range *V* > 0.3 V. The large nonideality factor *n*> 2 provides evidence on the tunneling model of charge transport. At large forward bais the space charge region becomes thin enough for direct tunneling and the *I–V* characteristics are well described by the Newman formula [12,14]:

$$I = I_t^0 \exp(\gamma T)\exp\left[\alpha(V - IR_s)\right] = I_t \exp\left[\alpha(V - IR_s)\right], \tag{3}$$

where I_t^0=2.3 · 10^{-12} A, α=11.8 eV, γ = 3.7 ·10^{-2} $K^{-1}$are constants.

In the case of an abrupt junction, the expression for the tunneling current at reverse bias has the form (4). Therefore, according to equation (4), the appearance of the reverse branches of the *I-V* characteristics as straight lines in the coordinates $\ln I_{rev} = f((\varphi_0 - qV)^{-1/2}$ (Figure 2c) confirms the dominance of the tunneling mechanism of current transport at reverse bias [23].

$$I_{rev} \approx a_0 \exp\left(\frac{b_0}{\sqrt{\phi_0(T) - eV}}\right) \tag{4}$$

where a_0 and b_0 are the voltage-independent parameters.

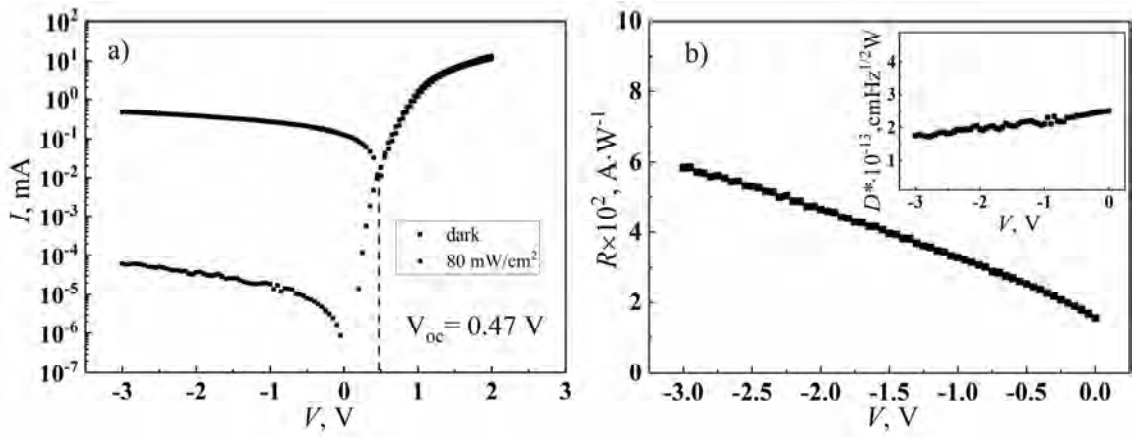

Figure 3. a) *I-V* characteristic of the PEDOT:PSS/*n*-CdTe heterojunction in the dark and under the white light illumination with the intensity of 80 mW/cm^2; b) voltage dependence of responsivity (*R*). The inset reveals the voltage dependence of detectivity (*D**).

Photoelectric properties

Figure 3a reveals the dark and light *I-V* characteristics of the hybrid heterojunction PEDOT:PSS/*n*-CdTe. The photovoltaic parameters of the heterojunction are the following: open-circuit voltage V_{oc} = 0.47 V, short-circuit current I_{sc} = 1.3 mA/cm^2, and fill factor FF = 0.31 under white light illumination with the intensity of 80 mW/cm^2.

The photodiode characteristics of the heterojunction can be quantified via its responsivity (R) and detectivity (D^*) in the shot noise-limited case [24,25]:

$$R=(I_{light}-I_{dark})/P_{opt}, \quad (5)$$

$$D^*=(RS/2qI_{dark})^{1/2}, \quad (6)$$

Where S is the photodetector area.

The responsivity R increases at larger reverse bias due to the widening of the depletion region, thus, improving the efficiency of separating photoinduced charge carriers (see Fig. 3b). The specific detectivity D^* describes the normalized radiation power required to obtain a signal from the photodetector at the noise level, remains relatively constant within the all tested range of reverse bias due to the counter compensating between the increasing I_{dark} and increasing R.

C-V characteristics

Figure 4a shows the capacitance-voltage characteristics of the hybrid heterojunction PEDOT:PSS/*n*-CdTe, the measurements were carried out at room temperature, in the frequency range 20 kHz - 1 MHz in the parallel RC circuit mode, the alternating current amplitude was 20 mV. Since part of the applied DC bias is dropped across the series resistance, so its effect was accounted for as follows: $V_{cor}=V-IR$.

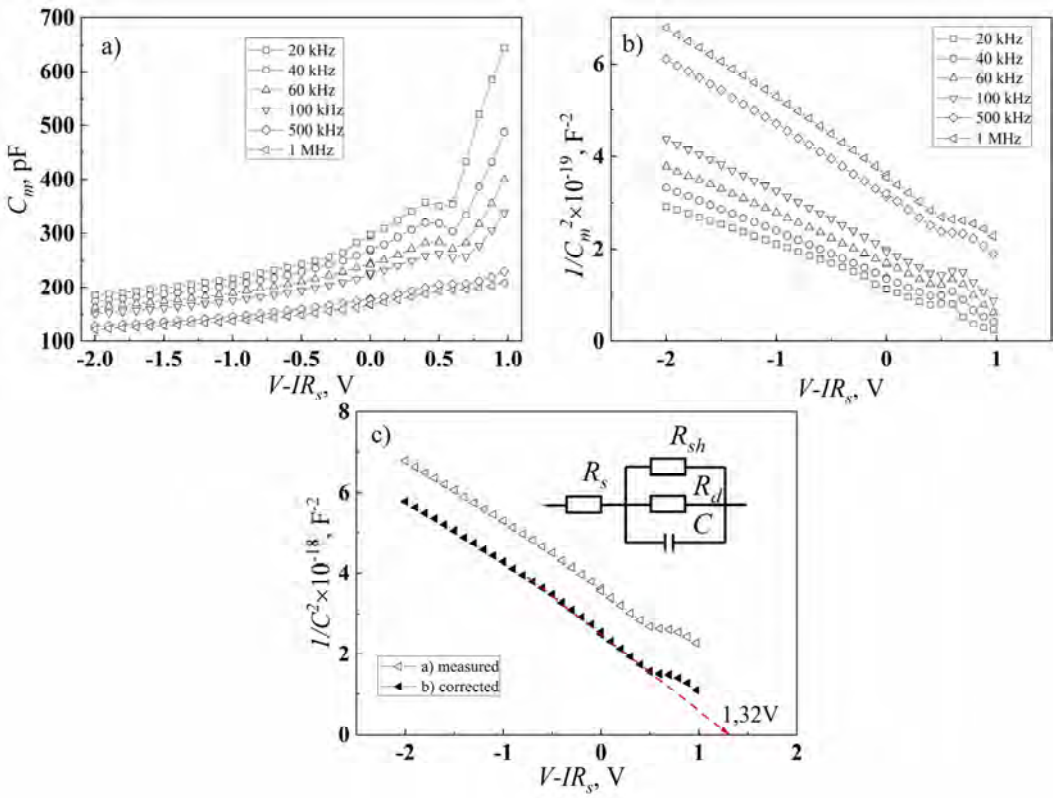

Figure 4. a) *C-V* characteristics of PEDOT:PSS/*n*-CdTe heterojunction at room temperature b) *C-V* characteristics in Mott-Schottky coordinates; c) Mott-Schottky dependence, measured at the frequency of 1 MHz: measured capacitance C_m, corrected capacitance by the effect of the series resistance C.

Let us consider the frequency dependence of the measured capacitance-voltage characteristics. It was shown in [26,27] that surface and bulk traps affect the measured capacitance C_m only at low frequencies while they can still follow the AC test signal. Thus, measuring C-V characteristics at high frequencies can mitigate the excessive capacitance originated from charging and discharging traps. At the same time, the series resistance parasitic contribution to the measured capacitance becomes more apparent with the increase of frequency (Fig. 4a). Therefore, the increase of the slope of the Mott-Schottky dependence in the frequency range 20 – 500 kHz dominantly results from the reduced capacitance originated from the charging-discharging surface and bulk traps. However, in the high-frequency range 500 kHz – 1 MHz, the parallel shift of the Mott-Schottky dependence is caused almost purely by the parasitic effect of the series resistance (Fig. 4b).

Since the effect of traps is negligible at the high frequency of 1 MHz, it is possible to analyze the *C-V* characteristics in this frequency range using a simplified equivalent circuit (the inset in Fig. 4c). The barrier capacitance of the heterojunction is calculated using the following formula, which accounts for the parasitic effect of the series resistance on measured high-frequency capacitance[27]:

$$C = \left[\frac{C_m^{-2} - 2R_s^2\omega^2 - \sqrt{\left(C_m^{-2} - 2R_s^2\omega^2\right)^2 - 4R_s^4\omega^4}}{2R_s^4\omega^4} \right]^{1/2}. \quad (7)$$

Plotting the high-frequency Mott-Schottky dependence, corrected by the effect of the series resistance (Fig. 4c), allows proper analysis of the height of the potential barrier and the concentration of uncompensated donor centers in the CdTe substrate. By extrapolating the linear part of the corrected Mott-Schottky dependence toward the intersection with the voltage axis, we determine the value of the built-in potential V_c = 1.32 V that is in good agreement with the value of the built-in potential determined from the *I–V* characteristic of the heterojunctions V_{bi} = 1.32 V.

According to the Donelly-Milns model [28], this is clear evidence of a high-quality heterojunction interface between the PEDOT:PSS layer and the n-CdTe substrate without charged interface defect states.

Having taken into account that the space charge region is almost entirely located in the CdTe substrate, the voltage dependence of the barrier capacitance can be expressed by the following equation [13]:

$$C = S\sqrt{\frac{e^2\varepsilon_n\varepsilon_0 N_D - N_A}{2\left(\phi_0 - e(V - IR_s)\right)}}, \quad (8)$$

Where S is the area of the heterojunction.

The density of uncompensated donors can be determined from the slope of the Mott-Schottky dependence [13]:

$$N_D - N_A = -\frac{2}{S^2 e\varepsilon_n\varepsilon_0 \dfrac{\Delta C^{-2}}{\Delta(V - IR_s)}}. \quad (9)$$

The determined densities of uncompensated donors in the base material for linear regions at a reverse bias (Figure 4c) are 8.79×10^{14} cm^{-3}.

CONCLUSION

The possibilities of using solution-processed PEDOT:PSS thin films for the fabrication of photosensitive hybrid organic-inorganic heterojunctions PEDOT:PSS/n-CdTe were experimentally revealed in this study.

It was established that PEDOT:PSS/*n*-CdTe heterojunctions possess quite decent diode properties with a high rectification ratio $RR \approx 10^5$, the height of the potential barrier $\varphi_0 = eV_{bi}$ = 0.95 eV and the values of the series R_s = 91 Ω and shunt resistance $R_{sh} = 5.7 \cdot 10^7$ Ω.

The analysis of the forward branches of the *I–V* characteristics of the heterojunctions has shown that the dominant mechanisms of charge transport are defined by emission-recombination processes at a low bias ($3kT$ / e < V < 0.3 V) and tunneling through the thin depletion layer at large bias (0.3 V < V < 0.6 V).

Mott-Schottky dependence, measured at the frequency of 1 MHz and corrected by the effect of the series resistance, was used to determine the built-in potential V_c = 1.32 V (in good correlation with the cut-off voltage of the measured *I-V* characteristics) and the concentration of uncompensated donors in the n-CdTe substrate N_D-N_A = 8.79×10^{14} cm^{-3}.

Although the photovoltaic parameters of the unoptimized PEDOT:PSS/*n*-CdTe heterojunctions are low, their photodiode performance is quite promising for further detail analysis and improvement. The proposed concept of a hybrid wide-bandgap organic-inorganic solution-processed Schottky-type heterojunction also has potential for applications in low-cost γ- and *x*-ray detectors [29].

ORCID IDs

Hryhorii P. Parkhomenko, https://orcid.org/0000-0001-5358-1505; **Mykhailo M. Solovan,** https://orcid.org/0000-0002-1077-5702
Andrii I. Mostovyi, https://orcid.org/0000-0001-9634-0058; **Ivan G. Orletskyi,** https://orcid.org/0000-0001-5202-8353
Viktor V. Brus, https://orcid.org/0000-0002-8839-124X

REFERENCES

[1] P. Handler, Science **159**, 185 (1968). https://doi.org/10.1126/science.159.3811.185
[2] H. Lin, Irfan, W. Xia, H.N. Wu, Y. Gao, and C.W. Tang, Solar Energy Materials and Solar Cells, **99**, 349 (2012). https://doi.org/10.1016/j.solmat.2012.01.001
[3] Y. Eisen, and A. Shor, Journal of Crystal Growth, **184–185**, 1302 (1998), https://doi.org/10.1016/S0022-0248(98)80270-4
[4] V.V. Brus, and P.D. Maryanchuk, Carbon **78**, 613 (2014), https://doi.org/10.1016/j.carbon.2014.07.021
[5] H. Parkhomenko, M. Solovan, V.V. Brus, E. Maystruk, and P.D. Maryanchuk, OE, **57**, 017116 (2018), https://doi.org/10.1117/1.OE.57.1.017116

[6] I.B. Olenych, O.I. Aksimentyeva, L.S. Monastyrskii, Y.Y. Horbenko, and L.I. Yarytska, Nanoscale Res Lett, **10**, 187 (2015), https://doi.org/10.1186/s11671-015-0896-1
[7] U. Lang, E. Müller, N. Naujoks, and J. Dual, Advanced Functional Materials, **19**, 1215 (2009), https://doi.org/10.1002/adfm.200801258
[8] Y. Lan, Y. Wang, and Y. Song, Flex. Print. Electron. **5**, 014001 (2020), https://doi.org/10.1088/2058-8585/ab5ce3
[9] C. Roldán-Carmona, O. Malinkiewicz, A. Soriano, G.M. Espallargas, A. Garcia, P. Reinecke, T. Kroyer, M. Ibrahim Dar, M. Khaja Nazeeruddin, and H. J. Bolink, Energy & Environmental Science, **7**, 994 (2014), https://doi.org/10.1039/C3EE43619E
[10] T.M. Schmidt, T.T. Larsen-Olsen, J.E. Carlé, D. Angmo, and F.C. Krebs, Advanced Energy Materials, **5**, 1500569 (2015), https://doi.org/10.1002/aenm.201500569
[11] W. Wang, N.R. Paudel, Y. Yan, F. Duarte, and M. Mount, J. Mater. Sci.: Mater. Electron. **27**, 1057 (2016), https://doi.org/10.1007/s10854-015-3850-1
[12] H. Parkhomenko, M. Solovan, A. Mostovyi, K. Ulyanytsky, and P. Maryanchuk, Semiconductors, **51**, 344 (2017). https://doi.org/10.1134/S1063782617030216
[13] M.M. Solovan, N.M. Gavaleshko, V.V. Brus, A.I. Mostovyi, P.D. Maryanchuk, and E. Tresso, Semicond. Sci. Technol. **31**, 105006 (2016), https://doi.org/10.1088/0268-1242/31/10/105006
[14] B.L. Sharma, and R.K. Purohit, *Semiconductor Heterojunctions*, (Elsevier, 2015).
[15] A. Fahrenbruch, and R. Bube, *Fundamentals Of Solar Cells: Photovoltaic Solar Energy Conversion*, (Elsevier, 2012).
[16] Y.J. Lee, C. Yeon, J.W. Lim, and S.J. Yun, Solar Energy, **163**, 398 (2018), https://doi.org/10.1016/j.solener.2018.02.026
[17] A.M. Nardes, M. Kemerink, M.M. de Kok, E. Vinken, K. Maturova, and R.A.J. Janssen, Organic Electronics, **9**, 727 (2008), https://doi.org/10.1016/j.orgel.2008.05.006
[18] L.A. Kosyachenko, X. Mathew, V.V. Motushchuk, and V.M. Sklyarchuk, Solar Energy, **80**, 148 (2006), https://doi.org/10.1016/j.solener.2005.01.009
[19] M.M. Solovan, V.V. Brus, P.D. Maryanchuk, M.I. Ilashchuk, J. Rappich, N. Nickel, and S.L. Abashin, Semicond. Sci. Technol. **29**, 015007 (2013), https://doi.org/10.1088/0268-1242/29/1/015007
[20] S.M. Sze, Y. Li, and K.K. Ng, *Physics of Semiconductor Devices*, (John Wiley & Sons, 2021).
[21] G. a. H. Wetzelaer, M. Kuik, M. Lenes, and P.W.M. Blom, Appl. Phys. Lett. **99**, 153506 (2011), https://doi.org/10.1063/1.3651752
[22] V.V. Brus, P.D. Maryanchuk, M.I. Ilashchuk, J. Rappich, I.S. Babichuk, and Z.D. Kovalyuk, Solar Energy, **112**, 78 (2015), https://doi.org/10.1016/j.solener.2014.11.023
[23] V.V. Brus, and P.D. Maryanchuk, Appl. Phys. Lett. **104**, 173501 (2014), https://doi.org/10.1063/1.4872467
[24] Y. Zhang, P. Huang, J. Guo, R. Shi, W. Huang, Z. Shi, L. Wu, F. Zhang, L. Gao, C. Li, X. Zhang, J. Xu, and H. Zhang, Advanced Materials, **32**, 2001082 (2020), https://doi.org/10.1002/adma.202001082
[25] S. Chakrabarti, A.D. Stiff-Roberts, P. Bhattacharya, S. Gunapala, S. Bandara, S.B. Rafol, and S.W. Kennerly, IEEE Photonics Technology Letters, **16**, 1361 (2004), https://doi.org/10.1109/LPT.2004.825974
[26] V.V. Brus, Semicond. Sci. Technol. **28**, 025013 (2013), https://doi.org/10.1088/0268-1242/28/2/025013
[27] V.V. Brus, A.K.K. Kyaw, P.D. Maryanchuk, and J. Zhang, Progress in Photovoltaics: Research and Applications, **23**, 1526 (2015), https://doi.org/10.1002/pip.2586
[28] J.P. Donnelly and A.G. Milnes, IEEE Transactions on Electron Devices, **14**, 63 (1967), https://doi.org/10.1109/T-ED.1967.15900
[29] V.V. Brus, O.L. Maslyanchuk, M.M. Solovan, P.D. Maryanchuk, I. Fodchuk, V.A. Gnatyuk, N.D. Vakhnyak, S.V. Melnychuk, and T. Aoki, Sci. Rep. **9**, 1065 (2019), https://doi.org/10.1038/s41598-018-37637-w

ЕЛЕКТРИЧНІ ТА ФОТОЕЛЕКТРИЧНІ ВЛАСТИВОСТІ ОРГАНІЧНО-НЕОРГАНІЧНИХ ГЕТЕРОПЕРЕХОДІВ PEDOT:PSS/*n*-CdTe

Г.П. Пархоменко[a], М.М. Солован[a], А.І. Мостовий[a], І.Г. Орлецький[a], В.В. Брус[b]
[a]Кафедра електроніки і енергетики, Чернівецький національний університет імені Юрія Федьковича 58012, Чернівці, Україна
[b]Кафедра фізики, Університет Назарбаєва, 010000, Нур-Султан, Казахстан

Тонкі плівки PEDOT:PSS знайшли широке використання в якості прозорих покритів в гнучких напівпровідникових приладах в тому числі сонячних елементах. Проте вони доволі мало використовуюся в якості просвітлюючих покриттів в поєднанні з кристалічними підкладками. В даній роботі показано можливість використання тонких плівок PEDOT: PSS як фронтального прозорого провідного шару в гібридних органічно-неорганічних гетеропереходах типу Шотткі PEDOT: PSS/*n*-CdTe, які були виготовлені шляхом нанесення тонких плівок PEDOT: PSS (використовуючи метод спінкоутингу) на кристалічні підкладки телуриду кадмію. Виміряно та проаналізовано вольт-амперні (в широкому діапазоні температур) та вольт-фарадні (при кімнатній температурі) характеристики гетеропереходів. Встановлено, що гетеропереходи PEDOT: PSS/*n*-CdTe володіють хорошими діодними властивостями з високим коефіцієнтом випрямлення RR≈10^5, висотою потенціального бар'єру φ_0 = 0,95 еВ та значеннями послідовного R_s = 91 Ом і шунтуючого R_{sh} = 5,7 × 10^7 Ом опорів. Аналіз прямих гілок ВАХ гетеропереходів показав, що домінуючі механізми переносу заряду визначаються процесами випромінювальної рекомбінації при малих зміщеннях (3kT/e <*V* <0,3 В) та тунелювання через тонкий збіднений шар при великих зміщеннях (0,3 В <*V*<0,6 В). Вольт-фаратні характеристики побудовані в кординатах Мотта-Шотткі з врахуванням впливу послідовного опору, виміряні при частоті 1 МГц. З ВФХ було визначено величину вбудованого потенціалу V_c= 1,32 В (яка добре корелює з напругою відсічки визначеною з вольт-амперних характеристик) та концентрацію незкомпенсованих донорів у підкладці *n*-CdTe N_D-N_A = 8,79 × 10^{14} $см^{-3}$. Хоча фотоелектричні параметри неоптимізованих гетеропереходів PEDOT:PSS/*n*-CdTe низькі, їх фотодіодні характеристики (детективність D^*> 10^{13} Джонс) є досить перспективними для подальшого детального аналізу та вдосконалення. Запропонована концепція гібридного органічно-неорганічного гетеропереходу типу діода Шотткі, також має потенціал для застосування в недорогих γ- та рентгенівських детекторах.

Ключові слова: PEDOT:PSS, CdTe, гетероперехід, фотодетектор, механізми струмопереносу.

EAST EUROPEAN JOURNAL OF PHYSICS. 4. 49-58 (2021)
DOI: 10.26565/2312-4334-2021-4-05 ISSN 2312-4334

FAMILY OF THE ATOMIC RADIAL BASIS FUNCTIONS OF THREE INDEPENDENT VARIABLES GENERATED BY HELMHOLTZ-TYPE OPERATOR†

Denys O. Protektor
V.N. Karazin Kharkiv National University
4, Svoboda Sq., Kharkiv, 61022, Ukraine
Corresponding Author: d.protector@karazin.ua
Received September 24, 2021; accepted November 24, 2021

The paper presents an algorithm for constructing the family of the atomic radial basis functions of three independent variables $AHorp_k(x_1,x_2,x_3)$ generated by Helmholtz-type operator, which may be used as basis functions for the implementation of meshless methods for solving boundary-value problems in anisotropic solids. Helmholtz-type equations play a significant role in mathematical physics because of the applications in which they arise. In particular, the heat equation in anisotropic solids in the process of numerical solution is reduced to the equation that contains the differential operator of the special form (Helmholtz-type operator), which includes components of the tensor of the second rank, which determines the anisotropy of the material. The family of functions $AHorp_k(x_1,x_2,x_3)$ is infinitely differentiable and finite (compactly supported) solutions of the functional-differential equation of the special form. The choice of compactly supported functions as basis functions makes it possible to consider boundary-value problems on domains with complex geometric shapes. Functions $AHorp_k(x_1,x_2,x_3)$ include the shape parameter k, which allows varying the size of the support and may be adjusted in the process of solving the boundary-value problem. Explicit formulas for calculating the considered functions and their Fourier transform are obtained. Visualizations of the atomic functions $AHorp_k(x_1,x_2,x_3)$ and their first derivatives with respect to the variables x_1 and x_2 at the fixed value of the variable $x_3 = 0$ for isotropic and anisotropic cases are presented. The efficiency of using atomic functions $AHorp_k(x_1,x_2,x_3)$ as basis functions is demonstrated by the solution of the non-stationary heat conduction problem with the moving heat source. This work contains the results of the numerical solution of the considered boundary-value problem, as well as average relative error, average absolute error and maximum error are calculated using atomic radial basis functions $AHorp_k(x_1,x_2,x_3)$ and multiquadric radial basis functions.

Keywords: atomic radial basis function, Helmholtz-type operator, meshless methods, boundary-value problems, anisotropic thermal conductivity.
PACS: 02.60.-x, 44.10.+i

Currently, meshless methods for the numerical solution of boundary-value problems are being actively developed [1-5]. In particular, methods that implement the approximation of a differential equation in the strong form (collocation methods) using compactly supported radial functions as basis [6-10]. The use of compactly supported radial basis functions leads to a sparse interpolation matrix and allows effectively avoiding ill-conditioning, and therefore, reduces computational costs. However, the lower order of accuracy of compactly supported radial basis functions compared to global supported functions is a serious obstacle to their practical use.

New opportunities for the practical implementation of meshless schemes appear with the use of atomic radial basis functions. The discovery of classes of atomic functions is due to Rvachev V. L. and Rvachev V. A. [11], who constructed the simplest one-dimensional atomic function $up(x)$ in 1971. The special properties of the function $up(x)$ (infinite differentiability and compact support) made it possible to construct algorithmically simple computational schemes for solving problems of interpolation and approximation of functions [12]. These functions were used to solve boundary-value problems through the application of variational methods. The expansion of the concept of atomic function in case of many independent variables was presented in the works of Kolodyazhny V. M., Rvachev V. A. and Lisina O. Yu. [13-17]. Atomic functions generated by various differential operators such as the Laplace, Helmholtz, Klein-Gordon, biharmonic operator, etc. have been constructed. The obtained atomic radial basis functions have demonstrated their efficiency in the numerical solution of unsteady heat conduction problems in isotropic solids using meshless schemes [18,19].

Currently, there are many natural and synthetic materials, whose thermophysical properties depend on the direction; they are called anisotropic materials. Common examples of anisotropic materials are crystals and single crystals, steel and alloy billets (rolling, stamping), fibrous materials and thin films, fiber reinforced plastics, quartz, graphite, etc. In this case the heat equation in anisotropic solids in the process of numerical solution is reduced to the equation that contains the differential operator of the special form (Helmholtz-type operator), which includes components of the tensor of the second rank, which determines the anisotropy of the material.

The study of heat conduction processes in anisotropic solids is a major focus of modern engineering research in the energy, machine-building, nuclear and other industries.

† ***Cite as:*** D. Protector, East. Eur. J. Phys. **4**, 49 (2021), https://doi.org/10.26565/2312-4334-2021-4-05

Goals of article is constructing family of the atomic radial basis functions generated by Helmholtz-type operator, which extends the subclass of functions used as basis functions in the implementation of meshless methods for solving boundary-value problems in anisotropic solids.

THE CONSTRUCTION ALGORITHM

Consider algorithm for constructing family of the atomic radial basis functions of three independent variables, which are the solution of the functional-differential equation of the following form:

$$L(K)u(x_1,x_2,x_3)-\delta^2 u(x_1,x_2,x_3)=\lambda\iint\limits_{\partial\Omega}u(k(x_1-\xi_1),k(x_2-\xi_2),k(x_3-\xi_3))d\omega+\mu u(kx_1,kx_2,kx_3), \tag{1}$$

where $L(K)-\delta^2=\sum\limits_{i,j=1}^{3}K_{ij}\dfrac{\partial^2}{\partial x_i\partial x_j}-\delta^2$ – Helmholtz-type operator; $K=\left[K_{ij}\right]_{1\le i,j\le 3}$ – symmetric positive definite tensor of the second rank, which determines the anisotropy of the material; $\partial\Omega$ – boundary of the sphere of radius $r_k:\sum\limits_{i=1}^{3}\xi_i^2=r_k^2$, $r_k=r_k(k)=\dfrac{k+1}{2k}$; k – shape parameter; λ, μ – parameters whose values are determined from the condition guaranteeing the existence of the compactly supported solution of equation (1); δ^2 – parameter of the Helmholtz-type operator.

Apply the three-dimensional Fourier transform to equation (1):

$$\begin{aligned}&\int\limits_{-\infty}^{+\infty}\int\limits_{-\infty}^{+\infty}\int\limits_{-\infty}^{+\infty}\left[L(K)u(x_1,x_2,x_3)-\delta^2u(x_1,x_2,x_3)\right]e^{-i(t_1x_1+t_2x_2+t_3x_3)}dx_1dx_2dx_3=\\&\quad=\lambda\int\limits_{-\infty}^{+\infty}\int\limits_{-\infty}^{+\infty}\int\limits_{-\infty}^{+\infty}\left\{\iint\limits_{\partial\Omega}u(k(x_1-\xi_1),k(x_2-\xi_2),k(x_3-\xi_3))d\omega+\mu u(kx_1,kx_2,kx_3)\right\}e^{-i(t_1x_1+t_2x_2+t_3x_3)}dx_1dx_2dx_3.\end{aligned} \tag{2}$$

Denote by $U(t_1,t_2,t_3)$ the result of applying the three-dimensional Fourier transform to the function $u(x_1,x_2,x_3)$:

$$U(t_1,t_2,t_3)=\int\limits_{-\infty}^{+\infty}\int\limits_{-\infty}^{+\infty}\int\limits_{-\infty}^{+\infty}u(x_1,x_2,x_3)e^{-i(t_1x_1+t_2x_2+t_3x_3)}dx_1dx_2dx_3.$$

Let $k(x_i-\xi_i)=\eta_i$, $i=1,2,3,$ in this case $x_i=\dfrac{\eta_i}{k}+\xi_i$. On the right-hand side of equation (2), we change the order of applying the operation of integration over the surface of the sphere and the operation of the three-dimensional Fourier transform. As a result, equation (2) can be rewritten as

$$\begin{aligned}&-\left(K_{11}t_1^2+K_{22}t_2^2+K_{33}t_3^2+2K_{12}t_1t_2+2K_{13}t_1t_3+2K_{23}t_2t_3\right)U(t_1,t_2,t_3)-\delta^2U(t_1,t_2,t_3)=\\&\quad=\lambda\iint\limits_{\partial\Omega}\left\{\int\limits_{-\infty}^{+\infty}\int\limits_{-\infty}^{+\infty}\int\limits_{-\infty}^{+\infty}u\left(k\frac{\eta_1}{k},k\frac{\eta_2}{k},k\frac{\eta_3}{k}\right)e^{-i\left[t_1\left(\frac{\eta_1}{k}+\xi_1\right)+t_2\left(\frac{\eta_2}{k}+\xi_2\right)+t_3\left(\frac{\eta_3}{k}+\xi_3\right)\right]}d\frac{\eta_1}{k}d\frac{\eta_2}{k}d\frac{\eta_3}{k}\right\}d\omega+\frac{\mu}{k^3}U\left(\frac{t_1}{k},\frac{t_2}{k},\frac{t_3}{k}\right).\end{aligned} \tag{3}$$

After applying the three-dimensional Fourier transform on the right-hand side of equation (3), we obtain

$$\begin{aligned}&-\left(K_{11}t_1^2+K_{22}t_2^2+K_{33}t_3^2+2K_{12}t_1t_2+2K_{13}t_1t_3+2K_{23}t_2t_3+\delta^2\right)U(t_1,t_2,t_3)=\\&\qquad=\frac{1}{k^3}U\left(\frac{t_1}{k},\frac{t_2}{k},\frac{t_3}{k}\right)\left[\lambda\iint\limits_{\partial\Omega}e^{-i(t_1\xi_1+t_2\xi_2+t_3\xi_3)}d\omega+\mu\right].\end{aligned} \tag{4}$$

For further solution, it is necessary to consider the integral over the surface of the sphere $\partial\Omega:\xi_1^2+\xi_2^2+\xi_3^2=r_k^2$ on the right-hand side of equation (4). It should be noted that the exponent of the integrand represents the dot product of two vectors $\vec{T}=(t_1,t_2,t_3)$, $\vec{\Xi}=(\xi_1,\xi_2,\xi_3)$.

We will assume that the vector $\vec{T}$ is directed along the z-axis of the Cartesian coordinate system in which the sphere $\partial\Omega$ is defined, and the vector $\vec{\Xi}$ is directed along the radius vector that describes this sphere. To simplify the integration procedure, we introduce spherical coordinates as $x = r\sin\theta\cos\varphi$, $y = r\sin\theta\sin\varphi$, $z = r\cos\varphi$. This representation allows the surface integral to be rewritten in the form

$$\iint\limits_{\partial\Omega} e^{-i\left(t_1\xi_1+t_2\xi_2+t_3\xi_3\right)}d\omega = r_k^2\int\limits_0^{2\pi}\int\limits_0^{\pi} e^{-i\sqrt{t_1^2+t_2^2+t_3^2}\sqrt{\xi_1^2+\xi_2^2+\xi_3^2}\cos\theta}\sin\theta d\theta d\varphi = r_k^2\int\limits_0^{2\pi}\int\limits_0^{\pi} e^{-ir_k\sqrt{t_1^2+t_2^2+t_3^2}\cos\theta}\sin\theta d\theta d\varphi. \tag{5}$$

The implementation of the integration procedure in (5) leads to the representation of the integral as the elementary function

$$\iint\limits_{\partial\Omega} e^{-i\left(t_1\xi_1+t_2\xi_2+t_3\xi_3\right)}d\omega = 4\pi r_k^2\frac{\sin r_k\sqrt{t_1^2+t_2^2+t_3^2}}{r_k\sqrt{t_1^2+t_2^2+t_3^2}}.$$

Based on the above, equation (4) can be rewritten as follows

$$U(t_1,t_2,t_3) = -\frac{U\left(\frac{t_1}{k},\frac{t_2}{k},\frac{t_3}{k}\right)\left[\lambda 4\pi r_k^2\frac{\sin r_k\sqrt{t_1^2+t_2^2+t_3^2}}{r_k\sqrt{t_1^2+t_2^2+t_3^2}}+\mu\right]}{k^3\left(K_{11}t_1^2+K_{22}t_2^2+K_{33}t_3^2+2K_{12}t_1t_2+2K_{13}t_1t_3+2K_{23}t_2t_3+\delta^2\right)}. \tag{6}$$

In order for the expression in braces to be an entire function, we will use the possibility of choosing the parameter μ, considering that $t_1^2+t_2^2+t_3^2\to 0$, $K_{11}t_1^2+K_{22}t_2^2+K_{33}t_3^2+2K_{12}t_1t_2+2K_{13}t_1t_3+2K_{23}t_2t_3\to 0$. In this case $\mu = -\frac{4\pi}{i\delta}\lambda r_k\sin(r_k i\delta)$.

The structure of equation (6) makes it possible to represent the ratio

$$f(x) = C(x)f\left(\frac{x}{a}\right),$$

where $f\left(\frac{x}{a}\right)$, $C(x)$ – functions which are analytic everywhere on the numerical axis, $a>0$, $a = const$, $C(0)=1$, $f(0)=1$, in the form of the infinite product [16]: $f(x)=\prod\limits_{h=0}^{+\infty}C\left(\frac{x}{a^h}\right)$. Thus, equation (6) can be written in the following form:

$$U(t_1,t_2,t_3) = \prod_{h=0}^{\infty}\frac{\mu - 4\pi r_k^2\lambda\frac{\sin\frac{r_k}{k^h}\sqrt{t_1^2+t_2^2+t_3^2}}{\frac{r_k}{k^h}\sqrt{t_1^2+t_2^2+t_3^2}}}{k^3\left(\frac{K_{11}t_1^2+K_{22}t_2^2+K_{33}t_3^2+2K_{12}t_1t_2+2K_{13}t_1t_3+2K_{23}t_2t_3}{k^{2h}}+\delta^2\right)}. \tag{7}$$

To ensure the convergence of the infinite product (7), we choose the parameter λ from the conditions: $h=0$, $t_1^2+t_2^2+t_3^2\to 0$, $K_{11}t_1^2+K_{22}t_2^2+K_{33}t_3^2+2K_{12}t_1t_2+2K_{13}t_1t_3+2K_{23}t_2t_3\to 0$, in this case $\lambda = -\frac{\left(k\delta\right)^3 i}{4\pi r_k\left(\sin\left(r_k i\delta\right)+r_k i\delta\right)}$.

Based on the generalization of the Paley-Wiener theorem [20] for the multidimensional case and the Polya-Plancherel theorem [21], we establish that the function $u(x_1, x_2, x_3)$ is an infinitely differentiable compactly supported function, for which the Fourier transform $U(t_1, t_2, t_3)$ is represented by the rapidly decreasing entire function of exponential type at $t_1^2 + t_2^2 + t_3^2 \to \infty$, $K_{11}t_1^2 + K_{22}t_2^2 + K_{33}t_3^2 + 2K_{12}t_1t_2 + 2K_{13}t_1t_3 + 2K_{23}t_2t_3 \to \infty$. Thus, as a result of applying the inverse Fourier transform to expression (7), we obtain the required finite function (the support of this function will be the sphere of unit radius). This function will be denoted by $AHorp_k(x_1, x_2, x_3)$, and will be called the atomic function.

From the above it is clear that the Fourier transform of the function $AHorp_k(x_1, x_2, x_3)$ is

$$AH\tilde{o}\tilde{r}p_k(t_1, t_2, t_3) = \prod_{h=0}^{\infty} \frac{\mu - 4\pi r_k^2 \lambda \dfrac{\sin \dfrac{r_k}{k^h}\sqrt{t_1^2 + t_2^2 + t_3^2}}{\dfrac{r_k}{k^h}\sqrt{t_1^2 + t_2^2 + t_3^2}}}{k^3\left(\dfrac{K_{11}t_1^2 + K_{22}t_2^2 + K_{33}t_3^2 + 2K_{12}t_1t_2 + 2K_{13}t_1t_3 + 2K_{23}t_2t_3}{k^{2h}} + \delta^2\right)}. \tag{8}$$

Function $AHorp_k(x_1, x_2, x_3)$ is even with respect to its variables and can be expanded in the triple Fourier series

$$AHorp_k(x_1, x_2, x_3) = \sum_{p=0}^{\infty}\sum_{q=0}^{\infty}\sum_{r=0}^{\infty} a_{pqr} \cos(p\pi x_1)\cos(q\pi x_2)\cos(r\pi x_3), \tag{9}$$

in which the Fourier coefficients are calculated by the following formulas:

$$\begin{aligned}
a_{000} &= \frac{1}{8};\\
a_{p00} &= \frac{1}{4}\int_{-\infty}^{+\infty} AHorp_k(\xi_1, 0, 0)\cos(p\pi\xi_1)\,d\xi_1;\\
a_{pq0} &= \frac{1}{2}\int_{-\infty}^{+\infty}\int_{-\infty}^{+\infty} AHorp_k(\xi_1, \xi_2, 0)\cos(p\pi\xi_1)\cos(q\pi\xi_2)\,d\xi_1 d\xi_2;\\
a_{0q0} &= \frac{1}{4}\int_{-\infty}^{+\infty} AHorp_k(0, \xi_2, 0)\cos(q\pi\xi_2)\,d\xi_2;\\
a_{0qr} &= \frac{1}{2}\int_{-\infty}^{+\infty}\int_{-\infty}^{+\infty} AHorp_k(0, \xi_2, \xi_3)\cos(q\pi\xi_2)\cos(r\pi\xi_3)\,d\xi_2 d\xi_3;\\
a_{p0r} &= \frac{1}{2}\int_{-\infty}^{+\infty}\int_{-\infty}^{+\infty} AHorp_k(\xi_1, 0, \xi_3)\cos(p\pi\xi_1)\cos(r\pi\xi_3)\,d\xi_1 d\xi_3;\\
a_{00r} &= \frac{1}{4}\int_{-\infty}^{+\infty} AHorp_k(0, 0, \xi_3)\cos(r\pi\xi_3)\,d\xi_3;\\
a_{pqr} &= \int_{-\infty}^{+\infty}\int_{-\infty}^{+\infty}\int_{-\infty}^{+\infty} AHorp_k(\xi_1, \xi_2, \xi_3)\cos(p\pi\xi_1)\cos(q\pi\xi_2)\cos(r\pi\xi_3)\,d\xi_1 d\xi_2 d\xi_3,
\end{aligned} \tag{10}$$

where $p, q, r = 1, 2, ...$

It is clear that, since the function $AHorp_k(x_1, x_2, x_3)$ is finite, $\operatorname{supp} AHorp_k \in [-1,1]\times[-1,1]\times[-1,1]$ and even with respect to variables x_1, x_2, x_3, in the expressions for the Fourier coefficients (10), improper integrals can be replaced by definite integrals, and integrands can be replaced by exponential functions. These transformations make it possible to rewrite the Fourier coefficients (10) of series (9) in the following form:

$$
\begin{aligned}
&a_{000} = \frac{1}{8};\\
&a_{p00} = \frac{1}{4}\int_{-1}^{1} AHorp_k(\xi_1,0,0)e^{-ip\pi\xi_1}d\xi_1 = \frac{1}{4}AH\tilde{o}\tilde{r}p_k(p\pi,0,0);\\
&a_{pq0} = \frac{1}{2}\int_{-1}^{1}\int_{-1}^{1} AHorp_k(\xi_1,\xi_2,0)e^{-ip\pi\xi_1}e^{-iq\pi\xi_2}d\xi_1 d\xi_2 = \frac{1}{2}AH\tilde{o}\tilde{r}p_k(p\pi,q\pi,0);\\
&a_{0q0} = \frac{1}{4}\int_{-1}^{1} AHorp_k(0,\xi_2,0)e^{-iq\pi\xi_2}d\xi_2 = \frac{1}{4}AH\tilde{o}\tilde{r}p_k(0,q\pi,0);\\
&a_{0qr} = \frac{1}{2}\int_{-1}^{1}\int_{-1}^{1} AHorp_k(0,\xi_2,\xi_3)e^{-iq\pi\xi_2}e^{-ir\pi\xi_3}d\xi_2 d\xi_3 = \frac{1}{2}AH\tilde{o}\tilde{r}p_k(0,q\pi,r\pi);\\
&a_{p0r} = \frac{1}{2}\int_{-1}^{1}\int_{-1}^{1} AHorp_k(\xi_1,0,\xi_3)e^{-ip\pi\xi_1}e^{-ir\pi\xi_3}d\xi_1 d\xi_3 = \frac{1}{2}AH\tilde{o}\tilde{r}p_k(p\pi,0,r\pi);\\
&a_{00r} = \frac{1}{4}\int_{-1}^{1} AHorp_k(0,0,\xi_3)e^{-ir\pi\xi_3}d\xi_3 = \frac{1}{4}AH\tilde{o}\tilde{r}p_k(0,0,r\pi);\\
&a_{pqr} = \int_{-1}^{1}\int_{-1}^{1}\int_{-1}^{1} AHorp_k(\xi_1,\xi_2,\xi_3)e^{-ip\pi\xi_1}e^{-iq\pi\xi_2}e^{-ir\pi\xi_3}d\xi_1 d\xi_2 d\xi_3 = AH\tilde{o}\tilde{r}p_k(p\pi,q\pi,r\pi),
\end{aligned}
\tag{11}
$$

where $p,q,r = 1,2,...$

Functions $AHorp_k(x_1,x_2,x_3)$ form the family of atomic functions that are generated by the differential operator $L(K)-\delta^2$. Fig. 1 shows the visualization of the function $AHorp_k(x_1,x_2,x_3)$ at the fixed value of the variable $x_3 = 0$ for isotropic (*a*) and anisotropic $(K_{11} = 0.5, K_{22} = 1.5, K_{33} = 2.0, K_{12} = K_{13} = K_{23} = 0)$ (*b*) cases.

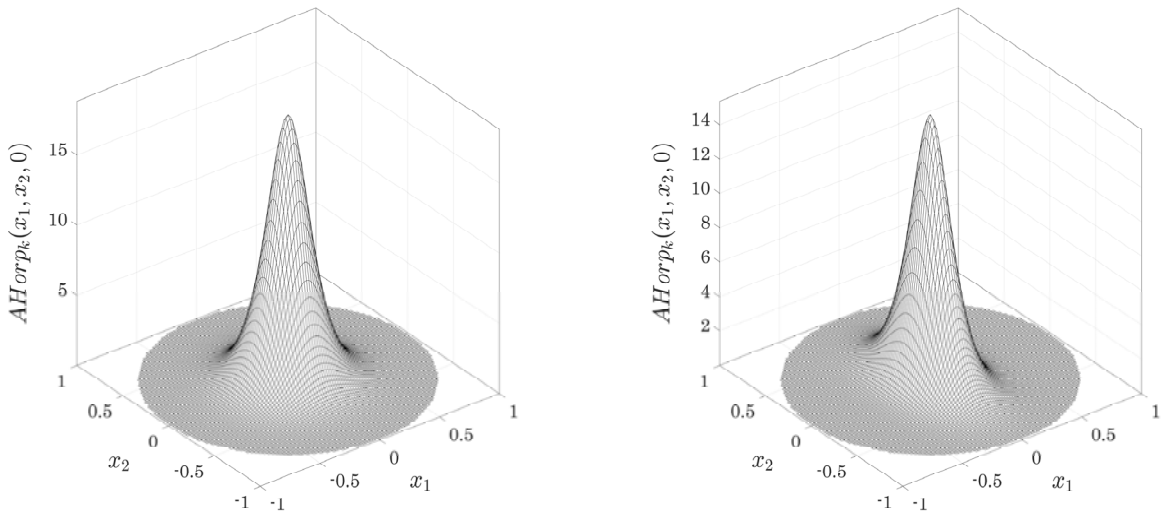

(*a*) *Isotropic case* (*b*) *Anisotropic case*

Figure 1. Visualization of the function $AHorp_k(x_1,x_2,x_3)$ at the fixed value of the variable $x_3 = 0$ for isotropic (*a*) and anisotropic (*b*) cases.

Theorem 1. *The family of atomic functions* $AHorp_k(x_1,x_2,x_3)$, *which are solutions of the functional-differential equation (1) with the values of the parameters*

$$\mu = -\frac{4\pi}{i\delta}\lambda r_k \sin(r_k i\delta); \quad \lambda = -\frac{(k\delta)^3 i}{4\pi r_k(\sin(r_k i\delta) + r_k i\delta)}$$

are finite, infinitely differentiable functions with support in the form of the sphere of unit radius, normalized by the condition $\int_{-\infty}^{+\infty}\int_{-\infty}^{+\infty}\int_{-\infty}^{+\infty} AHorp_k(x_1,x_2,x_3)dx_1dx_2dx_3 = 1$, *which are represented in the cube:* $[-1,1]\times[-1,1]\times[-1,1]$ *by the Fourier series (9) with the coefficients (11). The Fourier transform of functions* $AHorp_k(x_1,x_2,x_3)$ *(8) is rapidly decreasing function of exponential type at* $t_1^2+t_2^2+t_3^2\to\infty$, $K_{11}t_1^2+K_{22}t_2^2+K_{33}t_3^2+2K_{12}t_1t_2+2K_{13}t_1t_3+2K_{23}t_2t_3\to\infty$.

Fig. 2 shows the visualization of the first derivatives of the function $AHorp_k(x_1,x_2,x_3)$ with respect to the variables x_1 and x_2 at the fixed value of the variable $x_3=0$ for isotropic (*a*)-(*b*) and anisotropic $(K_{11}=0.5, K_{22}=1.5, K_{33}=2.0, K_{12}=K_{13}=K_{23}=0)$ (*c*)-(*d*) cases.

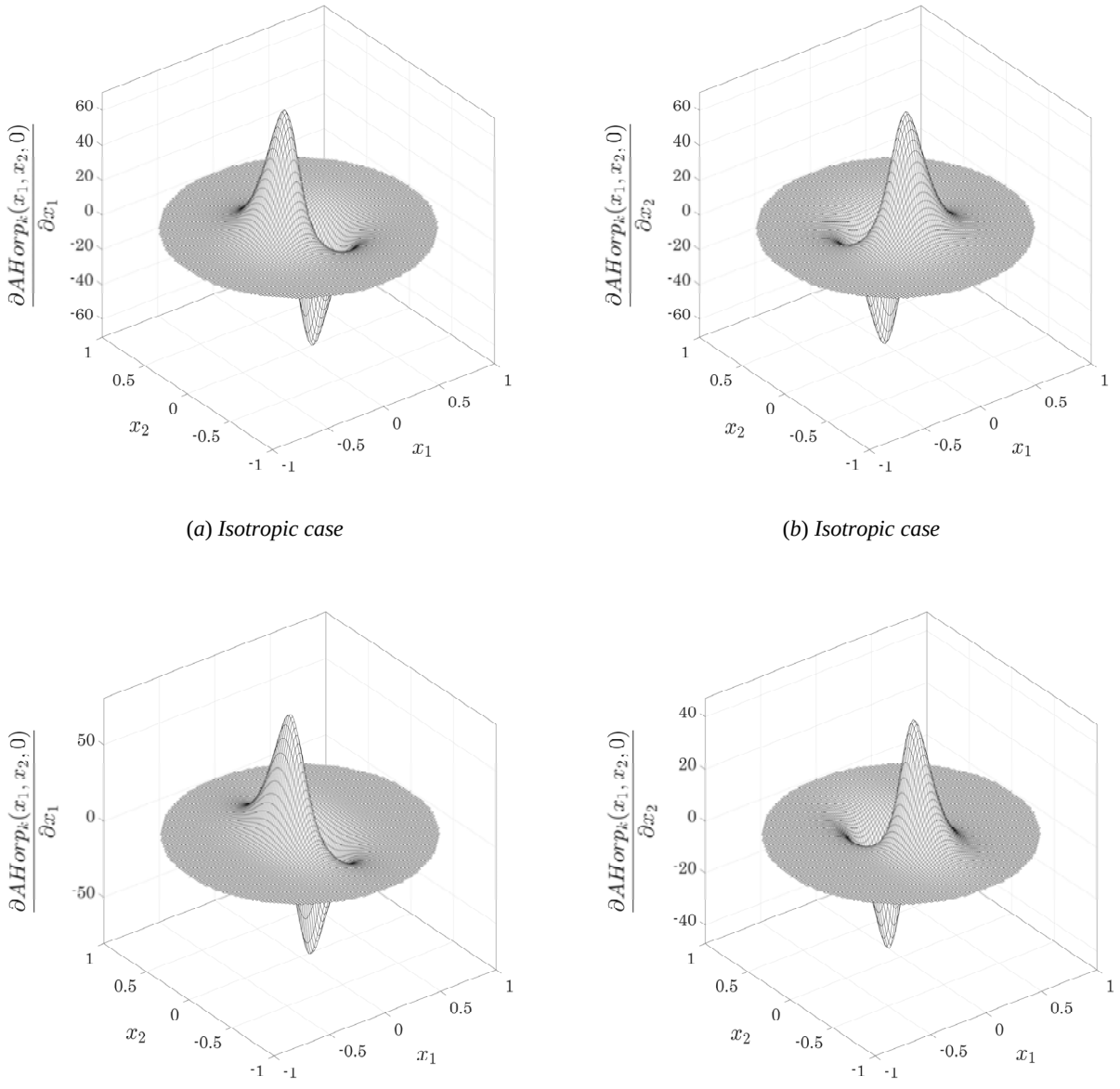

(*a*) *Isotropic case* (*b*) *Isotropic case*

(*c*) *Anisotropic case* (*d*) *Anisotropic case*

Figure 2. Visualization of the first derivatives of the function $AHorp_k(x_1,x_2,x_3)$ with respect to the variables x_1 and x_2 at the fixed value of the variable $x_3=0$ for isotropic (*a*)-(*b*) and anisotropic (*c*)-(*d*) cases.

Fig. 3 shows the visualization of the function $\left(L(K)-\delta^2\right)AHorp_k(x_1,x_2,x_3)$ at the fixed value of the variable $x_3=0$ for isotropic (*a*) and anisotropic $(K_{11}=0.5, K_{22}=1.5, K_{33}=2.0, K_{12}=K_{13}=K_{23}=0)$ (*b*) cases.

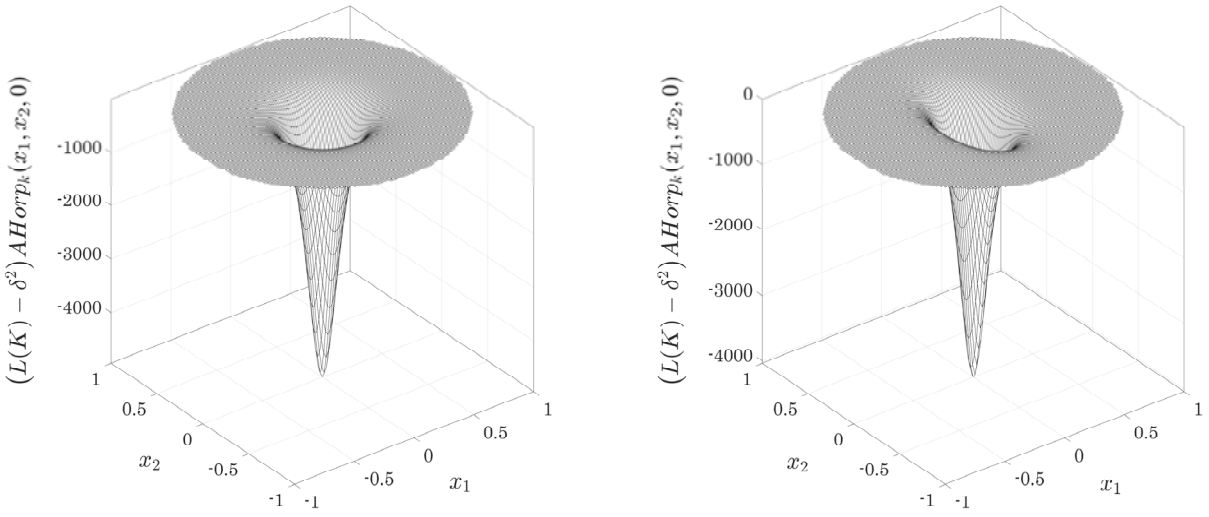

(*a*) *Isotropic case* (*b*) *Anisotropic case*

Figure 3. Visualization of the function $\left(L(K)-\delta^2\right)AHorp_k(x_1,x_2,x_3)$ at the fixed value of the variable $x_3=0$ for isotropic (*a*) and anisotropic (*b*) cases.

NUMERICAL RESULTS

We will illustrate the use of atomic functions $AHorp_k(x_1,x_2,x_3)$ as basis functions in the implementation of the meshless method for solving three-dimensional non-stationary heat conduction problems in materials with anisotropy, described in [1]. In this approach, the combination of the dual reciprocity method [22] using anisotropic radial basis function and the method of fundamental solutions [23] is used for solving boundary-value problem. The method of fundamental solutions is used for obtaining of homogenous part of the solution and the dual reciprocity method using anisotropic radial basis functions is used for obtaining of particular solution.

Problem statement

Consider the three-dimensional non-stationary heat conduction problem in the closed parallelepipedic domain $\Omega=[0,2]\times[0,2]\times[0,0.5]$ bounded by Γ. The unsteady heat equation in homogeneous anisotropic solids has the form:

$$\rho c_p\frac{\partial u}{\partial t}=K_{11}\frac{\partial^2 u}{\partial x^2}+K_{22}\frac{\partial^2 u}{\partial y^2}+K_{33}\frac{\partial^2 u}{\partial z^2}+2\left(K_{12}\frac{\partial^2 u}{\partial x\partial y}+K_{13}\frac{\partial^2 u}{\partial x\partial z}+K_{23}\frac{\partial^2 u}{\partial y\partial z}\right)+g$$

where $\rho=1$ – density, $c_p=1$ – specific heat at constant pressure, $u=u(x,y,z,t)$ – temperature, $g=g(x,y,z,t)$ – heat source, $t\in[0,2]$, $\Delta t=0.01$ – time step, $N=2646$ – the total number of interpolation nodes.

The initial condition is

$$u(x,y,z,0)=0,\quad (x,y,z)\in\Omega$$

The Dirichlet boundary conditions are

$$u(x,y,z,t)=0,\quad (x,y,z)\in\Gamma$$

Moving heat source is given by the equation:

$$g(x,y,z,t)=\exp\left(-80\left[\left(x-\frac{1}{2}\left(2+\sin(\pi t)\right)\right)^2+\left(y-\frac{1}{2}\left(2+\cos(\pi t)\right)\right)^2\right]\right),\quad (x,y,z)\in\Omega$$

The heat conduction tensor for this boundary-value problem has the form $K=\begin{bmatrix}5&0&0\\0&5&0\\0&0&10\end{bmatrix}$.

Fig. 4 shows the visualization of slices of the numerical solution by the plane $z = 0.3$ at different time moments.

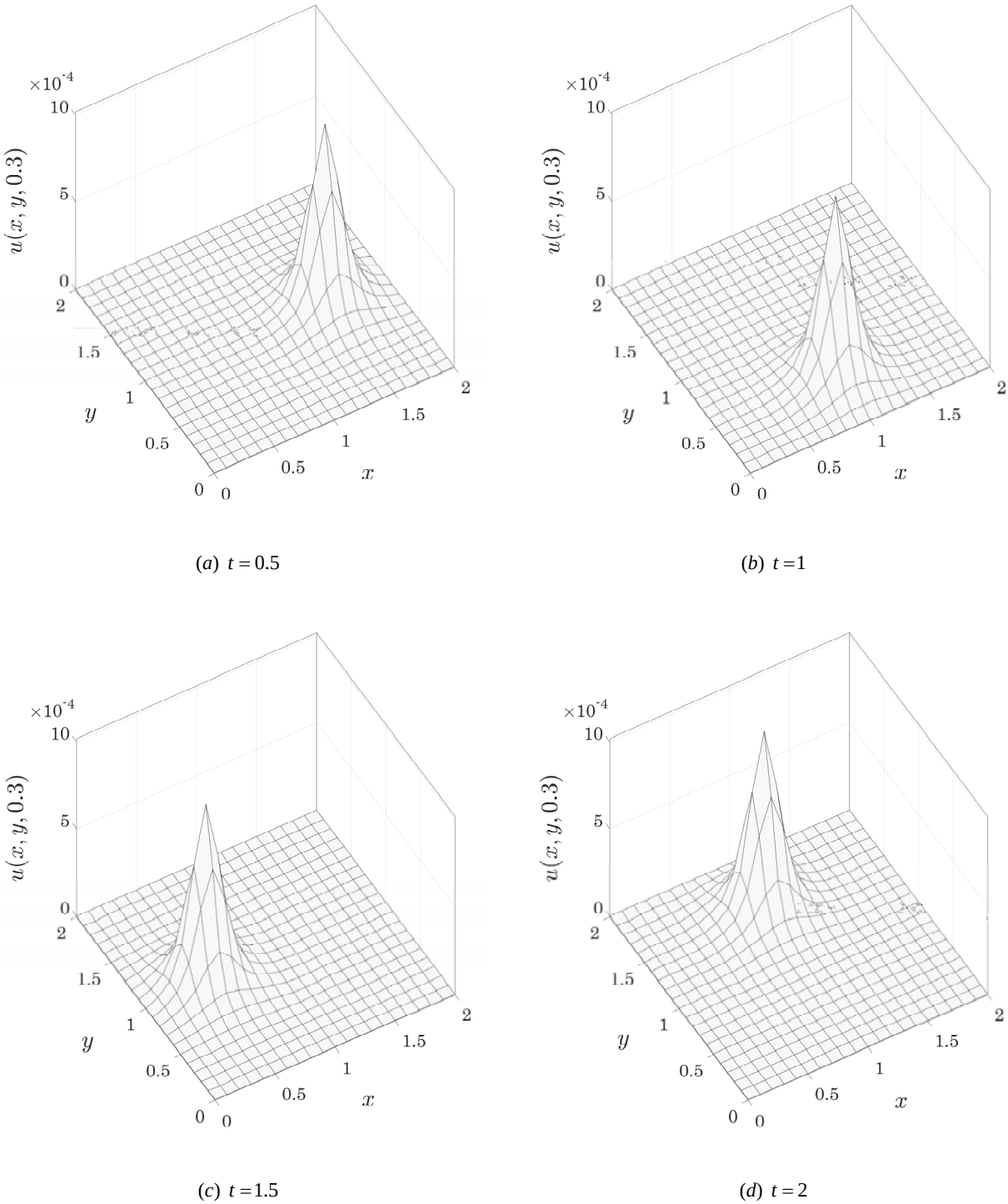

(*a*) $t = 0.5$ (*b*) $t = 1$

(*c*) $t = 1.5$ (*d*) $t = 2$

Figure 4. Visualization of slices of the numerical solution by the plane $z = 0.3$ at different time moments.

The exact solution for this boundary-value problem is:

$$u(x, y, z, t) = \sum_{m=1}^{\infty} \sum_{n=1}^{\infty} \sum_{k=1}^{\infty} u_{m,n,k}(t) \sin\left(\frac{\pi m}{l_1} x\right) \sin\left(\frac{\pi n}{l_2} y\right) \sin\left(\frac{\pi k}{l_3} z\right),$$

where $u_{m,n,k}(t)=\int_0^t\left[\frac{8}{l_1l_2l_3\rho c_p}\int_0^{l_1}\int_0^{l_2}\int_0^{l_3}g(\xi,\eta,\zeta,t)\sin\left(\frac{\pi m}{l_1}\xi\right)\sin\left(\frac{\pi n}{l_2}\eta\right)\sin\left(\frac{\pi k}{l_3}\zeta\right)d\xi\,d\eta\,d\zeta\right]\exp\left(-A_{m,n,k}(t-\tau)\right)d\tau$;

$A_{m,n,k}=a_{11}\left(\frac{\pi m}{l_1}\right)^2+a_{22}\left(\frac{\pi n}{l_2}\right)^2+a_{33}\left(\frac{\pi k}{l_3}\right)^2$; $a_{11}=\frac{K_{11}}{\rho c_p}$, $a_{22}=\frac{K_{22}}{\rho c_p}$, $a_{33}=\frac{K_{33}}{\rho c_p}$; $\{l_i\}_{i=1}^3$ – geometric dimensions of the parallelepipedic domain; $g(\xi,\eta,\zeta,t)$ – heat source.

To estimate the accuracy of the approximation of the numerical solution, the average relative error $rerr(u)$, the average absolute error $aerr(u)$ and the maximum error $merr(u)$ are used, which are calculated by the formulas:

$$rerr(u)=\sqrt{\frac{1}{N}\frac{\sum_{j=1}^{N}(u_j-\tilde{u}_j)^2}{\sum_{j=1}^{N}u_j^2}}$$

$$aerr(u)=\sqrt{\frac{1}{N}\sum_{j=1}^{N}(u_j-\tilde{u}_j)^2}$$

$$merr(u)=\max_j\left|u_j-\tilde{u}_j\right|$$

where u_j and $\tilde{u}_j$ are exact and numerical solutions, respectively.

Table 1 shows the errors of the numerical solution of the boundary-value problem regarding to the exact solution obtained using the atomic radial basis function (ARBF) and multiquadric radial basis function (MQ) at different time moments.

Table 1. Errors of the numerical solution of the boundary-value problem.

Basis function	t	$rerr(u)$	$aerr(u)$	$merr(u)$
ARBF	0.5	1.20529052×10^{-3}	4.44930401×10^{-6}	7.16979247×10^{-5}
	1	1.16163349×10^{-3}	4.28814625×10^{-6}	6.90741195×10^{-5}
	1.5	1.12912489×10^{-3}	4.16814019×10^{-6}	6.71658645×10^{-5}
	2	1.16305499×10^{-3}	4.29339239×10^{-6}	6.93488164×10^{-5}
MQ	0.5	3.41366269×10^{-3}	1.26014623×10^{-5}	1.05639294×10^{-4}
	1	3.27575942×10^{-3}	1.20923987×10^{-5}	1.10745011×10^{-4}
	1.5	2.98933244×10^{-3}	1.10350563×10^{-5}	1.04590253×10^{-4}
	2	2.99707792×10^{-3}	1.10636484×10^{-5}	1.07216618×10^{-4}

CONCLUSIONS

This paper presents the algorithm for constructing family of the atomic radial basis functions of three independent variables generated by Helmholtz-type operator. The functions $AHorp_k(x_1,x_2,x_3)$ extend the subclass of functions used as basis in the implementation of meshless methods for solving boundary-value problems in anisotropic solids. The efficiency of using atomic functions as basis functions is demonstrated by the benchmark problem, for which the average relative, average absolute and maximum errors were calculated. It should be noted that the shape parameter k of the functions $AHorp_k(x_1,x_2,x_3)$ allows varying the size of the support and may be adjusted in the process of solving the boundary-value problem. Increase of the parameter k leads to decrease of the size of the support of the basis function and increase of the sparsity of the interpolation matrix. The choice of the optimal shape parameter k remains the subject for future research.

ORCID IDs

Denys Protector, https://orcid.org/0000-0003-3323-7058

REFERENCES

[1] D.O. Protektor, V.M. Kolodyazhny, D.O. Lisin, and O.Yu. Lisina, Cybern. Syst. Anal. **57**, 470 (2021), https://doi.org/10.1007/s10559-021-00372-8.

[2] I.V. Garyachevskaya, and D.O. Protektor, Bulletin of V.N. Karazin Kharkiv National University, series Mathematical modeling. Information technology. Automated control systems. **45**, 10 (2020), https://doi.org/10.26565/2304-6201-2020-45-02. (in Ukrainian)

[3] D. Miotti, R. Zamolo, and E. Nobile, Energies. **14**(5), 1351 (2021), https://doi.org/10.3390/en14051351.

[4] X. Liang, D. Huang, T. Wang, Z. Liu, R. Zhu, L. Wang, and C. Huang, Int. J. Numer. Methods Eng. **122**(8), 1964 (2021), https://doi.org/10.1002/nme.6607.
[5] B. Zheng, S. Reutskiy, and J. Lu, Eur. Phys. J. Plus. **135**, 707 (2020), https://doi.org/10.1140/epjp/s13360-020-00547-w.
[6] S. Chantasiriwan, Int. Commun. Heat Mass Transf. **31**(8), 1095 (2004), https://doi.org/10.1016/j.icheatmasstransfer.2004.08.007.
[7] B. Sarler, and R. Vertnik, Comput. Math. with Appl. **51**(8), 1269 (2006), https://doi.org/10.1016/j.camwa.2006.04.013.
[8] R. Vertnik, and B. Sarler, Int. J. Numer. Method. H. **16**(5), 617 (2006), https://doi.org/10.1108/09615530610669148.
[9] B. Sarler, in: *Advances in Meshfree Techniques. Computational Methods in Applied Sciences*, edited by V. M. A. Leitao (Springer, Dordrecht, 2007), pp. 257-282.
[10] G. Kosec, and B. Sarler, Comput. Model. Eng. Sci. **25**(3), 197 (2008), https://www.techscience.com/CMES/v25n3/25100.
[11] V.L. Rvachev, and V.A. Rvachev, *Теория приближений и атомарные функции [Approximation theory and atomic functions]*, (Znanie, Moscow, 1978), pp. 64. (in Russian)
[12] V.L. Rvachev, and V.A. Rvachev, *Неклассические методы теории приближений в краевых задачах [Non-classical methods of approximation theory in boundary-value problems]*, (Naukova dumka, Kyiv, 1979), pp. 196. (in Russian)
[13] V.M. Kolodyazhny, and V.A. Rvachev, Dopov. Nac. akad. nauk Ukr. **5**, 17 (2004) (in Ukrainian)
[14] V.M. Kolodyazhny, and V.O. Rvachov, Dopov. Nac. akad. nauk Ukr. **1**, 12 (2005) (in Ukrainian)
[15] V.M. Kolodyazhny, and V.A. Rvachev, Cybern. Syst. Anal. **43**, 893 (2007), https://doi.org/10.1007/s10559-007-0114-y.
[16] O.Yu. Lisina, Bulletin of Taras Shevchenko National University of Kyiv. Maths. Mechanics. **21**, 53 (2009), http://nbuv.gov.ua/UJRN/VKNU_Mat_2009_21_15. (in Ukrainian)
[17] V.M. Kolodyazhny, and O.Yu. Lisina, Dopov. Nac. akad. nauk Ukr. **8**, 21 (2011), http://dspace.nbuv.gov.ua/handle/123456789/38513. (in Ukrainian)
[18] D.O. Protektor, Applied Questions of Mathematical Modelling. **1**, 89 (2018), http://nbuv.gov.ua/UJRN/apqmm_2018_1_11. (in Ukrainian)
[19] V.M. Kolodyazhny, and D.O. Lisin, Cybern. Syst. Anal. **49**, 434 (2013), https://doi.org/10.1007/s10559-013-9526-z.
[20] N. Wiener, and R.C. Paley, *Преобразование Фурье в комплексной области [Fourier Transforms in the Complex Domain]*, (Nauka, Moscow, 1964), pp. 268. (in Russian)
[21] L.I. Ronkin, *Элементы теории аналитических функций многих переменных [Elements of the theory of analytical functions of several variables]*, (Naukova dumka, Kyiv, 1977), pp. 125. (in Russian)
[22] M.S. Ingber, C.S. Chen, and J.A. Tanski, Int. J. Numer. Methods Eng. **60**(13), 2183 (2004), https://doi.org/10.1002/nme.1043.
[23] A. Bogomolny, SIAM J. Numer. Anal. **22**(4), 644 (1985), https://www.jstor.org/stable/2157574.

СІМЕЙСТВО АТОМАРНИХ РАДІАЛЬНИХ БАЗИСНИХ ФУНКЦІЙ ТРЬОХ НЕЗАЛЕЖНИХ ЗМІННИХ, ЯКІ ПОРОДЖУЮТЬСЯ ОПЕРАТОРОМ ТИПУ ГЕЛЬМГОЛЬЦА

Д.О. Протектор
Харківський національний університет імені В.Н. Каразіна
м. Свободи, 4, Харків, 61022, Україна

У статті представлено алгоритм побудови сімейства атомарних радіальних базисних функцій трьох незалежних змінних $AHorp_k(x_1,x_2,x_3)$, що породжуються оператором типу Гельмгольца, які використовуються в якості базисних при реалізації безсіткових методів розв'язку крайових задач в анізотропних твердих тілах. Рівняння типу Гельмгольца відіграють значну роль в математичній фізиці завдяки додаткам, в яких вони виникають. Зокрема, рівняння теплопровідності для анізотропних твердих тіл в процесі чисельного розв'язку зводиться до рівняння, яке містить диференціальний оператор спеціального виду (оператор типу Гельмгольца), який включає в себе компоненти тензора другого рангу, що визначає анізотропію матеріалу. Сімейство атомарних радіальних базисних функцій $AHorp_k(x_1,x_2,x_3)$ є нескінченно диференційованими фінітними розв'язками функціонально-диференціального рівняння спеціального виду. Вибір фінітних функцій в якості базисних дає можливість розглядати крайові задачі на областях зі складною геометричною конфігурацією. Функції $AHorp_k(x_1,x_2,x_3)$ містять параметр форми k, який дозволяє варіювати розмір носія та може уточнюватися в процесі розв'язку крайової задачі. Отримано явні формули для обчислення функцій $AHorp_k(x_1,x_2,x_3)$ та їх перетворення Фур'є. В роботі представлені візуалізації атомарних функцій $AHorp_k(x_1,x_2,x_3)$ та їх перших похідних за змінними x_1 і x_2 при фіксованому значенні змінної $x_3=0$ для ізотропного та анізотропного випадків. Ефективність використання атомарних функцій $AHorp_k(x_1,x_2,x_3)$ в якості базисних демонструється на прикладі тривимірної нестаціонарної задачі теплопровідності з рухомим джерелом тепла. Наведено результати чисельного розв'язку тестової крайової задачі, а також обчислені середня відносна, середня абсолютна і максимальна похибки наближених розв'язків, які отримані за допомогою атомарних радіальних базисних функцій $AHorp_k(x_1,x_2,x_3)$ та мультиквадратичних радіальних базисних функцій.

Ключові слова: атомарна радіальна базисна функція, оператор типу Гельмгольца, безсіткові методи, крайові задачі, анізотропна теплопровідність.

EAST EUROPEAN JOURNAL OF PHYSICS. 4. 59-67 (2021)
DOI: 10.26565/2312-4334-2021-4-06 ISSN 2312-4334

APPLICATION OF PARTICULAR SOLUTIONS OF THE BURGERS EQUATION TO DESCRIBE THE EVOLUTION OF SHOCK WAVES OF DENSITY OF ELEMENTARY STEPS[†]

Oksana L. Andrieieva[a,b,*], Victor I. Tkachenko[a,b], Oleksandr P. Kulyk[b,†], Oksana V. Podshyvalova[c], Volodymyr A. Gnatyuk[d], Toru Aoki[e]

[a]*National Science Center "Kharkiv Institute of Physics and Technology", 1 Akademichna St., Kharkiv 61108, Ukraine*
[b]*V.N. Karazin Kharkiv National University, 4 Svobody Sq., Kharkiv 61022, Ukraine*
[c]*National Aerospace University "Kharkiv Aviation Institute", 17 Chkalov St., Kharkiv 61070, Ukraine*
[d]*V.E. Lashkaryov Institute of Semiconductor Physics of the National Academy of Sciences of Ukraine, 41 Prospekt Nauky Kyiv 03028, Ukraine*
[e]*Research Institute of Electronics, Shizuoka University, 3-5-1 Johoku, Naka-ku, Hamamatsu 432-8011, Japan*
[*]*Corresponding author: andreevaoksana@kipt.kharkov.ua*
[†]*E-mail: kulykop@gmail.com*
Received October 1, 2021; revised November 1, 2021; accepted November 16, 2021

Particular solutions of the Burgers equations (BE) with zero boundary conditions are investigated in an analytical form. For values of the shape parameter a greater than 1, but approximately equal to 1, the amplitude of the initial periodic perturbations depends nonmonotonically on the spatial coordinate, i.e. the initial perturbation can be considered as a shock wave. Particular BE solutions with zero boundary conditions describe a time decrease of the amplitude of initial nonmonotonic perturbations, which indicates the decay of the initial shock wave. At large values of the shape parameter $a \gg 1$, the amplitude of the initial periodic perturbations depends harmoniously on the spatial coordinate. It is shown that over time, the amplitude and the spatial derivative of the profile of such a perturbation decrease and tend to zero. Emphasis was put on the fact that particular BE solutions can be used to control numerical calculations related to the BE-based description of shock waves in the region of large spatial gradients, that is, under conditions of a manifold increase in spatial derivatives. These solutions are employed to describe the profile of a one-dimensional train of elementary steps with an orientation near <100>, formed during the growth of a NaCl single crystal from the vapor phase at the base of a macroscopic cleavage step. It is shown that the distribution of the step concentration with distance from the initial position of the macrostep adequately reflects the shock wave profile at the decay stage. The dimensionless parameters of the wave are determined, on the basis of which the estimates of the characteristic time of the shock wave decay are made.
Keywords: Burgers equation, analytical solutions, zero boundary conditions, shock wave, decay
PACS: PhySH: Surface & interfacial phenomena

It is known that vicinal surfaces during crystal growth from the vapor phase or solutions are subject to a certain type of morphological instability – bunching of steps [1-4]. The formation of step bunching is a very serious problem when growing perfect crystals and obtaining surfaces that are atomically smooth on a macroscale [5-7]. On the other hand, such instabilities lead to the formation of large-scale nanostructured surfaces, which can be used to obtain low-dimensional structures actual for various technological applications [8-13]. A theoretical description of the nonlinear processes that result in the development of such kind of instabilities is very complicated due to a variety of causes leading to the step bunching in real experimental conditions (stochasticity of growth processes in general, presence of impurities, surface electromigration effect, Ehrlich-Schwöbel effect, elastic stress fields, variable macroscopic fields, non-quasi-static effects, etc.) [14-20]. The current state of research of step bunching, in particular, induced by electric currents, is presented in the references given in [21], where it is shown how the general picture of the process of bunching depends on the short-range repulsive force between the steps. It is customary to distinguish between the steps bunching as a result of morphological instability and as a shock in a kinematic wave, when the flux of steps is determined only by their local density [3].

The study of kinematic ("shock") waves of steps on crystal surfaces was first carried out by Frank [22], and by Cabrera and Vermilyea [23], who used the results of the general analysis of kinematic waves done by Lighthill and Whitham [24]. Later, it was shown that the appearance of shock waves is accompanied by a characteristic curvature of the vicinal surface profile, reflecting the space-time distribution of the step density[25]. At the level of optical microscopy, kinematic waves are usually perceived as steps of macroscopic height. At that, they should be distinguished from another type of macro-steps associated with the anisotropy of the surface energy ("true" macro-steps) [25]. Subsequently, based on the experimental data, it was concluded that the characteristic macroscopic relief of shock waves can be formed under certain conditions of crystal growth (evaporation) on vicinal thermodynamically stable surfaces [26, 27]. As follows from [25], the appearance of shock waves with a curved profile of the vicinal surface under such conditions is the main result of the diffusion interaction of moving elementary steps.

[†] ***Cite as:*** O.L. Andrieieva, V.I. Tkachenko, O.P. Kulyk, O.V. Podshyvalova, V.A. Gnatyuk, and T. Aoki, East. Eur. J. Phys. **4**, 59 (2021), https://doi.org/10.26565/2312-4334-2021-4-06

The dynamics of the macroscopic curved vicinal surface profile of a crystal growing from the vapor phase was studied in [28], in which the expressions for the average values of the ad atom concentration and the velocity of elementary steps were obtained by averaging over large spatial intervals. The nonlinear Korteweg-de Vries-Burgers (KVB) equation was obtained from the continuity equation for average values of the ad atom concentration and the velocity of elementary steps, taking phenomenological account of surface curvature [3, 29]. This equation describes the nonlinear dynamics of a train of parallel elementary steps on a macroscopically curved vicinal crystal surface. In a particular case, the KVB equation can transform into the Burgers equation (BE), which describes the formation and dynamics of shock waves.

The BE is a partial differential equation and it can be derived from the Navier-Stokes equations in the special case when the system under consideration has one spatial dimension [30].Following [30], the BE for the fluid flow velocity $u(x,t)$ is written in the next form:

$$\frac{\partial u}{\partial t}+u\frac{\partial u}{\partial x}=\mu\frac{\partial^2 u}{\partial x^2}, \tag{1}$$

where t and x are the time and coordinate along the flow, respectively, $\mu>0$ is the kinematic viscosity of the fluid. We consider the quantities t , x , and μ to be dimensionless.

Equation (1) is used in various fields of applied physics: to study the appearance of shock waves in hydrodynamic mediums[31], to describe the steepening and overturning of waves on the water surface [32]. The BE is also used in nonlinear acoustics to study cylindrical and spherical shock waves, as well as waves in relaxing mediums[33,34].

It is known that the BE can be reduced to the heat conduction equation using the Hopf-Cole transformation [35, 36]. The analytical solution obtained in this case describes the velocity of the medium for an arbitrary initial spatial distribution [37]. However, the integrals included in the solution cannot be always represented in an analytical form. Therefore, preference is given to such analytical solutions that are expressed in terms of elementary functions and can be easily applied to the problem being solved.

The scientific literature provides analytical and numerical methods for solving the BE [31, 35-37]. The asymptotic of solutions of the BE with initial or boundary conditions on a finite interval with periodic boundary conditions is analyzed in [38]. It is shown that in a viscous medium, the profile initially at rest transforms into a traveling wave with decreasing amplitude. At viscosity values approaching zero, the asymptotic profile takes on a saw tooth shape with periodic derivative discontinuities, similar to Fay's solution on the half-line.

Numerical calculations of the BE on a finite interval allow us not only to find new solutions, but also to verify experimentally their asymptotic using analytical estimates. It is noted that the numerical simulation of functions with a discontinuous derivative complicates the calculations, because in the vicinity of the discontinuities, the standard methods become unstable. The latter fact causes multiple oscillations, leading to a loss of accuracy and incorrect results. The only way to avoid that is to use an adaptive step length on the spatial coordinate, which corresponds to a step reduction of 10-20 times compared to the original step length. But the marked possibility is limited. Therefore, all calculations must be checked using model analytical solutions.

Analytical solutions of the BE with periodic boundary conditions were obtained in [39]. These solutions are proposed to be considered as a model for the development of stable and convergent grid methods for the numerical analysis of viscous media motion. However, the analytical solutions obtained in this work, as reference ones, do not describe the formation of a shock wave, but its decay.

The purpose of this work is to obtain analytical solutions of the BE that describe both the formation of a shock wave, which is expressed in an increase in the steepness of the wave profile, and its decay, accompanied by a decrease in the steepness of its profile in a sufficiently wide time interval. The obtained solutions are used to describe some experimental results related to growth from the vapor phase (or evaporation) of alkali-haloid crystals.

ANALYTICAL SOLUTIONS OF THE BE FOR SPATIALLY PERIODIC PERTURBATIONS WITH ZERO BOUNDARY CONDITIONS

Let us find the bounded solutions $|u(x,t)|<\infty$ of the BE (1) on the interval $x\in[0,L]$, for times $t\in[0,\infty]$with the boundary conditions:

$$u(0,t)=u(L,t)=0. \tag{2}$$

The Hopf-Cole transformation (HC) $u(x,t)=-2\mu\dfrac{1}{\mathrm{v}(x,t)}\dfrac{\partial \mathrm{v}(x,t)}{\partial x}$ [37] reduces the nonlinear equation (1) to the linear heat equation for the function $\mathrm{v}(x,t)$:

$$\frac{\partial \mathrm{v}(x,t)}{\partial t}=\mu\frac{\partial^2 \mathrm{v}(x,t)}{\partial x^2}. \tag{3}$$

The boundary condition (2) implies the property of the function $\mathrm{v}(x,t)$ in the range of its variation and its boundary conditions are the following:

$$\mathrm{v}(x,t) \neq 0, \tag{4}$$

$$\frac{\partial \mathrm{v}(0,t)}{\partial x} = \frac{\partial \mathrm{v}(L,t)}{\partial x} = 0, \tag{5}$$

where $0 \le x < L$, $0 \le t < \infty$.

Equation (3) has an infinite set of functions and conditions (4), (5) [39]:

$$\mathrm{v}_n(x,t) = \cos(\lambda_n x)\exp\left(-\mu\lambda_n^2 t\right), \tag{6}$$

where $\lambda_n = n\pi/L$, $n = 1,2,3,\ldots$.

Particular solutions (3) is determined up to a constant. Therefore, they can be represented as:

$$\mathrm{w}_n(x,t) = \mathrm{v}_n(x,t) + a, \tag{7}$$

where a is a constant. It follows from (4) that $a > 1$.

As a result of the HC transformation, we obtain particular BE solutions:

$$u_n(x,t) = 2\mu\lambda_n \frac{\sin(\lambda_n x)}{\cos(\lambda_n x) + a\exp\left(\mu\lambda_n^2 t\right)}. \tag{8}$$

Solution (8) describes an infinite number of BE particular solutions for different values of constants a, μ, n. Further, we call a the shape parameter of BE particular solutions, since its value determines the shape of the initial perturbation.

Let us consider the dependence of solutions (8) on the value of the parameter a.

DEPENDENCE OF THE BE SOLUTIONS ON TIME FOR DIFFERENT VALUES OF THE SHAPE PARAMETER a

At the initial moment of time ($t = 0$), ordinary BE particular solutions are described by a periodic function in the following form:

$$u_n(x,0) = 2\mu\frac{n\pi}{L}\frac{\sin(n\pi x/L)}{\cos(n\pi x/L) + a}. \tag{9}$$

For large positive values of the shape parameter $a >> 1$, the initial perturbation is close to a harmonic signal:

$$u_n(x,0) \approx 2\mu\frac{n\pi}{aL}\sin(n\pi x/L)\left(1 - a^{-1}\cos(n\pi x/L)\right). \tag{10}$$

For finite values of the shape parameter $a = 1+\zeta$, where $0 \le \zeta << 1$, a particular solution of the BE at the initial moment of time (9) is a periodic function which, at points $x = (2k+1)L/n$ when $\zeta \to 0$ ($a \to 1$), has a singularity of the form:

$$u_n(x,0) = 2\mu\frac{n\pi}{L}\mathrm{tg}\left(\frac{n\pi x}{2L}\right), \tag{11}$$

where $k = 0;\pm1;\pm2\ldots, (2k+1) \le n$.

It follows from (11) that solutions (8) are inapplicable for the shape parameter $a = 1$, since the boundedness condition of solutions is violated already for the initial perturbations ($t = 0$). Therefore, the range of variation of the shape parameter a, as noted above, is determined by the condition $a > 1$.

Let us determine the extreme values of the initial perturbation in the specified intervals of change in the shape parameter. For $0 < \zeta < 1$ at the initial moment of time (9) at points $x_{\mathrm{ext}}^{\pm} = \frac{2L}{n\pi}\arccos\left(\frac{\Delta_{\pm}}{\sqrt{1+2\Delta_{\pm}^2}}\right)$, the BE positive particular solutions are bounded and have extreme values:

$$u_n\left(x_{\text{ext}}^{\pm},0\right)=\pm 2\frac{\mu\lambda_n}{\sqrt{\zeta}\sqrt{2+\zeta}}, \tag{12}$$

where $\Delta_{\pm}=\pm\sqrt{\frac{\zeta}{2}}$.

It follows from (12) that, for example, for $n=2$, when ζ increases from zero to infinity, the parameter Δ_{-} changes from zero to minus infinity, and the coordinate of the maximum shifts from $L/2$ to $L/4$. When ζ increases from zero to infinity, the parameter Δ_{+}, on the contrary, changes from zero to plus infinity, and the coordinate of the minimum shifts from $L/2$ to $3L/4$. In all these cases, as ζ increases, the initial wave profile spreads and its amplitude decreases.

NUMERICAL ANALYSIS OF THE TEMPORAL DYNAMICS OF THE BE PARTICULAR SOLUTIONS

As an example of how the profile of (8) changes over time, let us plot the dependence of the dimensionless velocity $y_n\left(x,\tau_n\right)=u_n\left(x,t\right)/\left(2n\pi\mu/L\right)$ on the dimensionless time $\tau_n=\mu\left(n\pi/L\right)^2 t$ and the dimensionless coordinate $\xi=x/L$ for a given mode n. At that, the areas of time and coordinate changes remain the same: $0\le\tau_n<\infty$, $0\le\xi\le 1$.

The BE particular solution in new variables takes the form:

$$y_n\left(\xi,\tau_n\right)=\frac{\sin\left(n\pi\xi\right)}{\cos\left(n\pi\xi\right)+a\exp\left(\tau_n\right)}. \tag{13}$$

Figure 1(a) shows the time dynamics of the BE particular solution (13) for the mode $n=1$ and for the shape parameter value $a=1.001$. Such particular solution describes the decrease in the nonmonotonical initial perturbation amplitude (11) with time, which corresponds to shock waves. The figure shows an exponential decrease in $y_1\left(\xi,\tau_1\right)$ over time.

Figure 1(b) shows the time dynamics of the BE particular solution (13) for the mode $n=6$ and for a large value of the shape parameter $a=15$. The ordinary BE particular solution describes the decrease in the initial perturbation amplitude (10) with time. The figure shows an exponential decrease in $y_6\left(\xi,\tau_6\right)$ over time.

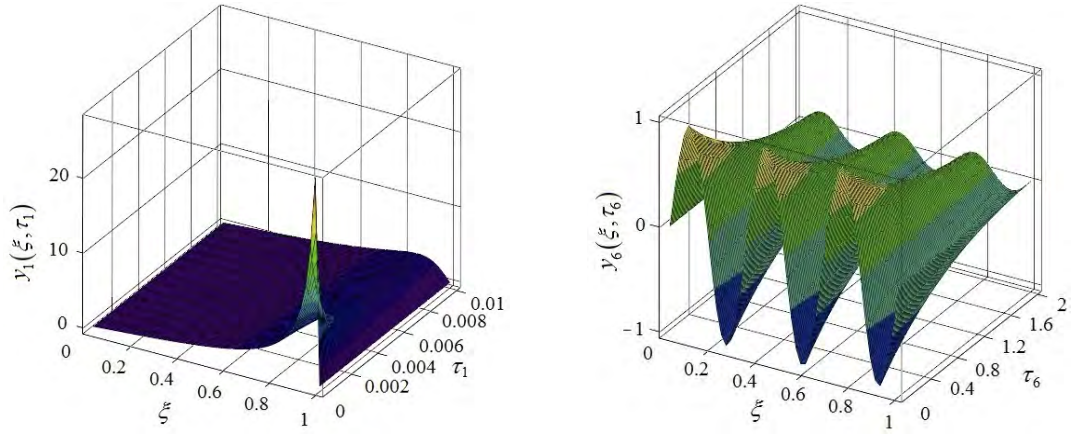

Figure. 1. Time dynamics of the BE particular solution (13): (a) - for $n=1$ and the shape parameter $a=1.001$; (b) - for $n=6$ and the shape parameter $a=15$.

Thus, the study of periodic particular BE solutions shows that the amplitude of the perturbation, as well as its spatial derivative, decreases with time to zero. This behavior of the perturbation indicates its decay and does not describe the formation of shock waves.

RESULTS AND DISCUSSION

Experimental results on the study of the growth of alkali halide crystals from the vapor phase

In [28], the density waves of monatomic steps with <10> orientation on thermodynamically stable vicinal surfaces of NaCl(100) were investigated under conditions of very low super saturation (10^{-5}-10^{-4})and high temperatures (~ 10^3 K). The wave structure is adequately described on the basis of the analytical solution of the KVB equation obtained by the

averaging method for the one-dimensional (1D) model of the train of steps. This allows, on the one hand, to confirm the conclusion that the observed step bunches have a kinematic origin, on the other hand, to show that they are monotonic shock waves without oscillations. Dimensionless characteristics of shock waves, such as the average step density $\rho_0\lambda_s$, amplitude A_0, wave number q_0 and velocity u_0 were determined. Here λ_s is the ad molecule mean free path, $\rho_0 = 1/l_0$, l_0 is the average width of the vicinal surface terrace. Since the dimensionless coefficients of the obtained KVB equation are determined by the crystal parameters at the growth (evaporation) stage, this allowed us to take a fresh look at the physics of the process and take into account the effects of dispersion and dissipation in the experimental studies. The value of the parameter $\nu^{-1} = \rho_0\lambda_s / q_0 \geq 1$ obtained in [28] indicated that, during the formation of the investigated kinematic waves, the contribution of the dispersion effect to the competition with nonlinear effects is quite significant. This value agrees with the ratio of the coefficients at spatial derivatives of higher order in the KVB equation obtained using the method of many scales [29], and allows us to conclude that shock waves described by the BE should be expected on vicinal NaCl (100) surfaces in the temperature range under study at higher values of super saturation, when $\nu \ll 1$. Such shock waves, characterized by the presence of a saw tooth profile and discontinuities in the density of elementary steps, were found on the pore growth surfaces formed during the thermally induced motion of pores in NaCl single crystals [40].

The microcrystallization conditions that can be created in pores (high temperatures and low super saturations [28]) are difficult to implement in conventional growth experiments. This is mainly due to the technical difficulties in maintaining and controlling both the required super saturation values and the temperatures themselves. The value of (super-) under saturation on the (growing) evaporating surfaces of pores inside a crystal can be controlled either by the value of the temperature gradient during their thermally induced motion, or by the difference in local surface curvatures during relaxation of their shape under isothermal conditions (see, references in [28]).

A similar technique for studying the processes of dissolution and growth of crystals from solutions has been developed for liquid inclusions (see references in [41, 42]). In the case of saturated solution inclusions in alkali-halide crystals, the activation energies of dissolution (growth) processes are quite small. This makes it possible to study the spontaneous displacement of inclusions as a whole by creating inhomogeneous distributions of structural defects in the crystal (point defects of radiation origin, dislocations, etc.) [41], as well as the transition from the kinetic regime of motion of inclusions, when the processes at the inclusion-matrix interface are determining, to the diffusion regime, when the processes of substance transfer through the inclusion volume are decisive [42].

Meanwhile, the use of the moving pore (liquid inclusion) technique excludes the possibility of studying the dynamics of elementary steps in-situ and allows one to study only stationary stages of the growth processes of alkali halide crystals. And in order to obtain data on the characteristic times of formation (decay) of shock waves of the elementary steps density, necessary for the interpretation of theoretical results, it is important to study exactly the non-stationary stages of the growth (evaporation) on the vicinal surfaces of crystals.

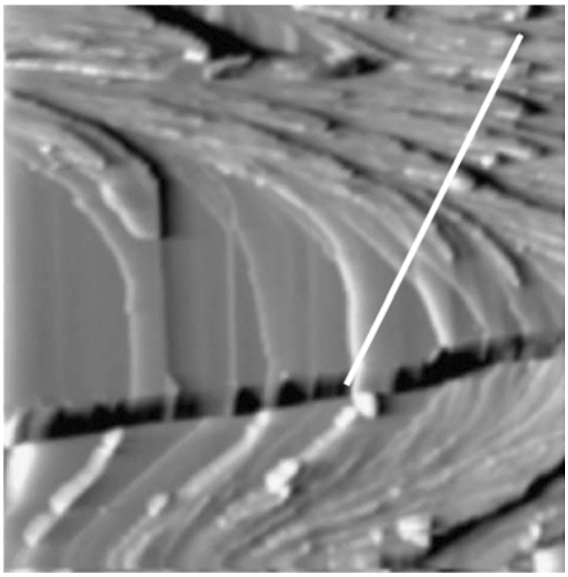

2200 nm × 2200 nm
(a)

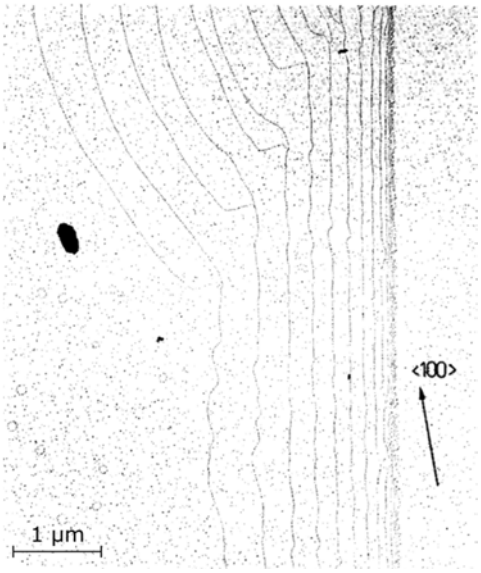

(b)

Figure 2.(a) - AFM micrograph showing the macrostep formed on the KCl(100) surface during crystal cleavage in vacuum [44] and (b) – the electron microscope image of the surface decorated with gold particles showing the "decay" of a similar macrostep into elementary steps during growth of NaCl(100) from the vapor phase ($T = 620$ K, $R/R_0 = 5$, $\Delta\mu = 0{,}09$ eV, $A = 10$ nm) [43].

Figure 2 shows the atomic force microscopy (AFM) image of the KCl(100) surface (a) and the electron microscope image of the NaCl(100) surface decorated with gold particles (b). The image (b) of the "decay" process during the growth

from the vapor phase of a macroscopic step formed on NaCl(100) upon cleavage of the crystal in vacuum is taken from [43]. The presence of such steps and their height can be reliably monitored by AFM, as it seen from Figure 2(a) taken from [44]. By decay we mean the process of forming a train of elementary steps of variable density at macrostep's base. At a distant stage of this process, one should expect a complete "splitting" of the macrostep into elementary steps. The reason is that vicinal NaCl surfaces near (100) are thermodynamically stable and the existence of such macrosteps is thermodynamically disadvantageous [28]. In this case, the elementary steps have a height of 2*a*, which is obviously due to a relatively high value of super saturation in the vapor phase at a given temperature ($T = 620$ K) [43]. However, Figure 2(b) clearly shows the process of simultaneous decay of double-height steps into monoatomic ones. This process is assisted by the deviation of the orientation of both the macrostep itself and the double steps attached to it from the dense packing direction. The observed faceting of the double steps indicates that their disintegration into monoatomic steps begins from the <11> directions, for which the speeds of the steps are greater than that in the <10> direction.

The area of the NaCl(100) growth surface decorated with gold particles, shown in Figure 2(b), allows us to reconstruct its topography quite accurately and estimate the formation time of the studied train of elementary (2*a*) steps of variable density. Therefore, the experimental data presented in Figure 2(b) were used to interpret the obtained theoretical results describing the decay of shock waves, i.e. the space-time evolution of perturbations with the amplitudes $a \geq 1$ at the initial moment of time. Here A is the thickness of the evaporated layer, R is the evaporation rate, R/R_0 is the super saturation coefficient calculated from T and R on the basis of the temperature dependence of the saturated vapor pressure P_0 [45], $\Delta\mu = kT\ln(R/R_0)$. The train of elementary (2*a*) steps in Figure 2(b) was digitized and the obtained values of the concentration ($\rho\lambda_s$) of steps, taking into account the width ($l = 1/\rho$) of the terraces adjacent to them, are presented as a function of the longitudinal coordinate x (in units λ_s) in Figure 3.

To make the values of the step density (ρ) and longitudinal coordinate dimensionless, we used the value λ_s, obtained at $T = 620$ K on the basis of the empirical temperature dependence presented in [29].This value agrees to within tenths with the data presented in [43] for the conditions of the considered growth experiment.

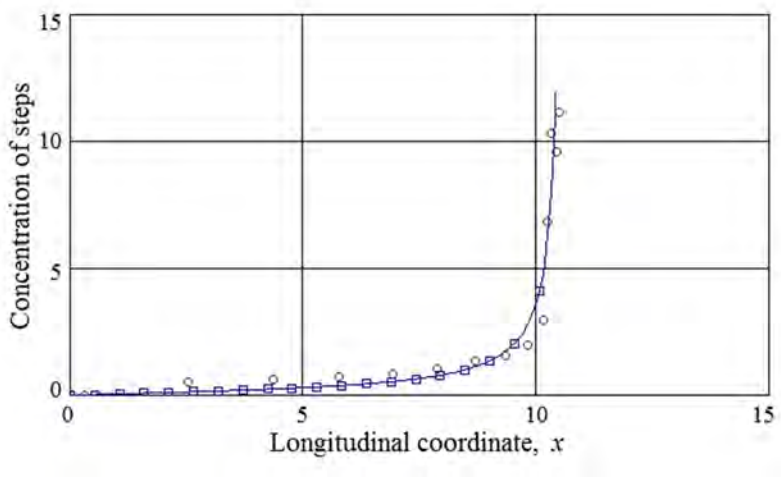

Figure 3. The structure of the shock wave of the elementary step density, shown in Figure 2(b), at the decay stage: symbols "○" are the experimental values of the step concentration in the wave; the solid line and symbols "□"are the result of calculations using formula (8).

Description of the experimental results of the NaCl crystal growth from the vapor phase by the BE particular solutions

The structure of the kinematic wave, represented by the grouping of elementary (2*a*) steps shown in Figure (b), is distinguished by the following characteristic features: the presence of a segment of the sharp change in the profile of the initial perturbation and its subsequent smooth decrease to the minimum value. Such the change in the step concentration with the distance from the macrostep initial position is in qualitative agreement with the profile of the shock wave described by the BE particular solution at the stage of its decay at a given mode $n = 1$ (Figure 1(a)).

Before moving on to the interpretation of the experimental data based on the analytical solutions (8) and (13), we made the estimates of the coefficient μ [28] taking into account the equilibrium concentration of ad molecules on an atomically smooth surface ξ_{a0}. Estimating $\xi_{a0} \sim 10^{-9}$ by the saturated vapor pressure of NaCl [45] and assuming $q \sim 0.01(\rho_0\lambda_s)$, with the known σ and λ_s [28], we found that the coefficient at the dissipative term in the BE is $\mu \sim 1$.

Using the Wolfram Mathematica package, the obtained experimental dependence of the step concentration on the longitudinal coordinate was approximated by the theoretical dependence based on equation (8) at $n = 1$ (solid line and symbols"□" in Figure 3). This made it possible to obtain the values of the dimensionless parameters of the shock wave at

the decay stage (Table 1). Here f_A is the amplitude of the wave, f_0 is its pedestal, a is the shape parameter of the initial perturbation, L is the half-width of the wave front, t is the dimensionless time.

Table 1. Parameters of the shock wave (Figure 3) at the decay stage.

μ	L	a	t	f_0	f_A
0.55	10.35	1.0001	0.005	1.37	11.50

To interpret the obtained values of the dimensionless parameters under the conditions of the considered experiment, the data on the real time of formation of the train of double-height steps in Figure 2(b) are needed. Unfortunately, these data are not given in [43]; however, the image of a spiral consisting of monoatomic height steps under the same experimental conditions at the nonstationary growth stage is presented. Earlier, when studying the morphology of evaporation (growth) spirals and the dynamics of motion of monatomic and double-height steps in a wide range of temperatures and under saturations, the normalized velocities of isolated steps were measured [46]. On their basis, the velocities of steps in the spiral and in the train (Figure 2(b)) were calculated, which, when reduced to the same effective super saturation under the experimental conditions [43], were $3.3\cdot10^{-10}$ m/s and $1.3\cdot10^{-10}$ m/s, respectively. This allowed us to estimate the time of the nonstationary growth stage in Figure 2(b) as $t_{exp} \sim 1$ hour, taking into account the value $R/R_0 = 5$.

In the kinematic wave theory, the characteristic time of a shock wave decay is considered to be the time during which the wave amplitude decreases by a factor of e. For the shock wave parameters presented in Table 1, the characteristic decay time was $t_d = 0.057$. During this time, under the conditions of the considered experiment, a train of elementary steps could propagate over a distance $L_2 \simeq 109.4$ in λ_s units with the speed of double steps, or over a distance $L_1 \simeq 277.9$ with the speed of monoatomic steps. Assuming $q \sim 1/2L$, we obtain for the parameter $\nu \sim q/(\rho_0\lambda_s) = 0.019$, which is close to the value used to estimate the value of μ. However, at that, the corresponding values of the average width of the terraces are several times greater than the value of $2\lambda_s$. This indicates that the diffusion interaction of elementary steps, which is responsible for the formation of shock waves, is very weak under these experimental conditions. Since, theoretically, the processes of formation and decay of shock waves are mutually reversible, their detection under the considered experimental conditions is practically unlikely. Anyway, despite the numerous published results of studies of the morphology of the growth (evaporation) surfaces of alkaline-halide crystals in the considered temperature range, we do not know such data. It should be noted that the considered experiment is a model one in the sense that it is not the decay of the "true" shock wave that is investigated, but its model in the form of a macrostep on the singular crystal surface, the vicinals to which are thermodynamically stable.

CONCLUSIONS

In this paper, particular solutions of the BE with zero boundary conditions are investigated in an analytical form to describe the decay of shock waves. It is shown that the amplitude of the initial periodic perturbation for values of the shape parameter a greater than 1, but about 1, nonmonotonically depends on the spatial coordinate. The particular solution of the BE describes a time decrease of the amplitude of the initial nonmonotonic perturbation, which can be considered as a shock wave. Such behavior of the perturbation indicates the decay of the initial shock wave. For large values of the shape parameter $a >> 1$, the amplitude of the initial periodic perturbation depends harmonically on the spatial coordinate. It is shown that over time the amplitude and the spatial derivative of such perturbation decrease and tend to zero. Particular solutions of the BE with zero boundary conditions may be used to control numerical calculations related to the BE-based description of shock waves in the region of large spatial gradients, that is, under conditions of a manifold increase in spatial derivatives. Such solutions were employed to describe the profile of a one-dimensional train of elementary steps with an orientation near <100>, formed during the growth of a NaCl single crystal from the vapor phase at the base of a macroscopic cleavage step. It is shown that the distribution of the step concentration with a distance from the initial position of the macrostep adequately reflected the shock wave profile at the decay stage. The dimensionless wave parameters were determined, on the basis of which the estimates of the characteristic decay time of the shock wave were performed.

ACKNOWLEDGEMENTS

This research was partly supported by the 2021 Cooperative Research Projects (grants 2073 and 2074) at the Research Center of Biomedical Engineering (RCBE) adopted as the 2021 Cooperative Research at Research Institute of Electronics, Shizuoka University, Japan.

ORCID IDs

Oksana L. Andrieieva, https://orcid.org/0000-0001-9757-8519; **Victor I. Tkachenko**, https://orcid.org/0000-0002-1108-5842
Oleksandr P. Kulyk, https://orcid.org/0000-0002-7389-3888; **Oksana V. Podshyvalova**, https://orcid.org/0000-0001-9680-9610
Volodymyr A. Gnatyuk, https://orcid.org/0000-0001-6412-2064, **Toru Aoki**, https://orcid.org/0000-0002-6107-3962

REFERENCES

[1] T.L. Einstein, in: *Handbook of Crystal Growth, vol. 1*,edited by T. Nishinaga, (Elsevier, Amsterdam, 2015), pp.215-264, https://doi.org/10.1016/B978-0-444-56369-9.00005-8
[2] N. Akutsu, and T. Yamamoto, in: *Handbook of Crystal Growth,vol. 1*, edited by T. Nishinaga (Elsevier, Amsterdam, 2015), pp.265-313, https://doi.org/10.1016/B978-0-444-56369-9.00006-X
[3] C. Misbah, O. Pierre-Louis, and Y. Saito, Rev. Modern Phys. **82**, 981 (2010), https://doi.org/10.1103/RevModPhys.82.981
[4] A.A. Chernov, J. Optoelectron. Adv. M. **5**(3) 575 (2003), https://old.joam.inoe.ro/arhiva/pdf5_3/Chernov.pdf
[5] T. Yamaguchi, K. Ohtomo, S. Sato, N. Ohtani, M. Katsuno, T. Fujimoto, S. Sato,H. Tsuge, and T. Yano, J. Cryst. Growth, **431**, 24 (2015), https://doi.org/10.1016/j.jcrysgro.2015.09.002
[6] T. Mitani, N. Komatsu, T. Takahashi, T. Kato, S. Harada, T. Ujihara, T. Ujihara, Y. Matsumoto, K. Kurashige, and H. Okumura, J. Cryst. Growth, **423**, 45 (2015),https://doi.org/10.1016/j.jcrysgro.2015.04.032
[7] A. Gura, G. Bertino, B. Bein, and M. Dawber, Appl. Phys. Lett. **112**(18), 182902-1-4 (2018), https://doi.org/10.1063/1.5026682.
[8] H. Morkoc, *Handbook of Nitride Semiconductors and Devices*, (Wiley-VCH, New-York, 2008), pp.1257.
[9] I. Berbezier, and A. Ronda, Surf. Sci. Rep. **64**(2), 47 (2009), https://doi.org/10.1016/j.surfrep.2008.09.003
[10] I. Goldfarb, Nanotechnology, **18**(33), 335304-1-7 (2007), https://doi.org/10.1088/0957-4484/18/33/335304
[11] J. Bao, O. Yasui, W. Norimatsu, K. Matsuda, and M. Kusunoki, Appl. Phys. Lett. **109**(8), 081602-1-5 (2016), https://doi.org/10.1063/1.4961630
[12] M. Hou, Z. Qin, L. Zhang, T. Han, M. Wang, F. Xu, X. Wang, T. Yu, Z. Fang, and B. Shen, Superlattices Microstruct. **104**, 397 (2017), https://doi.org/10.1016/j.spmi.2017.02.051
[13] K. Matsuoka, S. Yagi, and H. Yaguchi, J. Cryst. Growth, **477**, 201 (2017), https://doi.org/10.1016/j.jcrysgro.2017.05.021
[14] M. Kardar, G. Parisi, and Y.-C. Zhang, Phys. Rev. Lett. **56**(9), 889 (1986), https://doi.org/10.1103/PhysRevLett.56.889
[15] J.P. v.d. Eerden, and H. Müller-Krumbhaar, Phys. Rev. Lett. **57**9(19), 2431 (1986), https://doi.org/10.1103/PhysRevLett.57.2431
[16] S. Stoyanov, Jpn. J. Appl. Phys. **30**(1R), 1 (1991), https://doi.org/10.1143/JJAP.30.1
[17] M. Vladimirova, A. De Vita, and A. Pimpinelli, Phys. Rev. B. **64**(24), 24520-1-6 (2001), https://doi.org/10.1103/PhysRevB.64.245420.
[18] C. Duport, P. Nozières, and J. Villain, Phys. Rev. Lett. **74**(1), 134 (1995), https://doi.org/10.1103/PhysRevLett.74.134
[19] I. Derényi, C. Lee, and A.-L. Barabási, Phys. Rev. Lett. **80**(7), 1473 (1998), https://doi.org/10.1103/PhysRevLett.80.1473
[20] J.B. Keller, H.G. Cohen, and G.J. Merchant, J. Appl. Phys. **73**(8), 3694 (1993), https://doi.org/10.1063/1.352928
[21] H. Popova, F. Krzyzewski, M.A. Załuska-Kotur, and V. Tonchev, Cryst. Growth Des. **20**(11), 7246 (2020), https://doi.org/10.1021/acs.cgd.0c00927
[22] F.C. Frank, in: *Growth and Perfection of Crystals*, edited by R.H. Doremus, B.W. Roberts, and D. Turnbull (John Wiley& Sons, New York, 1958), pp. 411.
[23] N. Cabrera, and D.A. Vermilyea, in: *Growth and Perfection of Crystals*, edited by B.W. Roberts, and D. Turnbull (John Wiley& Sons, New York, 1958), pp.393.
[24] M.J. Lighthill, and G.B. Whitham, Proc. R. Soc. Lond., Ser. A. **229**(1178), 281 (1955), https://doi.org/10.1098/rspa.1955.0088
[25] A.A. Chernov, Sov. Phys. Uspekhi. **4**(1), 116 (1961),http://dx.doi.org/10.1070/PU1961v004n01ABEH003328
[26] Ya.E. Geguzin, and N.N. Ovcharenko, Sov. Phys. Uspekhi. **5**(1), 129(1962), https://dx.doi.org/10.1070/PU1962v005n01ABEH003403.
[27] Yu.S. Kaganovskii, V.V. Grischenko, and J. Zikkert, Sov. Phys. Crystallogr. **28**(3), 321 (1983). (in Russian).
[28] O.P. Kulyk, V.I Tkachenko, O.V. Podshyvalova, V.A. Gnatyuk, and T. Aoki, J. Cryst. Growth, **530**, 125296-1-7 (2020), https://doi.org/10.1016/j.jcrysgro.2019.125296
[29] V.G. Bar'yakhtar, A.E. Borovik, Yu.S. Kaganovskii. JETP Lett. **47**(8), 474 (1988), http://jetpletters.ru/ps/1095/article_16544.pdf
[30] J.M. Burgers, Adv. Appl. Mech. **1**, 171 (1948), https://doi.org/10.1016/S0065-2156(08)70100-5
[31] L. Landau, and E. Lifshitz, *Course of Theoretical Physics, vol. 6*, edited by L.D. Landau and E.M. Lifshitz (Elsevier,-Oxford, 2001), pp. 539, http://www.worldcat.org/isbn/0750627670
[32] G.M. Zaslavsky, and R.Z. Sagdeev, *An Introduction to Nonlinear Physics: From Pendulum to Turbulence and Chaos*, (Nauka, Moscow, 1988), pp. 368. (in Russian), https://www.twirpx.com/file/86242
[33] O.V. Rudenko, and S.I. Soluyan, *Theoretical Foundations of Nonlinear Acoustics*, (Nauka, Moscow, 1975), pp. 287. (in Russian), https://www.twirpx.com/file/255873.
[34] K.A. Naugolnykh, and L.A. Ostrovsky, *Nonlinear Wave Processes in Acoustics*, (Nauka, Moscow, 1990), pp. 237, https://www.twirpx.com/file/532109. (in Russian)
[35] .E. Hopf, Comm. Pure Appl. Math. **3**(3), 201 (1950), https://doi.org/10.1002/cpa.3160030302
[36] J.D. Cole, Quart. Appl. Math. **9**(3), 225 (1951), https://doi.org/10.1090/QAM/42889
[37] N.M. Ryskin, D.I. Trubetskov, *Nonlinear Waves*, (Fizmatlit, Moscow, 2000), pp. 272, https://www.twirpx.com/file/276239. (in Russian)
[38] A.V. Samokhin, Civil Aviation High Technologies. **220**, 82 (2015), https://avia.mstuca.ru/jour/article/view/308. (In Russian)
[39] A.V. Zaitsev, and V.N. Kudashov, Scientific Journal NRU ITMO. Processes and Food Production Equipment, **2**(20), https://www.processes.ihbt.ifmo.ru
[40] O. Kulyk, I. Hariachevska, O. Lisina, V. Tkachenko, O. Andrieieva, O. Podshyvalova, V. Gnatyuk, and T. Aoki, in: *Reiwa 1st Biomedicine Dental Engineering Collaborative Research Base Results Report Meeting* (Book of Abstracts, Yokohama, 2020), Presentation No 1-11, p. 37.
[41] A.P. Kulik, O.V. Podshyvalova, and I.G. Marchenko, Problems of Atomic Science and Technology, **2**(120), 13 (2019), https://vant.kipt.kharkov.ua/ARTICLE/VANT_2019_2/article_2019_2_13.pdf
[42] O.P. Kulyk, L.A. Bulavin, S.F. Skoromnaya, and V.I. Tkachenko, in: *Engineering for Sustainable Future. Inter-Academia 2019. Lecture Notes in Networks and Systems(LNNS), vol. 101*, edited by A.R. Varkonyi-Koczy (Springer, Cham, 2020) pp. 326-339, https://doi.org/10.1007/978-3-030-36841-8_32
[43] K.W. Keller, J. Cryst. Growth, **74**(1), 161 (1986), https://doi.org/10.1016/0022-0248(86)90260-5

[44] A.H. Ostadrahimi, H. Dabringhaus, and K. Wandelt, Surf. Sci. **521**(3), 139 (2002), https://doi.org/10.1016/S0039-6028(02)02311-7
[45] B.H. Zimm, and J.E. Mayer, J. Chem. Phys. **12**(9), 362 (1944), https://doi.org/10.1063/1.1723958
[46] Yu.S. Kaganovskii, O.P. Kulyk, in: *VIIth European Conference on Surface Crystallography and Dynamics (ECSCD-7), Book of Abstracts*, (Leiden, 2001), pp. 52.

ЗАСТОСУВАННЯ ЧАСТИННИХ РОЗВ'ЯЗКІВ РІВНЯННЯ БЮРГЕРСА ДЛЯ ОПИСУ ЕВОЛЮЦІЇ УДАРНИХ ХВИЛЬ ГУСТИНИ ЕЛЕМЕНТАРНИХ СХОДИН

Оксана Л. Андрєєва[a,b], Віктор І. Ткаченко[a,b], Олександр П. Кулик[b], Оксана В. Подшивалова[c], Володимир А. Гнатюк[d], Тору Аокі[e]
[a]ННЦ "Харківський фізико-технічний інститут" НАН України, Харків, Україна
[b]Харківський національний університет імені В.Н. Каразіна, Харків, Україна
[c]Національний аерокосмічний університет "Харківський авіаційний інститут", Харків, Україна
[d]Інститут фізики напівпровідників імені В.Є. Лашкарьова НАН України, Київ, Україна
[e]Науково-дослідний інститут електроніки, Університет Шизуоки, Хамамацу, Японія

Частинні розв'язки РБ з нульовими граничними умовами досліджені в аналітичній формі. Для значень параметра форми a більше, але приблизно рівному 1, амплітуда початкових періодичних збурень немонотонно залежить від просторової координати, тобто початкове збурення можна розглядати як ударну хвилю. Частинні розв'язки РБ з нульовими граничними умовами описують зменшення з часом початкової амплітуди немонотонних збурень, що свідчить про затухання початкової ударної хвилі. При великих значеннях параметра форми $a >> 1$ амплітуда початкових періодичних збурень гармонійно залежить від просторової координати. Показано, що з часом амплітуда та просторова похідна профілю такого збурення зменшуються і прагнуть до нуля. Наголошено, що періодичні аналітичні розв'язки РБ з нульовими граничними умовами можуть бути використані для контролю числових розрахунків, пов'язаних з описом ударних хвиль на основі РБ в області великих просторових градієнтів, тобто в умовах багаторазового збільшення просторових похідних. Ці розв'язки використані для опису профілю одновимірного ешелону елементарних сходинок з орієнтацією поблизу <100>, що сформувався при рості монокристала NaCl з парової фази біля основи макроскопічної сходини відколу. Показано, що розподіл концентрації сходинок з відстанню від початкового положення макросходини адекватно відображає профіль ударної хвилі на стадії розпаду. Визначено безрозмірні параметри хвилі, на підставі яких зроблено оцінки характерного часу її розпаду.

Ключові слова: рівняння Бюргерса, нульові граничні умови, аналітичні розв'язки, ударна хвиля, розпад

East European Journal of Physics. 4. 68-75 (2021)
DOI: 10.26565/2312-4334-2021-4-07 ISSN 2312-4334

ON THE IMPACT PARAMETER DEPENDENCE OF THE IONIZATION ENERGY LOSS OF FAST NEGATIVELY CHARGED PARTICLES IN AN ORIENTED CRYSTAL[†]

Sergii V. Trofymenko[a,b], Igor V. Kyryllin[a,b,*], Oleksandr P. Shchus[b]
[a]*Akhiezer Institute for Theoretical Physics, National Science Center "Kharkov Institute of Physics and Technology"*
Akademicheskaya Str., 1, Kharkiv, 61108, Ukraine
[b]*V.N. Karazin Kharkiv National University*
4, Svoboda Sq., Kharkiv, 61022, Ukraine
**Corresponding Author: kirillin@kipt.kharkov.ua*
Received July 27, 2021; revised September 29, 2021; accepted November 15, 2021

When a fast charged particle passes through matter, it loses some of its energy to the excitation and ionization of atoms. This energy loss is called ionization energy loss. In rather thin layers of matter, the value of such energy loss is stochastic. It is distributed in accordance with the law, which was first received by L.D. Landau. In amorphous substances, such a distribution (or spectrum), known as the Landau distribution, has a single maximum that corresponds to the most probable value of particle energy loss. When a particle moves in crystal in a planar channeling mode, the probability of close collisions of the particle with atoms decreases (for a positive particle charge) or increases (for a negative charge), which leads to a change in the most probable energy loss compared to an amorphous target. It has recently been shown that during planar channeling of negatively charged particles in a crystal, the distribution of ionization energy loss of the particles is much wider than in the amorphous target. In this case, this distribution can be two-humped, if we neglect the incoherent scattering of charged particles on the thermal oscillations of the crystal atoms and the electronic subsystem of the crystal. This paper explains the reason for this distribution of ionization energy loss of particles. The ionization energy loss distribution of high-energy negatively charged particles which move in the planar channeling mode in a silicon crystal are studied with the use of numerical simulation. The dependence of this distribution on the impact parameter of the particles with respect to atomic planes is considered. The dependence of the most probable ionization energy loss of particles on the impact parameter is found. It is shown that, for a large group of particles, the most probable ionization energy loss during planar channeling in a crystal is lower than in an amorphous target.
Keywords: ionization energy loss, planar channeling, negatively charged particles.
PACS: 61.85.+p; 34.50.Bw; 34.50.Fa

If a high-energy charged particle penetrates through a crystal having a small angle θ between its momentum and one of atomic planes, correlations in scattering by neighboring atoms may occur. This happens when θ is of the order of the critical angle of planar channeling θ_c [1] or smaller. In this case the distance between particle and atomic plane changes weakly upon scattering by neighboring atoms. This means that a large number of sequentially located atoms deflect the particle in the same direction, that is, they act coherently. This coherent interaction leads to existence of the so-called planar channeling, in which the particle moves in a potential well formed by adjacent planes. The particle motion in this case is periodic [1]. The ionization energy loss of particles in this mode of motion differs significantly from the ionization energy loss in an amorphous target. For positively charged particles, this loss has been well studied both theoretically and experimentally [see, e.g., 2–5]. In this case, planar channeling leads to a significant decrease in the most probable ionization energy loss (MPEL) due to the fact that particles less often approach close enough to the crystal atoms than in an amorphous target. The case of negatively charged particles has been much less studied. In the recent work [6] the distribution of ionization energy loss of high-energy negatively charged particles in the planar channeling mode was obtained via computer simulation. This distribution was broader than in the case of an amorphous target and had a peculiar shape (particularly, a two-humped structure in the case when dechanneling can be neglected). In [6] the physical reasons for such peculiarities of the distribution were not deeply investigated since the main attention there was focused on the possibility of applying the ionization loss for determining the dechanneling length of negatively charged particles. In the present paper we investigate the reasons for the above peculiarities of the distribution of ionization energy loss of negatively charged particles at planar channeling in a crystal. We show that the parameters of such distribution are directly correlated with the probability of close collisions between the incident particles and crystal atoms. It is demonstrated that a certain part of negatively charged channeled particles can move in the so-called 'hanging' mode (which is usually typical for over-barrier positive particles) having a decreased probability of close collisions and forming the low-energy peak of the two-humped distribution.

DISTRIBUTION OF IONIZATION ENERGY LOSS OF NEGATIVELY CHARGED PARTICLES DURING PLANAR CHANNELING IN A CRYSTAL

In [6] the case of 150 GeV/c π^- mesons impinging on a silicon crystal along the (110) plane was considered. The secondary beam of π^- mesons with such a momentum is delivered by SPS accelerator at CERN. The crystal thickness was chosen to equal 1 mm. Fig. 1 shows the distribution (spectrum) of the ionization energy loss for this case (solid

[†] ***Cite as:*** S.V. Trofymenko, I.V. Kyryllin, and O.P. Shchus, East. Eur. J. Phys. **4**, 68 (2021), https://doi.org/10.26565/2312-4334-2021-4-07

line) as well as the corresponding distribution for the case when the crystal is disoriented and behaves like an amorphous target (dashed line) (hereinafter in the text, by the term 'amorphous target' we mean a disoriented silicon crystal). For clarity, the spectrum for the oriented crystal is presented here without the account of incoherent scattering of the impinging particle on the crystal atoms, which leads to the particle dechanneling. It shows the distribution of ionization loss value of 10^6 particles which impinge on the crystal having arbitrary values of impact parameters with respect to the crystal plane, which models the incidence of a real beam on the crystal (neglecting the beam divergence).

We see that the spectrum for the disoriented crystal has a conventional shape of Landau-Vavilov distribution [7–9] with a single maximum corresponding to MPEL. The spectrum for oriented crystal differs significantly from it. It is much broader and has a two-humped structure. Its high-energy maximum at $\mathcal{E} \approx 700\,\text{keV}$ (which is larger than MPEL for the disoriented crystal) is intuitively expected as a result of the effect opposite to the one taking place for positive channeled particles, which have smaller MPEL values than in disoriented crystals. Indeed, positive particles are repelled from the atomic planes and spend a lot of time on relatively large distance from them in the region of low atomic electron density, while the negative ones are attracted to the planes and it is natural to expect the increase of their ionization loss while proceeding from the overbarrier to channeling mode. The existence of low-energy maximum of the two-humped distribution in Fig. 1, therefore, seems to be counterintuitive. Its explanation requires some deeper analysis of the impact parameter dependence of the particle ionization energy loss in crystal, which is the object of the present paper.

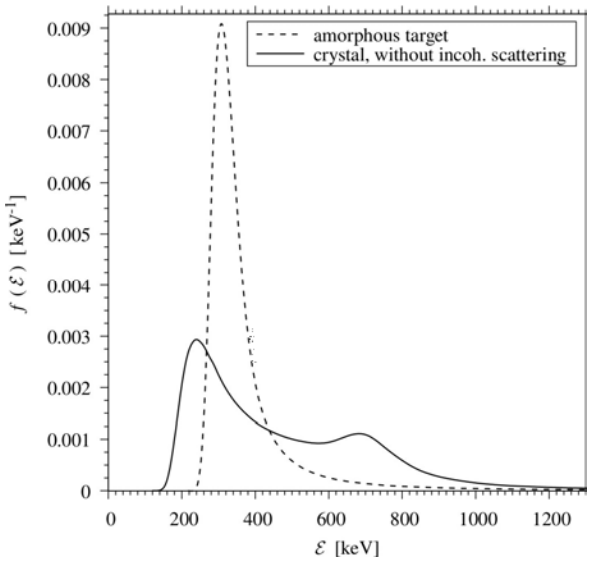

Figure 1. The distribution of ionization energy loss of 150 GeV/c π^- mesons during planar channeling in the field of (110) planes of Si crystal (solid line) and during motion in an amorphous target (dashed line).

The particle trajectory inside the crystal we define via numerical solution of the equation of particle motion (see formula (3) in the next section) in the field of crystalline atomic planes. For the latter field the Doyle-Turner model is applied. The probability for the particle to interact with an atom within the segment dl of its trajectory can be defined as $dP = n_{\text{eff}}\sigma dl$, where σ is the total collision cross section with an arbitrary energy transfer $\mathcal{E}$. The quantity n_{eff} here is some effective atomic electron density. It can be presented as a combination of two other quantities $n(\mathbf{r})$ and n as $n_{\text{eff}} = (1-\alpha)n + \alpha n(\mathbf{r})$ [1,6]. Here $n(\mathbf{r})$ is the real local electron density at the points of the particle trajectory, associated with the contribution of close collisions to the probability of particle interaction with the atom. The quantity n is the electron density averaged over a macroscopic volume inside the crystal, associated with the contribution of distant collisions to the above probability. The quantity α, belonging to the interval $0 < \alpha < 1$, defines the relative contributions of close and distant collisions to the particle ionization energy loss. At high particle energies these contributions can be considered as approximately equal [1,10,11], which corresponds to the choice $\alpha = 1/2$.

In case the collision takes place within dl, the value $\mathcal{E}$ of the particle energy loss in this collision can be further simulated using the probability distribution for this value $\rho(\mathcal{E}) = \sigma^{-1}(d\sigma/d\mathcal{E})$. For the differential cross section of energy transfer $d\sigma/d\mathcal{E}$ we apply the expression derived in [12], which proved its validity in comparisons with the experimental results for high-energy particles ionization loss in disoriented silicon targets, reported in the same paper. For very high particle energies, which we presently consider (namely, $\gamma >> 100$, where γ is the particle Lorenz-factor), it can be presented as follows:

$$\frac{d\sigma(\mathcal{E})}{d\mathcal{E}} = 6.25\times10^{11}\frac{2\pi e^4}{mc^2}\sum_i \frac{f_i}{\mathcal{E}}\left\{\ln\frac{2mc^2\mathcal{E}}{(\hbar\omega_p)^2}\delta(\mathcal{E}-E_i) \;+\; \mathcal{E}^{-1}H(\mathcal{E}-E_i)\right\}, \tag{1}$$

where the numerical factor in front of the formula ensures that all the quantities with the dimension of energy, i.e. $\mathcal{E}$, $\hbar\omega_p$ and mc^2 can be taken in eV, σ in cm^2, while e is the CGS value of the electron charge. Here m is the atomic electron mass, ω_p is the crystal plasma frequency, $\delta(x)$ and $H(x)$ are Dirac delta function and Heaviside step function, E_i are the effective ionization potentials of the atomic shells and f_i are the corresponding dipole oscillator strengths. The sum is performed over the occupied atomic K, L and M shells of silicon and the parameters E_i and f_i should be assigned the following values [12]: $E_K = 4033\,\mathrm{eV}$, $E_L = 241\,\mathrm{eV}$, $E_M = 17\,\mathrm{eV}$, $f_K = 2/14$, $f_L = 8/14$, $f_M = 4/14$.

Having simulated the particle energy loss on each segment of its trajectory we obtain the total particle ionization energy loss $\mathcal{E}$ inside the crystal. This value is stochastic and varies for different particles even if they travel along the same trajectory (which can take place for the particles impinging on the crystal with the same impact parameter only in the idealized case, when incoherent scattering is neglected). Fig. 1 shows the example of distribution of the value of $\mathcal{E}$ in the case when the impinging particles have arbitrary impact parameters.

IMPACT PARAMETER DEPENDENCE OF THE PROBABILITY OF CLOSE COLLISIONS OF NEGATIVELY CHARGED PARTICLES WITH CRYSTAL ATOMS DURING PLANAR CHANNELING

As we saw in the previous section, ionization energy loss of fast particles in a crystal is proportional to the probability of close collisions, associated with $n(\mathbf{r})$. Thus, in order to explain the peculiarities of ionization loss distribution, it is necessary to find the dependence of this probability on the impact parameter of negatively charged particles during planar channeling in a crystal. To do it analytically we will use a parabolic approximation of the planar potential, in which a particle with the charge of electron in the field of atomic planes has the potential energy

$$U(x) = -U_0\left[\left(2\frac{x}{d_p}-1\right)^2 H(x) + \left(2\frac{x}{d_p}+1\right)^2 H(-x)\right], \tag{2}$$

where the x-axis is perpendicular to the atomic plane, $|x| \le d_p/2$, d_p is the distance between neighboring atomic planes. Atomic planes are located in the points $x = nd_p$, $n \in \mathbb{Z}$, and presently we consider the particle channeled motion in the vicinity of the plane located at $x = 0$.

To find the particle trajectory in the field (2) we must solve the motion equation [13]

$$\frac{d^2x}{dt^2} = -\frac{v}{p}\frac{\partial U(x)}{\partial x}, \tag{3}$$

where p and v are respectively the particle momentum and velocity and c is the speed of light in vacuum. To solve the equation (3) it is necessary to divide the planar channel into two parts, $0 \le x \le d_p/2$ and $-d_p/2 \le x \le 0$, and consider the particle motion in each of them. For definiteness, we will assume that when the particle impinges on the crystal, its impact parameter with respect to the atomic plane with coordinate $x = 0$ is $x_0 > 0$. In this case, in the region $0 \le x \le d_p/2$ we need to solve the equation of motion

$$\frac{d^2x}{dt^2} = \frac{v}{p}\frac{4U_0}{d_p}\left(2\frac{x}{d_p}-1\right). \tag{4}$$

The solution to equation (4) can be written in the following form:

$$x(t) = \frac{d_p}{2} + C_1 e^{At} + C_2 e^{-At},$$

where C_1 and C_2 are constants, that can be found from the initial conditions, and $A = \frac{2}{d_p}\sqrt{\frac{2vU_0}{p}}$.

If x_0 and v_{x0} are the initial coordinate and velocity of the particle along the x-axis, then the constants C_1 and C_2 in the solution of motion equation in the region $0 \le x \le d_p/2$ can be found as

$$\begin{cases} C_1 = \frac{1}{2}\left(x_0 - \frac{d_p}{2} + \frac{v_{x0}}{A}\right) \\ C_2 = \frac{1}{2}\left(x_0 - \frac{d_p}{2} - \frac{v_{x0}}{A}\right) \end{cases}.$$

Here and below, as in [6], we set $v_{x0} = 0$, so that $C_1 = C_2 = \frac{1}{2}\left(x_0 - \frac{d_p}{2}\right)$ and

$$x(t) = \frac{d_p}{2} + \left(x_0 - \frac{d_p}{2}\right)\mathrm{ch}\left(At\right) \equiv g(t).$$

Now let us find the moment of time t_1 in which the particle will reach the point $x = 0$:

$$t_1 = \frac{1}{A}\mathrm{arch}\left(\frac{1}{1 - 2x_0 / d_p}\right). \tag{5}$$

In the region $-d_p / 2 \le x \le 0$ the solution of equation (3) is

$$x(t) = -\frac{d_p}{2} + C_3 e^{At} + C_4 e^{-At},$$

where C_3 and C_4 are constants. Taking into account that, in view of the symmetry of the potential relative to the point $x = 0$, at $t = 2t_1$ the value of $x(2t_1) = -x_0$ and $v_x(2t_1) = v_{x0} = 0$, we obtain the following solution of motion equation for $t_1 \le t \le 3t_1$

$$x(t) = -\frac{d_p}{2} - \left(x_0 - \frac{d_p}{2}\right)\mathrm{ch}\left(A\left(t - 2t_1\right)\right) = -g(t - 2t_1).$$

In general, the particle *x*-coordinate can be written as

$$x(t) = g\left(t - 2t_1 \,\mathrm{R}\left(\frac{t}{2t_1}\right)\right)\mathrm{sgn}\left(\cos\left(\frac{\pi}{2}\frac{t}{t_1}\right)\right), \tag{6}$$

where R(*t*) is a function that rounds its argument to the nearest integer.

Thus, in the parabolic potential model, we found the trajectories of negatively charged particles with different impact parameters. These trajectories are periodic non-sinusoidal oscillations with the period $T = 4t_1$. It is important that this period substantially depends on the impact parameter x_0 of the particles. To illustrate this fact, Fig. 2 shows several trajectories with different impact parameters.

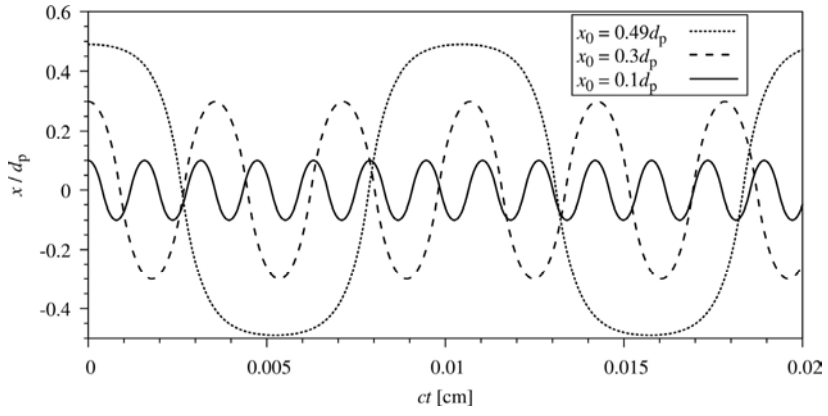

Figure 2. Trajectories of 150 GeV/*c* π^- mesons during planar channeling in the field of (110) planes of Si crystal.

The probability of close collisions of fast charged particle with atoms in a thin amorphous target can be written as a product of collision cross-section σ_c, atomic density *N* and thickness of the target *L*: $P = \sigma_c NL$. In a short oriented crystal this probability of close collisions can be written in a similar way with the help of integration over the particle trajectory inside the crystal: $P = \sigma_c \int N(x, y, z)dl$, where atomic density depends on the particle coordinate. In the case of motion in the field of atomic planes atomic density depends only on one coordinate: $N(x, y, z) = N(x)$. If we assume that atomic density near atomic plane has Gaussian distribution, then the probability of close collisions of fast charged particle with atoms during planar channeling can be found as

$$P(x_0) = B\int\limits_{T_{\text{in}}}^{T_{\text{out}}} \exp\left(-\frac{x^2(t)}{2r_T^2}\right) v(t)dt\,, \tag{7}$$

where r_T is the atomic root mean square thermal vibration amplitude in one direction, B is a constant that includes σ_c and takes into account crystal parameters, T_{in} and T_{out} are the moments of time at which the particle enters the crystal and exits from it. If one substitutes expression (6) into equation (7), then one obtains the probability of close collisions of fast negatively charged particle with atoms as a function of the impact parameter x_0. This dependence is shown in Fig. 3 for 150 GeV/c π^- mesons that pass through the silicon crystal of thickness 1 mm in the regime of planar channeling in (110) atomic planes. For convenience, $P(x_0)$ is normalized to the value of $P(0)$.

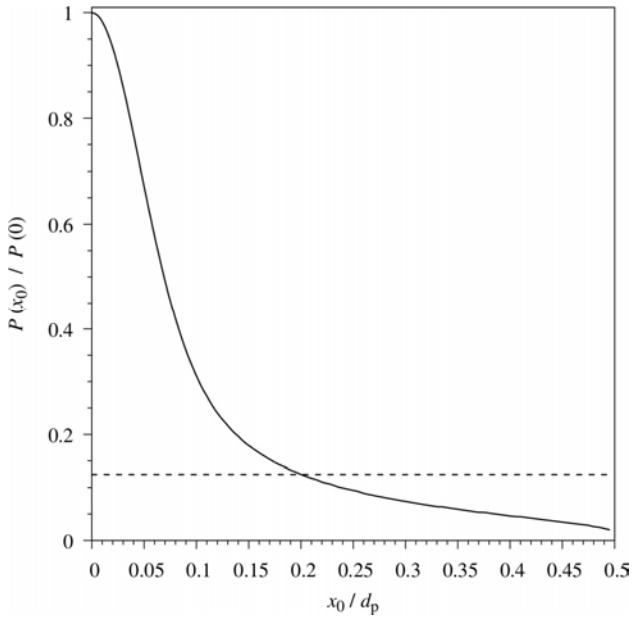

Figure 3. The dependence of probability of close collisions of 150 GeV/c π^- mesons with atoms on the impact parameter (solid line). Dashed line shows the mean probability of close collisions in the amorphous target.

It is also straightforward to estimate the probability of close collisions in a disoriented crystal when channeling is absent and the atoms can be considered as randomly located. Presently, at each moment of time the particle has equal chance to have an arbitrary value of impact parameter x_0 with respect to the atom it moves past. Let us choose the range of possible values of x_0 as $0 < x_0 < d_p/2$. In this case the average probability of close collisions, normalized to the corresponding probability for $x_0 = 0$ (as in Fig. 3) is

$$\overline{P}_{\text{dis}} = \frac{2}{d_p}\int\limits_0^{d_p/2} \exp\left(-\frac{x_0^{\,2}}{2r_T^2}\right) dx_0 \;=\; \frac{2}{\sqrt{\pi}\xi}\,\text{erf}(\xi)\,, \tag{8}$$

where $\xi = d_p/\left(2\sqrt{2}r_T\right)$ and $\text{erf}(x)$ is the error function. For the values $d_p \approx 1.92\times10^{-8}$ cm and $r_T \approx 7.5\times10^{-10}$ cm, typical for (110) planes of silicon crystal, $\xi \approx 9$ and $\text{erf}(\xi) \approx 1$, which gives $\overline{P}_{\text{dis}} \approx 0.125$. From Fig. 3 we see that this value is typical for channeled particles impinging on the crystal with the impact parameter of about $0.2d_p$.

IMPACT PARAMETER DEPENDENCE OF THE IONIZATION ENERGY LOSS DISTRIBUTION FOR NEGATIVELY CHARGED PARTICLES DURING PLANAR CHANNELING

Let us now study how the impact parameter dependence of close collisions, obtained in the previous section, manifests itself in the analogous dependence of the ionization energy loss distribution, resulting in a large width of the distribution for channeled particles in Fig. 1 (which is averaged with respect to impact parameters) and its two-humped structure. This study was carried out using numerical simulation of charged particles motion in oriented crystal, the principle of which is described in [14–17]. The simulation was carried out for 150 GeV/c π^- mesons that pass through the silicon crystal of 1 mm thickness in the regime of planar channeling in (110) atomic planes. For a clearer study of the reasons for appearance of the two-humped distribution, the simulation was carried out without taking into account the incoherent scattering of particles (except for the results shown in the last figure of this section). Some of the

obtained distributions are shown in Fig. 4 for the values of the impact parameter $x_0 = 0.05d_p$ (dash-dotted line), $x_0 = 0.25d_p$ (dashed line) and $x_0 = 0.45d_p$ (dashed line with two dots) and for scattering in amorphous target (solid line). The figure shows that each impact parameter corresponds to the Landau distribution with different values of MPEL. The lower is the value of the impact parameter, the higher is the value of MPEL of the particles. From Fig. 3 we see that, this dependence nicely correlates with the impact parameter dependence of probability of close collisions. With the decrease of impact parameter, the probability of close collisions of particles with the crystal atoms increases. This growth leads to the increase in parameter n_{eff}, and, consequently, to the increase in value of MPEL of the particles. The most interesting is the fact that at large values of the impact parameter, the value of MPEL of channeling negatively charged particles turns out to be lower than in an amorphous target. This is both due to the increase in oscillation period of the particles in the planar channel, which occurs with the increase in impact parameter x_0 (see eq. (5)), and to the fact that particles with large impact parameters 'hang' in the regions located close to the center of the gap between the atomic planes. The latter means that such particles have noticeable segments of their trajectory almost parallel to the atomic plane (see, e.g., the trajectory shown in Fig. 2 by the dotted line). The shape of trajectories of such particles is very far from the sinusoid and such particles spend much less time near the plane than far from it. It is such particles with relatively large impact parameters that form the low-energy peak of the two-humped distribution in Fig. 1, while the ones with small impact parameters are responsible for the corresponding high-energy peak. Let us note that such a two-humped structure of the distribution persists after taking into account the particle incoherent scattering on atoms as well, provided the dechanneling length is larger than the crystal thickness [6].

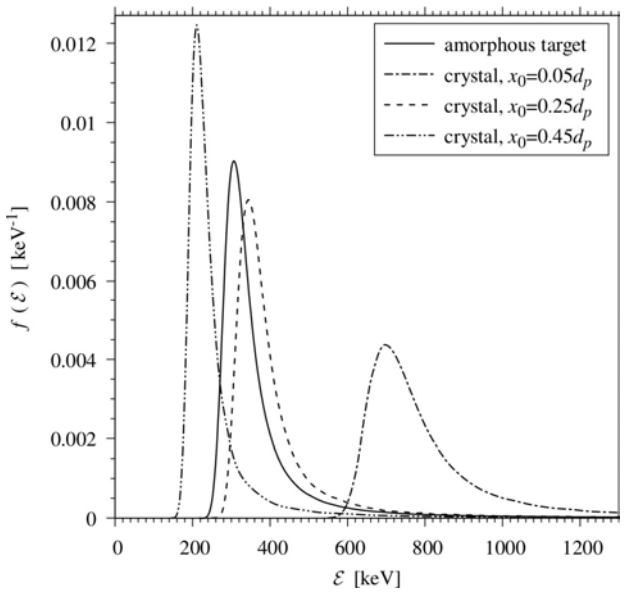

Figure 4. The distribution of ionization energy loss of 150 GeV/c π^- mesons during planar channeling in the field of (110) planes of Si crystal for different values of the impact parameter (dashed and dash-dotted lines) and during motion in an amorphous target (solid line).

The dependence of MPEL of 150 GeV/c π^- mesons on the impact parameter is shown in Fig. 5. The solid line corresponds to the motion of particles in the silicon crystal of 1 mm thickness in the regime of planar channeling in (110) atomic planes without taking into account incoherent scattering, while the dash-dotted line corresponds to the motion of particles in the same crystal, but taking such a scattering into account. Incoherent scattering was taken into account in the same way as in [18]. The behavior of these dependences is very similar to that of the dependence of probability of close collisions with atoms on the impact parameter, shown in Fig. 3. The dashed line in Fig. 5 shows the value of MPEL when particles pass through an amorphous target. It can be noted that taking incoherent scattering into account leads to the fact that the dependence of MPEL on the impact parameter becomes more similar to this dependence in an amorphous target. This is because incoherent scattering leads to dechanneling of some of the particles. The motion regime of these particles changes. They become overbarrier with respect to the potential of atomic planes. In this case, their motion becomes more similar to scattering in an amorphous target. At the same time, from Fig. 5 we see that even after taking into account the incoherent scattering of particles by thermal vibrations of atoms and electronic subsystem of the crystal, there remains a large group of particles, which MPEL in an oriented crystal is smaller than in an amorphous target. This group consists of particles with large impact parameters.

Fig. 5 indicates a rather wide spread of MPEL values in the allowed range of impact parameters, which explains the large width of the distribution in an oriented crystal in Fig. 1 compared to the one in the disoriented crystal. The significant dependence of MPEL of negatively charged particles on the impact parameter is quite unusual, since it is much less pronounced in the case of positively charged channeled particles, which have ionization loss distribution with

the width close to the one typical for the disoriented crystal [4]. In this regard, it would be highly desirable to carry out thorough experimental study of the ionization energy loss distribution of negatively charged channeled particles. For such a study it is best of all to use crystal targets of thickness smaller than the dechanneling length in order to minimize the effect of incoherent scattering.

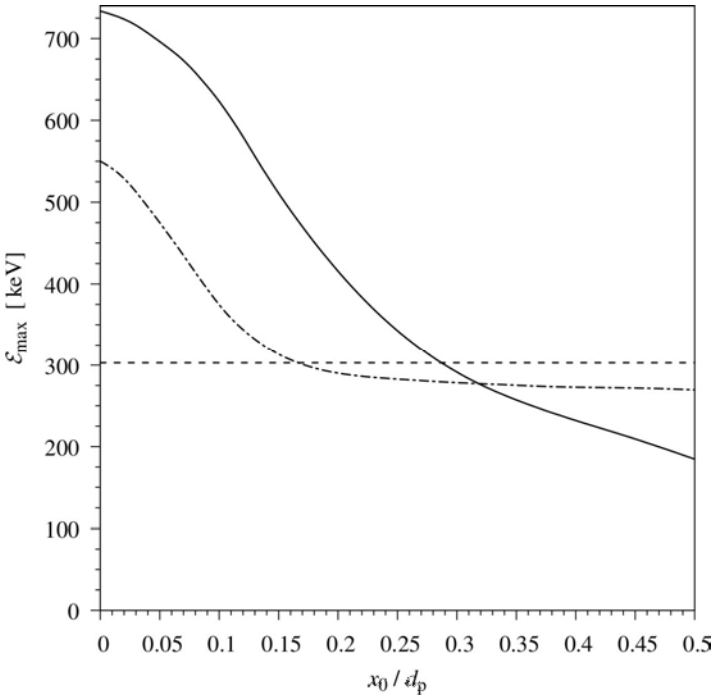

Figure 5. The impact parameter dependence of the most probable ionization energy loss of 150 GeV/c π^- mesons during planar channeling in the field of (110) planes of Si crystal with (dot-dashed line) and without (solid line) taking into account incoherent scattering and during motion in an amorphous target (dashed line).

CONCLUSION

The investigation of ionization energy loss distribution of high-energy negatively charged particles which move in the planar channeling mode in a silicon crystal showed a significant dependence of the value of the most probable energy loss on the impact parameter. It is quite unusual, since such a dependence is much less pronounced in the case of positively charged particles. It is shown that, for a large group of particles with large impact parameters, the most probable ionization energy loss during planar channeling in a crystal is lower than in an amorphous target, while for particles with small impact parameters the most probable ionization energy loss in a crystal is significantly higher than in an amorphous target. It is demonstrated that negatively charged channeled particles with large impact parameters can move in the 'hanging' mode (which resembles the case of positive over-barrier particles) having considerably suppressed probability of close collisions with the crystal atoms. The presented investigation explains the two-humped structure and considerable broadening of the ionization energy loss distribution for negatively charged channeled particles, revealed in our previous study. More detailed investigation of this problem requires taking into account the non-zero angle between the initial momentum of the particles and atomic planes, and is planned to be performed in the future.

ACKNOWLEDGEMENTS

This work was partially supported by the National Academy of Sciences of Ukraine (program "Support for the Development of Priority Areas of Scientific Research" 6541230, projects C-2/56-2021, F30-2021, 60-08/10-2021).

ORCID IDs

Sergii V. Trofymenko, https://orcid.org/0000-0002-1263-4444; **Igor V. Kyryllin**, https://orcid.org/0000-0003-3625-7521
Oleksandr P. Shchus, https://orcid.org/0000-0001-6063-197X

REFERENCES

[1] J. Lindhard, Danske Vid. Selsk. Mat. Fys. Medd. **34**(14), 1 (1965), https://www.osti.gov/biblio/4536390
[2] O. Fich, J.A. Golovchenko, K.O. Nielsen et al., Phys. Rev. Lett. **36**, 1245 (1976), https://doi.org/10.1103/PhysRevLett.36.1245
[3] H. Esbensen, O. Fich, and J.A. Golovchenko et al., Nucl. Phys. B, **127**, 281 (1977), https://doi.org/10.1016/0550-3213(77)90216-4
[4] H. Esbensen, O. Fich, and J.A. Golovchenko et al., Phys. Rev. B, **18**, 1039 (1978), https://doi.org/10.1103/PhysRevB.18.1039
[5] S. Pape Møller, and V. Biryukov, S. Datz et al., Phys. Rev. A, **64**, 032902 (2001), https://doi.org/10.1103/PhysRevA.64.032902
[6] Trofymenko S.V., and Kyryllin I.V., Eur. Phys. J. C. **80**, 689 (2020), https://doi.org/10.1140/epjc/s10052-020-8127-z

[7] L.D. Landau, J. Phys. USSR, **8**, 201 (1944).
[8] P.V. Vavilov, Sov. Phys. JETP, **5**, 749 (1957).
[9] P. Shulek, B.M. Golovin, L.A. Kuliukina et al., Sov. J. Nucl. Phys. **4**, 400 (1967).
[10] K. Dettmann, and M.T. Robinson, Phys. Rev. B, **10**, 1 (1974), https://doi.org/10.1103/PhysRevB.10.1
[11] K. Dettmann, Z. Phys. A, **272**, 227 (1975), https://doi.org/10.1007/BF01438014
[12] J.F. Bak, A. Burenkov, J.B.B. Petersen et al., Nucl. Phys. B, **288**, 681 (1987), https://doi.org/10.1016/0550-3213(87)90234-3
[13] A.I. Akhiezer, and N.F. Shul'ga, *High-energy electrodynamics in matter*, (Gordon and Breach Science Publishers, Amsterdam, 1996).
[14] I.V. Kirillin, N.F. Shul'ga, L. Bandiera et al., Eur. Phys. J. C, **77**, 117 (2017), https://doi.org/10.1140/epjc/s10052-017-4694-z
[15] I.V. Kirillin, Phys. Rev. Accel. Beams, **20**, 104401 (2017), https://doi.org/10.1103/PhysRevAccelBeams.20.104401
[16] I.V. Kyryllin, and N.F. Shul'ga, J. Instrum. **13**, C02020 (2018), https://doi.org/10.1088/1748-0221/13/02/C02020
[17] I.V. Kyryllin, and N.F. Shul'ga, Eur. Phys. J. C, **79**, 1015 (2019), https://doi.org/10.1140/epjc/s10052-019-7517-6
[18] N.F. Shul'ga, I.V. Kirillin, and V.I. Truten', J. Surf. Invest.: X-Ray, Synchrotron Neutron Tech. **7**(2), 398 (2013), https://doi.org/10.1134/S1027451013020468

ПРО ЗАЛЕЖНІСТЬ ІОНІЗАЦІЙНИХ ВТРАТ ЕНЕРГІЇ ШВИДКИХ НЕГАТИВНО ЗАРЯДЖЕНИХ ЧАСТИНОК В ОРІЄНТОВАНОМУ КРИСТАЛІ ВІД ПРИЦІЛЬНОГО ПАРАМЕТРА

С.В. Трофименко[a,b], І.В. Кирилін[a,b], О.П. Щусь[b]

[a]*Інститут теоретичної фізики імені Ахієзера Національного наукового центру «Харківський фізико-технічний інститут» Академічна вул., 1, Харків, 61108, Україна*

[b]*Харківський національний університет імені В.Н. Каразіна пл. Свободи, 4, Харків, 61022, Україна*

Коли швидка заряджена частинка рухається в речовині, вона втрачає частину своєї енергії на збудження та іонізацію атомів. Ці втрати енергії називаються іонізаційними втратами енергії. У досить тонких шарах речовини значення таких втрат енергії є стохастичним. Воно розподіляється відповідно до закону, що його вперше отримав Л.Д. Ландау. В аморфних речовинах такий розподіл (або спектр), відомий як розподіл Ландау, має єдиний максимум, який відповідає найбільш ймовірному значенню втрат енергії частинок. При русі частинки в режимі площинного каналювання у кристалі відбувається зменшення (при позитивному заряді частинки) або збільшення (при негативному заряді) ймовірності близьких зіткнень частинки з атомами, що призводить до зміни величини найбільш ймовірної втрати енергії порівняно з аморфною мішенню. Нещодавно було показано, що при каналюванні негативно заряджених частинок у кристалі розподіл іонізаційних втрат енергії частинок є значно більш широким, ніж у аморфній мішені. При цьому цей розподіл може бути двогорбим, якщо знехтувати некогерентним розсіянням заряджених частинок на теплових коливаннях атомів кристала та електронній підсистемі кристала. В даній роботі пояснюється причина виникнення такого розподілу іонізаційних втрат енергії частинок. За допомогою чисельного моделювання досліджено розподіл іонізаційних втрат енергії негативно заряджених частинок високої енергії, які рухаються в режимі площинного каналювання в кристалі кремнію. Розглянуто залежність цього розподілу від прицільного параметра частинок відносно атомних площин. Знайдено залежність найбільш ймовірних іонізаційних втрат енергії частинок від прицільного параметра. Показано, що для великої групи частинок найбільш ймовірні іонізаційні втрати енергії при площинному каналюванні у кристалі є нижчими, ніж у аморфній мішені.

Ключові слова: іонізаційні втрати енергії, площинне каналювання, негативно заряджені частинки.

East European Journal of Physics. 4. 76-85 (2021)
DOI: 10.26565/2312-4334-2021-4-08 ISSN 2312-4334

СТРУКТУРНІ, ЕЛЕКТРИЧНІ ТА ОПТИЧНІ ВЛАСТИВОСТІ ТОНКИХ ПЛІВОК CuO ОТРИМАНИХ МЕТОДОМ РЕАКТИВНОГО МАГНЕТРОННОГО РОЗПИЛЕННЯ[†]

С.І. Курищук[a,*], Т.Т. Ковалюк[a,b,‡], Г.П. Пархоменко[a,§], М.М. Солован[a,#]
[a]*Чернівецький національний університет імені Юрія Федьковича*
вул. Коцюбинського 2, 58012 Чернівці, Україна
[b]*Charles University in Prague, Faculty of Mathematics and Physics*
Ke Karlovu 5, 121 16 Prague 2, Czech Republic
**Corresponding Author: kuryshchuk.serhii@chnu.edu.ua*
[‡]*E-mail: t.kovaliuk@mag.mff.cuni.cz,* [§]*E-mail: h.parkhomenko@chnu.edu.ua,* [#]*E-mail: m.solovan@chnu.edu.ua*
Received October 1, 2021; revised November 29, 2021; accepted December 1, 2021

Виготовлено тонкі плівки CuO методом реактивного магнетронного розпилення при постійному струмі в універсальній вакуумній установці Leybold-Heraeus L560 на скляні підкладки, температура яких складала 300 К та 523 К. Досліджено структурні, електричні та оптичні властивості для отриманих зразків тонких плівок CuO, а саме було визначено: елементний склад, представлено розподіл елементів на поверхні, які входять до складу даних плівок, розмір зерен, енергію активації, оптичну ширину забороненої зони, показник заломлення, проведений аналіз кривих спектрів пропускання і відбивання для плівок CuO, нанесених на скляні підкладки. Елементний склад тонких плівок та морфологію поверхні отримано за допомогою скануючого електронного мікроскопа (MIRA3 FEG, Tescan) оснащеного детектором відбитих електронів (BSE) і енергодисперсним рентгенівським детектором (EDX). Встановлено, що розмір зерен для плівок отриманих при нижчій температурі підкладки D становить ~ 16 нм, а для плівок отриманих при вищій температурі – D ~ 26 нм. На дифрактограмах тонких плівок CuO спостерігається більша інтенсивність піків для тонких плівок отриманих при вищих температурах підкладки CuO №2, що може бути зумовлено кращою структурною досконалістю тонких плівок та більшим розміром зерен. З дослідження електричних властивостей, встановлено, що температурні залежності електричного опору для тонких плівок CuO мають напівпровідниковий характер, тобто опір зменшується при збільшенні T. Чотирьохзондовим методом виміряно величини поверхневого опору плівок: зразок №1 - ρ = 18,69 кОм/☐, зразок № 2 –- ρ = 5,96 кОм/☐. На основі незалежних вимірювань коефіцієнтів відбивання і пропускання визначили оптичну ширину забороненої зони (E_g^{op}) для двох зразків екстраполяцією прямолінійної ділянки кривої $(\alpha h\nu)^2 = f(h\nu)$ на вісь $h\nu$. Для зразка CuO №1 E_g^{op} = 1,62 еВ; для зразка CuO №2 E_g^{op} = 1,65 еВ. Для тонких плівок CuO №2 також використовували конвертний метод для визначення основних оптичних коефіцієнтів E_g^{op} = 1,72 еВ, отримані значення E_g^{op} визначені двома методами добре корелюють між собою.
Ключові слова: тонка плівка, CuO, оптичні властивості, енергія активації.
PACS: 68.65.Pq, 68.55.Jk, 68.37.Hk, 68.37.−d, 71.20.−b, 71.20.Nr

Останнім часом проводиться пошук і дослідження дешевих та нетоксичних матеріалів для використання у тонкоплівкових сонячних елементах. Оксид міді широко використовується в фотоелектричній галузі, літій-іонних батареях, біологічних датчиках, газових датчиках, магнітних накопичувачах, мікроприладах та в якості негативних електродів для сучасних літій-іонних акумуляторів [1-5]. Він є актуальним матеріалом для виготовлення сонячних елементів. Основною його перевагою є те, що він може утворювати сполуки CuO та Cu_2O з шириною забороненої зони для CuO 1,3 еВ – 2,1 еВ, а для Cu_2O 2,1 еВ – 2,6 еВ. Такі плівки можуть володіти n- або p- типом провідності. Завдяки цьому вченим вдалося створити тонкоплівкові сонячні елементи на основі гетеропереходів Cu_2O/CuO.

В останні роки основним питанням застосування оксидів міді в якості компонентів для конструкції сонячних елементів являється покращення оптичних, електричних і структурних характеристик цих оксидів. Теоретичний ККД сонячних елементів на основі оксиду міді становить 30,5 % при 1,6 еВ [6]. Мідь не є рідкоземельним металом, що робить її дешевшою в порівнянні з галієм та індієм, які використовуються у виробництві сонячних елементів. Відомо, що прямозонні напівпровідники успішно використовуються в фотовольтаїці [7,8], а CuO є прямозонним напівпровідником, тому він має високий коефіцієнт оптичного поглинання у видимій та ІЧ області спектра. Нетоксичність і економічність виробничого процесу могли б зробити оксиди міді альтернативою кремнію, який в основному використовується для виробництва сонячних елементів. Отже, тонкі плівки оксиду міді можуть бути використані для виготовлення сонячних елементів і фотоприймачів.

Тонкі плівки CuO створюють з використанням різних методів осадження тонких плівок [9,10], таких як хімічне осадження з парової фази, термічне випаровування, реактивне магнетронне розпилення. Однак електричні та оптичні властивості даних плівок суттєво залежать від технологічних режимів їх виготовлення. Тому дослідження технологічних режимів виготовлення тонких плівок оксиду міді залишається актуальною задачею.

[†] ***Cite as:*** S.I. Kuryshchuk, T.T. Kovalyuk, H.P. Parkhomenko, and M.M. Solovan, East. Eur. J. Phys. **4**, 76 (2021), https://doi.org/10.26565/2312-4334-2021-4-08

ЕКСПЕРИМЕНТАЛЬНА ЧАСТИНА

Виготовлення тонких плівок CuO проводилося в універсальній вакуумній установці Leybold-Heraeus L560. Напилювались тонкі плівки CuO методом реактивного магнетронного розпилення при постійному струмі [11, 12] на скляні підкладки, температура яких складала ($T_{підкл}$): для зразка №1 – 300 К та для зразка №2 – 523 К. Мідна мішень – шайба діаметром 100мм і товщиною 5мм, розміщується на столику магнетрона з водяним охолодженням на відстані 7см під підкладками. Вакуумна камера має товщину 10 мм і виготовлена з нержавіючої сталі. З неї проводиться відкачка газу до високого вакууму за допомогою турбомолекулярного насосу (30000 об/хв) до $5\cdot10^{-5}$ мбар ($5\cdot10^{-3}$ Па). Контролюється тиск залишкових газів за допомогою іонізаційного та термопарного манометричного перетворювача.

В табл.1. наведені технологічні параметри процесу виготовлення тонких плівок CuO. Протягом процесу напилення формування газової суміші в потрібних пропорціях аргону (P_{Ar}) і кисню (P_{O2}) відбувалося з 2-х незалежних джерел. Щоб запобігти неконтрольованому забрудненню поверхонь підкладки і мішені, ми використовували короткочасне протравлювання їх бомбардуючими іонами аргону.

Таблиця 1. Параметри тонких плівок CuO

№	*Плівка*	$P_{магн.}$, Вт	$T_{підк.}$, К	*t*, хв.	P_{Ar}, мбар	P_{O2}, мбар	E_g^{op}, еВ	*d*, нм
1	CuO	70	300	10	$4\cdot10^{-3}$	$4\cdot10^{-3}$	1,62	280
2	CuO	70	523	10	$4\cdot10^{-3}$	$4\cdot10^{-3}$	1,72(*1) 1,65(*2)	280

Примітка: *1 – оптична ширина забороненої зони визначена за допомогою конвертного методу; *2 – оптична ширина забороненої зони визначена з незалежних вимірювань коефіцієнтів відбивання і пропускання

Визначення елементного складу тонких плівок CuO та дослідження морфології поверхні було проведено за допомогою скануючого електронного мікроскопа (MIRA3 FEG, Tescan) оснащеного детектором відбитих електронів (BSE) і енергодисперсним рентгенівським детектором (EDX). Відносна похибка при вимірюванні атомних часток хімічних елементів, які входять до складу не перевищує 2,7 % у випадку Cu, а також 2,3 % у випадку O (Табл. 2). Дифрактограми плівок CuO були отримані на рентгенівському дифрактометрі XRD System - SmartLab, Rigaku.

Вимірювання поверхневого опору тонких плівок оксиду міді проводилося за допомогою чотирьохзондового методу. Електричні контакти для вимірювання температурних залежностей електричного опору (R) тонких плівок CuO були зроблені на протилежних сторонах плівок шляхом осадження нікелю методом магнетронного розпилення при температурі підкладки 400 К. Дослідження проводили в інтервалі температур T = 305 ÷ 375 К. Оскільки незворотні процеси, наприклад, окиснення при вимірюванні температурних залежностей опору можуть змінювати параметри плівки, тому вимірювання проводили, як при нагріванні, так і при охолодженні. Товщину (d) тонких плівок CuO вимірювали за допомогою інтерферометра МИИ-4 за стандартною методикою. Оптичні властивості тонких плівок CuO досліджувались на основі аналізу їх спектрів пропускання та відбивання виміряних на спектрофотометрах СФ-2000 та Nicolet 6700 в діапазоні довжин хвиль від 400 до 2800 нм.

РЕЗУЛЬТАТИ ТА ЇХ ОБГОВОРЕННЯ

Структурні властивості тонких плівок CuO

За допомогою скануючого електронного мікроскопа було одержано типові зображення поверхні утворені відбитими електронами (BSE) (рис. 1, а), які показано при збільшенні (1000х), а також на рисунку представлено розподіл елементів на поверхні, які входять до складу даних плівок.

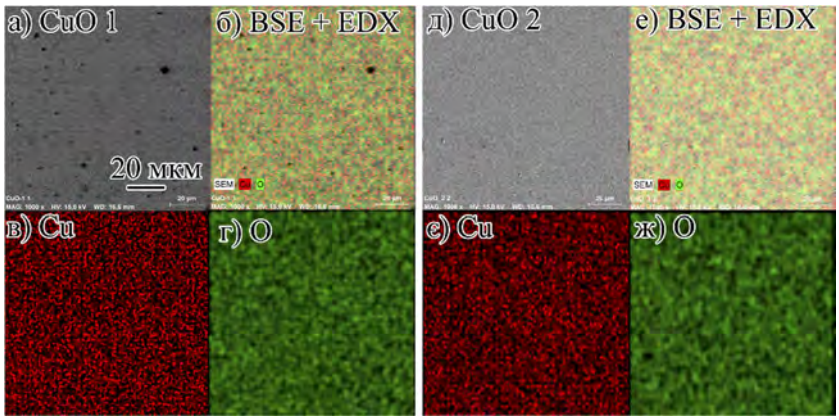

Рисунок 1. Типові SEM зображення поверхні плівки (а, д) утворені відбитими електронами (BSE) при збільшенні (1000х) для тонких плівок CuO 1 та CuO 2, відповідно. На рис. (б, е) представлено розподіл елементів на поверхні плівок CuO 1 та CuO 2, а також окремих хімічних елементів Cu (в, є) та O (г, ж), які входять до складу тонких плівок.

Зображення отримані за допомогою SEM для оксиду міді показали, що для тонких плівок відсутні видимі дефекти (проколи, особливо для плівки CuO 2), що в свою чергу свідчать про їх хорошу структурну досконалість, а також підтверджено рівномірний розподіл елементів на поверхні для двох плівок рис.1 (б, е). Краща структурна досконалість тонкої плівки CuO 2 може бути обумовлено вищою температурою підкладки під час осадження, а відповідно й кращою рухливістю атомів на підкладці у процесі формування плівки порівняно з плівкою CuO 1.

Опромінення зразків пучком електронів призвело не тільки до утворення вторинних і відбитих електронів, а також викликало появу характеристичного рентгенівського випромінювання (типові спектри представлено на рис. 2).

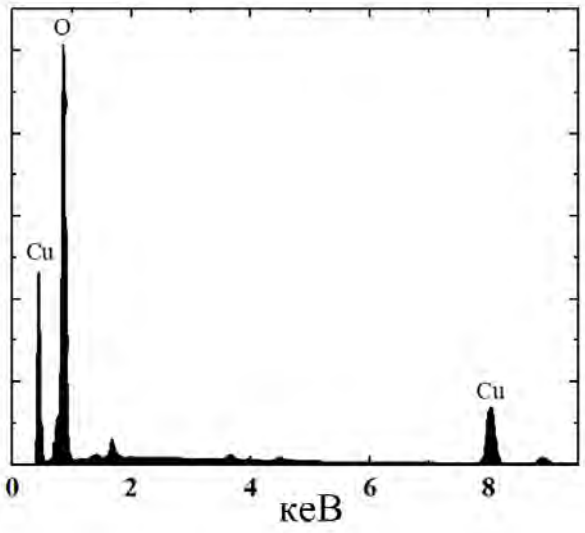

Рисунок 2. EDX-спектр для тонкої плівки CuO 1.

Аналіз характеристичного рентгенівського випромінювання дозволив визначити елементний склад досліджуваних тонких плівок (табл. 2). Визначений елементний склад відповідає стехіометричному для тонких плівок CuO, а також показано деяке відхилення від стехіометрії для тонких плівок CuO №2.

Таблиця 2. Елементний склад зразків

Назва	Атомні частки хімічних елементів, які входять до складу тонких плівок, %		Похибка, %	
	Cu	O	Cu	O
№1				
зона 1	51,38	48,62	2,6	2,2
зона 2	51,55	48,45	2,6	2,3
№2				
зона 1	54,24	45,76	2,7	2,0
зона 2	54.28	45,72	2,7	2,1

Враховуючи відносну похибку при вимірюванні атомних часток хімічних елементів, які входять до складу тонких плівок CuO для плівок отриманих при нижчих температурах підкладки зразок №1 склад плівок відповідає стехіометричному ~ 1,02:0,98 у випадку зі зразком №2 відбувається деяке відхилення від стехіометричного складу ~ 1,08:0,92. Відхилення від стехіометрії для зразка №2 може бути обумовлено формуванням кластерів Cu_2O при вищих температурах осадження тонких плівок. Це також підтверджується наявністю піків меншої інтенсивності для плівки CuO №2 на дифрактограмах рис.3 (б) де спостерігається відбивання від площин (200) при 42,4° та (220) при 61,5° [13].

На дифрактограмах тонких плівок CuO (Рис. 3) спостерігаються домінуюче відбивання від площини (-111/002) при 35.5° і відбивання меншої інтенсивності від площин (111) при 38,54° , (110) – 32,5° і (220) при 66,7°. Наявність цих піків узгоджуються з літературними даними отриманими в роботах [13-15]. Спостерігається більша інтенсивність піків для тонких плівок отриманих при вищих температурах підкладки, що може бути зумовлено кращою структурною досконалістю тонких плівок та більшим розміром зерен [16].

Використовуючи рівняння Шерера можна визначити розмір зерен для плівок CuO отриманих при різних температурах підкладки :

$$D = \frac{0.94\lambda}{\beta \cos\theta}, \qquad (1)$$

де D - розмір зерна, β - повна ширина на половині максимуму дифракційного піку, λ-довжина хвилі рентгенівського випромінювання, і θ - кут дифракції.

Встановлено, що розмір зерен для плівок отриманих при нижчій температурі підкладки D становить ~ 16 нм, а для плівок отриманих при вищій температурі – D ~ 26 нм.

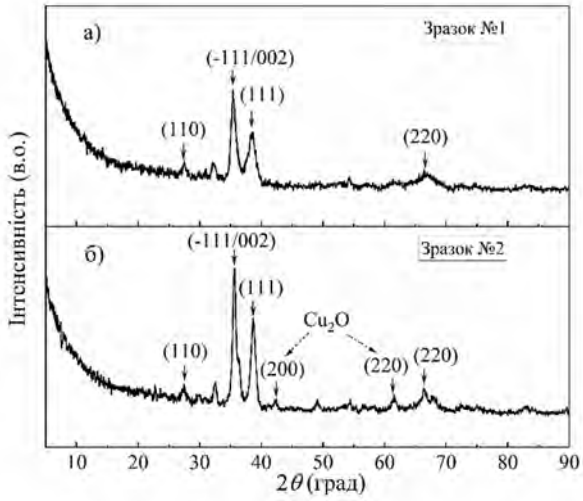

Рисунок 3. Дифрактограми тонких плівок CuO отриманих при різних температурах підкладки: а) Зразок №1; б) Зразок №2.

Електричні властивості тонких плівок CuO

Одну з основних задач для досягнення високої ефективності роботи напівпровідникових приладів відіграє ефективне відведення носіїв електричного струму. Ця функція виконується за допомогою металічних контактів, які підводяться до тонкої плівки або напівпровідникової структури. Основна вимога до них: вони повинні володіти омічними властивостями, тобто малим електричним опором та лінійною вольт-амперною характеристикою[17]. Ці умови виконуються, якщо створити приконтактну область (з боку напівпровідника), збагачену на основні носії заряду. Співвідношення між роботами виходу електронів з напівпровідника і металу – не єдиний фактор створення омічного контакту. Треба звернути особливу увагу на поверхневі явища речовини, на ступінь легування напівпровідникового матеріалу, на можливе утворення різних хімічних сполук або структур в місці контакту, та ін.

Щоб визначити електричні параметри тонких плівок оксиду міді, потрібно нанести якісні омічні контакти на них. В літературі на сьогоднішній день майже немає результатів детальних досліджень електричних властивостей омічних контактів для тонких плівок CuO. На рис. 4, зображені ВАХ нікелевого контакту, який був створений за допомогою магнетронного напилення до тонких плівок CuO.

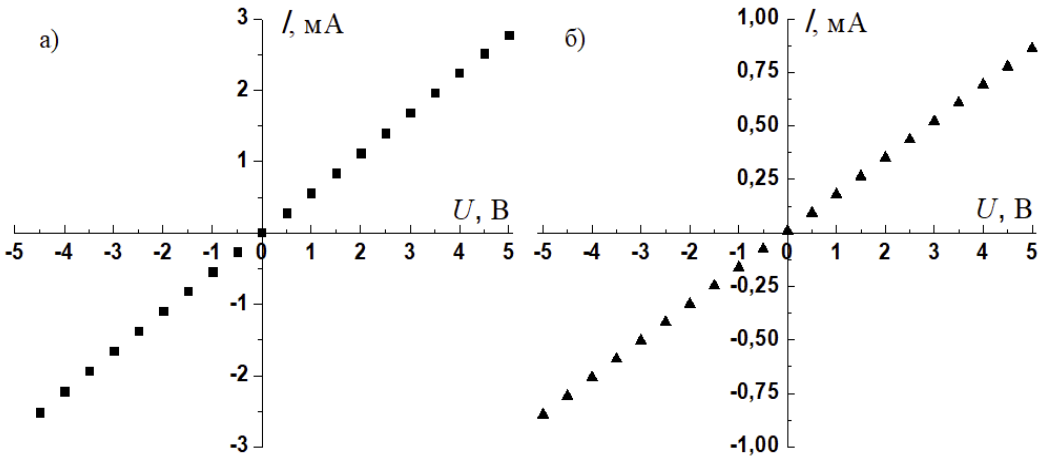

Рисунок 4. ВАХ нікелевого контакту до тонких плівок CuO: а) зразок №1; б) зразок №2.

З рис. 4 можна зробити припущення, що отримані нікелеві контакти відповідають критеріям омічності контакту, а саме - це симетричність і прямолінійність гілок ВАХ. Щоб виміряти температурні залежності електричного опору тонких плівок оксиду міді $R = f(T)$, створювали контакти на 2-х протилежних сторонах досліджуваної плівки. Вимірювання температурних залежностей проводилися в інтервалі температур 305 ÷ 375 К. Із рис. 5 видно, що після процесу нагрівання в плівках відбуваються незначні зміни (невелике

зростання питомого опору). Температурні залежності опору тонких плівок CuO приведені на рис. 5, мають активаційний характер провідності, з цього можна зробити висновок, що тонкі плівки оксиду міді мають напівпровідниковий тип провідності. З експоненційних ділянок отриманих експериментальних залежностей $R = f(T)$ визначали енергію активації для наших зразків CuO (рис. 4), яка складає 0,24 еВ і може відповідати глибині залягання робочого рівня.

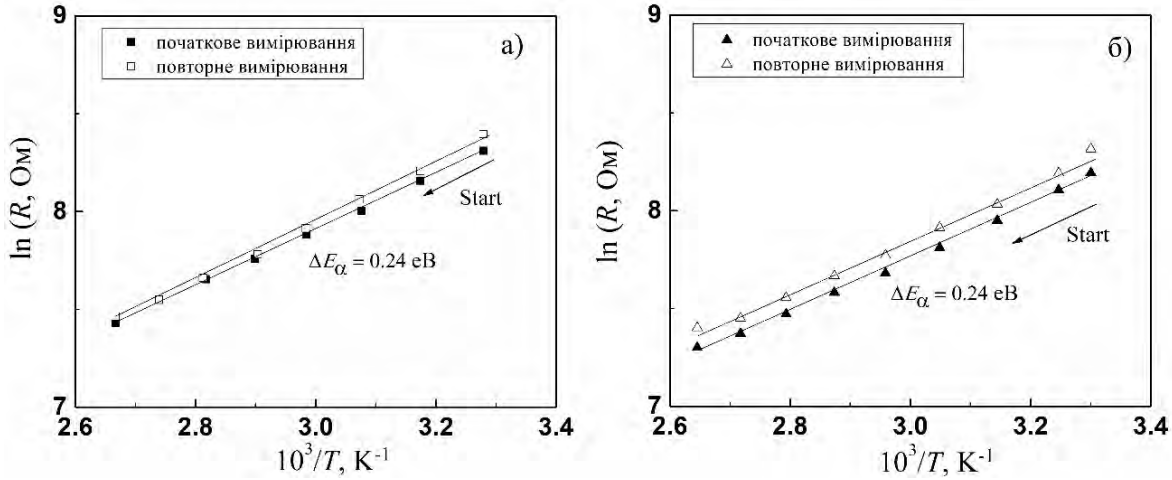

Рисунок 5. Температурна залежність опору тонких плівок CuO: а) зразок №1; б) зразок №2.

Були виміряні значення поверхневого опору тонких плівок CuO при кімнатній температурі чотирьохзондовим методом: зразок №1 складає ρ_s = 18,69 кОм/□, зразок № 2 - ρ_s = 5,96 кОм/□.

Оптичні властивості тонких плівок CuO

На рис. 6 зображено спектри пропускання тонких плівок CuO. На спектрі пропускання зразка №2 видно періодичні піки та впадини, які обумовлені інтерференційними явищами, що свідчить про хорошу однорідність та якість поверхні тонких плівок[18]. Оптичні коефіцієнти тонких плівок (показник заломлення *n(λ)*, товщина плівок *d*, коефіцієнти поглинання *α(λ)* та екстинції *k(λ)*) визначаються із спектрів пропускання, на яких спостерігаються інтерференційні явища, використовуючи конвертний метод[19]. Цей метод можна застосовувати при слабкому поглинанні тонкими плівками та прозорості підкладки, товщина якої значно більша від товщини плівки. У даній роботі ці вимоги задовольняються.

Однією з основних частин конвертного методу служать конвертні криві $T_{max}(\lambda)=T_M(\lambda)$ та $T_{min}(\lambda)= T_m(\lambda)$. Отримуються вони за допомогою екстраполяції попередньо визначених точок, які відповідають положенню інтерференційних екстремумів (рис. 6).

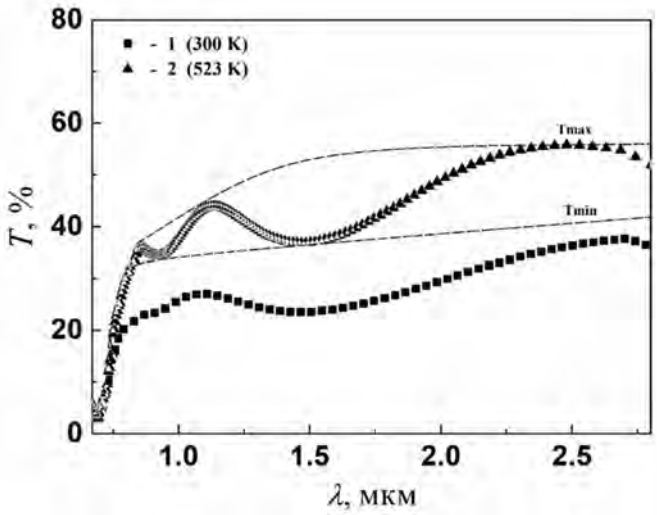

Рисунок 6. Спектр пропускання тонкої плівки CuO та конвертні криві для інтерференційних максимумів $T_{max}(\lambda)$ та мінімумів $T_{min}(\lambda)$

Після того, як ми отримали конвертні криві, можна визначити показник заломлення *n(λ)* тонкої плівки CuO, який знаходиться за допомогою рівняння:

$$n(\lambda)=\left[\sqrt{\left(\frac{2n_s\left(T_M(\lambda)-T_m(\lambda)\right)}{T_M(\lambda)T_m(\lambda)}+\frac{n_s^2+1}{2}\right)^2-n_s^2}+\left(\frac{2n_s\left(T_M(\lambda)-T_m(\lambda)\right)}{T_M(\lambda)T_m(\lambda)}+\frac{n_s^2+1}{2}\right)\right]^{\frac{1}{2}}, \quad (2)$$

де n_s – це показник заломлення підкладки, який визначається за виразом:

$$n_s=\sqrt{(\frac{1}{T_s^2}-1)}+\frac{1}{T_s}, \quad (3)$$

де T_s - пропускання підкладки і воно практично постійне в прозорій області.

Для підкладки, в якості якої використане покривне скло, T_s = 0,91. Тоді з рівняння (3) отримаємо, що n_s = 1,554.

Значення показника заломлення тонких плівок CuO розраховане з використанням рівняння (2). З рис. 7 видно, що при збільшенні довжини хвилі показник заломлення спадає і при довжинах хвиль λ > 1000 нм стабілізується. Великі значення n при довжинах хвиль λ < 800 нм обумовлене різким зменшенням пропускання біля краю власного поглинання тонких плівок оксиду міді. Наступним кроком конвертного методу є визначення товщини плівок CuO з рівняння (4):

$$d=\frac{A\lambda_1\lambda_2}{2\left[n(\lambda_1)\lambda_2-n(\lambda_2)\lambda_1\right]}, \quad (4)$$

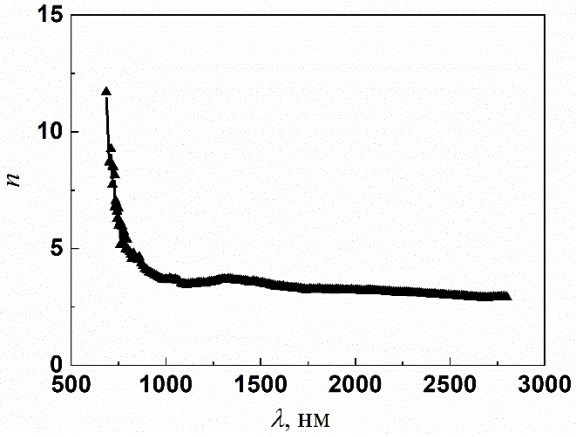

Рисунок 7. Графік залежності показника заломлення від довжини хвилі для тонкої плівки CuO (№2).

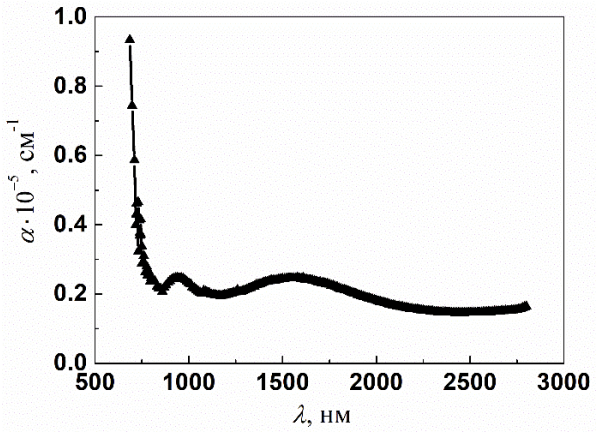

Рисунок 8. Графік залежності *α(λ)* тонкої плівки CuO (№2)

де: λ_1 та λ_2 – довжини хвиль, котрі відповідають сусіднім точкам екстремуму на спектрі пропускання, величина A = 1 для 2-х сусідніх точок екстремуму одного типу (min – min, max – max) і A = 0,5 для 2-х сусідніх екстремумів протилежного типу (min – max, max – min).

Товщина тонкої плівки оксиду міді, розрахована за допомогою виразу (4) складає 280 нм. Коефіцієнт поглинання *α(λ)* (рис. 8) для плівок оксиду міді можна обчислити за допомогою виразу (5):

$$\alpha(\lambda)=\frac{1}{d}\ln\left[\frac{\left(n(\lambda)-1\right)\left(n(\lambda)-n_s\right)\left[\left(\frac{T_M(\lambda)}{T_m(\lambda)}\right)^{\frac{1}{2}}+1\right]}{\left(n(\lambda)+1\right)\left(n(\lambda)+n_s\right)\left[\left(\frac{T_M(\lambda)}{T_m(\lambda)}\right)^{\frac{1}{2}}-1\right]}\right] \quad (5)$$

На рис. 8 можна побачити що значення коефіцієнта поглинання α в області коротких хвиль, біля краю власного поглинання є великими, а однорідним поглинання стає в області λ > 1000 нм. За допомогою рівняння (6) визначено коефіцієнт екстинкції, графік якого зображено на рис. 9.

$$k(\lambda)=\frac{\lambda\alpha(\lambda)}{4\pi} \quad (6)$$

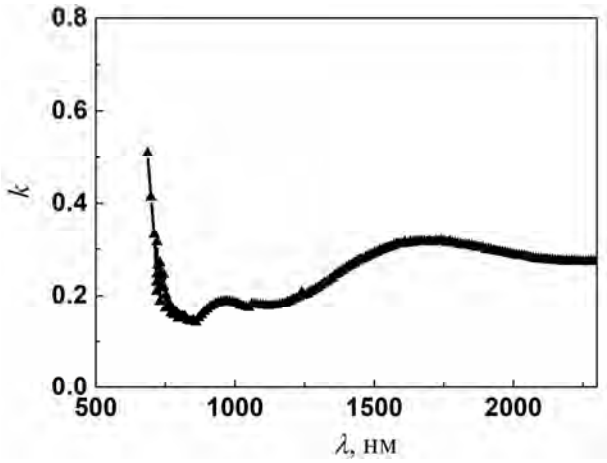

Рисунок 9. Графік залежності *k(λ)* тонкої плівки CuO (№2)

З рис. 9 видно, що біля краю області власного поглинання плівки коефіцієнт екстинції теж високий. В області $\lambda > 800$ нм значення коефіцієнта екстинції k слабо залежить від довжини хвилі λ. Даний метод застосовується тільки у межах області прозорості тонкої плівки. В області власного поглинання виконуються такі умови: сильне поглинання в тонкої плівки CuO, повністю прозора підкладка та $n^2>>k^2$.

Показник поглинання α в області власного поглинання тонкої плівки оксиду міді може бути визначений з наступного виразу[20]:

$$\alpha(\lambda)=\frac{1}{d}\ln\left[\frac{\left(1-R_1(\lambda)\right)\left(1-R_2(\lambda)\right)\left(1-R_{12}(\lambda)\right)}{T(\lambda)}\right], \tag{7}$$

де T – коефіцієнт пропускання; R_1, R_{12}, R_2 – це коефіцієнти відбивання від границь: плівка – підкладка, повітря – плівка, підкладка – повітря.

$$R_1=\left(\frac{n(\lambda)-1}{n(\lambda)+1}\right)^2,\ R_{12}=\left(\frac{n_s-n(\lambda)}{n_s+n(\lambda)}\right)^2,\ R_2=\left(\frac{1-n_s}{1+n_s}\right)^2\ [16] \tag{8}$$

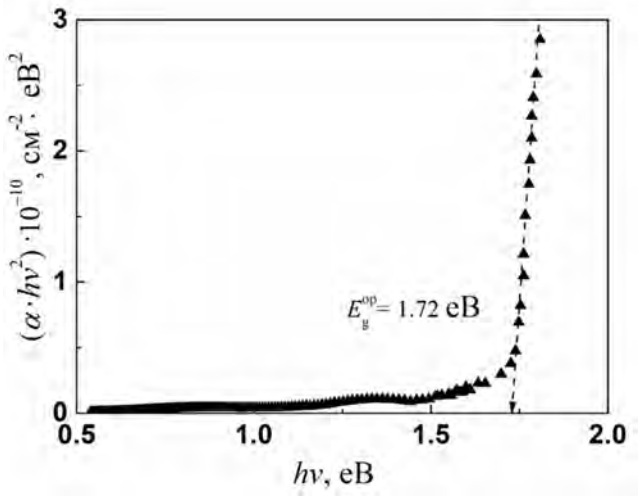

Рисунок 10. Графік залежності $(\alpha h\nu)^2 = f(h\nu)$ для зразка CuO №2

Коефіцієнт поглинання α для тонких плівок добре узгоджується із наступною залежністю:

$$(\alpha h\nu) = A\left(h\nu - E_g\right)^{1/2}, \tag{9}$$

де A – константа.

Визначено ширину забороненої зони тонкої плівки CuO (№2) E_g=1,72 еВ, здійснивши екстраполяцію прямолінійної ділянки кривої $(\alpha\ \ h\nu)^2 = f(h\nu)$ на вісь енергії $h\nu$ (рис. 10).

Також було проведено визначення оптичних властивостей за допомогою незалежних вимірювань коефіцієнтів пропускання (рис. 6) і відбивання (рис. 11) [21]. Оптичні коефіцієнти взаємо пов'язані з оптичними константами n і k [22]. Якщо падіння світлового пучка на поверхню зразка нормальне, то відбивна здатність поверхні визначається за формулою:

$$R = \frac{(n-1)^2 + k^2}{(n+1)^2 + k^2} \tag{10}$$

При низькому коефіцієнті поглинання світла в об'ємі напівпровідника, коли $k^2 << 1$ (або $k^2 << n^2$), із (10) одержуємо:

$$R = \frac{(n-1)^2}{(n+1)^2} \tag{11}$$

з якого отримуємо:

$$n = \frac{1+\sqrt{R}}{1-\sqrt{R}} \tag{12}$$

На рис. 11 наведені спектри відбивання і показник заломлення (вставка), який розрахований за формулою 12.

Встановлено, що коефіцієнт поглинання (рис. 12) тонких плівок CuO в області власного поглинання добре описується залежністю (9). Така залежність свідчить про те, що матеріал тонких плівок CuO, напилених методом реактивного магнетронного розпилення при постійній напрузі, є прямозонним напівпровідником. Шляхом екстраполяції лінійної ділянки кривої $(\alpha\ \ h\nu)^2 = f(h\nu)$ до перетину з віссю енергії $h\nu$, визначено оптичну ширину забороненої зони для зразка №1 CuO (E_g^{op} = 1,62 еВ); для зразка №2 CuO (E_g^{op} = 1,65 еВ).

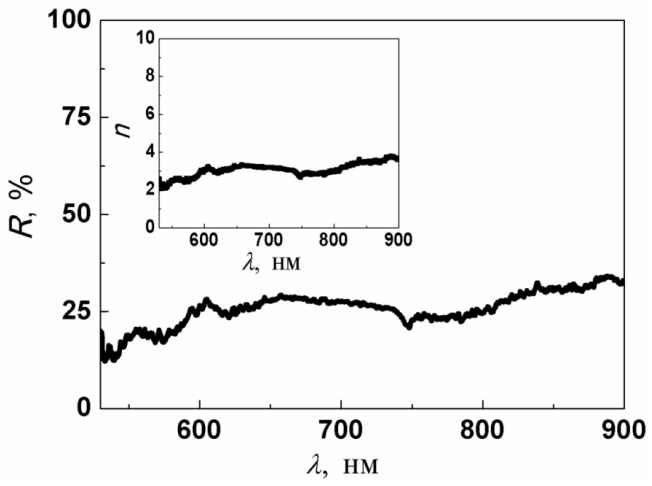

Рисунок 11. Спектральні залежності коефіцієнта відбивання тонкої плівки CuO (№2), на вставці залежність показника заломлення

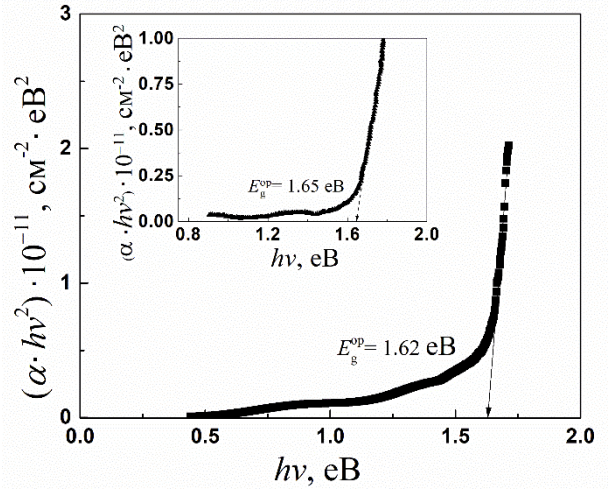

Рисунок 12. Графік залежності $(\alpha\ \ h\nu)^2 = f(h\nu)$ для зразка CuO №1. На вставці - для зразка №2.

Варто відмітити, що отримані плівки володіють шириною забороненої зони близькою до оптимальної ширини забороненої зони (1,5 еВ) матеріалів поглинача в конструкції сонячних елементів. Тому ці плівки можна використовувати в сонячних елементах.

ВИСНОВКИ

1. Визначено елементний склад тонких плівок CuO, представлено розподіл елементів на поверхні, які входять до складу даних плівок, встановлено, що розмір зерен для плівок отриманих при нижчій температурі підкладки D становить ~ 16 нм, а для плівок отриманих при вищій температурі – D ~ 26 нм. На дифрактограмах тонких плівок CuO спостерігається більша інтенсивність піків для тонких плівок отриманих

при вищих температурах підкладки CuO №2, що може бути зумовлено кращою структурною досконалістю тонких плівок та більшим розміром зерен.

2. На основі незалежних вимірювань коефіцієнтів відбивання і пропускання визначили оптичну ширину забороненої зони для двох зразків екстраполяцією прямолінійної ділянки кривої $(\alpha h\nu)^2 = f(h\nu)$ на вісь $h\nu$. Для зразка CuO №1 E_g^{op} = 1,62 еВ; для зразка CuO №2 E_g^{op} = 1,65 еВ. Для тонких плівок CuO №2 також використовували конвертний метод для визначення основних оптичних коефіцієнтів E_g^{op} = 1,72 еВ, отримані значення E_g^{op} визначені двома методами добре корелюють між собою.
3. З дослідження електричних властивостей, встановлено, що температурні залежності електричного опору для тонких плівок CuO мають напівпровідниковий характер, тобто опір зменшується при збільшенні T. Чотирьохзондовим методом визначено величини поверхневого опору плівок: зразок №1- ρ = 18,69 кОм/☐, зразок № 2 - ρ = 5,96 кОм/☐.

ORCID IDs

Taras T. Kovalyuk, https://orcid.org/0000-0002-7712-6758; **Hryhorii P. Parkhomenko,** https://orcid.org/0000-0001-5358-1505
Mykhailo M. Solovan, https://orcid.org/0000-0002-1077-5702

REFERENCES

[1] K. Deepthi Jayan, and V. Sebastian, International Journal of Energy Research. **45(11)**, 16618 (2021), https://doi.org/10.1002/er.6909
[2] Y. Su, T. Liu, P. Zhang, and P. Zheng, Thin Solid Films. **690**, 137522 (2019), https://doi.org/10.1016/j.tsf.2019.137522
[3] F. Wu, B.J. Harper, L.E. Crandon, and S.L. Harper, Environmental Science: Nano. **7(1)**, 105 (2020), https://doi.org/10.1039/C9EN01026B
[4] A. Nigussie, H.C. Ananda Murthy, and A. Bedassa, Research Journal of Chemistry and Environment. **25(6)**, 202 (2021), http://dx.doi.org/10.13005/msri/150311
[5] M.A. Kamyabi, N. Hajari, and M. Moharramnezhad, Chemical Papers. **75**, 5387 (2021), https://doi.org/10.1007/s11696-021-01584-0
[6] W. Shockley and H. J. Queisser, Journal of Applied Physics, **32**, 510 (1961), https://doi.org/10.1063/1.1736034
[7] M.M. Solovan, V.V. Brus, A.I. Mostovyi, P.D. Maryanchuk, E. Tresso, and N.M. Gavaleshko, Physica Status Solidi - Rapid Research Letters. **10(4)**, 346 (2016), https://doi.org/10.1002/pssr.201600010
[8] M.M. Solovan, V.V. Brus, , P.D. Maryanchuk, M. I. Ilashchuk, S. L. Abashin, and Z. D. Kovalyuk, Semiconductor Science and Technology. **30(7)** (2015), https://doi.org/10.1088/0268-1242/30/7/075006
[9] I.G. Orletskii, P.D. Maryanchuk, E.V. Maistruk, M.N. Solovan, D.P. Koziarskyi, and V.V. Brus, Inorganic Materials. **52**(8), 851 (2016), https://doi.org/10.1134/S0020168516080148
[10] I.G. Orletskii, P.D. Maryanchuk, E.V. Maistruk, M.N. Solovan, and V.V. Brus, Physics of the Solid State. **58**(1), 37 (2016), https://doi.org/10.1134/S1063783416010224
[11] R. Özmenteş, C. Temirci, A. Özkartal, K. Ejderha, and N. Yildirim, Materials Science-Poland. **36**(4), 668 (2018), https://doi.org/10.2478/msp-2018-0092
[12] W. Zheng, Y. Chen, X. Peng, K. Zhong, Y. Lin, and Z. Huang, Materials. **10**(7), 1253 (2018), https://doi.org/10.3390/ma11071253
[13] S. Dolai, R. Dey, S. Das, S. Hussain, R. Bhar, and A. K. Pal, Journal of Alloys and Compounds. **724**, 456 (2017), https://doi.org/10.1016/j.jallcom.2017.07.061
[14] N. Sangwaranatee, C. Chananonnawathorn, and M. Horprathum, Materials Today: Proceedings. **5**(6), 13896 (2018), https://doi.org/10.1016/j.matpr.2018.02.036
[15] A. Moumen, B. Hartiti, P. Thevenin, and M. Siadat, Optical and Quantum Electronics. **49**(2), 70 (2017), https://doi.org/10.1007/s11082-017-0910-1
[16] D.S. Murali, S. Kumar, R.J. Choudhary, A.D. Wadikar, M.K. Jain, and A. Subrahmanyam, AIP advances. **5**(4), 047143 (2015), https://doi.org/10.1063/1.4919323
[17] I.G. Orletskii, P.D. Mar'yanchuk, M.N. Solovan, E.V. Maistruk, and D.P. Kozyarskii, Technical Physics Letters. **42**(3), 291 (2016), https://doi.org/10.1134/S1063785016030263
[18] A.E. Lapshin, V.V. Karzin, V.I. Shapovalov, and P.B. Baikov, Glass Physics and Chemistry. **42**(1), 116 (2016), https://doi.org/10.1134/S1087659616010065
[19] M.N. Solovan, P.D. Maryanchuk, V.V. Brus and O.A.Parfenyuk, Inorganic Materials. **48**(10), 1026 – 1032, (2012), https://doi.org/10.1134/S0020168512100123
[20] E.A. Saied, M.M. Ismahil, and Y.M. Hassan, Arabian Journal for Science and Engineering. **45**(6), 4921 (2020), https://doi.org/10.1007/s13369-020-04367-z
[21] P. Dutta, R. Mandal, S. Bhattacharyya, R. Dey, and R.S. Dhar, Microsystem Technologies. **27**(9), 3475 (2021), https://doi.org/10.1007/s00542-020-05145-5
[22] V.V. Brus, L.J. Pidkamin, S.L. Abashin, Z.D. Kovalyuk, P.D. Maryanchuk, and O.M. Chugai, Optical Materials. **34**(11), 1940 (2012), https://doi.org/10.1016/j.optmat.2012.06.007

STRUCTURAL, ELECTRICAL AND OPTICAL PROPERTIES OF CuO THIN FILMS OBTAINED BY REACTIVE MAGNETRON SPUTTERING

S.I. Kuryshchuk[a], Taras T. Kovalyuk[a,b], Hryhorii P. Parkhomenko[a], Mykhailo M. Solovan[a]
[a]Yuriy Fedkovych Chernivtsi National University, st. Kotsyubyns'kogo 2, 58012, Chernivtsi, Ukraine
[b]Charles University in Prague, Faculty of Mathematics and Physics
Ke Karlovu 5, 121 16 Prague 2, Czech Republic

CuO thin films were produced by the method of reactive magnetron sputtering at direct current in a universal vacuum system Leybold-Heraeus L560 on glass substrates, the temperature of which was: 300 K and 523 K. The structural, electrical and optical properties for

the obtained samples of CuO thin films were studied, namely: elemental composition, distribution of elements on the surface, which are part of these films, grain size, activation energy, optical band gap, refractive index, analysis of curves of transmission and reflection spectra for CuO thin films deposited on glass substrates. The elemental composition of the thin films and the surface morphology were performed using a scanning electron microscope (MIRA3 FEG, Tescan) equipped with a reflected electron detector (BSE) and an energy-dispersed X-ray detector (EDX). It was found that the grain size for films obtained at a lower substrate temperature D is ~ 16 nm, and for films obtained at a higher temperature - D ~ 26 nm. On the diffractograms of CuO thin films, a higher peak intensity is observed for thin films obtained at higher CuO no. 2 substrate temperatures, which may be due to better structural perfection of thin films and larger grain size. From the study of electrical properties, it was found that the temperature dependences of the electrical resistance for CuO thin films have a semiconductor character, ie the resistance decreases with increasing *T*. The surface resistance of the films was measured by the four-probe method: no. 1- ρ = 18,69 kΩ/□, sample no. 2 – ρ = 5,96 kΩ/□. Based on independent measurements of the reflection and transmission coefficients, the optical band gap was determined for the two samples by extrapolation of the rectilinear section of the curve $(\alpha h\nu)^2 = f(h\nu)$ to the $h\nu$ axis. For the sample CuO №1 E_g^{op} = 1.62 eV; for the sample CuO no. 2 E_g^{op} = 1.65 eV. For CuO no. 2 thin films, the envelope method was also used to determine the basic optical coefficients E_g^{op} = 1.72 eV, and the obtained E_g^{op} values determined by the two methods correlate well with each other.
Keywords: thin film, CuO, optical properties, activation energy.

EAST EUROPEAN JOURNAL OF PHYSICS. 4. 86-90 (2021)
DOI: 10.26565/2312-4334-2021-4-09 ISSN 2312-4334

THERMAL-VACUUM METHOD FOR OBTAINING NANODISPERSED ZIRCONIUM DIOXIDE[†]

Volodymyr O. Kutovyi*, Dmitry G. Malykhin, Volodymyr D. Virych, Ruslan L. Vasilenko
National Scientific Center "Kharkov Institute of Physics & Technology" NASU
Kharkiv, 61108, Akademicheskaya st. 1, Ukraine
**Corresponding Author: kutovoy@kipt.kharkov.ua, Tel.: +38-057-349-10-82*
Received September 23, 2021; revised October 20, 2021; accepted November 16, 2021

An energy-efficient thermal-vacuum method for continuous production of nanodispersed powder of amorphous zirconium dioxide from zirconium hydroxide has been developed. This approach is based on a principle of creating an aerodynamic flow with an initial powder-like material in the cavity of the heating element of a thermal-vacuum installation. In this way, short-term contacts of particles of zirconium hydroxide with the inner surface of the heating element made in the form of the winding helical are created. As a result, the crushing of the particles is carried out due to the high thermal stresses in the particles contacted. This process is aggravated by the presence of residual moisture in the original powdery material. Transformations of the zirconium hydroxide in the process of thermal-vacuum treatment have been investigated. Amorphous dioxide has been obtained. The study of structural composition of the material in the initial state and processed in a thermal-vacuum installation was carried out using X-ray analysis and scanning microscopy. Experimental data on the structural-phase composition of the original material and data on the closest structural prototypes of crystalline-impurity compounds are presented. They are also given data on the volume of crystal cells and estimates of the molar concentration of the components. A mass spectrometric assessment of the elemental composition of the obtained zirconium dioxide is given. Thermal-vacuum method allows toobtain highly dispersed zirconium dioxide in its amorphous state directly from zirconium hydroxide without using liquid media and, moreover, in a short time – within 15...20 s.
Keywords: zirconium hydroxide, zirconium dioxide, fabrication, dispersion method, nanopowder.
PACS: 81.05.Je, 81.07.Wx, 81.16.-c

One of the problems of current interest associated with the needs of modern technology is the scientific and technical principles of creating nanostructured materials for products and structures of industrial production and other technical needs. Objects of interest include zirconium dioxide, which is widely used in the manufacture of fire-resistant materials, as well as in dentistry.

To create nanosized zirconium dioxide, the method of forced hydrolysis [1], as well as the method of pyrolysis of sprayed salt solutions [2], have recently been used. There is also a method for producing zirconium-dioxide nanopowders by the method of electron beam evaporation and vacuum deposition [3]. However, this process is lengthy and energy intensive. Hydrothermal synthesis is one of the most industry-wide methods for obtaining nanodispersed ZrO_2 powders [4]. But this process requires acid treatment. And in this case, it is necessary to change in a wide range the temperature, pressure, concentration and acidity of the solutions used. Nano-dispersed zirconium dioxide is obtained by its heterophase synthesis from zirconium oxychloride with the participation of solutions of different bases (for example, from the compound $ZrOCl_2 \cdot 8H_2O$ in aqueous solutions of KOH, NaOH or ammonia [5]).

So, the methods described above make it possible to obtain nanodispersed zirconium dioxide using aqueous solutions of acids, alkalis and alcohols.

The featured thermal-vacuum method makes it possible to obtain highly dispersed zirconium dioxide directly from the hydroxide without using liquid media and, moreover, in a short time – 15...20 s. This takes place in the air flow through the heating element duct. On the basis of this, in particular, a nanodispersed graphite powder was obtained – a material that can be used in printers and other copying equipment [6].

THERMAL-VACUUM INSTALLATION FOR DISPERSION AND DEHYDRATION

On the basis of the performed theoretical and experimental studies, an energy-efficient thermal-vacuum method for continuous dispersion and dehydration of wet powdery materials had been developed [7]. This method is based on combining a fast evacuation process – creating aerodynamic driving force – and thermal heating to a required temperature. This is accompanied by acts of direct contact of surface layer of particles of original material with the inner surface of the hollow heater, what provides instantaneous heating of the material particles in a vacuum.

For the closest contact with the initial powdery material, the heater is made in the form of a helical spiral. The physical principle of this technique is that the decrease in pressure inside the heating element, produced by a vacuum pump, creates a pressure gradient that stimulates an intense flow of air with powder. When such a flow moves in the spiral, due to its sufficient speed and inertia of the particles, an impact contact of the particles with the inner surface of the heater occurs, which makes it possible to efficiently use the heat of the heating element in this process. An instantaneous heating of the surface layer of zirconium hydroxide particles to a high temperature occurs. This stimulates the fragmentation of particles.

[†] ***Cite as:*** V.O. Kutovyi, D.G. Malykhin, V.D. Virych, and R.L. Vasilenko, East. Eur. J. Phys. **4**, 86 (2021), https://doi.org/10.26565/2312-4334-2021-4-09

Under the conditions of the existence of residual moisture in the original powder in combination with a reduced air pressure, the process of crushing particles can be aggravated. So, in this case, the temperature of the contacting layer becomes higher than the temperature of moisture evaporation. This causes intense vapor release from the surface layer of zirconium hydroxide – a steam explosion, which facilitates the crushing process. The physical details of the powder dispersion process are described in [6-7].

The thermal-vacuum installation is shown in Fig. 1[6, 8]. It consists of a feed hopper (1), a hollow heater (2), a vacuum pump (3), tunnels (4, 11), a cyclone (5), a receiver for dried raw materials (6), and a floodgate (7). The installation has a thermocouple (8, 13), a control panel (9), a conveyer (10), a filter (12), a level sensor for dried raw materials (14), and a vacuum gauge (15).

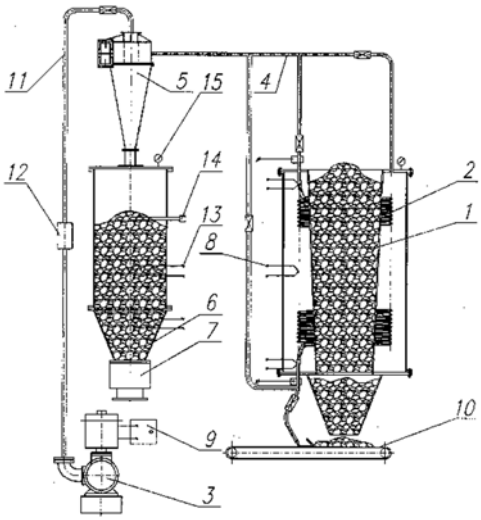

Figure 1. Thermal-vacuum scheme.

This design of the installation provides highly efficient dispersion of material in a space thermally insulated from the external environment, and, simultaneously, its continuous dehydration. In general, effectiveness of dispersion depends on thermal-physical properties of material and its state: on the relationship between thermal conductivity, heat capacity and thermal coefficient of expansion, on dispersion and moisture content of original material, on ambient pressure, and on the heater temperature. In our case, the heater temperature is 350ºC.

EXPERIMENTAL

As is known, zirconium hydroxide – the original material in our studying – is obtained by chemical processing zircon concentrate [4]:

$$ZrSiO_4 + [(Na,K)OH + CaF_4] \rightarrow \ldots \rightarrow (Na,K)_2ZrF_6 + ZrO_2 + CaSiO_3 \quad (1)$$

By treating the resulting mixture in a hydrochloric acid solution, zirconium oxychloride $ZrOCl_2$ is obtained from the first two products, from which zirconium hydroxide is then precipitated in an ammonia solution. In this case, insoluble impurities may remain [4].

The study of structural composition of the material in the initial state and processed in a thermal vacuum installation was carried out using X-ray structural analysis and scanning microscopy. The X-ray measurements were carried out on a DRON4-07 diffractometer with CuK_α radiation recording by a proportional counter using the pair of Soller slits.

A semi-quantitative phase analysis was performed using a full-profile X-ray diagram, and this referred to the original material. Based on the measurement results, the molar portion of the structural components of the material was estimated by integrating the intensity of X-ray reflection recorded as profiles of the $I(\theta)$ diagram in the coordinates of the diffraction angle θ. Integration was carried out over polar coordinates in the volume of the sphere of reflections (Ewald's sphere). The initial variable of integration is reduced to an analog of the diffraction vector: $s = \sin\theta/\lambda$, where λ is the radiation wavelength. The following formula was used to calculate the averaged parameter of the reduced intensity of an individual phase or fraction, which is directly related to the numerical content of the reflecting molecular units of this fraction:

$$i = \frac{u}{U}\int_{s_0}^{s_M}\frac{I(s)}{P(\theta)f^2(s)}s^2ds = \frac{u}{U}\frac{1}{\lambda^3}\int_{\theta_0}^{\theta_M}\frac{I(\theta)}{P(\theta)f^2(s)}\sin^2\theta\cos\theta d\theta \qquad \left[U = \int_{\theta_0}^{\theta_M} s^2ds,\right], \quad (2)$$

Herein the first integrand is the integration of the full-profile intensity of reflections from some of the phases or fractions, taken individually, over the volume of the reciprocal lattice space bounded by the limiting radii of the Ewald sphere s_0 and s_M; $P(\theta)$ – multiplier of correction for the polarization of the reflected beam: $P(\theta) = (1 + \cos^2 2\theta)/2$; U is the volume of the integration area in the space of reciprocal lattices; f is the atomic factor; u is the volume fraction of the

space of reflections attributable to any node of the reciprocal lattice: $u = 1/8v$, where v is the real volume of the molecular unit (~ 10^{-22} cm^3).

The f-factor expresses the diffraction effect due to the size of atoms and the number of its electrons (ordinal number N), and is presented as an algebraic sum over the atoms of a molecular unit with their stoichiometric numbers n_i:

$$f^2(s) = \sum_i n_i f_i^2(s) \tag{3}$$

We limited this to the region of non-large diffraction angles and the values of $f_i(0)$ as parametric coefficients when integrating according to the formula (2). This approach is sufficient for estimating the content of phases and fractions at the level of their scales.

In general, the molar concentration of the j-th phase or fraction was estimated by the ratio $c_j = i_j/\Sigma i_k$ (2), with which the normalization condition $\Sigma c_k = 1$ is met.

RESULTS

X-ray CuK$_\alpha$-diagrams of the original and processed material are shown in Figure 2.

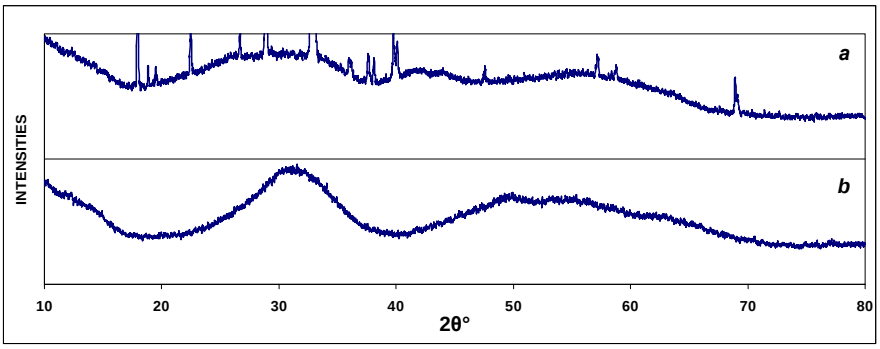

Figure 2. X-ray diagrams of the original zirconium hydroxide (a) and the dioxide obtained after thermal-vacuum treatment (b).

The presence of elements of similarity in the general form of angular distributions (Fig. 2a,b) gave grounds to believe that the original material contains a significant amount of zirconium dioxide.

According to the analysis of the complex of X-ray lines in the diagram (Fig. 2a), it was found that the original material contains two crystalline phases of an unidentifiable nature. Apparently, these are impurities of precipitates remaining after the preliminary treatment of zirconium oxychloride in an ammonia solution to obtain hydroxide. It is assumed that these are structures based on $(Na,K)_2ZrF_6$ and $CaSiO_3$ (1), modified by other elements in the course of chemical separation reactions.

Table 1 shows experimental data on the structural-phase composition of the original material and data on the closest structural prototypes of impurity compounds with a crystalline nature. Data on the volume of crystal cells and estimates of the molar concentration of the components are also given. Molar concentrations were estimated from chart analysis based on the approach described in the previous section.

Table 2 shows the mass spectrometric estimates of the elemental composition of the obtained zirconium dioxide.

Table 1. Structural-phase composition of the original material.

composition	structure	a (nm)	b (nm)	c (nm)	V (nm^3)	mol. %
exp.	cubic	0.667 (0.471)	0.667 (0.471)	0.667 (0.471)	0.296 (0.105)	0.5
K_2ZrF_6	rhombic	0.658	1.144	0.694	0.522	
exp.	rhombic	0.987	0.792	0.553	0.4325	3
$CaSiO_3$	triclinic	1.01 99.5°*	0.731 83.4°	1.106 100.6°	0.789	
Zr hydroxide	amorphous					32-45
ZrO_2	amorphous					53-66

(*) – angles between two other basal planes of the lattice.

Table 2. Elemental composition of the obtained zirconium dioxide.

el.	B	C	N	O	F	Na	Mg	Al	Si	P	S	Cl	K
at.%	0.0003	4.64	0.56	67.9	2.64	0.067	0.045	0.08	0.36	0.018	0.09	0.018	0.028
el.	Ca	Ti	V	Cr	Mn	Fe	Ni	Co	Cu	Zn	Sr	Zr	Sn
at.%	0.4	0.008	0.001	0.048	0.004	0.29	0.015	0.003	0.043	0.004	0.003	22.8	0.003

These data indicate the predominance of impurities C, N, Ca, Si, Fe and F in the resulted dioxide. This, in particular, confirms the result of the analysis of the crystalline-impurity composition of the original material (Table 1).

By the method of thermal-vacuum dispersion, amorphous zirconium dioxide was obtained with 20...200 nm size of the powder particles (Fig. 3). There were no conglomerates in the powder.

DISCUSSION

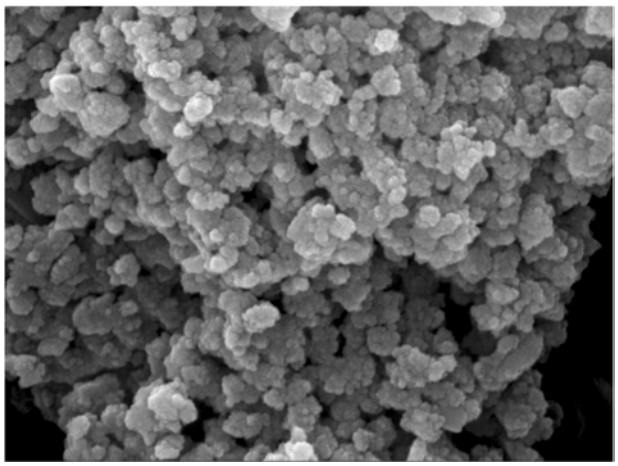

Figure 3. ZrO_2 in the amorphous state

The original material with zirconium hydroxide (Fig. 2a) was a powder with a moisture content of 12.5%. The obtained dioxide in the amorphous state (Figs. 2b, 3) has a moisture content of 1.8%. The presence of hydroxide in its environment, had noted by analyzing the diagrams (Fig. 2a,b), is associated with the time period before X-ray measurements, during which it gained atmospheric humidity up to 6%.

Of course, the dispersion process is determined by the physical capabilities of the thermal-vacuum installation. However, the actual result depends also on the characteristics of the filters. In our case, a system of two filters was used. Amorphous zirconium dioxide was retained by a fine filter (Fig. 3). Crystalline-impurity fractions were retained in the coarse filter. The process time of the entire technological cycle is 15...20 s.

As a result, the amorphous zirconium dioxide was obtained with a yield of 30 wt%, the apparent density of 1.64 g/cm^3, wherein the apparent density of zirconium hydroxide was 1.05 g/cm^3.

SUMMARY

1. As a result of thermal-vacuum treatment of a powder based on zirconium dioxide containing zirconium hydroxide, pure dioxide was obtained in the amorphous state with a moisture content of 1.8%, a particle size of 20...200 nm and an yield of 30%.

2. It is noted that this method makes it possible to obtain fine and nanodispersed powders in a cycle of 15...20 s. This is due to a combination of sharp thermal effects when particles come into contact with the heater surface, the design feature of the heater, and the aerodynamic conditions of the process – with a positive effect of the residual moisture content of the powder material on the process.

3. It is noted that in the process of thermal-vacuum treatment, the material is able to change the crystalline-structure state under the conditions of the existing variety of its known crystallographic modifications. Under such conditions, an amorphous state of zirconium dioxide was obtained.

The described thermal vacuum-method significantly reduces the technological process and energy consumption – and can be used for the continuous and energy-efficient production of nanodispersed materials, as well as for drying powder materials.

The principle of this method provides wide possibilities for physical-mathematical developments on optimization industrial dispersion processes for various specific types of powder materials.

ORCID IDs

D.G. Malykhin, https://orcid.org/0000-0003-0259-0211

REFERENCES

[1] M.Z.C. Hu, R.D. Hunt, E.A. Payzant, and C.R. Hubbard, J. Am. Ceram. Soc. **82**(9), 2313 (1999), https://doi.org/10.1111/j.1151-2916.1999.tb02085.x

[2] R.S. Mishra, V. Jayaram, B. Majumdar, C.E. Lesher, and A.K. Mukherjee, J. Mater. Res. **14**(3), 834 (1999), https://doi.org/10.1557/JMR.1999.0111

[3] B.A. Movchan, Nanosystems, nanomaterials, nanotechnologies, **2**(4), 1103-1126 (2004). (in Russian)

[4] L.M. Rudkovskaya. R.N. Pshenichnyy, T.V. Pavlenko, and A.A. Omel'chuk, Nanosystems, nanomaterials, nanotechnologies, **10**(2), 351-360 (2012). (in Russian)

[5] A.V. Zhukov, S.V. Chizhevskaya, P. Phyo, and V.A. Panov, Inorganic materials, **55**(10), 994-1000 (2019), https://doi.org/10.1134/S0020168519080193

[6] V.O. Kutovyi, D.G. Malykhin, O.S. Kalchenko, R.L. Vasilenko, V.D. Virych, and O.S. Germanov, East Eur. J. Phys. **2**, 111 (2020), https://doi.org/10.26565/2312-4334-2020-2-10

[7] V.A. Kutovoy, Yu.G. Kazarinov, A.S. Lutsenko, A.A. Nikolaenko, and V.I. Tkachenko, PAST, **2**(90), 153 (2014), https://vant.kipt.kharkov.ua/ARTICLE/VANT_2014_2/article_2014_2_153.pdf

[8] V.O. Kutovyi, Patent 81138 Ukraine, (10 December 2007).

ТЕРМОВАКУУМНИЙ СПОСІБ ОДЕРЖАННЯ НАНОДИСПЕРСНОГО ДІОКСИДУ ЦИРКОНІЮ

В.О. Кутовий, Д.Г. Малихін, В.Д. Вірич, Р.Л. Василенко

Національний науковий центр «Харківський фізико-технічний інститут» НАНУ

Україна, 61108, г. Харків, вул. Академічна 1

У даній роботі наведено енергоефективний термовакуумний спосіб безперервного отримання нанодисперсного діоксиду цирконію з гідроксиду цирконію. У цьому підході закладено принцип створення аеродинамічного потоку з вихідним порошкоподібним матеріалом в порожнині нагрівального елементу. Таким способом створюються короткомоментні контакти частинок з внутрішньою поверхнею нагрівального елементу. В результаті цього дроблення частинок здійснюється завдяки високим термічним напруженням в частинках, що контактують. Цей процес посилюється існуванням залишкової вологи у вихідному порошкоподібному матеріалі. Досліджено фазові перетворення у процесі термовакуумной обробки гідроксиду цирконію. Отримано аморфний діоксид цирконію. Дослідження структурного складу матеріалу в початковому стані і обробленого в термовакуумній установці здійснено за допомогою рентгеноструктурного аналізу і скануючої мікроскопії. Приведено експериментальні дані зі структурно-фазового складу вихідного матеріалу і дані по найближчим структурним прототипам домішкових сполук кристалічного характеру. Наведено також дані з об'єму кристалічних комірок і оцінка молярної концентрації компонентів. Дана мас-спектрометрична оцінка елементного складу отриманого діоксиду цирконію. Термовакуумний метод дозволяє отримувати високодисперсний діоксид цирконію у аморфному стані безпосередньо з гідроксиду цирконію без використання рідких середовищ і до того ж за короткий час – протягом 15...20 с.

Ключові слова: гідроксид цирконію, діоксид цирконію, виробництво, метод диспергувания, нанопорошок.

EAST EUROPEAN JOURNAL OF PHYSICS. 4. 91-98 (2021)
DOI: 10.26565/2312-4334-2021-4-10 ISSN 2312-4334

GEANT4 MODELING OF THE BREMSSTRAHLUNG CONVERTER OPTIMAL THICKNESS FOR STUDYING THE RADIATION DAMAGE PROCESSES IN ORGANIC DYES SOLUTIONS†

Tetiana V. Malykhina[a,b]*, Vladimir E. Kovtun[a], Valentin I. Kasilov[b], Sergey P. Gokov[b]
[a]*Kharkiv V.N. Karazin National University*
4, Svobody sq., 61022, Kharkiv, Ukraine
[b]*National Science Center "Kharkiv Institute of Physics and Technology"*
2, Academicheskaya str., 61108, Kharkiv, Ukraine
**Corresponding Author: malykhina@karazin.ua*
Received 20 July 2021; revised October 11, 2021; accepted November 14, 2021

The study of the processes occurring in a matter when ionizing radiation passes through is important for solving various problems. Examples of such problems are applied and fundamental problems in the field of radiation physics, chemistry, biology, medicine and dosimetry. This work is dedicated to computer modeling of the parameters of a tungsten converter for studying the processes of radiation damage during the interaction of ionizing radiation with solutions of organic dyes. Simulation was carried out in order to determine the optimal thickness of the converter under predetermined experimental conditions. Experimental conditions include: energies and type of primary particles, radiation intensity, target dimensions, relative position of the radiation source and target. Experimental studies of the processes of radiation damage occurring in solutions of organic dyes are planned to be carried out using the linear electron accelerator "LINAC-300" of the National Scientific Center "Kharkov Institute of Physics and Technology". Electrons with 15 MeV energy are chosen as primary particles. The interaction of electrons with the irradiated target substances is planned to be studied in the first series of experiments. Investigations of the interaction of gamma quanta with the target matter will be carried out in the second series of experiments. The tungsten converter is used to generate a flux of bremsstrahlung gamma rays. One modeling problem is determination of the converter thickness at which the flux of bremsstrahlung gamma will be maximal in front of the target. At the same time, the flow of electrons and positrons in front of the target should be as low as possible. Another important task of the work is to identify the possibility of determining the relative amount of radiation damage in the target material by the Geant4-modeling method. Radiation damage of the target substance can occur due to the effect of bremsstrahlung, as well as electrons and positrons. Computational experiments were carried out for various values of the converter thickness – from 0 mm (no converter) to 8 mm with a step of 1 mm. A detailed analysis of the obtained data has been performed. As a result of the data analysis, the optimal value of the tungsten converter thickness was obtained. The bremsstrahlung flux in front of the target is maximum at a converter thickness of 2 mm. But at the same time, the flux of electrons and positrons crossing the boundaries of the target does not significantly affect the target. The computational experiment was carried out by the Monte Carlo method. A computer program in C++ that uses the Geant4 toolkit was developed to perform calculations. The developed program operates in a multithreaded mode. The multithreaded mode is necessary to reduce the computation time when using a large number of primary electrons. The G4EmStandardPhysics_option3 model of the PhysicsList was used in the calculations. The calculations necessary for solving the problem were carried out using the educational computing cluster of the Department of Physics and Technology of V.N. Karazin Kharkiv National University.
Keywords: bremsstrahlung, Geant4-simulation, bremsstrahlung converter, interaction of radiation with matter.
PACS: 07.05.Tp, 02.70.Uu, 81.40wx

Linear electron accelerators are currently used to solve various applied and fundamental problems. In particular, accelerators are used in nuclear medicine, materials science, in the development of radiation detectors, etc. Experiments on the irradiation of organic dyes were carried out in [1]. Aqueous, alcoholic and glycerol solutions of methylene blue ($C_{16}H_{18}N_3SCl$), as well as methyl orange ($C_{14}H_{14}N_3O_3SNa$), were irradiated with an electron beam. The authors investigated the optical density of the irradiated dyes. The electron beam energy was 16 MeV. It was found that aqueous solutions have less radiation resistance than alcohol and glycerol solutions. Further experimental studies of radiation-stimulated chemical processes during the destruction of dyes organic molecules have become necessary.

An experimental stand with a bremsstrahlung converter is usually used to study the effects that occur in matter when interacting with a flux of gamma quanta. The generation of a gamma quanta flux occurs in the converter due to the conversion of part of the electron beam energy into bremsstrahlung. The converter must be made of a material with a high atomic number and a high density in order to obtain a sufficient amount of gamma quanta. Tantalum and tungsten are appropriate materials due to their physical and chemical properties [2].

Computer simulation using Geant4 allows virtual nuclear physics experiments. These experiments are necessary for preliminary assessment, as well as choice of the bremsstrahlung converter optimal parameters for real experiments.

The aim of this work is to select the optimal thickness of the bremsstrahlung converter as part of the experimental stand "LINAC-300" of the National Scientific Center "Kharkov Institute of Physics and Technology" for studying the

† ***Cite as:*** T.V. Malykhina, V.E. Kovtun, V.I. Kasilov, and S.P. Gokov, East. Eur. J. Phys. **4**, 91 (2021), https://doi.org/10.26565/2312-4334-2021-4-10

radiation resistance of organic dye solutions. The primary electron energy is 15 MeV. It is necessary to determine the optimal thickness of the tungsten converter, at which the bremsstrahlung flux will be maximum directly in front of the target containing the solution. At the same time, the flux of electrons and positrons should be as low as possible. A converter with these parameters will be necessary to study the nature of the mechanisms that lead to radiation damage that occurs when ionizing radiation interacts with organic dye solutions.

MATERIALS AND METHODS

The scheme of the planned experiment is shown in Figure 1. The primary electrons beam passes through the titanium outlet window foil of the LINAC accelerator. The electron energy is E_e=15 MeV. The thickness of the foil is 50 μm. The bremsstrahlung converter is located at a distance of 50 mm from the titanium foil. The converter is marked in black in Figure 1. The electrons beam is directed along the normal to the converter surface. The target containing the solution is located after the converter. The target is marked in light green in Figure 1. The irradiated target contains 1% aqueous solution of an organic dye. Methylene blue $C_{16}H_{18}N_3SCl$ was chosen as an organic dye, as one of the substances studied in [1].

Figure 1. Simplified scheme of the experiment. The target size is 10 mm × 10 mm × 10 mm

The dimensions of the target are 10 mm×10 mm×10 mm, i.e., rather small, due to the need for further studies of the target. The transverse dimensions of the converter are 40 mm × 40 mm. The irradiated target is located at a distance of 1 mm after the converter. The thickness of the tungsten converter is varied from 0 mm to 8 mm in 1 mm increment in a series of computational experiments. A value of 0 mm corresponds to the case when the converter is absent. This case is necessary to study the interaction of electrons with the target material in the absence of bremsstrahlung. In this case, there will still be a small amount of gamma quanta formed in the titanium foil material when primary electrons pass through it.

One of the objectives of this work is to determine the thickness of the converter at which the flux of bremsstrahlung gamma quanta immediately in front of the target will be maximum, regardless of the amount of electrons and positrons in front of the target. The number of electrons and positrons in front of the target in this case should be minimal. It is necessary to estimate the relative amount of radiation damage in the target containing the organic dye solution for each value of the tungsten converter thickness.

We have developed a computer model of the planned experiment to solve the problem. The model is based on a computer program. The program is developed in C++ and uses the Geant4 toolkit of version 10.6 [3, 4].

The Geant4 toolkit has a complete set of tools for computer modeling of nuclear physical processes of radiation with matter interaction. Geant4 modules used in our program include Instrumentation for describing the detectors geometry and the experimental setup as a whole, description of particles and physical processes, transport and tracking of particles, simulation of the detector response. The Geant4 library uses CLHEP classes [5] and has a wide range of utility functions as well as random number generators.

The developed program contains the definition of several main classes that correspond to the specifics of the task when using the Geant4 library. All these classes must be registered in a special object-instance of the G4RunManager class, which controls the modeling process. The main classes are G4VUserDetectorConstruction, G4VPhysicsList, G4VUserPrimaryGeneratorAction [3]. The G4VUserDetectorConstruction class contains the geometry definition of the experimental setup model and its constituent parts, their mutual arrangement, as well as their materials. The G4VPhysicsList class is necessary to describe the models of physical processes [4] that occur during the interaction of ionizing radiation with materials of experimental setup components. We specify the primary particles source in the simulation, their type and energies in the G4VUserPrimaryGeneratorAction class. We also specify the particles movement direction and other parameters that characterize the radiation source in the G4VUserPrimaryGeneratorAction class. In addition, optional classes, for example, G4UserEventAction, G4UserSteppingAction [3], etc. can also be registered in the instance of the G4RunManager class. These classes allow one to control the behavior of the developed program at various stages of its execution, as well as set the required level of detail when displaying results.

The Geant4 toolkit developers offer about 30 predefined PhysicsList models to date. These models are described in detail in the documentation [6], and have application in modeling of almost any problem - from problems in high energy physics to applications in microdosimetry. We have chosen the G4EmStandardPhysics_option3 model of the PhysicsList module to solve our problem. This model is the most suitable [6] for simulating the passage of 15 MeV electron beam through the blocks of the studied facility. A monoenergetic electron beam is used in our problem to simulate ideal experimental conditions. The electron beam diameter in the model is specified to be 2 mm due to the fact that this series of calculations is preliminary. We will be able to find out the real parameters of the beam after carrying out a real experiment in order to use them in further calculations. The particle transport-tracking threshold was specified

to be 0.1 mm in length units. We used the setCut() function to calculate the threshold for tracking particle transport in units of energy. The threshold is approximately 351 keV for electrons in tungsten, and 36 keV for gamma rays in tungsten. The tracking threshold for particle transport is, respectively, 85 keV for electrons and 1 keV for gamma quanta in an aqueous solution of methylene blue.

The program we have developed contains a visualization module that uses the OpenGL library. A screen shot of the visualization module is shown in Figure 2 (a, b) in order to visualize the relative position of the experimental setup components, as well as to demonstrate the result of the particles passage through the converter.

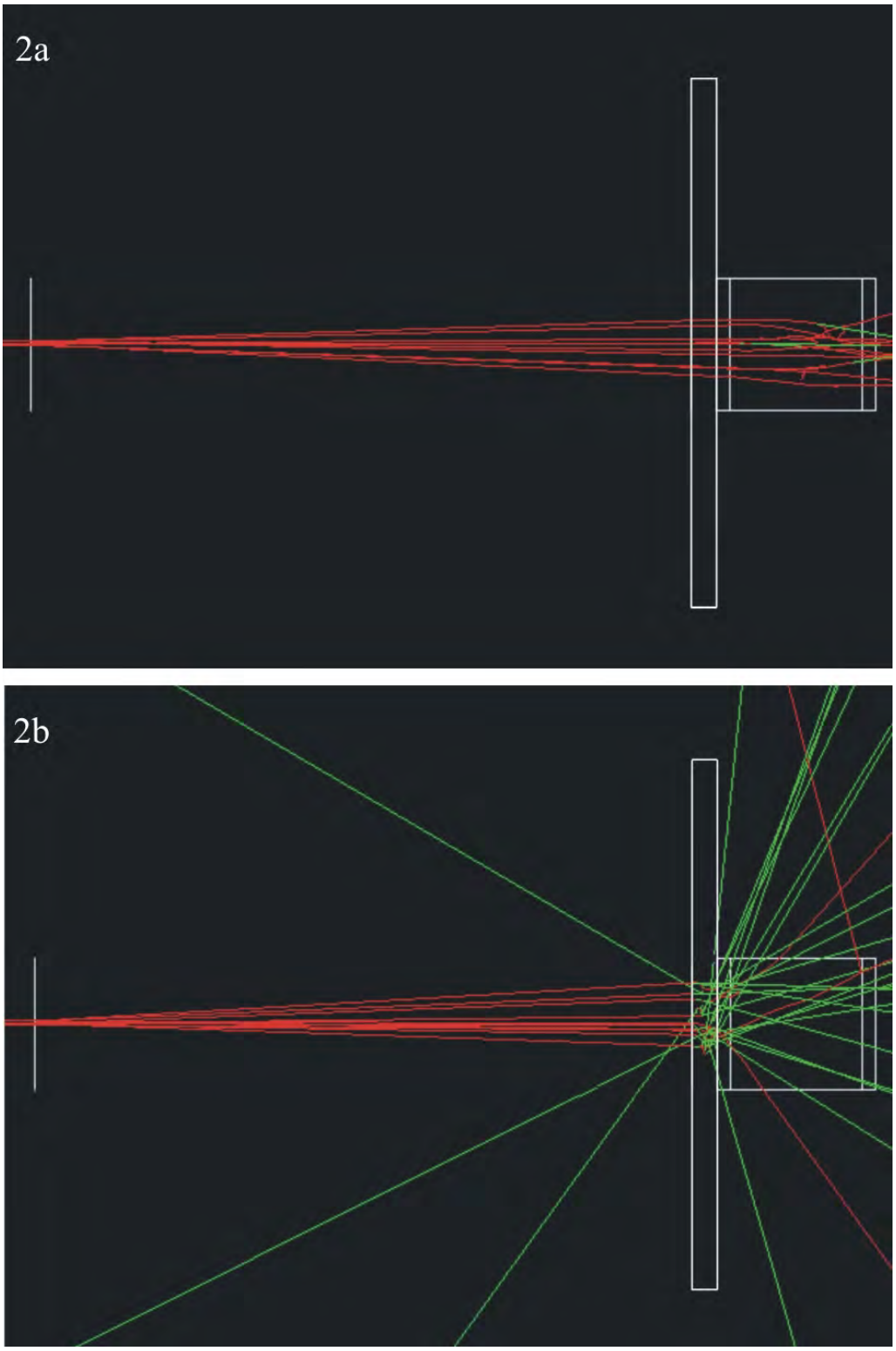

Figure 2. Passage of 10 primary electrons through the facility. The electron energy is 15 MeV.
(Figure 2a – The converter is absent; Figure 2b – We use a bremsstrahlung converter, its thickness is 2 mm)

Figure 2 shows the converter with a thickness of 2 mm. The converter thickness increases by 1 mm in each subsequent series of computational experiments. The energy of primary electrons is 15 MeV. The trajectories of electrons are shown in red in Figure 2, the trajectories of bremsstrahlung gamma quanta are shown in green. The OpenGL visualization of 10 primary electrons passing through the setup is shown in Figure 2a. There is no bremsstrahlung converter in this case, but the outline of the converter is shown in the screen shot in order to to keep the scale. We use air instead of a tungsten converter in the DetectorConstruction module in this case. A slight deviation of the electron beam can be seen after passing through the thin titanium foil. All primary electrons hit the target.

The passage of 10 electrons through a tungsten bremsstrahlung converter is shown in Figure 2b. The trajectories of gamma quanta are shown in green, the trajectories of electrons are shown in red in Figure 2b, similar to the marking in Figure 2a. It can be seen that primary electrons are decelerated in the converter, and bremsstrahlung gamma quanta are formed. A certain amount of gamma quanta does not hit the target in this case due to the small size of the target. Therefore, calculations using a large number of events are necessary, as well as an analysis of the obtained results.

The program developed by us has a batch mode for performing calculations by the Monte Carlo method for the purpose of further statistical data processing. The passage of 10^7 primary electrons with energy E_e=15 MeV through the setup containing the target was simulated in the batch mode. The statistical error of the Monte Carlo method will be less than 1% for this amount of primary electrons.

The calculations required to solve the problem were carried out using the educational computing cluster of the Scientific and Educational Institute "Physics and Technology Faculty" of V.N. Karazin Kharkiv National University. The educational compute cluster (Figure 3) consists of Dell Power Edge 1850 blocks of various configurations. These blocks are integrated into a local network, and use the Linux operating system.

Figure 3. Educational computing cluster of the Scientific and Educational Institute "Physics and Technology Faculty"

We used the multi-threaded mode of the Geant4 toolkit. The required additional libraries have been installed for this. In addition, we modified the source codes of the G4MPI module [3, 7] in order to uniformly load the computing blocks of the cluster, depending on their performance.

RESULTS AND DISCUSSION

The series of computational experiments were carried out using the batch mode of the developed program. The energy spectra of bremsstrahlung gamma quanta (Figure 4) in front of the target containing an organic dye solution were obtained as a result of data processing. The values of the gamma quanta flux directly in front of the target were also calculated for different converter thicknesses (Figure 5). The values of the electron flux in front of the target (Figure 6) were obtained depending on the thickness of the converter. In addition, the energy spectra of electrons in front of the target were calculated for two values of the converter thickness (Figure 7), at which a significant flux of gamma quanta is observed in front of the target. All presented results are normalized to 1 incident electron. The transverse dimension of the target is 10 mm×10 mm. The transverse dimension of the converter is 40 mm×40 mm.

The energy spectra of bremsstrahlung gamma quanta for primary electrons with energy E_e = 15 MeV in front of the target are shown in Figure 4. These spectra have 100 keV resolution and are presented in a log scale on Y-axis. It can be noted that the maximum relative amount of gamma rays crossing the target boundary will occur for tungsten converter thickness of 2 mm.

The relative amount of bremsstrahlung gamma quanta crossing the target boundary, depending on the converter thickness, is shown in Figure 5. The flux is normalized to 1 incident electron. It can be seen that the maximum flux of bremsstrahlung gamma quanta in front of the target will be at the converter thickness of 2 mm for primary electrons with energy of 15 MeV. The flux of gamma quanta decreases when the converter thickness is 3 mm.

The electron flux values in front of the target (Figure 6) were obtained for the same values of the converter thickness from 0 mm to 8 mm with a step of 1 mm.

It can be seen that with a converter thickness of 2 mm, when the largest amount of bremsstrahlung gamma quanta is observed in front of the target, there is also a significant amount of electrons in front of the target. The relative electrons number in front of the target, depending on the converter thickness, is presented in Table 1. The presented results are normalized to 1 incident electron.

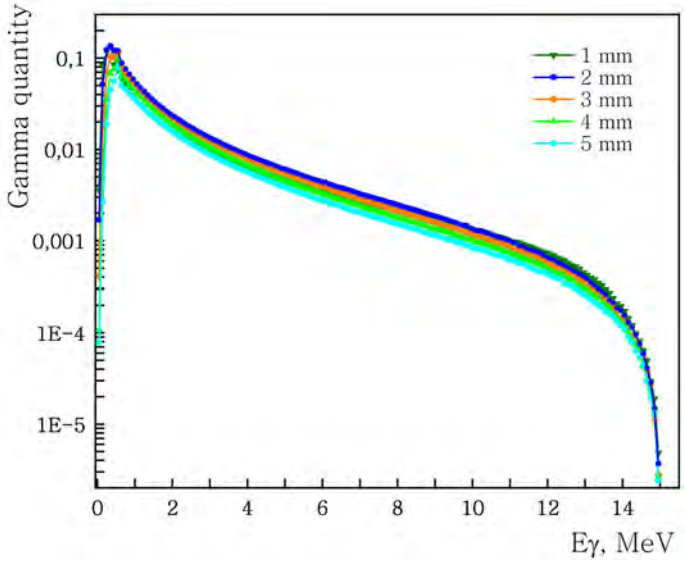

Figure 4. Energy spectra of gamma quanta crossing the target boundary

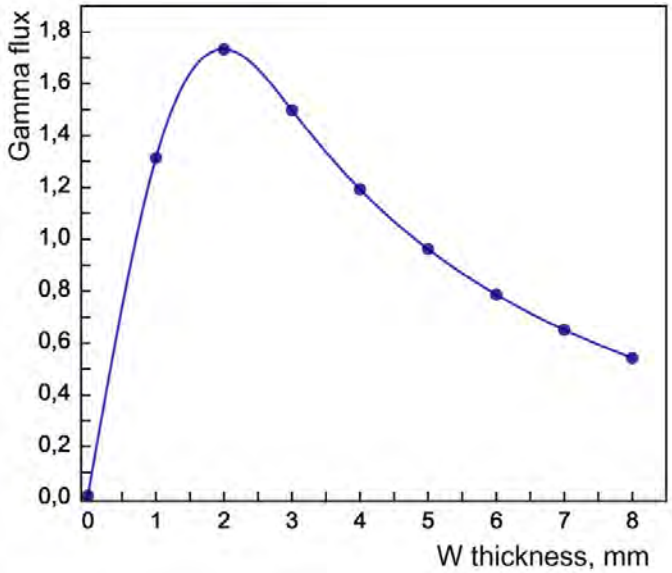

Figure 5. The gamma quanta flux crossing the target boundaries, depending on the converter thickness

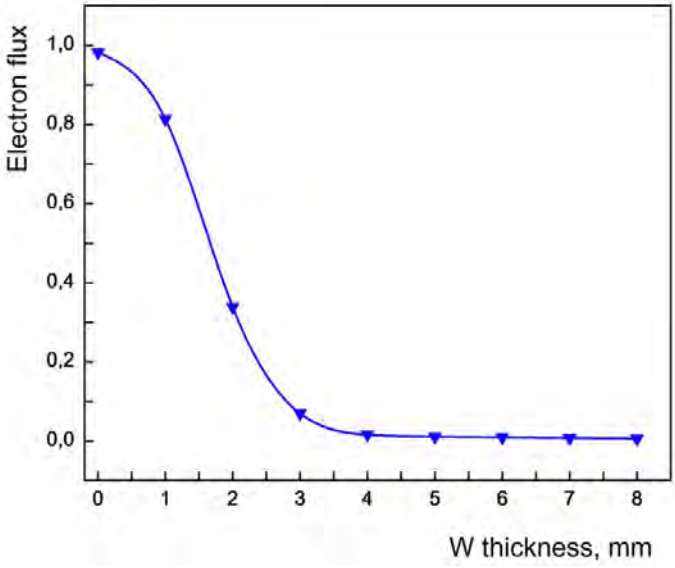

Figure 6. The electrons flux crossing the target boundaries, depending on the converter thickness

Table1. Relative number of electrons crossing the target boundary, depending on the bremsstrahlung converter thickness for primary electrons with energy E_e = 15 MeV

Tungsten thickness, mm	0	1	2	3	4	5	6	7	8
Amount of electrons in front of the target	0.982	0.815	0.339	0.0703	0.0162	0.0112	0.0092	0.0076	0.0064

Comparison of the electrons energy spectra in front of the target was carried out for two values of the tungsten converter thickness. These studies are necessary to choose the optimal converter thickness, at which it is expedient to study the mechanisms of radiation damage in the target. Two values of thickness for the tungsten converter are 2 mm and 3 mm (Figure 7). The calculations of spectra were done in same steps of 1 MeV for the convenience of results comparing.

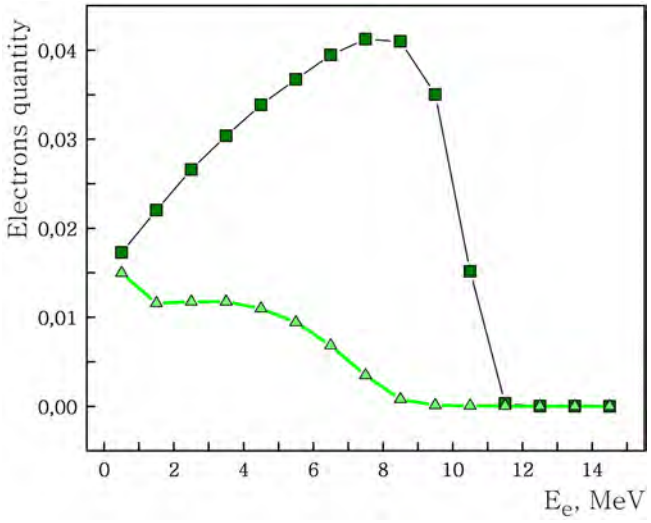

Figure 7. Comparison of the electrons energy spectra in front of the target for two values of the tungsten converter thickness. These values are 2 mm and 3 mm. The energy of primary electrons is E_e = 15 MeV. The electrons spectrum in the case of 2 mm converter is indicated by dark squares. The electrons spectrum in the case of 3 mm converter is indicated by light triangles

It can be seen (Figure 7) that a significant amount of high-energy electrons are still present in front of the target with a converter thickness of 2 mm. However, the energies of electrons in front of the target noticeably decrease with increasing the converter thickness to 3 mm. The relative amount of electrons also decreases. The electrons energy spectra (Figure 7) are normalized to 1 incident electron. A significant decreasing the number of electrons in front of the target, as well as decreasing the electron energy, suggests us that it is desirable to use a 3 mm thick tungsten bremsstrahlung converter irradiated with 15 MeV primary electrons to study the radiation damages processes in organic solutions irradiated by gamma quanta.

The simulation of the ^{16}O nuclei formation in the target was carried out in order to determine the possibility of a preliminary assessment of radiation damage occurring in a 1% aqueous solution of an organic dye upon irradiation by primary electrons. We took into account ^{16}O nuclei with energies above 5 eV. This simulation was carried out for various values of the tungsten converter thickness. The dependence of the number of ^{16}O nuclei with energies above 5 eV on the converter thickness is shown in Figure 8.

It can be noted that the rupture of water molecules' chemical bonds is practically not observed in the absence of bremsstrahlung gamma quanta, i.e., with a converter thickness of 0 mm. The relative number of such events is approximately 3.7×10^{-5}. A significant increase in radiation-stimulated chemical processes of the target substance destruction [8] is observed with increasing the number of gamma quanta (Figure 4 and Figure 5) crossing the target boundaries. The number of water molecules chemical bonds rupture is 5.4×10^{-4} per one primary electron with energy of 15 MeV at 1 mm tungsten thickness. The relative number of ruptures of water molecules chemical bonds is now about 10 times greater than in case of absent converter. Approximately 6×10^{-4} ruptures of water molecules chemical bonds per 1 incident electron occur when tungsten is 2 mm thick.

The attenuation of the gamma-ray beam occurs due a further increase in the converter thickness [9]. This fact explains decreasing (Figure 8) of the number of water molecules chemical bonds ruptures while increasing the converter thickness.

Therefore, further experimental studies of the interaction of radiation with organic dye solutions are necessary to reveal the mechanisms leading to radiation damage of dye solutions.

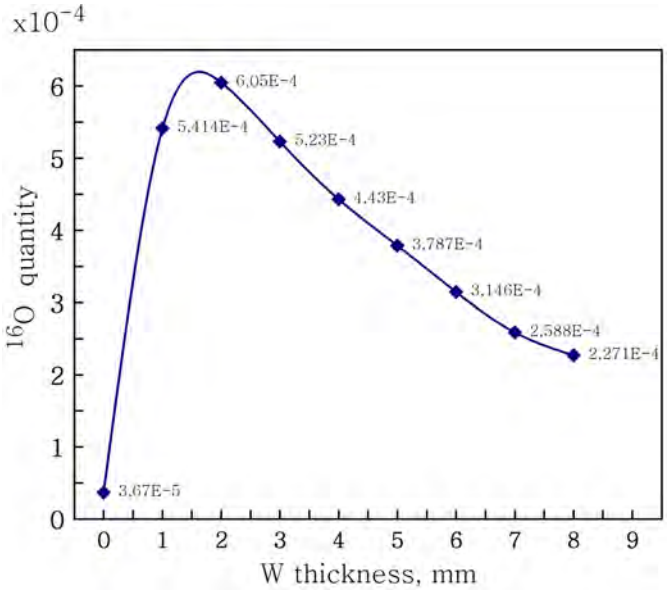

Figure 8. Formation of ^{16}O nuclei with energies above 5 eV depending on the thickness of the converter

CONCLUSIONS

The simulation of the passage of electrons flux with energy of 15 MeV through tungsten converters of various thickness values, from 0 mm to 8 mm, was carried out with a step of 1 mm. The values of the bremsstrahlung gamma flux immediately in front of a small target containing 1% aqueous solution of an organic dye were obtained as a result of simulation. It is shown that it is necessary to locate the target at the minimum possible distance from the converter due to the rather small dimensions of the target. The values of the converter thickness for carrying out experimental studies at the linear electron accelerator "LINAC-300" of the National Scientific Center "Kharkov Institute of Physics and Technology" were obtained as a result of a computational experiment. It is shown that the flux of gamma quanta in front of the target is maximum at 2 mm of tungsten, but there are also high-energy electrons in front of the target. The electron flux in front of the target is much less for a 3 mm thick tungsten converter. The gamma quanta flux decreased slightly in this case.

The method of radiation damage preliminary estimation in the target for different converter thickness values, and, therefore, different values of the gamma quanta flux crossing the target boundaries, was investigated by the computer simulation method using Geant4 toolkit.

The possibility to optimize the experimental stand for studying the main mechanisms leading to the ruptures of organic dye molecules appeared on the basis of the obtained results. It is planned to receive specific proposals for optimizing the experimental stand in further research.

Acknowledgements

The authors thank the Department of Astronomy & Astrophysics at the University of Toronto for the provided hardware calculating facilities, as well as Meest corporation and the “Computers for Ukraine” project for crucial logistical assistance in the transfer of these facilities to Ukraine.

ORCID IDs

Tetiana V. Malykhina, https://orcid.org/0000-0003-0035-2367; **Valentin I. Kasilov**, https://orcid.org/0000-0002-1355-311X
Vladimir E. Kovtun, https://orcid.org/0000-0001-8966-7685; **Sergey P. Gokov**, https://orcid.org/0000-0002-3656-3804

REFERENCES

[1] A.Yu. Buki, S.P. Gokov, Yu.G. Kazarinov et al. PAST, **5**(93), 98 (2014),
[2] M. Tanabashi et al. (Particle Data Group), Phys. Rev. D, **98**, 030001 (2018), https://doi.org/10.1103/PhysRevD.98.03000
[3] Geant4 Collaboration, Book For Application Developers, Release 10.6, http://cern.ch/geant4-userdoc/UsersGuides/ForApplicationDeveloper/BackupVersions/V10.6c/fo/BookForApplicationDevelopers.pdf
[4] Geant4 Collaboration, Physics Reference Manual, http://cern.ch/geant4-userdoc/UsersGuides/PhysicsReferenceManual/BackupVersions/V10.6c/fo/PhysicsReferenceManual.pdf
[5] CLHEP – A Class Library for High Energy Physics, https://proj-clhep.web.cern.ch/proj-clhep/
[6] Geant4 Guide For Physics Lists, Release 10.6, https://geant4-userdoc.web.cern.ch/UsersGuides/PhysicsListGuide/BackupVersions/V10.6c/fo/PhysicsListGuide.pdf
[7] Open MPI Documentation, 2020, https://www.open-mpi.org/doc/
[8] R. Huszank, Gy. Nagy, I. Rajta, and A.M. Czegledi, Radiation Physics and Chemistry, **180**, 109322 (2020), https://doi.org/10.1016/j.radphyschem.2020.109322
[9] C. Grupen, and I. Buvat, *Handbook of Particle Detection and Imaging*, (Springer, 2012), pp. 1226.

GEANT4-МОДЕЛЮВАННЯ ОПТИМАЛЬНОЇ ТОВЩИНИ КОНВЕРТЕРУ ГАЛЬМІВНОГО ВИПРОМІНЮВАННЯ ДЛЯ ДОСЛІДЖЕННЯ ПРОЦЕСІВ РАДІАЦІНИХ ПОШКОДЖЕНЬ ПРИ ВЗАЄМОДІЇ ВИПРОМІНЮВАННЯ З РОЗЧИНАМИ ОРГАНІЧНИХ БАРВНИКІВ

Т.В. Малихіна[a,b], В.Є. Ковтун[a], В.Й. Касілов[b], С.П. Гоков[b]

[a]*Харківський національний університет імені В.Н. Каразіна, майдан Свободи, 4, 61022, Харків, Україна*

[b]*Національний науковий центр «Харківський фізико-технічний інститут», вул. Академічна, 1, 61108, Харків, Україна*

Дослідження процесів, що відбуваються у речовині при проходженні через нього іонізуючого випромінювання, має важливе значення для вирішення різних задач. Прикладом таких задач є прикладні та фундаментальні завдання в галузі радіаційної фізики, хімії, біології, медицини та дозиметрії. Представлена робота присвячена комп'ютерному моделюванню параметрів вольфрамового конвертера для дослідження процесів радіаційних ушкоджень при взаємодії іонізуючого випромінювання з розчинами органічних барвників. Моделювання проведено з метою визначення оптимальної товщини конвертера при заздалегідь визначених умовах експерименту. До умов експерименту відносяться: енергії і тип первинних частинок, інтенсивність випромінювання, розміри мішені, взаємне розташування джерела випромінювання і мішені. Експериментальні дослідження процесів радіаційних ушкоджень, що відбуваються в розчинах органічних барвників, планується проводити з використанням лінійного прискорювача електронів «ЛУЕ-300» Національного наукового центру «Харківський фізико-технічний інститут». В якості первинних частинок обрані електрони з енергією 15 МеВ. У першій серії експериментів планується дослідити взаємодію електронів з речовиною мішені. У другій серії експериментів будуть проводитися дослідження взаємодії гамма-квантів з речовиною мішені. Для отримання потоку гамма-квантів використовується конвертер з вольфраму. Одним із завдань моделювання є визначення товщини конвертера, при якій потік гальмівних гамма-квантів безпосередньо перед мішенню буде максимальним. У той же час потік електронів і позитронів перед мішенню повинен бути мінімально можливим. Ще одним важливим завданням роботи є виявлення можливості визначення методом Geant4-моделювання відносної кількості радіаційних ушкоджень в речовині мішені під дією гальмівних гамма-квантів, а також під дією електронів і позитронів. Обчислювальні експерименти для різних значень товщини конвертера – від 0 мм (немає конвертера) до 8 мм проведені з кроком 1 мм. Виконано детальний аналіз отриманих даних. В результаті аналізу даних проведених обчислювальних експериментів отримані значення товщини вольфрамового конвертера, при якій потік гальмівного випромінювання безпосередньо перед мішенню є максимальним, але в той же час потік електронів і позитронів, що перетинають межі мішені, не робить істотного впливу на мішень. Обчислювальний експеримент проведений методом Монте-Карло. Для проведення розрахунків нами була розроблена комп'ютерна програма мовою C++, яка використовує бібліотеки класів Geant4, і працює у багатопотоковому режимі. Багато потоковий режим необхідний для зменшення часу обчислень при використанні великої кількості первинних електронів. При проведенні розрахунків використовувалася модель G4EmStandardPhysics_option3 модуля PhysicsList. Необхідні для вирішення завдання розрахунки здійснені з використанням навчального обчислювального кластера Науково-навчального інституту «Фізико-технічний факультет» Харківського національного університету імені В.Н. Каразіна.

Ключові слова: гальмівне випромінювання електронів, Geant4-моделювання, конвертер гальмівного випромінювання, взаємодія випромінювання з речовиною.

EAST EUROPEAN JOURNAL OF PHYSICS. 4. 99-106 (2021)
DOI: 10.26565/2312-4334-2021-4-11 ISSN 2312-4334

THERMODYNAMIC AND KINETIC PARAMETERS OF THE PROCESSES OF DEUTERIUM INTERACTION WITH TUNGSTEN PROTECTIVE COATINGS†

Sergiy Karpov, Valeryi Ruzhytskyi, Galyna Tolstolutskaya*, Ruslan Vasilenko, Oleksandr Kuprin, Sergiy Leonov

National Science Center "Kharkov Institute of Physics and Technology", Kharkov, Ukraine
**Corresponding Author: g.d.t@kipt.kharkov.ua*
Received September 30, 2021; revised October 22, 2021; accepted November 18, 2021

The effect of radiation damage on the retention of deuterium in tungsten (W) was examined. A vacuum-arc plasma source with magnetic stabilization of the cathode spot was used for tungsten coatings preparation. W samples were treated with D ions at temperatures 300-600 K with a fluence of (1 – 10) 10^{20} D_2^+/m^2 and ion energies of 12 keV/D_2^+. The influence of radiation damage on microstructure and accumulation of deuterium implanted in W samples at room temperature and after annealing have been studied. Thermal desorption (TD) spectroscopy was used to determine the D retained throughout the bulk of the sample. The structure of TD spectra represents the multi-stage process of deuterium release suggesting the trapping of gas atoms by a number of defect types. Computational evaluation of deuterium desorption within the framework of the diffusion-trapping model allows to associate characteristics of experimental TD spectra with specific trapping sites in the material. Experimental TD spectrum was fitted by assigning four binding energies of 0.55 eV, 0.74 eV, 1.09 eV and 1.60 eV for the peaks with maxima at 475, 590, 810 and 1140 K, respectively. The low temperature peak in the TD spectra is associated with desorption of deuterium bounded to the low energy natural traps, whereas the other peaks are related to the desorption of deuterium bounded to the high energy ion induced traps: monovacancies and vacancy clusters.
Keywords: tungsten, irradiation, damage, microstructure, thermal desorption, deuterium trapping, activation energies, de-trapping processes
PACS: 52.40HF, 28.52FA, 68.49SF, 79.20RF

An important problem in the development of fusion plasma devices that utilize tritium is the loss of tritium from the fuel cycle. The tritium leaking can cause safety issues because of the regulatory limits for the amount of tritium in the vessel walls. In addition, operational problems due to possible uncontrolled hydrogen isotopes recycling fluxes can affect global plasma stability. It is therefore advisable to investigate the features of the thermal release of hydrogen isotopes from plasma-facing materials in order to evaluate their applicability as candidate materials with respect to fuel retention [1].

Currently, tungsten is selected as the main armor material for the plasma-facing components of the next step fusion reactor due to a high melting point, low tritium retention, low sputtering ration as well as good behavior under neutron irradiation. A lot of works has been performed to qualify existing materials related to issues for fusion reactor ITER, in particular for W, as plasma facing materials for first wall and diverter [2]. However, it is now believed that fabrication the first wall of a fusion reactor completely from tungsten is not economically feasible due to the high cost, as well as the difficulties with machining due to the hardness and brittleness of tungsten. Recently, tungsten coatings on a stainless steel substrate have come to be considered as an alternative option from the point of view of economics and protection of structural material against plasma exposure [3]. In order to evaluate the applicability of W-coatings as plasma-facing materials, it is necessary to carefully examine the behavior of these materials under intense neutron irradiation from the fusion reaction and plasma exposure. Understanding the mechanisms of microstructural changes during operation is also of high importance.

Extensive studies have been made on the interaction of hydrogen isotopes with various tungsten materials [1–10]. The surface topography of W bulk prepared by powder sintering (20 μm thickness), and W coatings deposited by cathodic arc evaporation and by argon ion sputtering was studied under the influence of low-energy hydrogen (deuterium) and helium plasma at room temperature [4, 5]. The exposure predominantly resulted in the formation of blisters and sputtering. After helium and deuterium plasma irradiation, numerous blisters were observed on the surface of W foils samples and coatings deposited by argon ion sputtering. The surface of W coatings deposited by cathodic arc evaporation was undergone only sputtering process under the same irradiation conditions [4]. Processes of sputtering, surface modification and deuterium retention in W coatings deposited on stainless steel by cathodic arc evaporation were studied under the influence of low-energy (500 eV) deuterium plasma with a fluence of $4 \cdot 10^{24}$ D^+/m^2 at room temperature. The values of the experimentally measured sputtering yield of the tungsten coatings exposed to the D plasma are two times higher compared to bulk W but almost an order of magnitude smaller compared to ferritic martensitic steels. The total D retentions of W coatings were on the order of $5 \cdot 10^{19}$ D/m^2 [5].

Since the solubility of hydrogen isotopes in tungsten is very low, the trapping at defects mainly determines the retention. These defects are either natural defects which are present after fabrication or they may be created by treatment

† ***Cite as:*** S. Karpov, V. Ruzhytskyi, G. Tolstolutskaya, R. Vasilenko, O. Kuprin, and S. Leonov, East. Eur. J. Phys. **4**, 99 (2021), https://doi.org/10.26565/2312-4334-2021-4-11

after fabrication such as, for example, radiation-induced defects. Therefore, parameters of trapping are essential for predicting hydrogen isotope transport in irradiated tungsten. Many aspects of hydrogen retention in bulk tungsten have been investigated in the past and the available literature is extensive [6-10]. However, there are few data on the behavior of hydrogen isotopes in tungsten coatings.

The objective of this study is to evaluate the role of radiation defects on deuterium retention in tungsten coatings prepared by cathodic arc evaporation (CAE) and irradiated with energetic deuterium ions.

MATERIAL AND METHODS

Tungsten coatings were deposited on tungsten substrates by means of PVD method using unfiltered cathodic arc evaporation in a "Bulat-6" system equipped with a W (99.9%) cathode of 60 mm diameter. Magnetic stabilization of the cathode spot was used in a vacuum-arc plasma source [11]. The main advantage of the cathodic arc evaporation method over conventional magnetron sputtering deposition is a much higher degree of plasma ionization and energy of metallic ions [12]. This can be the explanation of the high quality and adhesion of such deposited coatings.

Tungsten foil was chosen as a substrate material to eliminate the possible influence of various effects from other substrate materials, for example, differences in thermal expansion coefficients, mutual diffusion of elements, eutectic formation, etc., during high-temperature annealing in TD experiments. This approach in choosing W foils as substrates was used to study the TD of deuterium [13, 14], helium blistering [15], TD of helium [16], as well as in determining the thermal stability [17] of the W coatings deposited by magnetron sputtering.

The tungsten foil substrates (8×5×0.3 mm) were chemically degreased and ultrasonically cleaned in a hot alkaline bath for 10 min and dried in warm air. After cleaning they were mounted on a substrate holder without rotation. The substrate-cathode distance was about 250 mm. The chamber was evacuated to a pressure of 2×10^{-3} Pa before the coating deposition. The substrates were ion etched with tungsten ion bombardment by applying a DC bias of -1300 V during 3 min. The arc current was 120 A. Noble gas Ar (99.9 %) was introduced in to vacuum chamber up to pressure of 2 Pa for stabilization of the arc discharge. The deposition of tungsten coating was performed at a substrate bias voltage of -30 V and a substrate temperature of ~ 400 °C. The deposition time was 60 min. The coating thickness was ~ 8 μm. The concentration of impurities ions (oxygen, nitrogen and carbon) did not exceed 3 at.% in accordance with the EDX and WDS data.

Hydrogen isotopes trapping by irradiation damages is often simulated using higher energy ion irradiation technique to introduce the defects, such as dislocation loops, vacancies and voids, etc [9]. In the current study, W foils and coatings have been irradiated with deuterium ions at temperatures 300 - 600 K with a fluence of $(1 - 10)\cdot10^{20}$ D_2^+/m^2 and ion energies of 12 keV/D_2^+. The SRIM code [18] was used to evaluate the ion projected ranges (R_p) and range straggling (ΔR_p), the concentration of gas atoms, and the dpa (displacement per atom) (Fig. 1). The calculations were performed with a target density of 19.35 g cm^{-3} and a displacement threshold energy of 90 eV [9].

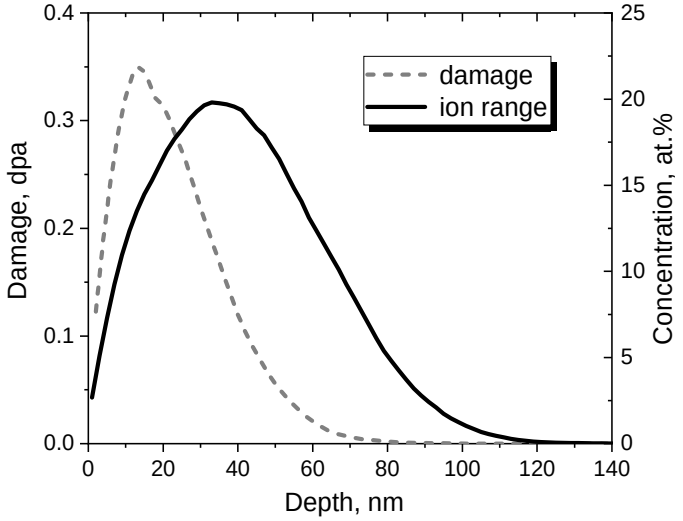

Figure1. Depth distribution profiles of damage and concentration for 12 keV/D_2^+ in tungsten calculated for a fluence of $1\cdot10^{21}$ m^{-2}

The specimen temperature was measured by the thermocouple and was maintained at about (27±2.5) °C during irradiation. The experimental ion flux and fluence were calculated from the measured ion currents and beam spot areas. The deuterium release from irradiated specimens was investigated by the thermal desorption technique in the temperature range from 300 to 1400 K at a rate of 6 K s^{-1}. This temperature range is expected to encompass the characteristic detrapping temperatures of hydrogen isotopes with radiation defects in tungsten materials [6]. The gas release was registered by a monopole mass-spectrometer. Irradiations and measurements of TD spectra were performed in one chamber, to exclude contact of the specimens with air that prevented the formation of artifact trap sites associated with the surface. The residual gas pressure in the experimental chamber was measured to be $\sim5\cdot10^{-5}$ Pa.

The microstructure of tungsten substrate and coatings was investigated using transmission electron microscopy at room temperature, employing standard bright–field techniques on JEM-2100 electron microscope. Investigations of surface microstructure were performed using scanning electron microscope JEOL JSM-7001F. Chemical composition of the coatings was determined by energy dispersive X-ray spectroscopy – EDS.

RESULTS AND DISCUSSION

Fig. 2 shows SEM images of surface morphology, cross-section images and TEM microstructure of tungsten foil substrates and W coatings deposited by CAE in the initial state.

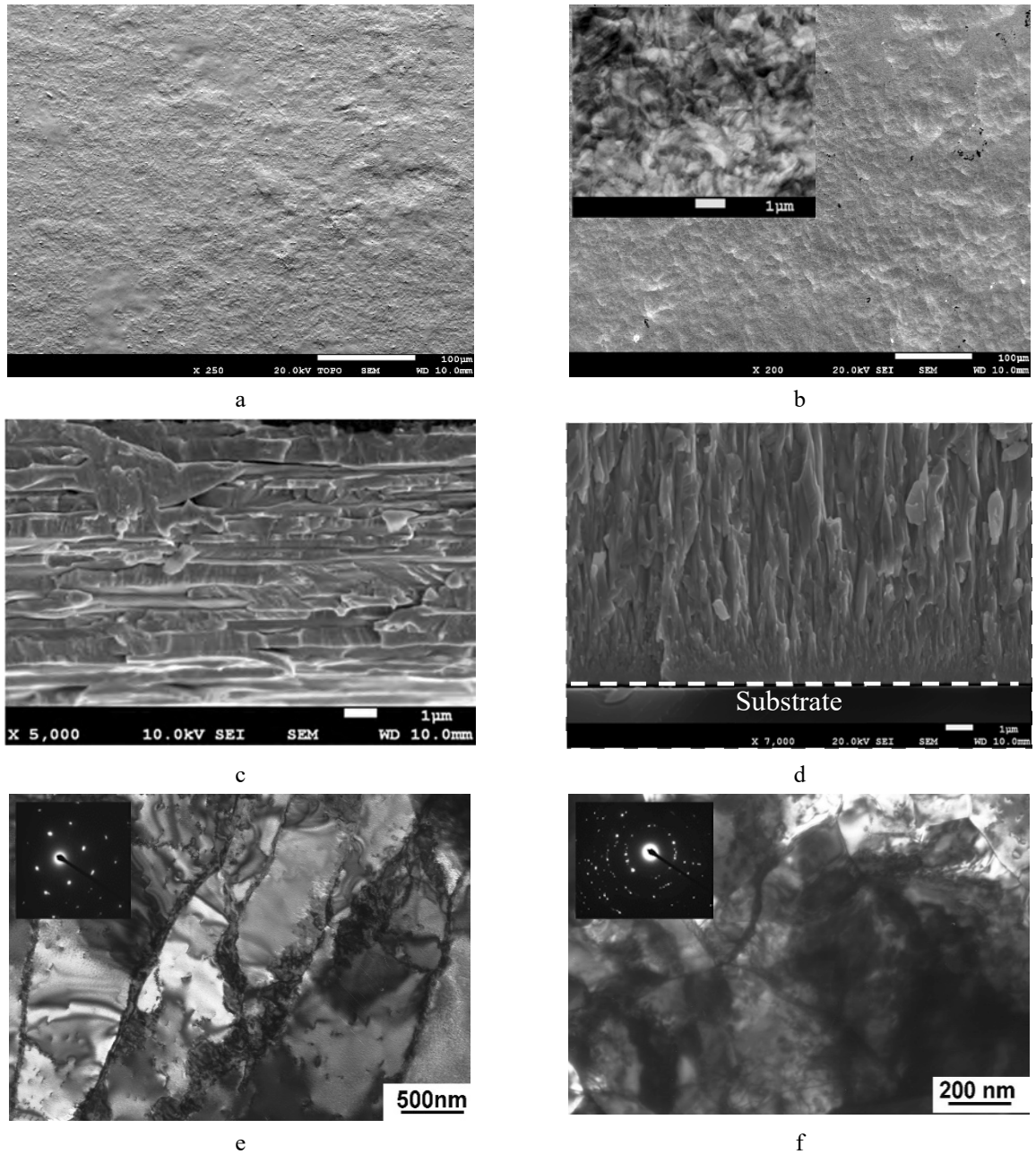

Figure 2. Structure of tungsten foil (a,c,e) and coating (b,d,f): SEM surface morphology (a,b) and cross-section (c,d); TEM plan view (e,f). Higher magnification detail of the 'nanoridges' coating morphology (insert fig. 2, b). The interface between the coating and substrate is indicated by the dashed horizontal line (Fig. 2, d).

Surface morphology of tungsten foil substrates has 'smoothening' relief (Fig. 2a). The microstructure of the tungsten foil substrates was characterized by layers with high elongation grains arranged parallel to the surface, see Fig. 2c. TEM investigation demonstrated high elongation grains with dimensions in the 0.5-1.5 µm range. Dislocations were distributed inhomogeneously even within a single grain (Fig. 2e). The dislocation density was found to be about $1 \cdot 10^{14}\,m^{-2}$. The dislocation density was measured by counting the number of intersections with dislocation lines made by random strips drawn on micrographs.

The as-deposited W coatings have a rough surface (Fig. 2b). Surface morphology of initial W coatings exhibit surfaces of densely packed "nanoridges" or overlapping tiles, which is the typical morphology of refractory metal films deposited at the relatively low temperatures (see Fig. 2b, insert). These "nanoridges" were observed on the α-W phase film surfaces irrespective of the film thickness. It is found that many individual grains contain two types of "nanoridge" domains oriented with each other with an angle ranging between 109 and 124º. Each domain has ridges with an average height and period of (1.5±0.5) and (7.5±1.0) nm, respectively [4]. As-deposited W coating show a typical columnar epitaxial growth with grain boundaries preferentially oriented perpendicular to the substrate (Fig. 2d). The structure of W-coating is dense and without pores, as shown on SEM cross-section image (Fig. 2d).

According to the TEM analysis data, a single α-W phase with an average grain size of 180 nm is formed in the tungsten coatings. The density of dislocations was found to be about $2.2 \cdot 10^{14}$ m^{-2}. The structure of coatings may be explained by sufficiently high relative energy of tungsten ions (140 eV) and by the high degree of plasma ionization (90 %) of the tungsten cathodic arc [12, 19].

Figs. 3-4 shows deuterium TD spectra from tungsten substrates and coatings irradiated with deuterium ions at temperature 300 K with a fluence of $(2–10) \cdot 10^{20}$ D_2^+/m^2 and ion energy of 12 keV/D_2^+.

Gas evolution from both types of specimens is characterized by the following common features: (i) initial temperature of desorption is consistent with the terminal temperature of exposure; (ii) the structure of TD spectrum represents the multi-stage process with well-defined desorption peaks at about 600, 850 and 1150 K for all studied irradiation fluences with the exception of high-temperature desorption stage for smallest fluences; (iii) the broad low temperature desorption stage looks like a peak with shoulders, and thus appears to consist of several narrow peaks.

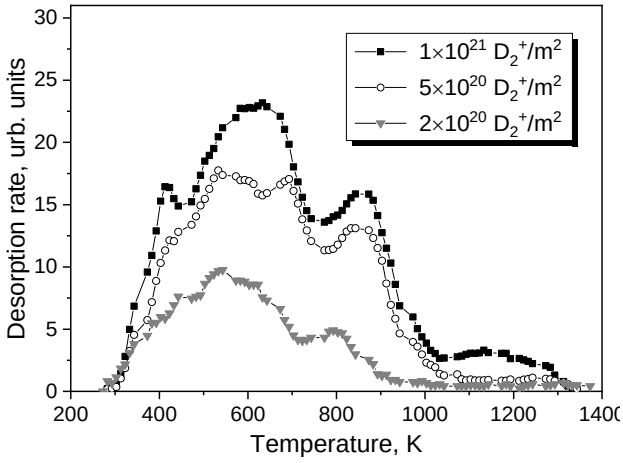

Figure 3. Deuterium TD spectra from tungsten foils after deuterium ions irradiation at temperature 300 K

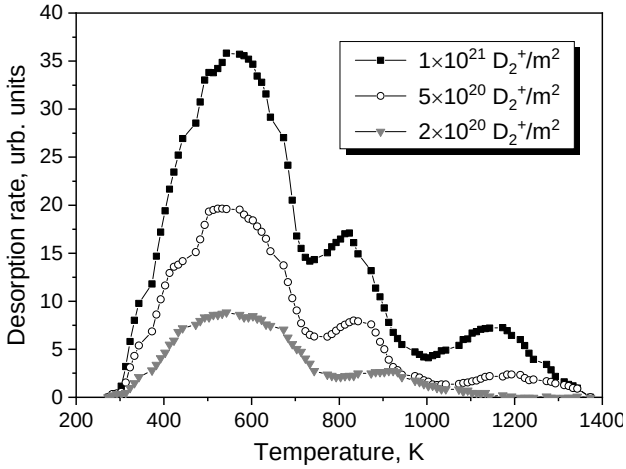

Figure 4. Deuterium TD spectra from tungsten coatings after deuterium ions irradiation at temperature 300 K

Characteristic temperatures of TD spectra depend on hydrogen retention parameters, predominantly on activation energy of de-trapping processes. In the case of the keV implantation, both radiation-induced and natural trap types are present in the material.

Energetic ion irradiation can greatly increase the local point defects concentration by displacing the lattice atoms through collisions. The 6 keV D^+ energy is well above the threshold for displacement damage [20] and capable of creating Frenkel pair defects within the implantation zone. At room temperature, the interstitials are mobile [21] and most of them quickly recombine with vacancies, however a fraction of vacancies survives and becomes the dominant deuterium traps in near surface layer of material. On the other hand, several studies [6,7] of the damage structure produced in W crystals under D ion implantation have revealed that in addition to radiation-induced defects, intrinsic defects strongly influence deuterium retention. Moreover, intrinsic defects like dislocations and grain boundaries are thought to be responsible for accumulation of large amounts of deuterium, especially in polycrystalline W at near room temperatures.

The deuterium concentration is found to be inhomogeneous throughout the bulk, according to previously published data on the evolution of the deuterium depth distribution as a function of fluence [22, 23]. The highest deuterium content is observed in the ion stopping range, while a decreasing tail of deuterium concentration with reaching the plateau is detected at depths of up to several microns. It has been shown, that the near surface high concentration layer is associated with radiation-induced defects, whereas the latter zone is related to natural defects in the material, since certain portion of the D atoms implanted in tungsten at room temperature diffuse deep into the bulk and is captured by dislocations and grain boundaries.

Computational evaluation of deuterium desorption within the framework of the diffusion-trapping model [24] provides the ability to assess activation energies of de-trapping processes and to associate characteristics of experimental TD spectra with specific trapping sites in the material. This was accomplished by numerically solving the equations for diffusion in a field of traps.

$$\frac{\partial C(x,t)}{\partial t} = D(T)\frac{\partial^2 C(x,t)}{\partial x^2} - \sum_k \frac{\partial G_k(x,t)}{\partial t} + \phi(x) \tag{1}$$

$$\frac{\partial G_k(x,t)}{\partial t} = 4\pi R_k D(T)\left\{C(x,t)\left[W_k(x,t) - G_k(x,t)/m_k\right] - G_k(x,t)zN_V \exp\left(-\frac{Q_k}{k_B T}\right)\right\},$$

where C is the concentration of hydrogen in the solution; G_k is the concentration of hydrogen in traps of k-type; R_k is the radius of defect trap; m_k is the number of hydrogen atoms per trap; z is the number of solution sites per host atom; N_v is the atomic density of the host; W_k is trap concentration; φ(x) is the distribution of the hydrogen introduction rate through depth; Q_k is the binding energy of hydrogen atom with the trap; $k_в$ is Boltzmann's constant; and $D(T) = D_o \exp(-E_m/k_в T)$ is the deuterium diffusivity.

Since solute deuterium atoms remain mobile in tungsten at room temperature, the calculations include two steps imitating the experimental procedure: deuterium implantation at room temperature, and then linear heating of the sample to the certain temperature.

Present calculations assumed up to four different trap energies. This assumption is supported by the thermal desorption data (see Fig. 4) that show at least three clearly visible peaks, and by preliminary estimations indicating the complex structure of low temperature desorption stage, which is not a simple single peak, but rather composed of several narrower peaks that suggest the presence of multiple trap energies.

Model calculations also assumed that injected deuterium diffuses through the material, interacting with intrinsic and radiation defects. The defect traps representing radiation-induced displacement defects are distributed along the depth according to the damage profile calculated using SRIM (see Fig. 1) and located in the near-surface region within 100 nm of the surface. Obviously, natural defects are distributed over the whole thickness of the sample, but in present calculations they were assumed to distribute uniformly in the depth range of 0-2 microns. Both these assumptions are supported by the results [25, 26] of experimentally measured depth distribution of keV-energy deuterium in tungsten after implantation at 300 K.

Modeling of thermal desorption data suggest a rate-dependent boundary conditions, that requires the value for the recombination coefficient. The obtained values for the hydrogen recombination coefficient on tungsten vary by more than six orders of magnitude [27-29]. Current calculations utilize recently published data [30] for experimentally measured recombination coefficient for a pristine and clean W surface under well-controlled surface conditions by means of X-ray photoelectron spectroscopy. We used the coefficient $K_r = 3.8\times10^{-26} \exp(-0.15/kT)$ m^4s^{-1} for the pristine surface due to special preparation of specimens' surface was not performed.

Other necessary calculation parameters include $N_V = 6{,}3\cdot10^{28}$ m^{-3}, $D = 2.9\times10^{-7} \exp(-0.39/kT)$ m^2s^{-1} [31]; $R_k = 3{,}16\cdot10^{-10}$ m; z = 6.

The system of equations (1) was solved numerically by previously described and used method [24, 32]. The best agreement between the calculated and experimental deuterium TD spectrum is shown in Fig. 5.

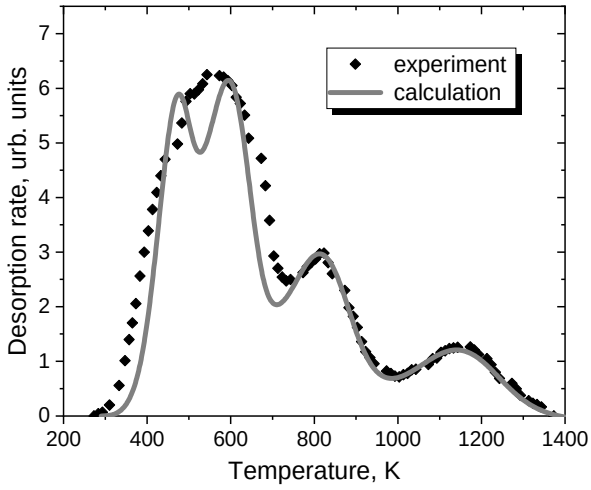

Figure 5. Experimental points and the calculated curve of thermal desorption of deuterium from W coating irradiated at temperature 300 K by 12 keV D_2^+ ions to a fluence of $1\cdot10^{21}$ m^{-2}

Experimental TD spectrum is rather well fitted by assigning four binding energies of 0.55 eV, 0.74 eV, 1.09 eV and 1.60 eV for the peaks with maxima at 475, 590, 810 and 1140 K, respectively. The corresponding trapping energies representing binding energies plus the activation energy for diffusion (0.39 eV [31]) are 0.94 eV, 1.13 eV, 1.48 eV and 1.99 eV. The first peak in the TD spectra appears to be associated with desorption of deuterium bounded to the low energy natural traps, whereas the other peaks are related to desorption of deuterium bounded to the high energy ion induced traps.

The low-temperature desorption peak with binding energy of 0.5-0.6 eV is often attributed to natural defects without separation of trap types into impurities, dislocations, grain boundaries, etc. In present study high dislocation density has

been observed in the microstructure of W coatings (Fig. 2) that suggests the dominative role of dislocation type defects on the formation of 475 K low-temperature peak. In addition, the derived binding energy value of 0.55 eV for this peak correlates well with results of ab initio atomistic calculations [33] demonstrating that hydrogen atoms in tungsten are bound to the screw dislocation core with the binding energy of ~0.6 eV.

Hydrogen isotope retention in various W grades has been studied quite extensively under different experimental conditions. Under low-energy irradiation, vacancies are considered to be the predominant radiation-induced defects. The value of hydrogen de-trapping energy from a single vacancy in W varies among different researchers in the range of 1.3-1.6 eV [34-36]. Therefore, it appears reasonable to suppose that the desorption peak with a de-trapping energy of 1.48 eV in our spectrum can be interpreted as the deuterium release from monovacancies.

Recent ab-initio calculations have demonstrated that multiple hydrogen atoms can be trapped around a single defect, leading to a distribution of binding energies [36-38]. Furthermore, trapping of multiple hydrogen atoms in one monovacancy is quite possible and the binding energy of subsequent H atoms decreases with increasing occupancy. Following density functional theory calculations [36-37, 39], hydrogen capturing with de-trapping energy in the range of 1.1-1.2 eV can be attributed to hydrogen multiplicity binding in monovacancies, where it is energetically favorable for up to six hydrogen atoms to participate in the occupancy. Based on these findings, desorption stage with a maximum at 590 K and characterized in our simulations by de-trapping energy of 1.13 eV is associated with deuterium release from multiply occupied monovacancies.

The ion-irradiated tungsten coatings also showed deuterium desorption in the high-temperature region, i.e. 1000-1300 K. The high temperature peak is usually associated with deuterium trapped in vacancy clusters [23, 40-42]. The de-trapping energy of 1.99 eV attributed to this peak in our calculations correlates with previously published values of hydrogen de-trapping energy from vacancy cluster – in the range of 1.7–2.2 eV [23, 34-35, 43-44]. It is worth noting, that this desorption stage is absent at lowest implantation fluence (see Fig. 4) due apparently to impeded vacancy clustering caused by the deficiency of monovacancies.

Fig. 6 shows deuterium TD spectra for tungsten coating after deuterium ions irradiation to a fluence of $1 \cdot 10^{21}$ D_2^+/m^2 at different temperatures T_{room} – 600 K. The D retention is strongly reduced at high implantation temperatures of 500-600 K compared to that at 300 K. These observations agree with [45] where it was shown the deuterium retention of Plansee tungsten decreased at irradiation with energy upon 200 eV/D^+ and increasing irradiation temperature in the 300-500 K range. The highest retention level was ~$1.7 \cdot 10^{20}$ D^+/m^2 at 300 K, followed by a linear decreasing trend, reaching ~$5 \cdot 10^{19}$ D^+/m^2 at 500 K [45].

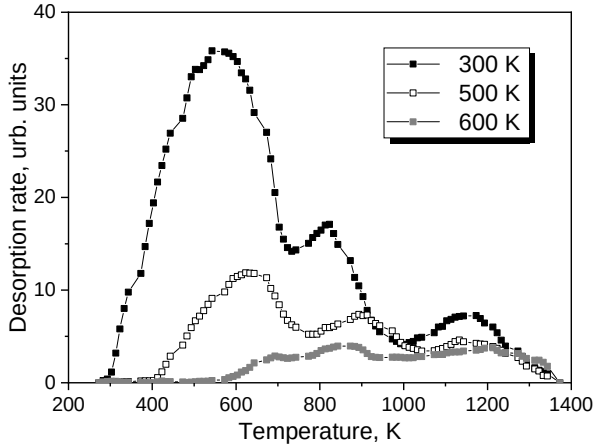

Figure 6. Deuterium TD spectra from tungsten coatings after deuterium ions irradiation to a fluence of $1 \cdot 10^{21}$ D_2^+/m^2 at different temperatures 300 – 600 K

The desorption stage associated with natural defects is characterized by a noticeable gas release already at ~400 K and a maximum at about 475 K. Therefore, the amount of trapped deuterium in low-energy intrinsic traps decreases rapidly at implantation temperature of 500 K, whereas the population in the stronger radiation-induced traps varies slightly at this temperature. High-energy traps population begin to decrease considerably after 600 K as the sample temperature is high enough for de-trapping of deuterium from those traps.

CONCLUSIONS

In the present study, deuterium interaction with tungsten protective coatings deposited by cathodic arc evaporation has been investigated by means of ion irradiation combined with thermal desorption spectroscopy. Scanning and transmission electron microscopy were used for specimen's microstructure characterization. W samples were treated with D ions at temperatures 300 - 600 K with a fluence of $(1 – 10) \cdot 10^{20}$ D_2^+/m^2 and ion energies of 12 keV/D_2^+. Characteristics of experimental TD spectra were associated with specific trapping sites in the material on the base of computational evaluation of deuterium desorption within the framework of the diffusion-trapping model. The main results are summarized as follows.

Deuterium gas release from tungsten coatings and tungsten foils demonstrates similar trend.

The trapping of ion-implanted deuterium in tungsten is attributed to the interaction of gas atoms with natural and radiation-induced defects.

The trapping energies of deuterium with traps are determined within the framework of the diffusion-trapping model. The derived trapping energy values of 0.94 eV, 1.13 eV, 1.48 eV and 1.99 eV are associated with deuterium interaction with intrinsic dislocations, radiation-induced monovacancies at multiple and single deuterium occupation, and vacancy clusters, respectively.

It was found that an increasing of the implantation temperature leads to a significant decrease of deuterium retention in tungsten coatings.

Acknowledgements

The work was financially supported by the National Academy of Science of Ukraine (program "Support of the development of main lines of scientific investigations" (KPKVK 6541230)).

ORCID IDs

Sergiy Karpov, https://orcid.org/0000-0002-6607-8455; **Valeriy Ruzhytskyi,** https://orcid.org/0000-0002-7856-1188
Galyna Tolstolutska, https://orcid.org/0000-0003-3091-4033; **Ruslan Vasilenko**, https://orcid.org/0000-0002-4029-9727
Oleksandr Kuprin, https://orcid.org/0000-0003-4293-4197; **Sergiy Leonov**, https://orcid.org/0000-0002-0338-9168

REFERENCES

[1] M.A. Abdou, E.L. Vold, C.Y. Gung, M.Z. Youssef, and K. Shin, Fusion Technology, **9**, 250 (1986), https://doi.org/10.13182/FST86-A24715
[2] R.A. Pitts, X. Bonnin, F. Escourbiac, H. Frerichs, J.P. Gunn, T. Hirai, A.S. Kukushkin, E. Kaveeva, M.A. Miller, D. Moulton, V. Rozhansky, I. Senichenkov, E. Sytova, O. Schmitz, P.C. Stangeby, G.De Temmerman, I. Veselova, and S. Wiesen, Nucl. Mater. Energy, **20**, 100696 (2019), https://doi.org/10.1016/j.nme.2019.100696
[3] C. Ruset, E. Grigore, H. Maier, R. Neu, H. Greuner, M. Mayer, and G. Matthews, Fusion Eng. Des., **86**(9-11), 1677 (2011), https://doi.org/10.1016/j.fusengdes.2011.04.031
[4] A.V. Nikitin, A.S. Kuprin, G.D. Tolstolutskaya, R.L. Vasilenko, V.D. Ovcharenko, and V.N. Voyevodin, PAST, **2**(114), 29 (2018), https://vant.kipt.kharkov.ua/ARTICLE/VANT_2018_2/article_2018_2_29.pdf
[5] G.D. Tolstolutskaya, A.S. Kuprin, A.V. Nikitin, I.E. Kopanets, V.N. Voyevodin, I.V. Kolodiy, R.L. Vasilenko, A.V. Ilchenko PAST, 2(126), 54 (2020), https://vant.kipt.kharkov.ua/ARTICLE/VANT_2020_2/article_2020_2_54.pdf
[6] V.Kh. Alimov, J. Roth, Phys. Scr. **2007**, 6 (2007), https://doi.org/10.1088/0031-8949/2007/T128/002
[7] O.V. Ogorodnikova, J. Roth, and M. Mayer, J. Appl. Phys. **103**, 034902 (2008), https://doi.org/10.1063/1.2828139
[8] J. Roth, K. Schmid, Phys. Scr. **2011**, 014031 (2011), https://doi.org/10.1088/0031-8949/2011/T145/014031
[9] M. Kobayashi, M. Shimada, Y. Hatano, T. Oda, B. Merrill, Y. Oya, and K. Okuno, Fus. Eng. Des. **88**, 1749 (2013), https://doi.org/10.1016/j.fusengdes.2013.04.009
[10] A. Manhard, K. Schmid, M. Balden, and W. Jacob, J. Nucl. Mater. **415**, S632 (2011), https://doi.org/10.1016/j.jnucmat.2010.10.045
[11] A.S. Kuprin, S.A. Leonov, V.D. Ovcharenko, E.N. Reshetnyak, V.A. Belous, R.L. Vasilenko, G.N. Tolmachova, V.I. Kovalenko, and I.O. Klimenko, PAST, **5**(123), 154 (2019), https://vant.kipt.kharkov.ua/ARTICLE/VANT_2019_5/article-_2019_5_154.pdf
[12] A. Anders, Surf. Coat. Technol. **257**, 308 (2014), https://doi.org/10.1016/j.surfcoat.2014.08.043
[13] P. Wang, W. Jacob, L. Gao, S. Elgeti, and M. Balden, Phys. Scr. **T159**, 014046 (2014), https://doi.org/10.1088/0031-8949/2014/T159/014046
[14] P. Wang, W. Jacob, and S. Elgeti, J. Nucl. Mater. **456**, 192 (2015), http://doi.org/10.1016/j.jnucmat.2014.09.023
[15] J. Yu, W. Han, Z. Chen, and K. Zhu, Nucl. Mater. Energy, **12**, 588 (2017), http://doi.org/10.1016/j.nme.2016.10.001
[16] J. Yan, X. Li, Z. Wang, and K. Zhu, Nucl. Mater. Energy, **22**, 100733, (2020), https://doi.org/10.1016/j.nme.2020.100733
[17] N. Gordillo, C. Gómez de Castro, E. Tejado, J.Y. Pastor, G. Balabanian, M. Panizo-Laiz, R. Gonzalez-Arrabal, J.M. Perlado, and J.del Rio, Surf. Coat. Technol. **325**, 588 (2017), http://dx.doi.org/10.1016/j.surfcoat.2017.06.070
[18] R.E. Stoller, M.B. Toloczko, G.S. Was, A.G. Certain, S. Dwaraknath, and F.A. Garner, Nucl. Instrum. Methods Phys. Res. Sect. B: Beam Interact. Mater. Atoms, **310**, 75 (2013), http://dx.doi.org/10.1016/j.nimb.2013.05.008
[19] I.I. Aksenov, A.A. Andreev, V.A. Belous, V.E. Strel'nitskij, and V.M. Khoroshikh, *Vacuum arc: plasma sources, deposition of coatings, surface modification*, (Naukova Dumka, Kyiv, 2012).
[20] W. Eckstein, *Springer Series in Materials Science, vol. 10*, (Springer, Berlin, 1991), https://doi.org/10.1007/978-3-642-73513-4
[21] P. Jung, *Atomic Defects in Metals, Landolt–Bornstein New Series III/25*, edited by H. Ullmaier, (Springer, Berlin, 1991)
[22] V. Kh. Alimov, J. Roth, and M. Mayer, J. Nucl. Mater. **337-339**, 619 (2005), http://dx.doi.org/10.1016/j.jnucmat.2004.10.082
[23] O.V. Ogorodnikova, J. Roth, and M. Mayer, J. Appl. Phys. **103**, 034902, (2008), https://doi.org/10.1063/1.2828139
[24] S.O. Karpov, V.V. Ruzhits' ky, I.M. Neklyudov, V.I. Bendikov, and G.D. Tolstoluts'ka, Metallofiz. Noveishie Tekhnol. **26**, 1661 (2004).
[25] V. Kh. Alimov, K. Ertl, J. Roth, and K. Schmid, Phys. Scr. **T94**, 34 (2001), https://doi.org/10.1238/Physica.Topical.094a00034
[26] T. Ahlgren, K. Heinola, K. Vörtler, and J. Keinonen, J. Nucl. Mater. **427**, 152 (2012). https://doi.org/10.1016/j.jnucmat.2012.04.031
[27] R.A. Anderl, D.F. Holland, G.R. Longhurst, R.J. Pawelko, C.L. Trybus, and C.H. Sellers, Fusion Tech. **21**, 745 (1992), https://doi.org/10.13182/FST92-A29837
[28] C. Garcia-Rosales, P. Franzen, H. Plank, J. Roth, and E. Gauthier, J. Nucl. Mater. **233-237**, 803 (1996), https://doi.org/10.1016/S0022-3115(96)00185-7
[29] P. Franzen, C. Garcia-Rosales, H. Plank, and V.Kh. Alimov, J. Nucl.Mater. **241-243**, 1082, (1997). https://doi.org/10.1016/S0022-3115(97)80198-5
[30] M. Zhao, S. Yamazaki, T. Wada, A. Koike, F. Sun, N. Ashikawa, Y. Someya, T. Mieno, and Y. Oya, Fusion Eng. Des. **160**, 111853 (2020), https://doi.org/10.1016/j.fusengdes.2020.111853

[31] R. Frauenfelder, J. Vac. Sci. Technol. **6**, 388 (1969), https://doi.org/10.1116/1.1492699
[32] G.D. Tolstolutskaya, V.V. Ruzhytskyi, V.N. Voyevodin, I.E. Kopanets, S.A. Karpov, and A.V. Nikitin, J. Nucl. Mater. **442**(1-3), S710 (2013), https://doi.org/10.1016/j.jnucmat.2013.02.053
[33] D. Terentyev, V. Dubinko, A. Bakaev, Y. Zayachuk, W.V. Renterghem, and P. Grigorev, Nucl. Fusion, **54**, 042004 (2014), https://doi.org/10.1088/0029-5515/54/4/042004
[34] H. Eleveld, and A. van Veen, J. Nucl. Mater. **191–194**(Part A), 433 (1992), https://doi.org/10.1016/s0022-3115(09)80082-2
[35] M. Poon, A.A. Haasz, and J.W. Davis, J. Nucl. Mater. **374**, 390 (2008), https://doi.org/10.1016/j.jnucmat.2007.09.028
[36] K. Heinola, T. Ahlgren, and K. Nordlund, J. Keinonen, Phys. Rev. B, **82**, 094102 (2010), https://doi.org/10.1103/PhysRevB.82.094102
[37] N. Fernandez, Y. Ferro, and D. Kato, Acta Mater. **94**, 307 (2015), https://doi.org/10.1016/j.actamat.2015.04.052
[38] K. Ohsawa, J. Goto, M. Yamakami, M. Yamaguchi, and M. Yagi, Phys. Rev. B, **82**, 184117 (2010), https://doi.org/10.1103/PhysRevB.82.184117
[39] Y.-W. You, X.-S. Kong, X.-B. Wu, Y.-C. Xu, Q.F. Fang, J.L. Chen, G.-N. Luo, C.S. Liu, B.C. Pan, and Z. Wang, AIP Adv. **3**, 012118 (2013), https://doi.org/10.1063/1.4789547
[40] M. Fukumoto, H. Kashiwagi, Y. Ohtsuka, Y. Ueda, M. Taniguchi, T. Inoue, K. Sakamoto, J. Yagyu, T. Arai, I. Takagi, and T. Kawamura, J. Nucl. Mater. **390-391**, 572 (2009), https://doi.org/10.1016/j.jnucmat.2009.01.107
[41] I.I. Arkhipov, S.L. Kanashenko, V.M. Sharapov, R.Kh. Zalavutdinov, and A.E. Gorodetsky, J. Nucl. Mater. **363-365**, 1168 (2007), https://doi.org/10.1016/j.jnucmat.2007.01.150
[42] Yu. Gasparyan, M. Rasinski, M. Mayer, A. Pisarev, and J. Roth, J. Nucl. Mater. **417**, 540 (2011). https://doi.org/10.1016/j.jnucmat.2010.12.119
[43] A. van Veen, H.A. Filius, J. de Vries, K.R. Nijkerk, G.J. Rozing, and D. Segers, J. Nucl.Mater. **155-157**, 1113 (1988), https://doi.org/10.1016/0022-3115(88)90478-3
[44] Yu.M. Gasparyan, O.V. Ogorodnikova, V.S. Efimov, A. Mednikov, E.D. Marenkov, A.A. Pisarev, S. Markelj, and I. Čadež, J. Nucl. Mater. **463**, 1013 (2015), https://doi.org/10.1016/j.jnucmat.2014.11.022
[45] Z. Tian, J.W. Davis, and A.A. Haasz, J. Nucl. Mater. **399**, 101 (2010), https://doi.org/10.1016/j.jnucmat.2010.01.007

ТЕРМОДИНАМІЧНІ ТА КІНЕТИЧНІ ПАРАМЕТРИ ПРОЦЕСІВ ВЗАЄМОДІЇ ДЕЙТЕРІЮ ІЗ ЗАХИСНИМИ ПОКРИТТЯМИ ВОЛЬФРАМУ

Сергій Карпов, Валерій Ружицький, Галина Толстолуцька, Руслан Василенко, Олександр Купрін, Сергій Леонов
Національний науковий центр "Харківський фізико-технічний інститут", Харків, Україна

Досліджено вплив радіаційних пошкоджень на утримування D в вольфрамі (W). Для приготування вольфрамових покриттів використовувалося вакуумно-дугове плазмове джерело з магнітною стабілізацією катодної плями. Зразки W опромінювали іонами D при температурах 300-600 К до дози (1-10) 10^{20} $D_2^+/м^2$ з енергією іонів 12 кеВ / D_2^+. Досліджено вплив радіаційних пошкоджень на мікроструктуру і накопичення дейтерію, імплантованого в зразки W при кімнатній температурі і після відпалу. Термодесорбційна спектроскопія (ТДС) використовувалася для визначення D, утримуваного в об'ємі зразків. Структура ТД-спектра являє собою багатоступінчастий процес виділення дейтерію, який свідчить про захоплення атомів газу дефектами кількох типів. Розрахункова оцінка десорбції дейтерію в рамках моделі дифузійного захоплення дозволила зв'язати характеристики експериментальних ТД-спектрів з конкретними центрами захоплення в матеріалі. Експериментальний ТД-спектр досить добре апроксимується шляхом присвоєння чотирьох енергій зв'язку 0,55 еВ, 0,74 еВ, 1,09 еВ і 1,60 еВ для піків з максимумами при 475, 590, 810 і 1140 К, відповідно. Низькотемпературний пік в спектрах TD, вірогідно, пов'язаний з десорбцією дейтерію, асоційованого з природними пастками з низькою енергією зв'язку, тоді як інші піки пов'язані з десорбцією дейтерію з пасток, індукованих іонами високої енергії: моновакансій та вакансійних кластерів.

Ключові слова: вольфрам, опромінення, пошкодження, мікроструктура, термодесорбція, уловлювання дейтерію, енергія активації

EAST EUROPEAN JOURNAL OF PHYSICS. 4. 107-113 (2021)
DOI: 10.26565/2312-4334-2021-4-12 ISSN 2312-4334

INTERACTIONS OF NOVEL PHOSPHONIUM DYE WITH LIPID BILAYERS: A FLUORESCENCE STUDY†

Olga Zhytniakivska
Department of Medical Physics and Biomedical Nanotechnologies, V.N. Karazin Kharkiv National University
4 Svobody Sq., Kharkiv, 61022, Ukraine
**E-Mail: olga.zhytniakivska@karazin.ua*
Received October 1, 2021; revised November 11, 2021; accepted November 16, 2021

The phosphonium-based optical probes attract ever growing interest due to their excellent chemical and photophysical stability, high aqueous solubility, long wavelength absorption and emission, large extinction coefficient, high fluorescence quantum yield, low cytotoxicity, etc. The present study was focused on assessing the ability of the novel phosphonium dye TDV to monitor the changes in physicochemical properties of the model lipid membranes. To this end, the fluorescence spectral properties of TDV have been explored in lipid bilayers composed of zwitterionic lipid phosphatidylcholine (PC) and its mixtures with cholesterol (Chol) or/and anionic phospholipid cardiolipin (CL). It was observed that in the buffer solution TDV possesses one well-defined fluorescence peak with the emission maximum at 533 nm. The dye transfer from the aqueous to lipid phase was followed by the enhancement of the fluorescence intensity coupled with a red shift of the emission maximum up to 67 nm, depending on the liposome composition. The quantitative information about the dye partitioning into lipid phase of the model membranes was obtained through approximating the experimental dependencies of the fluorescence intensity increase *vs* lipid concentration by the partition model. Analysis of the partition coefficients showed that TDV has a rather high lipid-associating ability and displays sensitivity to the changes in physicochemical properties of the model lipid membranes. The addition of CL, Chol or both lipids to the PC bilayer gives rise to the increase of the TDV partition coefficients compared to the neat PC membranes. The enhancement of the phosphonium dye partitioning in the CL and Chol-containing lipid bilayers has been attributed to the cardiolopin- and cholesterol-induced changes in the structure and physicochemical characteristics of the polar membrane region.
KEYWORDS: phosphonium probe, lipid membranes, fluorescence, partitioning
PACS: 87.14.C++c, 87.16.Dg

During the last decades the phosphonium-based optical probes attract ever growing interest due to their favorable characteristics, namely, the excellent chemical and photophysical stability, high aqueous solubility, long wavelength absorption and emission, large extinction coefficient, high fluorescence quantum yield, low cytotoxicity, etc [1-14]. The above properties render phosphonium dyes highly suitable for the selective staining of mitochondria [3-5], antioxidants detection [6, 7], probing the structural differences of DNA/RNA grooves [1, 2], exploring the tumor multidrug resistance [8], to name only a few. More specifically, the cyanine-based phosphonium dyes can be used for the kinetic differentiation between homo-and alternating AT-DNA forming dimers within DNA minor grooves [1, 2]. Moreover, the cyanine-based phosphonium dyes demonstrated the strongly selective antiproliferative activity toward HeLa cancer cell lines [1]. The phosphonium-tagged coumarin derivatives can be used for the identification of the peptide fragment [9]. In recent years it was shown that phosphonium-based fluorophores are highly efficient for mitochondria imaging with phosphonium groups serving as specific targeting sites toward mithochondria [3-5]. Specifically, Li and colleagues developed a perylene-based phosphonium fluorophore possessing the dual-emissive luminescence in living cells [3]. The possibility of mitochondria imaging in living cells was described also for a new conjugated phosphonium salt TPP characterized by the high intracellular selectivity toward mitochondria and the aggregation-induced emission [4]. A highly efficient cellular uptake and specific accumulation in mitochondria was observed for cyanine-based phosphonium probes possessing the potential dependent mitochondria-related fluorescent signal without exhibiting the cell toxicity [5]. Moreover, the phosphonium conjugates proved to be very effective in monitoring the oxygen variations within mitochondria [10] and measuring the hydrogen peroxide levels [11]. Furthermore, numerous studies have demonstrated that phosphonium fluorescent dyes can be effectively used for optical detection of disease-related protein aggregates, amyloid fibrils [12,13]. In particular, a phosphonium dye TDV was used as a mediator in the amyloid-scaffolded multichromophoric systems for monitoring the amyloid transformation of the N-terminal fragment of apolipoprotein A-I [12] and insulin [13]. Moreover, previous studies suggested that phosphonium dyes may prove of value in elucidating the mechanism of DNA interactions with pathogenic protein aggregates [14].

As a next logical step in evaluating the biomedical potential of phosphonium-based fluorescent probes, the present study was directed at assessing an ability of the novel phosphonium dye TDV to monitor the properties of lipid bilayers. More specifically, the aim of the present study was two fold: i) to obtain the quantitative information about the dye partitioning into lipid phase of the model membranes and ii) to assess the TDV sensitivity to the changes in the physicochemical properties of the lipid bilayer.

† ***Cite as***: O. Zhytniakivska, East. Eur. J. Phys. **4**, 107 (2021), https://doi.org/10.26565/2312-4334-2021-4-12

EXPERIMENTAL SECTION

Materials

Egg yolk phosphatidylcholine, beef heart cardiolipin and cholesterol were purchased from Sigma (St. Louis. MO, USA). The phosphonium dye TDV (Fig.1) was provided by Professor Todor Deligeorgiev, University of Sofia, Bulgaria. All other materials were commercial products of analytical grade and were used without further purification.

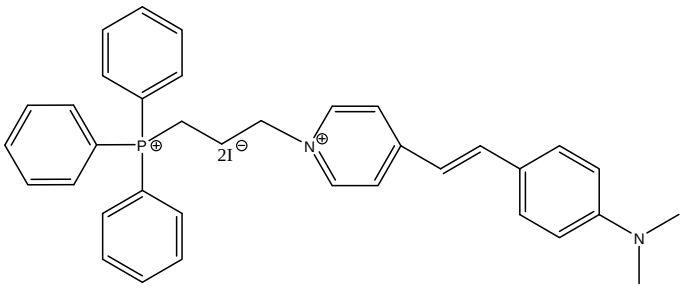

Figure 1. The structural formula of TDV

Preparation of lipid vesicles

Unilamellar lipid vesicles composed of zwitterionic lipid phospatidylcholine (PC) or PC mixtures with anionic lipid cardiolipin (CL) and sterol cholesterol (Chol) were prepared by the extrusion method [15]. The thin lipid films were obtained by evaporation of lipids' ethanol solutions. The dry lipid residues were subsequently hydrated with 5 mM sodium phosphate buffer, pH 7.4 at room temperature to yield lipid concentration of 1 mM. Thereafter, lipid suspension was extruded through a 100 nm pore size polycarbonate filter (Millipore, Bedford, USA). In this way, 6 types of lipid vesicles containing PC and 5, 10 or 20 mol% CL, 30 mol% of Chol or the combination of 10 mol% CL and 30 mol% of Chol with the content of phosphate being identical for all liposome preparations. Hereafter, the liposomes containing 5, 10 or 20 mol% CL are referred to as CL5, CL10 or CL20, respectively, while the liposomes bearing 30 mol% Chol are denoted as Chol30, respectively. Accordingly, the liposomes with cardiolipin content 10 mol% and cholesterol content 30 mol% were marked as CL10/Chol30.

Spectroscopic measurements

The stock solution of TDV was prepared by dissolving the dye in 10 mM Tris buffer, pH 7.4. The concentration of TDV was determined spectrophotometrically, using the extinction coefficient $\varepsilon_{480} = 2.1\times10^5 M^{-1}cm^{-1}$ The dye-liposome mixtures were prepared by adding the proper amounts of the probe stock solutions in buffer to the liposome suspension of different composition varying the lipid concentration from 0 to 4.76 μM. The dye-liposome mixtures were incubated for an hour. The steady-state fluorescence spectra were recorded with FL-6500 spectrofluorimeter (Perkin-Elmer Ltd., Beaconsfield, UK) at 20°C using 10 mm path-length quartz cuvettes. The excitation wavelength was 480 nm. The excitation and emission slit widths were set at 10 nm.

Partitioning model

The TDV binding to the model lipid membranes has been analyzed in terms of the partition model [16]. The total concentration of the dye distributing between aqueous and lipid phases (Z_{tot}) can be represented as:

$$Z_{tot} = Z_F + Z_L , \tag{1}$$

where subscripts *F* and *L* denote free and lipid-bound dye, respectively. The coefficient of dye partitioning between the two phases (K_P) is defined as [16]:

$$K_P = \frac{Z_L V_W}{Z_F V_L}, \tag{2}$$

where V_W , V_L are the volumes of the aqueous and lipid phases, respectively. Given that under the employed experimental conditions the volume of lipid phase is much less than the total volume of the system V_t , we assume that $V_W \approx V_t = 1$ sm^3. Therefore

$$Z_F = \frac{Z_{tot} V_W}{V_W + K_P V_L} = \frac{Z_{tot}}{1 + K_P V_L}. \tag{3}$$

The dye fluorescence intensity measured at a certain lipid concentration can be calculated as:

$$I = a_f Z_F + a_L Z_L = Z_F \left(a_f + a_L \frac{K_P V_L}{V_W} \right) = Z_F \left(a_f + a_L K_P V_L \right), \tag{4}$$

where a_f, a_L represent molar fluorescence of the dye free in solution and in a lipid environment, respectively. From the Eqs. (3) and (4) one obtains:

$$I = \frac{Z_{tot}(a_f + a_L K_P V_L)}{1 + K_P V_L}. \quad (5)$$

The volume of lipid phase can be determined from:

$$V_L = N_A C_L \sum v_i f_i, \quad (6)$$

where C_L is the molar lipid concentration, f_i is mole fraction of the i-th bilayer constituent, v_i is its molecular volume taken as 1.58 nm^3, 3 nm^3 and 0.74 nm^3 for PC, CL and Chol respectively.

The relationship between K_p and fluorescence intensity increase (ΔI) upon the dye transfer from water to lipid phase can be written as [16]:

$$\Delta I = I_L - I_W = \frac{K_p V_L (I_{\max} - I_W)}{1 + K_p V_L}, \quad (7)$$

where I_L is the fluorescence intensity observed in the liposome suspension at a certain lipid concentration C_L, I_W is the dye fluorescence intensity in a buffer, $I_{\max}$ is the limit fluorescence in a lipid environment.

Lipophilicity calculation

The resources of the virtual computational laboratories (http://biosig.unimelb.edu.au/pkcsm/prediction#, http://www.swissadme.ch/ and https://mcule.com/apps/property-calculator/) were used for the calculation of the lipophilicity of the examined dye.

RESULTS AND DISCUSSION

To examine how the TDV lipid associating ability depends on the membrane physical properties, at the first step of our study the emission spectra of this phosphonium dye were recorded in the buffer solution and liposomal suspensions of different composition. TDV was found to be weakly-emissive in the buffer with the fluorescence maximum at 533 nm. Typical fluorescence spectra measured at increasing lipid concentration are presented in Fig. 1.

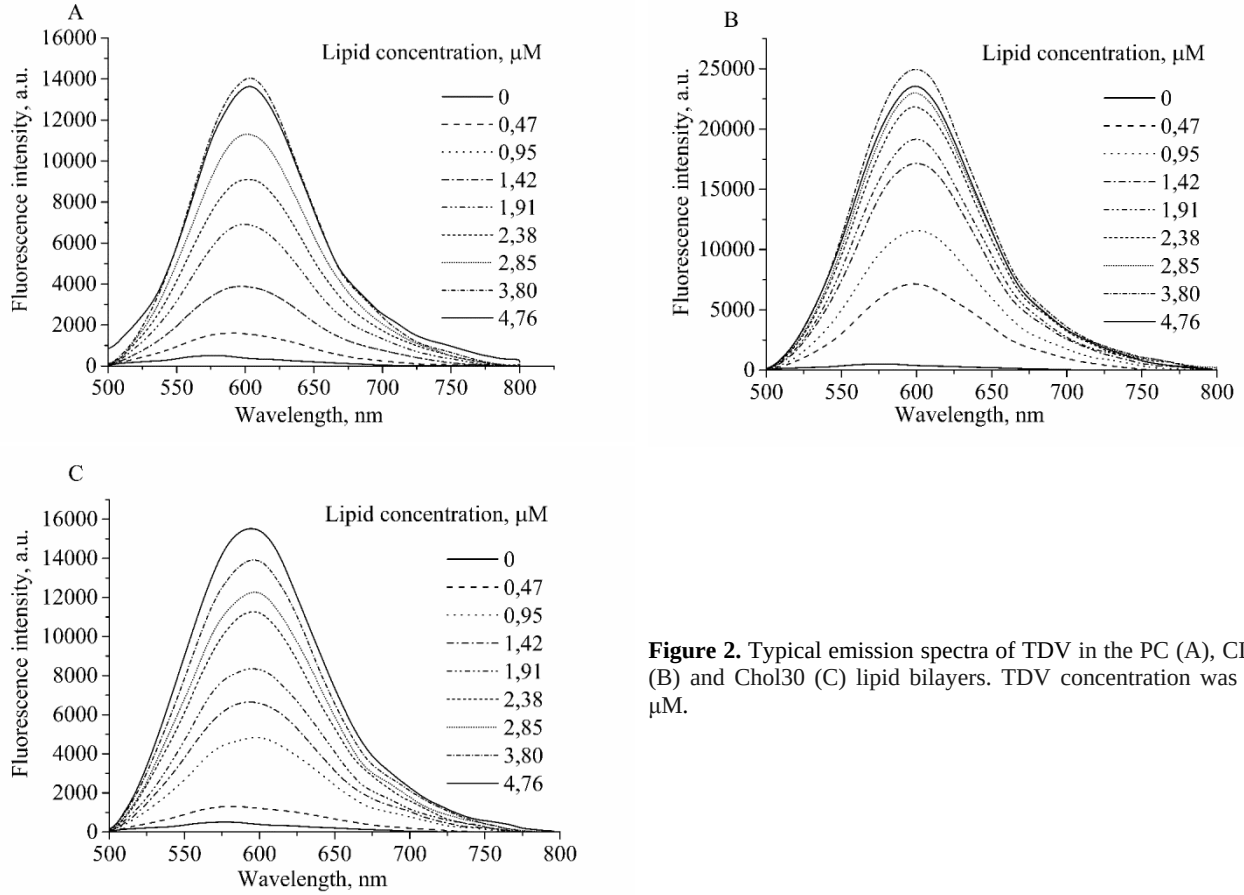

Figure 2. Typical emission spectra of TDV in the PC (A), CL20 (B) and Chol30 (C) lipid bilayers. TDV concentration was 1.0 μM.

As seen in Fig. 1, the TDV transfer from the aqueous to lipid phase resulted in a significant increase of the fluorescence intensity coupled with a red shift of the emission maximum λ_F up to 67 nm, depending on liposome composition (Table 1). The observed fluorescence enhancement is most likely to arise from the decreased mobility of the fluorophore and the reduced polarity of its surroundings. To quantitate the dye partitioning in the lipid phase of the model membranes, the experimental dependencies $\Delta I(C_L)$ were obtained (Fig. 2). The resulting binding isotherms were hyperbolic in shape for all dye-lipid systems under study. To obtain the quantitative parameters of the TDV partitioning into lipid bilayers of varying composition the binding curves were approximated by the equation (7).

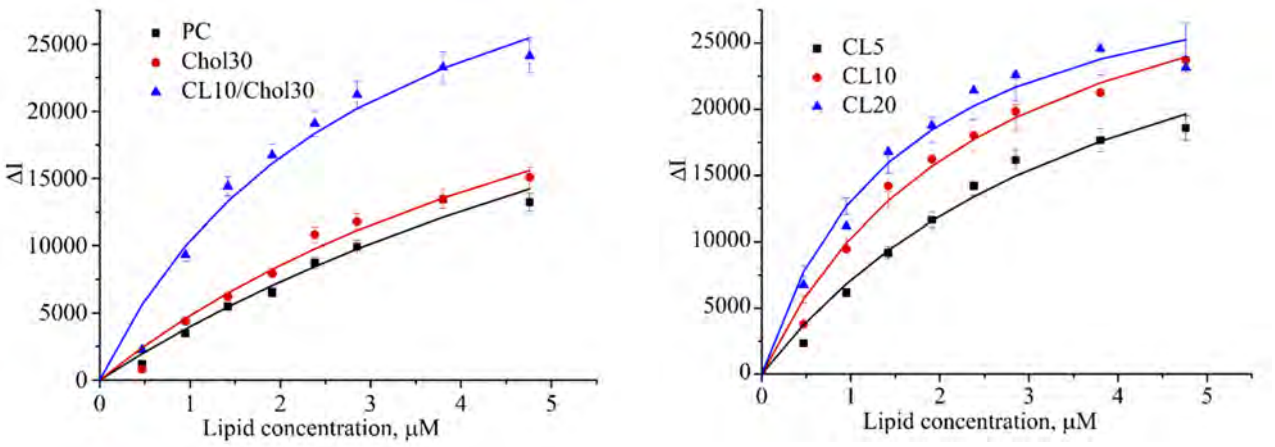

Figure 2. Isotherms of TDV binding to the model lipid membranes. TDV concentration was 1.0 μM. Solid lines represent an approximation of the experimental profiles $\Delta I(C_L)$ by equation (7).

The parameters of TDV partitioning into lipid bilayers are presented in Table 1. The analysis of partition coefficients showed that TDV possesses a rather high lipid-associating ability. Importantly, the estimated K_p values for the model membranes of different lipid composition are in good agreement with the lipophilicity of TDV evaluated using the resources of different virtual computing laboratories (Table 2). A molecular parameter, such as lipophilicity, is commonly used to characterize the tendency of a molecule to distribute between water and water-immiscible solvent [17] and can be expressed by a term accounting for hydrophobic and dispersion forces, and polarity term [18,19].

Table 1. Parameters of TDV partitioning into lipid systems

	λ_F, nm	$K_p \times 10^5$	$\Delta I_{max} \times 10^4$	Fluorescence anisotropy
PC	602	0.96±0.2	4.8±0.9	0.165
CL5	600	2.4±0.4	3.7±0.6	0.161
CL10	600	3.9±0.6	3.5±0.6	0.161
CL20	600	6.4±1.1	3.7±0.7	0.163
Chol30	594	1.4±0.4	5.7±0.8	0.169
CL10/Chol30	596	3.3±0.5	6.1±0.6	0.160

It turned out that addition of CL and Chol to PC bilayer gives rise to the increase of partition coefficients compared to the neat PC membrane. In terms of the modern theories of membrane electrostatics partition coefficient can be represented as consisting of electrostatic and nonelectrostatic terms [20,21]:

$$K_p = exp\left(\left\{w_{el} + w_{Born} + w_h + w_n + w_d\right\} / kT\right) \quad (8)$$

where w_{el} characterizes the Coulombic ion-membrane interactions; w_{Born} corresponds to the free energy of charge transfer between the media with different dielectric constants; w_n is the term determined by hydrophobic, van der Waals and steric factors; w_h related to the membrane hydration; w_d depends on the membrane dipole potential [21-23]. Considering the cationic nature of TDV, the observed increase in K_p values with an increase of the CL content can be explained by electrostatic dye-lipid interaction.

However, in an attempt to interpret the observed increase of the partition coefficients for TDV in the presence of the anionic lipid CL, one should bear in mind the ability of CL to modify the physicochemical properties of the lipid bilayers [24, 25]. Specifically, Shibata et al, based on the FTIR data, demonstrated that CL negative charge tends to move the N^+ end of P-N dipole parallel to the membrane surface, causing the rearrangement of water bridges at the

bilayer surface and stabilizing the intermolecular hydrogen-bonded network including hydrational water [24]. They hypothesized that the above perturbations in the bilayer surface are coupled with the increased amount of the membrane-bound water in the presence of a cone-shaped CL molecules, leading to the enhancement of the hydration of ester C=O groups in the presence of cardiolipin [24]. Moreover, the ability of CL to increase bilayer hydration was also evidenced from the molecular dynamic simulations of lipid membranes with cardiolipin [25].

Table 2. Lipophilicity of TDV calculated using the resources of the virtual computational laboratories

Resource	Method	LogP
http://www.swissadme.ch/	XLOGP3	8.01
	WLOGP	6.21
	MLOGP	6.25
	SILICOS-IT	7.61
	Consensus	6.00
https://mcule.com/apps/property-calculator/		6.2095
http://biosig.unimelb.edu.au/pkcsm/prediction#)		6.2095

To determine whether i) the novel phosphonium dye is sensitive to the changes in lipid packing density and reflects the CL-induced changes in the hydrophobic membrane part; or ii) TDV preferentially resides in the polar part of the lipid bilayer and the increase in K_p values in the CL-containing membranes is caused by alterations in the bilayer physicochemical properties produced by cardiolipin, the fluorescence anisotropy of TDV was measured (Table 1). It is known that the fluorescence anisotropy of the membrane-bound dye is determined by the rate of its rotational diffusion and reflects the changes in lipid packing density. As illustrated in Table 1, the anisotropy values of TDV appeared to be insensitive to the changes in membrane composition, indicating that the dye is most probably located in the polar membrane region. Most likely, the phosphonium part of TDV resides in the polar water/membrane interface, while the rest part of its molecule penetrates more deeply into the membrane interior.

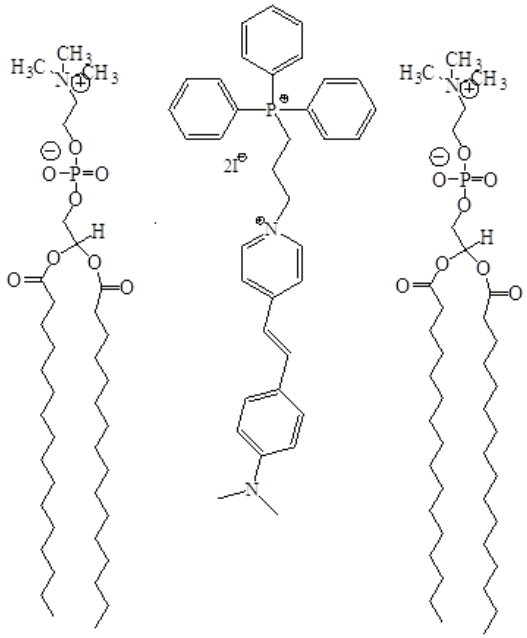

Figure 3. Possible bilayer location of TDV

Additional argument in favour of the TDV ability to monitor the physicochemical properties of the polar membrane part comes from the fluorescence response of this phosphonium dye to the presence of Chol. As seen in Table 1, the measured anisotropy values in the Chol-containing membranes are comparable with those obtained in pure PC and PC/CL membranes, therefore the TDV location in the non-polar membrane part seems less probable due to a well-known ability of Chol to produce tighter lateral packing of lipid molecules (condensing effect) [26]. An assumption was made that the observed increase in K_p value in the presence of cholesterol is associated with the ability of Chol to alter hydration and packing density of lipid membranes [27-30]. It was previously shown that cholesterol is

capable of producing the increase in separation of phospholipid headgroups [27]. Moreover, numerous studies provide evidence for the decreased polarity at the level of glycerol backbone of phospholipids in the presence of cholesterol [28-30]. The TDV sensitivity to the membrane hydration is confirmed by the observed blue shift of the position of emission maxima in the presence of Chol in comparison with CL-containing and pure PC membranes, indicating that TDV accommodates in the less polar environment in the presence of cholesterol. The blue shift of the emission maxima in the presence of cholesterol was observed also for Prodan and Laurdan [30,31]. Given that addition of Chol to PC bilayer gives rise to the increase of partition coefficients compared to the neat PC membrane, the possibility of the TDV preferential interactions with cholesterol cannot be excluded. Most probably, similarly to Prodan, TDV tends to reside in the cholesterol-rich regions of the lipid bilayer [31]. Moreover, one cannot rule out the possibility that TDV is sensitive to the Chol-induced changes in the dipole potential of lipid bilayer [3,4,32]. To uncover the factors contributing to the membrane association of TDV, further studies are needed.

CONCLUSIONS

To summarize, the present study has been undertaken to evaluate the potential of the novel phosphonium dye to trace the changes in the physicochemical properties of the model lipid membranes. TDV was found to display a marked lipid-associating ability and high sensitivity to the physicochemical properties of lipid bilayers. Based on the comprehensive analysis of the binding parameters and spectral characteristics of TDV in the different lipid systems it was assumed that membrane electrostatics and hydration can contribute to the membrane association of TDV. High environmental sensitivity of the examined posphonium dye allowed us to recommend this probe for membrane studies.

Acknowledgements

This work was supported by the Ministry of Education and Science of Ukraine (the Young Scientist projects № 0120U101064 “Novel nanomaterials based on the lyophilic self-assembled systems: theoretical prediction, experimental investigation and biomedical applications” and the project № 0119U002525 “Development of novel ultrasonic and fluorescence techniques for medical micro- and macrodiagnostics”). The author is grateful to Dr.Sci. Galyna Gorbenko, V. N. Karazin Kharkiv National University, for useful comments and discussions.

ORCID IDs

Olga Zhytniakivska, https://orcid.org/0000-0002-2068-5823

REFERENCES

[1] I. Crnolatac, L.-M. Tumir, N. Lesev, A. Vasilev, T. Deligeorgiev, K. Mišković, L. Glavaš-Obrovac, O. Vugrek, and I. Piantanida, ChemMedChem. **8**, 1093 (2013), https://doi.org/10.1002/cmdc.201300085
[2] L.-M. Tumir, I. Crnolatac, T. Deligeorgiev, A. Vasilev, S. Kaloyanova, M. Grabar Branilovic, S. Tomic, and I. Piantanida, Chem. Eur. J. **18**, 3859 (2012), https://doi.org/10.1002/chem.201102968.
[3] G. Li, K. Yang, J. Sun, and Y. Wang, RSC Adv. **6**, 94085 (2016), https://doi.org/10.1039/C6RA21848B.
[4] W. Chen, D. Zang, W. Gong, Y. Lin, and G. Ning, Spectrochim. Acta A Mol. Biomol. Spectrosc. **110**, 471 (2013), https://doi.org/10.1016/j.saa.2013.03.088.
[5] A. Šarić, I. Crnolatac, F. Bouillaud, S. Sobočanec, A.-M. Mikecin, Ž. Mačak Šafranko, T. Delgeorgiev, I. Piantanida, T. Balog, and P. X Petit, Methods Apl. Fluoresc. **5**, 015007 (2017), https://doi.org/10.1088/2050-6120/aa5e64
[6] R.A. J. Smith, C. M. Porteous, C.V. Coulter, and M.P. Murphy, Eur. J. Biochem. **263**, 709 (1999), https://doi.org/10.1046/j.1432-1327.1999.00543.x.
[7] G.F. Kelso, C. M. Porteous, C.V. Coulter, G. Hughes, W.K. Porteous, E.C. Ledgerwood, R.A.J. Smith, and M.P. Murphy, J. Biol. Chem. **276**, 4588 (2001), https://doi.org/10.1074/jbc.M009093200
[8] K. Li, S. Chen, Z. Liu, Z. Zhao, and J. Lu, J. Organomet. Chem. **871**, 28 (2018), https://doi.org/10.1016/j.jorganchem.2018.07.003
[9] A. Lizzul-Jurse, L. Bailly, M. Hubert-Roux, C. Afonso, P. Rehard, and C. Sabot, Org. biomol. Chem. **14**, 7777 (2016), https://doi.org/10.1039/C6OB01080F
[10] X. H. Wang, H. S. Peng, L. Yang, F.T. You, F. Teng, L.L. Hou, and O.S. Wolbeis, Angew. Chemie. **53**, 12471 (2014), https://doi.org/10.1002/ange.201405048
[11] B.C. Dickinson, and C.J. Chang, J. Am. Chem. Soc. **130**, 9638 (2008), https://doi.org/10.1021/ja802355u
[12] G. Gorbenko, V. Trusova, T. Deligeorgiev, N. Gadjev, C. Mizuguchi, and H. Saito, J. Mol. Liq. **294**, 111675 (2019), https://doi.org/10.1016/j.molliq.2019.111675
[13] G. Gorbenko, O. Zhytniakivska, K.Vus, U. Tarabara, and V. Trusova, Phys. Chem. Chem. Phys. **23**, 14746 (2021), https://doi.org/10.1039/D1CP01359A
[14] O. Zhytniakivska, U. Tarabara, K.Vus, V. Trusova and G. Gorbenko, East. Eur. J. Phys. **2**, 19 (2019), https://doi.org/10.26565/2312-4334-2019-2-03
[15] B. Mui, L. Chow, and M. Hope, Meth. Enzymol. **367**, 3 (2003), https://doi.org/10.1016/S0076-6879(03)67001-1
[16] N. Santos, M. Prieto, and M. Castanho, Biochim. Biophys. Acta **1612**, 123 (2003), https://doi.org/10.1016/S0005-2736(03)00112-3
[17] F. Lombardo, M. Shalaeva, K. Tupper, F. Gao, and M. Abraham, J. Med. Chem. **43**, 2922 (2000), https://doi.org/10.1021/jm0000822
[18] G. van Balen, C. Martinet, G. Caron, G. Bouchard, M. Reist, P. Carrupt, R. Fruttero, A. Gasco, and B. Testa, Med. Res. Rev. **3**, 299 (2004), https://doi.org/10.1002/med.10063
[19] C. Giaginis, and A. Tsantili-Kakoulidou, J. Pharmaceut. Sci. **97**, 2984 (2008), https://doi.org/10.1002/jps.21244
[20] G. Cevc, Biochim. Biophys. Acta **1031**, 311 (1990), https://doi.org/10.1016/0304-4157(90)90015-5
[21] J. Tocanne, and J. Teissie, Biochim. Biophys. Acta **1031**, 111 (1990), https://doi.org/10.1016/0304-4157(90)90005-W
[22] R. Flewelling, and W. Hubbel, Biophys. J. **49**, 541 (1986), https://doi.org/10.1016/S0006-3495(86)83664-5

[23] M. Belaya, M.V. Feigel'man, and V.G. Levadnyii, Langmuir **3**, 648 (1987), https://doi.org/10.1021/la00077a011
[24] A. Shibata, K. Ikawa, T. Shimmoka, and H. Terada, Biochim. Biophys. Acta **1192**, 71 (1994), https://doi.org/10.1016/0005-2736(94)90144-9
[25] M. Dahlberg, and F. Maliniak J Phys Chem B **112**, 11655 (2008), https://doi.org/10.1021/jp803414g
[26] W.-C. Hung, M.-T. Lee, F.-Y. Chen, and H.W. Huang, Biophys. J. **92**, 3960 (2007), https://doi.org/10.1529/biophysj.106.099234
[27] Y. Levine, Prog. Biophys. Mol. Biol. **24**, 1 (1972), https://doi.org/10.1016/0079-6107(72)90003-X
[28] H.A. Perez, A. Disalvo, and M. de los Angeles Frias, Colloid Surf. B. **178**, 346 (2019), https://doi.org/10.1016/j.colsurfb.2019.03.022
[29] H.A. Perez, L.M. Alarcon, A.R. Verde, G.A. Appignanesi, R.E. Gimenez, E.A. Disalvo, and M.A. Frias, Biochim. Biophys. Acta **1863**, 183489 (2021), https://doi.org/10.1016/j.bbamem.2020.183489
[30] T. Parasassi, M. Stefano, M. Loiero, G. Ravagnan, and E. Gratton, Biophys J. **66**, 120 (1994), https://doi.org/10.1016/S0006-3495(94)80763-5
[31] O.P. Bondar, and E.S. Rowe, Biophys J. **76**, 956 (1999), https://doi.org/10.1016/S0006-3495(99)77259-0
[32] S. Bandari, H. Chakraborty, D. Covey, and A. Chattopadhyay, Chem. Phys. Lipids **184**, 25 (2014), https://doi.org/10.1016/j.chemphyslip.2014.09.001

ВЗАЄМОДІЯ НОВОГО ФОСФОНІЄВОГО ЗОНДУ З ЛІПІДНИМИ МЕМБРАНАМИ: ФЛУОРЕСЦЕНТНЕ ДОСЛІДЖЕННЯ

О. Житняківська

Кафедра медичної фізики та біомедичних нанотехнологій, Харківський національний університет імені В.Н. Каразіна м. Свободи 4, Харків, 61022, Україна

Останнім часом оптичні зонди на основі фосфонію привертають все більший інтерес завдяки їх чудовій хімічній та фотофізичній стабільності, високій розчинності у воді, поглинанню та випромінюванню в довгохвильовій області, великих коефіцієнтах екстинкції, високому квантовому виходу флуоресценції, низькій цитотоксичності, тощо. Дана робота була спрямована на оцінку чутливості нового фосфонієвого барвника TDV до змін фізико-хімічних властивостей модельних ліпідних мембран. З цією метою, було досліджено флуоресцентні спектральні властивості TDV в ліпідних бішарах, що складались із цвіттеріонного ліпіду фосфатидилхоліну (ФХ) та його сумішей з холестерином (Хол) та/або аніонним фосфоліпідом кардіоліпіном (КЛ). Виявилось, що в буферному розчині TDV має один добре виражений пік емісії з на довжині хвилі 533 нм. Перехід барвника з водної в ліпідну фазу супроводжувався зростанням інтенсивності флуоресценції зонду, поряд із червоним зсувом максимуму випромінювання, величина якого досягала 67 нм, залежно від складу ліпосом. Була отримана кількісна інформація щодо розподілу барвника в ліпідну фазу модельних мембран шляхом апроксимації експериментальних залежностей зміни інтенсивності флуоресценції зонду від концентрації ліпіду моделлю розподілу. Аналіз отриманих коефіцієнтів розподілу демонструє високу ліпід-асоціюючу здатність TDV та його чутливість до змін фізико-хімічних властивостей модельних ліпідних мембран. Включення КЛ, Хол або обох ліпідів до ФХ бішару спричиняло збільшення коефіцієнтів розподілу TDV, порівняно з чистими ФХ мембранами. Зростання коефіцієнтів розподілу фосфонієвого барвника в ліпідних мембранах, що містили КЛ та Хол, було інтерпретовано в рамках уявлень про зміни структури та фізико-хімічних характеристик полярної області мембрани під впливом кардіоліпіну та холестерину.

Ключові слова: фосфонієвий зонд, ліпідні мембрани, флуоресценція, розподіл.

East European Journal of Physics. 4. 114-119 (2021)
DOI: 10.26565/2312-4334-2021-4-13 ISSN 2312-4334

CLINICAL COMMISSIONING AND DOSIMETRIC VERIFICATION OF THE RAYSTATION TREATMENT PLANNING SYSTEM[†]

Taylan Tuğrul
Department of Radiation Oncology, Medicine Faculty of Van Yüzüncü Yıl University, Van, TURKEY
E-mail: taylantugrul@gmail.com
Received September 22, 2021; accepted November 15, 2021

Background: The software used by treatment planning systems (TPS) plays an important role for treatments using radiation. The accuracy of the calculated dose in radiation treatments depends on the assumptions made by the TPS. In this study, we summarize our methods and results regarding clinical commissioning of the basic functions needed for photon therapy. Materials and Method: Measurements were obtained for the 6 and 15 MV photon energies obtained from the Siemens Artiste linear accelerator device. Important data such as percent deep dose, profile and output measurements were taken in the water phantom and transferred to the RayStation Treatment Planning System. Results: When the absolute dose values calculated by the RayStation TPS are compared with the water phantom data, the differences obtained are less than 3%. When the 2-dimensional quality control of asymmetrical areas and patients with IMRT plan was controlled by gamma analysis method, the gamma rate was more than 95%. Conclusion: One of the most important quality control tests is TPS acceptance tests, which must be performed before clinical use. In this study, in which we checked the basic dose measurement and patient planning, it was seen that the RayStation TPS can be used in patient treatment for clinical use. The doses calculated by the RayStation TPS were found to be reliable and within the expected accuracy range. These results are sufficient for the application of 3-dimensional conformal radiotherapy (3D-CRT) and IMRT technique.
Keywords: RayStation, Commissioning, Dosimetric Verification
PACS: 87.55.Qr

The software used by treatment planning systems (TPS) plays an important role for treatments using radiation [1]. The accuracy of the calculated dose in radiation treatments depends on the assumptions made by the TPS. In TPS, operations such as defining the target volume, making the treatment plan, determining the treatment areas, and calculating the appropriate Monitor Unit (MU) value are performed. Considering what has been done, it is extremely important to carry out quality controls before TPSs are put into use for clinical use [2,3,4].

The International Atomic Energy Agency (IAEA) has published a report on the quality control of TPSs [5]. In addition, IAEA has also prepared a technical document file numbered TECDOC 1583, which includes practical tests for dosimetric calculations [6]. Reports published by the Association of Physicist in Medicine (AAPM) are also available in the literature [7,8].

RayStation (RaySearch Labs, Stockholm/Sweden) is a good example of advanced TPS. Raysearch laboratories have an important place in the world in the field of advanced software and are the creators of the RayStation TPS for radiation therapy [9]. Studies for the commissioning of TPS models are available in the literature [10,11,12,13].

RayStation is a treatment planning system that has just started to be used in our country. It started to be used in our clinic in 2021. We aimed to check the accuracy of the radiation dose calculations of the RayStation TPS before it is used in the clinic. In this study, we summarize our methods and results regarding clinical commissioning of the basic functions needed for photon therapy.

MATERIALS AND METHODS

In the study, Somatom Sensation 4 (Siemens, Erlangen) device was used for computed tomography images. Measurements were obtained for the 6 and 15 MV photon energies obtained from the Siemens Artiste linear accelerator (Linac) device. IBA Bule Phantom-2 (IBA dosimetry, Schwarzenbruck, Germany) water phantom device was used in the study. The compact ion chambers used in the water phantom are CC04 (13808) (IBA dosimetry, Schwarzenbruck, Germany). All absolute measurements were obtained with DOSE 1 (IBA dosimetry, Schwarzenbruck, Germany) electrometer. PTW OCTAVIUS was used for 2D quality control measurements (PTW, Freiburg, Germany).

For 6 and 15 MV photons, Percent deep dose (PDD) measurements were obtained in field sizes of 2x2 cm^2-40x40 cm^2, on the central axis and at 100 cm source to skin distance (SSD). In addition, profile measurements were taken at maximum dose depth (dmax), 5 cm, 10 cm and 20 cm depths and inplane-crossplane directions.

For 2x2 cm^2-40x40 cm^2 fields, 100 MU irradiation was made at SSD=100 cm, 10 cm depth, and Output measurements were taken for both photon energies and normalized to 10x10 cm^2.

The MLC transmission factor was calculated by irradiating the multi-leaf collimators (MLC) in the closed state while the jaws were open at maximum width.

After all data were transferred to the TPS system, dose measurements at different depths for asymmetrical areas were taken in a water phantom and compared with the doses calculated by the RayStation TPS. In addition, dose

[†] ***Cite as:*** T. Tuğrul, East. Eur. J. Phys. **4**, 114 (2021), https://doi.org/10.26565/2312-4334-2021-4-13

distribution results obtained in patients planned for Intensity Modulated Radiotherapy (IMRT) and in different asymmetrical areas in TPS were compared with the dose distribution calculated by RayStation's QA module using gamma analysis test. For the gamma index, dose confirmation distance and dose difference criteria were chosen as 3 mm and 3%, respectively[1,14]. Absorbed dose measurements were made according to the IAEA TRS-398 protocol [15].

RESULTS

The 6 MV and 15 MV photon beam data required for the RayStation TPS were measured with the water phantom. Then, the measured beam data was transferred to the RayStation system by normalizing the maximum dose. Figure 1 and Figure 2 show the PDD and profile results measured in the water phantom.

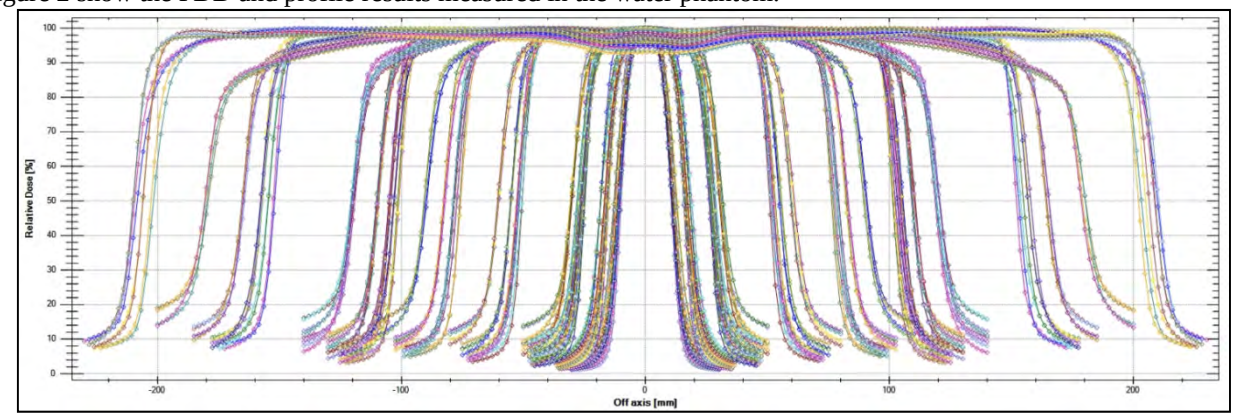

Figure 1. Profile results obtained in the water phantom.

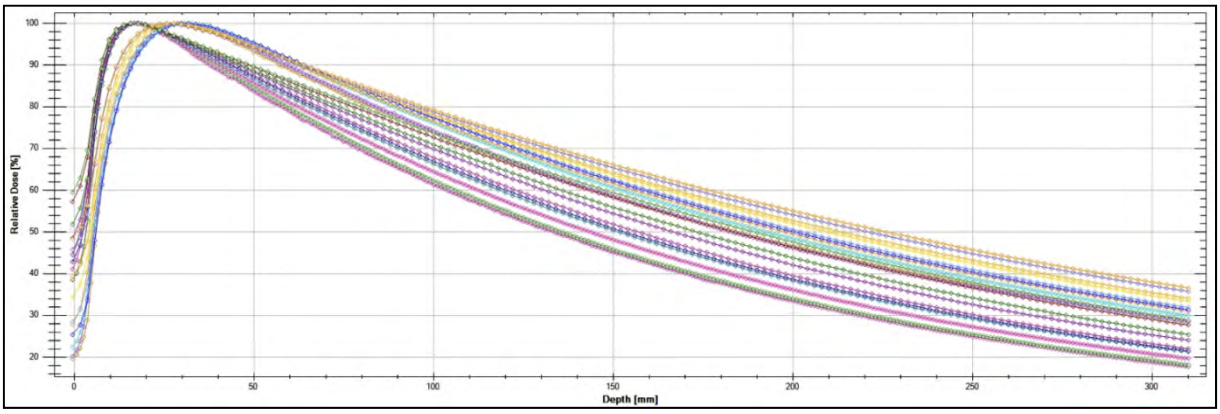

Figure 2. PDD results obtained in the water phantom.

Output values obtained for different fields at a depth of 10 cm and the results normalized to 10x10 cm^2 are shown in Table 1 and Table 2.

Table 1. For 6 MV photon energy, the dose values obtained as a result of 100 MU irradiation in different areas, at a depth of 10 cm, and the ratios normalized to 10x10 cm^2.

Field Size (cm^2)	Detector Model	6 MV				
		1st Measurement (pC)	2nd Measurement (pC)	3rd Measurement (pC)	Average	Ratio
2x2	**CC04**	1661,3	1661,3	1661,3	1661,3	0, 783928
3x3	**CC04**	1764	1764	1764	1764	0, 83239
4x4	**CC04**	1835,8	1835,8	1835,8	1835,8	0, 86627
5x5	**CC04**	1893,6	1893,6	1893,45	1893,55	0, 893521
7x7	**CC04**	2000,1	2000,2	2001,2	2000,5	0, 943988
10x10	**CC04**	2118,2	2119,2	2120,2	2119,2	1
10x20	**CC04**	2220,5	2217,3	2220	2219,267	1, 047219
12x12	**CC04**	2177,1	2176,4	2177,4	2176,967	1, 027259
15x15	**CC04**	2246,9	2244,6	2244,5	2245,333	1, 059519
20x20	**CC04**	2332,7	2331,3	2333	2332,333	1, 100573
20x10	**CC04**	2192,7	2192,7	2193,2	2192,867	1, 034762
25x25	**CC04**	2398,9	2396,1	2395,1	2396,7	1, 130946
30x30	**CC04**	2446	2442,3	2441,3	2443,2	1, 152888
40x40	**CC04**	2497	2498,4	2495,3	2496,9	1, 178228

Table 2. For 15 MV photon energy, the dose values obtained as a result of 100 MU irradiation in different areas, at a depth of 10 cm, and the ratios normalized to 10x10 cm^2.

Field Size (cm^2)	Detector Model	15 MV				
		1st Measurement (pC)	2nd Measurement (pC)	3rd Measurement (pC)	Average	Ratio
2x2	**CC04**	1916,5	1916,5	1916,5	1916,5	0,779086
3x3	**CC04**	2109	2109	2109	2109	0,85734
4x4	**CC04**	2203,5	2203,5	2203,5	2203,5	0,895756
5x5	**CC04**	2272,1	2272,5	2272,2	2272,267	0,923711
7x7	**CC04**	2363,5	2366,6	2364	2364,7	0,961286
10x10	**CC04**	2460	2459,5	2460,3	2459,933	1
10x20	**CC04**	2538,7	2537,4	2538,6	2538,233	1,03183
12x12	**CC04**	2501,7	2501,7	2504,8	2502,733	1,017399
15x15	**CC04**	2555,3	2554,1	2554	2554,467	1,038429
20x20	**CC04**	2617,2	2616,8	2617,7	2617,233	1,063945
20x10	**CC04**	2509,2	2511,8	2511,7	2510,9	1,020719
25x25	**CC04**	2661,9	2661,4	2660,8	2661,367	1,081886
30x30	**CC04**	2696	2698,6	2696,6	2697,067	1,096398
40x40	**CC04**	2734,5	2734,8	2734,4	2734,567	1,111643

After taking measurements in accordance with the IAEA TRS-398 protocol and determining the desired factors in the protocol, absolute dose measurements were taken in different areas and at different points and compared with the dose values obtained in the RayStation system. the differences in percentages are shown in Table 3 and Table 4.

Table 3. For 6 MV photon energy, absolute dose values obtained in RayStation and water phantom as a result of 100 MU irradiation in different areas and at different points.

Field Size (cm^2)	Points X,Y,Z (cm)	RayStation TPS (cGy)	Water Phantom (cGy)	Difference (%)
3x3	(0,1,5)	72,1	70,85	1,73
10x10	(3,-3,8)	73,5	73,96	0,63
15x15	(0,0,5)	89,6	90,16	0,62
20x20	(-3,7,10)	73,4	73,76	0,50
30x30	(5,12,7)	87,4	88,92	1,73
3x5	(0,0,5)	77,4	78,12	0,93
10x5	(0,0,7)	73,4	73,93	0,72
10x20	(1,1,9)	73,9	73,83	0,10
30x15	(5,-3,11)	70,2	71,01	1,16
20x9	(3,0,6)	84	85,18	1,41
30x40	(2,-5,5)	95	96,88	1,9
5x40	(0,-1,9)	69,7	69,77	0,10

Table 4. For 15 MV photon energy, absolute dose values obtained in RayStation and water phantom as a result of 100 MU irradiation in different areas and at different points.

Field Size (cm^2)	Points X,Y,Z (cm)	RayStation TPS (cGy)	Water Phantom (cGy)	Difference (%)
4x4	(0,1,5)	83,5	84,52	1,22
7x7	(1,0,8)	79,3	79,97	0,84
10x10	(3,-3,6)	90,5	91,13	0,70
15x15	(0,0,7)	89,8	90,01	0,23
20x20	(-3,7,7)	91,7	91,93	0,26
30x30	(0,0,5)	100	100,50	0,50
	(5,12,9)	84,9	85,81	1,07
40x40	(0,0,5)	100	100,92	0,92
4x7	(0,0,5)	88,8	89,59	0,89
10x5	(0,0,4)	93,5	93,92	0,45
10x20	(1,1,7)	88	88,82	0,93
30x15	(5,-3,5)	99,5	100,50	1,01
20x9	(3,0,10)	78,6	78,59	0,02
30x40	(2,-5,5)	102,5	103,84	1,31
5x40	(0,-1,12)	69,4	69,70	0,43

Before starting the gamma analysis measurements, a calibration factor for the 2D-array was obtained by irradiating 100 MU in a 10x10 cm^2 area. Comparison of 2-dimensional measurement results was made in 4 different ways.

The images of the 2D-Array, whose computerized tomography was taken, were sent to the RayStation system. In the RayStation system, 20x20 cm^2 area was opened on the 2D-Array images and 100 MU irradiation was made. Then, the MLCs were closed by 2 cm and 100 MU irradiation was performed again. This process was repeated 5 times. The Figure 3 demonstrates gamma analysis results from the comparison between measurement maps and calculated plan maps.

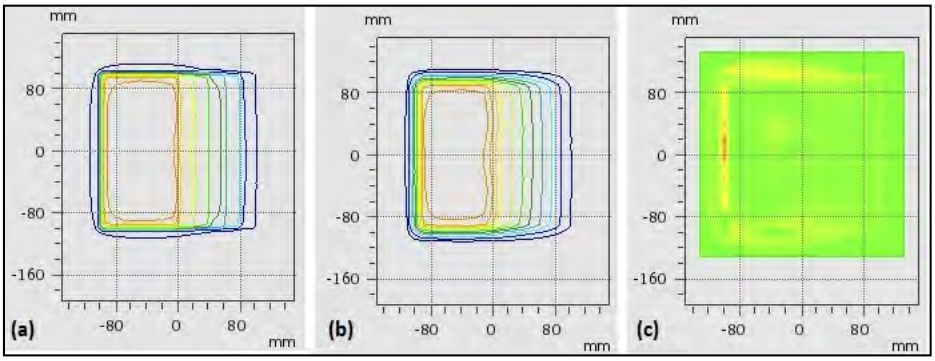

Figure 3. (a) Dose distribution calculated by RayStation; (b) Dose distribution measured by PTW OCTAVIUS; (c) Gamma Index results.

Then, with the help of MLCs, an irregular area was created on the RayStation and this area was controlled in 2 dimensions. The field created on the RayStation TPS and gamma analysis results are shown in Figures 4 and 5, respectively.

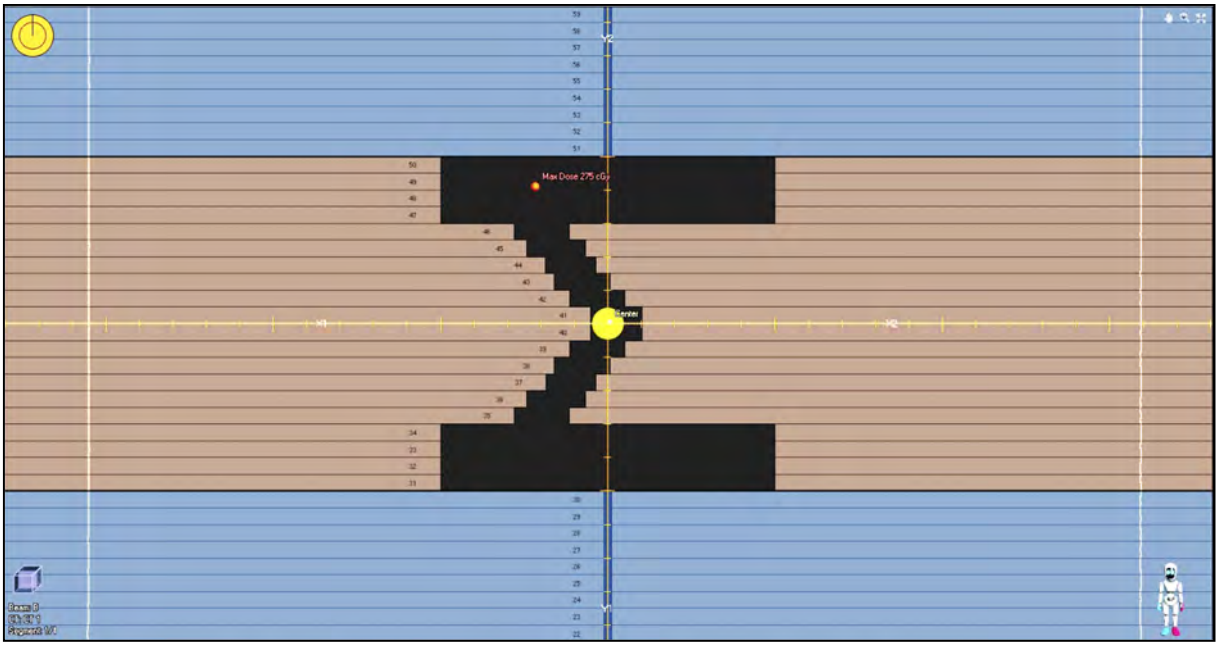

Figure 4. The irregular area created with the help of MLCs in the TPS system.

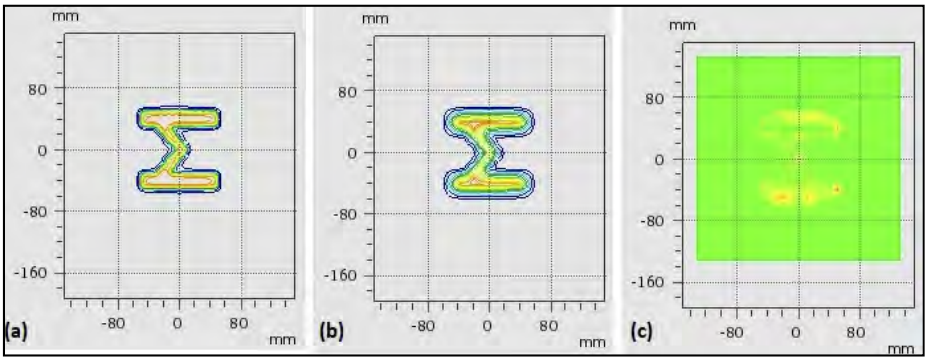

Figure 5. (a) Dose distribution calculated by RayStation; (b) Dose distribution measured by PTW OCTAVIUS; (c) Gamma Index results.

In order to see the effect of MLC leakage and Tongue and Groove effect on planning, MLCs were closed by leaving a gap in the +x direction and 100 MU irradiation was made. Then, the MLCs in the -x direction were closed by leaving a gap and 100 MU irradiation was made. The dose distribution obtained as a result of the irradiation was compared with the gamma analysis method. The fields of MLC created on the RayStation TPS and gamma analysis results are shown in Figures 6 and 7, respectively.

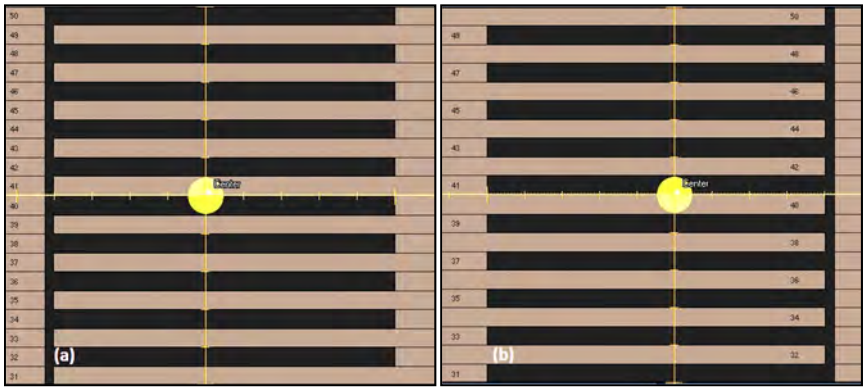

Figure 6. For MLC leakage and Tongue and Groove effect, the fields created with the help of MLCs in the TPS system. (a) The MLC's are in the +x direction. (b) The MLC's are in the -x direction.

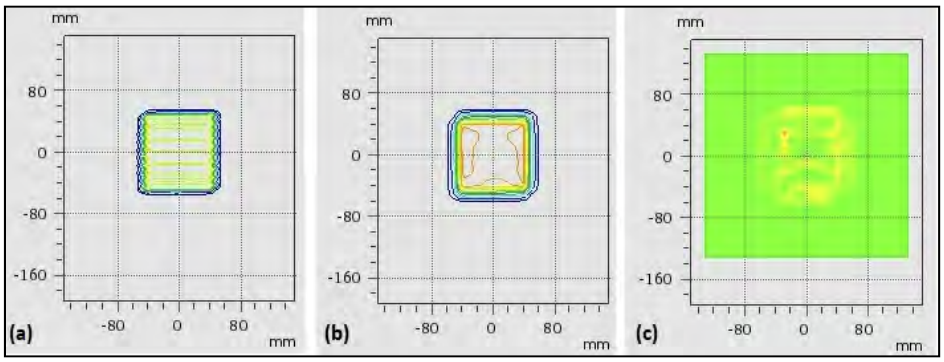

Figure 7. (a) Dose distribution calculated by RayStation; (b) Dose distribution measured by PTW OCTAVIUS; (c) Gamma Index results.

IMRT plans were made with the 9-field Step and Shoot technique for 5 different patients. The plans made were set to have 150 segments. Then, with the help of the QA mode in the RayStation system, the dose distribution created by these patients was obtained and 2-dimensional quality controls were made. The dose distribution obtained for an exemplary patient is shown in Figure 8.
All 2-dimensional dosimetric controls performed have a gamma rate of over 95%.

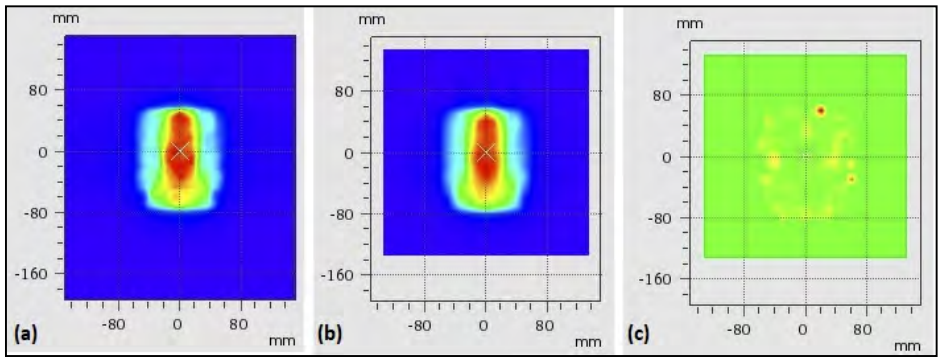

Figure 8. (a) Dose distribution calculated by RayStation; (b) Dose distribution measured by PTW OCTAVIUS; (c) Gamma Index results.

CONCLUSION

One of the most important quality control tests is TPS acceptance tests, which must be performed before clinical use. The necessary data of the Linac device should be measured completely and accurately and transferred to the Treatment planning system. The dosimetric accuracy of the RayStation treatment planning system was investigated for 6 MV and 15 MV beams obtained from the Siemens Artiste Linac. In the study, acceptable differences were observed between the treatment planning

system and the measurement results. As a result of the examinations made in homogeneous and heterogeneous environments, it was observed that there was a high level of agreement between the treatment planning system and the measurement data. The difference between the absolute dose data measured and calculated according to the AAPM Task Group 53 should not be more than 3%. In the results we found, the difference was less than 3%. In this study, in which we checked the basic dose measurement and patient planning, it was seen that the RayStation TPS can be used in patient treatment for clinical use. The doses calculated by the RayStation TPS were found to be reliable and within the expected accuracy range. These results are sufficient for the application of 3-dimensional conformal radiotherapy (3D-CRT) and IMRT technique.

Acknowledgement

Thank you to Ali Yeşil for his contribution.

ORCID IDs

Taylan Tuğrul, https://orcid.org/0000-0002-0557-1334

REFERENCES

[1] C. Bäumer, D. Geismar, B. Koska, P.H. Kramer, J. Lambert, M. Lemke, S. Plaude, L. Pschichholz, S. Qamhiyeh, A. Schiemann, B. Timmermann, and X. Vermeren, Physica Medica, **43**, 15–24 (2017), https://doi.org/10.1016/j.ejmp.2017.09.136

[2] *Investigation of an Accidental Exposure of Radiotherapy Patients in Panama*. (IAEA, Vienna, 2001), https://www-pub.iaea.org/MTCD/Publications/PDF/Pub1114_scr.pdf

[3] *Lessons Learned from Accidental Exposures in Radiotherapy, Safety Reports Series No. 17*, (IAEA, Vienna, 2000), http://www-pub.iaea.org/MTCD/Publications/PDF/Pub1084_web.pdf

[4] L. Rutonjski, B. Petrović, M. Baucal, M. Teodorović, O. Čudić, E. Gershkevitsh, and J. Izewska, Radiation Oncology, **7**, 155 (2012), https://doi.org/10.1186/1748-717x-7-155

[5] *Commissioning and Quality Assurance of Computerized Planning Systems for Radiation Treatment of Cancer, Technical Reports Series No. 430*, (IAEA, Vienna, 2004), http://www-pub.iaea.org/MTCD/Publications/PDF/TRS430_web.pdf

[6] *Commissioning of radiotherapy treatment planning systems: testing for typical external beam treatment techniques, TECDOC 1583*, (IAEA, Vienna, 2008), https://www-pub.iaea.org/MTCD/Publications/PDF/te_1583_web.pdf

[7] American Association of Physicists in Medicine Radiation Therapy Committee Task Group 23 "*Radiation Treatment Planning Dosimetry Verification*" (AIP, New York, 1995), https://www.aapm.org/pubs/reports/RPT_55.pdf

[8] G.J. Kutcher, L. Coia, M. Gillin, W.F. Hanson, S. Leibel, R.J. Morton, et al, Med. Phys. **21**(4), 581 (1994); https://doi.org/10.1118/1.597316

[9] D. Bodensteiner, Medical Dosimetry, **43**, 168 (2018), https://doi.org/10.1016/j.meddos.2018.02.013

[10] J. Saini, N. Cao, S.R. Bowen, M. Herrera, D. Nicewonger, T. Wong, and C.D. Bloch, Int. J. Particle Therapy, **3**(1), 51 (2016), https://doi.org/10.14338/IJPT-16-0000.1

[11] B. Mzenda, K. Mugabe, R. Sims, G. Godwin, and D. Loria, Modeling and dosimetric performance evaluation of the RayStation treatment planning system. J. Appl. Clin. Med. Phys. **15**(5), 29 (2014), https://doi.org/10.1120/jacmp.v15i5.4787

[12] B. Fraass, K. Doppke, M. Hunt, G. Kutcher, G. Starkschall, R. Stern, and J. Van Dyke, Med. Phys. **25**, 1773 (1998), https://doi.org/10.1118/1.598373

[13] B. Mijnheer, A. Olszewska, C. Fiorino, et al, Quality assurance of treatment planning systems. Practical examples for non-IMRT photon beams. (ESTRO, Brussels, 2005). ESTRO Booklet no. 7, in: *8th Biennial ESTRO Meeting on Physics and Radiation Technology for Clinical Radiotherapy*, Radiotherapy and Oncology, **73**, Suppl. 1, S417, (2004), https://doi.org/10.1016/s0167-8140%2804%2982857-3

[14] G.A. Ezzell, J.W. Burmeister, N. Dogan, T.J. LoSasso, J.G. Mechalakos, D. Mihailidis, et al, Med. Phys. **36**(11), 5359 (2009), https://doi.org/10.1118/1.3238104

[15] *Absorbed dose determination in external beam radiotherapy. An International Code of Practice for Dosimetry Based on Standards of Absorbed Dose to Water Technical Report Series 398*, (IAEA, Vienna, 2000), http://www-naweb.iaea.org/nahu/DMRP/documents/CoP_V12_2006-06-05.pdf

КЛІНІЧНИЙ ПУСК ТА ДОЗИМЕТРИЧНА ПЕРЕВІРКА СИСТЕМИ ПЛАНУВАННЯ ЛІКУВАННЯ ПРОМЕНЕВОЮ СТАНЦІЄЮ

Тайлан Тугрул

Кафедра радіаційної онкології, медичний факультет Університету Ван Юзюнджю Йіл, Ван, ТУРЕЦІЯ

Програмне забезпечення, яке використовується системами планування лікування (TPS), відіграє важливу роль для лікування з використанням радіації. Точність розрахункової дози при радіаційних обробках залежить від припущень, зроблених TPS. У цьому дослідженні ми підсумовуємо наші методи та результати щодо клінічного введення в дію основних функцій, необхідних для фотонної терапії. Матеріали та метод. Вимірювання проведено для енергій фотонів 6 і 15 МВ, отриманих з лінійного прискорювача Siemens Artiste. Важливі дані, такі як відсоток глибинної дози, профіль та вимірювання виходу, були зроблені у водному фантомі та передані в систему планування обробки RayStation. Результати: Коли абсолютні значення дози, розраховані RayStation TPS, порівнюються з даними водних фантомів, отримані відмінності становлять менше 3%. Коли двовимірний контроль якості асиметричних ділянок та пацієнтів із планом IMRT контролювали методом гамма-аналізу, рівень гамма-потужності становив більше 95%. Висновок: одним з найважливіших тестів контролю якості є приймальні тести TPS, які необхідно виконати перед клінічним використанням. У цьому дослідженні, в якому ми перевірили основне вимірювання дози та планування пацієнта, було виявлено, що RayStation TPS можна використовувати для лікування пацієнтів для клінічного використання. Дози, розраховані за допомогою RayStation TPS, виявилися надійними та в межах очікуваного діапазону точності. Цих результатів достатньо для застосування 3-вимірної конформної променевої терапії (3D-CRT) та техніки IMRT.

Ключові слова: променева станція, введення в експлуатацію, дозиметрична повірка

East European Journal of Physics. 4. 120-123 (2021)
DOI: 10.26565/2312-4334-2021-4-14 ISSN 2312-4334

INVESTIGATION OF THE STRUCTURAL COMPOSITION OF Fe-Mn-Si-Ti-Al-NC ALLOYS AND THE SOLUBILITY OF ELEMENTS IN α-IRON†

Nataliia Yu. Filonenko[a,b,*], Olexander I. Babachenko[b], Hanna A. Kononenko[b], Alexander S. Baskevich[c]

[a]*Dnipro State Medical University*
9, Vernadsky Str., Dnipro,49044, Ukraine
[b]*Z. I. Nekrasov Iron and Steel Institute of National Academy of Sciences of Ukraine*
1, Ak. Starodubova K.F. sq., Dnipro, 49107, Ukraine
[c]*Ukrainian State University of Chemical Technology*
8, Gagarin Av., Dnipro, 49000, Ukraine
**Corresponding Author: natph2016@gmail.com*
Received September 29, 2021; revised October 27, 2021; accepted November 16, 2021

The study of the structural components of Fe-Mn-Si-Ti-Al-N-C with the carbon content of 0.50-0.60% (wt.), Silicon 0.80-0.90% (wt.), Manganese 0.90-0.95% (wt.), Aluminum - 0.20-0.30% (wt.), Titanium - 0.02-0.03% (wt.), Nitrogen - 0.015-0.02% (wt.), the rest - iron. Microstructural, micro-X-ray spectral and X-ray phase analyzes were used to determine the structural state of the alloys. It is shown that after crystallization and a number of phase transformations the structure of the alloy was presentedα - iron alloyed with cementite, oxides, nitrides and carbonitrides. Using the quasi-chemical method, the free energy dependence of the solid solution of α-iron alloyed with silicon, manganese and titanium was obtained. In α-iron, it can dissolve up to 0.016% (at.) Carbon, manganese up to 1.3% (at.), Silicon - 1.0% (at.), and titanium up to 0.5% (at.), which is consistent with experimental results.
Keywords: complex alloying of steel with aluminum, titanium and nitrogen; inclusions; oxides; nitrides; carbonitrides; ferrite; free energy of ferrite.
PACS: 61.50.Ah, 64.10.+h

It is known that alloying elements have an effect on phase transformations and the formation of excess phases in steels. Alloying elements can be divided into (where) stabilizing carbides and ferrite in the formation of perlite [1]. Carbide-forming elements include Mn, V, Ti, Cr and Mo [2-3], while non-carbide-forming elements such as Si, Al, Ni and Co [1-3] have high concentrations in the α-Fe phase. The authors found that there is a strong repulsive force between Si and Mn atoms in α-Fe structure of BCC [4]. Si atoms predominantly dissolve in α-Fe and push Mn atoms into cementite. For Fe-4.18C-0.71Mn-0.42Si and Fe-4.16C-0.72Mn-1.82Si alloys, the distribution coefficient between the ratio of the concentration of manganese in cementite and silicon in ferrite was 3.66 ... 8.16, depending on the content of these elements in steel. The manganese content in the ferrite of Fe – 4.18C – 0.71Mn – 0.42Si and Fe – 4.16C – 0.72Mn – 1.82 Si alloys was 0.7% (at.), Silicon - 0.8… 3% (at.), and in manganese cementite - 2.0% (at.), and silicon 0.1% (at.) [4].

With the silicon content of 0.95% (at.) in the cementite of both alloys, its content is 0.06 ± 0.01% (at.) and the silicon content of 0.22% (at.) is 0.09 ± 0.02% (at.), respectively [1]. The content of Mn in α-Fe and in the cementite of the alloy with the content of 0.95% silicon is 0.41 ± 0.02% (at.) and 1.60 ± 0.03% (at.), and for the alloy with the content of 0.22% (at.) Si - 0.50 ± 0.04% (at.) and 1.45 ± 0.31% (at.), respectively [1].

Studies of the content of alloying elements in the ferrite of Fe-3.2Mn-1.0Al-1.2 C alloy showed that the content of manganese in α-iron - 3… 10% (at.), Aluminum - 3… 9% (at.) and carbon <0.4 % (at.) [5]. In paper [6], it is indicated that the maximum solubility of elements in α-iron is: carbon - 0.017% (wt.), Manganese - 1.5% (wt.), Silicon - 1.3% (wt.), which is consistent with the results given in paper [7].

The authors of paper [8] note that the microstructure of steel Fe – 1.5% Mn – 0.6% Si –0.8% C had the ferrite-perlite structure, and Fe – 2 / 2.5% Mn – 0.6% Si – 0.8% C is pearlitic, which had higher hardness. The authors explain the obtained result by the joint effect of Mn and Si on the eutectic point of Fe-Fe $_3$ C system - both alloying elements shift S point (eutectoid point on the iron-carbon phase diagram) to the higher carbon content, which leads to the increase in the volume fraction of perlite in steel.

It is known that Si and Al inhibit the formation of carbides, and Si is more efficient than aluminum. Phosphorus and sulfur occupy the position of carbon substitution in all carbides, while Si can replace carbon in two of them - Fe $_3$ C and Fe_5C_2 [9]. Currently, the literature contains insufficient data on the structural components and features of the phases of high-alloy alloys, in particular, alloys of Fe-Mn-Si-Ti-Al-N-C system.

The aim of this work was to investigate the phase composition of alloys of Fe-Mn-Si-Ti-Al-NC system and to determine the solubility of elements in α-iron.

† ***Cite as:*** N.Yu. Filonenko, A.I. Babachenko, H. A. Kononenko, and A.S. Baskevich, East. Eur. J. Phys. **4**, 120 (2021), https://doi.org/10.26565/2312-4334-2021-4-14

MATERIALS AND RESEARCH METHODS

The study was performed on alloys of Fe-Mn-Si-Ti-Al-NC system with the carbon content of 0.50-0.60% (wt.), Silicon 0.80-0.90% (wt.), Manganese 0.90-0.95 % (wt.), aluminum - 0.20-0.30% (wt.), titanium - 0.02-0.03% (wt.), nitrogen - 0.015-0.02% (wt.), the rest - iron.

The smelting of the alloy was carried out in the furnace in alundum crucibles in the argon atmosphere. The cooling rate of the alloy after casting was 10 K/s. Metallographic sections of the alloy were made according to standard methods using diamond pastes. Chemical and spectral analysis were used to determine the chemical composition of the alloy [10]. The phase composition of the alloy was determined using the optical microscope "Neofot-21". The main results of micro-X-ray spectral analysis were obtained using the electron microscope JSM-6490 with the scanning prefix ASID-4D and energy-dispersive X-ray microanalyzer "Link Systems 860" with software. X-ray diffraction analysis was performed on DRON-3 diffractometer in monochromatized Fe-K $_{\alpha}$ radiation.

RESULTS AND THEIR DISCUSSION

The microstructure of the alloy in the cast state was represented by perlite and ferrite. Perlite had the fine morphology (Fig. 1, a).

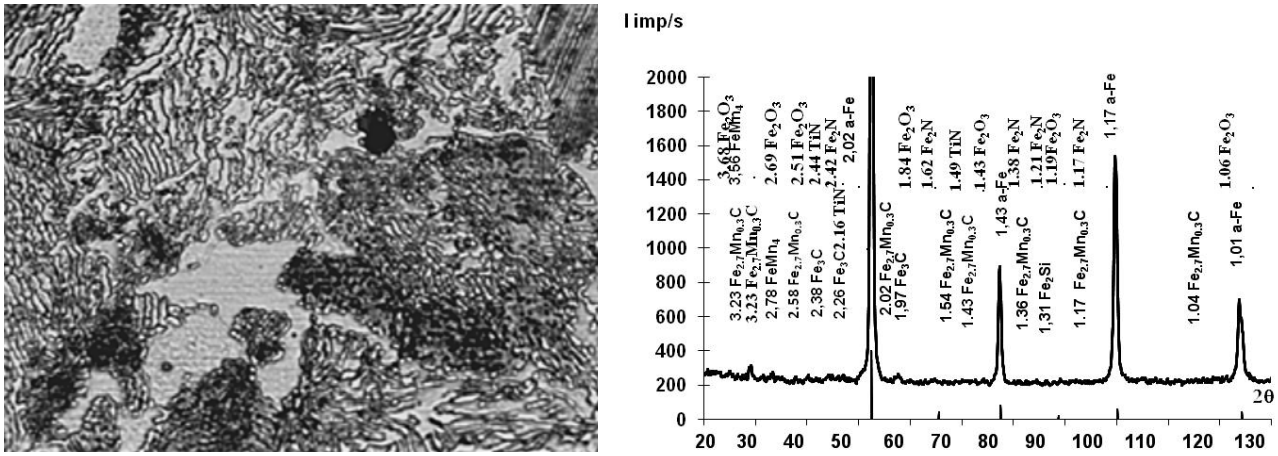

a b

Figure 1. - Microstructure (a) and diffraction pattern (b) of the alloy system Fe-Mn-Si-Ti-Al-NC

In the structure of the alloys were found multilayer inclusions, which had a size of 1.5-2 μm. The formation of the multiphase inclusion begins with the formation of the phase melt L → $Al(TiFe)_2O_3$. This phase additionally contains manganese 2.55% (at.), Silicon 1.0% (at.), Nitrogen 4.23% (at.) (Fig. 2).

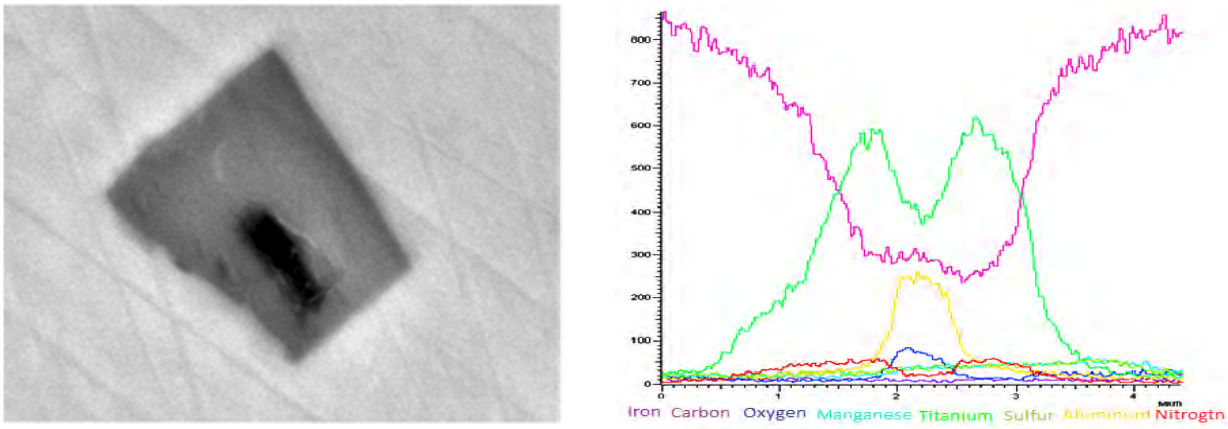

a b

Figure 2. Microstructure of multiphase inclusion (a) and diffractogram of chemical elements distribution

The phase ($Ti_{0.3}$ $Fe_{0.2}$) ($N_{0.3}$ $C_{0.2}$) is placed around it, with stereometry of TiN phase. The formation of the phase ($Ti_{0.3}$ $Fe_{0.2}$) ($N_{0.3}$ $C_{0.2}$) occurs by peritectic reaction – L + $Al(TiFe)_2O_3$ → ($Ti_{0.3}$ $Fe_{0.2}$) ($N_{0.3}$ $C_{0.2}$). This phase is alloyed with manganese up to 2.4% (at.), Silicon up to 0.3% (at.), Aluminum up to 2.0% (at.). It should be noted that the nitrides that were formed during the crystallization of this alloy contained sulfur up to 0.9% (at.). In addition, the following inclusions were identified in the microstructure using X-ray phase and micro-X-ray diffraction analyzes: oxides - Fe_3AlO_2 with FeO stereometry, $(FeAl)_2O_3$ with Fe_2O_3 stereometry, $F_{21}Ti_{18}O_{24}N_{17}C_{17}$, $Fe_{40}Al_{15}O_{31}$; nitrides - FeTiN with stereometry TiN, Ti_2 FeN ($Ti_{41}Fe_{26}N_{27}$); carbonitrides - $Fe_{50}N_{15}C_{30}$, Fe_3NC_2, $Fe_3Ti_2N_3C$ ($Fe_{20}Ti_{28}$ $N_{35}C_{15}$), FeTiNC, $Fe_2(NC)$, which were alloyed

with manganese up to 0.5% (at.), silicon 1.0% (at.), titanium up to 5.0% (at.). At doping the iron alloys with manganese, silicon and titanium, any pure carbides of manganese, silicon and titanium do not exist, but there are complex carbides [11]. In addition, the formation of $Fe_{2.7}Mn_{0.3}C$, carbide was determined in the structure and phase $FeMn_4$, Fe_2Si.

It should be noted that the inclusions found in the microstructure were located not only along the grain boundaries, but also in the pearlite grain.

The presence of ferrite was observed around the inclusions and along the boundaries of perlite. On the diffraction pattern, the α-iron lines were shifted toward larger angles compared to pure α-iron (Fig. 1, b). The obtained result can be explained by the fact that the ferrite is alloyed with manganese, silicon, titanium, aluminum and the lattice parameter of α-iron changes. Micro X-ray spectral studies of the surface of the samples performed in this work showed that ferrite could contain up to 1.0% (at.) Manganese, 1.7% (at.) Silicon, 1.0% (at.) Titanium, 0.032% (at.) Carbon.

Thus, additional alloying with titanium and aluminum leads to the decrease in the content of manganese silicite in ferrite in comparison with the data given in [6-7]. Perlite cementite was alloyed with manganese up to 2.0% (at.), Titanium 1.2% (at.), Silicon 1.2% (at.), And aluminum 0.4% (at.).

It is known that the lattice parameter of the BCC of iron at room temperature has the numerical value of 2,862 Å [12]. As can be seen from table 1, additional doping of the Fe-Mn-Si-C alloy with titanium, aluminum and nitrogen leads to the increase in the lattice parameter of α-iron [6]. The obtained result can be explained by the fact that in the α-iron lattice it is possible to replace iron atoms with manganese, silicon, titanium or aluminum.

Table 1. Lattice parameter, crystallite size, dislocation density, degree of microstresses in α-Fe

Lattice parameter, Å	Block sizes L, Å	Degree of microstress	Dislocation density, cm^{-2}
2.867	1184	$1.05\cdot10^{-3}$	$28\cdot10^{10}$

The structure of α-Fe has the volume-centered lattice and belongs to the spatial group O_h^9 - Im3m with 8 atoms in the first coordination sphere [13]. Each atom of the BCC lattice has six tetrahedral and three octahedral pores. Of the six atoms surrounding the octahedral pore, two are closest to the others. The arrangement of carbon atoms in theBCC lattice can be described as follows: the arrangement of carbon atoms in the octahedral pore, which has four nearest metal atoms at the distance of 2.02 Å, and two at the distance of 1.43 Å, each metal atom has 8 neighbors, which are located on distances of 2.48 Å from each other.

To determine the solubility limit of manganese, silicon, aluminum, titanium in α-iron and the effect of these elements on the solubility of carbon, the quasi-chemical method was used [14].

The interaction of Fe-Fe, Fe-C, Fe-Si, Fe-Mn, Fe-Al, Fe-Tit and Fe-V_a atoms, where V_a is the vacancy which can be considered as follows: the interaction energies of atomic pairs $\nu_{FeFe}, \nu_{FeSi}, \nu_{Fe\mathrm{Va}}, \nu_{FeMn}, \nu_{FeAl}, \nu_{FeTi}$. The energy of interaction between metal and carbon atoms at the distance of 2.02 Å is denoted by – ν_{FeC}, $\nu_{SiC}, \nu_{TiC}, \nu_{MnC}$. For carbon atoms located at the distance of 1.43 Å – $\nu^1_{FeC}, \nu^1_{SiC}, \nu^1_{TiC}, \nu^1_{MnC}$. The results presented in paper [7] were used for numerical values of the interaction energy of pairs of atoms.

The free energy of ferrite can be determined by the formula: $F = E - kT\ln W$, where E is the internal energy of ferrite, W is the thermodynamic probability of the placement of atoms in the nodes of the crystal lattice of ferrite, k = 1.38 ·10^{-23} J / K is the Boltzmann constant, T is the absolute temperature. Thus, the free energy of ferrite is determined as follows:

$$
\begin{aligned}
F = &-8\left(N_{Fe}N_{\mathrm{Ti}}\nu_{FeTi} + N_{Fe}N_{Fe}\nu_{FeFe} + N_{Mn}N_{Fe}\nu_{MnFe} + N_{Si}N_{Fe}\nu_{SiFe}\right)\\
&-4\left(N_{Fe}N_C\nu_{FeC} + N_{Mn}N_C\nu_{MnC} + N_{Si}N_C\nu_{SiC} + N_{Ti}N_C\nu_{TiC} + N_{Fe}N_{\mathrm{Va}}\nu_{FeN_{Ti}}\right) -\\
&-2\left(N_{Fe}N_C\nu^1_{FeC} + N_{Mn}N_C\nu^1_{MnC} + N_{Si}N_C\nu^1_{SiC} + N_{Ti}N_C\nu^1_{TiC} + N_{Fe}N_{\mathrm{Va}}\nu^1_{FeN_{Ti}}\right) -\\
&-kT(8(N_{Fe} + N_{Mn} + N_{Si} + N_{\mathrm{Ti}} + N_{Va})(\ln(N_{Fe} + N_{Mn} + N_{Si} + N_{\mathrm{Ti}} + N_{Va}) - 1) -\\
&-8N_{Fe}(\ln N_{Fe} - 1) - 8N_{Mn}(\ln N_{Mn} - 1) - 8N_{Si}(\ln N_{Si} - 1) - 8N_{Ti}(\ln N_{Ti} - 1)) -\\
&-4(N_C + N_{Va})(\ln(N_C + N_{Va}) - 1) - N_C(\ln N_C - 1) -\\
&-N_{Va}(\ln N_{Va} - 1)
\end{aligned}
$$

To calculate the solubility of carbon in α-iron, we need to find the solution of the system of equations:

$$
\frac{\partial F}{\partial N_C} = 0,\ \frac{\partial F}{\partial N_{Va}} = 0,\ \frac{\partial F}{\partial N_{Si}} = 0,\ \frac{\partial F}{\partial N_{Mn}} = 0,\ \frac{\partial F}{\partial N_{Fe}} = 0,\ \frac{\partial F}{\partial N_{Ti}} = 0. \qquad (1)
$$

The resulting system of equations (1) is transcendental. Usually the solution of such equations can be obtained graphically or numerically. But in the framework of this problem, it is expedient to consider the asymptotic solution of the equations. To do this, we present the logarithm included in each of the equations of system (1) in the form of Taylor series (this is acceptable under the conditions of its convergence):

To obtain the asymptotic estimate of the solution of system (1), it suffices to consider the first two terms of the development of logarithms.

The results of solving the system of equations showed that in α-iron it could dissolve in 0.016% (at.) Carbon, manganese up to 1.3% (at.), Silicon - 1.0% (at.), and titanium up to 0.5% (at.). It should be noted that additional alloying of Fe-Mn-Si-C alloy with titanium, aluminum and nitrogen leads to the decrease in the content of silicon, manganese and carbon in α-iron [6-7].

The obtained results can be explained by the fact that additional alloying of Fe-Mn-Si-C alloy with titanium, aluminum and nitrogen promotes the formation of complex carbides of oxides, nitrides and carbonitrides, and reduces the content of doped elements in α-iron.

CONCLUSIONS

1. The analysis of the phase composition of alloys of Fe-Mn-Si-Ti-Al-NC system with the carbon content of 0.50-0.60% (wt.), Silicon 0.80-0.90% (wt.), Manganese 0, 90-0.95% (wt.), Aluminum - 0.20-0.30% (wt.), Titanium - 0.02-0.03% (wt.), Nitrogen - 0.015-0.02% (wt.), the rest - iron. It is determined that after crystallization and a number of phase transformations the structure of the alloy was presented by α -iron, alloyed with cementite, oxides, nitrides and carbonitrides.

2. Using the quasi-chemical method we obtain or the dependence of the free energy of the solid solution of α-iron doped with silicon, manganese and titanium. It was found that in α-iron it can dissolve in 0.022% (at.) carbon, manganese up to 1.6% (at.), Silicon - 1.0% (at.), and titanium up to 0.5% (at.), which is in agreement with the experimental results.

3. It is established that the maximum solubility of carbon, manganese, titanium and silicon in α-iron of Fe-Mn-Si-C alloys is lower in comparison with their solubility in the corresponding binary systems.

The work was performed within the project КС.013.17 “Development of a scientifically-coated complex of technological solutions for the production of new generation railings with new operating authorities” (State Str. No. 0117U004145)

ORCID IDs

Nataliia Yu. Filonenko, https://orcid.org/0000-0003-1219-348X; **Olexander I. Babachenko,** https://orcid.org/0000-0003-4710-0343
Hanna A. Kononenko, https://orcid.org/0000-0001-7446-4105; **Alexander S. Baskevich**, https://orcid.org/0000-0002-3227-5637

REFERENCES

[1] Y. Tu, L. Huang,, et al., Materials Science and Technology, **34(7)**, 780 (2018), https://doi.org/10.1080/02670836.2017.1407558
[2] C. Zhu, et. al. Ultramicroscopy, **107**(9), 808 (2007), https://doi.org/10.1016/j.ultramic.2007.02.033
[3] G. Miyamoto, Oh J, Hono K, et al., Acta Mater. **55(15)**, 5027 (2007), https://doi.org/10.1016/j.actamat.2007.05.023
[4] Y.Y. Tu, Z. G. Mao, Q. Zhang, et. al, Mater Lett. **134**, 84 (2014), https://doi.org/10.1016/j.matlet.2014.07.057
[5] I. Gutierrez-Urrutia, ISIJ International, **61**(1), 16 (2021), https://doi.org/10.2355/isijinternational.ISIJINT-2020-467
[6] N. Filonenkoa A. Babachenko, G. Kononenko, and E. Domin, East. Eur. J. Phys, **4**, 90 (2020), https://doi.org/10.26565/2312-4334-2020-4-12
[7] J. Miettinen, V.-V. Visuri, and T. Fabritius, *Thermodynamic description of the Fe–Al–Mn–Si–C system for modelling solidification of steels,* (University of Oulu, Oulu, 2019). pp. 704, http://jultika.oulu.fi/files/isbn9789526222516.pdf
[8] P. Głowacz, M. Tenerowicz-Żaba, M. Sułowski, and J. Konstanty, International Journal NDTDays, II(3), (2019).
[9] Ch. Krishna Ande, H.F. Marce, Metallurgical and Materials Transactions, **A 4436**, 43A (2012), https://doi.org/10.1007/s11661-012-1229-y
[10] S.V. Tverdokhlebova, Visnyk Dnipropetrovskogo nacionalnogo universitetu. Serija Fizika. Radioelektronika, **14**(12/1), 100 (2007).
[11] O.V. Akymov, and S.M. Nury, Eastern-European Journal of Enterprise Technologies, **6**(11/78), 35 (2015), https://doi.org/10.15587/1729-4061.2015.56370
[12] A.P. Huliaev, and A.A. Huliaev, *Металловедение* [*Metalscience*], (Midalliance, 2011), pp. 644. (in Russian)
[13] M.P. Shaskolskaya, *Кристаллография* [*Crystallography*], (Vyisshay Shkola, Moscow, 1984), pp.376. (in Russian)
[14] Z.A. Matysina, and M.I. Milyan, *Теория растворимости примеси в упорядоченных фазах* [*Solubility theory residual element in ordered phase*], (DGU, Dnipro, 1991). pp.180.(in Russian).

ДОСЛІДЖЕННЯ СТРУКТУРНОГО СКЛАДУ СПЛАВІВ СИСТЕМИ Fe-Mn-Si-Ti-Al-N-C ТА РОЗЧИННОСТІ ЕЛЕМЕНТІВ В α- ЗАЛІЗІ

Н.Ю. Філоненко[a,b], О. І. Бабаченко[b], Г. А. Кононенко[b], О.С. Баскевич[c]
[a]Дніпровський державний медичний університет
[b]Інститут чорної металургії ім. З.І. Некрасова НАН України (ІЧМ НАНУ)
[c]Український державний хіміко-технологічний університет

В роботі проведене дослідження структурних складових сплавів системи Fe-Mn-Si-Ti-Al-N-C з вмістом карбону 0,50-0,60 % (мас.), силіцію 0,80-0.90 % (мас.), мангану 0,90-0.95 % (мас.), алюмінію – 0.20-0.30 % (мас.), титану – 0.02-0.03 % (мас.), азоту – 0.015-0.02 % (мас.) решта – залізо. Для визначення структурного стану сплавів використовували мікроструктурний, мікрорентгеноспектральний та рентгенофазовий аналізи. Показано, що після кристалізації та низки фазових перетворень структура сплаву була представлена α- залізом, легованим цементитом, оксидами, нітридами та карбонітридами. З застосуванням квазіхімічного методу отримали залежність вільної енергії твердого розчину α-заліза легованого силіцієм, манганом та титаном. В α-залізі може розчинятись до 0,016 % (ат.) карбону, мангану до 1,3 % (ат.), силіцію – 1,0 % (ат.), а титану до 0.5 % (ат.), що узгоджується з експериментальними результатами.

Ключові слова: комплексне легування сталі алюмінієм, титаном і азотом; включення; оксиди; нітриди; карбонітриди; ферит, вільна енергія фериту

EAST EUROPEAN JOURNAL OF PHYSICS. 4. 124-129 (2021)
DOI: 10.26565/2312-4334-2021-4-15 ISSN 2312-4334

SIMULATION OF A HIGH-ENERGY ELECTRON BEAM TRANSMISSION THROUGH TITANIUM AND KAPTON® THIN FILMS†

Tetiana V. Malykhina[a,b,*], Stepan G. Karpus[b], Oleg O. Shopen[b], Valerii I. Prystupa[b]
[a]*Kharkiv V.N. Karazin National University*
4, Svobody sq., 61022, Kharkiv, Ukraine
[b]*National Science Center "Kharkiv Institute of Physics and Technology"*
2, Academicheskaya str., 61108, Kharkiv, Ukraine
**Corresponding Author: malykhina@karazin.ua*
Received 30 September 2021; revised October 10, 2021; accepted November 15, 2021

The results of computer simulation of the high-energy electrons passage through thin layers of titanium (Ti) and polyimide Kapton® ($C_{22}H_{10}N_2O_5$) in the energy range from 3 MeV to 20 MeV are presented. Simulation is carried out using the Geant4 toolkit. The number of primary electrons is 6.24×10^7 for each series of calculations. The thickness of the titanium foil in the model experiment is 50 μm, the thickness of the Kapton® film is 110 μm. The energies of primary electrons are chosen as following: 3 MeV, 5 MeV, 10 MeV, 15 MeV, and 20 MeV. The purpose of the calculations is to reveal the possibility of using the Kapton® film in the output devices of linear electron accelerators. It was necessary to calculate the probable values of the energy absorbed in a Kapton® film and in a titanium foil for each value of primary electrons energy. Another important characteristic is the divergence radius of the electron beam at a predetermined distance from the film, or the electron scattering angle. As a result of calculations, the energy spectra of bremsstrahlung gamma-quanta, formed during the passage of electrons through the materials of the films, are obtained. The most probable values of the energy absorbed in the titanium foil and in the Kapton® film are calculated. The scattering radii of an electron beam for the Kapton® film and also for the titanium foil at a distance of 20 centimeters are estimated. These calculations are performed for electron energies of 3 MeV, 5 MeV, 10 MeV, 15 MeV, and 20 MeV. A comparative analysis of the obtained results of computational experiments is carried out. It is shown that the ratio of the total amount of bremsstrahlung gamma quanta in the case of use the Kapton® film is approximately 0.56 of the total amount of bremsstrahlung gamma quanta when using the titanium foil. The coefficients of the ratio of the electrons scattering radius most probable value after passing through Kapton® to the most probable value of the scattering radius after passing through titanium are from 0.62 at electrons energy of 3 MeV to 0.57 at electrons energy of 20 MeV. The analysis of the calculated data showed that the use of Kapton® ($C_{22}H_{10}N_2O_5$) as a material for the manufacture of output devices for high-energy electron beams is more preferable in comparison to titanium films, since the use of Kapton® instead of titanium makes it possible to significantly reduce the background of the generated bremsstrahlung gamma quanta and reduce the scattering radius of the electron beam.
Keywords: bremsstrahlung, Geant4-simulation, LINAC, Kapton® film, ($C_{22}H_{10}N_2O_5$), interaction of radiation with matter, electron angular scattering.
PACS: 07.05.Tp, 02.70.Uu, 81.40wx

Linear electron accelerators are used to solve various applied problems related to the processes and effects occurring during the interaction of ionizing radiation with matter. These problems include irradiation of samples required for research in nuclear and medical physics, in particular, the improvement of methods for the production of radioisotopes. Applied studies of irradiated materials properties, as well as many other problems, are no less important tasks. All these tasks in most cases require an electron beam with certain characteristics. For example, there is a requirement to minimize the radius of the electron beam, as well as to reduce the bremsstrahlung background after passing through the output device of the electron accelerator. Great attention is paid to the study of the influence of the primary electron flux angular distribution on the irradiated object in work [1]. In particular, the study of the absorbed dose distribution was carried out depending on the penetration depth of the electron beam. The electron scattering angle at low energies (up to 10 MeV) was calculated for polyethylene layers. The layers thickness was more than 1 radiation length. The results of these studies suggest the expediency of studying the angular scattering of electrons after passing through thin polymer films, which could be used in the output devices of accelerators. We chose Kapton® ($C_{22}H_{10}N_2O_5$) as an object to study the possibility of optimizing the accelerator beams parameters in the energy range from 3 MeV to 20 MeV. We took into account the physical and chemical properties [2, 3] of Kapton®, in particular, the Kapton® density, the value of the critical energy, etc. Kapton® is a fairly stable material in the range from low temperatures to +400°C [4]. Despite the widespread use of Kapton® [3, 4] in medicine, aircraft construction, astronautics, vacuum technology, and other industries, the possibility of its use in accelerator technology has not been sufficiently studied.

MATERIALS AND METHODS

We carried out a computer simulation of the passage of electron beams of various initial energies through a titanium foil. This simulation is carried out in order to study the possibility of optimizing the parameters of the output

† ***Cite as:*** T.V. Malykhina, S.G. Karpus, O.O. Shopen, and V.I. Prystupa, East. Eur. J. Phys. **4**, 124 (2021), https://doi.org/10.26565/2312-4334-2021-4-15

devices of linear electron accelerators. The output window of a typical LINAC usually is made of titanium foil. We consider the titanium foil thickness of 50 microns. This value of the titanium foil thickness is selected in accordance to the real foil thickness used in the LINAC-300 accelerator at National Scientific Center "Kharkiv Institute of Physics and Technology". The energies of primary electrons are equal to 3 MeV, 5 MeV, 10 MeV, 15 MeV, and 20 MeV in the simulation. The fluencies of bremsstrahlung gamma quanta and the electron beam scattering radii are calculated at a distance of 20 centimeters after the foil, since an irradiated target is supposed to be installed in this position. Similar calculations are performed for the Kapton® film with a thickness of 110 μm. This thickness of the Kapton® film was chosen for our research because of studies of the mechanical properties of various thicknesses of Kapton® films were carried out earlier in laboratory conditions. The obtained data were in good agreement with the data from the manufacturers' catalogs [5], as well as with the literature data [6].

We have developed a computer program in the C++ language that uses the Geant4 toolkit [7–9] for modeling the processes of interaction of radiation with matter. The primary electrons amount is 6.24×10^7, and the threshold E_{cut} for particle tracking [7] is 0.1 μm. We have used the low energy `emlivermore` model of the `PhysicsList` unit. This model is based on the data of EEDL, EPDL libraries [9], and is applicable for electromagnetic processes modeling in the energy range from 100 eV to 20 GeV.

The results of Monte Carlo simulation of the absorbed energy spectra in the titanium foil and in the Kapton® film are shown in Figure 1. The calculation results are normalized to 1 primary electron. It can be seen that the most probable value of the absorbed energy in the case of using Kapton® is slightly less than the most probable value of the absorbed energy in the case of using titanium. The value of the absorbed energy is calculated for two values of the primary electrons energy. These values are 3 MeV and 15 MeV. The most probable values of the absorbed energy in Kapton® and titanium are obtained as a result of statistical data processing. The value of the electron energy absorbed in Kapton® is 17 keV for both values of the primary electron energy. The most probable energy absorbed in titanium is 20 keV for primary electrons with energy of 3 MeV, and 21 keV for primary electrons with an energy of 15 MeV. The statistical error is no more than 1%. The step of creating histograms when calculating the energy spectra is 1 keV.

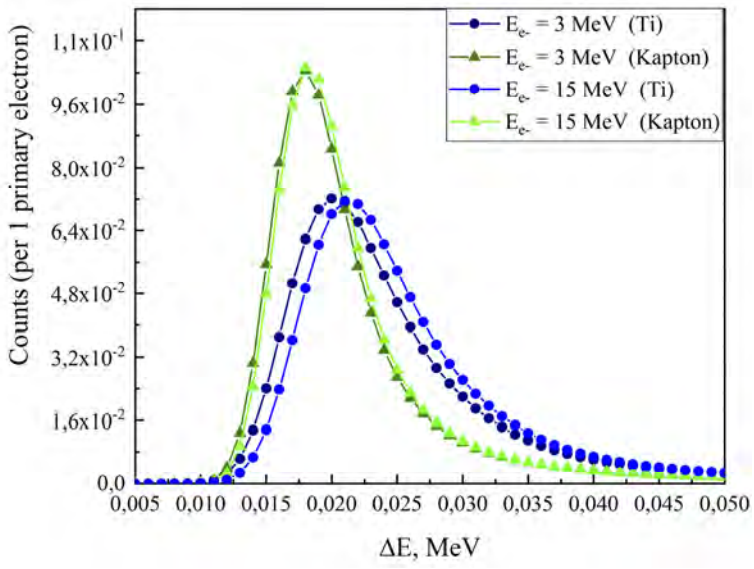

Figure 1. Energy spectra of absorbed energy in the titanium foil and in the Kapton® film for primary electron energies of 3 MeV and 15 MeV (triangles indicate values for Kapton®, circles indicate values for titanium)

The total and average values of the energy absorbed in titanium and in Kapton® during the passage of 3 MeV electrons beam, as well as 15 MeV electrons beam are presented in Table 1.

Table 1. Total (for $N_e=6.24\times10^7$) and average values of energy absorbed in titanium and in Kapton®

Titanium 50 microns		
Electrons energy, MeV	Total absorbed energy, MeV	Average value of absorbed energy, MeV
3	Sum= 1.79×10^6	Sum/N_e= 0.0286
15	Sum= 1.82×10^6	Sum/N_e= 0.0292
Kapton® 110 microns		
Electrons energy, MeV	Total absorbed energy, MeV	Average value of absorbed energy, MeV
3	Sum=1.514×10^6	Sum/N_e= 0.0243
15	Sum=1.514×10^6	Sum/N_e= 0.0243

The scattering radii of electrons at a distance of 20 cm after passing through a 50 μm thick titanium foil are estimated by the Monte Carlo method. A similar series of simulations is carried out to estimate the scattering radii of electrons after passing through a Kapton® film with a thickness of 110 μm. The distance of 20 cm after the foil is chosen as the position at which we estimate the electron scattering radius, because the irradiated sample will be placed at this position. The calculations are carried out for several values of the primary electrons energy. These values are 3 MeV, 5 MeV, 10 MeV, 15 MeV, 20 MeV. The number of simulated events is 6.24×10^7. The graphs characterizing the value of the scattering radius of the electron beam after passing through the titanium foil, as well as after passing through the Kapton® film, for each energy of primary electrons are shown in Figure 2. The corresponding values of the scattering radii, as well as the comparison result, are presented in Table 2. The error in determining the scattering radii of electrons is 0.1 mm. This error is due to the size of the histograms calculating step during data processing. Graphs of changes in the values of the electrons scattering radii depending on the primary electrons energy for each of two materials are shown in Figure 3.

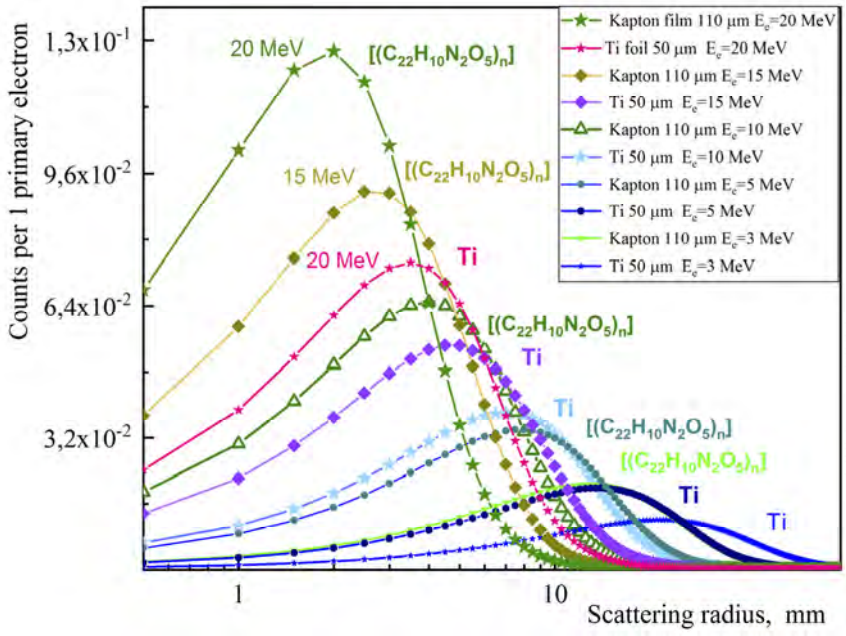

Figure 2. The scattering radius of electrons of various energies after passing through the titanium foil as well as after the Kapton® film at 20 cm distance after the film or foil

Table 2. The most probable values of scattering radii of electrons at the distance of 20 cm after the titanium foil or the Kapton® film, as well as the ratio coefficient of the electron scattering radii

Electrons energy, MeV	The most probable scattering radius (mm) of electrons after the Kapton® film, 110 μm	The most probable scattering radius (mm) of electrons after the Ti foil 50 μm	The coefficient of the scattering radii ratio
3	13	21	0.62
5	8	14	0.57
10	4	7	0.57
15	2.5	4.5	0.56
20	2	3.5	0.57

It can be noted (Fig. 2, Table 2) that with an increase in the primary electrons energy, the scattering radius decreases both in the case of using titanium and in the case of using Kapton®. However, in the case of using the Kapton® film, we have a much smaller scattering radius. For example, the scattering radius for 10 MeV electrons when using Kapton® is 4 mm (Table 2). This value is even less than the scattering radius of 15 MeV electrons in the case of using the titanium film. The scattering radius of 15 MeV electrons is 4.5 mm.

It can be noted that the general tendency towards a decrease in the electrons scattering radius persists with an increase in the electron energy from 3 MeV to 20 MeV (Table 2). The scattering radius of electrons at the distance of 20 cm after passing through the Kapton® film is smaller than the scattering radius of electrons after passing through the titanium foil. Therefore, we can assume that the use of the Kapton® film instead of the titanium foil in the design of the linear electron accelerators output devices would make it possible to obtain narrower electron beam.

One of the tasks of this work is to determine the possibility of reducing the bremsstrahlung background after passing through the output device of the electron accelerator. The energy spectra of bremsstrahlung gamma quanta at

the distance of 20 cm after passing through the titanium foil, as well as after the Kapton® film, are shown in Figure 4. The calculation step for each spectrum is 100 keV.

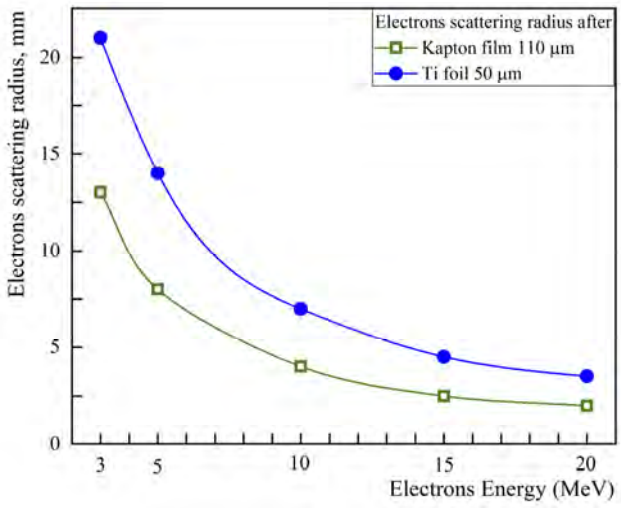

Figure 3. The comparison of the electrons scattering radii at the distance of 20 cm after the titanium foil (blue solid dots) as well as after the Kapton® film (green open points)

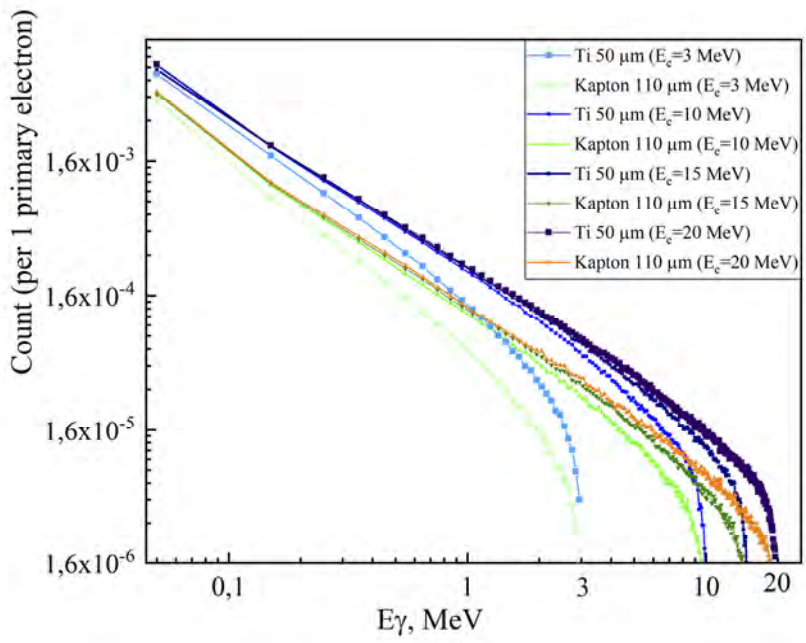

Figure 4. The comparison of the bremsstrahlung spectra at the distance of 20 cm after the titanium foil as well as after the Kapton® film for different values of the primary electrons energies

It can be seen (Figure 4) that the amount of bremsstrahlung gamma quanta at the distance of 20 cm after a 110 μm thick Kapton® film is less than the amount of bremsstrahlung gamma quanta after a 50 μm thick titanium foil for the same values of the primary electrons energy. The numerical values of the bremsstrahlung gamma quanta amount for each material, as well as the coefficient of their ratio, are presented in Table 3.

Table 3. The numerical values of the bremsstrahlung gamma quanta amount (S) for each material, as well as the coefficient of their ratio, at the distance of 20 cm after Kapton® or titanium

Electrons energy, MeV	S (for Kapton®)	S (for Ti)	S(Kapton®) / S (Ti)
3	452486	804833	0.562
10	634884	1.148E6	0.553
15	676580	1.198E6	0.564
20	724679	1.309E6	0.554

Figure 5 shows the values of the bremsstrahlung amount at the distance of 20 cm after the foil. Data are normalized to 1 primary electron.

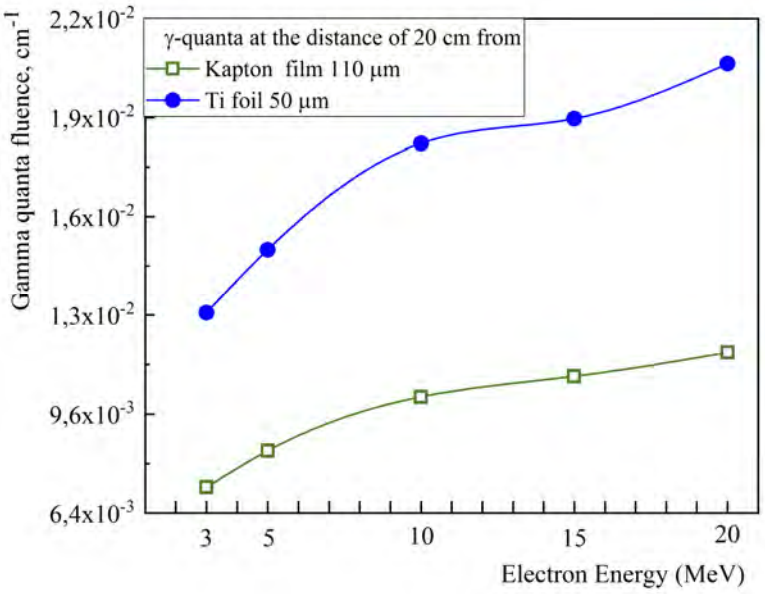

Figure 5. The comparison of the bremsstrahlung fluences at the distance of 20 cm after the titanium foil (blue solid points) as well as after the Kapton® film (green open points)

Gamma quanta are formed as a result of the primary electrons passage through the titanium foil, or the Kapton® film (Figure 5). It can be noted that in the case of using Kapton®, the fluence of bremsstrahlung gamma quanta is significantly less.

CONCLUSIONS

A series of simulations of the electron beam passage through 50 μm thick titanium foil, as well as through 110 μm thick Kapton® film, are carried out for electrons of various energies. The electron energies are 3 MeV, 5 MeV, 10 MeV, 15 MeV, and 20 MeV. The fluence values of bremsstrahlung gamma quanta after the passage of the foil as well as after the film are obtained as a result of simulation. The most probable values of the absorbed energy in the titanium foil and in the Kapton® film are calculated for each value of the primary electrons energy. The values of the most probable scattering radius of an electron beam after passing through a 50 μm thick titanium foil and after passing through a 110 μm thick Kapton® film were calculated for the same values of the primary electrons energy. A comparative analysis of the obtained results of computational experiments is carried out. It is shown that the ratio of the total amount of bremsstrahlung gamma quanta when using a Kapton® film is approximately 0.56 to the total amount of bremsstrahlung gamma quanta when using a titanium film. The ratio coefficients of the most probable values of the scattering radii of electrons at a distance of 20 cm after passing through Kapton® to those after titanium are from 0.62 at 3 MeV electrons energy to 0.57 at 20 MeV electrons energy.

Analysis of the calculated data showed that the use of Kapton® ($C_{22}H_{10}N_2O_5$) as a material for the manufacture of high-energy electron beam output devices is promising in comparison to titanium films. The use of Kapton® instead of titanium makes it possible to significantly reduce the background of the produced bremsstrahlung gamma rays, as well as to reduce the scattering radius of the electron beam. Additional studies of the material thermal stability are necessary for the final decision on the experimental research.

ORCID IDs

Tetiana V. Malykhina, https://orcid.org/0000-0003-0035-2367; **Stepan G. Karpus**, https://orcid.org/0000-0002-1087-9245
Oleg O. Shopen, https://orcid.org/0000-0003-3158-8081; **Valerii I. Prystupa**, https://orcid.org/0000-0002-0789-2991

REFERENCES

[1] V.G. Rudychev, V.T. Lazurik, and Y.V. Rudychev, Radiation Physics and Chemistry, **186**, 109527 (2021), https://doi.org/10.1016/j.radphyschem.2021.109527
[2] M. Tanabashi et al. (Particle Data Group), Phys. Rev. D, **98**, 030001 (2018), https://doi.org/10.1103/PhysRevD.98.030001
[3] K.L. Mittal, *Polyimides: Synthesis, Characterization, and Applications Vol. 1*, (Springer, 1984), pp. 626.
[4] K.L. Mittal, *Polyimides and Other High Temperature Polymers: Synthesis, Characterization, and Applications, Vol. 5*, (Taylor & Fransis Group, 2009), pp. 436.
[5] *Kapton® Polyimide Films*, https://www.dupont.com/electronic-materials/kapton-polyimide-film.html
[6] A. Sharma, N.L.Singh, M.S.Gadkari, V. Shrinet, and D.K. Avasthi, Journal of Macromolecular Science, Part A: Pure and Applied Chemistry, **42**(2), 149 (2004), http://dx.doi.org/10.1081/MA-200046970
[7] Geant4 Collaboration, Book For Application Developers, Release 10.6, http://cern.ch/geant4-userdoc/UsersGuides/ForApplicationDeveloper/BackupVersions/V10.6c/fo/BookForApplicationDevelopers.pdf

[8] Geant4 Collaboration, *Physics Reference Manual*, http://cern.ch/geant4-userdoc/UsersGuides/PhysicsReferenceManual/BackupVersions/V10.6c/fo/PhysicsReferenceManual.pdf
[9] *Geant4 Guide For Physics Lists, Release 10.6*, https://geant4-userdoc.web.cern.ch/UsersGuides/PhysicsListGuide/BackupVersions/V10.6c/fo/PhysicsListGuide.pdf

МОДЕЛЮВАННЯ ПРОХОДЖЕННЯ ПУЧКА ВИСОКОЕНЕРГЕТИЧНИХ ЕЛЕКТРОНІВ ЧЕРЕЗ ТОНКІ ПЛІВКИ ТИТАНУ ТА КАПТОНУ®

Т.В. Малихіна[a,b], С.Г. Карпусь[b], О.О. Шопен[b], В.І. Приступа[b]
[a]*Харківський національний університет імені В.Н. Каразіна*
[b]*Національний науковий центр «Харківський фізико-технічний інститут»*

Представлені результати комп'ютерного моделювання проходження високоенергетичних електронів через тонкі шари титану (Ti) та Каптону® ($C_{22}H_{10}N_2O_5$) у діапазоні енергій від 3 МеВ до 20 МеВ. Моделювання проведено з використанням бібліотеки класів Geant4. Кількість первинних електронів дорівнювала 6.24×10^7 для кожної серії розрахунків. Товщина титанової фольги у модельному експерименті дорівнювала 50 мкм, товщина плівки з Каптону® дорівнювала 110 мкм. Енергії первинних електронів обрані такими: 3 МеВ, 5 МеВ, 10 МеВ, 15 МеВ та 20 МеВ. Метою розрахунків є виявлення можливості використання плівки з Каптону® у вивідних пристроях лінійних прискорювачів електронів. Тому необхідно розрахувати вірогідні значення поглиненої у каптоні та у титані енергії для кожної енергії первинних електронів. Також важливою характеристикою є радіус розходження пучка електронів на певній відстані від плівки, або кут розсіювання електронів. У результаті розрахунків отримано енергетичні спектри гальмівних гамма-квантів, що утворюються під час проходження електронів через речовину плівок. Розраховані найбільш вірогідні значення поглиненої у титані та у Каптоні® енергії. Оцінені радіуси розходження пучка електронів для плівки з каптону, а також для титанової плівки, на відстані 20 сантиметрів. Ці розрахунки проведені для енергії електронів 3 МеВ, 5 МеВ, 10 МеВ, 15 МеВ та 20 МеВ. Проведений порівняльний аналіз отриманих результатів обчислювальних експериментів. Показано, що коефіцієнт відношення сумарної кількості гальмівних гамма-квантів у разі використання плівки з Каптону® становить приблизно 0.56 до сумарної кількості гальмівних гамма-квантів у разі використання плівки з титану. Коефіцієнти відношення найбільш вірогідного значення радіусу розсіювання електронів після проходження Каптону® до найбільш вірогідного значення радіусу розсіювання після титану дорівнює від 0.62 при енергії електронів 3 МеВ до 0.57 при енергії електронів 20 МеВ. Аналіз розрахункових даних показав перспективність використання Каптону® ($C_{22}H_{10}N_2O_5$), як матеріалу для виготовлення вивідних пристроїв пучків високоенергетичних електронів у порівнянні з плівками титану, оскільки дозволяє суттєво знизити супутній фон утворених гальмівних гамма-квантів та зменшити радіус розсіювання пучка електронів.

Ключові слова: гальмівне випромінювання, Geant4-моделювання, лінійний прискорювач електронів, плівка з Каптону®, $C_{22}H_{10}N_2O_5$, взаємодія випромінювання з речовиною, кутове розсіювання електронів.

EAST EUROPEAN JOURNAL OF PHYSICS. 4. 130-134 (2021)
DOI: 10.26565/2312-4334-2021-4-16 ISSN 2312-4334

RESEARCH OF INTERACTION PROCESSES OF FAST AND THERMAL NEUTRONS WITH SOLUTION OF ORGANIC DYE METHYL ORANGE†

Sergey P. Gokov[a], Yuri G. Kazarinov[a,b], Sergiy A. Kalenik[a], Valentin Y. Kasilov[a], Tetiana V. Malykhina[a,b], Yegor V. Rudychev[a,b], Vitaliy V. Tsiats'ko[a,*]

[a]National Science Center "Kharkiv Institute of Physics and Technology"
1, Akademichna str., 61108, Kharkiv, Ukraine
[b]Kharkiv V.N. Karazin National University
4, Svobody sq., 61022, Kharkiv, Ukraine
**Corresponding Author: stek@kipt.kharkov.ua*
Received September 28, 2021; revised October 25, 2021; accepted November 26, 2021

The emergence of powerful sources of ionizing radiation, the needs of nuclear energy, technology and medicine, as well as the need to develop reliable methods of protection against the harmful effects of penetrating radiation stimulated the development of such branches of science as radiation chemistry, radiation biology, radiation medicine. When an organic dye solution is exposed to ionizing radiation, it irreversibly changes color. As a result, the absorbed dose can be determined. The processes of interaction of neutron fluxes with an aqueous solution of an organic dye methyl orange (MO) – $C_{14}H_{14}N_3O_3SNa$, containing and not containing 4% boric acid, have been investigated. The work was carried out on a LINAC LUE-300 at NSC KIPT. A set of tungsten plates was used as a neutron-generating target. The electron energy was 15 MeV, the average current was 20 μA. The samples were located behind the lead shield and without it, with and without a moderator. Using the GEANT4 toolkit code for this experiment, neutron fluxes and their energy spectra were calculated at the location of experimental samples without a moderator and with a moderator of different thickness (1-5 cm). An analysis of the experimental results showed that when objects without lead shielding and without a moderator are irradiated, the dye molecules are completely destroyed. In the presence of lead protection, 10% destruction of the dye molecules was observed. When a five-centimeter polyethylene moderator was installed behind the lead shield, the destruction of dye molecules without boric acid on thermal neutrons was practically not observed. When the fluxes of thermal and epithermal neutrons interacted with a dye solution containing 4% boric acid, 30% destruction of dye molecules was observed due to the exothermic reaction 10B (n, α). The research has shown that solutions of organic dyes are a good material for creating detectors for recording fluxes of thermal and epithermal neutrons. Such detectors can be used for radioecological monitoring of the environment, in nuclear power engineering and nuclear medicine, and in the field of neutron capture therapy research in particular.
Keywords: organic dye, neutrons, dosimeters
PACS: 61.72.Cc, 61.80.Hg, 78.20.Ci, 87.80.+s, 87.90.+y, 07.05.Tp , 78.70.−g

The emergence of powerful sources of ionizing radiation, the needs of nuclear energy and technology, as well as the need to develop reliable methods of protection against the harmful effects of penetrating radiation stimulated the rapid development of radiation chemistry, radiation biology, and radiation medicine. At present, intensive development of chemical dosimetry methods is underway. The most convenient model objects for researching the processes of interaction of ionizing radiation with a substance are liquid and solid solutions of organic dyes and pigments [1-14]. Organic dye solutions have intense absorption and fluorescence bands in the visible region of the spectrum. When the dye solution is exposed to ionizing radiation, an irreversible loss of dye color occurs (a decrease in the intensity of the long-wavelength band of the absorption spectrum). In this case, the shape of the absorption spectrum band, as a rule, does not change.

Previous researches [12-13] have shown that irreversible radiation destruction of dyes in solutions occurs as a result of the oxidation of organic dyes by radicals and radical ions formed during the radiolysis of solvents ($OH^{\cdot}$, $HO_2^{\cdot}$, etc.). A relatively stable product of the radiolysis of solvents, hydrogen peroxide, also participates in the decolorization of dye solutions.

The rate of radiation destruction of a dye in a solution essentially depends on both the chemical nature of the dye and the nature and physicochemical properties of the solvent. The lowest radiation resistance of dyes is observed in aqueous solutions, the highest - in solvents whose molecules do not contain oxygen atoms (for example, in dimethylamine), and in solid solutions (for example, in polymer films) [1-14]. So, from the decrease in the intensity of the long-wave absorption band of the dye solution under the action of ionizing radiation, it is possible to determine the value of the radiation dose. Thus, an organic dye solution can serve as a radiation dose detector and be used for radiation monitoring of the environment [2-6]. For example, aqueous solutions of dyes can be successfully used to visually determine the radiation dose in the range of 0.003 – 0.5 Mrad, and polymer films colored with dyes- 0.3 – 40 Mrad.

According to literature data, the USA and England produce polymethyl methacrylate and paper coated with polyvinyl chloride containing a dye for use in dosimetry. Depending on the degree of degradation of the dye, it is

† ***Cite as:*** S.P. Gokov, Yu.G. Kazarinov, S.A. Kalenik, V.Y. Kasilov, T.V. Malykhina, Ye.V. Rudychev, and V.V. Tsiats'ko, East. Eur. J. Phys. **4**, 130 (2021), https://doi.org/10.26565/2312-4334-2021-4-16

possible to determine doses in the range from 0.1 to 6 Mrad. The US industry produces cellophane films containing some colorants. These films are widely used to measure doses of various types of radiation because they change color when exposed to them. The degree of discoloration is linearly dependent on the dose. In this case, the dose range is from 0.1 to 10 Mrad. All these systems are characterized by the independence of the readings from changes in the dose rate and temperature during irradiation. These systems retain their properties for a sufficiently long period of time after irradiation, which greatly simplifies the measurement process. Before irradiation, they can be stored in the dark for a long time. These systems can be used to determine the spatial distribution of absorbed doses that are received under the influence of high-energy electrons. With their help, the processes of radiation processing of various materials are controlled in production conditions. To solve such problems, a chemical dosimetry method [14] was developed at the Pisarzhevsky Institute of Physical Chemistry of the Academy of Sciences of the Ukrainian SSR, based on the use of films made of colored polyvinyl alcohol. Thus, irradiation of organic dyes can lead to various photochemical reactions. At present, the nature of these processes is still poorly understood.

FORMULATION OF THE PROBLEM

In this work, the processes of interaction of neutron fluxes with an aqueous solution of an organic dye methyl orange (MO) – $C_{14}H_{14}N_3O_3SNa$, containing and not containing 4% boric acid, have been researched. The work was carried out on a LINAC LUE – 300 at NSC KIPT. The work was carried out with the aim of researching the processes of interaction of neutrons with matter, as well as the possibility of creating detectors based on these materials for registering fluxes of thermal and fast neutrons.

A number of nuclear reactions are used to register neutrons, such as: ^{10}B (n, α) ^{7}Li, ^{6}Li (n, α) T, ^{3}He (n, p) T, elastic, inelastic scattering, etc. The methods used in the work are elastic neutron scattering and nuclear reaction ^{10}B (n, α) ^{7}Li.

Elastic neutron scattering

In the case of researching fast neutron fluxes in the elastic scattering reaction, the neutron transfers part of its kinetic energy to the nucleus. The neutron gives up the maximum share of energy in a central (head-on) collision with nuclei. The mass of the neutron differs little from the mass of the proton. A neutron transfers all of its kinetic energy to the nucleus of a hydrogen atom in the event of a central collision. Elastic neutron scattering by hydrogen nuclei is used to register fast neutrons from recoil protons. In this work, an aqueous solution of methyl orange was used. Irreversible radiation destruction of the dye occurred due to the radiolysis of water as a result of oxidation by radicals ($OH^{\cdot}$, $HO_2^{\cdot}$, etc.) and the kinematic destruction of dye molecules in collisions with fast neutrons.

Nuclear reaction ^{10}B (n, α) ^{7}Li

Natural boron consists of two isotopes: ^{10}B (18.2%) and ^{11}B (81.8%). Slow neutrons interact intensely with the nuclei of the ^{10}B isotope. In the exothermic reaction ^{10}B (n, α), α-particles and a ^{7}Li nucleus appear. This reaction takes place through two channels:

$$^{10}B+n\rightarrow(^{7}Li)^{*}+\alpha+E_1;$$

$$^{10}B+n\rightarrow{}^{7}Li+\alpha+E_2,$$

where E_1 and E_2 – the reaction energy, is released in the form of the kinetic energy of the reaction products. In the first channel, the ^{7}Li nucleus is formed in an excited state with an excitation energy of 0.48 MeV. The excited state of ^{7}Li is indicated by an asterisk. The transition of the nucleus from the excited state to the ground state is accompanied by the emission of a γ-quantum with an energy of E_γ = 0.48 MeV. Therefore, the first reaction channel can be rewritten as follows:

$$^{10}B + n \rightarrow {}^{7}Li + \alpha + E_\gamma + E_1.$$

The energy of the ^{10}B (n, α) ^{7}Li reaction is 2.78 MeV. One part of the energy (E_γ = 0.48 MeV) is carried by the γ-quantum, the other part (E_1 = 2.30 MeV) is released in the form of the kinetic energy of the α-particle and the lithium nucleus. At the same time, the Energy E_1 = 2.30 MeV is made up of E_α and E_{Li}. The fraction of the α-particle is E_α = 1.47 MeV, and the fraction of the lithium nucleus is E_{Li} = 0.83 MeV. The probability of the reaction proceeding through the first channel is 93% for free neutrons with an energy of about 10 keV. Then this probability gradually decreases, reaching a value of 0.3 at a neutron energy of 1.8 MeV and again increases to 0.5 at a neutron energy of 2.5 MeV. In the second channel, the ^{10}B (n, α) ^{7}Li reaction proceeds with a 7% probability for slow neutrons and, accordingly, with a higher probability for fast neutrons. The reaction energy E_2 = 2.78 MeV in this case is completely carried by the α particle and the lithium nucleus.

Thus, when boric acid is added to the dye solution and it is irradiated with a flux of thermal neutrons, the above reactions occur. In this case, the interaction of high-energy α-particles and ^{7}Li nuclei with dye molecules leads to their destruction, and the presence of a gamma quantum in the first reaction leads to radiolysis of water and ionization of atoms in molecules.

EXPERIMENTAL RESEARCHES

The work was carried out at the NSC KIPT on the linear electron accelerator LUE – 300. The electron beam was exposed to a neutron-generating target located at a distance of 40 cm from the output foil. The electron energy was 15 MeV, and the average beam current was 20 μA. The neutron-producing target was a set of tungsten plates. In the immediate vicinity of the target, a lead shield was assembled against scattered electrons and the accompanying gamma background 5 cm thick.

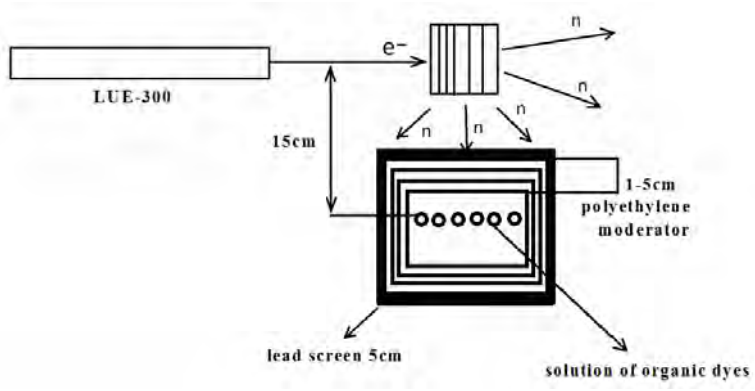

Figure 1. Experiment scheme

The schematic of the experiment is shown in Fig. 1. The dye solution in a glass test tube was placed inside a lead shield at a distance of 15 cm from the electron beam axis. The irradiation time was 1 hour, which corresponds to a total neutron flux of 10^{11} n/cm^2 at the location of the samples. The thickness of the lead shield was 5 cm. Between the lead shield and the test tube, there was a moderator made of polyethylene with a thickness of 1–5 cm.

Figure 2. Photo of the exit of the LUE – 300 accelerator and the lead shielding of the samples under study.

Figure 2 shows a photograph of the output of the LUE-300 accelerator and the lead shielding of the samples under study.

Using the GEANT4 program code [9] for this experiment, the energy spectra of neutron fluxes inside the lead shield at the location of the experimental samples were calculated. The simulation results are shown in Fig. 3. Six cases were considered: 0 - the spectrum of neutrons inside the shield at the location of the sample without a polyethylene moderator, 1–5– spectra of neutrons inside the shield with a gradual increase in the thickness of the moderator from 1 to 5 cm. From Fig. 3 it can be seen that with an increase in the thickness of the moderator layer, the number of fast neutrons decreases significantly (with an increase in the thickness of the moderator from 0 to 5 cm, the number of fast neutrons decreases by a factor of 10). At the same time, the number of thermal neutrons increases insignificantly, approximately 2 times in comparison with the case without a moderator. The total neutron flux for the case without a moderator at the location of the samples for the presented experiment was 10^{11} n/cm^2.

Several experiments were carried out in the work. In one case, tubes with an aqueous solution of the organic dye methyl orange without boric acid were placed inside and outside the lead shield at a distance of 15 cm from the neutron-producing target.

The main absorption spectra of the irradiated and unirradiated dye are shown in Fig. 4

Fig. 4 that when objects without lead shielding and without a moderator are irradiated, the dye molecules are completely destroyed. This is mostly due to their interaction with scattered electrons and gamma quanta. In the presence of lead shielding, a 10% destruction of dye molecules was observed due to their interaction with fast neutron fluxes.

In another case, one tube with an aqueous solution of an organic dye containing boric acid and the second tube without boric acid were located inside a lead shield in the presence of a polyethylene moderator 5 cm thick. These test tubes were located at a distance of 15 cm from the neutron-forming target. The main absorption spectra of the irradiated and unirradiated dye with and without boric acid are shown in Fig. 5 and 6.

In Fig. 5 and 6, it can be seen that when a polyethylene moderator was installed after a lead shield 5 cm thick and in front of the target, the destruction of dye molecules without 4% boric acid on thermal neutrons was practically not observed. The target consisted of test tubes with solutions of dye (MO) – $C_{14}H_{14}N_3O_3SNa$. When a dye solution containing 4% boric acid interacted with fluxes of thermal and epithermal neutrons, a 30% destruction of dye molecules was observed due to the exothermic reaction 10B (n, α). Researches have shown that solutions of organic dyes, on the

one hand, can be a good material for creating detectors of ionizing radiation, in particular, for fluxes of thermal and epithermal neutrons. On the other hand, solutions of organic dyes are a convenient object for studying the processes of interaction of ionizing radiation with matter as a whole.

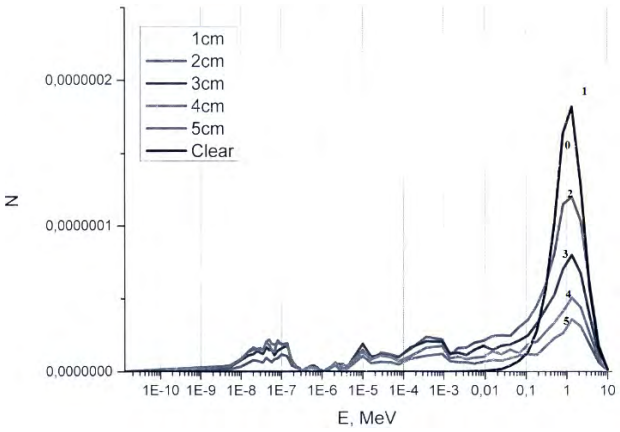

Figure 3. Simulation results using the GEANT4 code of the energy spectra of neutron fluxes from a neutron-producing target (electron energy 15 MeV, current 20 μA) with polyethylene moderators of different thicknesses: 1–5 cm and without them.

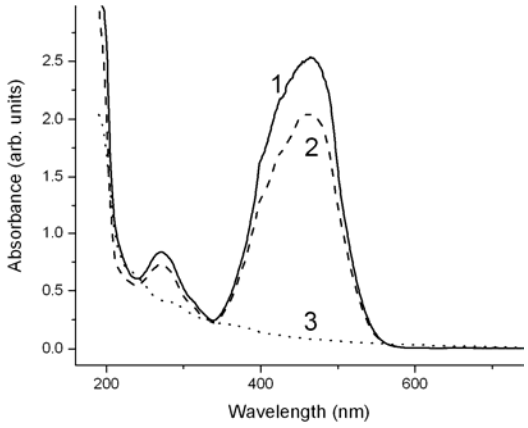

Figure 4. Main absorption spectra of irradiated and unirradiated dye.1 – before irradiation; 2 – irradiated with Pb shield; 3 – irradiated without Pb shield

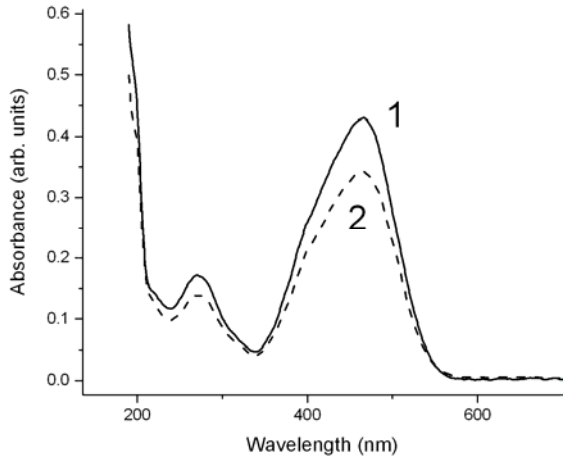

Figure 5. Optical absorption spectra of an aqueous solution of a dye before (1) and after (2) irradiation with neutron fluxes in the presence of a polyethylene moderator

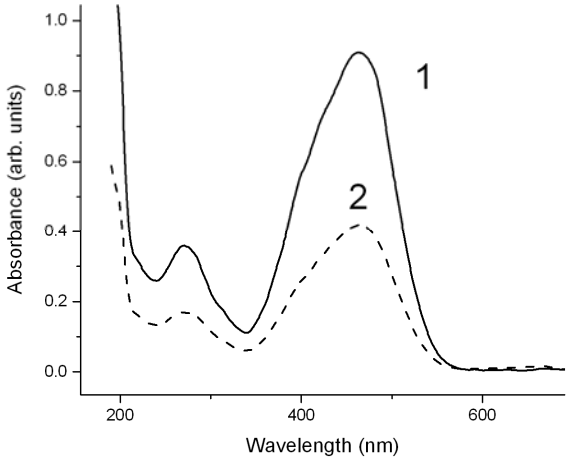

Figure 6. Optical absorption spectra of an aqueous solution of a dye with boric acid before (1) and after (2) irradiation with neutron fluxes in the presence of a polyethylene moderator.

CONCLUSION

In this work, the processes of interaction of neutron fluxes with an aqueous solution of an organic dye methyl orange (MO) – $C_{14}H_{14}N_3O_3SNa$, containing 4% boric acid, and with an aqueous solution of the same dye without boric acid were investigated. In the experimental and simulated parts of the work, these samples were located behind the lead screen and without it. Also, a polyethylene moderator with a thickness of 0 to 5 cm was used in the work.

The energy spectra of neutron fluxes at the location of the experimental samples were calculated using the GEANT4 program code.

An analysis of the experimental results showed that when objects without lead shielding and without a moderator are irradiated, the dye molecules are completely destroyed. This happens mostly due to organic dye interaction with scattered electrons and gamma quanta. In the presence of lead shielding, 10% destruction of dye molecules was observed due to their interaction with fast neutron flux. When a five-centimeter polyethylene moderator was installed behind the lead shield, the destruction of dye molecules without boric acid on thermal neutrons was practically not observed. When the fluxes of thermal and epithermal neutrons interacted with a dye solution containing 4% boric acid, 30% destruction of dye molecules was observed due to the exothermic reaction ^{10}B (n, α).

The researches have shown that a solution of organic dye MO is a good material for creating detectors for recording fluxes of thermal and epithermal neutrons, which currently have no analogues. Such detectors can be used for radiation monitoring of the environment, in nuclear power engineering and nuclear medicine, and in the field of neutron capture therapy research in particular.

ORCID IDs
Sergey P. Gokov, https://orcid.org/0000-0002-3656-3804; **Yuri G. Kazarinov**, https://orcid.org/0000-0001-5143-8545
Sergiy A. Kalenik, https://orcid.org/0000-0002-1460-5081; **Valentin I. Kasilov**, https://orcid.org/0000-0002-1355-311X
Tetiana V. Malykhina, https://orcid.org/0000-0003-0035-2367; **Yegor V. Rudychev**, https://orcid.org/0000-0002-1453-2062
Vitaliy V. Tsiats'ko, https://orcid.org/0000-0002-7347-0500

REFERENCES

[1]. B.I. Stepanov, *Введение в химию и технологию органических красителей* [*Introduction to the chemistry and technology of organic dyes*], (Khimiya, Moscow, 1977), pp. 488, (in Russian)
[2]. V.I. Popechits, in: *Spektroskopiya i lyuminestsentsiya molekulyarnykh sistem* [*Spectroscopy and luminescence of molecular systems*], edited by E. S. Voropai, K. N. Soloviev, D. S. Umreiko, (BSU, Minsk, 2002), pp. 275-286. (in Russian)
[3]. V.I. Popechits, Vestnik BSU. Ser. 1, **3**, 33 (2002). (in Russian)
[4]. V.I. Popechits, Journal of Applied Spectroscopy, **70**(1), 34 (2003). (in Russian)
[5]. V.I. Popechits, and O.N. Kravtsova, in: *Применение молекулярной люминесценции и спектроскопии к исследованию структуры и свойств вещества* [*Application of molecular luminescence and spectroscopy to the study of the structure and properties of matter*] edited by D.S. Umreyko, A.A. Min'ko, (BSU, Minsk, 2006), pp. 53–56. (in Russian)
[6]. V.I. Popechits, Vestnik BSU. Ser. 1, **2**, 49 (2008). (in Russian)
[7]. Milinchuk V.K., Klinshpont E.R., and Tupikov V.I. *Основы радиационной стойкости органических материалов* [*Fundamentals of Radiation Resistance of Organic Materials*], (Energoatomizdat, Moscow, 1994). Pp. 256. (in Russian)
[8]. V.K. Milinchuk, Radiation Chemistry, Soros Educational Journal, **4**, 24 (2000). (in Russian)
[9]. Geant4 Collaboration, *Physics Reference Manual*, http://cern.ch/geant4-userdoc/UsersGuides/PhysicsListGuide/fo/PhysicsListGuide.pdf
[10]. Y.A. Afanas′eva, V.V. Bobkov, S.P. Hokov, V.V. Hrytsyna, O.V. Sukhostavets′, and D.I. Shevchenko, UFZH, **55**(2), p.182 (2010). (in Ukrainian)
[11]. S.S. Alimov, I.O. Afanas′yeva, V.V. Bobkov, S.P. Hokov, V.V. Hrytsyna, and D.I. Shevchenko, UFZH, **56**(3), 211 (2011). (in Ukrainian)
[12]. A.Yu. Buki, S.P. Gokov, Yu.G. Kazarinov, S.A. Kalenik, V.I. Kasilov, S.S. Kochetov, P.L. Makhnenko, I.V. Mel'nitskiy, A.V. Tverdokhvalov, V.V. Tsyats'ko, and O.A. Shopen, PAST, **5**(93), 98 (2014), https://vant.kipt.kharkov.ua/ARTICLE/VANT_2014_5/article_2014_5_98.pdf
[13]. Ayzatskiy N.I., Afanas'yev S.N., Buki A.Yu., Gokov S.P., Ozhegov L.S., Parkhomenko A.A., Khvastunov V.M., and Shevchenko N.G. *Исследования атомных ядер электронами и фотонами с энергией до 300 МэВ* [*Investigation of Atomic Nuclei with Electrons and Photons with Energy Up to 300 MeV*], (*NSC "Kharkiv Institute of Physics and Technology"*, Kharkiv, 2017), pp. 393. (in Russian)
[14]. V.S. Ivanov, Радиационная химия полимеров [Radiation chemistry of polymers], (Khimiya, Leningrad, LO, 1988), pp. 320. (in Russian)

ДОСЛІДЖЕННЯ ПРОЦЕСІВ ВЗАИМОДІЇ ПОТОКІВ ШВИДКИХ І ТЕПЛОВИХ НЕЙТРОНІВ З РОЗЧИНОМ ОРГАНІЧНОГО БАРВНИКА МЕТИЛОВИЙ ОРАНЖЕВИЙ

С.П. Гоков[a], Ю.Г. Казарінов[a,b], С.О. Каленик[a], В.І. Касілов[a], Т.В. Малихіна[a,b], Е.В. Рудичев[a,b], В.В. Цяцько[a]
[a]Національний науковий центр Харківський фізико-технічний інститут
вул. Академічна, 1, 61108, Харків, Україна
[b]Харківський національний університет імені В.Н. Каразіна
майдан Свободи, 4, 61022, Харків, Україна

Поява потужних джерел іонізуючого випромінювання, потреби ядерної енергетики, технологій і медицини, а також необхідність розробки надійних способів захисту від шкідливої дії проникаючої радіації стимулювали розвиток таких галузей науки, як радіаційна хімія, радіаційна біологія, радіаційна медицина. При впливі іонізуючого випромінювання на розчин органічного барвника відбувається його необоротне знебарвлення. У наслідок чого, можна визначити величину поглиненої дози. У даній роботі досліджувалися процеси взаємодії потоків нейтронів з водним розчином органічного барвника метиловий оранжевий (МО) - $C_{14}H_{14}N_3O_3SNa$, що містить і не містить 4% борної кислоти. Робота виконувалася на лінійному прискорювачі електронів ЛУЕ-300 ННЦ ХФТІ. У якості мішені, що продукує нейтрони, використовувався набір вольфрамових пластин. Енергія електронів становила 15 МеВ, середній струм 20 мкА. Зразки перебували за свинцевим захистом і без нього з отеплювачем і без нього. З використанням бібліотеки класів GEANT4 для даного експерименту були розраховані потоки нейтронів і їх енергетичні спектри в місці розташування експериментальних зразків без сповільнювача і зі сповільнювачем різної товщини (1-5 см). Аналіз результатів експерименту показав, що при опроміненні об'єктів без свинцевого захисту і без отеплювача відбувається повне руйнування молекул барвника. При наявності свинцевої захисту спостерігалося 10-процентне руйнування молекул барвника. При установці п'яти сантиметрового поліетиленового сповільнювача за свинцевим екраном руйнування молекул барвника без борної кислоти на теплових нейтронах практично не спостерігалося. При взаємодії потоків теплових і епітеплових нейтронів із розчином барвника, що містить 4% борну кислоту, спостерігалося 30% руйнування молекул барвника за рахунок протікання екзотермічної реакції ^{10}B (n, α). Проведені дослідження показали, що розчини органічних барвників, є хорошим матеріалом для створення детекторів реєстрації потоків теплових і епітеплових нейтронів. Такі детектори можуть використовуватися для радіаційного моніторингу навколишнього середовища, в ядерній енергетиці і ядерній медицині, зокрема в галузі досліджень нейтрон-захоплювальной терапії.

Ключові слова: органічний барвник, нейтрони, дозиметри

EAST EUROPEAN JOURNAL OF PHYSICS. 4. 135-139 (2021)
DOI: 10.26565/2312-4334-2021-4-17 ISSN 2312-4334

POSITIVE DEVIATION OF THE HALL-PETCH RELATIONSHIP FOR ALUMINUM CONDENSATES ALLOYED WITH IRON†

Evgeniy Lutsenko[a,*], Anatoly Zubkov[b], Maria Zhadko[b], Eduard Zozulya[b]
[a]*National Science Center "Kharkiv Institute of Physics and Technology", 1, Akademichna str., Kharkiv 61108, Ukraine*
[b]*National Technical University "Kharkiv Polytechnic Institute", 2, Kyrpychova str., 61002 Kharkiv, Ukraine*
**Corresponding Author: lytsenko87@gmail.com*
Received July 23, 2021; revised November 17, 2021; accepted November 19, 2021

The structure and strength properties of vacuum aluminum condensates alloyed with iron in the concentration range of 0.1 – 3.2 at. % is studied in the paper. It is shown that up to a concentration of about 2 at. % Fe, the grain size decreases, the strength properties increase and the lattice parameter values of these objects remain unchanged. It is found that at an iron concentration of up to ~ 2 at. % its atoms are concentrated in the grain boundaries of the aluminum matrix metal in the form of grain boundary segregation. At high concentrations, the structure of condensates is a supersaturated solution of iron in the FCC crystal lattice of aluminum. Highly dispersed $Al_{13}Fe_4$ intermetallic compounds are present at the grain boundaries and within the volume of grains. It has been found that the Hall-Petch coefficient for one-component aluminum condensates is 0.04 MPa·m$^{1/2}$, which is typical for this metal. For Al-Fe condensates, a positive deviation from the Hall-Petch dependence is observed and the coefficient k increases to 0.4 MPa·m$^{1/2}$ for a structure with grain boundary segregations and to 0.14 MPa·m$^{1/2}$ for condensates containing intermetallic compounds. The obtained experimental results are explained by the different structural-phase state of the grain boundaries of the aluminum matrix.
Keywords: Grain boundary segregation, vacuum condensate, intermetallic compound, Al-Fe, grain size.
PACS: 61.66.Dk, 64.75.Op, 68.35.Fx, 68.55.Ln, 81.05.Ni, 81.10.Fq, 81.15.Kk

The level of strength properties of nanostructured metals is mainly determined by grain boundary hardening. Its value depends on the grain size and the state of the grain boundaries. A large number of theoretical and experimental studies are devoted to the problem of dispersing the grain structure of metallic materials. Less attention has been paid to the study of the chemical composition and structure of grain boundaries. First of all, this was due to the problems of testing grain boundaries at the atomic level. As a result, it became possible to purposefully influence the properties of grain boundaries by varying their chemical composition and structural-phase state, which can lead to a dramatic increase in various properties of nanostructured metals. For example, alloying of aluminum films, foils, or coatings obtained by physical vapor deposition in vacuum (PVD-technology) with iron allows reducing the grain size of these materials to nanoscale dimension, increasing their strength properties and recrystallization temperature. As a result, these objects are widely used in the aviation and aerospace industries, primarily in parts exposed to thermal effects [1-3]. At the same time, the physical mechanisms of the modifying effect of iron on aluminum are currently controversial and insufficiently studied.

In this regard, the purpose of this work is to study the effect of iron concentration on the structure and strength properties of vacuum Al-Fe condensates.

LITERATURE REVIEW

The grain boundary hardening of metallic materials is described by the Hall-Petch strengthening [4, 5], which for the yield strength has the following form

$$\sigma_y = \sigma_0 + kd^{-1/2}$$

where σ_y is the yield strength, σ_0 is the resistance to the motion of dislocations in a single crystal, k is the Hall-Petch coefficient, d is the grain size.

The authors of various studies use the Hall-Petch equation to describe various strength properties: tensile strength, yield strength, hardness, however, the most correct is to use the yield stress in order to avoid veiling effects associated with strain hardening, brittleness, plasticity, etc. [6].

For the majority of one-component metals and alloys in a wide range of grain sizes from several to hundreds of micrometers, the constancy of the values of the exponent (-1/2) and the k value is maintained [7]. At the same time, in a number of studies [8, 9] facts of deviation from dependence (1) are noted both due to the change in the value of k and the exponent from -1/2 to -1. To explain these experimental results, many theoretical models have been proposed [6], among which the most famous are the following. 1. Compositional model of the grain structure, suggesting different properties of grain boundaries and intragranular volume, predicting changes in the exponent depending on grain size [10]. 2. Dislocation mechanisms, which involve changes in the value of k due to various ways of transferring deformation through the grain boundary [11]. 3. Models providing various options for the transition of translational

† ***Cite as:*** E. Lutsenko, A. Zubkov, M. Zhadko, and E. Zozulya, East. Eur. J. Phys. **4**, 135 (2021), https://doi.org/10.26565/2312-4334-2021-4-17

deformation mechanisms to rotational [12]. For nanostructured aluminum and its alloys, these circumstances are enhanced due to a significant spread in the values of the Hall-Petch coefficient, even for a single-component metal, the value of which is in the range of 0.02 – 0.29 MPa·m$^{1/2}$, depending on the production methods [11, 13], the method of the grain size measurement [6, 13], chemical purity of metal [14], etc. The authors of some studies have noted both positive [7] and negative deviations from the Hall-Petch dependence [15]. It should be noted that there is no unambiguous interpretation of the observed experimental results in the available literature [6]. An important feature of these studies is the underestimation or ignoring of impurities, alloying elements or modifiers, which can radically change the structural-phase state of grain boundaries. Suffice it to note that the content of the second component constituting ~ $1 \cdot 10^{-4}$ at. % in the volume of a matrix metal with a grain size of about 100 μm is capable of covering the entire area of grain boundaries with a monoatomic adsorption layer [16]. This state of the adsorption layers provides for the formation of strong interatomic bonds between the segregating substance and the matrix metal. As a result, the cohesive strength of grain boundaries increases, the tendency to brittle intercrystalline fracture increases and other properties improve. Depending on the combination of physical and mechanical properties of the constituent components of the metal, such grain boundary segregation can significantly change the strength and other properties of metals in general [17, 18].

RESEARCH METHODOLOGY

The objects of study were Al and Al-Fe condensates up to 50 μm thick, obtained by the PVD method, by evaporation of the constituent components from different sources and subsequent condensation of a mixture of their vapors on a non-orienting substrate in vacuum. The substrate temperature was 200–250°C. The concentration of alloying elements was monitored by the X-ray spectral method. Mechanical tests were carried out at room temperature in the active tension mode with a strain rate of 0.36 mm/min on a TIRATEST-2300 setup. The samples had the following geometry: width – 3 mm, thickness – 30 μm, length – 30 mm. Thus, the test conditions and geometric dimensions of these objects correspond to the methodology developed in [19]. The structure of the condensates was studied by X-ray diffractometry, light and transmission microscopy using DRON-3M, OptikaM XDS-3Met, and JEM-2100 devices, respectively.

RESULTS

Fig. 1, 2, 3 shows the concentration dependences of the grain size (d), lattice parameter (a) and yield strength (σ_y) of the aluminum matrix on the iron content in the condensates. It can be seen that up to a concentration of about 2 at. %, the value of d decreases and the value of a remains. It should be noted that the observed increased solubility of Fe is characteristic of such objects and exceeds the equilibrium solubility at room temperature, which is 0.025 at.% [20].

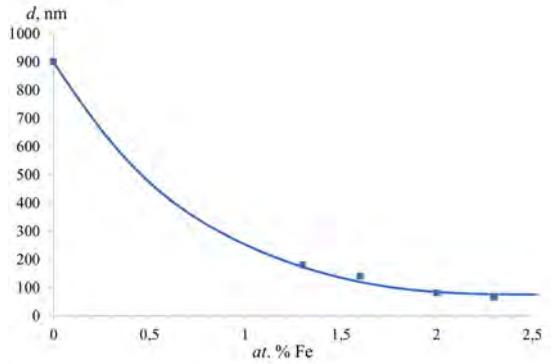

Figure 1. Dependence of the grain size of aluminum on the concentration of Fe.

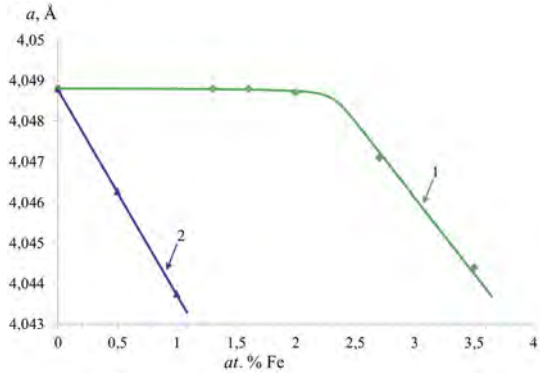

Figure 2. Dependence of the crystal lattice parameter of aluminum on the concentration of Fe
1 – lattice parameter, 2 – Vegard's law.

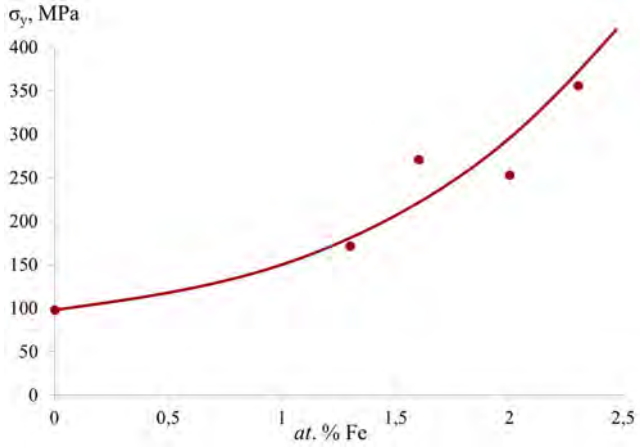

Figure 3. Dependence of the yield strength of aluminum on the concentration of Fe.

The electron diffraction patterns contain only diffraction reflections belonging to the FCC lattice of aluminum (Fig. 4). With a further increase in the iron content, the diffraction reflections of the intermetallic compound with the stoichiometric composition $Al_{13}Fe_4$ appear in the electron diffraction patterns (Fig. 5).

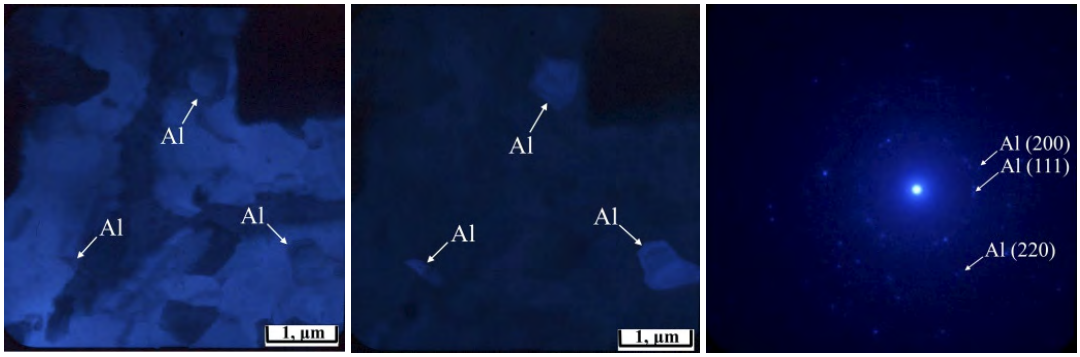

a b c

Figure 4. Electron-microscopic images of aluminum condensate
a – bright field image, b – dark field image, c – electron diffraction pattern.

A decrease in the lattice period of the FCC aluminum matrix is also observed, which indicates the formation of a supersaturated solution of iron in aluminum (Fig. 2).

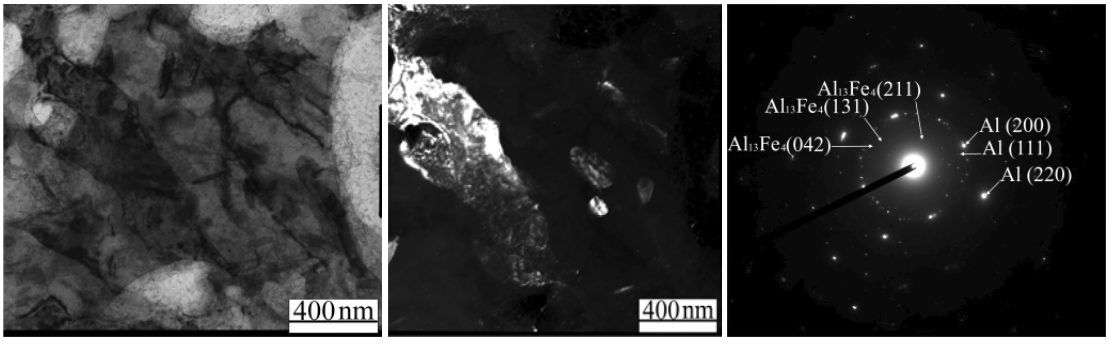

a b c

Figure 5. Electron-microscopic images of Al-3.2 at. % Fe condensate
a – bright field image, b – dark field image, c – electron diffraction pattern.

In the entire range of concentrations, an increase in the yield stress occurs (Fig. 3). It should be noted that the yield stress of unalloyed condensates is an order of magnitude higher than that of single-component aluminum obtained by crystallization from a melt, which strongly depends on the chemical purity of the matrix metal. For example, for aluminum A99 the yield stress is 10 MPa, for A8 is 20 MPa, and for A6 is 30 MPa [20].

These experimental results and the data of [17] allow us to conclude that in the concentration range of 0.1 - 2 at. % iron atoms are located in grain boundaries in the form of grain boundary segregation. At such iron content within the

grain, the structure is uniform, the grain size changes due to the blocking effect of monoatomic segregation of iron atoms during the condensate formation. According to the Seah theory [21], such grain boundary segregation of Fe in aluminum should increase the cohesive strength of grain boundaries. With a further increase in the iron content (over 2 at. %), a fundamental change in the structural state of the condensates occurs. The aluminum matrix is a supersaturated solution of iron in the FCC lattice of aluminum, as evidenced by a decrease in the lattice parameter (Fig. 2). Simultaneously, first at the grain boundaries, and then in the volume of the aluminum matrix, the formation of highly dispersed intermetallic compounds $Al_{13}Fe_4$ occurs (Fig. 5) [17].

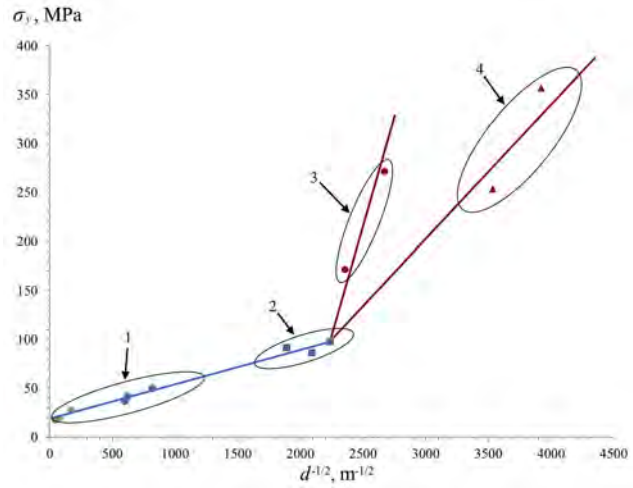

Figure 6. Hall-Petch dependences: 1 – [7, 22], 2 – Al condensates, 3 – Al-Fe condensates (up to 2 at. % Fe), 4 – Al-Fe condensates (over 2 at. % Fe).

Thus, there are three concentration regions with the following structural states: one-component condensates; two-component single-phase condensates with an iron concentration of up to 2 at. %, the grain boundaries of which contain segregation of iron, presumably in an atomic form, the so-called 2D structures; and finally condensates containing more than 2 at. % Fe, having a different intragranular structure and state of grain boundaries. These distinctive circumstances are reflected in the Hall-Petch dependence shown in Fig. 6. The value of the Hall-Petch coefficient determined for one-component aluminum is 0.04 MPa·m$^{1/2}$, which is in good agreement with the literature data for high-purity aluminum obtained by crystallization from the melt. For condensates containing grain-boundary monolayer segregation, the Hall-Petch coefficient increases significantly to 0.4 MPa m$^{1/2}$ (plot 3, Fig. 6). A further increase in the iron concentration leads to a decrease in the slope of the Hall-Petch dependence and the value of the coefficient k is 0.14 MPa m$^{1/2}$. Thus, in the concentration range from 0.1 to 3.2 at. % Al-Fe condensates have different states of grain boundaries and intragranular volume, resulting in a change in the value of k. Grain-boundary segregation of iron in the form of monoatomic layers increase the value of the k from 0.04 MPa·m$^{1/2}$ to 0.4 MPa·m$^{1/2}$, that is, there are positive deviations from the Hall-Petch dependence. It should be noted that a similar effect was observed by the authors of [8], who paid no attention and did not study the possibility of the formation of grain boundary segregation of iron.

Intermetallic compounds formed during condensation of a vapor mixture of aluminum and iron in the grain boundaries lead to the destruction of the adsorption layers and, as a result, the value of k decreases. For these objects, the level of strength properties is determined by the total action of solid solution, dispersion and grain boundary hardening.

CONCLUSIONS

1. The structure and strength properties of one-component and alloyed with iron aluminum condensates have been studied.

2. It was found that for one-component aluminum condensates the Hall-Petch dependence is observed. The Hall-Petch coefficient is 0.04 MPa m$^{1/2}$. This is in good agreement with the literature data obtained for high-purity aluminum crystallized from the melt.

3. Alloying with iron up to 2 at. % of aluminum condensates leads to a positive deviation from the Hall-Petch dependence and increases the Hall-Petch coefficient to 0.4 MPa·m$^{1/2}$.

4. Al-Fe condensates containing more than 2 at. % Fe, which is located within the grain boundaries of the matrix metal in the form of intermetallic compounds, have a Hall-Petch coefficient of 0.14 MPa·m$^{1/2}$. This value is higher than the analogous value for single-component aluminum, but less in comparison with condensates with grain-boundary segregations of iron in the form of monolayers.

ORCID IDs
Evgeniy Lutsenko, https://orcid.org/0000-0003-4523-9253; **Anatoly Zubkov**, https://orcid.org/0000-0001-9013-8158
Maria Zhadko, https://orcid.org/0000-0002-7979-9550; **Eduard Zozulya**, https://orcid.org/0000-0003-4598-8182

REFERENCES

[1] E.V. Lutsenko, V.A. Kreshchenko, N.D. Rud', O.V. Sobol', M.A. Glushchenko, and A.I. Zubkov, Metallofiz. Noveishie Tekhnol. **39**(5), 607 (2017), https://doi.org/10.15407/mfint.39.05.0607
[2] A. Inoue, F. Kong, S. Zhu, C.T. Liu, and F. Al–Marzouki, Materials Research, **18** (6), 1414 (2015), https://doi.org/10.1590/1516-1439.058815
[3] I.I. Tashlykova–Bushkevich, E.S. Gut'ko, V.G. Shepelevich, and S.M. Baraishuk, J Surf Investig X–RA, **2**(2), 310 (2008), https://doi.org/10.1134/S1027451008020286
[4] E.O. Hall, Proceedings of the Physical Society. Section B, **64** (9), 747 (1951), https://doi.org/10.1088/0370-1301/64/9/303
[5] N.J. Petch, Progress in Metal Physics, **5**, 1 (1954), https://doi.org/10.1016/0502-8205(54)90003-9
[6] R.W. Armstrong, *Hall–Petch Relationship: Use in Characterizing Properties of Aluminum and Aluminum Alloys* (Department of Mechanical Engineering University of Maryland College Park), (2016), pp. 1–30.
[7] N. Hansen, Acta Metall. **25**, 863 (1977), https://doi.org/10.1016/0001-6160(77)90171-7
[8] H.J. Choi, S.W. Lee, J.S. Park, and D.H Bae. Materials Transactions. **50**(3), 640 (2009), https://doi.org/10.2320/matertrans.MRA2008343
[9] S.A. Firstov, T.G. Rogul, and O.A. Shut, Fiz. Khim. Mekh. Mater. **6**, 5 (2009).
[10] O.O. Shut, Reports of the NAS of Ukraine, **9**, 70 (2014), https://doi.org/10.15407/dopovidi2014.09.070
[11] D. Tian, Ch–J Zhou, and J–H. He, Fractals, **26**(06), 1850083 (2018), https://doi.org/10.1142/S0218348X18500834
[12] S.N. Naik, and S.M. Walley, Journal of Materials Science, **55**, 2661 (2020), https://doi.org/10.1007/s10853-019-04160-w
[13] N. Kamikawa, T. Hirochi, and T. Furuhara, Metallurgical and Materials Transactions A, **50**(1), 234 (2018), https://doi.org/10.1007/s11661-018-5007-3
[14] W. Xu, and L.P. Dávila, Materials Science and Engineering: A. **710**, 413 (2018), https://doi.org/10.1016/j.msea.2017.10.021
[15] M.A. Tschopp, H.A. Murdoch, L.J. Kecskes, and K.A. Darling, The Minerals, Metals & Materials Society, **66**(6), 1000 (2014), https://doi.org/10.1007/s11837-014-0978-z
[16] E.V. Lutsenko, O.V. Sobol', and A.I. Zubkov, J. Nano–Electron. Phys. **7**(3), 03042 (2015), https://jnep.sumdu.edu.ua/en/full_article/1562
[17] Z.C. Cordero, B.E. Knight, and C.A. Schuh, International Materials Reviews. **61**(8), 495 (2016), https://www.tandfonline.com/doi/abs/10.1080/09506608.2016.1191808.
[18] S. Takaki, D. Akama, N. Nakada, and T. Tsuchiyama, Mater. Trans. **55**(1) 28 (2014), https://doi.org/10.2320/matertrans.MA201314
[19] A.I. Ilinskii, *Структура и Прочность Слоистых и Дисперсноупрочненных Пленок* [*Structure and Strength of Laminated and Dispersion Hardened Films*] (Metallurgiya, Moskow, 1986) pp. 143. (in Russian)
[20] J.E. Hatch, editor, *Aluminum: Properties and Physical Metallurgy* (American Society for Metals, Metals Park, Ohio, 1984), pp. 424.
[21] M.P. Seah, and E.D. Hondros, Proceedings of the Royal Society A. Mathematical and Physical Sciences, **335**(1601), 191 (1973), https://doi.org/10.1098/rspa.1973.0121
[22] H. Fujita, and T. Tabata, Acta Metall. **21** (4), 355 (1973), https://doi.org/10.1016/0001-6160(73)90191-0

ПОЗИТИВНЕ ВІДХИЛЕННЯ СПІВНОШЕННЯ ХОЛЛА-ПЕТЧА ДЛЯ КОНДЕНСАТУ АЛЮМІНІЮ, ЛЕГОВАНОГО ЗАЛІЗОМ

Є.А. Луценко[a], А.Б Зубков[b], М.Б. Жадько[b], Є.Б. Зозуля[b]
[a]Національний науковий центр «Харківський фізико-технічний інститут»
вул. Академічна, 1, м. Харків, Україна, 61108
[b]НТУ «Харківський політехнічний інститут»
вул. Кирпичова 2, м. Харків, Україна, 61002

В роботі вивчено структуру і характеристики міцності вакуумних конденсатів алюмінію, легованих залізом в діапазоні концентрацій 0,1 – 3,2 ат. %. Показано, що до концентрації приблизно 2 ат. % заліза відбувається зниження розміру зерна, підвищуються характеристики міцності і зберігається значення періоду кристалічної решітки даних об'єктів. Встановлено, що при вмісті заліза до ~ 2 ат. % Його атоми зосереджені в границях зерен матричного металу – алюмінію у вигляді зернограничних сегрегацій. При великих концентраціях структура конденсатів є пересиченим розчином заліза в ГЦК кристалічній решітці алюмінію. На границях і всередині об'єму зерен присутні високодисперсні інтерметалліди $Al_{13}Fe_4$. Виявлено, що для однокомпонентних конденсатів алюмінію виконується залежність Холла-Петча. Величина коефіцієнта Холла-Петча становить 0,05 МПа·м$^{1/2}$, яка характерна для цього металу. Для конденсатів Al-Fe спостерігається позитивне відхилення від залежності Холла-Петча і коефіцієнт k збільшується до 0,4 МПа·м$^{1/2}$ для структури з зернограничною сегрегацією і до 0,14 МПа·м$^{1/2}$ для конденсатів, які містять інтерметалліди. Отримані експериментальні результати пояснюються різним структурно-фазовим станом границь зерен алюмінієвої матриці.

Ключові слова: Зернограничная сегрегація, вакуумний конденсат, інтерметалід, Al-Fe, розмір зерна

EAST EUROPEAN JOURNAL OF PHYSICS. 4. 140-144 (2021)
DOI: 10.26565/2312-4334-2021-4-18 ISSN 2312-4334

X-RAY INDUCED LIGHT EMISSION OF YTTRIUM OXIDE†

Sergiy Kononenko, Oganes Kalantaryan, Vitaliy Zhurenko, Volodymyr Chishkala, Sergii Lytovchenko, Ruslan Skyba
V.N. Karazin Kharkiv National University
4 Svobody Sq., Kharkov, 61022, Ukraine
**Corresponding Author: sergiy.i.kononenko@gmail.com*
Received October 1, 2021; revised November 17, 2021; accepted November 19, 2021

The paper presents the experimental results of light radiation from Y_2O_3 ceramics caused by X-rays with energy up to 50 keV. The samples were made from commercial Y_2O_3 nanopowder by pressing and subsequent sintering in air at different temperatures from 1300 to 1500°C. Some samples sintered at 1500°C were additionally annealed at 1000°C for 10 hours. X-ray diffraction analysis of all samples did not reveal differences in the crystal structure that could be explained by heat treatment during sintering and annealing. The spectra of light emission in the wavelength range of 250-750 nm showed the presence of radiation from the electronic transitions of YO structures on the background of the luminescence of trivalent yttrium oxide. The presence of such lines of YO systems were observed also for the powder, which allows us to conclude that these structures appear on the surface of the crystallites during production. As the sintering temperature of the sample increased, the intensity of optical radiation increased. A significant difference in the effect of both temperature and sintering (annealing) time on the intensity of light emission of yttrium oxide was revealed. The intensity of the luminescent band, which is associated with the self-trapped exciton, increased with increasing thermal contribution (to estimate the contribution, we introduced a parameter equal to the product of temperature and the time of thermal action). The increase in spectral intensity in the second, third, fourth, and fifth line systems (especially for the system of lines with a maximum of λ=573.5 nm) considerably exceeded the one for self-trapped exciton. Our experimental results on the second, fourth and fifth systems of lines, which coincide well with the molecular lines YO, suggest that the heat treatment of the samples sintered from pressed Y_2O_3 powder leads to an increase in YO structures on the surface of the crystallites.
Keywords X-ray light emission, yttrium oxide, spectrum, YO structure, powder sintering.
PACS: 78

Development of new technologies is associated with the use of materials basing on wide class of inorganic refractory compounds (oxides, carbides, nitrides, borides and others), which, in addition to high melting temperatures, have high resistance, high fire-resistant and anti-corrosion properties in combination with important electrophysical and optical characteristics [1–2]. The sintering process is of particular importance for powder formation of ceramics. Herewith powder consolidation technologies can be divided into two main methods. The first is the molding of a material pressed at room temperature followed by sintering; the second, called sintering under pressure, is the simultaneous pressing and sintering of powders [1].

In most materials, including ceramics, physical and mechanical properties depend on the homogeneity of structure and density. As a rule, with increasing porosity, these characteristics decrease. The initial powders of ceramics of different fractions are subjected to different methods of shaping and heating at different rates. The larger the size of ceramic specimen, the slower it is necessary to raise the temperature during sintering, sometimes up to 0.1÷10 degree per minute, to suppress nonuniform heating processes caused by low thermal conductivity of oxides: nonuniform solidification contraction of ceramics on the surface and in the middle of specimen. At nonoptimal heating rate, ceramics with a large number of macro- and microdefects (pores, macro-and microcracks, dislocations) are formed. For small samples (laboratory) the rate of temperature rise can be much higher.

Among a wide class of ceramics, yttrium oxide (Y_2O_3) is of particular interest. This material has many applications, such as a supplement component in the processing of ceramic materials, substrates for semiconductor films, optical windows and doped with rare earth components elements for lasers and so on [3]. Structural stability in combination with unique mechanical properties also permits to consider Y_2O_3 as an interesting material for other applications. Its optical properties have been widely studied in terms of its use as a host matrix material for doping with rare earth ions such as samarium, erbium, gadolinium and europium for luminescence applications [see, for example, 4-6]. As for pure yttrium oxide, its optical properties have been less studied, nevertheless, in recent years a number of works has paid attention to its luminescent properties in connection with new possibilities of using as active elements of solid-state lasers [7-8] and luminophores [9].

Due to spectroscopic study (spectroscopy is the most versatile remote monitoring tool) astronomers have revealed presence of YO-components in various astrophysical sources. That is why YO-molecule spectrum is of considerable astrophysical interest because it is one of the main features in the spectra of cool star atmosphere [see, for example, 3-4]. Note that the presence of isolated YO-lines in the spectra of sintered ceramics of Y_2O_3 samples was confirmed in a number

† ***Cite as:*** S. Kononenko, O. Kalantaryan, V. Zhurenko, V. Chishkala, S. Lytovchenko, and R. Skyba, East. Eur. J. Phys. **4**, 140 (2021), https://doi.org/10.26565/2312-4334-2021-4-18

of works [12-13]. The authors [12] identified series of narrow bands that are located in the blue (435–510 nm), orange (515–640 nm), red (645–700 nm), and infrared (785–840 nm) spectral ranges as most pronounced in the spectra of commercially available powder and Y_2O_3 ceramics. They assumed that these series are emitted by bound YO-radicals, which are a part of the surface structure of yttria crystals. In our earlier experimental work [13], we also paid attention to the fact that isolated YO molecular lines were observed in the spectrum of ceramics sintered from yttrium oxide (sintering of the samples compacted from pure Y_2O_3 nanopowder).

This paper deals with an experimental study of X-ray light emission of Y_2O_3 (nanopowder and ceramics) making an emphasis on changes in spectral series which are responsible for YO band systems depending on heat treatment of the samples.

EXPERIMENT

The experiment were done with commercially available yttrium powder «ITO-Lyum», consisting of pure Y_2O_3 (purity of the powder was approximately 99.9828 %). The samples were produced by compaction procedure of the powder. «ITO-Lyum» powder hitch with mass of 1 g were placed inside the cylindrical pressform with a diameter of 10.8 mm. A hydraulic press worked in the following regime: the pressure inside the pressform was grown from 0 up to the value of 3000 kgf per cm^2 (327.5 MPa) during 1 minute without an additive exposure at maximum pressure. So pressed cylindrical pellets of 10 mm in diameter and approximately 3 mm thickness were prepared. Thermal treatment was performed in commercial electric furnace «Naberthem LHT 04/18». To avoid possible penetration of impurities into the sample (contamination by volatile oxides from the furnace) we used special a container made from the same yttrium oxide ceramics. Sintering was carried out in in air atmosphere. The heat treatment cycle included the following stages (see Fig. 1): 1) slow increase of the temperature during approximately 3 h (the average rate was 8÷10 °C per min) up to sintering temperature 1300 °C (sample #1), 1400 °C (sample #2), 1500 °C (sample #3); 2) sintering at this temperature for 1 h; 3) cooling to room temperature for 4 h in an air atmosphere. Some of the samples were additionally annealed at 1000 °C for 10 h, followed by cooling for the same time (the sample #4). It is generally accepted that sintering of yttrium oxide ceramics begins at temperatures of about 700 °C [15] (Fig. 1 shows the area (filled by gray color) that corresponds to the most efficient sintering process).

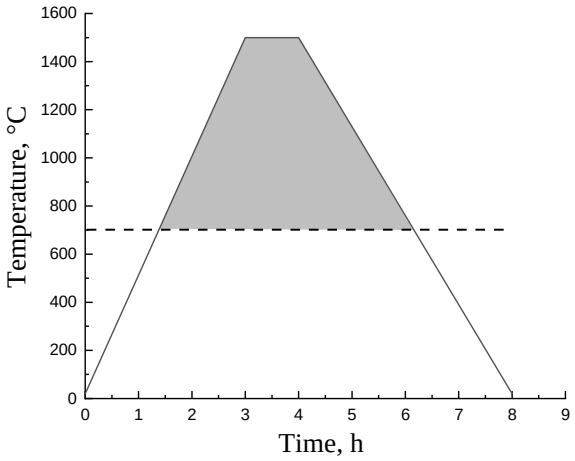

Figure. 1. Typical heat treatment shown by the example of the sample T=1500 °C.

The samples were examined by some diagnostics: X-ray diffraction analysis (XRD) and Scanning electron microscopy (SEM). Light emission excited by X-ray irradiation was studied on spectrometric complex (see details in [13]). X-ray vacuum tube source operated at voltage of up to 50 kV. Spectra were measured by grating monochromator at wavelength range of 250–750 nm. The measuring channel was calibrated with taking into account corresponding spectral sensitivity of the apparatus.

RESULTS AND DISCUSSION

X-ray diffraction

X-ray diffractometer DRON-4-07 (Cu-Kα radiation with applying Ni selectively absorbing filter, diffracted radiation was registered by a scintillation detector) was applied for crystallographic analysis of the samples. X-ray diffraction pattern showed presence of single-phase and cubic yttrium oxide (space group No. 206). No traces of other phases were found within the sensitivity of the method. XRD demonstrated that the samples #1-4 were almost identical; no significant differences were found in the pattern.

The lattice parameters were slightly higher than database (ICDD PDF-2 International database). The distribution of the intensities of the diffraction lines corresponded to a polycrystalline non-textured state.

Scanning electron microscopy

SEM-examination of our ceramics was done by means of commercial Scanning Electron Microscope JEOL JSM-7001F. Fig. 2 shows the morphology of Y_2O_3. The prepared samples showed good morphology and homogeneity with grains of nano- and micro- sizes. We have seen that the images for plane surface and fresh cleavage demonstrated no noticeable differences. SEM-study of the the samples #3 and #4 demonstrated minor differences in the images before and after additional 10 h annealing, which indicates the absence of significant changes in the structure of Y_2O_3 ceramics associated with long heating. Also, no significant difference was found on the surfaces and fresh cleavage of the additionally annealed sample.

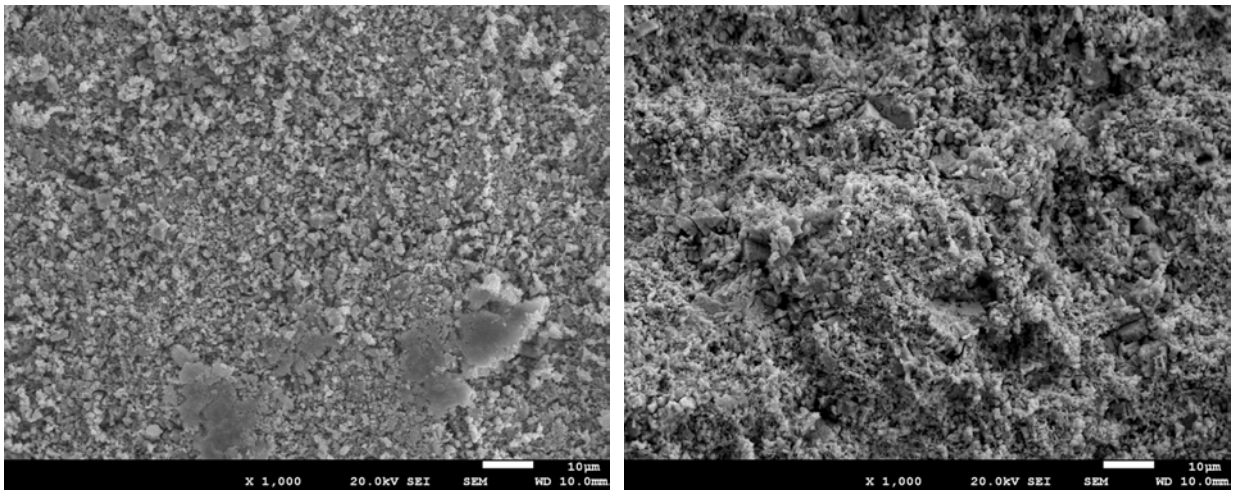

a b

Figure. 2. SEM-image of Y_2O_3 (sample #3, T=1500 °C): *a* is plane surface, *b* is fresh cleavage.

Luminescence measurements

Figure 3 shows typical light emission spectra induced by X-ray irradiation for powder and ceramics, sintered at 1500 °C (sample #3). To compare the spectra for different samples and experimental conditions, we performed the normalization to the maximum value of the first band, which is usually associated with self-trapped exciton (STE) [16]. As it could be seen, the spectra contained one wide band and four systems of lines, which we have already observed earlier [13]. The maxima of the first band lied near 350 nm, the other maxima of line systems were 487 nm, 545 nm, 573.5 nm and 670.5 nm. It should be noted that the spectrum observed for ceramic sample #3 was also similar to the spectra for samples #1, #2 and #4.The origin of light generation of the bands has been already discussed [13]. We only note that the first broad band is associated with an exciton [16], while the second, fourth, and fifth systems of lines are identified with good accuracy as lines of molecular yttrium oxide [17]. The origin of the third peak has not yet been established and requires further research. As for the doublet in the region 314–316 nm, its identification turned out to be difficult, since it did not correspond to any known radiation from up-to-date atomic and molecular spectral databases.

As can be clearly seen from Fig. 3 for the spectra of the powder that was not subjected to heat treatment, the lines associated with YO molecule system of lines are small, except for a peak at approximately λ=573.5 nm. For samples that were heat treated, the situation changed. The emission peaks of YO molecules have increased significantly compared to the maximum of the STE band. Heat treatments with the temperatures at which the samples were sintered hardly led to a significant increase in the size of Y_2O_3 crystallites, and, consequently, to an increase in the maximum of the band associated with STE light emission. The significant increase in YO systems of lines is apparently associated with a significant increase in the number of YO structures on the crystal surface.

The processes of sintering and annealing of powder ceramics strongly depend on both temperature at which these processes effectively occur and on the time of exposure of the sample to these temperatures. As we mentioned above, yttrium oxide the sintering and annealing processes begin to proceed effectively at temperatures above 700 °C [15]. We took into account the influence of these factors on the properties of the samples under study by applying such a parameter as temperature multiplied by the time of exposure of a given temperature to the sample (some analogy of the energy contribution parameter). We calculated the value of this parameter for our samples and plot the dependences of the maximum values of the light intensities for 5 band systems on the energy contribution parameter during heat treatment (Fig. 4).

As it can be seen from the figure, with an increase of the energy contribution parameter, the intensity of the line systems associated with YO structures increases. The last points for all experimental curves, corresponded to the sample #5 sintered at a temperature of 1500 °C with additional annealing at a temperature of 1000 °C, tend to influence slightly the YO line system light emission.

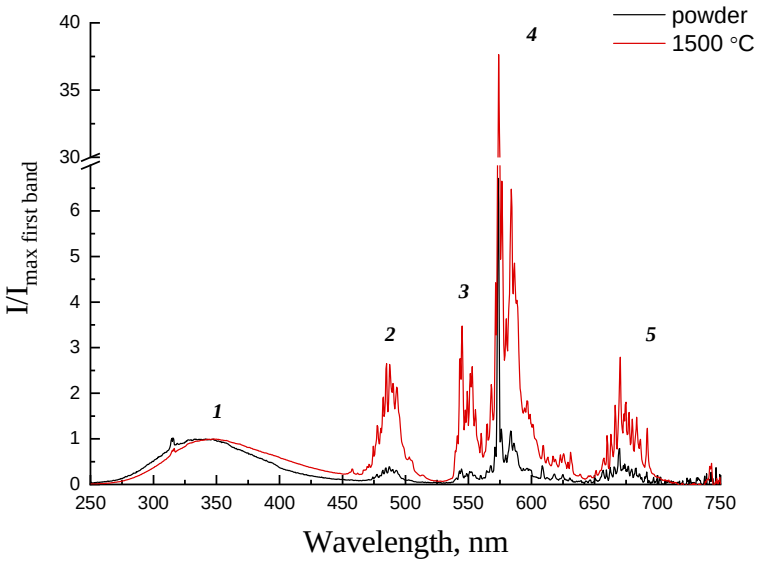

Figure 3. X-ray luminescence spectra of yttrium oxide powder and ceramic sample (sintering temperature of 1500 °C).

The numbers from 1 to 5 indicate the wavelength ranges of the corresponding first band and systems of lines (vertical bars are shown to guide eye, it indicate the borders of the bands).

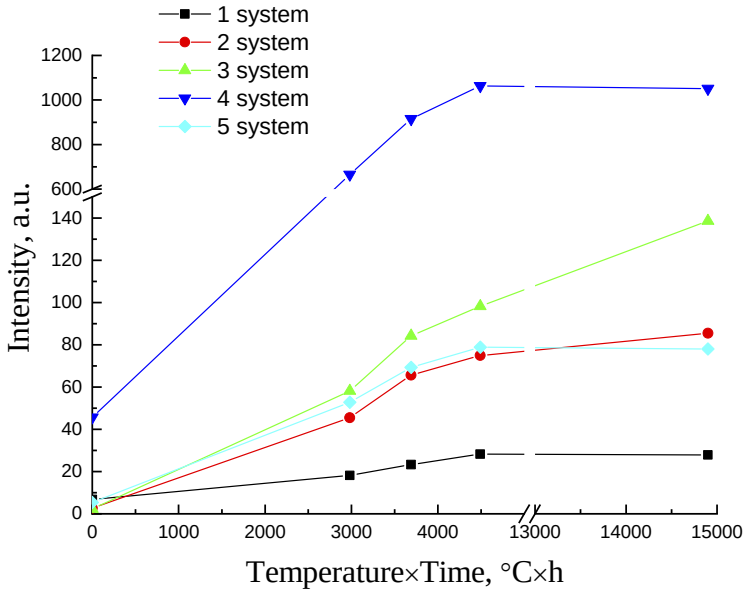

Figure 4. Luminescence light intensity as function of sintering temperature multiplied by time for different wavelength bands of Y_2O_3 spectra.

CONCLUSIONS

The performed study of the light emission from the powder and sintered ceramics exposed to X-ray irradiation up to 50 keV made it possible to conclude the following. As shown by X-ray structural analysis, as a result of sintering and annealing, Y_2O_3 crystal lattice does not change, and new types of the crystal lattice are not formed. Meanwhile, the luminescence measurements revealed that besides light emissions associated with Y_2O_3 band systems corresponded to self-trapped exciton decay (generation of radiation in the entire volume of ceramics), there were intensive YO band systems (molecular character of the spectral lines pointed out on light emission from molecule structures on surface of the crystallites). The linear structure of the YO spectra suggests that YO structures are weakly bound to Y_2O_3 crystal structure. The influence of the sintering temperature on peak maximum intensities, which allows us to talk about growth of energy contribution to the Y_2O_3 pellet, leads to an increase in the intensity of the band and systems of lines associated with YO structures. The presence of YO structures on the surface of the initial ITO-LUM powder, which is clearly seen on the spectra, makes it possible to draw a conclusion about the synthesis of these structures during production process of Y_2O_3 powder. It should be noted that the number of these structures on the surface of Y_2O_3 crystallites increasing with heat treatment process.

Acknowledgment

The authors consider it their duty to thank Bogdan Mazilin for his help in preparing the samples being studied.

ORCID IDs

Sergiy Kononenko, https://orcid.org/0000-0001-6060-2589; **Volodymyr Chishkala**, https://orcid.org/0000-0002-8634-4212
Vitaliy Zhurenko, https://orcid.org/0000-0002-4738-094X; **Oganes Kalantaryan,** https://orcid.org/0000-0002-5625-6908
Sergey Lytovchenko, https://orcid.org/0000-0002-3292-5468

REFERENCES

[1] M.I. Alymov, V.S. Shustov, A.S. Ustuhin, E.V. Evstratov, Composites and Nanostructures, **3**, 5 (2012), http://www.issp.ac.ru/journal/composites/2012/CN_03_2012.pdf (in Russsian).
[2] X. J. Song, H. Z. Cui, L. L. Cao, Transactions of Nonferrous Metals Society of China, **26**, 1878 (2016), https://doi.org/10.1016/S1003-6326(16)64265-6
[3] V.H. Mudavakkat, V.V. Atuchin, V.N. Kruchinin, A. Kayani, C.V. Ramana, Optical Materials, **34**, 893 (2012), https://doi.org/10.1016/j.optmat.2011.11.027
[4] R. Srinivasan, N.R. Yogamalar, J. Elanchezhiyan, R.J. Joseyphus, A.C. Bose, Journal of Alloys and Compounds, **496**, 472 (2010), https://doi.org/10.1016/j.jallcom.2010.02.083
[5] L. Mariscal-Becerra, R. Vázquez-Arreguín, U. Balderas, S. Carmona-Téllez, H. Murrieta Sánchez, and C. Falcony, Journal of Applied Physics, **121**, 125111-1 (2017); https://doi.org/10.1063/1.4979209
[6] W. Wang, P. Zhu, Optics Express, **26**, 34820 (2018), https://doi.org/10.1364/OE.26.034820
[7] A. Ikesue, Y. L. Aung, T. Taira, T. Kamimura, and K. Yoshida, Ann. Rev. Mater. Res. **36**, 397 (2006), https://doi.org/10.1146/annurev.matsci.36.011205.152926
[8] V. V. Osipov, V. A. Shitov, R. N. Maksimov, V. I. Solomonov, K. E. Luk'yashin, and A. N. Orlov, Photonics, **12**, 318 (2018). https://doi.org/10.22184/1993-7296.2018.71.3.318.334
[9] 9. V. V. Osipov, A. V. Ishchenko, V. A. Shitov, R. N. Maksimov, K. E. Lukyashin, V. V. Platonov, A. N. Orlov, S. N. Osipov, V. V. Yagodin, L. V. Viktorov, and B. V. Shulgin, Opt. Mater. **71**, 98 (2017), https://doi.org/10.1016/j.optmat.2016.05.016
[10] A. Bernard and R. Gravina, The Astrophysical Journal Supplement Series, **44**, 223 (1980).
[11] M. Singh and J. P. Chaturvedi, Astrophysics and Space Science, **135**, 1 (1987).
[12] V. V. Osipov, A. V. Rasuleva, and V. I. Solomonov, Optics and Spectroscopy **105**, pp. 524–530 (2008), https://doi.org/10.1134/S0030400X08100068
[13] O. Kalantaryan, V. Zhurenko, S. Kononenko, R. Skiba, V. Chishkala and M. Azarenkov, in: *2020 IEEE 10th International Conference Nanomaterials: Applications & Properties (NAP)*, 2020, pp. 01NP03-1-01NP03-5, https://doi.org/10.1109/NAP51477.2020.9309672
[14] O. Kalantaryan, S. Kononenko, E. Barannik, V. Zhurenko and V. Chishkala, in: *2021 IEEE 11th International Conference Nanomaterials: Applications & Properties (NAP)*, 2021, pp. 1-4, https://doi.org/10.1109/NAP51885.2021.9568608
[15] Joanna R. Groza, NanoStmchmd Materials, **12**, 987 (1999), https://doi.org/10.1016/S0965-9773(99)00284-6
[16] A. Lushchik, M. Kirm, Ch. Lushchik, I. Martinson, G. Zimmerer Journal of Luminescence, **87**, 232 (2000), https://doi.org/10.1016/S0022-2313(99)00271-9
[17] K.P. Huber, G. Herzberg, *Molecular spectra and molecular structure, IV. Constants of diatomic molecules, vol. 4* (Springer Science+Business Media, New York, 1979), pp. 19-24.

ЛЮМІНЕСЦЕНЦІЯ ОКСИДУ ІТРІЮ, СПРИЧИНЕНА РЕНТГЕНІВСЬКИМ ОПРОМІНЕННЯМ

С. Кононенко, О. Калантар'ян, В. Журенко, В. Чішкала, С. Литовченко

Харківський Національний університет ім. В.Н. Каразіна
61022, Україна, м. Харків, пл. Свободи, 4

Наведено результати експериментальних досліджень світлового випромінювання кераміки Y_2O_3, спричиненого рентгенівським випромінюванням з енергією до 50 кеВ. Зразки виготовлялися з комерційного нанопорошку Y_2O_3 методом пресування та подальшого спікання в атмосфері повітря за різних температур від 1300 до 1500°С. Деякі зразки, спечені за температури 1500°С, додатково відпалювалися за температури 1000°С протягом 10 годин. Рентгеноструктурні дослідження всіх зразків не виявили відмінностей у кристалічній структурі, які могли бути пов'язані з температурною обробкою під час спікання та відпалу. Спектри світлового випромінювання в діапазоні 250-750 нм показують наявність випромінювання від електронних переходів YO структур на тлі люмінесценції оксиду тривалентного ітрію. Наявність такого випромінювання було зафіксовано і для порошку, що дозволяє зробити висновок щодо виникнення цих структур на поверхні кристалітів у процесі виробництва. Зі зростанням температури спікання зразка інтенсивність оптичного випромінювання зростала. Виявлено суттєву відмінність впливу як температури, так і часу спікання (відпалу) на інтенсивність люмінесценції та свічення оксидів ітрію. Інтенсивність люмінесцентної смуги, яка пов'язується із самозахопленим екситоном, зі зростанням теплового вкладу зростала (для оцінки вкладу ми в роботі запровадили параметр, що дорівнює добутку температури на час теплового діяння). Зростання інтенсивності випромінювань у другій, третій четвертій і п'ятій системах ліній (особливо для системи ліній з максимумом λ=573,5 нм) помітно перевищувало таке для само захопленого екситону. Отримані нами експериментальні результати щодо другої, четвертої та п'ятої систем ліній, які добре збігаються молекулярними лініями YO, дозволяють припустити, що теплова обробка зразків кераміки, спеченої з пресованого порошку Y_2O_3, призводить до збільшення YO структур на поверхні кристалітів.

Ключові слова: рентгенівська емісія світла, оксид ітрію, спектр, YO структура, запікання порошків.

East European Journal of Physics. 4. 145-151 (2021)
DOI: 10.26565/2312-4334-2021-4-19 ISSN 2312-4334

PHOTOLUMINESCENCE, IMPEDANCE, THERMAL CHARACTERISTICS AND HIRSHFELD SURFACE ANALYSIS OF POTASSIUM BISULPHATE SINGLE CRYSTALS FOR THIRD ORDER NLO APPLICATIONS[†]

K. Thilaga[a,d,#], P. Selvarajan[b,*], S.M. Abdul Kader[c,‡]
[a]*Research scholar, Reg.No.19221192132006, Department of Physics, Sadakathullah Appa College Tirunelveli -627011, Tamilnadu, India*
[b]*Department of Physics, Aditanar College of Arts and Science, Tiruchendur -628216, Tamilnadu, India*
[c]*Department of Physics, Sadakathullah Appa College, Tirunelveli -627011, Tamilnadu, India (Manonmaniam Sundaranar University, Abishekapatti, Tirunelveli – 627012, Tamilnadu, India)*
[d]*Department of Physics, Sri S.R.N.M College, Sattur-626203, Tamilnadu, India*
**Corresponding Author: pselvarajanphy@gmail.com*
[#]E-mail: kthilaga@gmail.com, [‡]E-mail: aksac.physics@gmail.com
Received October 7, 2021; revised November 12, 2021; accepted December 20, 2021

Good quality potassium bisulphate (KHS) single crystals have been grown by slow evaporation method at room temperature. The KHS crystal was found to be crystallizing in orthorhombic crystal structure with Pbca space group. The photoluminescence behaviour of the crystal was analysed in the visible region. This study disclosed that the grown KHS crystal has intense blue emission peak at 490 nm. Impedance analysis was performed to investigate the frequency dependent electrical characteristics at various temperatures. From the impedance studies the bulk resistance, grain boundary resistance and DC conductivity values of the grown crystal were found out. The KHS crystal was subjected to TGA/DTA and the results have been investigated. The electrical parameters like Fermi energy and average energy gap of KHS crystal have been determined. The evaluated values are used to estimate the electronic polarizability. The intermolecular interactions were predicted using Hirshfeld surface analysis. This analysis exhibited that the utmost contribution to the crystal structure was the K···O (46.7%) interaction. The 2D fingerprint plot provides the percentage contribution of each atom-to-atom interaction. Since KHS material is a centrosymmetric crystal, it could be used for third order nonlinear optical (NLO) applications.
Keywords: Inorganic crystal; solution growth; XRD; photoluminescence; impedance; TGA/DTA; electronic polarizability; 3-D Hirshfeld surface.
PACS: 81.10.Dn, 81.10.−h

In recent years, single crystals with good electrical, thermal, and nonlinear optical properties are in high demand for the development of solid state devices. Accordingly, many researchers have focused on the feasibility and applicability of crystal in the fabrication of devices [1]. Nowadays, the study of NLO materials has garnered much attention since its technological needs are obvious [2]. Some researchers have reported that the inorganic crystals gaining its popularity in the area of nonlinear optics owing to its good physical and chemical stabilities [3]. Many useful inorganic crystals have been discovered and used in laser sources. One such inorganic NLO active substance is potassium bisulphate, often known as potassium hydrogen sulphate (KHS). Though KHS is reusable, affordable, non-toxic and can be employed in both homogeneous and heterogeneous conditions, only few research works have been reported to understand its physical properties. Loopstra has reported the crystal structure of KHS crystal [4]. And the thermoelastic properties of single crystals of KHS have been studied by some investigators [5, 6]. To the best of our knowledge, here we are reporting for the first time the photoluminesnce behaviour, electrical properties and intermolecular interactions of the KHS crystal. Also the experimental and theoretical value of density of the KHS crystal has been compared.

GROWTH OF KHS CRYSTAL

The mixture to grow single crystals of KHS was prepared from high grade potassium hydrogen sulfate using aqueous solution. The solution was stirred for three hours using magnetic stirrer. The prepared mixture was then filtered and placed undisturbed in a reasonably dustless atmosphere. The KHS crystal was harvested within 30 days. The photograph of the grown KHS crystal is shown in Fig. 1.

RESULTS AND DISCUSSION

Structural characterization

The grown KHS crystal was exposed to single crystal X-ray diffraction investigations using MoK_α radiation ENRAF NONIUS CAD4 diffractometer to identify the crystal system. The data acquired from single crystal XRD investigation displayed in Table 1 shows that the KHS crystal belongs to the orthorhombic crystal system with Pbca space group and 16 molecular units per unit cell. The results of this study appear to be in excellent accord with the published values [4]. Because the Pbca group is a centrosymmetric space group, no second order nonlinear optical (NLO) characteristics will be observed in this sample.

[†] ***Cite as:*** K. Thilaga, P. Selvarajan, and S.M. Abdul Kader, East. Eur. J Phys. **4**, 145 (2021), https://doi.org/10.26565/2312-4334-2021-4-19

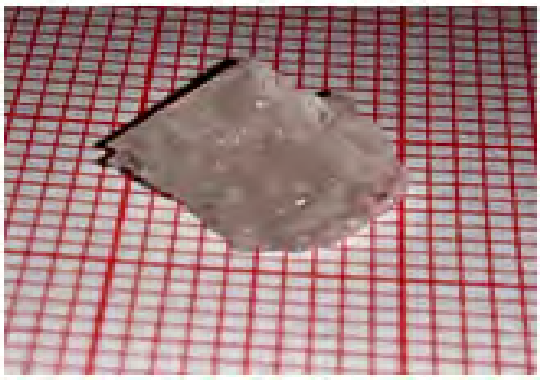

Figure 1. Grown crystal of KHS

Table 1. Single crystal XRD data for KHS crystal

Chemical formula	$KHSO_4$
Refinement method	Full matrix Least square method
Molecular weight	136.17 g/mol
Crystal habit	Colorless, transparent
Crystal Symmetry	Orthorhombic
Space group	Pbca
a	8.411(4) Å
b	9.802 (3) Å
c	18.961(2) Å
α	90°
β	90°
γ	90°
Z	16
Volume of unit cell	1563.23(4) $Å^3$
Density	2.313 g/cc

Photoluminescence studies

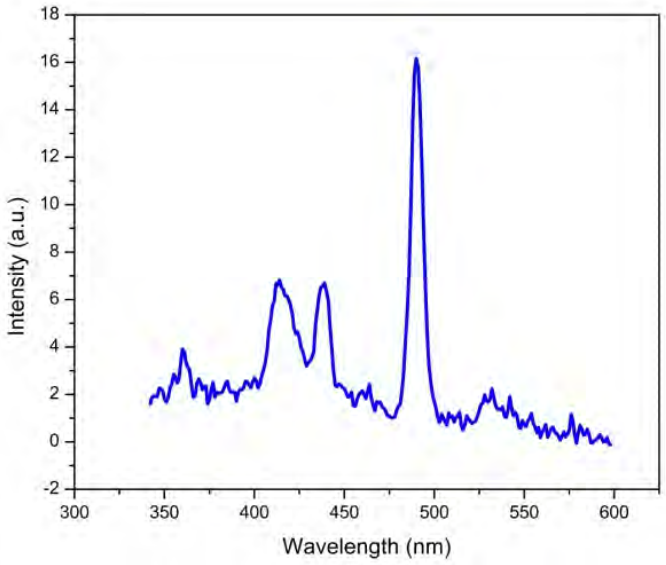

Figure 2. PL spectrum of the KHS crystal excited at 320 nm.

The PL analysis of KHS single crystal was performed out in the range between 350- 600 nm with an excited wavelength 320 nm and it is shown in Fig. 2. The prepared KHS crystal shows both UV and broad visible emissions. The strength of the peak emitted in the visible range is higher when compared to the UV region. The PL spectrum recorded indicates a less intense UV emission at ~ 359 nm and the blue emission bands at ~ 412 nm, ~ 438 nm and ~ 490 nm. And the emission in the UV and visible region is attributed to the free exciton recombination through an exciton–exciton collision process and the presence of intrinsic defects respectively [7]. The occurrence of charge transfer [8] in the molecules might explain the sharp emission peak at 490 nm. The spectrum indicates that the KHS crystal can be beneficial for fluorescence in blue LED applications [9].

Impedance Studies

Impedance analysis was used to understand the electrical behaviour of the KHS crystal. Fig. 3 and 4 depict changes in the real (Z') and imaginary (Z'') portions of impedance for the KHS crystal against frequency. As seen in the graph, the real part (Z') of impedance drops as the temperature and frequency rises. Fig. 4 shows that the amplitude of Z'' rises at first, then declines with increasing frequency after reaching a peak $(Z''_{\max})$. As the temperature rises, the peak widening and shift to higher frequency regions is observed which shows the presence of an electrical relaxation phenomenon. Moreover, the impedance curves at all temperatures were combined at higher frequency due to a decrease in space charge polarization [10].

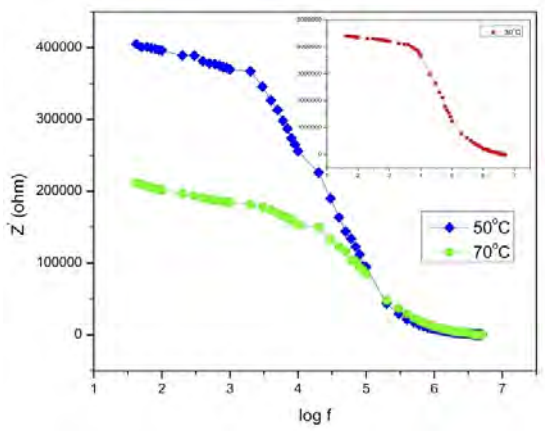

Figure 3. Real term of impedance against frequency

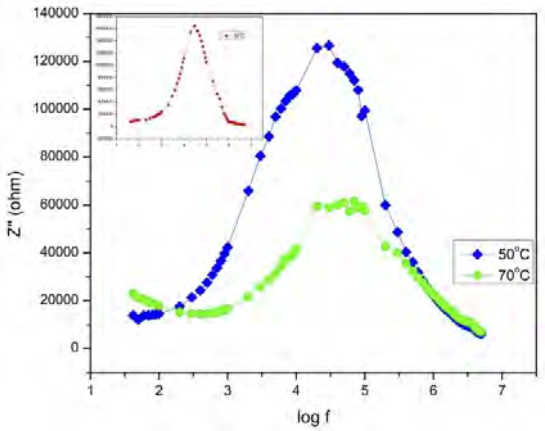

Figure 4. Imaginary term of impedance against frequency

Fig. 5 shows the Nyquist plots for the grown KHS crystal between Z' and Z'' of impedance at various temperatures. The existence of a single semicircular arc and spike suggests that the material's electrical characteristics are mostly attributable to bulk and grain boundary influences [11]. Table 2 shows the bulk resistance R_b as well as the grain boundary resistance R_{gb} of the sample derived from the plot. The data clearly shows that when the temperature rises, R_b and R_{gb} decreases. Furthermore, this finding supports the insulating nature of KHS sample. Moreover the conductivity of the KHS crystal presented in table 2 was estimated using the formula [12] $\sigma = d / AR_b$, where A is the area of the face of the crystal in contact with the electrode and d is the thickness of the KHS crystal. The low conductivity of grown KHS crystal supports its quality of dielectric material.

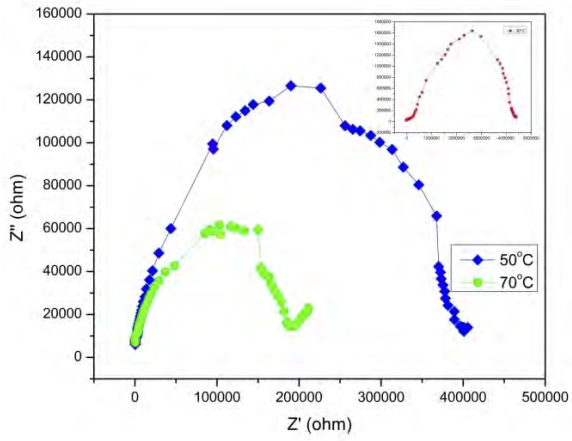

Figure 5. Nyquist plot for KHS crystal

Table 2. Bulk resistance, grain boundary resistance and DC conductivity values of the KHS crystal

Temperature (°C)	Bulk resistance R_b (ohm)	Grain boundary resistance R_{gb} (ohm)	DC conductivity (ohm m)$^{-1}$
30	4.40 x 10^6	2.63 x 10^6	2.49 x 10^{-6}
50	4.00 x 10^5	1.90 x 10^5	2.74 x 10^{-5}
70	1.90 x 10^5	1.02 x 10^5	5.76 x 10^{-5}

Thermal studies

The thermal feature of KHS crystal was investigated using the Perkin Elmer STA 600 TG-DTA instrument in the temperature range of 40–730 °C. In a nitrogen environment, the experiment was performed at a pace of 10 °C per minute. Fig. 6 shows the TGA and DTA graph of the KHS crystal. At the beginning of experiment, mass of the sample was 19.90 mg and it had a mass of 14.4 mg at the end. The slight weight loss in the TGA curve over the temperature range 40-50 °C is attributed to the removal of adsorbed water molecules by the sample from the atmosphere. Chemical dehydration is responsible for the endothermic peak at 195°C. And the peak in the DTA curve at 210°C, which corresponds to the weight loss in the TGA curve, indicates simultaneous melting and disintegration of the KHS crystal. The wide peak after the disintegration point is due to the evaporation of gaseous materials [13-15]. Thermal stability of the grown KHS crystal ascertains that they may be used at higher temperatures [16]. The result indicates that 72% of the sample retained even at 720°C. Hence the sample has an imperative quality for device manufacturing.

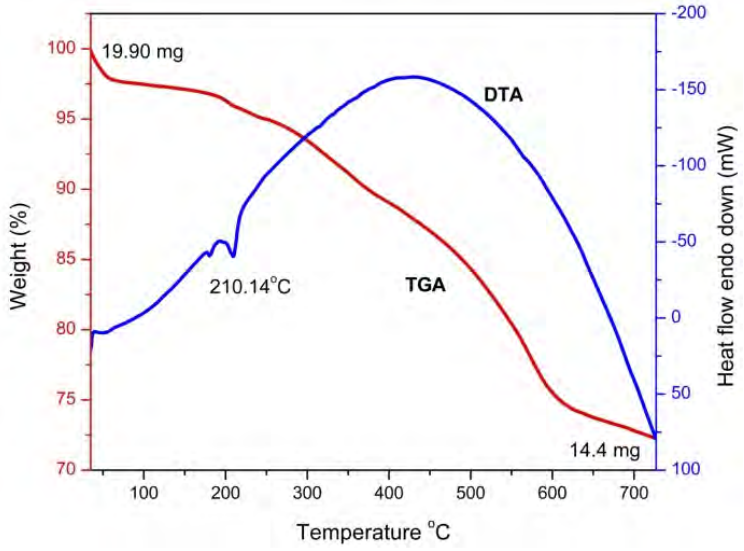

Figure 6. TG/DTA curves for KHS sample

Electronic polarizability of KHS crystal

The tendency of a charge distribution to be deformed from its usual shape when an electric field is applied to a sample consisting of atoms or molecules is known as electronic polarizability. The estimation of electronic polarizability relies upon certain solid state parameters such as plasma energy of valence electron (E_v), Fermi energy (E_F) and Penn gap energy (E_p). The value of E_v is estimated from the following equation

$$E_v = 28.8\left[(Z' \times \rho)/M\right]^{1/2}$$

where Z' is the number of valence electrons of KHS molecule, ρ is the density of the crystal and M is the molecular weight of KHS crystal. Here M = 136.17 g mol^{-1}, ρ = 2.313 g/cc, Z' = 32.

Penn gap energy or average energy gap can be estimated using the dielectric constant [17] from the relationship $E_p = E_v(\varepsilon' - 1)^{-1/2}$ where ε' is the dielectric permittivity, often known as the dielectric constant, has a value of 4.5 at 1 MHz [18]. Fermi energy is the kinetic energy of particles in their most occupied state, and it may be calculated theoretically using the equation $E_F = 0.2948 \times E_v^{4/3}$. Table 3 shows the calculated values of E_v, E_p, and E_F for the KHS crystal.

The electronic polarizability (α) of KHS crystal may be determined using the Penn analysis from the relationship

$$\alpha = \left[\left(E_v^2 S\right)/\left(E_v S + 3E_p^2\right)\right] \times (M/\rho) \times 0.369 \times 10^{-24}$$

where $S = 1 - \left(E_p/4E_F\right) + 1/3\left(E_p/4E_F\right)^2$ is a specific constant of the material [19, 20]. The electronic polarizability of the KHS crystal is determined to be 2.196 x 10^{-23} cm^3 using Penn analysis.

The value of α of KHS crystal may also be computed using the Clausius-Mossotti relation given below

$$\alpha = \left(3M/4\pi N\rho\right)\left[(\varepsilon' - 1)/(\varepsilon' + 2)\right]$$

where N is the Avogadro's number [21] and the estimated value of electronic polarizability is 1.256 x 10^{-23} cm^3. The results show that the electronic polarizability of KHS crystal determined using both techniques is almost identical.

Table 3. Values of E_v , E_p , and E_F for KHS crystal

Energy parameters	Values (eV)
Plasma energy (E_v)	21.233
Penn gap energy (E_p)	11.350
Fermi energy (E_F)	17.315

Experimental determination of density of crystal

Flotation method was employed to estimate the density of the KHS crystal. A tiny part of crystal was submerged in the mixture of liquid bromoform and carbon tetra chloride in a specific gravity container. When the sample was in the condition of mechanical equilibrium, the density of both the crystal and the combination of liquids would be equivalent. Then using the following relation density can be estimated

$$\rho = (w_3 - w_1)/(w_2 - w_1)$$

where w_1 represents the weight of a specific gravity bottle, w_2 and w_3 represents the weight of a specific gravity bottle filled with water and the solution mixture respectively. The experimentally estimated density of KHS crystal is 2.325 g/cc, which is nearly identical to the density of KHS crystal, determined using the XRD technique [22].

Kurtz-Perry powder technique for SHG

The Kurtz and Perry approach was used to determine the second harmonic generation (SHG) efficiency of the powdered form of the grown KHS crystal [23]. Nd: YAG laser beam (λ = 1064 nm) of very high intensity with a pulse length of about 6 ns was incident over the prepared material. The reference sample in this experiment was KDP. The grown crystal was crushed into a powder with a grain size of 300-350 m and the SHG was measured. It is noticed that no green radiation is emitted during the experiment. However, at an input energy of 0.70 J, the typical KDP sample produced green radiation with a SHG signal of 8.90 mJ. From the SHG analysis it is observed that the magnitude of SHG for the KHS sample is zero and is attributed to the centrosymmetric nature of the grown crystal. Third order NLO property (Z-scan) analysis of KHS sample is in progress.

Hirshfeld surface analysis

The Crystal Explorer 17.5 programme was used to analyze Hirshfeld surfaces and generate the corresponding 2D fingerprint plots for the KHS crystal. The intercontacts in the KHS crystal were seen utilizing the normalized contact distance d_{norm} , distance between Hirshfeld surface and the closest atom inside the surface d_i and distance between Hirshfeld surface and the closest atom outside the surface d_e maps on the Hirshfeld surface displayed in Fig. 7.

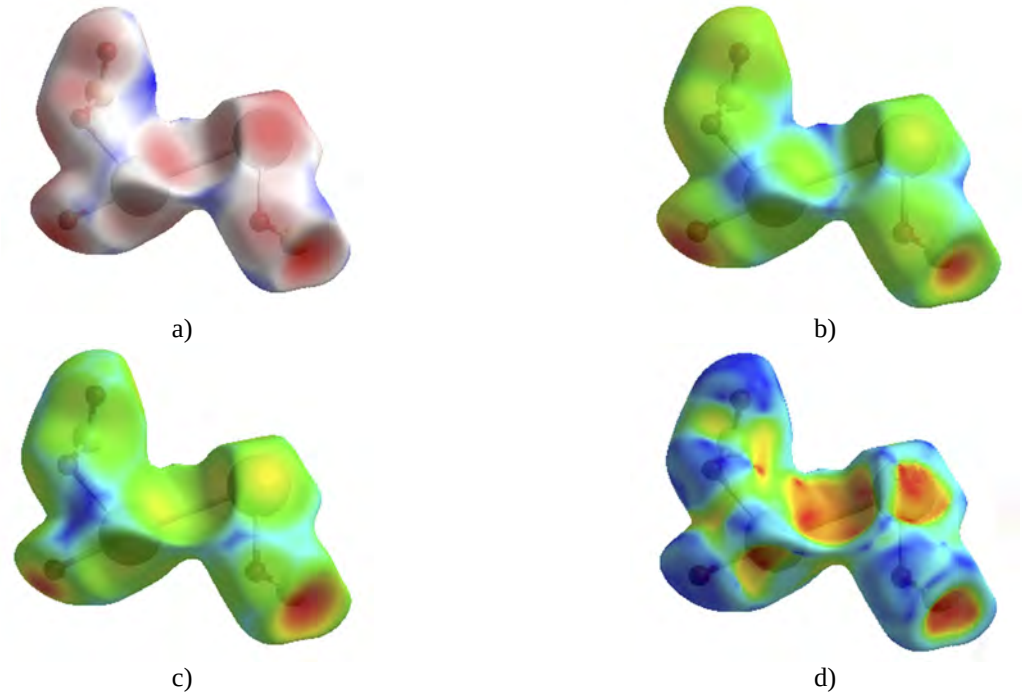

Figure 7. The Hirshfeld surface of the compound mapped with a) d_{norm} b) d_i c) d_e d) shape index

The surfaces were made transparent so that molecules and the crystals interacting environment could be seen clearly. The colors red, white and blue in the d_{norm} mapped Hirshfeld surface show that the interatomic contacts [24-26] are shorter longer, Van der Waals separated and longer respectively. The bright red zone in the d_{norm} mapping shows the presence of hydrogen bond interactions (S–HO) in the Hirshfeld surface of the investigated crystal. The shape index elucidates molecular packing in more depth. The donor of an intermolecular interaction is represented by the blue bump-shape with a shape-index greater than 1, while the acceptor is represented by the red hollow with a shape-index less than 1. The hydrogen-donor and hydrogen-acceptor groups were represented by the blue and red areas on the shape-index map of KHS crystal displayed in Fig. 7 d). Fig 8 shows a 2D fingerprint plot depiction of a Hirshfeld surface. With 46.7 percent of the Hirshfeld surface of the title molecule, the K…O intercontact makes a significant contribution. Other intercontacts discovered in the Hirshfeld surface of the investigated compound include O...O (27.9%) and S...O (25.4%).

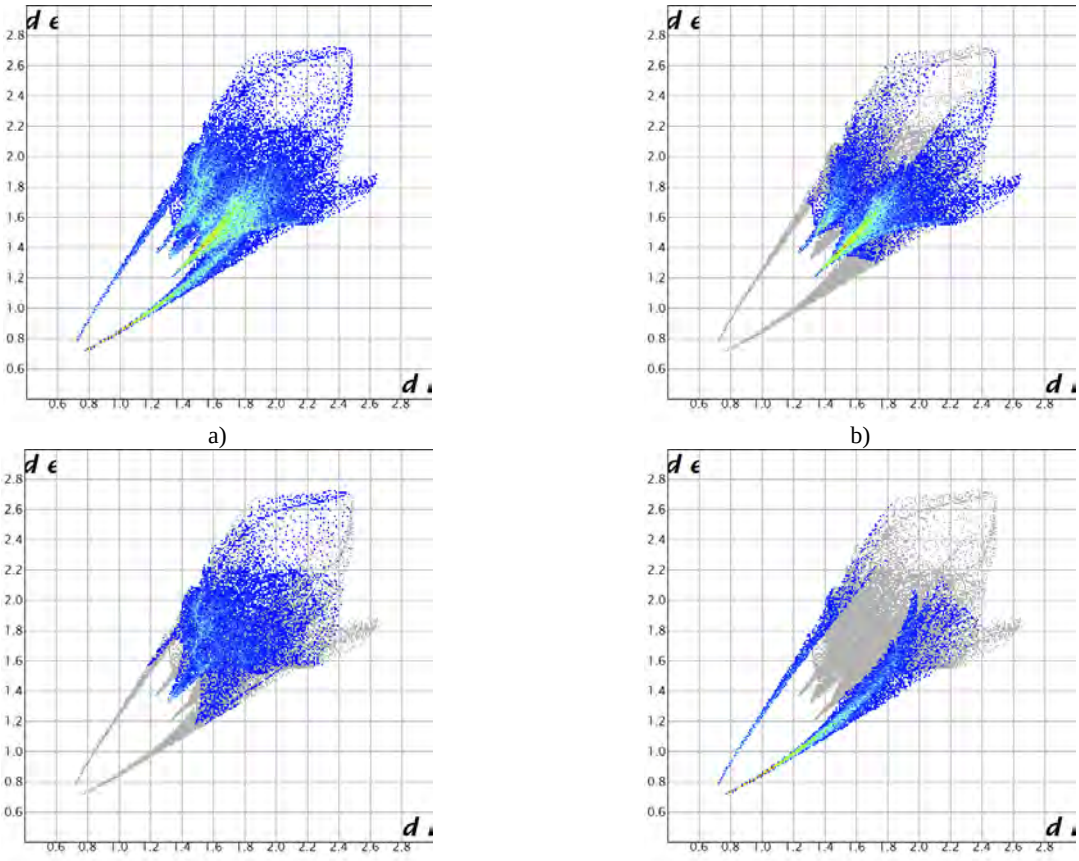

Figure 8. a) title compound b) K..O c) O..O d) S..O interactions and their contribution to the Hirshfeld surface

CONCLUSION

High optical quality single crystals of KHS were grown by slow evaporation technique. The crystal structure and space group of grown KHS crystal were determined by XRD technique. The photoluminescence feature of the grown crystal indicates that it is appropriate for the photonic devices manufacturing. The electrical properties have been studied using impedance spectroscopic technique and can be used as a tool to identify the good quality dielectric crystal. Thermal steadiness and decomposition point were found by TGA/DTA analysis and it suggests that the sample can be employed for device fabrication. The solid state electronic parameters and the electronic polarizability of KHS crystal were calculated. And the SHG analysis divulges that the KHS crystal is centrosymmetric. The percentages of the intermolecular interactions of the grown sample are revealed using 3D Hirshfeld surface analysis and 2D fingerprint plots.

Acknowledgement

The authors are thankful to the management of Aditanar College of arts and science, Tiruchendur, Sadakathullah Appa College, Tirunelveli and Sri S. R. N. M College, Sattur for their encouragement to carry out the research work. Also the authors acknowledge the research centers like STIC (Cochin University), St. Joseph's College (Trichy), and Crescent Engineering College (Chennai) for getting the research data of the sample.

ORCID IDs

K. Thilaga, https://orcid.org/0000-0003-1124-8733; **P. Selvarajan,** https://orcid.org/0000-0003-1097-4207
S.M. Abdul Kader, https://orcid.org/0000-0001-6130-3855

REFERENCES

[1] Mohd. Shkir, S. Alfaify, Haider Abbas, and G. Bhagawannarayan, Materials Chemistry and Physics, **155**, 36 (2015), https://doi.org/10.1016/j.matchemphys.2015.01.062
[2] P. Maadeswaran, J. Chandrasekaran, S. Thirumalairajan, Optik - International Journal for Light and Electron Optics, **122** (3), 259 (2011), https://doi.org/10.1016/j.ijleo.2009.11.031
[3] M.K. Dhatchaiyini, , G. Rajasekar, , M. NizamMohideen, and A. Bhaskaran, Journal of Molecular Structure, **1210**, 128065 (2020), https://doi.org/10.1016/j.molstruc.2020.128065
[4] L.H. Loopstra, and C.H. MacGillavry, Acta Cryst. **11**, 349 (1958), https://doi.org/10.1107/s0365110x58000943
[5] D. Gerlich, and H. Seigert, Acta Cryst. **A31**, 207(1975), https://doi.org/10.1107/s0567739475000411
[6] J.E. Diosa, R.A. Vargas, E. Mina, E. Torijano, and B.E. Mellander, Phys, Stat. Sol. **220**, 641(2000), https://doi.org/10.1002/1521-3951(200007)220:1%3C641::aid-pssb641%3E3.0.co;2-x
[7] P.K. Giri, S. Bhattacharyya, R. Kesavamoorthy, B.K. Panigrahi, and K.G.M. Nair, Journal of Nanoscience and Nanotechnology, **9**, 5389 (2009). https://doi.org/10.1166/jnn.2009.1137
[8] S.P. Puppalwar, and S.J. Dhoble, and A. Kumar, Luminescence, **26**, 456 (2011), https://doi.org/10.1002/bio.1252
[9] P. Anandan, S. Vetrivel, R. Jayavel, C. Vedhi, G. Ravi, and G. Bhagavannarayana, Journal of Physics and Chemistry of Solids, **73**, 1296 (2012), https://doi.org/10.1016/j.jpcs.2012.06.015
[10] J. Uma Maheswari, C. Krishnan, S. Kalyanaraman, and P. Selvarajan, Physica B: Physics of Condensed Matter, **502**, 32 (2016), https://doi.org/10.1016/j.physb.2016.08.042
[11] D. Shanthi, P. Selvarajan, and S. Perumal, Materials Today: Proceedings, **2**, 943 (2015), https://doi.org/10.1016/j.matpr.2015.06.013
[12] T. Rhimi, G. Leroy, B. Duponchel, K. Khirouni, S. Guermazi, and M. Toumi, Ionics, **24**, 1305 (2018), https://doi.org/10.1007/s11581-017-2306-4
[13] P. Karuppasamy, Muthu Senthil Pandian, P. Ramasamy, and Sunil Verma, Optical Materials, **79**, 152 (2018), https://doi.org/10.1016/j.optmat.2018.03.041
[14] Z. Sun, G. Zhang, X. Wang, Z. Gao, X. Cheng, S. Zhang, and D. Xu, Crystal growth & design, **9**, 3251 (2009), https://doi.org/10.1021/cg801360q
[15] R. Manickam, and G.Srinivasan, Materials Today: Proceedings, **8**, 57 (2019), https://doi.org/10.1016/j.matpr.2019.02.080
[16] S. Vediyappan, R. Arumugam, K. Pichan, R. Kasthuri, S.P. Muthu, and R. Perumal, Applied Physics A, **123**, 780 (2012), https://doi.org/10.1007/s00339-017-1394-3
[17] P. Karuppasamy, V. Sivasubramani, M. Senthil Pandian, and P. Ramasamy, RSC Adv. **6**, 109105 (2016), https://doi.org/10.1039/c6ra21590d
[18] D.R. Penn, Phys. Rev. **128**, 2093 (1962), https://doi.org/10.1103/physrev.128.2093
[19] N.M. Ravindra, and V.K. Srivastava, J. Infrared Phys. **20**, 67 (1980), https://doi.org/10.1016/0020-0891(80)90009-3
[20] R.R. Reddy, Y. Nazeer Ahammed, and M. Ravi Kumar, J. Phys. Chem. Solids, **56**, 825(1995), https://doi.org/10.1016/0022-3697(94)00268-1
[21] R. Robert, C. Justin Raj, S. Krishnan, and S. Jerome Das, Physica B, **405**, 20 (2010), https://doi.org/10.1016/j.physb.2009.08.015
[22] C. Krishnan, P. Selvarajan, and T.H. Freeda, Materials letters, **62**, 4414 (2008), https://doi.org/10.1016/j.matlet.2008.07.045
[23] S.K. Kurtz, and T.T. Perry, J. Appl. Phys. **39**, 3798 (1968), https://doi.org/10.1063/1.1656857
[24] Tarun Kumar Pal, Subrata Paul, Jewel Hossen, Ashraful Alam, Chanmiya Sheikh, Arkajyoti Paul, and Ryuta Miyatake, Journal of Molecular Structure, **1226**, 129397 (2021), https://doi.org/10.1016/j.molstruc.2020.129397
[25] M. Manikandan, P. Rajesh, and P. Ramasamy, Journal of Molecular Structure, **1195**, 659 (2019), https://doi.org/10.1016/j.molstruc.2019.06.001
[26] N. Tyagi, H. Yadav, A. Hussain, and B. Kumar, Journal of Molecular Structure, **1224**, 129190 (2021), https://doi.org/10.1016/j.molstruc.2020.129190
[27] K. Indira, T. Chitravel, R.R. Saravanan, and P. Indumathi, Materials Research Innovations, **23**, 113 (2019), https://doi.org/10.1080/14328917.2017.1392692

ФОТОЛЮМІНЕСЦЕНЦІЯ, ІМПЕДАНС, ТЕРМІЧНІ ХАРАКТЕРИСТИКИ ТА АНАЛІЗ ПОВЕРХНІ ХІРШФЕЛЬДА МОНОКРИСТАЛІВ БІСУЛЬФАТУ КАЛІЮ ДЛЯ ЗАСТОСУВАНЬ NLO ТРЕТОГО ПОРЯДКУ

К. Тілага[a,d], П. Селварайян[b], С.М. Абдул Кадер[c]

[a]Дослідник, реєстраційний номер 19221192132006, факультет фізики, коледж Садакатуллаха Аппа Тірунелвелі -627011, Тамілнаду, Індія

[b]Кафедра фізики, Коледж мистецтв і науки Адітанар, Тіручендур -628216, Тамілнаду, Індія

[c]Кафедра фізики, Коледж Садакатуллаха Аппа, Тірунелвелі -627011, Тамілнаду, Індія

(Університет Манонманіам Сундаранар, Абішекапатті, Тірунелвелі – 627012, Тамілнаду, Індія)

[d]Кафедра фізики, Sri S.R.N.M College, Sattur-626203, Тамілнаду, Індія

Високоякісні монокристали бісульфату калію (KHS) були вирощені методом повільного випаровування при кімнатній температурі. Встановлено, що кристал KHS кристалізується в ромбічній кристалічній структурі з просторовою групою Pbca. Проаналізовано поведінку фотолюмінесценції кристала у видимій області. Це дослідження показало, що вирощений кристал KHS має інтенсивний синій пік емісії при 490 нм. Для дослідження частотно-залежних електричних характеристик при різних температурах проводили аналіз імпедансу. З досліджень імпедансу були виявлені величини об'ємного опору, опору межзеренних меж і провідності по постійному струму вирощеного кристала. Кристал KHS був підданий TGA/DTA, і результати були досліджені. Визначено такі електричні параметри, як енергія Фермі та середня енергетична ширина кристала KHS. Оцінені значення використовуються для оцінки електронної поляризуємості. Міжмолекулярні взаємодії були передбачені за допомогою аналізу поверхні Гіршфельда. Цей аналіз показав, що найбільшим внеском у кристалічну структуру була взаємодія K···O (46,7%). Двовимірна діаграма відбитків надає відсотковий внесок кожної взаємодії атома з атомом. Оскільки матеріал KHS є центросиметричним кристалом, його можна використовувати для нелінійно-оптичних додатків третього порядку (NLO).

Ключові слова: неорганічний кристал; зростання розчину; XRD; фотолюмінесценція; імпеданс; TGA/DTA; електронна поляризуємість; 3-D поверхня Гіршфельда.

East European Journal of Physics. 4. 152-159 (2021)
DOI: 10.26565/2312-4334-2021-4-20 ISSN 2312-4334

PLASMA CONVERSION OF CO_2 IN DC GLOW DISCHARGE WITH DISTRIBUTED GAS INJECTION AND PUMPING[†]

Valeriy A. Lisovskiy*, Stanislav V. Dudin, Pavlo P. Platonov, Vladimir D. Yegorenkov
V.N. Karazin Kharkiv National University, 4 Svobody Sq., Kharkiv, 61022, Ukraine
**Corresponding Author: lisovskiy@yahoo.com*
Received October 1, 2021; revised November 23, 2021; accepted November 29, 2021

Accumulation of carbon dioxide in the Earth's atmosphere leads to an increase in the greenhouse effect and, as a consequence, to significant climate change. Thus, the demand to develop effective technologies of carbon dioxide conversion grows year to year. Additional reason for research in this direction is the intention of Mars exploration, since 96% of the Martian atmosphere is just carbon dioxide, which can be a source of oxygen, rocket fuel, and raw materials for further chemical utilization. In the present paper, the plasma conversion of carbon dioxide have been studied in the dc glow discharge at the gas pressure of 5 Torr in a chamber with distributed gas injection and evacuation from the same side for the case of narrow interelectrode gap. The conversion coefficient and the energy efficiency of the conversion were determined using mass spectrometry of the exhaust gas mixture in dependence on CO_2 flow rate and the discharge current and voltage. Maximum conversion rate was up to 78% while the energy efficiency of the conversion was always less than 2%. It was found that the discharge at this pressure can operate in normal and abnormal modes and the transition between the modes corresponds just to the maximum value of the conversion coefficient for a given gas flow. It was shown that even in anomalous regime, when the cathode is completely covered by the discharge, the discharge contraction occurs in whole range of parameters studied. The anode glow and the plasma column outside the cathode layer occupy the central part of the discharge only that reduces the conversion efficiency. Optical emission spectra from the carbon dioxide plasma were measured in the range of 200-1000 nm, which allowed to make a conclusion that the Oxygen atom emission is mostly origins from the exited atoms appearing after dissociation rather than after electron impact excitation.
Keywords: carbon dioxide, plasma conversion, dc glow discharge
PACS: 52.80.Hc

In recent years, the processes of conversion of carbon dioxide (CO_2) have attracted considerable attention of researchers [1–3] due to at least two reasons. First, the accumulation of CO_2 in the Earth's atmosphere leads to an increase in the greenhouse effect and, as a consequence, to significant climate change. The main source of carbon dioxide emission into the atmosphere is energy enterprises that burn fossil fuels and organic materials. In order to reduce the concentration of CO_2 in the atmosphere, it is necessary both to reduce its emission by various sources and to develop effective methods for its utilization. Secondly, humanity plans to explore Mars and other planets and satellites of the solar system. However, 96% of the Martian atmosphere is CO_2 [3]. Under such conditions, it is possible to convert carbon dioxide molecules into carbon monoxide CO and oxygen O_2. In this case, carbon monoxide CO can be a raw material for further chemical utilization, and the CO/O_2 mixture has proven itself as a rocket fuel [3].

Plasma methods are among the most efficient for CO_2 conversion. Detailed studies were carried out with dielectric barrier discharges [4–6], gliding arc [7–9] and microwave [10–13] discharges. There are also a small number of studies on CO_2 conversion in nanosecond pulse discharge [14], corona [15, 16], glow [17–19], radiofrequency CCP [20, 21], capillary [22] and other types of discharges [23, 24]. Recently, a number of review papers have appeared (see for example [1, 2]), where the advantages and disadvantages of various methods of CO_2 conversion are analyzed in detail as well as applicability of various types of gas discharges for this process.

All plasma methods investigated to date can be divided into three different groups. Discharges of the first group (dielectric barrier, glow, microwave discharges, radiofrequency CCP, ICP [23]) allow to obtain high conversion coefficients (the ratio of the number of converted molecules to the initial number of CO_2 molecules entering the plasma volume) of more than 50%, but at the same time the energy efficiency of the conversion (the fraction of the discharge power spent specifically for the conversion of CO_2 molecules) is of the order of 1–10% and lower. The second group of discharges (gliding arcs) gives the opposite results – the energy efficiency of the conversion can exceed 50%, but the conversion rate is usually small and comparable to 10%. In the discharges of the third group (nanosecond pulse, corona, pulsed corona discharges [25]), both the conversion rate (less than 30%) and the energy efficiency of the conversion (less than 10%) are quite low. Obviously, these three groups can hardly be called effective for an economically viable production process for the conversion of carbon dioxide. Therefore, additional searches for optimal plasma technologies are needed. To do this, it is necessary to find out what types of discharges and chamber geometries will allow one to simultaneously obtain high values of both the conversion rate and the energy efficiency of the conversion.

In our recent work [19], the process of CO_2 conversion in DC discharge performed in the device possessing the distributed same-side gas supply and pumping for the distance between the electrodes of 60 mm was already investigated. In that work, the conversion rate reached 70%, but the energy efficiency of the conversion remained low

[†] ***Cite as:*** V.A. Lisovskiy, S.V. Dudin, P.P. Platonov, and V.D. Yegorenkov, East. Eur. J. Phys. 4, 152 (2021), https://doi.org/10.26565/2312-4334-2021-4-20

and usually did not exceed 1–3%. The reason for this was revealed in [26], where it was shown using the COMSOL software that with the large gap between the electrodes (as was the case in [19]), gas molecules between entering the discharge chamber and exit into the pumping system spend longer time in the discharge chamber than is necessary for their effective conversion in plasma that leads to excessive power loss. Therefore, in this work, we investigated the CO_2 conversion process for lower distance between the electrodes (11 mm).

EXPERIMENTAL

For the experiments, a discharge chamber was used, in which the CO_2 feeding and reaction products evacuation are performed through the same electrode (shower-like electrode, see photo in Fig. 1). This electrode had 265 holes evenly distributed over its surface. The inlet and outlet holes are located on a regular hexagonal grid with a step of 5 mm along the diagonals. This electrode was grounded to prevent parasitic discharges in the holes and in the pipes connected to it. The second, solid electrode was supplied with a positive voltage from the DC power supply; therefore, it was the anode. The electrodes were made of stainless steel.

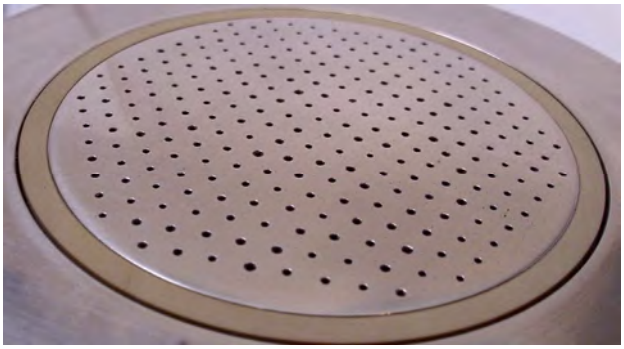

Figure 1. Photo of shower-like electrode

Turbomolecular and rotary vane pumps were used to evacuate the vacuum chamber. The electrodes described above were external, a section of a quartz tube with an inner diameter of 93 mm was sealed between the electrodes spaced by 11 mm gap. Note that in narrower gaps the ignition of the discharge will be difficult, since the breakdown curves are shifted to the range of high gas pressures [27, 28]. The experiments were carried out at carbon dioxide pressure of 5 Torr. To measure the gas pressure, a Baratron 627 capacitive manometer (MKS Instruments) with a maximum measured value of 10 Torr was used. The carbon dioxide flux Q varied from 1 sccm to 200 sccm using a mass-flow controller.

The CO_2 conversion rate can be estimated using mass spectrometry of the exhaust gas. The gas mixture leaving the discharge chamber consists mainly of CO_2, CO, O and O_2. Using a thin capillary with inner diameter of 1 mm, the analyzed portion of gas was taken from the pumping system near the outlet of the discharge chamber and fed through a valve into the ROMS-4 mass spectrometer pumped by separate ion pump. Note that oxygen atoms recombine on the walls of the capillary with the formation of O_2 molecules. The ion peak in the mass spectrum corresponding to the 16th mass (O^+) origins from O_2 molecules dissociation in the mass spectrometer ionizer. Therefore, we analyzed the peaks of M = 28 (CO^+), M = 32 (O_2^+) and M = 44 (CO_2^+) mass. Before each experiment, the mass spectrum of the residual gas in the mass spectrometer was measured and then subtracted from the obtained mass spectra of the analyzed gas mixture.

The optical emission of the discharge was measured by optical emission spectroscopy. The optical fiber was in a fixed position 5 mm from the grounded cathode electrode (almost in the center of the gap between the electrodes) and supplied the collected discharge radiation to the Horiba iHR-320 optical spectrometer. This spectrometer has a diffraction grating of 1800 lines/mm allowing spectrum measurement in wide wavelength range (200–1000 nm), with high resolution (better then 1 Å).

Note that the following three parameters are used to characterize the process of carbon dioxide conversion: specific energy input (SEI), absolute conversion coefficient χ and energy efficiency of the process η. Specific energy input is the ratio of the power supplied to the discharge to the value of the gas flow:

$$SEI\left[J\cdot cm^{-3}\right]=\frac{P\left[kW\right]}{\frac{dm}{dt}\left[L\cdot\min^{-1}\right]}\cdot 60\left[s\cdot\min^{-1}\right]\times$$
$$\times\frac{6.24\cdot 10^{21}\left[eV\cdot kJ^{-1}\right]\cdot 24.5\left[L\cdot mol^{-1}\right]}{6.022\cdot 10^{23}\left[mol^{-1}\right]},$$

where P is the power, dm/dt is the gas flow rate. The absolute conversion rate is the ratio of the number of CO_2 molecules that have been converted as the gas passes through the plasma volume to their initial number:

$$\chi = \frac{N_{in} - N_{out}}{N_{in}},$$

where N_{in} and N_{out} are CO_2 fluxes entering and pumping out of the chamber, respectively. Energy efficiency compares the energy consumption of a given conversion technique with the standard enthalpy of the process:

$$\eta = \chi \cdot \frac{\Delta H}{SEI},$$

where ΔH = 2.93 eV per molecule.

Thus, SEI, conversion coefficient χ and energy efficiency η can be determined if the concentration of CO_2 molecules without plasma and with a burning discharge were measured using a mass spectrometer, while simultaneously registering the power *P* deposited into the plasma and gas flow *Q* fed into the chamber. This technique is described in detail in [23, 24].

EXPERIMENTAL RESULTS

Let us consider our results obtained for a carbon dioxide pressure of 5 Torr. This pressure is interesting because the average atmospheric pressure of Mars is close to this value, therefore, a significant part of the experiments of other authors on the conversion of CO_2 were carried out precisely for this pressure.

Figure 2 shows a photograph of the discharge with current of 100 mA for the considered CO_2 pressure. At a lower current the normal mode is observed where the discharge covers only a part of the cathode surface.

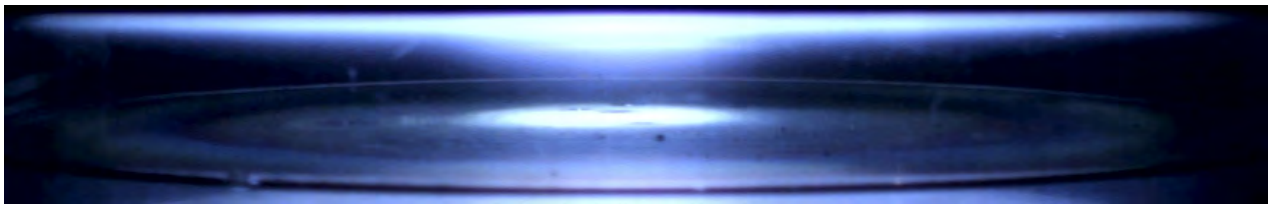

Figure 2. Photo of the discharge at CO_2 pressure of 5 Torr, gas flow rate of 2 sccm, and discharge current of 100 mA.

In this case, an increase in the current (until the moment of complete coverage of the entire cathode by the discharge) occurs at a constant or even decreasing voltage across the electrodes [29]. Figure 3 shows that the current-voltage characteristics of the discharge have two branches: falling (the current decreases with increasing voltage) and growing (current and voltage increase simultaneously).

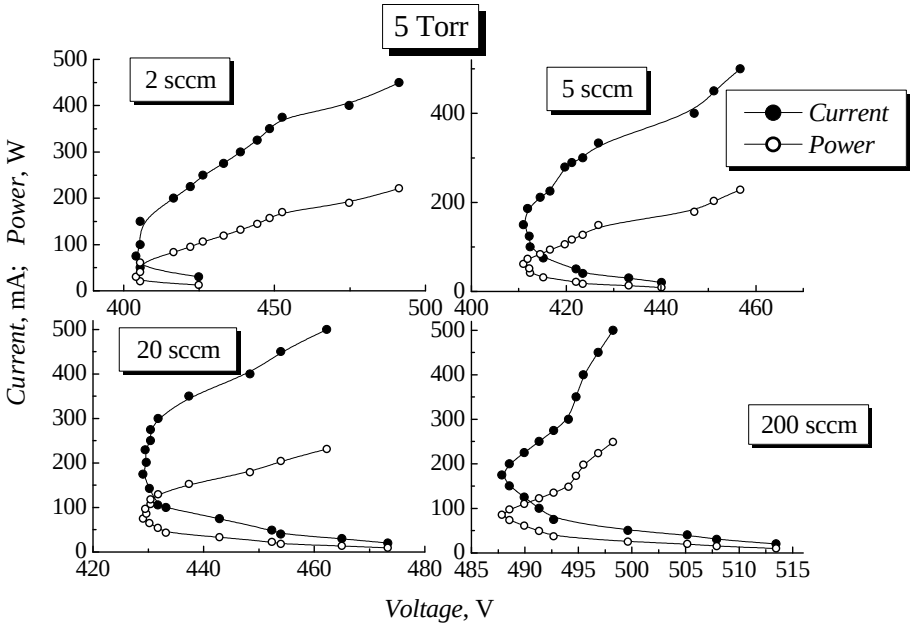

Figure 3. Dependences of the current and the power supplied to the discharge on the applied voltage at various gas flow rates (2 sccm, 5 sccm, 20 sccm and 200 sccm).

The falling branch belongs to the normal mode. The growing branch describes an anomalous regime in which the cathode surface is already completely covered by the discharge, and to further increase the current, it is necessary to increase the voltage across the cathode layer (and over the entire discharge gap) to enhance the ionization production of

charged particles. The values of the power supplied to the discharge presented in Fig. 3 will be used below to determine the SEI and the energy efficiency η of the process.

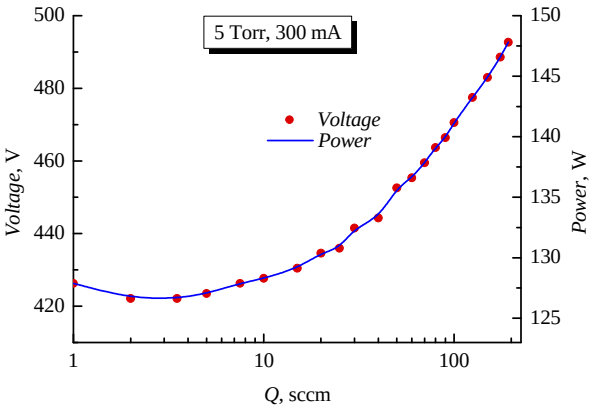

Figure 4. Dependence of the voltage across the electrodes and the power applied to the discharge on the gas flow *Q* at the pressure of 5 Torr and the current of 300 mA

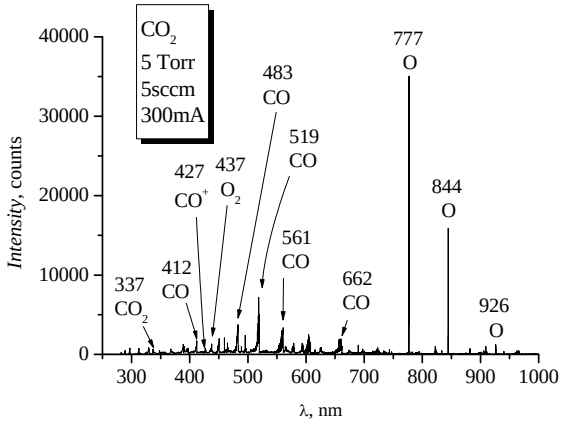

Figure 5. Optical emission spectrum measured at carbon dioxide pressure of 5 Torr, flow rate of 5 sccm, and discharge current of 300 mA.

Note that even when the discharge completely covers the cathode surface the glow occupies only a part of the anode area. If the distance between the electrodes is increased, then, starting from the anode, with a sufficiently large gap, a contracted positive column is formed, which occupies only a part of the cross section of the discharge tube. The photograph of the discharge shown in Fig. 2 shows that the cathode layer (which is practically invisible) and the negative glow jointly extend only 2–3 mm from the cathode surface. Deceleration of the bulk of fast electrons (born and accelerated in the strong electric field of the cathode layer) occurs just in the negative glow. The negative glow transforms into the dark Faraday space and then, in the region of the plasma column, into the anode glow. However, outside this column, a significant part of the discharge volume is occupied by decaying plasma with low density of charged particles. Therefore, as will be shown below, at a carbon dioxide pressure of 5 Torr, the energy efficiency of the conversion is low.

Figure 4 shows that with an increase in the carbon dioxide flux *Q* both the voltage between the electrodes and the power applied to the discharge first decrease, reach a minimum at a flux of about 2.5–3 sccm, and then increase. The discharge current during this experiment was kept constant.

The optical emission spectrum of the discharge (see Fig. 5) consists of lines of atomic oxygen O (777 nm, 844 nm and 926 nm), as well as a large number of bands of CO molecules (they mainly relate to the Angstrom system, the $B\ ^1\Sigma \rightarrow A\ ^1\Pi$ transition from the second to the first state of electronic excitation of the molecule).

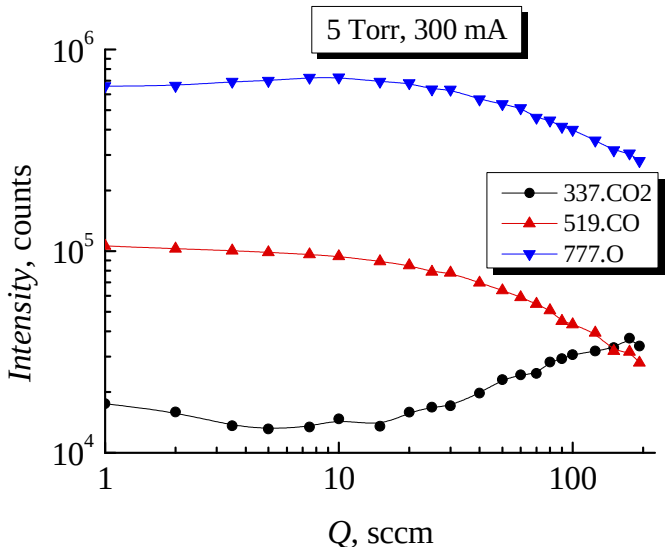

Figure 6. Dependences of the intensities of emission lines for CO_2 (337 nm), CO (519 nm) and O (777 nm) on the gas flow rate at pressure of 5 Torr and discharge current of 300 mA.

In addition, there are weak lines of O_2 (Schumann-Runge system, $B\ ^3\Sigma \rightarrow X\ ^3\Sigma$), CO^+ ("comet tail" system, $A\ ^2\Pi \rightarrow\ ^2\Sigma$ transition from the first excited electronic state to the ground state). The glow of CO_2 molecules is

represented by a weak line with a wavelength of 337 nm. Note that the luminescence of atomic oxygen can be caused both by the dissociation process itself (in this case, the CO_2 molecule decays into CO in the ground state and into an excited O atom [1, 2]), and by the excitation of oxygen atoms by subsequent electron impacts. That is why the intensities of the lines of atomic oxygen are so high in comparison with the lines of CO molecules. Moreover, the intensities of the CO, CO_2 and O_2 lines (which are excited only by electron impact) are usually tens of times lower than the intensities of the atomic oxygen lines. Thus, we suppose that the glow of oxygen atoms at wavelengths of 777 nm and 844 nm is almost completely associated with the process of dissociation of CO_2 molecules.

The difference in the mechanisms of excitation of CO molecules and O atoms is clearly seen in Fig. 6, which shows the dependences of the intensities of the emission lines of CO_2, CO and O on the gas flow rate.

It follows from the figure that the emission intensity of carbon dioxide molecules first decreases with the gas flow rate increase, reaches a minimum, and then increases. The opposite behavior is shown by the intensity of the lines of oxygen atoms, first increasing with the flow rate increase, then reaching a maximum, and finally decreasing. This behavior of the CO_2 and O lines can be explained by the assumption that at low gas flow rates ($Q \sim 1$ sccm) carbon dioxide molecules have time not only to be converted into CO and O, but also to partially recombine back into CO_2 molecules. With the flow rate increase, the residence time of molecules in the discharge chamber decreases, the process of CO and O recombination in CO_2 plays a lesser role, thus, the CO_2 concentration decreases, and the concentration of oxygen atoms increases. At higher flows ($Q > 10$ sccm), the gas is removed from the discharge without having time to be converted. However, the intensity of the CO line decreases monotonically with increasing gas flow, without reaching any extrema. Therefore, a clear correlation between the behavior of the CO_2 and O intensities is associated with the fact that the loss of CO_2 molecules during dissociation is accompanied by the appearance of excited O atoms. But CO molecules emit light only after they experience inelastic collisions with electrons after the conversion. Consequently, the intensity of their luminescence decreases with an increase in the gas flow due to the intensification of their removal from the discharge chamber.

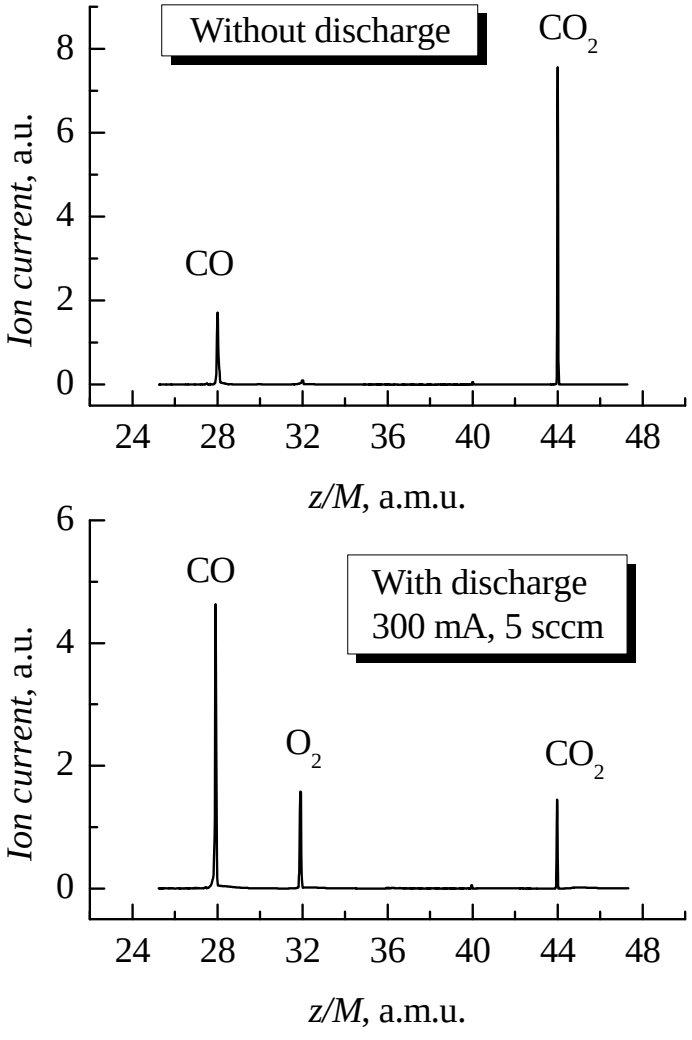

Figure 7. Mass spectra of the gas mixture leaving the discharge on and off. The gas flow rate is 5 sccm. The discharge current is 300 mA.

Now let us consider the mass spectra of the exhaust gas mixture (see Fig. 7). The mass spectrum of the gas leaving the chamber without discharge should only consist of CO_2^+ (M = 44). The CO^+ peak (M = 28) and a weak O_2^+ peak (M = 32) are observed, which are formed inside the mass spectrometer as a result of CO_2 dissociation and subsequent ionization of its products. The appearance of plasma in the chamber leads to a significant decrease in the CO_2^+ peak and a simultaneous increase of CO^+ and O_2^+ peaks.

From the measured mass spectra, the intensities of the CO_2^+, CO^+ and O_2^+ peaks were determined. Fig. 8 shows the dependences of the intensities of these peaks on the gas flow. It can be seen from the figure that the lowest values of the CO_2^+ peak are observed at low gas flows, and with increasing Q the CO_2^+ peak grows. This indicates that an increase in gas flow leads to the fact that more and more carbon dioxide molecules are removed from the discharge chamber, without having time and enough power to convert into CO and O.

Using the measured mass spectra and current-voltage characteristics of the glow discharge, the values of the conversion coefficient χ and the energy efficiency of the conversion η were determined, the dependences of which on the gas flow rate are shown in Fig. 9. It can be seen from the figure that at low gas flows the conversion coefficient reaches 78%, but with an increase in Q the conversion coefficient monotonically decreases down to 23% at

Q = 100 sccm due to a decrease in the residence time of CO_2 molecules in the discharge. The energy efficiency of conversion η at low flow rates is quite low and amounts to only 0.07%, but at high flows it reaches 1.6%.

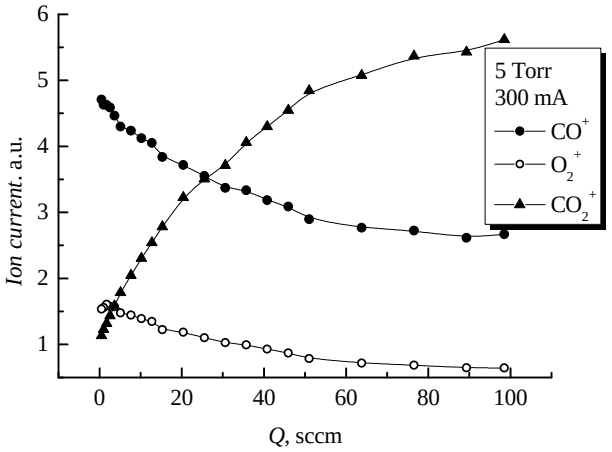

Figure 8. Dependences of the peak intensities in the mass spectra of the gas mixture leaving the discharge chamber into the pumping system on the gas flow at the gas pressure of 5 Torr and discharge current of 300 mA.

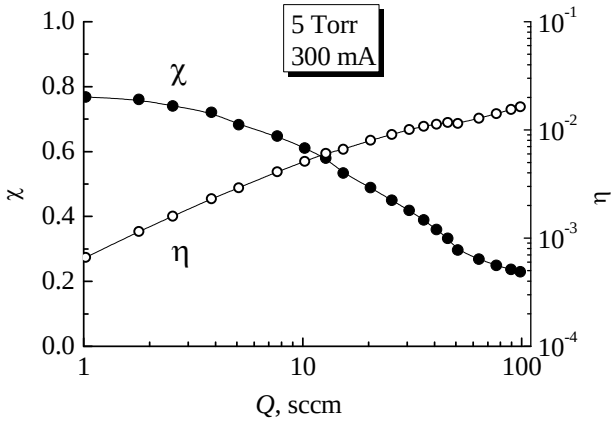

Figure 9. Dependences of the conversion coefficient χ and the energy efficiency of the conversion η on the gas flow at pressure of 5 Torr and discharge current of 300 mA.

Since the specific energy input SEI is inversely proportional to the gas flow, the dependences of χ and η on the gas flow rate shown in Fig. 9 are mirrored when plotting them as a function of SEI (see Fig. 10). That is, the low Q range corresponds to high SEI values. Conversely, at high gas flows the SEI becomes small. It should be kept in mind that SEI is proportional to the power input into the discharge, which depends on the gas flow (see Fig. 4).

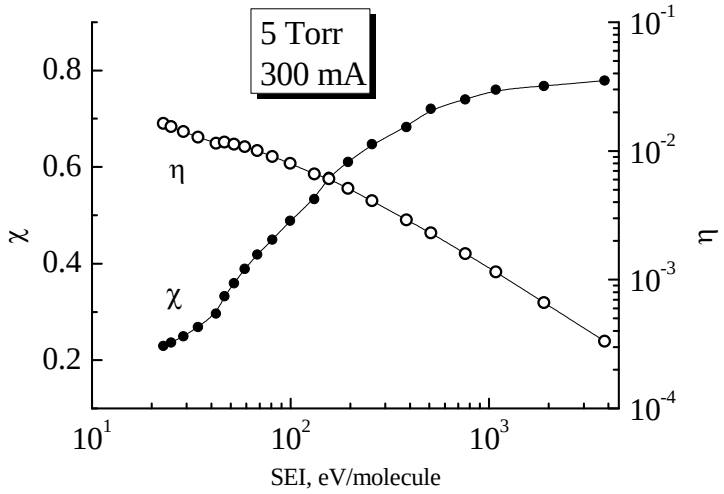

Figure 10. Dependences of the conversion coefficient χ and the energy efficiency of conversion η on SEI at the pressure of 5 Torr and the discharge current of 300 mA.

A convenient tool for comparison of carbon dioxide conversion processes under various conditions (types of discharges, ranges of gas pressure, current, gas flow, etc.) is the dependence of η on χ. Such dependence at fixed pressure and discharge current, but different gas flow rates, is shown in Fig. 11. From the economical point of view, the most optimal case is when both η and χ are close to 100%. However, at present, such a technology for the conversion of carbon dioxide has not yet been developed, as we mentioned in the Introduction. It follows from Figure 11 that higher values of the energy efficiency η are observed at low values of the conversion coefficient χ. An increase in χ is accompanied by a rapid decrease in energy efficiency. Under the conditions of our experiments, it was possible to achieve the maximum conversion rate χ = 78%, but at the same time the energy efficiency of the conversion is approximately equal to 0.07%.

A similar dependence of η on χ at the 5 Torr pressure with various flow rates is shown in Fig. 12. To obtain these dependences, the current varied from the minimum value at which it was possible to maintain a stable discharge burning (several milliamperes) to 500 mA. Recall that at low currents, the glow discharge burns in the normal mode, covering only a part of the cathode surface. The complete filling of the cathode with a discharge is observed at approximately a current of 100–200 mA (which depends on the gas flow). From Fig. 12 it can be seen that for a flow of Q = 1 sccm, the dependence of η on χ has two branches: an upper (corresponding to low currents) and a lower (high-current branch).

The transition from the upper to the lower branch occurs at the maximum value of the conversion coefficient χ for a given gas flow. The more the gas flow was, the less pronounced the lower branch was. In this case, the use of higher gas flows led to an increase in the energy efficiency of the conversion η. At a flow rate of Q = 25 sccm, it was possible to simultaneously achieve the values χ > 50% and η ≈ 1 %; moreover, the value of the energy efficiency η changed little over a wide range of values of the discharge current. Note that the presented results on the conversion efficiency are generally close to the same results of the paper [19] with wider discharge gap.

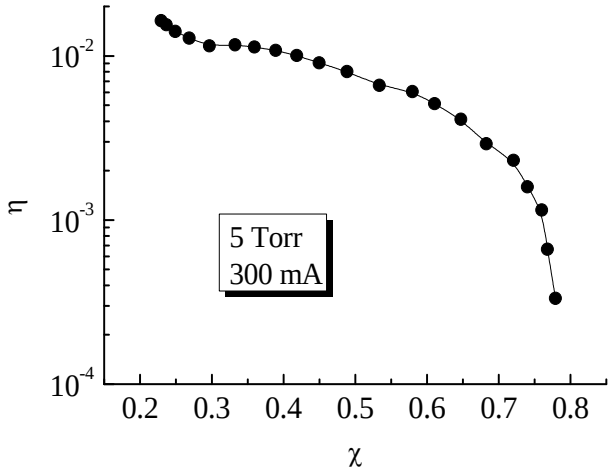

Figure 11. Relation between the energy efficiency of conversion η and the conversion coefficient χ at a pressure of 5 Torr and a discharge current of 300 mA.

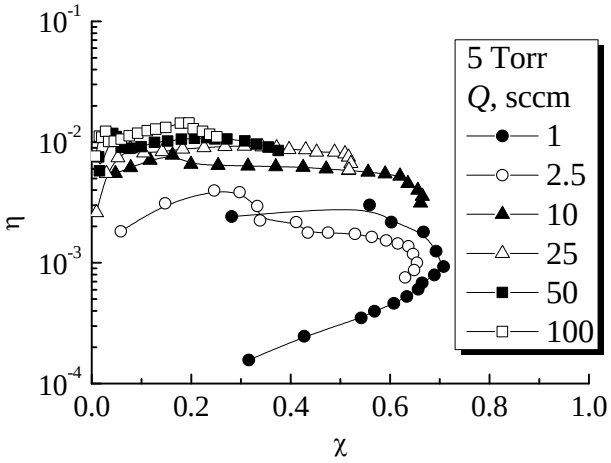

Figure 12. Dependence of the energy efficiency of conversion η on the conversion coefficient χ at the 5 Torr pressure with various gas flow rates

CONCLUSION

In the present research, we have studied the conversion of carbon dioxide in the dc glow discharge at the gas pressure of 5 Torr in a chamber with distributed gas injection and evacuation from the same side for the case of narrow interelectrode gap. The conversion coefficient χ and the energy efficiency of the conversion η were determined using mass spectrometry of the exhaust gas mixture in dependence on CO_2 flow rate and the discharge current and voltage. Under the conditions of our experiments, it was possible to achieve the maximum conversion rate χ = 78%, but the energy efficiency of the conversion was always less then 2%. Optical emission spectra from the carbon dioxide plasma were measured in the range of 200-1000 nm, which allowed to make a conclusion that the oxygen atom emission is mostly origins from the excited atoms appearing after dissociation rather than after electron impact excitation.

It is shown that at the studied pressure the discharge can operate in two different modes. At low discharge current the normal mode reveals where the discharge covers only a part of the cathode. At higher currents the anomalous regime appears, in which the cathode surface is already completely covered by the discharge, and to further increase the current, it is necessary to increase the discharge voltage. We have found that the transition between the modes occurs just at the maximum value of the conversion coefficient χ for a given gas flow. The use of higher gas flows led to an increase in the energy efficiency of the conversion η. At a flow rate of Q = 25 sccm, it was possible to simultaneously achieve the values χ > 50% and η ≈ 1 %.

It was found that even in anomalous regime, when the cathode is completely covered by the discharge, the discharge contraction occurs in whole range of parameters studied. The plasma column outside the cathode layer and the anode glow occupy the central part of the discharge only. Outside this column, in a significant part of the discharge volume only low density decaying plasma is present that reduces the energy efficiency of the conversion.

Acknowledgement

This research was conducted under financial support of National Research Foundation of Ukraine.

ORCID IDs

Valeriy A. Lisovskiy, https://orcid.org/0000-0002-6339-4516; **Stanislav V. Dudin**, https://orcid.org/0000-0001-9161-4654

REFERENCES

[1] R. Snoeckx, and A. Bogaerts, Chem. Soc. Rev. **46**, 5805 (2017), https://doi.org/10.1039/C6CS00066E
[2] A. Bogaerts, and G. Centi, Frontiers in Energy Research. **8**, 111 (2020), https://doi.org/10.3389/fenrg.2020.00111
[3] P. Ogloblina, A.S. Morillo-Candas, A.F. Silva, T. Silva, A. Tejero-del-Caz, L.L. Alves, O. Guaitella, and V. Guerra, Plasma Sources Sci. Technol. **30** 065005 (2021), https://doi.org/10.1088/1361-6595/abec28
[4] R. Aerts, W. Somers, and A. Bogaerts, Chem. Sus. Chem. **8**, 702 (2015), https://doi.org/10.1002/cssc.201402818
[5] S. Paulussen, B. Verheyde, X. Tu, C. De Bie, T. Martens, D. Petrovic, A. Bogaerts, and B. Sels, Plasma Sources Sci. Technol. **19**, 34015 (2010), https://doi.org/10.1088/0963-0252/19/3/034015

[6] A. Ozkan, A. Bogaerts, and F. Reniers, J. Phys. D: Appl. Phys. **50**, 84004 (2017), https://doi.org/10.1088/1361-6463/aa562c
[7] S.R. Sun, H.X. Wang, D.H. Mei, X. Tu, and A. Bogaerts, J. CO_2 Util. **17**, 220 (2017), http://dx.doi.org/10.1016/j.jcou.2016.12.009
[8] T. Nunnally, K. Gutsol, A. Rabinovich, A. Fridman, A. Gutsol, and A. Kemoun, J. Phys. D: Appl. Phys. 2011, 44, 274009, https://doi.org/10.1088/0022-3727/44/27/274009
[9] F. Ouni, A. Khacef and J. M. Cormier, Chem. Eng. Technol. 2006, 29, 604–609, https://doi.org/10.1002/ceat.200500333
[10] A. Fridman, *Plasma chemistry*, (Cambridge University Press, New York, 2008), pp. 978, https://doi.org/10.1017/CBO9780511546075
[11] W. Bongers, H. Bouwmeester, B. Wolf, F. Peeters, S. Welzel, D. van den Bekerom, N. den Harder, A. Goede, M. Graswinckel, P.W. Groen, J. Kopecki, M. Leins, G. Van Rooij, A. Schulz, M. Walker, and R. van de Sanden, Plasma Processes Polym. **14**, e1600126 (2017), https://doi.org/10.1002/ppap.201600126
[12] A.P.H. Goede, W.A. Bongers, M.F. Graswinckel, R.M.C.M. Van De Sanden, M. Leins, J. Kopecki, A. Schulz, and M. Walker, EPJ Web Conf. **79**, 01005 (2014), https://doi.org/10.1051/epjconf/20137901005
[13] L.F. Spencer and A.D. Gallimore, Plasma Sources Sci. Technol. **22**, 15019 (2013), https://doi.org/10.1088/0963-0252/22/1/015019
[14] M.S. Bak, S.K. Im, and M. Cappelli, IEEE Trans. Plasma Sci. **43**, 1002 (2015), https://doi.org/10.1109/TPS.2015.2408344
[15] G. Horváth, J.D. Skalný, and N.J. Mason, J. Phys. D: Appl. Phys. 2008, 41, 225207, https://doi.org/10.1088/0022-3727/41/22/225207
[16] T. Mikoviny, M. Kocan, S. Matejcik, N.J. Mason, and J.D. Skalny, J. Phys. D: Appl. Phys. 2004, 37, 64, https://doi.org/10.1088/0022-3727/37/1/011
[17] S.L. Suib, S.L. Brock, M. Marquez, J. Luo, H. Matsumoto, and Y. Hayashi, J. Phys. Chem. B, **102**, 9661 (1998), https://doi.org/10.1021/jp9822079
[18] S.L. Brock, T. Shimojo, M. Marquez, C. Marun, S.L. Suib, H. Matsumoto, and Y. Hayashi, J. Catal. **184**, 123 (1999), https://doi.org/10.1006/jcat.1999.2440
[19] V.A. Lisovskiy, S.V. Dudin, P.P. Platonov, and V.D. Yegorenkov. Studying CO_2 conversion in DC glow discharge, PAST, **6**, 179 (2020), https://vant.kipt.kharkov.ua/ARTICLE/VANT_2020_6/article_2020_6_179.pdf
[20] L.F. Spencer, and A.D. Gallimore, Plasma Chem. Plasma Process. **31**, 79 (2010), https://doi.org/10.1007/s11090-010-9273-0
[21] V.D. Rusanov, A.A. Fridman, and G.V. Sholin, Sov. Phys. Usp. **24,** 447 (1981), https://doi.org/10.1070/PU1981v024n06ABEH004884
[22] S. Mori, A. Yamamoto, and M. Suzuki, Plasma Sources Sci. Technol. **15**, 609 (2006), https://doi.org/10.1088/0963-0252/15/4/003
[23] S.V. Dudin, A.V. Zykov, and S.D. Yakovin, PAST, **4**, 141 (2019), https://vant.kipt.kharkov.ua/article/VANT_2019_4/article_2019_4_141.pdf
[24] S.V. Dudin, and A.N. Dakhov, PAST, **6**, 194 (2018), https://vant.kipt.kharkov.ua/ARTICLE/VANT_2018_6/article_2018_6_194.pdf
[25] Y. Wen, and X. Jiang, Plasma Chem. Plasma Process. **21**, 665 (2001), https://doi.org/10.1023/A:1012011420757
[26] P.P. Platonov, S.V. Dudin, and V.A. Lisovskiy, PAST, **1**, 131 (2021), https://vant.kipt.kharkov.ua/ARTICLE/VANT_2021_1/article_2021_1_131.pdf
[27] V.A. Lisovskiy, V.A. Koval, and V.D. Yegorenkov, Physics Letters A, **375**(19), 1986 (2011), https://doi.org/10.1016/j.physleta.2011.03.035
[28] V.A. Lisovskiy, R.O. Osmayev, A.V. Gapon, S.V. Dudin, I.S. Lesnik, and V.D. Yegorenkov, Vacuum, **145**, 19 (2017), https://doi.org/10.1016/j.vacuum.2017.08.022
[29] V.A. Lisovskiy, K.P. Artushenko, and V.D. Yegorenkov, PAST, **6**, 223 (2016), https://vant.kipt.kharkov.ua/ARTICLE/VANT_2016_6/article_2016_6_223.pdf

ПЛАЗМОВА КОНВЕРСІЯ CO_2 У ТЛІЮЧОМУ РОЗРЯДІ ПОСТІЙНОГО СТРУМУ З РОЗПОДІЛЕНИМ НАПУСКОМ ТА ВІДКАЧУВАННЯМ ГАЗУ

В.А. Лісовський, С.В. Дудін, П.П. Платонов, В.Д. Єгоренков
Харківський національний університет імені В.Н. Каразіна, майдан Свободи 4, Харків, 61022, Україна

Накопичення вуглекислого газу в атмосфері Землі призводить до посилення парникового ефекту і, як наслідок, до значної зміни клімату. Таким чином, попит на розробку ефективних технологій конверсії вуглекислого газу з кожним роком зростає. Додатковим приводом для досліджень у цьому напрямку є намір дослідження Марса, оскільки 96% марсіанської атмосфери — це вуглекислий газ, який може бути джерелом кисню, ракетного палива та сировини для подальшої хімічної утилізації. У цій роботі досліджено плазмова конверсія вуглекислого газу в тліючому розряді постійного струму при тиску газу 5 Торр в камері з розподіленим напуском та відкачуванням газу з одного боку для випадку вузького міжелектродного проміжку. Коефіцієнт конверсії та її енергоефективність визначали за допомогою мас-спектрометрії суміші вихлопних газів залежно від потоку CO_2 та струму та напруги розряду. Максимальний коефіцієнт конверсії становив до 78%, тоді як енергоефективність конверсії завжди була менша за 2%. Встановлено, що розряд при цьому тиску може існувати в нормальному і аномальному режимах, а перехід між режимами відповідає якраз максимальному значенню коефіцієнта конверсії для даного потоку газу. Показано, що навіть в аномальному режимі, коли катод повністю покритий розрядом, контракція розряду відбувається в усьому діапазоні досліджуваних параметрів. Анодне світіння і стовп плазми поза катодним шаром займають лише центральну частину розряду, що знижує ефективність конверсії. Виміряно спектри оптичного випромінювання з плазми вуглекислого газу в діапазоні 200-1000 нм, що дозволило зробити висновок, що випромінювання атома Оксигену здебільшого відбувається від збуджених атомів, які виникають після дисоціації, а не після збудження електронним ударом.

Ключові слова: вуглекислий газ, плазмова конверсія, тліючий розряд постійного струму

EAST EUROPEAN JOURNAL OF PHYSICS. 4. 160-163 (2021)
DOI: 10.26565/2312-4334-2021-4-21 ISSN 2312-4334

CONCEPT OF NEUTRON SOURCE CREATION FOR NUCLEAR MEDICINE BASED ON LINEAR ELECTRON ACCELERATOR[†]

Valentin I. Kasilov*, Sergey P. Gokov, Sergiy A. Kalenik, Sergey S. Kochetov, Leonid D. Saliy, Vitaliy V. Tsyats'ko, Evgen V. Tsyats'ko, Oleg A. Shopen
NSC "Kharkov Institute of Physics and Technology"
Akademicheskaya 1 st., Kharkov, Ukraine, 61108
**Corresponding Author: kasilovvi@kipt.kharkov.ua*
Received August 26, 2021; revised November 22, 2021; accepted November 23, 2021

We review the current status of the development of sources of epithermal neutrons sources based on reactors and accelerators for boron neutron capture therapy (BNCT), a promising method of malignant tumor treatment. The scheme is proposed of the source prototype for the production of thermal and epithermal neutrons using the delayed neutrons generated with help of linear electron accelerator at the target containing the fissile material. The results of an experiment are presented in which the half-life curves of radioactive nuclei formed during fission and emitting delayed neutrons are measured. It is shown that an activated target containing fissile material is a compact small-sized source of delayed neutrons. It can be delivered to the shaper, where, using a moderator, an absorber, and a collimator, neutrons of thermal or epithermal energies are formed over a certain period of time, after which this target is sent to the activator, and another target comes in its place. Thus, a pulsed neutron flux is formed. Such a neutron beam can be used in nuclear medicine, in particular, in neutron capture therapy in the treatment of cancer. An important task in the implementation of neutron capture therapy, when irradiating patients, is to control both the intensity and the energy spectrum of the neutron flux. To solve this problem, an earlier developed activation-type neutron ball spectrometer can be used, which will allow optimization of various parameters of the shaper, collimator and filters in order to obtain the most powerful neutron fluxes.
Keywords: nuclear medicine, delayed neutrons, thermal neutrons, linear accelerator, neutron source
PACS: 29.25.Dz

CONCEPT OF NEUTRON CAPTURE THERAPY

Treatment of tumor by means of neutron capture therapy requires formatted beams of thermal or epithermal neutrons with the flux density (2-3) 10^9 neutron/(cm^2 s), which can be generated at different devices, namely, reactors and charged particle accelerators. The essence of the method consists in preliminary injection to the patient of medication containing ^{10}B or ^{157}Gd which are accumulated predominantly in the tumor.

When thermal or epithermal neutrons interact with the these elements reaction products are obtained. E.g., stable isotope ^{10}B transforms after absorbing the neutron into the excited nucleus ^{11}B which decays within 10^{-12} seconds into the kernel ^7Li and -particle having large energy (about 2 MeV). These charged particles are quickly slowed down within the cancer cell. 80 % of the energy is released in the same cell which contained the Boron kernel what leads to the distraction of this cell.

Up to now, nuclear reactor were the most convenient sources of thermal or epithermal neutrons for neutron capture therapy [1-5]. In such an installation, patient is located in a special box behind the biological protection which has a neutron channel for the output of the formatted beam of thermal or epithermal neutrons to the distances up to 3-5 m. This is due to the fact that neutron flux density is decreasing inversely with the square of distance, and this density at larger distances is not sufficient for the irradiation of the patient despite the high neutron flux in the active zone which is of the order of 10^{14}-10^{15} neutrons/cm^2. Unfortunately such installations cannot be used directly in clinics because this is a large scale, complex and very expensive equipment. Moreover, a trend appeared recently is to use in clinics compact sources of thermal or epithermal neutrons. E.g., a project of 10 kW reactor device «Mars» for the treatment of oncological deceases has been developed in Russia.

During the last decade, an increasing interest is seen to the creation of compact, relatively cheap straight flow accelerators which are capable to generate neutrons for neutron and neutron capture therapy directly at oncological centers [6-8]. Creation of the compact source of thermal and epithermal neutrons on the basis of linear electron accelerator is also an actual task. For this purpose, we have performed preliminary studies of the new method of neutron generation using a linear electron accelerator [6]. This method is based on the use of delayed fission neutrons which are released from the activated target containing the fissile material.

The purpose of the present work is the analysis of the results obtained earlier in the studies of the method [9] of generation of thermal and epithermal neutrons, and, based on these results, creation of the prototype of the compact source on the basis of linear electron accelerator LINAC-300. This source can be a prototype for the full scale source of thermal and epithermal neutrons, which can be built on the basis of existing at NSC KIPT linear accelerator with 20 kW power in the outgoing electron beam. This allows to generate necessary neutron fluxes for the use in nuclear medicine.

[†] ***Cite as:*** V.I. Kasilov, S.P. Gokov, S.A. Kalenik, S.S. Kochetov, L.D. Saliy, V.V. Tsyats'ko, E.V. Tsyats'ko, and O.A. Shopen, East. Eur. J. Phys. **4**, 160 (2021), https://doi.org/10.26565/2312-4334-2021-4-21

METHOD OF GENERATION OF THERMAL AND EPITHERMAL NEUTRONS USING THE LINEAR ELECTRON ACCELERATOR

Usually generation of neutrons with help of the linear electron accelerator uses the outgoing beam with the energy 20 MeV at the target from the heavy material. In this work, it is proposed to use a target containing the fissile material ^{238}U with 2% enrichment with ^{235}U and with the volume of 1 cm^3 located in the activator on exit from the electron accelerator.

Activator consists of the moderator and reflector which are needed for the creation of the field of thermal neutrons. These neutrons are produced as a result of slowing down of delayed fast neutrons appearing in process of interaction of the electron beam with the target consisting of fissile material.

It is known that the interaction of electron beam with the target of fissile material leads to the generation of γ -quanta and photo-neutrons which stimulate nuclear fission reaction with formation of derbies. Photo-fission reaction results in instantaneous as well as in delayed neutron generation. Relative contribution of delayed neutrons is 1% of all neutrons.

Group parameters [10] of delayed neutrons in case of ^{235}U fission by the thermal neutrons are presented in Table.

Group	Relative contribution $a_i \pm \Delta a_i$	Half-decay period $T_i \pm \Delta T_i$
1	0.038 ± 0.001	53.95 ± 0.028
2	0.211 ± 0.004	22.34 ± 0.13
3	0.197 ± 0.004	6.40 ± 0.08
4	0.396 ± 0.005	2.26 ± 0.03
5	0.132 ± 0.004	0.494 ± 0.017
6	0.026 ± 0.001	0.179 ± 0.006

As seen from Table 1, half-decay periods change depending on the group from hundreds of milliseconds to 54 seconds. Note that after activation of the target containing fissile material by the electron beam and by the field of thermal neutrons formed in the activator, target becomes a compact source of delayed neutrons. Such a target can be transported during 1-2 s to the distance of 20-50 m from the active zone of the accelerator to the device-formator located in a different room. It is seen from Table 1 that the main contribution to the emission of delayed neutrons is made by groups 2,3 and 4. First group contributes less than 4% while 5 and 6 groups give practically no contribution because of a short half-decay period as compared to the transportation time of the activated target to the formator where it emits delayed neutrons. Device-formator consists of the moderator, reflector, filter, absorber and collimator which are needed for the achievement of neutron beam parameters necessary for the neutron capture therapy of oncological diseases.

Based on the above conclusions one can propose a principal scheme of the prototype of the device for the generation of thermal or epithermal neutrons. This scheme is shown in Fig.1 where it is seen that one can use two-path pneumatic mail connecting the activator of target and the formator of thermal and epithermal neutrons.

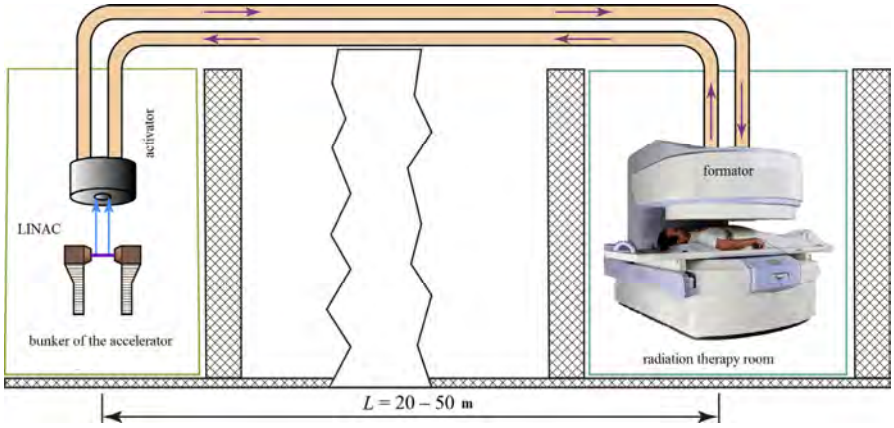

Figure 1. Principal scheme of the prototype of the device for the generation of thermal or epithermal neutrons

We suppose that system shown schematically in Fig.1 uses two targets. One is currently located in the activator where it is activated by the electron beam and the other one is located in the block-formator where it emits delayed neutrons during a certain time period. When time of presence in the formator emitting delayed neutrons is over targets are exchanged with help of pneumatic mail. Such a procedure can be repeated as many times as needed for the accumulation of the therapeutic dose at irradiated object. The activated target is a compact source of delayed neutrons which can be moved during the time about 1-2 s to the formator located near the irradiated object at the distance of 20-50 m from the activator.

In the earlier studies [9], we have measured decay curves for delayed neutrons released from the activated target and converted by the formator into thermal and epithermal neutrons. The results of the measurements are presented in Fig. 2.

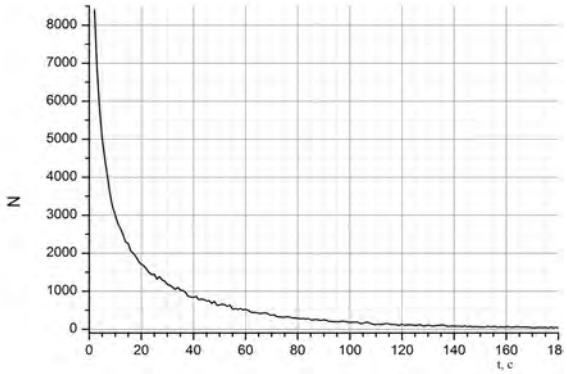

Figure 2. Decay curve of delayed neutrons slowed down to the energies in the range from 0.5 eV to 10 keV.

After the procession of the decay curve presented in Fig. 2, the dependence of the average flux density of slowed down neutrons at the supposed object on the emission time from the activated target in the device-formator has been obtained. The results of data procession are presented in the form of the histogram in Fig.3.

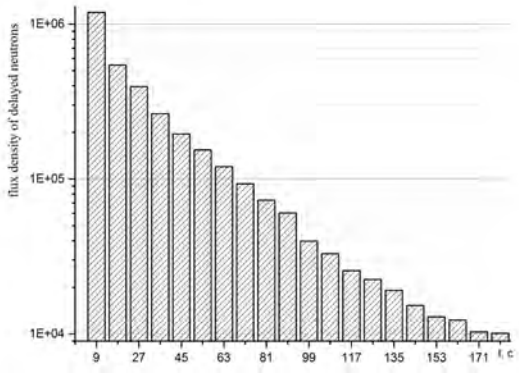

Figure 3. Flux density of delayed neutrons as function of time of emission in the device-formator (in the logarithmic scale)

It is seen from the figure that flux density of delayed neutrons decays exponentially with emission time of delayed neutrons by the sample activated in the device-formator. E.g., the shorter is the emission time interval the higher is the delayed neutron flux. Thus, if two targets are used which are subsequently exchanged with help of pneumatic mail between the activator and formator as shown in Fig.1, the procedure described above can be used for the creation of the so called pulsed source of thermal and epithermal neutrons. Then the duration of neutron pulse will be determined by the time of presence of the activated target in the formator, and the distance between pulses will be determined by the transportation time of the activated target to the formator. After slowing down of delayed neutrons and their passage through the filters, absorbers and collimator we obtain the neutron beam with necessary parameters for the neutron capture therapy. The dose achieved will be determined by the number of pulses of thermal or epithermal neutrons. As shown in [6], such a neutron beam can be created on the basis of a linear electron accelerator.

An important task in the implementation of neutron capture therapy, when irradiating patients, is to control both the intensity and the energy spectrum of the neutron flux. To solve this problem, an earlier developed spherical neutron spectrometer of activation type can be used [11]. The neutron spectrometer will also allow optimization of various parameters of the formator, collimator and filters in order to obtain the most powerful neutron fluxes that would meet the requirements of neutron capture therapy.

CONCLUSIONS

A scheme of the prototype of the compact neutron source has been proposed on the basis of the new method for the generation of thermal and epithermal neutrons with help of linear electron accelerator using delayed neutrons from the activated target containing fissile material. This prototype can be used for the development of the full-scale neutron source for neutron and neutron capture therapy of oncological diseases.

It has been also shown that the use of the above method for the generation of thermal and epithermal neutrons allows to create compact neutron sources on the basis of linear electron accelerators. Development of such sources opens the prospects to place them directly at the territory of clinic, to carry out the treatment of oncological patients and to create at operating accelerators of the radiation therapy cabinets.

ORCID IDs
Valentin I. Kasilov, https://orcid.org/0000-0002-1355-311X; **Sergey P. Gokov,** https://orcid.org/0000-0002-3656-3804
Sergiy A. Kalenik, https://orcid.org/0000-0002-1460-5081; **Vitaliy V. Tsiats'ko,** https://orcid.org/0000-0002-7347-0500
Oleg A. Shopen, https://orcid.org/0000-0003-3158-8081

REFERENCES

[1] H. Hatanaka, Y. Nakagava, Intern. J. Rad. Oncol. Biol. Phys. **28**, 1061 (1994), https://doi.org/10.1016/0360-3016(94)90479-0
[2] L.W. Wang, Y.H. Liu, F.I. Chou, S.H. Jiang, Cancer Commun (Lond), **38**(1), 37 (2018), https://doi.org/10.1186/s40880-018-0295-y
[3] H. Shiba, K. Takeuchi, R. Hiramatsu, M. Furuse, N. Nonoguchi, S. Kawabata, et al. Neurol Med Chir (Tokyo), **58**(12), 487 (2018), https://doi.org/10.2176/nmc.oa.2018-0111
[4] V.A. Trivillin, E.C.C. Pozzi, L.L. Colombo, S.I. Thorp, M.A. Garabalino, M.A. Hughes, et al. Radiat. Environ. Biophys. **56**(4), 365 (2017), https://doi.org/10.1007/s00411-017-0704-7
[5] J. Miyabe, R. Ohgaki, K. Saito, L. Wei, L. Quan, C. Jin, et al. J Pharmacol. Sci. **139**, 215 (2019), https://doi.org/10.1016/j.jphs.2019.01.01
[6] S.Y. Taskaev, Phys Part Nucl. **46**, 956 (2015), https://doi.org/10.1134/S1063779615060064
[7] S.Y. Taskaev, Boron Neutron Capture Therapy. Physics of Atomic Nuclei, **84**(2), 207 (2021), https://doi.org/10.1134/S106377882101021X
[8] M. Suzuki, Int. J. Clin. Oncol. **25**, 43 (2019), https://doi.org/10.1007/s10147-019-01480-4
[9] V.I. Kasilov, S.P. Gokov, A.N. Dovbnya, S.A. Kalenik, K.S. Kokhnyuk, S.S. Kochetov, A.A. Khomich, and O.A. Shopen, East Eur. J. Phys. **3**(3), 64 (2016), https://doi.org/10.26565/2312-4334-2016-3-05
[10] V.M. Pixaykin, L.E. Kazakov, G.G. Korolev, S.G. Isaev, V.A. Roschenko, and M.Z. Tarasko, Atomic energy, **92**(2), 135 (2002), http://elib.biblioatom.ru/text/atomnaya-energiya_t92-2_2002/go,0/. (in Russian)
[11] A.Yu. Buki, S.A. Kalenik, I.L. Semisalov, I.S. Timchenko, A.S. Zadvorny, M.G. Shevchenko, V.J. Kasilov, S.P. Gokov, S.S. Kochetov, G.I. Ledovskoy, and P.L. Makhnenko, The Journal of Kharkiv National University, physical series «Nuclei, Particles, Fields», **1025**(4), 35 (2012), http://nuclear.univer.kharkov.ua/lib/1025_4(56)_12_p35-42.pdf. (in Russian)

КОНЦЕПЦІЯ СТВОРЕННЯ ДЖЕРЕЛА НЕЙТРОНІВ ДЛЯ ЯДЕРНОЇ МЕДИЦИНИ НА ОСНОВІ ЛІНІЙНОГО ПРИСКОРЮВАЧА ЕЛЕКТРОНІВ

В.Й. Касілов, С.П. Гоков, С.О. Каленик, С.С. Кочетов, Л.Д. Салій, В.В. Цяц'ко, Е.В. Цяц'ко, О.О. Шопен
ННЦ «Харківський фізико-технічний інститут», Харків, Україна
вул. Академічна, 1, 61118, Харків, Україна

Розглянуто сучасний стан розробки джерел епітеплових нейтронів на базі реакторів та прискорювачів для бор-нейтронозахватної терапії (БНЗТ), перспективного методу лікування злоякісних пухлин. Запропоновано схему прототипу джерела для отримання теплових і епітеплових нейтронів з використанням запізнілих нейтронів, що генеруються за допомогою лінійного прискорювача електронів на мішені, що містить подільний матеріал. Наводяться результати експерименту, в якому виміряні криві напіврозпаду радіоактивних ядер, що утворилися в процесі поділу і випускають запізнілі нейтрони. Показано, що активована мішень, що містить подільний матеріал є компактним малогабаритним джерелом запізнілих нейтронів. Вона може бути доставлена в формувач, де за допомогою сповільнювача, поглинача і коліматора відбувається формування нейтронів теплових або епітеплових енергій протягом певного проміжку часу, після чого ця мішень відправляється в активатор, а на її місце приходить інша. Таким чином, утворюється імпульсний потік нейтронів. Такий пучок нейтронів може бути використаний в ядерній медицині, зокрема, в нейтронозахватної терапії при лікуванні онкологічних захворювань. Важливим завданням при реалізації нейтронозахватної терапії, при опроміненні пацієнтів, є проведення контролю, як інтенсивності так і енергетичного спектра потоку нейтронів. Для вирішення цього завдання може бути використаний раннє розроблений кульовий спектрометр нейтронів активаційного типу, який дозволить провести оптимізацію різних параметрів формувача, коліматора і фільтрів з метою отримання найбільш потужних потоків нейтронів.

Ключові слова: ядерна медицина, запізнілі нейтрони, теплові нейтрони, лінійний прискорювач електронів, джерело нейтронів

East European Journal of Physics. 4. 164-171 (2021)
DOI: 10.26565/2312-4334-2021-4-22 ISSN 2312-4334

ENHANCING SI SOLAR CELLS EFFICIENCY BY ADDING SiO_2/TiO_2 THIN FILMS USING TRANSFER MATRIX METHOD†

Wedad Ahmed Abdullah Garhoom†, Zina A. Al Shadidi*
Department of Physics, Faculty of Education/Saber, University of Aden, Yemen
**Corresponding Author: zabaqer@yahoo.com, †E-mail: garhoomwedad@gmail.com*
Received June 26, 2021; revised November 24, 2021; accepted November 25, 2021

Thin film silicon solar cells are nowadays the best choice to get electricity due to their low cost compared to the crystalline solar cells. However, thin film silicon solar cells have weak absorption of incident light. To deal with such a weakness and get better efficiency of these cells, an efficient back reflector composed of multilayer thin films (Silver, Silicon dioxide (SiO2) and Titanium dioxide (TiO2)) will be used. The transmitted light from the first silicon layer will be reflected by the next layer, and the reflected light will go back to the first silicon layer. By this way, the absorbance of the silicon solar cell can be increased by an increase in the probability of the light reflection from the SiO2, TiO2 and Ag. The transfer matrix method (TMM) by Matlab program will be used to analyze the results of the reflectance, transmittance and absorbance of the thin film layer and these results can prove the efficiency of the cells by using MATLAB codes.
Keywords: SiO2, TiO2, TMM, Efficiency, Optical Properties, Thin Film, Matlab.
PACS: 42.79.Ek

The need for clean energy sources has increased lately due to the increasing demand for cheaper and cleaner energy. The solar cell itself relies primarily on thin film and it is often made of semiconducting materials because of the scholars' ability to control the energy gap of these materials in the first place. The theoretical side is very important for the engineers interested in manufacturing the solar cells because theoretical calculations provide the optimum conditions for manufacturing such important devices and the electrical and optical properties of these materials.

Many studies were done to improve the solar cells efficiency. One of these studies was conducted by Saravanan, Dubey, Kalainathan, More and Gautam (2015). They used in their research the ultra film solar cells of 40 nm thickness and discovered that the efficiency of the solar cells increased by 15%, and the current density increased by 23mA/cm2. Another study was done by Xu, Chen, Ding, Pan, Hu, Yang, Zhu and Dai (2018). They controlled the recombination of the charge carriers in the interface in material of the different layers of the solar cells. As a result of this control, a positive change happens in the efficiency and current density when using SiO2; the efficiency increased from 3% to 3.9%, Voc from 0.523v to 0.558v and FF from 56.5% to 68.1 %.

For Sheng, Johnson, Broderick, Michel and Kimerling (2012), they recommended to employ the reflection idea in the form of DBR by using materials like SiC in the energy researches. These materials have small absorption coefficient α and big reflection. In comparison, Yang, Lien, Chu, Kung, Cheng and Chen (2013) used ARCs to increase both the reflection and efficiency. The results show that there was an increase in the reflection by 9% and in efficiency by 16.3%. Additionally, there are several mathematical methods to analyze the equations and the easiest one is TMM. Perez (2007) used TMM to find the transmittance and absorbance because this method is easy in studying a model of multilayers.

The specific scope of this research is numerical modeling for thin film solar cells. Photovoltaic array systems are familiar and are widely utilized in electric power generation. They are very important and useful devices, and the attempts to improve them and to get higher efficiency have not been stopped until now.

The research aims at getting solar cells of higher efficiency. To achieve this aim, a-Si, SiO2 and TiO2 will be used. Thin film silicon solar cells are the best choice to get power due to their low cost as compared to other types of solar cells. However, thin film silicon solar cells suffer from the problem of weak absorption of incident light. To solve this problem and improve the performance of solar cells, an efficient back reflector composed of layer thin film (SiO2/TiO2/Ag) will be used in this research

The properties of Si/SiO2/TiO2/Ag compounds will be examined by using TMM and their analysis will take place by Matlab code. The parameters will give information on the efficiency of the solar cells and this efficiency can be improved by putting layers of SiO2 and TiO2 under the first silicon's layer and analyses by using Matlab program.

The model used in this research consists of a glass substrate and a thin layer of thickness 50 nm from silver (Ag) is put on the substrate. The sliver does like a reflector of the incident light to the upper layers made of TiO2 and SiO2, which in turn, do like charge carrier collectors in addition to their role as reflectors for the light to the upper effective layer of silicon a-Si. The SiO2 & TiO2 layers collect the charge carriers faster than the process of the carrier's recombination effects. This research has found that the best thickness of Si is 100nm to absorb the charge carriers well, while it is 90 nm for SiO2 and TiO2. Consequently, better efficiency and current density can be got.

† ***Cite as***: W.A.A. Garhoom, Z.A.Al Shadidi, East. Eur. J. Phys. **4**, 164 (2021), https://doi.org/10.26565/2312-4334-2021-4-22

MATHEMATICAL METHOD

A. TMM for Thin Film Optics

TMM can be used for the analysis of the wave propagation of quantum particles, such as electrons and electromagnetic, acoustic, and elastic waves. In this research, a simulation of transfer matrix equations will be employed to examine the transmission and reflectance as functions of wavelength. The reflectance transmittance characteristics of optical thin-film will also be analyzed and visualized.

TMM in electromagnetics and optics is a powerful and convenient mathematical formalism for determining the plane wave reflection and transmission characteristics of an infinitely extended slab of a linear material. While the TMM was introduced for a homogeneous uniaxial dielectric-magnetic material in the 1960s, and subsequently was extended for multilayered slabs, it has more recently been developed for the most general linear materials. By means of the rigorous coupled-wave approach, slabs that are periodically nonhomogeneous in the thickness direction can also be accommodated by TMM.

Calculating the optical properties for the thin films paves the way to build a simulation for a solar cell system based on the results from TMM by using Matlab programming algorithms.

B. The Reflectance of a Thin Film

As it has been said before, the research method is TMM which will be used to analyze the propagation of waves in thin film which, in turn, will be studied for calculating transmission and reflection amplitude and their properties. Accordingly, it is supposed that there is one layer or two layers made of homogeneous substances, more particularly (Si, SiO_2 and TiO_2). The indexes of refraction of every medium will be different from each other, and changes with wavelength. The incident waves on the boundaries will be analyzed in electric and magnetic fields. Then, the equations will be solved to get the transmission and reflection. TMM has been applied to a single layer and multilayers.

a. The Single Layer Film

It can be noticed from Figure (1) that there is one layer film on a substrate. If this film is thin, the interfaces of the wave will increase. The occurrence of these interfaces of monochromatic leads to the existence of transmission and reflectance of the waves when analyzing them in their electric and magnetic fields. In this process, it should be taken into consideration the boundaries between the thin film, the air and the substrate. To go back to Maxwell's equations, the new equation will be used to describe the magnetic and electric fields at separating boundaries.

Some symbols are used in the Figures below to refer to the directions of the fields which make up waves. It is assumed that the sign (+) refers to the direction of incidence and the sign (-) refers to the direction of the light reflection. Besides, the boundary between the air and the first medium is named (a), the boundary between the second medium and the substrate is named (b), whereas the boundary between the third medium and the substrate is named (c). After the analyses of the research data, the following equations are got:

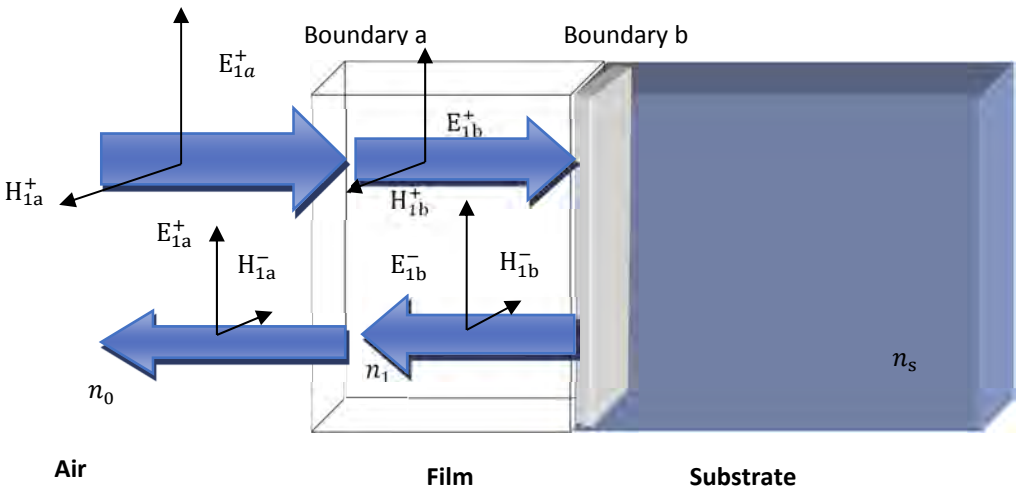

Figure 1. The wave incident on one layer thin film.

From the Figure (1), the tangential components of E and H are:

$$\pounds_b = \pounds_{1b}^{+} + \pounds_{1b}^{-}, \tag{1}$$

$$\mathcal{H}_b = \eta_1 \pounds_{1b}^{+} - \eta_1 \pounds_{1b}^{-}, \tag{2}$$

where

£ – total tangential electric field amplitude, that is, the field parallel to the thin film boundaries
$\mathcal{H}$ – total tangential magnetic field amplitude, that is, the field parallel to the thin-film boundaries.

The formulation of the optical admittance at oblique incidence angle according to Ahmed (2006) is

$$\eta_1 = n_1\eta_0 \cos\theta_1 \text{.....for S-polarization} \quad (3)$$

$$\eta_2 = \frac{n_1\eta_0}{\cos\theta_1} \text{..... for p-polarization} \quad (4)$$

where
η_1 – Characteristic admittance of a material thin film layer
η_0 – Characteristic admittance of the incident medium.
η_m – Characteristic admittance of the emergent medium
η_{sub} – Characteristic admittance of substrate.
θ – The angle of incidence in the thin film layer

From the Snell's law (Kolle, 2011):

$$n_0 \sin\theta_0 = n_1 \sin\theta_1, \quad (5)$$

$$n_1 \sin\theta_1 = n_{sub} \sin\theta_{sub}, \quad (6)$$

$$\therefore \ £_{1b}^{+} = \frac{1}{2}\left[\frac{\mathcal{H}_b}{\eta_1} + £_b\right], \quad (7)$$

$$£_{1b}^{-} = \frac{1}{2}\left[\frac{-\mathcal{H}_b}{\eta_1} + £_b\right], \quad (8)$$

$$\mathcal{H}_{1b}^{+} = \eta_1 £_{1b}^{+} = \frac{1}{2}[\mathcal{H}_b + \eta_1 £_b], \quad (9)$$

$$\mathcal{H}_{1b}^{-} = -\eta_1 £_{1b}^{-} = \frac{1}{2}[\mathcal{H}_b - \eta_1 £_b]. \quad (10)$$

The phase factor of the positive wave will be multiplied by ($e^{i\delta}$), while the phase factor the negative wave will be multiplied by ($e^{-i\delta}$) by using

$$\delta = 2\pi n_1 d \frac{\cos\theta_1}{\lambda}, \quad (11)$$

where:
δ – phase retardation in the thin film layer, d – the thickness of thin film, n – the refraction index for medium, λ – the wavelength of incident light .

$$\therefore \ £_{1a}^{+} = £_{1b}^{+} e^{i\delta} = \frac{1}{2}\left[\frac{\mathcal{H}_b}{\eta_1} + £_b\right] e^{i\delta} \quad (12)$$

$$£_{1a}^{+} = £_{1b}^{-} e^{-i\delta} = \frac{1}{2}\left[\frac{-\mathcal{H}_b}{\eta_1} + £_b\right] e^{-i\delta} \quad (13)$$

$$\mathcal{H}_{1a}^{+} = \mathcal{H}_{1b}^{+} e^{i\delta} = \eta_1 £_{1b}^{+} = \frac{1}{2}[\mathcal{H}_b + \eta_1 £_b] e^{i\delta} \quad (14)$$

$$\mathcal{H}_{1a}^{-} = \mathcal{H}_{1b}^{-} e^{-i\delta} = -\eta_1 £_{1b}^{-} = \frac{1}{2}[\mathcal{H}_b - \eta_1 £_b] e^{-i\delta} \quad (15)$$

The result of the field in boundary a is

$$£_a = £_{1a}^{+} + £_{1a}^{-} = £_{1b}^{+} \quad (16)$$

By using eqs (12) and (13), the following is produced:

$$£_a = \frac{1}{2}\frac{\mathcal{H}_b}{\eta_1} e^{i\delta} + \frac{1}{2} £_b e^{i\delta} - \frac{1}{2}\frac{\mathcal{H}_b}{\eta_1} e^{-i\delta} + \frac{1}{2} £_b e^{-i\delta} \quad (17)$$

$$£_a = £_b\left[\frac{e^{i\delta} + e^{-i\delta}}{2}\right] + \mathcal{H}_b\left[\frac{e^{i\delta} - e^{-i\delta}}{2\eta_1}\right] \quad (18)$$

The relationships:

$$\cos\theta = \left[\frac{e^{i\theta} + e^{-i\theta}}{2}\right] \quad (19)$$

$$i \sin\theta = \left[\frac{e^{i\theta} - e^{-i\theta}}{2}\right] \quad (20)$$

are used in eq. (18), so the result is

$$£_a = £_b \cos\delta + \mathcal{H}_b \frac{i \sin\delta}{\eta_1} \quad (21)$$

By using eqs (14) and (15), the following will exist:

$$\mathcal{H}_a = \mathcal{H}_{1a}^{+} + \mathcal{H}_{1a}^{-} = \mathcal{H}_{1b}^{+} e^{i\delta} + \mathcal{H}_{1b}^{-} e^{-i\delta} \tag{22}$$

$$\mathcal{H}_a = \eta_1 £_{1b}^{+} - \eta_1 £_{1b}^{-} \tag{23}$$

$$\mathcal{H}_a = \mathcal{H}_{1a}^{+} + \mathcal{H}_{1a}^{-} = \frac{1}{2}[\mathcal{H}_b + \eta_1 £_b] e^{i\delta} = \frac{1}{2}[\mathcal{H}_b - \eta_1 £_b] e^{-i\delta} \tag{24}$$

$$\mathcal{H}_a = \frac{1}{2}\mathcal{H}_b\, e^{i\delta} + \frac{1}{2}\eta_1 £_b e^{i\delta} + \frac{1}{2}\mathcal{H}_b e^{-i\delta} - \frac{1}{2}\eta_1 £_b e^{-i\delta} \tag{25}$$

$$\mathcal{H}_a = \eta_1 £_b \left[\frac{e^{i\delta} - e^{-i\delta}}{2}\right] + \mathcal{H}_b \left[\frac{e^{i\delta} + e^{-i\delta}}{2}\right] \tag{26}$$

By using the relationships (19) and (20), the result will be

$$\mathcal{H}_a = \eta_1 £_b \ \mathrm{i}\sin\delta + \mathcal{H}_b \cos\delta \tag{27}$$

$$£_a = £_b \cos\delta + \mathcal{H}_b \frac{\mathrm{i}\sin\delta}{\eta_1} \tag{28}$$

$$\mathcal{H}_a = \mathrm{i}\,\eta_1 £_b \ \sin\delta + \mathcal{H}_b \cos\delta \tag{29}$$

Now, eq. (28) and eq. (29) are changed to matrix notation which is between the boundaries a and b:

$$\begin{bmatrix} \cos\delta & \dfrac{\mathrm{i}\sin\delta}{\eta_1} \\ \mathrm{i}\,\eta_{1_b} \sin\delta & \cos\delta \end{bmatrix}$$

$$\therefore \begin{bmatrix} £_a \\ \mathcal{H}_a \end{bmatrix} = \begin{bmatrix} \cos\delta & \frac{\mathrm{i}\sin\delta}{\eta_1} \\ \mathrm{i}\,\eta_{1_b} \sin\delta & \cos\delta \end{bmatrix} = \begin{bmatrix} £_b \\ \mathcal{H}_b \end{bmatrix} \tag{30}$$

By supposing that the transfer matrix M has the following matrix notation:

$$M = \begin{bmatrix} \cos\delta & \frac{\mathrm{i}\sin\delta}{\eta_1} \\ \mathrm{i}\,\eta_{1_b} \sin\delta & \cos\delta \end{bmatrix} \tag{31}$$

$$\begin{bmatrix} £_a \\ \mathcal{H}_a \end{bmatrix} = M \begin{bmatrix} £_b \\ \mathcal{H}_b \end{bmatrix} \tag{32}$$

It is supposed that the symbol Y stands for input optical admittance to compare it with this eq.:

$$\eta = \frac{\mathcal{H}}{£} \tag{33}$$

So, according to Ahmed (2006):

$$\therefore Y = \frac{\mathcal{H}_a}{£_a} \tag{34}$$

To find the reflectance of a sample interference between an incident medium of admittance η_0 and the medium of admittance Y (Macleod, 2010):

$$r = \frac{\eta_0 - Y}{\eta_0 + Y} \tag{35}$$

$$R = \left[\frac{\eta_0 - Y}{\eta_0 + Y}\right]\left[\frac{\eta_0 - Y}{\eta_0 + Y}\right]^{*} \tag{36}$$

Now eq. (30) is changed by dividing it by $£_b$, so the following is produced:

$$\begin{bmatrix} £_a/£_b \\ \mathcal{H}_a/£_b \end{bmatrix} = \begin{bmatrix} B \\ C \end{bmatrix} = \begin{bmatrix} \cos\delta & \frac{\mathrm{i}\sin\delta}{\eta_1} \\ \mathrm{i}\,\eta_{1_b} \sin\delta & \cos\delta \end{bmatrix} \begin{bmatrix} 1 \\ \eta_2 \end{bmatrix} \tag{37}$$

Where $\begin{bmatrix} \mathrm{B} \\ \mathrm{C} \end{bmatrix}$ means the characteristic matrix

$$\frac{\mathcal{H}_a}{£_b} = \eta_2 \tag{38}$$

where

$$B = \frac{\mathcal{E}_a}{\mathcal{E}_b} \tag{39}$$

$$C = \frac{\mathcal{H}_a}{\mathcal{E}_b} \tag{40}$$

B and C are the normalized electric and magnetic fields at the interface.
From eqs (34) and (35), the following is got:

$$Y = \frac{\mathcal{H}_a}{\mathcal{E}_b} = \frac{\mathcal{E}_a/\mathcal{E}_b}{\mathcal{E}_a/\mathcal{E}_b} = \frac{B}{C} = \frac{\eta_2 \cos\delta + i\eta_1 \sin\delta}{\cos\delta + i\left(\frac{\eta_2}{\eta_1}\right)\sin\delta} \tag{41}$$

From eqs (36) and (37), the reflectance can be found.

b. The Reflectance of a (Assembly) Multilayers Film

The matrix notation of the film is near the substrate:

$$\begin{bmatrix} \cos\delta_2 & \frac{i\sin\delta_2}{\eta_1} \\ i\,\eta_2 \sin\delta_2 & \cos\delta_2 \end{bmatrix}$$

$$\begin{bmatrix} \mathcal{E}_a \\ \mathcal{H}_a \end{bmatrix} = \begin{bmatrix} \cos\delta_2 & \frac{i\sin\delta_2}{\eta_1} \\ i\,\eta_2 \sin\delta_2 & \cos\delta_2 \end{bmatrix} \begin{bmatrix} \mathcal{E}_c \\ \mathcal{H}_c \end{bmatrix} \tag{42}$$

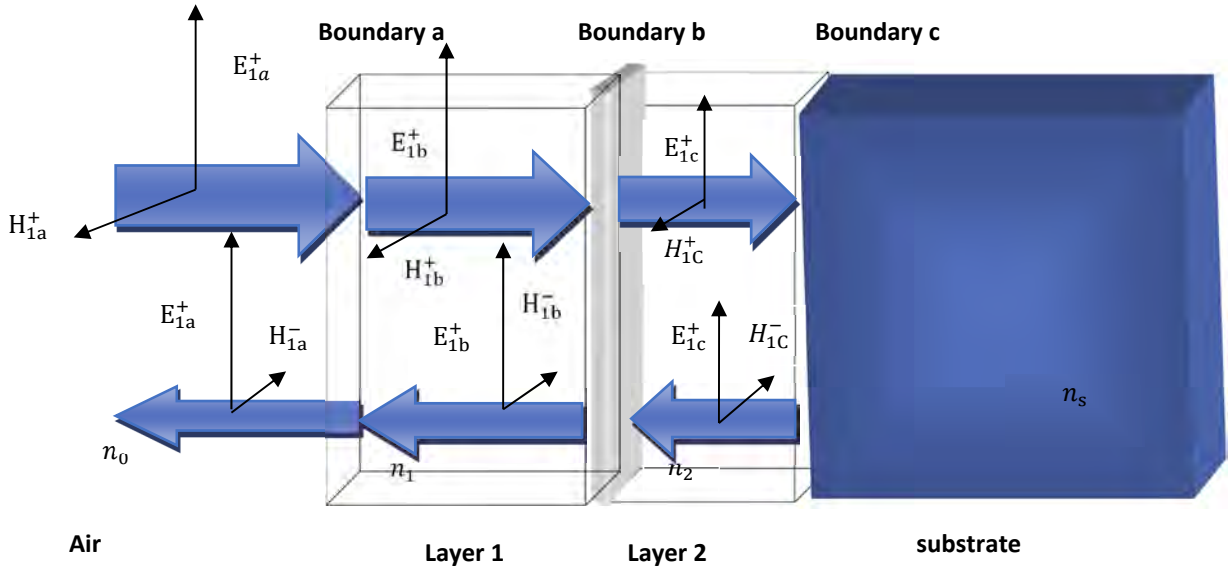

Figure 2. The incident wave on the two layer thin film.

For two layer films, the following equations exist:

$$\begin{bmatrix} \mathcal{E}_a \\ \mathcal{H}_a \end{bmatrix} = \begin{bmatrix} \cos\delta_1 & \frac{i\sin\delta_1}{\eta_1} \\ i\,\eta_1 \sin\delta_1 & \cos\delta_1 \end{bmatrix} \begin{bmatrix} \cos\delta_2 & \frac{i\sin\delta_2}{\eta_2} \\ i\,\eta_2 \sin\delta_2 & \cos\delta_2 \end{bmatrix} \begin{bmatrix} \mathcal{E}_c \\ \mathcal{H}_c \end{bmatrix} \tag{43}$$

$$\begin{bmatrix} B \\ C \end{bmatrix} = \left\{ \prod_{r=1}^{q} \begin{bmatrix} \cos\delta_r & \frac{i\sin\delta_r}{\eta_r} \\ i\eta_r \sin\delta_r & \cos\delta_r \end{bmatrix} \right\} \begin{bmatrix} 1 \\ \eta_{sub} \end{bmatrix} \tag{44}$$

$$\text{Where} \quad \delta_r = 2\pi d \frac{\cos\theta}{\lambda} \tag{45}$$

$$\begin{bmatrix} B \\ C \end{bmatrix} = [M_1][M_2][M_3] \ldots\ldots [M_q] \begin{bmatrix} 1 \\ \eta_{sub} \end{bmatrix} \tag{46}$$

The reflectance R, transmission T and absorbance A will be got by the following eqs (Macleod, 2010):

$$R = \left[\frac{\eta_0 B - C}{\eta_0 B + C}\right]\left[\frac{\eta_0 B - C}{\eta_0 B + C}\right]^* \quad (47)$$

$$T = \frac{4\eta_0 \mathrm{Re}(\eta_m)}{(\eta_0 B + C)(\eta_0 B + C)^*} \quad (48)$$

$$A = \frac{4\eta_0 \mathrm{Re}(BC^* - \eta_m)}{(\eta_0 B + C)(\eta_0 B + C)^*} \quad (49)$$

Where adding these parameters is equal to 1 according to Al-Shadidi & Falih (2019, p.77):

$$R+T+A=1 \quad (50)$$

THE RESULTS

To design a model for the silicon solar cell in this research, a set of thin film layers has been assumed. The thickness of each layer has been calculated, taking into consideration the interference between the incident and the reflected rays from each layer. These calculations have been done by using Matlab code for TMM, to investigate the higher possible absorption to be obtained.

As in equation (46), the M matrices have been calculated for different thickness of each layer and different angles of incident rays. The thickness of Si layer has varied from 100 nm to 1000 nm, with 100 nm steps, while the SiO2 & TiO2 thickness has been changed from 10 nm to 100 nm with 10 nm steps, for each layer thickness of Si. These calculations have been repeated for three angles of incident (0º, 45º, 90º).

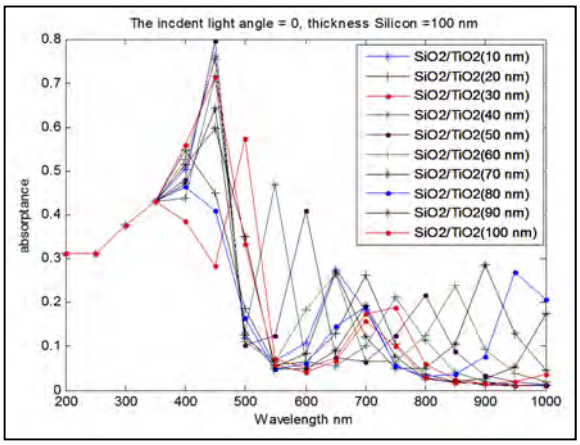

a

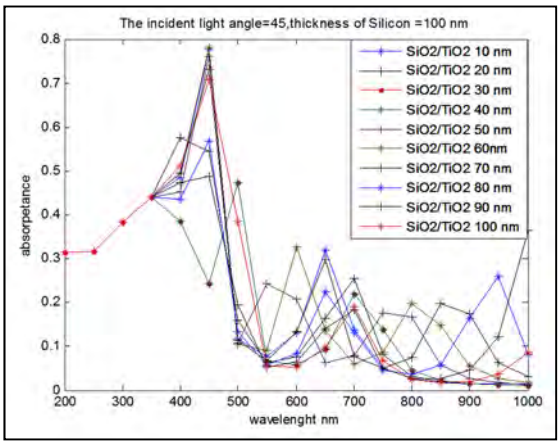

a

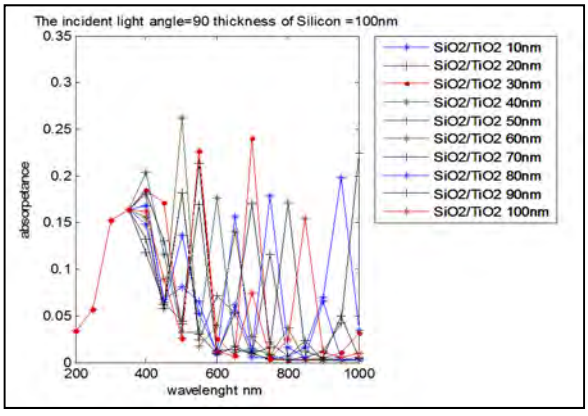

c

Figure 3. Absorbance as a function of wavelength (nm), the thickness of Silicon 100(nm) by different light incident angles (a) angle = 0^0,(b) angle = 45^0,(c) angle = 90^0

As shown in Figure (3), maximum absorbance has occurred at wavelength equal to 450nm which belongs to the interface between blue and violet color from the visible spectrum region. In Figure (3a) & (3b), many other peaks can be seen at different frequencies. At an angle of incident equal to zero, there are several peaks for absorption at other wavelength within the visible spectrum. It is possible to control the increase in absorbance within the whole light spectrum through controlling the thin films thickness. From Figure (3)a, a distinctive peak can be seen at wavelength equal to 900nm, when the (SiO2/TiO2) thickness is equal to 90nm, which is in the IR region.

At the angle of incident equal to 45º, it can be observed many peaks of absorbance within the visible and infrared spectrum. The highest absorbance is at wavelength equal to 450nm which is the interface between the violet and blue

color region in the visible spectrum. Then, the absorbance decreases. Moreover, there are many other peaks can be distinguished within the Visible- IR spectrum. One noticeable peak is at the end of IR region and it belongs to the SiO2/TiO2 90nm thickness.

Figure (3)c shows the absorbance at the angle of incident equal to 90º. The absorbance at average is less than that at another angle of incident. In detail, the absorbance reaches (0.8) at the highest peaks for other angles of incident, while the highest peak equal to (0.28) at angle of incident equal to (90º). In general, the absorption rate in this case is close to each other. The highest peak is at wavelength equal to 450nm. Other peaks of absorption have been seen at wavelength equal to (550, 700, 800, 900 and another high peak at the end of the infrared region 1000nm).

The above calculations have been repeated for different silicon thickness levels (100, 200,….100nm). The best absorbance has happened when Silicon thickness was equal to 100nm, while the SiO2 & TiO2 thickness was equal to 90 nm. These calculations have been done by using a 50 nm Ag layer thickness. The Ag has worked as a reflector to return the rays to the effective Silicon layer.

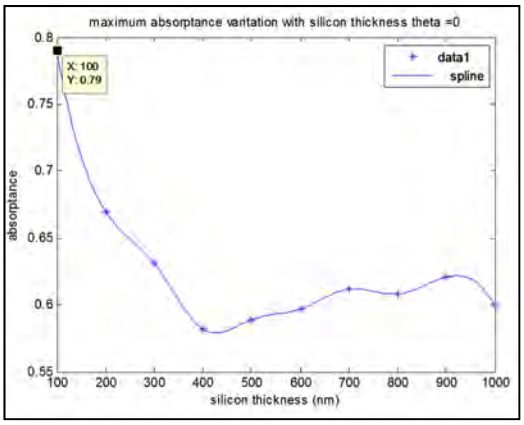

a

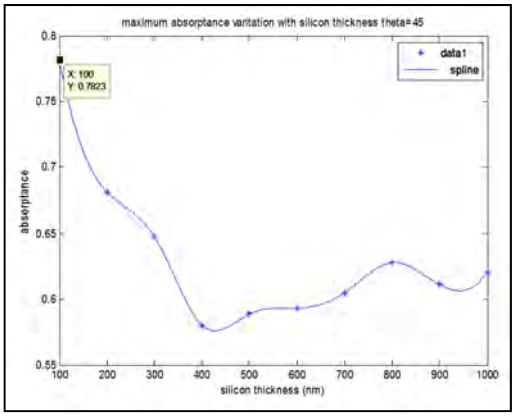

b

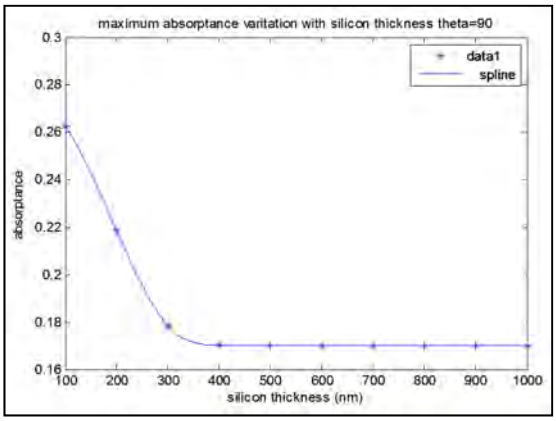

c

Figure 4. Absorbance of the solar cell as a function of Silicon thickness (nm) by different light incident angles (a) angle=0º, (b) angle=45º, (c) angle= 90^0.

In Figure (4), the maximum absorbance from each layer, and the relationship between the absorbance and the thickness of silicon layers have changed according to the change in silicon layer thickness.

The maximum point at the absorbance curve is got at the thickness of 100 nm. For lower absorbance at the other layer thicknesses, it happens because the interference of the light waves. At the thickness of 100 nm in the active material (a-Si), the interference effect is clear and a-Si becomes disordered in its behavior, so the change appears in the absorbance with thickness. As a result, the change of the incident angle of the unpolarized light leads to the best absorbance when the thickness is equal to 100 nm. It can be noticed from Figures (4a) and (4b) that there is a very little difference for the maximum absorbance between the cases of zero and 45º angle of incident. The maximum absorbance is very little in the case of normal incident as shown in Figure (4c). When silicon thickness increases, the recombination for the charge carriers will be done before reaching the SiO2/TiO2 layers. Therefore, the best results will be seen at a thickness equal to 100nm. However, decreasing silicon layer thickness less than 100nm interface effect will be dominant.

From Figure (5), it can be seen the curve of Jsc and the thickness of SiO_2 /TiO_2 layers. Jsc curve increases if the thickness of SiO_2 and TiO_2 layers increases. The highest point of Jsc curve increase occurs when the thickness of SiO_2 / TiO_2 is 90 nm. At this level of thickness, the best absorbance accrued at the effective silicon layer. For, the short circuit current, it was (15.16) mA. The results of this research are similar to the ones of Burkhard, Hoke & McGhee's research (2010) and Sahouane & Zerga's research (2014).

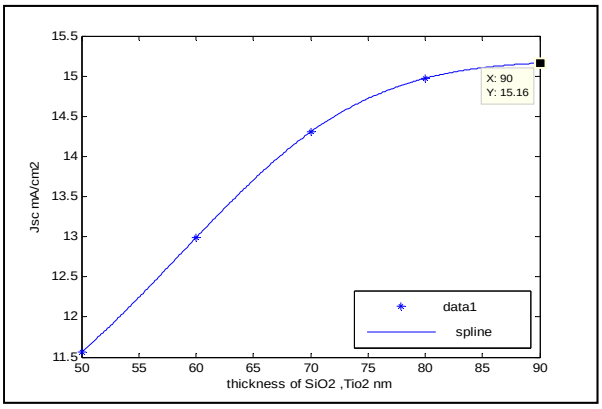

Figure 5. The curve of the thickness of SiO_2,TiO_2 (nm) and Jsc (mA/cm^2)

CONCLUSION

The efficiency of solar cells has been improved by using a multilayer thin film made of different materials. The choice of the thickness of these layers has been determined using the Matlab code to have the best absorbance of first layer (a-Si) and (SiO_2 and TiO_2). The absorbance of the charge carriers happens faster than their recombination. Hence, this model (SiO_2 and TiO_2) has the best efficiency at the thickness of 90 nm and at 100 nm for a-Si.

The novelty of this research is the new combination of thin film layers to build a high efficiency thin solar cell. The cell contains two layers that can collect the charge carriers before reassembly. In addition to an excellent reflector to ensure the use of the most possible radiation falling on the cell.

ORCID IDs

Zina A. Al Shadidi, https://orcid.org/0000-0002-2633-9446

REFERENCES

[1] N. Ahmed, Doctorate Thesis Malaysia, *Design and Experimental Studies of Multilayer Coating for Application Gallium Nitraide Light Emitting Devices*, University Sains Malaysia, 2006.
[2] Z. Alshadidi, and A. Falih, American Journal of Materials Synthesis and Processing, **4**(2), 75 (2019), https://doi.org/10.11648/j.ajmsp.20190402.14
[3] G. Burkhard, E. Hoke, and M. McGhee, Adv. Mater, **22**, 3293 (2010), https://doi.org/10.1002/adma.201000883
[4] O. Heavens, (1954). *Optical Properties of Thin Solid Films*. (Dover Publications, USA, 1954).
[5] M. Kolle, *Photonic Structures Inspired by Nature*, (Springer Verlag, Berlin Heidelberg, 2011).
[6] H. Macleod, *Thin-Film Optical Filters*. (Taylor & Francis Group, USA, 2010).
[7] E. Perez, *Design, Fabrication and Characterization of Porous Silicon Multilayer Optical Devices*. (Universtat Rovira I Virgili, 2007).
[8] N. Sahouane, and A. Zerga, Energy Procedia, **44**, 118 (2014), https://doi.org/10.1016/j.egypro.2013.12.017
[9] S. Saravanan, R. Dubey, S. Kalainathan, M. More, and D. Gautam, AIP Advances, **5**, 057160 (2015), https://doi.org/https://doi.org/10.1063/1.4921944
[10] X. Sheng, S. Johnson, L. Broderick, J. Michel, and L. Kimerling, Applied Physics Letters, **100**, 111110 (2012), https://doi.org/10.1063/1.3693613
[11] Y. Xu, W. Chen, X. Ding, X. Pan, L. Hu, S. Yang, J. Zhu, and S. Dai, Inorganic Chemistry Frontiers, **5**, 1370 (2018), https://doi.org/10.1039/C8QI00076J
[12] C. Yang, S. Lien, C. Chu, C. Kung, T. Cheng, and P. Chen, International Journal of Photoenergy, **2013**, Article ID 2325, (2013), https://doi.org/10.1155/2013/823254

ПІДВИЩЕННЯ ЕФЕКТИВНОСТІ КРЕМНІЄВИХ СОНЯЧНИХ ЕЛЕМЕНТОВ ШЛЯХОМ ДОДАВАННЯ ТОНКИХ ПЛІВОК SiO_2/TiO_2 МЕТОДОМ МАТРИЦІ ПЕРЕНОСУ

Ведад Ахмед Абдулла Гархум, Зіна А. Аль Шадіді
Кафедра фізики, Педагогічний факультет/Сейбер, Університет Адена, Ємен

Тонкоплівкові кремнієві сонячні батареї сьогодні є найкращим вибором для отримання електроенергії через їх низьку вартість порівняно з кристалічними сонячними елементами. Однак тонкоплівкові кремнієві сонячні батареї мають слабке поглинання падаючого світла. Щоб впоратися з такою слабкістю та отримати кращу ефективність цих батарей, буде використаний ефективний задній відбивач, що складається з багатошарових тонких плівок (срібла, діоксиду кремнію (SiO_2) та діоксиду титану (TiO_2)). Світло, що проходить від першого шару кремнію, буде відбиватися наступним шаром, а відбите світло повернеться до першого шару кремнію. Таким чином, поглинання кремнієвого сонячного елемента можна збільшити за рахунок збільшення ймовірності відбиття світла від SiO_2, TiO_2 та Ag. Метод матриці переносу (TMM) від програми Matlab буде використовуватися для аналізу результатів відбиття, пропускання та поглинання тонкого плівкового шару, і ці результати можуть довести ефективність батарей за допомогою кодів MATLAB.

Ключові слова: SiO_2, TiO_2, TMM, ефективність, оптичні властивості, тонка плівка, Matlab.

EAST EUROPEAN JOURNAL OF PHYSICS. 4. 172-180 (2021)
DOI: 10.26565/2312-4334-2021-4-23 ISSN 2312-4334

PRESSURE OF ELECTROMAGNETIC RADIATION ON A LINEAR VIBRATOR†

Mykola G. Kokodii*, Sergey L. Berdnik, Victor O. Katrich, Mikhail V. Nesterenko, Marina V. Kaydash
V.N. Karazin Kharkiv National University, 4, Svobody Sq., 61022, Kharkiv, Ukraine
**Corresponding Author: kokodiy.n.g@gmail.com*
Received October 1, 2021; revised December 4, 2021; accepted December 6, 2021

Nowadays the pressure of electromagnetic radiation in the optical range is widely used in laser traps (so called optical tweezers or single-beam gradient force trap) to control the position of microparticles, biological cells and other microscopic objects. This is possible by focusing the laser radiation into the area of several micrometers in size. The intensity of the radiation in the area is sufficient to hold particles in the beam and manipulate them. We are interested to research similar possibility in the microwave range of wavelengths. However we had faced a number of difficulties in this range: the size of the focal region is much larger, the radiation intensity is less, and to control microscopic objects by means of radiation pressure very high powers are required. And we decided to consider the known effect of a very strong interaction of thin conducting fibers (metal, semiconductor, graphite) with microwave radiation. The efficiency factor of radiation pressure on such objects reaches values of several hundreds and thousands. This can be used to control objects in the form of electrically thin metal conductors by means of radiation pressure. Methods for calculating the pressure of electromagnetic radiation on an infinitely long circular cylinder are known. In this paper we propose a method for calculating the radiation pressure on a circular cylinder (vibrator), the length of which is comparable to the radiation wavelength. We have found out that when the vibrator length is close to half the wavelength, the radiation pressure efficiency factor is much larger than for an infinite cylinder. We have obtained the dependence of the radiation pressure efficiency factor on the length and diameter of an absolutely reflecting and impedance vibrator. It decreases with decreasing conductivity. An infinite cylinder at a certain value of conductivity has a maximum of the radiation pressure efficiency factor.
Key words: microwave radiation, thin conductors, impedance vibrator, radiation pressure.
PACS: 78.70.Gq; 84.40.-x; 84.90.+a

Electromagnetic radiation presses on an object located in free space with the force determined by the following formula

$$F = \frac{P}{c} Q_{pr}, \tag{1}$$

where P is the power of the radiation that hits the object, c is the speed of light, Q_{pr} is the efficiency factor for radiation pressure. For a completely absorbing body $Q_{pr} = 1$ and for a reflecting plane $Q_{pr} = 2$. The radiation pressure on objects of a more complex shape (a sphere, a cylinder, an ellipsoid, a linear vibrator) can be found in two ways:

1. Having solved the problem of diffraction of an electromagnetic wave on an object (having found the distribution of fields in the object vicinity) and having calculated the forces and moments of forces acting on the object by the help of the Maxwell tension tensor. This method was first used by P. Debye in 1909 in his work on the pressure of light on a sphere [1], and then by G. Thilo in 1920 in his work on the pressure of light on an infinite circular cylinder [2]. They both had got the expressions for the radiation pressure efficiency factors in the form of series, the terms of which are expressed through the Bessel and Hankel functions.

2. Having found the strength of the currents interaction in an object with magnetic field in its vicinity. This method seems to be simpler, since it is related to the well-known problems on currents arising in a receiving linear antenna, but in fact it still requires solving the problem of wave diffraction on the antenna.

The problem on a linear vibrator of finite length is three-dimensional, in contrast to the two-dimensional problem for an infinite cylinder, and was actively researched in the middle of 20th century during the period of intensive development of radiolocation. The results of its solution for the cross section of radar scattering were obtained in a series of papers [3-5] and the book [6] summarizing them. Scattering by a thin conductor and the cross section of radar scattering were researched in These works. The authors have considered the cases when the vibrator length did not exceed the radiation wavelength. The distribution of currents induced in the conductor by the field of the incident plane wave was found through an approximate solution of the integral equation. The main term in the obtained solution was substituted into the integral that determines the electric field in the far zone, and the value of the backscattering cross section was calculated. The methods used by the authors differed mainly in the form of used zero approximation for the current and in the methods of subsequent calculation of the integrals. The results obtained through these methods are consistent with each other and with the results of experiments with vibrator lengths not exceeding one wavelength [7,8]. For longer vibrators zero approximation for currents is not sufficient. In [6] the authors had expanded the field of

† ***Cite as:*** M.G. Kokodii, S.L. Berdnik, V.O. Katrich, M.V. Nesterenko, and M.V. Kaydash, East. Eur. J. Phys. **4**, 172 (2021), https://doi.org/10.26565/2312-4334-2021-4-23

application of the theory onto vibrators with a length of several wavelengths by complex calculations, which are essentially equivalent to the usage of currents expressions with an accuracy of the first order. We did not found any published results of further researches in recent time.

Difficulties in solving these problems are created by the vibrator edges causing the reflection of currents from them. The solution of some problems of diffraction by such objects is given in [9, 10]. In books on antenna theory the problems of calculating currents in a receiving antenna are considered [11, 12]. But as a rule, only electromotive force at the antenna output is determined in them. The case closest to ours is considered in the paper [13] where a method for the numerical solution of the problem of electromagnetic scattering on a thin dielectric cylinder of a finite length is proposed and the results of numerical calculations are presented. To facilitate the solution of the problem, it was assumed that there are spherical rounding at the ends of the cylinder reducing the reflection of the wave.

In [14] the authors had proposed to use the results of problem solution of the electromagnetic wave diffraction on an ellipsoid. In [15-17], the problems of radiation pressure and torques acting on ellipsoids and systems of ellipsoids located in a rectangular waveguide are considered. These problems have been solved by the authors during the development of ponderomotive microwave measuring devices. Limitation in them is the condition of smallness of the size of objects in comparison with the wavelength.

The paper [18] analyzes the magnitude of the ponderomotive action of a plane electromagnetic wave on a thin vibrator with weakly perturbed surface impedance. The currents in the vibrator were calculated by the methods given in [19]. When solving the integral equation for the current in the vibrator the authors took into account the disturbances in the impedance distribution by averaging its value over the vibrator length. During the simulation the vibrators with distributed reactive impedance were researched. It is shown that such impedance scatterers experience a lower wave pressure force under resonance conditions than ideally conducting vibrators.

Below we will be using the results obtained in the mentioned papers.

Research is underway on the use of radiation pressure in technology. In work [20] studies micromachines, in [21] studies laser material processing. The features of the radiation pressure in thin films are studied in [22].

PONDEROMOTIVE FORCE ACTING ON THE VIBRATOR

The geometry of the problem is shown in Figure 1. A plane wave is incident on a thin vibrator with a length of 2*L* in the direction opposite to the direction of the *Oz* axis:

$$E_y = E_0\, e^{ik_1 z}, \qquad H_x = -\frac{E_0}{Z_0} e^{ik_1 z}$$

where k_1 is the wave number for the surrounding space, E_0 is the electric field strength of the incident wave, Z_0 is the wave impedance of free space.

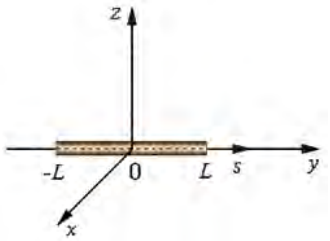

Figure 1. Geometry of the problem

The force *f* acting on a conductor element of length *ds* in a magnetic field with an intensity *H*, through which an electric current *J* flows, is determined by the following formula:

$$f(s) = \frac{1}{2}\mathrm{Re}\left\{J(s)\cdot \mu_0 H^*\right\} ds\,. \tag{2}$$

Expressions for the current and magnetic field are complex:

$$J(s) = J_0\, e^{i(\psi+\omega t)}, \quad H = H_0 e^{i(k_1 z+\omega t)}\,.$$

Here J_0, H_0 are modulus of the complex quantities *J* and *H*, ψ is the argument of the complex expression for the current, the * sign denotes the complex conjugate quantity. Having substituted them in (2) we obtain

$$\begin{aligned} f(s) &= \frac{1}{2}\mathrm{Re}\left\{J_0\, e^{i(\psi+\omega t)}\cdot \mu_0 H_0{}^{-i(k_1 z+\omega t)}\right\} ds = \frac{\mu_0 H_0}{2}\mathrm{Re}\left\{J_0\, e^{i(\psi-k_1 z)}\right\} ds = \\ &= -\frac{\mu_0 E_0}{2Z_0}\mathrm{Re}\left\{J_0\, e^{i(\psi-k_1 z)}\right\} ds \approx -\frac{\mu_0 E_0}{2Z_0}\mathrm{Re}\left\{J_0\, e^{i\psi}\right\} ds = -\frac{\mu_0 E_0}{2Z_0}\mathrm{Re}\left\{J(s)\right\} ds \end{aligned} \tag{3}$$

The force acting on the vibrator can be obtained by integrating expression (3) along the *Oz* axis along the vibrator:

$$F = -\frac{\mu_0 E_0}{2Z_0}\int_{-L}^{L} \mathrm{Re}\{J(s)\}ds \tag{4}$$

The reader can see that it depends only on the real part of the current in the vibrator.

Having calculated the force *F*, we can use expression (1) to find the efficiency factor of the radiation pressure:

$$Q_{pr} = \frac{F\,c}{P}. \tag{5}$$

Vibrator current

In order to use formula (4) to calculate the force with which the radiation presses on the vibrator, we need to find the distribution of the current along the vibrator. The needed expression was obtained in [21]:

$$J(s) = \alpha\frac{i\omega E_0}{k\tilde{k}}\left\{1-\cos\tilde{k}(s+L)-\frac{\sin\tilde{k}(s+L)+\alpha P^s(s)}{\sin 2\tilde{k}L+\alpha P^s(L)}\left(1-\cos 2\tilde{k}L\right)\right\}, \tag{6}$$

where *s* is the coordinate directed along the vibrator. The expression includes:

$$P^s(s) = \int_{-L}^{s}\left[\frac{e^{-ikR(s',-L)}}{R(s',-L)}+\frac{e^{-ikR(s',L)}}{R(s',L)}\right]\sin\tilde{k}(s-s')ds',$$

$\alpha = \dfrac{1}{2\ln[r/2L]}$ is a small parameter, E_0 is the electric field amplitude of incident wave, $R(s',s) = \sqrt{(s'-s)^2+r^2}$, $\tilde{k}^2(s) = k_1^2\left[1+i\alpha\omega\varepsilon_1 z_i(s)/k_1^2\right] = k_1^2\left[1+i2\alpha\bar{Z}_S(s)/(\mu_1 kr)\right]$, $z_i(s)$ is resistance per unit length, Ω/m, $\bar{Z}_S(s) = 2\pi r z_i(s)/Z_0$, $Z_0 = \sqrt{\dfrac{\mu_0}{\varepsilon_0}} = 377\ \Omega$ is the wave impedance in free space, $k_1 = k\sqrt{\varepsilon_1\mu_1}$, $k = 2\pi/\lambda$, is wavelength in free space, λ is circular frequency.

Expression (6) is valid for vibrators with a length of less than λ. It is written in the Gauss system of units. Therefore, before using formula (4) to calculate the ponderomotive force, the values of the electric field E_0 and the current $J(s)$ must be converted to SI. It is reasonable to calculate the value of $\tilde{k}(s)$ directly in SI units.

Radiation pressure on an absolutely reflective vibrator

For an absolutely reflecting vibrator, $z_i(s) = 0$. Figure 2 shows the dependence of the efficiency factor of radiation pressure with a wavelength of 8 mm on an absolutely reflecting vibrator on the length of the vibrator for several diameters, calculated according to formulas (1) - (6). The abscissa shows the values of $2L/\lambda$; the ordinate indicates the radiation pressure efficiency factor Q_{pr}.

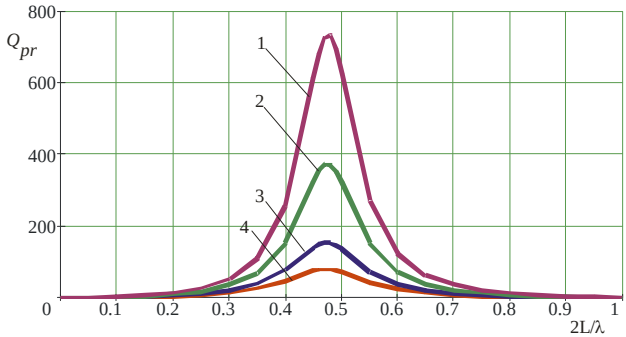

Figure 2. Dependence of the efficiency factor of radiation pressure on an absolutely reflecting vibrator on its electrical length and diameter 1 – *D* = 10 μ, 2 – *D* = 20 μ, 3 – *D* = 50 μ, 4 – *D* = 100 μ

The following features are visible:

1) There is a resonance at which the radiation pressure rises strongly. It occurs when the vibrator length is slightly less than half the wavelength ($2L/\lambda = 0.48$)

2) When the length of the vibrator is equal to the wavelength ($2L/\lambda = 1$) the radiation pressure is zero.

For the comparison, we took the graph (Figure 3) from [9], which shows the dependence of the effective cross-section of backscattering σ_I of a linear vibrator on its length. The solid line is calculation results; dots are experimental data.

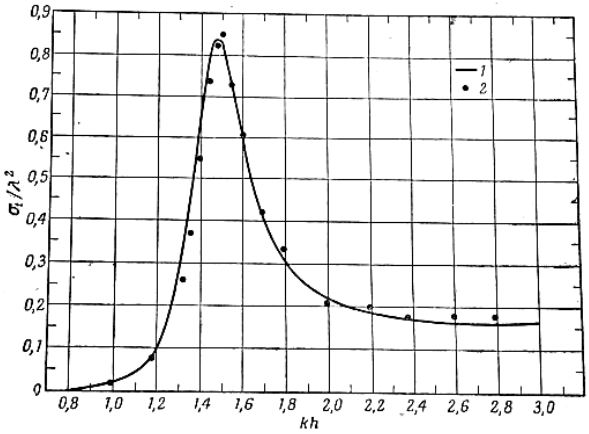

Figure 3. Dependence of the effective cross-section of backscattering of a linear vibrator on its length

The vibrator is a steel-silvered rod with a radius of 0.35 mm. The wavelength of radiation is 10 cm.

There is a resonance at $kh = 1.5$, where h is a half of the vibrator length, therefore, $2h/\lambda = 0.48$. It coincides with the resonance condition for the radiation pressure. This is normal, since the radiation pressure depends on the magnitude and direction of the scattered field.

The backscattering efficiency factor defined as the ratio of the effective backscattering cross section to the vibrator geometric cross section is

$$Q_{rev\,sca} = \frac{\sigma}{S} = 253.$$

The radiation pressure efficiency factor calculated from the vibrator data is

$$Q_{pr} = 121.$$

These values are of the same order of magnitude, which confirms the correctness of the method for calculating the radiation pressure.

But it can be seen in Fig. 3 that for vibrator length equal to the radiation wavelength, the effective cross-section of backscattering is not zero. This is probably due to the fact that the current calculation method can only be applied to vibrators whose length is shorter than the wavelength.

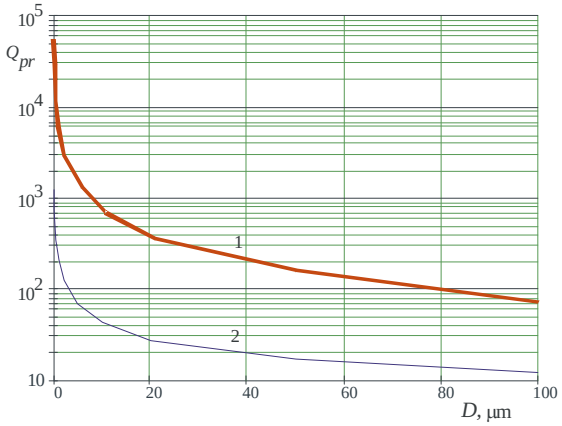

Figure 4. Dependence of the efficiency factor of the radiation pressure on the vibrator on its diameter
1 - half-wave vibrator, 2 - electrically long vibrator

Figure 4 shows the dependencies of the efficiency factor of radiation pressure on an absolutely reflecting vibrator on its diameter. Curve 1 shows the dependence for a half-wave vibrator at a resonance; curve 2 shows the dependence for an infinitely long cylinder of the same diameter.

Curve 2 is plotted by means of the approximate formula for an *E*-polarized wave [23]:

$$Q_{pr} = \frac{\pi^2}{2\rho(\ln\rho)^2},$$

where $\rho = \pi D/\lambda$.

The formula can be obtained when only the first terms of the series for the radiation pressure efficiency factor [2] and the Bessel and Hankel functions are taken into account.

Both curves in Figure 4 show that the radiation pressure efficiency factor grows indefinitely when vibrator diameter decreases.

The fact that the efficiency factor of the radiation pressure on the vibrator increases when its diameter is reducing does not mean that the force acting on the vibrator increases. The power of the radiation incident on the vibrator decreases. Figure 5 shows the dependence of the force on the diameter, calculated under the following conditions:
I = 40,000 W/m^2 is the average radiation intensity at the output of a waveguide with a cross section of 7.2×3.4 mm at a power of 1 W, $2L$ = 4 mm is the vibrator length, $\lambda = 8\ mm$ mm is the radiation wavelength.

The acting force is determined by the formula

$$F = \frac{PQ_{pr}}{c} = \frac{2IDLQ_{pr}}{c}$$

The reader can see that the force acting on the vibrator tends to zero when the diameter is decreasing, although the radiation efficiency factor increases indefinitely.

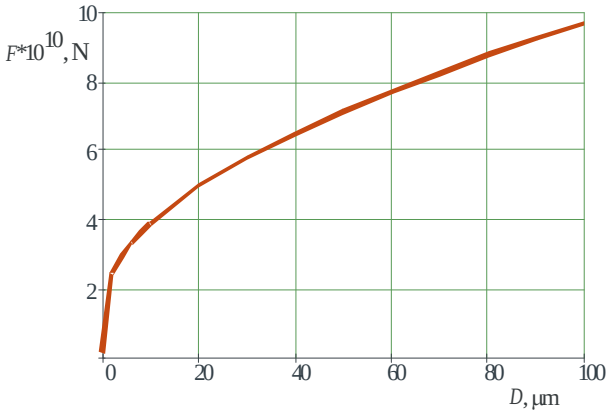

Figure 5. Dependence of the force acting on the vibrator on its diameter

Surface impedance of the vibrator

The surface resistance of metal has an inductive character and is determined by the following expression [24]:

$$Z = \sqrt{\frac{\pi c \mu_0}{\lambda \sigma}}(1+i), \tag{7}$$

where σ is the electrical conductivity of metal. Units for the surface resistance are Ω/m^2. The surface resistance of copper (σ = 5.8×10^7 1/(Ω×m)) at a wavelength of 8 mm equals to Z = 0.0505 (1 + i) Ω/m^2.

We had defined the surface resistance of the vibrator per unit length z_i in the following manner: a square on the surface of a round conductor of radius r has a side equal to $2\pi r$. Thus, a vibrator with a length of $2\pi r$ has a resistance defined by formula (7). Then the surface resistance of the vibrator per unit length is equal to

$$z_i = \frac{Z}{2\pi r}.$$

For a copper vibrator with a radius of r = 50 μm at a wavelength of 8 mm

$$z_i = 161\ (1+i)\ \Omega/\text{m}.$$

The expression for the current in the vibrator includes the parameter

$$\tilde{k} = k_1\sqrt{1 + i\frac{2\alpha\bar{Z}_s(s)}{\mu_1 kr}},$$

where $k_1 = k\sqrt{\varepsilon_1 \mu_1}$, $k = 2\pi/\lambda$ = 786m^{-1}, ε_1, μ_1 are relative dielectric and magnetic permeabilities of the environment ($\varepsilon_1 = 1$, $\mu_1 = 1$),

$$\alpha = \frac{1}{2\ln\frac{r}{2L}} = -0.114 \text{ at } L = 2 \text{ mm } (2L/\lambda = 0.5).$$

$$\bar{Z}_s(s) = \frac{2\pi r z_i}{Z_0} = 0.000134(1+i)$$

$Z_0 = \sqrt{\frac{\mu_0}{\varepsilon_0}} = 120\pi\ \Omega$ is the wave impedance in free space.

We have obtained:

$$\tilde{k} = 786 - 0.306i\ \text{m}^{-1}, \tag{8}$$

The reader can see that the difference from $k_1 = k = 786\ \text{m}^{-1}$, which is characteristic of an absolutely reflecting vibrator when $z_i = 0$, is very small. This is normal, since the conductivity of copper is very high and its reflection coefficient at a wavelength of 8 mm differs little from 1.0 (approximately 0.999).

Radiation pressure on the impedance vibrator

We had explored the impact of the conductivity of the vibrator material on the radiation pressure. We have found out that the radiation pressure on the copper vibrator, with an accuracy of tenths of a percent, coincides with the radiation pressure on the absolutely reflecting vibrator. But when the length of the vibrator is equal to the wavelength, the efficiency factor of the radiation pressure on the copper vibrator is not zero, while being a very small value. For a vibrator with a diameter of 10 microns, it is approximately 0.0004.

We had made the comparison of the radiation pressure on an infinitely long cylinder calculated by the formulae [2] (Fig. 6), and the radiation pressure on a half-wave vibrator calculated by the formulae given in the actual paper (Fig. 7). It is can see that for vibrator diameters larger than several micrometers, the radiation pressure on the absolutely reflecting vibrator and on the copper vibrator are almost equal. This is an expected result, since the radiation reflection coefficient with a wavelength of 8 mm from copper is approximately 0.999. Nevertheless, for diameters less than 2 microns, the radiation pressure on an infinite copper cylinder becomes greater than on an absolutely reflecting cylinder. At a certain diameter it reaches a maximum and then, with a decrease in the diameter, drops to zero. The maximum is a consequence of the effect of strong interaction of electromagnetic radiation with very thin cylinders, the diameter of which is comparable to the thickness of the skin layer in the cylinder material [23]. The efficiency factor of the radiation pressure on an absolutely reflecting cylinder increases indefinitely with a decrease in its diameter.

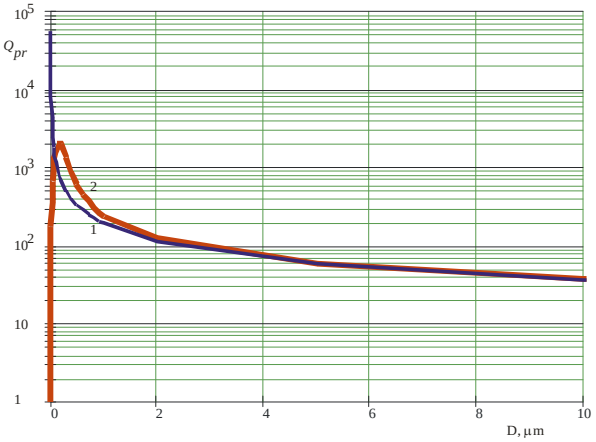

Figure 6. Dependence of the radiation pressure efficiency factor on an electrically long vibrator on its diameter
1 - absolutely reflective vibrator, 2 - copper vibrator

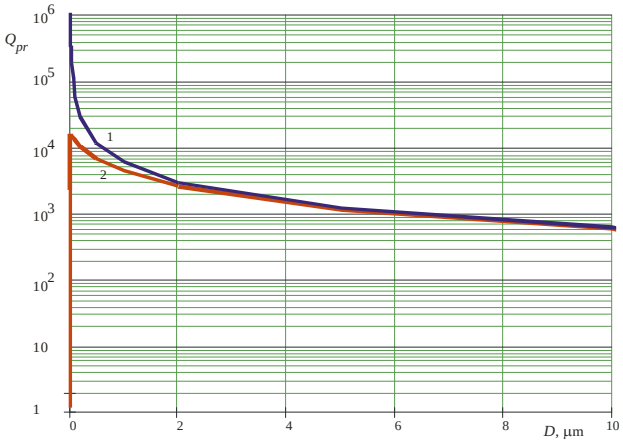

Figure 7. Dependence of the radiation pressure efficiency factor on a half-wave vibrator on its diameter
1 - absolutely reflective vibrator, 2 - copper vibrator

The calculation results for a half-wave vibrator are different (Fig. 7). The radiation pressure efficiency factor for a copper vibrator is always less than the one for an absolutely reflective vibrator. The maximum pressure exists, but at extremely small diameters of thousandths of a micrometer. For such diameters, the calculations we have presented above may be incorrect because in this range of sizes and at larger diameters the physics of the processes may differ.

It is likely that the difference in the dependences of the radiation pressure on the long vibrator and half-wave vibrator on the diameter is explained by the limitations on the method for calculating the current in the vibrator.

We had examined the dependence of the radiation pressure efficiency factor on the conductivity of the vibrator material and the type of impedance (inductive or capacitive). We have assumed that the values of the real and imaginary parts of the impedance in both cases were determined by formula (7), and its type is determined by the sign in front of the imaginary part. Figure 8 represents the dependencies for a vibrator with a diameter of 10 μm. Curves 1 and 2 show that when the conductivity decreases the efficiency factor of the radiation pressure decreases too regardless of the conductivity nature. For a vibrator with capacitive impedance, the radiation pressure efficiency factor is slightly higher than for a vibrator with inductive impedance. Dots on the curve 1 represent different materials. The radiation pressure efficiency factor is much less for an infinitely long metal cylinder than for a resonant half-wave vibrator. It also decreases when the conductivity is decreasing. But at some of conductivity value, there is a maximum which is caused by the effect of strong interaction of thin conductive fibers with microwave radiation. There is no such maximum on the graphs for a half-wave vibrator.

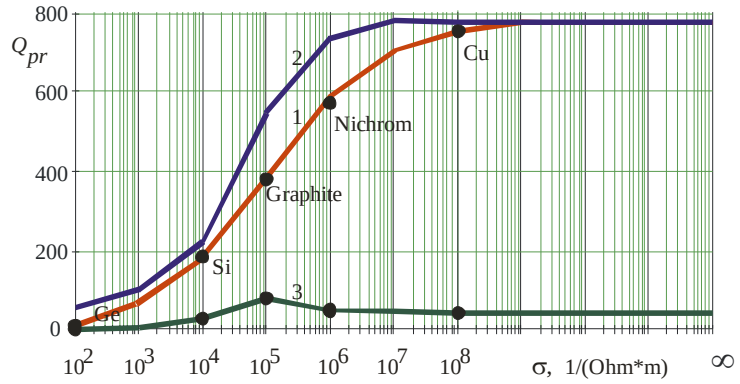

Figure 8. Dependence of the efficiency factor of the radiation pressure on the conductivity of the vibrator (diameter 10 μm)
1 - Inductive half-wave vibrator, 2 - capacitive half-wave vibrator, 3 - infinitely long metal cylinder

Figure 9 shows the same dependences but for a vibrator with a diameter of 100 μm. Their shape is the same as in Figure 8, but the values of the radiation pressure efficiency factor are much less, and the position of the maximum for an infinitely long cylinder is different. This can be explained by the fact that the condition for the maximum is the approximate equality of the cylinder diameter and the thickness of the skin layer in it [23].

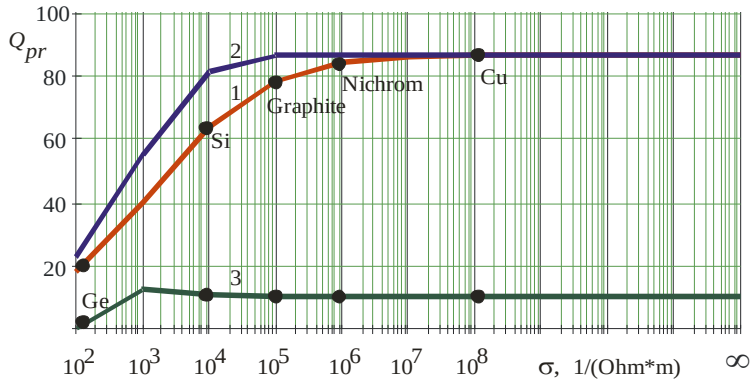

Figure 9. Dependence of the efficiency factor of the radiation pressure on the conductivity of the vibrator (diameter 100 μm)
1 - inductive half-wave vibrator, 2 - capacitive half-wave vibrator, 3 - infinitely long metal cylinder

CONCLUSIONS

1. We have proposed a method for calculating the efficiency factor of radiation pressure on an impedance linear vibrator, the length of which does not exceed the radiation wavelength.

2. We have found out that the resonance occurs when the length of the vibrator is close to half the wavelength. The radiation pressure efficiency factor reaches values tens of times larger for an infinitely long cylinder of the same diameter. With a vibrator length equal to the wavelength, the radiation pressure efficiency factor is very small, and for an absolutely reflecting cylinder it is equal to zero.

3. We have established that with a decrease in the diameter of an impedance vibrator of a finite length, the radiation pressure efficiency factor increases indefinitely, in contrast to an infinite cylinder of the same diameter, in which it reaches a certain maximum, and then decreases to zero. The maximum is explained by the existence of the effect of strong interaction of very thin conducting fibers with electromagnetic radiation.

4. We have discovered that an increase in the efficiency factor of radiation pressure on thin vibrators does not mean an increase in the force with which radiation presses on them. This is due to the fact that with a decrease in the diameter, the energy of the radiation hitting the vibrator decreases, and the force decreases too.

5. We have detected that with a decrease in the conductivity of an impedance vibrator of a finite length, the radiation pressure decreases monotonically, regardless of the type of the impedance (inductive or capacitive). The radiation pressure on an infinitely long cylinder reaches a maximum in a certain region, which is explained by the existence of the effect of strong interaction of radiation with very thin conducting fibers.

6. To summarize the results of our research we want to say that the effect of large values of the radiation pressure efficiency factor on thin conductive vibrators can be used to levitate and control the movement of targets in the microwave range, similar to how it is done in the optical range with the help of lasers.

ORCID IDs
Victor O. Katrich, https://orcid.org/0000-0001-5429-6124; **Maryna V. Kaydash,** https://orcid.org/0000-0003-0610-1489
Mykola G. Kokodii, https://orcid.org/0000-0003-1325-4563; **Sergey L. Berdnik,** https://orcid.org/0000-0002-0037-6935
Mikhail V. Nesterenko, https://orcid.org/0000-0002-1297-9119

REFERENCES

[1] P. Debye, Annalen der Physik, **335**(11), 57 (1909), https://doi.org/10.1002/andp.19093351103
[2] G. Thilo, Annalen der Physik, **367**(14), 531 (1920), https://onlinelibrary.wiley.com/doi/abs/10.1002/andp.19203671404
[3] J.H. van Vleck, F .Bloch, and M. Hamermesh, Journal of Applied Physics, **18**, 274 (1947), https://doi.org/10.1063/1.1697649
[4] S.H. Dike, and D.D. King, Proceedings of the IRE, **40**, 853 (1952), https://doi.org/10.1109/JRPROC.1952.273853
[5] S.H. Dike, and D.D. King, Proceedings of the IRE, **41**, 926 (1953), https://ieeexplore.ieee.org/document/4051412
[6] R. King, and U. Tai-Zun. *Рассеяние и дифракция электромагнитных волн [The Scattering and Diffraction of Electromagnetic Waves]*, (Inostrannaya Literatura, Moskow, 1962), pp. 194. (in Russian).
[7] B.-O. As, H.J. Schmitt, Scientific Rep. Cruft Laboratory, Harvard University, No. 18 (August 1958).
[8] J. Sevick, Techn. Rep. Cruft Laboratory, Harvard University. – No. 150 May 1952.
[9] P.Ya. Ufimtsev, *Метод краевых волн в физической теории дифракции [Metod of Edge Waves in Physical Theory of Diffraction]*, (Sovetskoe Radio, Moskva, 1962), pp. 244. (in Russian).
[10] P.Ya. Ufimtsev, *Theory of Edge Diffraction in electromagnetics*, (University of California, 2012), pp. 372.
[11] Yu. V. Shubarin, *Антенны сверхвысоких частот [Antennas of microwaves]*. (University of Kharkov, 1960), pp. 288. (in Russian).
[12] G.Z. Aizenberg, *Антенны ультракоротких волн [Antenas of microwaves]*, (Radio i svyaz, Moskow, 1957), pp 362. (in Russian).
[13] A.G. Dmitrenko, and E.P. Holzvart, Reports of TUSUR, No. 2 (22), Part 2, 41 (2010) (in Russian).
[14] M.G. Belkina, *Дифракция электромагнитных волн на некоторых телах вращения [Diffraction of Electromagnetic Waves on Same Objecs of Rotating]* (Sovetskoe Radio, Moskva, 1957), pp. 174. (in Russian).
[15] N.A. Khyzhnyak, G.P. Shcherbinin, L.K. Gal, and V.S. Zhylkov, Radiotechnik, **25**, (1973). (in Russian).
[16] A.I. Sirotnikov, V.S. Zhylkov, and N.A. Khyzhnyak, Radiotechnik, **29**, 144 (1974). (in Russian).
[17] N.A. Khyzhnyak, L.K. Gal, V.S. Zhylkov, A.V. Orlova, and G.P. Shcherbinin, Radiotechnik, **26**, 112 (1973). (in Russian).
[18] Yu.M. Penkin, V A. Katrich, M.V. Nesterenko, and S.L. Berdnik. Telecommunications and Radio Engineering, **79**(14), 1205 (2020).
[19] M.V Nesterenko, V.A. Katrich, Yu. M. Penkin, V.M. Dakhov, and S.L. Berdnik, *Thin Impedance Vibrators: Theory and Applications*, (Springer Science+Business Media, New York, 2011).
[20] I. Ryger, A.B. Artusio-Glimpse, P.A. Williams et al. IEEE Sensors Journal, **18**(18), 7941 (2018), https://doi.org/10.1109/JSEN.2018.2863607
[21] A. Mahrie, E. Beyer. Physics Scripta, **94**, 075004 (2019), https://doi.org/10.1088/1402-4896/ab04c3
[22] D. Ma, and J.N. Munday, Sci Rep. **8**, 15930 (2018), https://doi.org/10.1038/s41598-018-34381-z
[23] M.S. Kalambet, N.G. Kokodii, V.A. Maslov, and K.I. Muntean, in: *IEEE Ukrainian Microwave Week Proceedings*, (Kharkiv, Ukraine, 2020), pp. 720-725.
[24] V.M. Sedov, and T.A. Gaynutdinov, *Электромагнитные поля и волны [Electromagnye Polya i Volny]* (Moscow University, Moscow, 2018), pp. 282.

ТИСК ЕЛЕКТРОМАГНІТНОГО ВИПРОМІНЮВАННЯ НА ЛІНІЙНИЙ ВІБРАТОР

М.Г. Кокодій, С.Л. Бердник, В.О. Катрич, М.В. Нестеренко, М.В. Кайдаш

Харківський національний університет імені В.Н. Каразіна, м. Свободи 4, 61022 Харків, Україна

В теперішній час тиск електромагнітного випромінювання в оптичному діапазоні широко використовується в лазерних пастках (так званих оптичних пінцетах або однопроменевих градієнтних силових пастках), для управління положенням мікрочастинок, біологічних клітин та інших мікроскопічних об'єктів. Це можливо, завдяки фокусуванню лазерного випромінювання в область розміром в кілька мікрометрів. Інтенсивність випромінювання в ній є достатньою для утримання частинок у промені та маніпуляцій з ними. Ми вважаємо, що буде доцільно дослідити таку можливість й у мікрохвильовому діапазоні довжин хвиль. Однак, у цьому діапазоні розміри фокальної області набагато більші, інтенсивність випромінювання тут менша, і для управління малими об'єктами за допомогою тиску випромінювання необхідні дуже великі потужності. Ми вирішили використати відомий ефект дуже сильної взаємодії тонких провідних волокон (металевих, напівпровідникових, графітових) з мікрохвильовим випромінюванням. Фактор ефективності тиску випромінювання на такі об'єкти досягає значень у кілька сотень та тисяч. Це можна використовувати для керування об'єктами у вигляді електрично-тонких металевих провідників за допомогою радіаційного тиску. Відомий метод розрахунку тиску електромагнітного випромінювання на нескінченно довгий круговий циліндр. У цій статті ми пропонуємо метод розрахунку тиску випромінювання на круговий циліндр (вібратор), довжина якого порівняна з довжиною хвилі випромінювання. Ми з'ясували, що коли довжина вібратора близька до половини довжини хвилі, фактор ефективності тиску випромінювання набагато більший, ніж для нескінченного циліндра. Ми отримали залежність фактора ефективності тиску випромінювання від довжини та діаметра абсолютно відбиваючого та імпедансного вібратора. Він зменшується при зменшенні провідності. Нескінченний циліндр при певному значенні провідності має максимум фактора ефективності радіаційного тиску.

Ключові слова: мікрохвильове випромінювання, тонкі провідники, імпедансний вібратор, тиск випромінювання.

East European Journal of Physics. 4. 180-188 (2021)
DOI: 10.26565/2312-4334-2021-4-24 ISSN 2312-4334

THE NONLINEAR MAGNETOSONIC WAVES IN MAGNETIZED DENSE PLASMA FOR QUANTUM EFFECTS OF DEGENERATE ELECTRONS[†]

Neelam Rani*, Manikant Yadav
Department of Physics, J. C. Bose University of Science and Technology, YMCA, Faridabad, Haryana, 121006
**Corresponding Author: neelamraheja344@gmail.com*
Received July 27, 2021; accepted October 29, 2021

The nonlinear magnetosonic solitons are investigated in magnetized dense plasma for quantum effects of degenerate electrons in this research work. After reviewing the basic introduction of quantum plasma, we described the nonlinear phenomenon of magnetosonic wave. The reductive perturbation technique is employed for low frequency nonlinear magnetosonic waves in magnetized quantum plasma. In this paper, we have derived the Korteweg-de Vries (KdV) equation of magnetosonic solitons in a magnetized quantum plasma with degenerate electrons having arbitrary electron temperature. It is observed that the propagation of magnetosonic solitons in a magnetized dense plasma with the quantum effects of degenerate electrons and Bohm diffraction. The quantum or degeneracy effects become relevant in plasmas when fermi temperature and thermodynamic temperatures of degenerate electrons have same order.
Keywords: Magnetosonic wave, Quantum Plasma, Korteweg-de Vries equation (KdV) equation.
PACS: 52.35.Fp, 52.35.Sb, 67.10.Db, 67.10.Jn

The study of quantum plasma has been growing interest during the last decade due to its enormous applications on large scale systems in compact astrophysical objects such as white dwarfs, neutron stars and pulsars containing dense plasmas and on short scale systems such as in semiconductors, quantum devices and on nanometer scales such as quantum wells, quantum dots, nano-tubes and spintronics. The quantum or degeneracy effects become relevant in plasmas when the de Broglie wavelength associated with charge carriers becomes of the order of the average inter-particle distance so that there is a significant overlap of the corresponding wave functions or the Fermi temperature is same as the temperature of the system.

Firstly, Haas [1] introduced the quantum hydrodynamic (QHD) model used for quantum corrections in plasma. Thereafter, the proposal of QMHD model explaining spin-1/2 effect of degenerate electrons for low-frequency waves in magnetized quantum plasmas was given by Marklund and Brodin [2]. In a quantum magnetoplasma, the quantum Bohm potential and electron spin-1/2 effects using the Sagdeev potential approach was studied for magnetosonic solitons [3]. In the system of QMHD, the electron spin-1/2 changes to the shape of the magnetosonic solitary waves due to the balance between the nonlinearity and quantum diffraction/ tunneling effects. Spin Alfv´en solitons were investigated in magnetized electron-positron plasmas [4] by deriving a modified KdV equation in the MHD limit. It was shown that the collective spin effects may influence the wave characteristics in a strongly magnetized quantum plasma.The QHD model can be generalized by adding the quantum statistical pressure term (the Fermi-Dirac distribution) and the quantum diffraction term (the Bohm potential) to the fluid model [5, 6].

The QHD was used to investigate the quantum magnetosonic waves and a deformed Korteweg-de Vries (KdV) equation was derived by Haas et al. [7]. In classical plasma, the KdV equation is well known for the small but limited amplitude of ionic sound wave [8], [9]. Both degenerate (without spin) and non-degenerate (with spin) quantum plasmas were studied respectively by using small amplitude limited perturbation scheme obliquely two-dimensional nonlinear magnetosonic waves [10 – 11]. Many authors have studied the linear and nonlinear low-frequency waves in quantum plasma such as ion acoustic waves, drift waves etc. [12 - 14].

It has been proved that by adding positrons to the plasma as usual, their collective behavior has changed considerably [15] - [18]. Plasma [29] smashing [18], [20] the early universe, the vital role of survival and electron-positron (E-P) have collective behavior. Although most of the astronomical environments can be considered by the EP plasma existent senses [21], [22], the EP plasma combination in nonrelativistic regimes is astronomical plasma in some aspects [20], [23]. Verheest et al. studied through a reductive disturbance analysis, large amplitude in electron-positron plasma studied solitary electromagnetic waves and received a modified Korteweg-de verse (mKdV) equation [24]. Using two fluid plasma samples, Kourakis et al. [25] the pair studied parallel wavelength packets in parallel magnetic plasma in pairs. With this approach, Esfandyari-Kalejahi et al. E-P-I is considered nonlinear propagation of amplitude collective electrostatic wave-packets in Plasma [26]. Esfandyari-Kalejahi et al. [27] Studied electrostatic waves which unmagnified collision pair modulation of nonlinear amplitude propagation in plasma. Furthermore, many researchers have examined solder tissue structures in magnetic plasma, which are derived from the Zakharov-Kuznetsov (ZK) equation in various media. For example, Kourakis et al. have studied Magnetic mixed pair-ion plasma molecular electrostatic reactions are equated with linear dissemination analysis and forming their dimensional solutions [28]. The spread of shear Alfven waves in a strongly magnetic e-P-I plasma has been investigated by U. et al. [29], and also in Quantum E-P-I plasma, solitary waves were examined [20]. In the presence of stable ions, in the presence of Mahmoud et al., QHD for

[†] ***Cite as:*** N. Rani, and M. Yadav, East. Eur. J. Phys. **4**, 180 (2021), https://doi.org/10.26565/2312-4334-2021-4-24

disseminating nonlinear acoustic wave in dense magnetic e-p plasma, ZK has found the equation and found that the positron concentration decreases the wave dimension increases.

THEORETICAL FORMULATION

In order to study the nonlinear low frequency magnetosonic wave propagation, we take the set of dynamic equations for solving our problem. The set of quantum magnetohydrodynamic include the ion continuity equation and momentum equations as follows.

The ion continuity equation and for nondegenerate ions fluid are –

$$\frac{\partial n_i}{\partial t}+\nabla.(n_i u_i)=0\,, \tag{1}$$

$$\frac{\partial u_i}{\partial t}+(u_i.\nabla)u_i=\frac{e}{m_i}\left(\vec{E}+u_i\times\vec{B}\right), \tag{2}$$

where u_i is ion fluid velocity, n_i is ionic number density and m_i is the ion mass.
The electron continuity equation and momentum equation for degenerate electrons are –

$$\frac{\partial n_e}{\partial t}+\nabla.(n_e u_e)=0\,, \tag{3}$$

$$\frac{\partial u_e}{\partial t}+u_e.\nabla u_e=-\frac{e}{m_e}\left(\vec{E}+u_e\times\vec{B}\right)-\frac{\nabla P_e}{n_e m_e}+\frac{\alpha}{3}\frac{\hbar^2}{2m_e{}^2}\nabla\left(\frac{\nabla^2\sqrt{n_e}}{\sqrt{n_e}}\right), \tag{4}$$

where n_e is unperturbed electron number density, P_e is electron pressure and the term $\hbar^2$ arises due to electron tunneling through the Bohm potential. The numerical coefficient α is expressed as-

$$\alpha=\frac{Li_{\frac{3}{2}}(-e^{\beta\mu})Li_{-\frac{1}{2}}(-e^{\beta\mu})}{[Li_{\frac{1}{2}}(-e^{\beta\mu})]^2}. \tag{5}$$

Let $z = \exp(\beta\mu)$. In the classical limit ($z << 1$) then $\alpha \approx 1$, whereas in the full degenerate limit ($z >> 1$) then $\alpha \approx 1/3$.
The Fermi-Dirac particle distribution function for electron is –

$$f(u,r,t)=\frac{A}{1+e^{\beta(E-\mu)}}\,, \tag{6}$$

where $\beta=1/k_BT$, $E=m_ev^2/2$, $v=|u|$, k_B is the Boltzmann constant and μ is the chemical potential regarded as a slowly varying function of position **r** and time t.
The scalar pressure for equilibrium with zero drifts velocity as -

$$P=\frac{1}{3}m_e\int fu^2d^3u\,. \tag{7}$$

This is equal to –

$$\mathrm{P}=\frac{n_e}{\beta}\frac{Li_{\frac{5}{2}}(-e^{\beta\mu})}{Li_{\frac{3}{2}}(-e^{\beta\mu})}. \tag{8}$$

The Maxwell's equations are -

$$\nabla\times\vec{E}=-\frac{\partial\vec{B}}{\partial t}\,, \tag{9}$$

$$\nabla\times\vec{B}=\mu_0\vec{J}+\frac{1}{c^2}\frac{\partial\vec{E}}{\partial t}\,. \tag{10}$$

The current density is –

$$\vec{J}=e\left(n_iu_i-n_eu_e\right). \tag{11}$$

The equilibrium $n_{i0} = n_{e0} = n_0$ (say) has been defined. In order to study the obliquely propagating nonlinear magnetosonic wave propagating in x direction, i.e., $\nabla = (\partial_x, 0, 0)$ and electric field in a plane (xy) i.e., $\vec{E} = E_x\hat{i} + E_y\hat{j}$ .The linear dispersion relation for magnetosonic waves in a quantum plasma with arbitrary electron degeneracy is written as –

$$\omega^2 = \left(\upsilon_s^2 + \frac{\alpha}{12}\frac{\hbar^2}{m_i m_e}k^2\right)k^2 + \frac{k^2 u_a^2}{1+k^2\lambda_e^2}, \tag{12}$$

where υ_s is ion acoustic speed and defined as –

$$\upsilon_s = \left(\frac{1}{\beta m_i}\frac{Li_{\frac{3}{2}}(-e^{\beta\mu_{(0)}})}{Li_{\frac{1}{2}}(-e^{\beta\mu_{(0)}})}\right)^{1/2}. \tag{13}$$

The dispersion relation is described as -

$$\omega^2 = \left(\upsilon_s^2 + \frac{\alpha}{12}\frac{\hbar^2}{m_i m_e}k^2\right)k^2 + \Omega_i\Omega_e. \tag{14}$$

The phase velocity is defined as –

$$\frac{\omega}{k} = \sqrt{\upsilon_s^2 + \upsilon_A^2}, \tag{15}$$

where υ_A is Alfven speed.

$$\omega^2 = \upsilon_s^2 k^2 + \frac{k^2 u_a^2}{1+k^2\lambda_e^2}. \tag{16}$$

The dispersion relation for magnetosonic waves in quantum plasma with fully degenerate case can be written as –

$$\omega^2 = \left(\upsilon_s^2 + \frac{\hbar^2}{36 m_i m_e}k^2\right)k^2 + \frac{k^2 u_a^2}{1+k^2\lambda_e^2}. \tag{17}$$

To explore the nonlinear structures, it is convenient to write governing equations in dimensionless and component form and it is convenient to use of normalized quantities. For this, we introduce the following dimensionless variables:

$\bar{u}_{e,i} = u_{e,i}/\upsilon_s$, $\tilde{n}_{e,i} = n_{e,i}/n_0$, $\tilde{x}_{e,i} = \omega_p x/\upsilon_s$, $\tilde{t} = \omega_p t$ $\bar{\vec{E}} = e\vec{E}/m_i\upsilon_s\omega_p$ and $\bar{\vec{B}} = \vec{B}/B_0$,

here

$$\bar{H} = \frac{\beta\hbar\omega_{pe}}{\sqrt{3}}\left(\frac{Li_{-1/2}(-e^{\beta\mu})}{Li_{3/2}(-e^{\beta\mu})}\right)^{1/2},$$

is the quantum diffraction dimensionless parameter and $\beta = k_B T$, k_B is the Boltzmann constant, T is the temperature and μ is the equilibrium chemical potential and $\gamma = mi / me$ is ion electron mass ratio. The space (x) and time (t) variables are normalized by ion plasma frequency. Hereafter, we will be using these new variables and remove all the bars for simplicity of notations. The normalized ion continuity and momentum equations in the component form of dimensionless variables can be written as follows:

$$\frac{\partial n_i}{\partial t} + \frac{\partial}{\partial x}(n_i u_{ix}) = 0, \tag{18}$$

$$\frac{\partial u_{ix}}{\partial t} + u_{ix}\frac{\partial}{\partial x}u_{ix} = E_x + \Omega u_{iy}B, \tag{19}$$

$$\frac{\partial u_{iy}}{\partial t} + u_{iy}\frac{\partial}{\partial x}u_{iy} = E_y - \Omega u_{ix}B. \tag{20}$$

The normalized electron continuity and momentum equations in the component form of dimensionless variables can be written as follows:

$$\frac{\partial n_e}{\partial t}+\frac{\partial}{\partial x}(n_e u_{ex})=0\,, \tag{21}$$

$$\frac{\partial u_{ex}}{\partial t}+u_{ex}\frac{\partial}{\partial x}u_{ex}=-E_x-\Omega u_{ey}B-\frac{Li_{1/2}(-e^{\beta\mu_{(0)}})}{Li_{1/2}(-e^{\beta\mu_{(0)}})}\frac{\partial}{\partial x}n_e+\frac{\bar{H}^2}{2}\frac{\partial}{\partial x}\left[\frac{1}{\sqrt{n_e}}\frac{\partial^2}{\partial x^2}\sqrt{n_e}\right], \tag{22}$$

$$\frac{\partial u_{iy}}{\partial t}+u_{iy}\frac{\partial}{\partial x}u_{iy}=E_y-\Omega u_{ix}B\,. \tag{23}$$

The component form of Faraday's law –

$$\frac{\partial \vec{E}}{\partial x}=-\Omega\frac{\partial \vec{B}}{\partial t}\,. \tag{24}$$

The components form of Ampere's law -

$$0=n_i u_{ix}-n_e u_{ex}\,, \tag{25}$$

$$\Omega\frac{\partial \vec{B}}{\partial x}=\frac{\upsilon_s^2}{c^2}\left(n_e u_{ey}-n_i u_{iy}\right), \tag{26}$$

where $\Omega = \omega_{ci}/\omega_{pi}$ has been defined as normalized parameter of ion cyclotron and ion plasma frequency ratio. Where $\omega_{ci} = eB_0/m_i$ is the ion cyclotron frequency and $\omega_{pi}=\sqrt{\frac{n_0e^2}{\varepsilon_0 m_i}}$ is the ion plasma frequency respectively.

DERIVATION OF KDV EQUATION FOR MAGNETOSONIC WAVES

Now, we derive the Korteweg-de Vries equation from (18)-(26) by employing the reductive perturbation technique and the stretched coordinates –

$$\delta=\varepsilon^{1/2}(x-v_p t) \text{ and } \tau=\varepsilon^{3/2}t, \tag{27}$$

where ε is a smallness parameter proportional to the amplitude of the perturbation and v_p is the phase velocity of wave.

We can expand the variables $n_{e(i)}$, $u_{e(i)}$, E, B and μ in a power series of ε as –

$$n_{e(i)}=1+\varepsilon n_{e(i)}^{(1)}+\varepsilon^2 n_{e(i)}^{(2)}+\ldots\,, \tag{28}$$

$$u_{e(i)x}=0+\varepsilon u_{e(i)x}^{(1)}+\varepsilon^2 u_{e(i)x}^{(2)}+\ldots\,, \tag{29}$$

$$u_{e(i)y}=\varepsilon^{3/2}u_{e(i)y}^{(1)}+\varepsilon^{5/2}u_{e(i)y}^{(2)}+\ldots\,, \tag{30}$$

$$E_x=\varepsilon^{3/2}E_x^{(1)}+\varepsilon^{5/2}E_x^{(2)}+\ldots\,, \tag{31}$$

$$B=1+\varepsilon B_z^{(1)}+\varepsilon^2 B_z^{(2)}+\ldots\,, \tag{32}$$

$$\mu=\varepsilon^{(1)}\mu+\varepsilon^2\mu^{(2)}+\ldots\,. \tag{33}$$

Now collecting the lowest order ($\varepsilon^{3/2}$) terms from ion continuity and momentum equations of components form (18) to (20) give –

$$-v_p \frac{\partial n_i^{(1)}}{\partial \delta} + \frac{\partial u_{ix}^{(1)}}{\partial \delta} = 0 \,, \tag{34}$$

$$-v_p \frac{\partial u_{ix}^{(1)}}{\partial \delta} = E_x^{(1)} + \Omega u_{iy}^{(1)} \,, \tag{35}$$

$$E_y^{(1)} = \Omega u_{ix}^{(1)} \,. \tag{36}$$

Now collecting the lowest order ($\varepsilon^{3/2}$) terms from electron continuity and momentum equations of components form (21) to (23) give –

$$-v_p \frac{\partial n_e^{(1)}}{\partial \delta} + \frac{\partial u_{ex}^{(1)}}{\partial \delta} = 0 \,, \tag{37}$$

$$-v_p \frac{\partial u_{ex}^{(1)}}{\partial \delta} = dE_x^{(1)} + d\Omega u_{ey}^{(1)} + d\frac{\partial n_e^{(1)}}{\partial \delta} \,, \tag{38}$$

$$E_y^{(1)} = \Omega u_{ex}^{(1)} \,. \tag{39}$$

The lowest order ($\varepsilon^{3/2}$) terms from component form of Faraday's law (24) –

$$\frac{\partial E_y^{(1)}}{\partial \delta} = v_p \Omega \frac{\partial B_z^{(1)}}{\partial t} \,. \tag{40}$$

The lowest order ($\varepsilon^{3/2}$) terms from components form of Ampere's law (25-26) -

$$0 = u_{ix}^{(1)} - u_{ex}^{(1)} \,, \tag{41}$$

$$\Omega \frac{\partial B_z^{(1)}}{\partial \delta} = \frac{\upsilon_s^2}{c^2}\left(u_{ey}^{(1)} - u_{iy}^{(1)}\right) \,. \tag{42}$$

Now, using (34) – (42) we have –

$$v_p = \pm\sqrt{1+\left(\frac{\upsilon_a}{\upsilon_s}\right)^2} \,. \tag{43}$$

Now collecting the next higher order (ε) terms can be written as following -

$$v_p \frac{\partial n_i^{(2)}}{\partial \delta} - \frac{\partial u_{ix}^{(2)}}{\partial \delta} = \frac{\partial n_i^{(1)}}{\partial \tau} + \frac{\partial}{\partial \delta}\left(n_i^{(1)} u_{ix}^{(1)}\right) \,, \tag{44}$$

$$v_p \frac{\partial n_e^{(2)}}{\partial \delta} - \frac{\partial u_{ex}^{(2)}}{\partial \delta} = \frac{\partial n_e^{(1)}}{\partial \tau} + \frac{\partial}{\partial \delta}\left(n_e^{(1)} u_{ex}^{(1)}\right) \,, \tag{45}$$

$$v_p \frac{\partial u_{ix}^{(2)}}{\partial \delta} + E_x^{(2)} + \Omega u_{iy}^{(2)} = \frac{\partial u_{ix}^{(1)}}{\partial \tau} + u_{ix}^{(1)} \frac{\partial u_{ix}^{(1)}}{\partial \delta} - \Omega u_{iy}^{(1)} B_z^{(1)} \,, \tag{46}$$

$$E_y^{(2)} - \Omega u_{ix}^{(2)} = -v_p \frac{\partial u_{iy}^{(1)}}{\partial \delta} + \Omega u_{ix}^{(1)} B_z^{(1)} \,, \tag{47}$$

$$v_p \frac{\partial u_{ex}^{(2)}}{\partial \delta} - dE_x^{(2)} - d\Omega u_{ey}^{(2)} - d\frac{\partial n_{ex}^{(2)}}{\partial \delta} = \frac{\partial u_{ex}^{(1)}}{\partial \tau} + u_{ex}^{(1)} \frac{\partial u_{ex}^{(1)}}{\partial \delta} + d\Omega u_{ey}^{(1)} B_z^{(1)} - d\alpha n_e^{(1)} \frac{\partial n_e^{(1)}}{\partial \delta} - d\frac{H^2}{4}\frac{\partial^3 n_e^{(1)}}{\partial \delta^3} \,, \tag{48}$$

$$dE_y^{(2)} - d\Omega u_{ex}^{(2)} = v_p \frac{\partial u_{ey}^{(1)}}{\partial \delta} + d\Omega u_{ex}^{(1)} B_z^{(1)}, \tag{49}$$

$$\frac{\partial E_y^{(2)}}{\partial \delta} - \Omega v_p \frac{\partial B_z^{(2)}}{\partial \delta} = -\Omega \frac{\partial B_z^{(1)}}{\partial \tau}, \tag{50}$$

$$u_{ix}^{(2)} - u_{ex}^{(2)} = (n_e^{(1)} - n_i^{(1)}) u_x^{(1)}, \tag{51}$$

$$\frac{\upsilon_s^2}{c^2}(u_{iy}^{(2)} - u_{ey}^{(2)}) + \Omega \frac{\partial B_z^{(2)}}{\partial \delta} = \frac{\upsilon_s^2}{c^2}(n_e^{(1)} u_{ey}^{(1)} - n_i^{(1)} u_{iy}^{(1)}). \tag{52}$$

In order to study the nonlinear magnetosonic wave propagation characteristics we using this equation $u_{ey}^{(1)} = -du_{iy}^{(1)}$ and other variables can be expressed in terms of $u_{ex}^{(1)}$ as followings-

$$u_{ey}^{(1)} = -du_{iy}^{(1)}, \tag{53}$$

$$u_{ex}^{(1)} = u_{ix}^{(1)}, \tag{54}$$

$$n_e^{(1)} = n_i^{(1)} = \frac{u_{ex}^{(1)}}{v_p}, \tag{55}$$

$$B_z^{(1)} = \frac{u_{ex}^{(1)}}{v_p}, \tag{56}$$

$$E_x^{(1)} = -\frac{1}{v_p d}(v_p d + 1)\frac{\partial u_{ex}^{(1)}}{\partial \delta} = -v_p \frac{\partial u_{ex}^{(1)}}{\partial \delta}, \tag{57}$$

$$u_{iy}^{(1)} = \frac{1}{\Omega v_p d}\frac{\partial u_{ex}^{(1)}}{\partial \delta}, \tag{58}$$

$$u_{ey}^{(1)} = \frac{1}{\Omega v_p}(v_p^2 - 1)\frac{\partial u_{ex}^{(1)}}{\partial \delta}. \tag{59}$$

Now, using above equation and eliminating $n_{e(i)}$, u_i, E and B we obtain –

$$\frac{\partial \psi}{\partial \tau} + A_1 \psi \frac{\partial \psi}{\partial \delta} + A_2 \frac{\partial^3 \psi}{\partial \delta^3} = 0. \tag{60}$$

Equation (60) is the Korteweg-de Vries (KdV) equation of the nonlinear magnetosonic wave in magnetized quantum plasma in terms of $u_{ex}^{(1)} = \psi$. Where the nonlinear coefficient A_1 and the dispersion coefficients A_2 are given by –

$$\left.\begin{aligned} A_1 &= \frac{1}{2}\left(3 - \frac{\alpha}{v_p^2}\right) \\ A_2 &= \frac{1}{2v_p}\left(1 - \frac{H^2}{4}\right) \end{aligned}\right\}. \tag{61}$$

The solution of the Korteweg-de Vries (KdV) equation is found by transforming the independent variables X and τ to -

$$K = \delta - C_0\tau, \ \tau = \tau, \tag{62}$$

where, C_0 is a constant velocity normalized by c.

Therefore, the solution of the Korteweg-de Vries (KdV) equation is –

$$\psi = \psi_m \operatorname{sech}^2\left(\frac{K}{\Delta}\right). \tag{63}$$

In order to get the existence of solitons structures, it is necessary to apply the boundary condition on wave. The exact solution of KdV is not possible because this equation is not exactly integral solution. However, a particular solution of KdV is possible. The boundary condition is –

$$\psi \to 0, \frac{d\psi}{dK} \to 0, \frac{d^2\psi}{dK^2} \to 0 at K \to \infty,$$

where ψ_m is the amplitude and $\Delta = 1/\alpha$ is the width of magnetosonic soliton is given by –

$$\left.\begin{aligned} \psi_m &= \frac{3C_0}{A_1} \\ \Delta &= \sqrt{\frac{4A_2}{C_0}} \end{aligned}\right\}. \tag{64}$$

RESULT AND DISCUSSION

1. The theory of magnetosonic waves can be applied to all degeneracy of electrons. However, here the Fermi temperature and thermodynamic temperatures have same order and strong interactions between charge carriers. The quantum diffraction parameter depends on electron thermal temperatures as shown in Figure 1. It can be seen from the figure that quantum diffraction parameter attains large value for cold plasma.

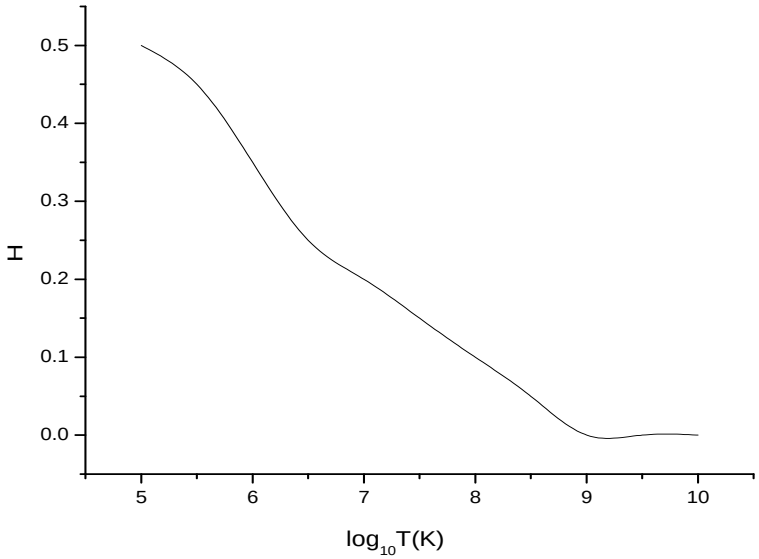

Figure 1. Variation of Quantum diffraction parameter H with temperature

2. Variation of Nonlinear dispersive coefficient A_2 as a function of temperature for magnetosonic waves is shown in Figure 2.

(a) The rarefactive magnetosonic solitons structures are formed only when velocity of nonlinear structure $C_0 < 0$ and nonlinear coefficient A_1 remains positive and nonlinear dispersive coefficient $A_2 < 0$ for electron temperature $T > 10^6$K. The speed of the nonlinear rarefactive soliton will be less than the phase speed of the magnetosonic waves.

(b) But the compressive magnetosonic solitons structures are formed when velocity of nonlinear structure $C_0 > 0$ and nonlinear coefficient A_1 remains positive and nonlinear dispersive coefficient $A_2 > 0$ for electron temperature $T < 10^6$K and it moves with a speed greater than the speed of the magnetosonic waves in the plasma with arbitrary degeneracy of electrons. The formation of magnetosonic dip structures in the higher temperature region is decreased with the increase of the magnetic field intensity.

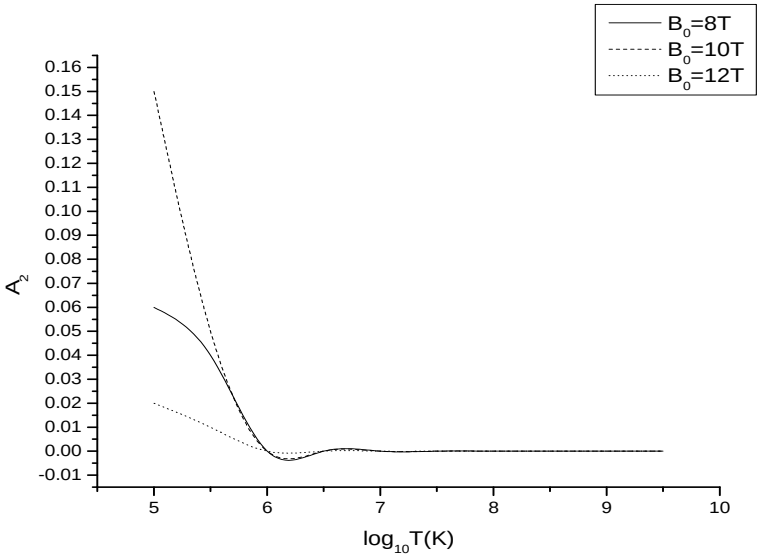

Figure 2. Nonlinear dispersive coefficient A_2 as a function of temperature

3. The variation of $\Omega = \omega_{ci}/\omega_{pi}$ as normalized parameter of ion cyclotron and ion plasma frequency ratio with different values of temperature as shown in Figure 3. It can be seen from the figure that the value of Ω decreases with increase in electron thermal temperature as well as magnetic field intensity.

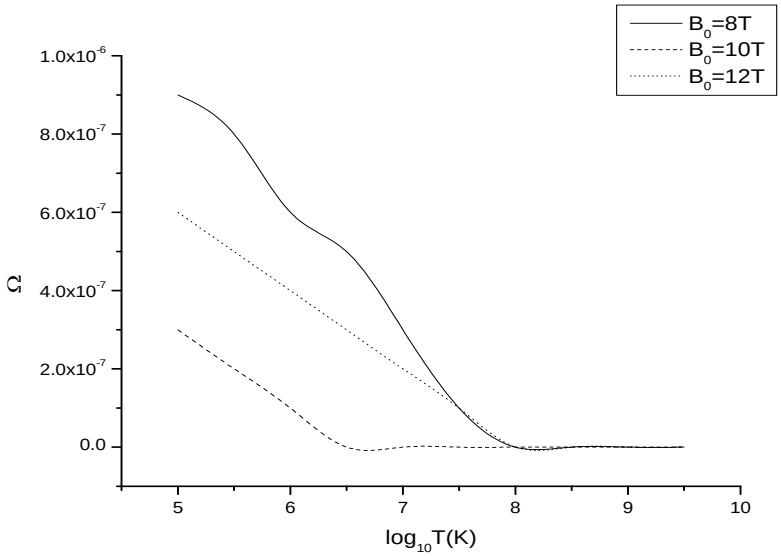

Figure 3. The ratio Ω of ion cyclotron to ion plasma frequency as a function of temperature

CONCLUSION

The weakly nonlinear propagation of magnetosonic soliton in magnetized dense plasma has been analyzed with the quantum effects of degenerate electrons, pressure degeneracy and Bohm diffraction. The reductive perturbation theory was used to derive Korteweg-de Vries (KdV) equation for the propagation of quantum magnetosonic waves in magnetized dense plasma. In weakly nonlinear limits, condition of shock wave has been discussed. Finally, we observed that this result relevant in plasma when fermi temperature and thermodynamic temperatures have same order.

Funding statement

- The authors did not receive support from any organization for the submitted work.
- No funding was received to assist with the preparation of this manuscript.

Declaration of interests

- The authors declare that they have no known competing financial interests or personal relationships that could have appeared to influence the work reported in this paper.

Author contributions

The first draft of the manuscript was written by [Neelam Rani]. All authors read and approved the final manuscript.

Availability of data and material

Authors have cited the data.

Compliance with ethical standards

- The manuscript has not submitted to other journal for simultaneous consideration.
- The submitted work is original and has not been published elsewhere.

Consent to participate

All authors agreed with the content and that all gave consent to submit the article.

Consent for Publication

All authors whose names appear on the submission have approved the content to be published.

Acknowledgment

The authors acknowledge the Prof. Ashok Kumar Arora, Director, YMCA Institute of Engineering, Faridabad, India for his continuous encouragement.

REFERENCES

[1] F. Haas, Physics of Plasmas, **12**, 062117 (2005), https://doi.org/10.1063/1.1939947
[2] M. Marklund and G. Brodin, Physical Review letters, **98**, 025001 (2007), https://doi.org/10.1103/PhysRevLett.98.025001
[3] M. Marklund, B. Eliasson, and P.K. Shukla, Physical Review E, **76**, 067401 (2007), https://doi.org/10.1103/PhysRevE.76.067401
[4] G. Brodin, and M. Marklund, Physics of Plasmas, **14**, 112107 (2007), https://doi.org/10.1063/1.2793744
[5] B. Eliasson and P.K. Shukla, Plasma Fusion Research, **4**, 032 (2009), https://doi.org/10.1585/pfr.4.032
[6] P. K. Shukla, and B. Eliasson, Physics-Uspekhi, **53**, 51 (2010), https://doi.org/10.3367/UFNe.0180.201001b.0055
[7] F. Haas, L.G. Garcia, J. Goedert, and G. Manfredi, "Quantum ionacoustic waves," Physics of Plasmas, **10**, 3858 (2003), https://doi.org/10.1063/1.1609446
[8] A. Kakad, B. Kakad, A. Lotekar, and G.S. Lakhina, Physics of Plasmas, **26**, 42112 (2019), https://doi.org/10.1063/1.5056227
[9] F.F. Chen, *Introduction to Plasma Physics and Controlled Fusion*, (Springer International Publishing, Switzerland, 2016), https://doi.org/10.1007/978-3-319-22309-4
[10] A. Mushtaq, and A. Qamar, Physics of Plasmas, **16**, 022301 (2009), https://doi.org/10.1063/1.3073669
[11] A. Mushtaq, and S.V. Vladimirov, Physics of Plasmas, **17**, 102310 (2010), https://doi.org/10.1063/1.3493632
[12] S. Ali, W. Moslem, P. Shukla, and R. Schlickeiser, Physics of Plasmas, **14**, 082307 (2007), https://doi.org/10.1063/1.2750649
[13] A. Misra, P. Shukla, and C. Bhowmik, Physics of Plasmas, **14**, 082309 (2007), https://doi.org/10.1063/1.2769322
[14] S. Mahmood, and Q. Haque, Physics Letters A, **374**, 872 (2010), http://dx.doi.org/10.1016%2Fj.physleta.2009.12.008
[15] P. Shukla, B. Dasgupta, and P. Sakanaka, Physics Letters A, **269**, 144 (2000), https://doi.org/10.1016/S0375-9601(00)00235-8
[16] S. Mahmood, A. Mushtaq, and H. Saleem, New Journal of Physics, **5**, 28 (2003), https://doi.org/10.1088/1367-2630/5/1/328
[17] P. Shukla, B. Eliasson, and L. Stenflo, Physical Review E, **84**, 037401 (2011), https://doi.org/10.1103/PhysRevE.84.037401
[18] M. Momeni, International Journal of Modern Physics C, **26**, 1550058 (2015), https://doi.org/10.1142/S0129183115500588
[19] M. Rehman, and M. Mishra, Physics of Plasmas, **23**, 012302 (2016), https://doi.org/10.1063/1.4939802
[20] S. Mahmood, N. Akhtar, and H. Ur-Rehman, Physica Scripta, **83**, 035505 (2011), https://doi.org/10.1088/0031-8949/83/03/035505
[21] B. Hosen, M.G. Shah, M.R. Hossen, and A. Mamun, Plasma Physics Reports, **44**, 976 (2018), https://doi.org/10.1134/S1063780X18100045
[22] S. Iwamoto, and F. Takahara, The Astrophysical Journal, **565**, 324480 (2002), https://doi.org/10.1086/324480
[23] J. Wang, Y. Zeng, Z. Liang, Y. Xu, and Y. Zhang, Open Physics, **16**, 563 (2018), https://doi.org/10.1515/phys-2018-0073
[24] F. Verheest, and T. Cattaert, Physics of Plasmas, **11**, 3078 (2004), https://doi.org/10.1063/1.1735714
[25] I. Kourakis, A. EsfandyariKalejahi, M. Mehdipoor, and P.K. Shukla, Physics of Plasmas, **13**, 052117 (2006), https://doi.org/10.1063/1.2203951
[26] A. Esfandyari-Kalejahi, I. Kourakis, M. Mehdipoor, and P. Shukla, Journal of Physics A: Mathematical and General, **39**, 13817 (2006), https://doi.org/10.1088/0305-4470/39/44/014
[27] A. Esfandyari-Kalejahi, I. Kourakis, and P. Shukla, Physics of Plasmas, **13**, 122310 (2006), https://doi.org/10.1063/1.2405328
[28] I. Kourakis, W. M. Moslem, U. M. Abdelsalam, R. Sabry, and P. K. Shukla, Plasma and Fusion Research, **4**, 018 (2009), https://doi.org/10.1585/pfr.4.018
[29] Q. Haque, S. Mahmood, and A. Mushtaq, Physics of Plasmas, **15**, 082315 (2008), http://dx.doi.org/10.1063/1.2974798

НЕЛІНІЙНІ МАГНІТОЗВУКОВІ ХВИЛІ В НАМАГНІЧЕНІЙ ЩІЛЬНОЇ ПЛАЗМІ ДЛЯ КВАНТОВИХ ЕФЕКТІВ ВИРОЖЕНИХ ЕЛЕКТРОнів

Нілам Рані, Манікант Ядав

Кафедра фізики, Університет науки і техніки Дж. К. Бозе, YMCA, Фаридабад, Хар'яна, 121006

У цій роботі досліджуються нелінійні магнітозвукові солітони в намагніченій щільній плазмі для квантових ефектів вироджених електронів. Ознайомившись з основним впровадженням квантової плазми, ми описали нелінійне явище магнітозвукової хвилі. Використовується метод відновного збурення для низькочастотних нелінійних магнітозвукових хвиль у намагніченій квантовій плазмі. У цій роботі ми вивели рівняння Кортевега-де Фріза (KdV) магнітозвукових солітонів у намагніченій квантовій плазмі з виродженими електронами, що мають довільну електронну температуру. Спостерігається, поширення магнітозвукових солітонів у намагніченій щільній плазмі з квантовими ефектами вироджених електронів і дифракції Бома. Квантові або ефекти виродження стають актуальними в плазмі, коли температура Фермі і термодинамічна температура вироджених електронів мають однаковий порядок.

Ключові слова: магнітозвукова хвиля, квантова плазма, рівняння Кортевега-де Фріза (КдВ).

EAST EUROPEAN JOURNAL OF PHYSICS. 4. 189-196 (2021)
DOI: 10.26565/2312-4334-2021-4-25 ISSN 2312-4334

THERMOELECTRIC COEFFICIENTS OF HEAVILY DOPED N-TYPE SILICON†

Mulugeta Habte Gebru
Department of Physics, Arba Minch University, Arba Minch, Ethiopia
E-mail: mulugeta1970@gmail.com
Received April 27, 2021; revised December 14, 2021; accepted December 15, 2021

In this study the thermoelectric effect is investigated in terms of thermoelectric power, Figure of merit(ZT), and power factor. The calculations were carried out based on Boltzmann transport equation by taking ionized impurity scattering as a dominant mechanism for heavily doped n-type silicon at 300K with charge concentration varies from 2×10^{18} /cm^3 – 20×10^{20} /cm^3. It is known that doping of materials can induce Fermi level shifts and doping can also induce changes of the transport mechanisms. The result of this study shows doping also induces changes in thermoelectric power, Figure of merit, and power factor. The magnitude of the change is different for consideration of parabolic density of states and non-parabolic modified density of states which amounts to 16.7% for thermoelectric power, from 0.059% - 84.1% for Figure of merit(ZT) in favor of non-parabolic consideration respectively. There is also a difference of 39.9% for power factor with respect to relaxation time between the two cases in favor of the parabolic consideration.
Key words: doping, thermoelectric effect, thermoelectric power
PACS: 72.20.Pa

A semiconductor can be considered heavily doped when the impurity band associated with the doped impurity merges with either in the conduction and valence band. There are two aspects with direct influence on the carrier transport namely tailing of states into the band gap. It thus seems useful to determine theoretically the location of the Fermi level in heavily doped silicon taking into account the density of states in the tails [1-3]. According to [1], the density of state for heavily doped silicon is expressed in [4] as

$$\rho(z) = \frac{m_b^{*\frac{3}{2}} 2^{\frac{3}{4}} \delta^{\frac{1}{2}}}{\pi^2 \hbar^3} y(z) \tag{1}$$

whereas,

$$\rho(\mathrm{E}) = \frac{8\sqrt{2}\pi m_n^{*\frac{3}{2}}}{h^3} \mathrm{E}^{\frac{1}{2}} \tag{2}$$

represents the parabolic total density of states in the conduction band.

In Eq. (1) for non-parabolic modified density of states, the term y(z) is given by

$$\mathrm{y(z)} = \frac{1}{2}\int_{-\infty}^{z} (\mathrm{z}-\zeta)^{\frac{1}{2}} \exp(-\zeta^2) \mathrm{d}\zeta \tag{3}$$

and

$$\mathrm{z} = \frac{\mathrm{E}}{\sqrt{2}\delta} \tag{4}$$

The standard deviation of the Gaussian distribution for the impurity potential energy is

$$\delta = \left(\frac{n e^4 a_s}{8\pi\epsilon_0^2\epsilon_d^2}\right)^{\frac{1}{2}} = \left(\frac{N_d e^4 a_s}{8\pi\epsilon_0^2\epsilon_d^2}\right)^{\frac{1}{2}} \tag{5}$$

For a screened coulomb potential of impurity atoms with ϵ_d is the dielectric constant of the given semiconductor. The Thomas-Fermi screening length according to [5] is

$$a_s = \left(\frac{\pi^{\frac{4}{3}}\epsilon_0\epsilon_d\hbar^2}{3^{\frac{1}{3}}N_d^{\frac{1}{3}}e^2 m_n^*}\right)^{\frac{1}{2}} \tag{6}$$

The density of states function given by Eq. 1 is very complicated and thus is not useful for making any calculation. Slotboom [2] has however; suggested the following approximation for y(z).

$$\mathrm{y(z)} \cong \mathrm{z}^{\frac{1}{2}}\left[1 - \frac{1}{16z^2}\right] \tag{7}$$

† ***Cite as***: M.H. Gebru, East. Eur. J. Phys. **4**, 189 (2021), https://doi.org/10.26565/2312-4334-2021-4-25

for z > 0.601, equally, E > 0.85δ.
and

$$y(z) \cong \frac{1}{2\pi^{\frac{1}{2}}}\exp(-z^2)\{1.225 - 0.906[1 - \exp(2z)]\} \tag{8}$$

for z ≤ 0.601.

Using Eqs. (7) and (8) for y(z), we obtain the following expression of the electron concentration in the conduction band for modified density of states having band tails

$$n = 2\int f_0\,\rho(E)dE = \frac{m_n^{*\frac{3}{2}}2^{\frac{5}{4}}\delta^{\frac{3}{2}}}{\pi^2\hbar^3}\psi_0 \tag{9}$$

where ψ_0 is obtained by setting λ = 0 into

$$\psi_\lambda = \frac{1}{2\pi^{\frac{1}{2}}}\int_{-\infty}^{0.601}|z|^\lambda\exp(-z^2)\left(\frac{0.319+0.906\mathrm{Exp}(2z)}{1+\mathrm{Exp}\left\{1.494n_n^{\frac{5}{12}}z-\eta\right\}}\right)dz + \int_{0.601}^{\infty}\frac{z^{\frac{1}{2}}\left[1-\frac{1}{16z^2}\right]}{1+\exp\left\{1.494n_n^{\frac{5}{12}}z-\eta\right\}}dz \tag{10}$$

It is more convenient to introduce normalized electron concentration n_n given by

$$n_n = \frac{n}{10^{25}/m^3} \tag{11}$$

In this study the semi-classical and quantum treatments are applied in the calculations of scattering mechanisms under the assumptions of the electron concentrations from $2x10^{18}$ - $2x10^{20}/cm^3$ and in the temperature range 77 – 300K.

LINEARIZED BOLTZMANN EQUATION WITH RELATION TIME APPROXIMATION

All the quantities of interest to us may be expressed immediately in terms of Fermi-Dirac distribution f(**r**,**k**.t). The Boltzmann transport equation is therefore

$$\frac{\partial f}{\partial t} + \mathbf{v}.\boldsymbol{\nabla}f + \mathbf{F}.\boldsymbol{\nabla}_{\mathbf{k}}f = \left(\frac{\partial f}{\partial t}\right)_{\mathbf{c}} \tag{12}$$

Consider a time dependent but spatially homogenous situation in the absence of applied fields. Thus Eq. (12) becomes

$$\frac{\partial f}{\partial t} = \left(\frac{\partial f}{\partial t}\right)_c \tag{13}$$

where the term $\left(\frac{\partial f}{\partial t}\right)_c$ is expressed in terms of collision operator **C** as

$$\left(\frac{\partial f}{\partial t}\right)_c = \boldsymbol{C}\phi(\boldsymbol{r},\boldsymbol{k}) = \beta\int V(\boldsymbol{k}',\boldsymbol{k})[\phi(\boldsymbol{k}') - \phi(\boldsymbol{k})]d\boldsymbol{k} \tag{14}$$

for arbitrary function(ϕ) and potential(V). In the relaxation time approximation, we suppose that $\left(\frac{\partial f}{\partial t}\right)_c$ has the simplest form which will yield the behavior

$$\left(\frac{\partial f}{\partial t}\right)_c = -\frac{f(K)}{\tau} \tag{15}$$

Now for all mechanisms of interest to us, E is not much changed in a single event. For elastic scattering such as ionized impurity scattering this is strictly true, while for acoustic deformation potential scattering(through local band perturbation), it is only approximate. Actually in the cases for which τ is well defined, it is a function of E alone. Thus the relaxation time can be written as

$$\tau = \tau_0 E^\lambda \tag{16}$$

The value of the superscript λ depends on the scattering mechanism 3/2 for ionized mpurities and -1/2 for acoustic phonons. In the case of optical phonons the electron scattering is not elastic the relaxation time cannot be applied [6].

ELECTRON AND HEAT FLUX DENSITIES

In the steady state in a homogeneous system with electric E applied along the x-axis, in the absence of magnetic field, the distribution can be written as

$$f = f_0 + f' \tag{17}$$

which is the solution of

$$-\frac{e}{\hbar}\boldsymbol{E}'.\boldsymbol{\nabla}_{\mathbf{k}}f_0 = \left(\frac{\partial f'}{\partial t}\right)_{coll} \tag{18}$$

where f_0 is the thermal equilibrium distribution and f' is a first order perturbation given by

$$f' = v_x f_x + v_y f_y + v_z f_z \tag{19}$$

Furthermore,

$$v\left(-\frac{\partial f}{\partial E}\right) = -\frac{1}{\hbar}\frac{\partial f}{\partial k} \tag{20}$$

And Eq. (18) can be solved to find f_x for one-dimensional case using Eqs. (15), (19), and (20) to give

$$f_x = \tau e\left(\frac{\partial f_0}{\partial E}\right)E'_x \tag{21}$$

Since E'_x in Eq. (21) is the d.c. electric field along x-direction, and the x-component of the electric current density is given by

$$J_x = -\frac{2em_n^{*3}}{\hbar^3}\int v_x^2 f_x dv_x dv_y dv_z \tag{22}$$

Finally after transformation to spherical coordinates (v, θ, φ) for velocity components and making use of Eq. (21) for f_x , we get

$$J = -\frac{e^2 m_n^{*3} E' v_0^5}{6\pi^2\hbar^3}\int_0^\infty \tau(E)\frac{\partial f_0}{\partial E}\varepsilon^{\frac{3}{2}}d\varepsilon \tag{23}$$

where we make change of variable from v to $\varepsilon = E/k_BT$.

Thus for the case of parabolic density of states we obtain the following expression for the electrical conductivity

$$\sigma = \frac{2ne^2\tau_0}{m_n^*}\frac{\int_0^\infty \varepsilon^2 f_0 d\varepsilon}{\int_0^\infty \varepsilon^{\frac{1}{2}} f_0 d\varepsilon} = \frac{2ne^2\tau_0}{m_n^*}\frac{F_2}{F_{\frac{1}{2}}} \tag{24}$$

where $F_{1/2}$ and F_2 can obtained as family of the well known tabulated Fermi-integral by setting p equals to 3 and 4 respectively.

$$\int_0^\infty \frac{\varepsilon^p d\varepsilon}{1+\exp(\varepsilon-\eta)} \tag{25}$$

where $\eta = E_F/k_BT$ is normalized Fermi energy.

We can obtain similar expression for electrical conductivity for the case of non-parabolic modified density of states having band tails in Eq. (1) by inserting into Eq. (24) which gives

$$\sigma = \frac{2e^2 n\tau_0}{3m_n^*}\left(\frac{\sqrt{2}\delta}{k_BT}\right)^{\frac{5}{2}}\frac{\psi_{\frac{5}{2}}}{\psi_0} \tag{26}$$

where $\psi_{\frac{5}{2}}$ is obtained from Eq. (10) by setting $\lambda = 5/2$.

To obtain thermal current density, we use from[7,8]

$$Q_x = \frac{2m_n^{*3}}{h^3}\int\left(\frac{1}{2}m_n^* v^2\right)v_x f d^3v = \frac{-4\pi m_n^{*4}}{5\hbar^4}\int_0^\infty v^6 f_x dv \tag{27}$$

after integrating over spherical coordinates θ and φ.

In the presence of an external d.c. field E'_x and a temperature gradient dT/dx along the x-direction, the Boltzmann transport equation is written as

$$v_x\frac{\partial f_0}{\partial x} - \frac{eE'_x}{m_n^*}\frac{\partial f_0}{\partial v_x} = v_x\frac{\partial f_0}{\partial x} - \frac{eE'_x}{m_n^*}\frac{v_x}{v}\frac{\partial f_0}{\partial v} = -\frac{f-f_0}{\tau} = -\frac{v_x f_x}{\tau} \tag{28}$$

One can solve $\frac{\partial f_0}{\partial x}$ in Eq. (28) as

$$\frac{\partial f_0}{\partial x} = \frac{\partial f_0}{\partial T}\frac{\partial T}{\partial x}$$

$$= \left(-\frac{\partial f_0}{\partial E}\right)\left[\frac{E}{T} + k_B T\frac{\partial}{\partial T}\left(\frac{E_F}{k_BT}\right)\right]\left(\frac{dT}{dx}\right) \tag{29}$$

Inserting Eq. (29) into Eq. (28) and solving for f_x, we get

$$f_x = \tau \frac{dT}{dx}\frac{\partial f_0}{\partial E}\left[\frac{E}{T} + k_B T \frac{\partial}{\partial T}\left(\frac{E_F}{k_B T}\right)\right] + eE'_x \tau \frac{\partial f_0}{\partial E} \tag{30}$$

Substituting Eq. (30) into Eq. (23), J_x becomes

$$J_x = -\frac{em_n^{*3}}{3\pi^2\hbar^3}\int_0^\infty \tau v^4 \frac{\partial f_0}{\partial E}\left[\frac{E}{T} + k_B T \frac{\partial}{\partial T}\left(\frac{E_F}{k_B T}\right)\right]\left(\frac{dT}{dx}\right)dv - \frac{e^4 m_n^{*3} E'_x}{3\pi^2\hbar^3}\int_0^\infty \tau v^4 \frac{\partial f_0}{\partial E}dv \tag{31}$$

Since a small current flows, $J_x = 0$ is assumed for measured thermoelectric voltages(V), and we obtain the following relationship between E'$_x$ and dT/dx.

$$E'_x = -\left(\frac{dT}{dx}\right)\frac{\left[\int_0^\infty \tau v^4\left(-\frac{\partial f_0}{\partial E}\right)\frac{E}{T}dv + \int_0^\infty \tau v^4\left(-\frac{\partial f_0}{\partial E}\right)k_B T\frac{\partial}{\partial T}\left(\frac{E_F}{k_B T}\right)\right]dv}{e\int_0^\infty \tau v^4\left(-\frac{\partial f_0}{\partial E}\right)dv} \tag{32}$$

If there are no gradients of concentration, then the second term in numerator is cancelled. The Seebeck coefficient(α) referred to as the thermal emf or thermoelectric power [9] is given by

$$\alpha = \frac{dV}{dT} = -\frac{1}{eT}\frac{\int_0^\infty \tau v^4\left(-\frac{\partial f_0}{\partial \varepsilon}\right)\frac{E}{T}dv}{\int_0^\infty \tau v^4\left(-\frac{\partial f_0}{\partial E}\right)dv} = -\frac{1}{eT}\frac{\int_0^\infty E^4 f_0 dE}{\int_0^\infty E^3 f_0 dE} = -\frac{k_B}{e}\frac{\int_0^\infty \varepsilon^4 f_0 d\varepsilon}{\int_0^\infty \varepsilon^3 f_0 d\varepsilon} = -\frac{k_B}{e}\frac{F_4}{F_3} \tag{33}$$

According to [10] dimensionless figure-of-merit(ZT) for a material in terms of Seebeck coefficient(α) , electrical conductivity (σ), and the electronic thermal conductivity (K_e) is

$$ZT = \frac{\alpha^2\sigma T}{K_e} = \frac{\left(-\frac{k_B F_4}{e F_3}\right)^2\left(\frac{2ne^2\tau_0 F_2}{m_n^* F_{\frac{1}{2}}}\right)T}{\left(\frac{2n\tau_0(k_B T)^2}{m_n^* T}\left[\frac{10F_4}{3F_{\frac{1}{2}}} - \frac{32}{9}\frac{F_3^2}{F_{\frac{1}{2}}F_2}\right]\right)} = \frac{1}{T}\left[\frac{10}{3}\frac{F_3^2}{F_2F_4} - \frac{32}{9}\frac{F_3^4}{F_2^2F_4^2}\right]^{-1} \tag{34}$$

The power factor (P_{FF}) for the case of parabolic density of state is

$$P_{FF} = \alpha^2\sigma = \left(-\frac{k_B}{e}\frac{F_4}{F_3}\right)^2\left(\frac{2ne^2\tau_0}{m_n^*}\frac{F_2}{F_{\frac{1}{2}}}\right) = \frac{2nk_B^2\tau_0}{m_n^*}\frac{F_4^2F_2}{F_3^2F_{1/2}} \tag{35}$$

where F_3 and F_4 can obtained as family of the well known tabulated Fermi-integral by setting p equals to 3 and 4 respectively.

We can obtain expressions for α, ZT and P_{FF} for the case of modified density of states using the corresponding expressions, i.e., Eqs. (33-35) obtained based on standard model with parabolic density of states (which doesn't incorporate the effect of band tails) by substituting Eq. (1) for modified density of states and by extending the integration limits from -∞ to ∞. This yields the following expressions

$$\alpha = -\frac{\sqrt{2}\delta}{eT}\frac{\psi_{7/2}}{\psi_{5/2}} \tag{36}$$

and

$$ZT = \frac{\alpha^2\sigma T}{K_e} = \frac{\left(-\frac{\sqrt{2}\delta}{eT}\frac{\psi_{7/2}}{\psi_{5/2}}\right)^2\left(\frac{2e^2n\tau_0}{3m_n^*}\left(\frac{\sqrt{2}\delta}{k_B T}\right)^{\frac{5}{2}}\frac{\psi_{\frac{5}{2}}}{\psi_0}\right)}{\frac{2n\tau_0(k_B T)^2}{3m_n^* T}\left(\frac{\sqrt{2}\delta}{k_B T}\right)^{\frac{9}{2}}\left[\frac{\psi_{\frac{9}{2}}}{\psi_0} - \frac{\psi_{\frac{7}{2}}^2}{\psi_0\psi_{\frac{5}{2}}}\right]} = \frac{1}{T}\left[\frac{\psi_{\frac{5}{2}}\psi_{\frac{9}{2}}}{\psi_{\frac{7}{2}}^2} - 1\right]^{-1} \tag{37}$$

Finally

$$P_{FF} = \left(-\frac{\sqrt{2}\delta}{eT}\frac{\psi_{7/2}}{\psi_{5/2}}\right)^2\left(\frac{2e^2n\tau_0}{3m_n^*}\left(\frac{\sqrt{2}\delta}{k_B T}\right)^{\frac{5}{2}}\frac{\psi_{\frac{5}{2}}}{\psi_0}\right) = \frac{2n\tau_0\left(\frac{\sqrt{2}\delta}{T}\right)^{\frac{9}{2}}}{3m_n^* k_B^{\frac{5}{2}}}\frac{\psi_{7/2}^2}{\psi_{5/2}\psi_0} \tag{38}$$

where $\psi_{5/2}$, $\psi_{7/2}$, $\psi_{9/2}$ are obtained from Eq. (10) by setting λ = 5/2, 7/2, 9/2 respectively.

RESULTS

Thomas-Fermi screening length in Eq.(6) is calculated to be

$$a_s = 7.87X10^{-10} n_n^{-\frac{1}{6}}\, m \tag{39}$$

and the value of the Gaussian distribution for impurity potential energy is

$$\delta = 4.375\, X10^{-21} n_n^{\frac{5}{12}} J \tag{40}$$

Thus the electron concentration in the conduction band for modified density of states having band tails in Eq. (9) becomes

$$n = \frac{m_n^{*\frac{3}{2}} 2^{\frac{5}{4}}}{\pi^2\hbar^3} \frac{1}{2\pi^{\frac{1}{2}}} \int_{-\infty}^{0.601} \delta^{\frac{3}{2}} exp(-z^2) \left(\frac{0.319+0.906exp(2z)}{1+exp\left\{1.494 n_n^{\frac{5}{12}} z-\eta\right\}} \right) dz + \int_{0.601}^{\infty} \frac{\delta^{\frac{3}{2}} z^{\frac{1}{2}} \left[1-\frac{1}{16z^2}\right]}{1+exp\left\{1.49 n_b^{\frac{5}{12}} z-\eta\right\}} dz$$

$$= \frac{(1.18)^{\frac{3}{2}} X (9.11)^{\frac{3}{2}} X (10^{-31})^{\frac{3}{2}} X 2^{\frac{5}{4}} X (4.375)^{\frac{3}{2}} X (10^{-21})^{\frac{3}{2}} (0.3)^{\frac{5}{8}}}{\pi^2 X (1.054)^3 X 10^{-102}}$$

$$[\int_{-\infty}^{0.601} (0.28) exp(-z^2) \left(\frac{0.319+0.906exp(2z)}{1+exp\{1.494X0.603z-\eta\}} \right) dz + \int_{0.601}^{\infty} \frac{z^{\frac{1}{2}} \left[1-\frac{1}{16z^2}\right]}{1+exp\{1.49X0.603z-\eta\}} dz \,] = 3.2X10^{25}\text{X}$$

$$[\int_{-\infty}^{0.601} (0.28) exp(-z^2) \left(\frac{0.319+0.906exp(2z)}{1+exp\{0.9z-\eta\}} \right) dz + \int_{0.601}^{\infty} \frac{z^{\frac{1}{2}} \left[1-\frac{1}{16z^2}\right]}{1+exp\{0.9z-\eta\}} dz \,] \quad (41)$$

Thus

$$n_n = 3.2[\int_{-\infty}^{0.601} (0.28) exp(-z^2) \left(\frac{0.319+0.906exp(2z)}{1+exp\{0.9z-\eta\}} \right) dz + \int_{0.601}^{\infty} \frac{z^{\frac{1}{2}} \left[1-\frac{1}{16z^2}\right]}{1+exp\{0.9z-\eta\}} dz \,] \quad (42)$$

Similarly for parabolic density of states

$$\mathrm{n_n} = 3.2\mathrm{F}_{1/2}(\eta) \quad (43)$$

and the rest all integrals are evaluated by inserting them directly in the mathematical v.5 installed in the sun ultra 5 work station computer[11]. The above values of n_n and η obtained by an iterative method which was employed in the above simplified expressions to relate them for parabolic and modified density of states cases.
The table of values(in the Appendix part of Table 1 and 2), $F_{1/2}$ (-2.6) is evaluated as

$$\text{NIntegrate}\left[x^{1/2}/(1+\text{Exp}[x+2.6])\,/\right], \{x, 0, \infty\}$$

The result is $F_{1/2}$ (-2.6) = 0.0641614 and the corresponding normalized concentration is

$$n_n = 3.2\ F_{1/2}(-2.6) = 3.2*0{,}0641614 = 0.2048$$

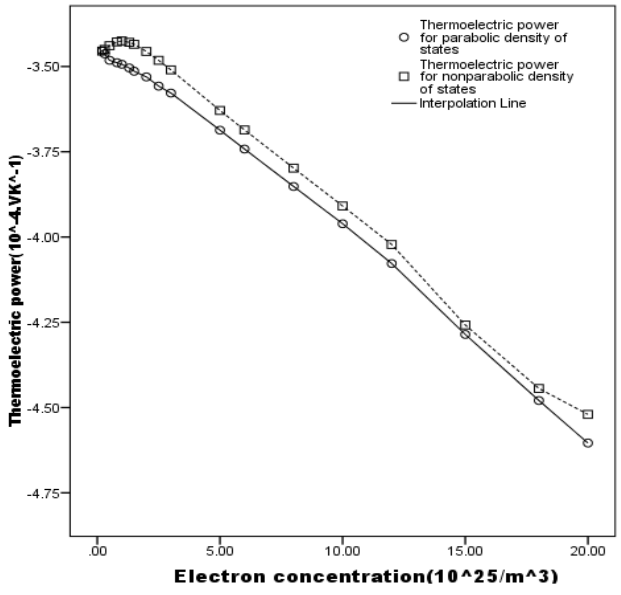

Figure 1. Thermoelectric power as a function of electron concentration with the solid line marked by circles is for parabolic band and dashed line marked by squares is for modified density of states.

Note that iterative method is not one shot process but it takes certain thoughtful steps to get the best value of η which gives to the nearest possible value of n_n = 0.2 that is η = -2.6. This procedure was followed to evaluate all values in the table including the corresponding values for F_3, and F_4 for parabolic case.

It is straightforward to use the same procedure for the case of modified density of states. In the same way as the previous case, in the table of values, n_n = 0.2 corresponds to η = -2.9. Mathematica software 5.0 is used to obtain 0.0333945 + 0.13557 = 0.16896 which was taken as the best approximation of n_n = 0.2 during the iterating method corresponding to η = -2.9. The same procedure was used for the other pair of values in the table. The values of the other integrals ψ_0 , $\psi_{\frac{5}{2}}$, $\psi_{\frac{7}{2}}$, $\psi_{\frac{9}{2}}$ (in Appendix part of Table 2) were evaluated straight forward(even copy and paste of expressions is possible that facilitates the process) by using mathematica v.5.

Graph in Figure 1 represents the dependence of thermoelectric power, defined as the voltage difference (ΔV) developed due to temperature difference (ΔT), as a function of electron concentration ranging 0.2 – 20×10^{25}/m^3 for two different cases. The quadratic equation fitting results are given by $y = -0.006x^2 + 0.06x - 3.584$ and with goodness of fit $R^2 = 0.987$ for parabolic case

whereas $y = -0.007x^2 + 0.072x - 3.577$ and with goodness of fit $R^2 = 0.99$ for non-parabolic case. When we compare the quadratic terms for each case the corresponding coefficients -0.007 and -0.006 differ by (-0.006 + 0.007)/0.006 = 16.7%, the coefficients of the linear terms differ by (0.072 -0.06)/0.06 = 16.7%, and the difference b/n the constant terms is negligible. Thus the values of the seebeck coefficient differ by 16.7% in favor of non-parabolic density of states consideration.

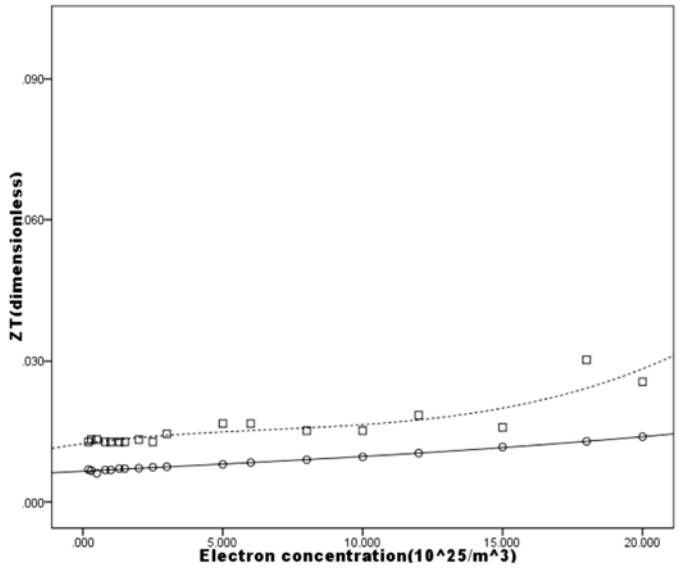

Figure 2. Merit(ZT) as a function of electron concentration with the solid line marked by circles is for parabolic band and dashed line marked by squares is for non-parabolic band consideration.

The graph for values of Figure of merit (ZT) for both parabolic and non-parabolic cases are presented in Figure 2. The cubic curve fitting was used with $R^2 = 0.994$ for parabolic case and $R^2 = 0.814$ for non-parabolic case. The maximum value of ZT for parabolic case is 0.0139 and for non-parabolic case it is 0.0256 corresponding to the maximum carrier concentration of $2 \times 10^{26}/m^3$. The minimum value of ZT for parabolic case is 0.0069 and for the non-parabolic case it is 0.0128 corresponding to the minimum carrier concentration of $2X10^{24}/m^3$. The difference in the values of ZT ranges up to 0.59% - 84.1% in favor of the non-parabolic consideration.

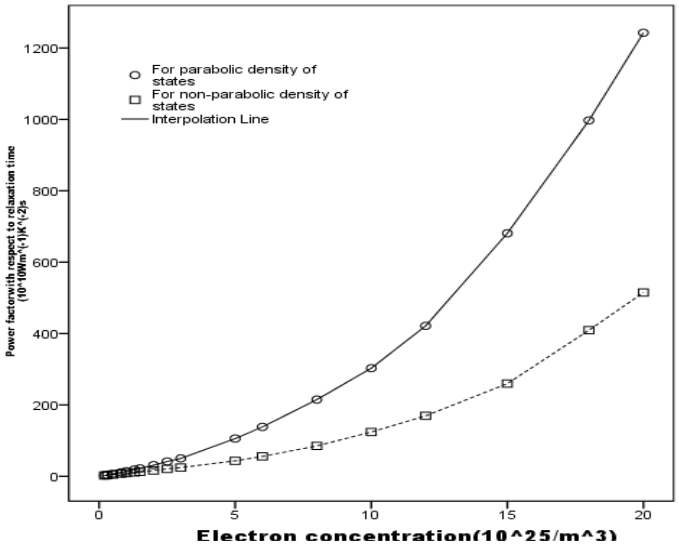

Figure 3. Power factor with respect to relaxation time plotted as a function of electron concentration

The power factor per relaxation time is plotted as shown in Figure 3. An exponential curve fitting is performed for the calculated data to obtain $y = 2.059e^{0.355x}$ and with goodness of fit $R^2 = 0.993$ for parabolic case while $y = 1.66e^{0.307x}$ and with goodness of fit $R^2 = 0.987$ is obtained for non-parabolic case. The two curves differ as shown by the respective exponential functions as the first is growing by a factor of 0.355 while the second is growing by a factor of 0.307 with a difference of .2% in favor of the non-parabolic consideration. On the other hand the amplitudes of the exponential functions are 2.059 for the first case and 1.66 for the second case which differ by 39.9% in favor of the parabolic consideration.

The results about calculations of Seebeck coefficient(α), Figure of merit(ZT), and Power factor with respect to relaxation time(P_{FF}/τ_0) for the parabolic and non-parabolic considerations do differ as much as 16.7%, from 0.059% to 84.1%, 39.9% respectively. The magnitude of the difference 16.7% is obtained in favor of parabolic density of states consideration as compared to non-parabolic density of states. It tells us as the carrier concentration increases with incorporation of more impurities the Seebeck coefficient changes significantly in both cases with respective difference of 16.7%. This is evident in the pattern of the calculated data fitted with a quadratic curve where the good-of-fit has a maximum value than other curves. When it comes to the Figure-of-merit(ZT) the maximum value of goodness-of-fit of the calculated data is obtained for cubic curve as shown in Figure 2. The comparison is made between the respective values of ZT at the minimum and maximum carrier concentration which gives the difference that ranges from 0.059% - 84.1% where the gap between the values in the two cases increases as the carrier concentration increases. The calculation of the power factor with respect to relaxation time is compared for the two cases with help of an exponential curve fitting which has a maximum value of goodness-of-fit than other fitted curves. Therefore the calculations for the two cases differ as much as 39.9% in favor of the parabolic density of states. This result reminds care should be taken in our calculation of thermoelectric coefficients for higher carrier concentrations where non-parabolic density of states consideration is preferable.

The experimental work by [12] reported that, despite limited information available about thermoelectric properties of single crystal silicon for higher doping concentration at higher temperature, they measured electrical conductivity, Seeback coefficient, and thermal conductivity to get calculated value of ZT as much as 0.015 for n-type silicon and 0.008 for p-type silicon in the heavily doping range(10^{18} – 10^{20}/cm^3) at temperature range from 300 – 1000K. In the current study the maximum value is 0.0256 slightly different by 1.06% from the experimental value for the non-parabolic density of consideration as it is closer than the parabolic consideration which differs as much as 12.4% from the experimental value. Thermoelectric devices provide cooling when an applied current pumps heat from the cold side towards the hot side through the Peltier effect, or enable waste heat recovery by converting a heat gradient to electrical power through the Seebeck effect[13]. As cited in [13], a good thermoelectric material should possess a large Seebeck coefficient, a high electrical conductivity, and low thermal conductivity to maximize the dimensionless Figure of merit for the thermoelectric performance of a material. Reducing the thermal conductivity is therefore a natural way to improve the performance(indicated by power factor and efficiency) of a thermoelectric material. [13] found that the thermal conductivity is strongly reduced due to nanostructuration and the incorporation of impurities.

CONCLUSION

The thermoelectric effect is investigated in terms of thermoelectric power, Figure of merit, and power factor which have primary importance in device application. There is considerable difference of 16.7% between calculated value of thermoelectric power based on the parabolic density of states and the modified density of states in favor of the latter case. The difference between Figure of merit values calculated for two cases ranges from 0.059% - 84.1%% in favor of the non-parabolic case. The same trend is expected for the electron concentration exceeding $2x10^{26}$/m^3. The calculated values of the power factor with respect to the relaxation time differ between the two case by 39.9% in favor of parabolic consideration. Laws of modern physics are used in the derivation of modified non-parabolic density of states to make corrections for parabolic density of states consideration as applied for heavily doped silicon, by doing so we get significant agreement with experimental results.

ORCID IDs

Mulugeta Habte Gebru, https://orcid.org/0000-0001-7341-2717

REFERENCES

[1] E.O. Kane, Phys. Rev. **131**, 79 (1963), https://doi.org/10.1103/PhysRev.131.79.
[2] J.W. Slotboom, Solid-state Electron. **20**, 279 (1977), https://doi.org/10.1016/0038-1101(77)90108-3
[3] C.J. Hwang, "Calculation of Fermi energy and band tail parameters in heavily doped and degenerate n-type GaAs", J. Appl. Phys. **41**, 2268-2674, (1970).
[4] M.H. Gebru, "Electrical and thermal conductivity of heavily doped n-type silicon", Eur. Phys. J. Appl. Phys. **90**, 10102 (2020), https://doi.org/10.1051/epjap/2020190332
[5] C. Kittel, *Introduction to solid state physics*, (John Wiley & Sons, Inc., New York, 1996).
[6] Cantarero A., Àlvarez F.X. in: *Thermoelectric Effects: Semiclassical and Quantum Approaches from the Boltzmann Transport Equation*, (Springer International Publishing, Switzerland, 2014), pp. 1-39, https://doi.org/10.1007/978-3-319-02012-9_1
[7] W.A. Harrison, *Solid State Theory*, (McGram-Hill Book Company, Inc. New York, 1976).
[8] F. Seiltz, *The Modern Theory of Solids*, (McGram-Hill book Company. Inc. New York, 1940).
[9] D.M. Rowe, *Thermoelectrics handbook: Macro-to-Nano*, (Taylor & Fracis Group, New York, 2006).
[10] H.W. Cong, American journal of modern physics, 4 (2018), https://doi.org/10.11648/j.ajmp.20180704.13
[11] Wolfram Research, Inc., Mathematica 5.0. 2008.
[12] Y. Ohishi, J. Xie, Y. Miyazaki, Y. Aikebaier, H. Muta, K. Kurosaki, S. Yamanaka, N. Uchida, and T. Tada, "Thermoelectric properties of heavily boron and phosphorus-doped silicon, Jpn. J. Appl. Phys. **54**, 071301 (2015). https://doi.org/10.7567/JJAP.54.071301
[13] T. Claudio, G. Schierning, R. Theissmann, H. Wiggers, H. Schober, M.M. Koza, and R.P. Hermann, J. Mater. Sci. **48**, 2836 (2013), https://doi.org/10.1007/s10853-012-6827-y

APPENDIX

Table 1. Calculated values for parabolic density of states

Serial No	n_n	η	$F_{1/2}$	F_2	F_3	F_4	$\alpha(\times10^{-4}$ VK$^{-1})$	ZT	$P_{FF}/\tau_0(10^{10}$W·m^{-1}·K^{-2}·s$^{-1})$
1	0.2	-2.6	0.064	0.147	0.444	1.778	-3.4539	0.0069	2.607564
2	0.3	-2.2	0.095	0.22	0.66	2.65	-3.4631	0.0067	3.964446
3	0.5	-1.7	0.15	0.37	1.08	4.36	-3.4819	0.0061	7.1154
4	0.8	-1.2	0.24	0.58	1.77	7.16	-3.489	0.0068	11.20056
5	1	-0.9	0.32	0.78	2.38	9.64	-3.4935	0.0068	14.15646
6	1.3	-0.6	0.41	1.03	3.19	12.96	-3.5041	0.0071	19.08449
7	1.5	-0.5	0.445	1.13	3.51	14.3	-3.5139	0.0071	22.38165
8	2	-0.1	0.626	1.65	5.17	21.163	-3.5306	0.0072	31.27236
9	2.5	0.2	0.781	2.16	6.87	28.337	-3.5576	0.0074	41.63925
10	3	0.4	0.94	2.583	8.288	34.38	-3.5778	0.0075	50.21136
11	5	1.2	1.56	5.105	17.214	73.58	-3.6867	0.008	105.8283
12	6	1.5	1.875	6.494	22.41	97.230	-3.7421	0.0084	138.4848
13	8	2	2.5	9.513	34.3	153.18	-3.8518	0.009	214.9205
14	10	2.4	3.125	12.68	47.5	218.15	-3.9611	0.0096	302.9532
15	12	2.8	3.75	16.65	65.06	307.59	-4.0777	0.0104	421.5715
16	15	3.4	4.688	24.35	101.6	504.83	-4.2856	0.0117	680.95
17	18	3.9	5.625	32.64	144.13	748.52	-4.4793	0.0129	997.218
18	20	4.2	6.25	38.5	176.12	940.14	-4.604	0.0139	1242.752

Table 2. Calculated values for modified density of states having band tails

Serial No	n_n	η	ψ_0	$\psi_{5/2}$	$\psi_{7/2}$	$\psi_{9/2}$	$\alpha(\times10^{-4}$ VK$^{-1})$	ZT	$P_{FF}/\tau_0(10^{10}$W·m^{-1}·K^{-2}·s$^{-1})$
1	0.2	-2.9	0.08	0..9627	5.047	33.1	-3.455	0.0128	2.32
2	0.3	-2.57	0.09	0.6821	3.015	16.7	-3.45	0.0133	3.35
3	0.5	-2.09	0.12	0.472	1.6809	7.5	-3.439	0.0133	4.9
4	0.8	-1.69	0.14	0.3227	0.9416	3.46	-3.428	0.0128	7.44
5	1	-1.5	0.15	0.2681	0.7124	2.38	-3.425	0.0128	9.09
6	1.3	-1.28	0.17	0.2167	0.5167	1.55	-3.429	0.0128	11.1
7	1.5	-1.15	0.18	0.1933	0.4351	1.23	-3.435	0.0128	12.57
8	2	-0.89	0.2	0.1533	0.3079	0.77	-3.456	0.0133	16.3
9	2.5	-0.68	0.21	0.1287	0.2373	0.55	-3.482	0.0128	20.87
10	3	-0.49	0.23	0.1125	0.1938	0.41	-3.51	0.0145	24.57
11	5	0.1	0.28	0.0803	0.1156	0.20	-3.629	0.0167	43.4
12	6	0.34	0.3	0.0726	0.0984	0.16	-3.686	0.0167	55.94
13	8	0.77	0.33	0.0642	0.0795	0.12	-3.798	0.0152	85.28
14	10	1.16	0.36	0.0606	0.0704	0.1	-3.909	0.0152	124.18
15	12	1.52	0.39	0.0592	0.0656	0.086	-4.022	0.0185	169.64
16	15	2.0	0.42	0.058	0.062	0.08	-4.258	0.0159	259.83
17	18	2.46	0.45	0.059	0.061	0.07	-4.444	0.0303	409.6
18	20	2.74	0.47	0.0604	0.0608	0.069	-4.520	0.0256	514.98

ТЕРМОЕЛЕКТРИЧНІ КОЕФІЦІЄНТИ СИЛЬНО ЛЕГОВАНОГО КРЕМНІЮ N-ТИПУ

Мулугета Хабте Гебру
Фізичний факультет Університету Арба Мінч, Арба Мінч, Ефіопія

Досліджено термоелектричний ефект з точки зору термоелектричної потужності, добротності (ZT) і коефіцієнта потужності. Розрахунки проводили на основі рівняння переносу Больцмана, взявши іонізоване розсіювання домішок як домінуючий механізм для сильно легованого кремнію n-типу при 300 К з концентрацією заряду від 2×10^{18}/см^3 – 20×10^{20}/см^3. Відомо, що легування матеріалів може викликати зміщення рівня Фермі, а легування також може викликати зміни транспортних механізмів. Результати цього дослідження показують, що легування також викликає зміни термоелектричної потужності, добротності та коефіцієнта потужності. Величина зміни різна для врахування параболічної щільності станів і непараболічної модифікованої щільності станів, яка становить 16,7% для термоелектричної енергії, від 0,059% - 84,1% для показника якості (ZT) на користь непараболічної відповідно. Існує також різниця в 39,9% для коефіцієнта потужності щодо часу релаксації між двома випадками на користь параболічного розгляду.

Ключові слова: легування, термоелектричний ефект, термоелектрична енергія

INSTRUCTIONS FOR PREPARING MANUSCRIPT IN THE EAST EUROPEAN JOURNAL OF PHYSICS

Nikita F. Author[a,*], Peter V. Co-Author(s)[b,†]
[a]*Affiliation of first author*
[b]*Affiliation of second author (if different from the first Author)*
**Corresponding Author: corresponding_authors@mail.com, [a]ORCID ID*
[†]*E-mail: co_authors@mail.com, [b]ORCID ID*
Received December 25, 2021; revised January 25, 2022 accepted February 5, 2022

Each paper must begin with an abstract. The abstract should be typed in the same manner as the body text (see below). Please note that these Instructions are typed just like the manuscripts should be. The abstract must have at least **1800 phonetic symbols (about 250-300 words)**, supplying general information about the achievements, and objectives of the paper, experimental technique, methods applied, significant results and conclusions. Page layout: the text should be printed on the paper **A4** format, at least **5 pages**, with margins of: **Top - 3, Bottom, Left and Right - 2 cm**. The abstract, keywords should be presented **in English** (only for foreign authors), **and Ukrainian**.
Keywords: there, must, be, 5-10 keywords
PACS: specify PACS code(s) here

This is **Introduction** section. This paper contains instructions for preparing the manuscripts. The text should be prepared in "**doc" or "docx"** format.

INSTRUCTIONS

The text should be typed as follows:

- **title**: Times New Roman, 12 pt, ALL CAPS, bold, 1 spacing, centred;
- **authors**: name, initials and family names; Times New Roman, 12 pt, bold, 1 spacing, centred;
- **affiliation(s)**: Times New Roman, 9 pt, italic, 1 spacing, centred;
- **abstract**: Times New Roman, 9 pt, 1 spacing, justified;
- **body text**: Times New Roman, 10 pt, 1 spacing, justified; paragraphs in sections should be indented right (tabulated) for 0.75 cm;
- **section titles**: Times New Roman, 10 pt, bold, 1 spacing, centred, without numbering, one line should be left, blank above section title;
- **subsection titles**: Times New Roman, 10 pt, bold, 1 spacing, centred, without numbering in accordance to the section (see below), one line should be left blank above subsection title;
- **figure captions**: width of the figure should be 85 or 170 mm, Figures should be numbered (**Figure 1**.) and titled below Figures using sentence format, Times New Roman, 9 pt, 1 spacing, centred (if one line) or justified (if more than one line); one line should be left blank below figure captions;
- **table captions**: width of the table should be 85 or 170 mm, tables should be numbered (**Table 1.**) and titled above tables using sentence format, Times New Roman, 10 pt, 1 spacing, justified, Tables should be formatted with a single-line box around the outside border and single ruling lines between rows and columns; one line should be left blank below tables;
- **equations**: place equations centred, numbered in Arabic: (1), the number is aligned to the right; equations should be specially prepared in **MathType** or "**Microsoft Equation"**, Times New Roman, 10 pt, one line should be left blank below and above equation.

Additional instructions

Numerated figures and tables should be embedded in your text and placed after they are cited. Only sharp photographs and drawings are acceptable. Letters in the figures should be 3 mm high. The figures should be presented in one of the following graphic formats: jpg, gif, pcx, bmp, tif.

REFERENCES

List of References must contain **at least 50% of articles published over the past 5 years** and **no more than 20% of links to their own work**. Cite References by number in AIP style (https://aip.scitation.org/php/authors/manuscript). Numbering in the order of referring in the text, e.g. [1], [2-5], etc. References should be listed in numerical order of citation in the text at the end of the paper (justified), Times New Roman, 9 pt, 1 spacing:

Journal Articles

[1] T. Mikolajick, C. Dehm, W. Hartner, I. Kasko, M.J. Kastner, N. Nagel, M. Moert, and C. Mazure, Microelectron. Reliab. **41**, 947 (2001), https://doi.org/10.1016/S0026-2714(01)00049-X.

[2] S. Bushkova, B.K. Ostafiychuk, and O.V. Copaiev, Physics and Chemistry of Solid State. **15**(1), 182 (2014), http://page.if.ua/uploads/pcss/vol15/!1501-27.pdf. (in Ukrainian)

[3] M. Yoshimura, E. Nakai, K. Tomioka, and T. Fukui, Appl. Phys. Lett. **103**, 243111 (2013), http://dx.doi.org/10.7567/APEX.6.052301.

E-print Resourses with Collaboration Research or Preprint

[4] M. Aaboud et al. (ATLAS Collaboration), Eur. Phys. J. C, **77**, 531 (2017), http://dx.doi.org/10.1140/epjc/s10052-017-5061-9

[5] Sjöstrand et al., *Comput. Phys. Commun.* **191,** 159 (2015), https://doi.org/10.1016/j.cpc.2015.01.024.

[6] Boudreau, C. Escobar, J. Mueller, K. Sapp, and J. Su, (2013), http://arxiv.org/abs/1304.5639.

Books

[7] S. Inoue, and K.R. Spring, *Video Microscopy*: *The fundamentals*, 2nd ed. (Plenum, New York, 1997), pp. 19-24.

[8] I. Gonsky, T.P. Maksymchuk, and M.I. Kalinsky, *Біохімія Людини [Biochemistry of Man]*, (Ukrmedknyga, Ternopil, 2002), pp. 16. (in Ukrainian)

Edited Books

[9] Z.C. Feng, editor, *Handbook of Zinc Oxide and Related Materials: Devices and Nano Engineering, vol. 2*, (CRC Press/Taylor & Francis, Boca Raton, FL, 2012)

Book Chapters

[10] P. Blaha, K. Schwarz, G.K.H. Madsen, D. Kvasnicka, and J. Luitz, in: *WIEN2K, An Augmented Plane Wave Plus Local Orbitals Program for Calculating Crystal Properties*, edited by K. Schwarz (Techn. Universität Wien, Austria, 2001).

[11] M. Gonzalez-Leal, P. Krecmer, J. Prokop, and S.R. Elliot, in: *Photo-Induced Metastability in Amorphous Semiconductors*, edited by A.V. Kolobov (Wiley-VCH, Weinheim, 2003), pp. 338-340.

[12] A. Kochelap, and S.I. Pekar, in: *Теория Спонтанной и Стимулированной Хемилюминесценции Газов [Theory of Spontaneous and Stimulated Gas Chemiluminescence]* (Naukova dumka, Kyiv, 1986), pp. 16-29. (in Russian)

Conference or Symposium Proceedings

[13] C. Yaakov, and R. Huque, in: *Second International Telecommunications Energy Symposium Proceedings*, edited by E. Yow (IEEE, New York, 1996), pp. 17-27.

[14] V. Nikolsky, A.K. Sandler, and M.S. Stetsenko, in: *Автоматика-2004: Матеріали 11 Міжнародної Конференції по Автоматичному Управлінню [Automation-2004: Materials of the 11th International Conference on Automated Management]* (NUHT, Kyiv, 2004), pp. 46-48. (in Ukrainian)

Patent

[15] I.M. Vikulin, V.I. Irha, and M.I. Panfilov, Patent Ukraine No. 26020 (27 August 2007). (in Ukrainian)

Thesis / Dissertation

[16] R.E. Teodorescu, Ph.D. dissertation, The George Washington University, 2009.

Special Notes

1. Use International System of Units (SI system). 2. It is undesirable to use acronyms in the titles. Please define the acronym on its first use in the paper. 3. Refer to isotopes as ^{14}C, ^{3}H, ^{60}Co, etc.

Наукове видання

СХІДНО-ЄВРОПЕЙСЬКИЙ ФІЗИЧНИЙ ЖУРНАЛ

Номер 4, 2021

EAST EUROPEAN JOURNAL OF PHYSICS

No 4, 2021

Збірник наукових праць
англійською та українською мовами

Коректор – Коваленко Т.О.
Технічний редактор – Гірник С.А.
Комп'ютерне верстання – Гірник С.А.

Підписано до друку 29.11.2021. Формат 60×84/8. Папір офсетний.
Друк цифровий.
Ум. друк. арк. 16,1. Обл.-вид. арк. 16,5
Тираж 50 пр. Зам. № . Ціна договірна

Видавець і виготовлювач
Харківський національний університет імені В.Н. Каразіна
61022, Харків, майдан Свободи, 4
Свідоцтво суб'єкта видавничої справи ДК № 3367 від 13.01.09

Видавництво Харківський національний університет імені В.Н. Каразіна
тел. +380-057-705-24-32